WOODHEAD PUBLISHING IN MATERIALS

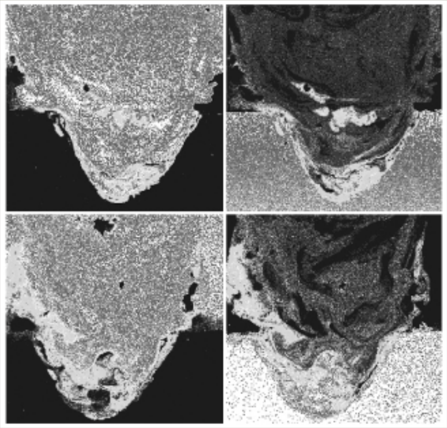

Welding and joining of magnesium alloys

Edited by Liming Liu

WP
WOODHEAD
PUBLISHING

Welding and joining of magnesium alloys

Related titles:

Failure mechanisms of advanced welding processes
(ISBN 978-1-84569-536-1)
Many new, or relatively new, welding processes such as friction stir welding, resistance spot welding and laser welding are being increasingly adopted by companies to replace or improve on traditional welding techniques. Improvements in welding speed and ease of automation are often used as reasons for choosing advanced welding processes. Before advanced techniques are employed, their potential failure mechanisms should be well understood and their suitability for welding particular metals and alloys in different situations should be assessed. This important book will provide a critical analysis of advanced welding techniques and their potential failure mechanisms.

Materials, design and manufacturing for lightweight vehicles
(ISBN 978-1-84569-463-0)
Research programs into the manufacture of lightweight automobiles have led to the consideration of a variety of materials, such as high strength steels, aluminium alloys, magnesium alloys, plastics and composites. This research is driven by a need to reduce fuel consumption to preserve dwindling hydrocarbon resources without compromising other attributes such as safety, performance, recyclability and cost. This important book will make it easier for engineers to not only learn about the materials being considered for lightweight automobiles, but also to compare their characteristics and properties. It also covers issues such as crashworthiness and recycling.

The welding of aluminium and its alloys
(ISBN 978-1-85573-567-5)
The welding of aluminium and its alloys is a practical user's guide to all aspects of welding aluminium and aluminium alloys, giving a basic understanding of the metallurgical principles involved. The book is intended to provide engineers with perhaps little prior acquaintance with the welding processes involved, a concise and effective reference to the subject. It covers weldability of aluminium alloys, process descriptions, advantages, limitations, proposed weld parameters, health and safety issues, preparation for welding, quality assurance and quality control issues. It is essential reading for welding engineers, production engineers, production managers, designers and supervisors involved in the aluminium fabrication industry.

Details of these and other Woodhead Publishing materials books can be obtained by:

- visiting our web site at www.woodheadpublishing.com
- contacting Customer Services (e-mail: sales@woodheadpublishing.com; fax: +44 (0) 1223 893694; tel.: +44 (0) 1223 891358 ext. 130; address: Woodhead Publishing Limited, Abington Hall, Granta Park, Great Abington, Cambridge CB21 6AH, UK)

If you would like to receive information on forthcoming titles, please send your address details to: Francis Dodds (address, telephone and fax as above; e-mail: francis.dodds@woodheadpublishing.com). Please confirm which subject areas you are interested in.

Welding and joining of magnesium alloys

Edited by
Liming Liu

WOODHEAD
PUBLISHING

Oxford Cambridge Philadelphia New Delhi

Published by Woodhead Publishing Limited, Abington Hall, Granta Park, Great Abington, Cambridge CB21 6AH, UK
www.woodheadpublishing.com

Woodhead Publishing, 525 South 4th Street #241, Philadelphia, PA 19147, USA

Woodhead Publishing India Private Limited, G-2, Vardaan House, 7/28 Ansari Road, Daryaganj, New Delhi – 110002, India
www.woodheadpublishingindia.com

First published 2010, Woodhead Publishing Limited
© Woodhead Publishing Limited, 2010
The authors have asserted their moral rights.

This book contains information obtained from authentic and highly regarded sources. Reprinted material is quoted with permission, and sources are indicated. Reasonable efforts have been made to publish reliable data and information, but the authors and the publisher cannot assume responsibility for the validity of all materials. Neither the authors nor the publisher, nor anyone else associated with this publication, shall be liable for any loss, damage or liability directly or indirectly caused or alleged to be caused by this book.

Neither this book nor any part may be reproduced or transmitted in any form or by any means, electronic or mechanical, including photocopying, microfilming and recording, or by any information storage or retrieval system, without permission in writing from Woodhead Publishing Limited.

The consent of Woodhead Publishing Limited does not extend to copying for general distribution, for promotion, for creating new works, or for resale. Specific permission must be obtained in writing from Woodhead Publishing Limited for such copying.

Trademark notice: Product or corporate names may be trademarks or registered trademarks, and are used only for identification and explanation, without intent to infringe.

British Library Cataloguing in Publication Data
A catalogue record for this book is available from the British Library.

Library of Congress Cataloging in Publication Data
A catalog record for this book is available from the Library of Congress.

ISBN 978-1-84569-692-4 (print)
ISBN 978-0-85709-042-3 (online)

The publisher's policy is to use permanent paper from mills that operate a sustainable forestry policy, and which has been manufactured from pulp which is processed using acid-free and elemental chlorine-free practices. Furthermore, the publisher ensures that the text paper and cover board used have met acceptable environmental accreditation standards.

Typeset by RefineCatch Limited, Bungay, Suffolk
Printed by TJI Digital, Padstow, Cornwall, UK

Contents

Contributor contact details *xi*

Part I General **1**

1 Introduction to the welding and joining of magnesium 3
L. LIU, Dalian University of Technology, China

1.1 Background 3
1.2 Characteristics of magnesium alloy welded joints under dynamic load 4
1.3 Efficient gas metal arc welding of magnesium alloys 5
1.4 Dissimilar welding of magnesium alloys to other metals 6
1.5 References 7

2 Welding metallurgy of magnesium alloys 9
L. LIU, Dalian University of Technology, China

2.1 Introduction 9
2.2 Weldability of magnesium alloys 10
2.3 Weldability of magnesium alloys to other metals 12
2.4 References 14

3 Preparation for welding of magnesium alloys 16
L. LIU, Dalian University of Technology, China

3.1 Introduction 16
3.2 Surface treatment of magnesium alloys 16
3.3 Welding groove for magnesium alloys 18
3.4 Preheating and postweld treatments for magnesium alloys 20
3.5 References 22

4 Welding materials for magnesium alloys 23
L. Liu, Dalian University of Technology, China

4.1 Introduction 23
4.2 Hot extrusion process of welding materials 27
4.3 Component design of welding materials 32
4.4 Hot pull process of welding materials 34
4.5 Microstructure and strength of welding materials 35
4.6 References 36

5 Welding and joining of magnesium alloys to aluminum alloys 38
L. Liu, Dalian University of Technology, China

5.1 Introduction 38
5.2 Hybrid laser-tungsten inert gas welding of magnesium and aluminum 39
5.3 Diffusion bonding magnesium to aluminum technology 44
5.4 Laser weld bonding magnesium to aluminum technology 49
5.5 Conclusion and future trends 60
5.6 References 61

6 The joining of magnesium alloy to steel 63
L. Liu, Dalian University of Technology, China

6.1 Introduction 63
6.2 Existing problems in the joining of magnesium alloys to steel 64
6.3 Welding principles for the joining of magnesium alloys to steel 66
6.4 Direct joining of magnesium alloys to mild steel 69
6.5 Nickel-added joining of magnesium alloys to steel 74
6.6 Conclusion and future trends 77
6.7 References 77

7 Corrosion and protection of magnesium alloy welds 79
L. Liu, Dalian University of Technology, China

7.1 Introduction 79
7.2 Corrosion characteristics of magnesium alloy weldment 80
7.3 Improvement in the corrosion resistance of magnesium alloy weldment 86
7.4 Conclusion and future trends 92
7.5 References 93

Part II Particular welding and joining techniques 95

8 Brazing and soldering of magnesium alloys 97
T. Watanabe, Niigata University, Japan

8.1 Surface preparation of magnesium alloys before joining 97
8.2 Brazing of magnesium alloys using flux and filler metal 103
8.3 Ultrasonic brazing of magnesium alloys with no flux 112
8.4 Soldering of magnesium alloys 117
8.5 References 120

9 Mechanical joining of magnesium alloys 122
M. Heger, Böllhoff, Germany and M. Horstmann,
Hella KGaA Hueck & Co., Germany

9.1 Introduction 122
9.2 Technologies with pre-punching operation and one-sided accessibility 123
9.3 Technologies with pre-punching operation and two-sided accessibility 130
9.4 Technologies without pre-punching operation and one-sided accessibility 133
9.5 Technologies without pre-punching operation and two-sided accessibility 138
9.6 Linear technology: hemming 145
9.7 References 147

10 Adhesive bonding of magnesium alloys 149
L. Liu, Dalian University of Technology, China

10.1 Introduction 149
10.2 Surface treatments of magnesium alloys 149
10.3 Adhesive for the bonding of magnesium alloys 154
10.4 Cure for the bonding of magnesium alloys 154
10.5 Applications of the bonding of magnesium alloys 154
10.6 Future trends 158
10.7 References 158

11 Gas-tungsten arc welding of magnesium alloys 160
L. Liu, Dalian University of Technology, China

11.1 Introduction 160
11.2 Gas-tungsten arc welding of magnesium alloys without filling wire 161
11.3 Gas-tungsten arc filler welding of magnesium alloys 168
11.4 References 175

12 Metal inert gas welding of magnesium alloys 178
G. Song, Dalian University of Technology, China

12.1 Introduction 178
12.2 Pulsed metal inert gas welding for magnesium alloys 179
12.3 Alternating current metal inert gas welding for magnesium alloys 185
12.4 Conclusion and future trends 194
12.5 References 194

13 Variable polarity plasma arc welding of magnesium alloys 197
Z.D. Zhang, Dalian University of Technology, China

13.1 Introduction 197
13.2 Variable polarity plasma arc welding of magnesium alloys 199
13.3 Variable polarity plasma arc weld bonding of magnesium alloys 211
13.4 Conclusion and future trends 226
13.5 References 227

14 Hybrid laser-arc welding of magnesium alloys 229
G. Song, Dalian University of Technology, China

14.1 Introduction 229
14.2 Low-power laser/arc hybrid welding of magnesium 230
14.3 Hybrid welding process with filler metal 244
14.4 Practical application 250
14.5 Conclusion and future trends 251
14.6 References 251

15 Activating flux tungsten inert gas welding of magnesium alloys 253
Z.D. Zhang, Dalian University of Technology, China

15.1 Introduction 253
15.2 Welding mechanism 254
15.3 Welding parameters 258
15.4 Microstructure of welding joints 267
15.5 Mechanical properties 271
15.6 Future trends 272
15.7 References 272

16 Friction stir welding of magnesium alloys 274
H. Zhang, University of Science and Technology, Beijing, China

16.1 Introduction 274
16.2 Welding parameters and procedures 276
16.3 Welding tools and equipment 280

16.4 Materials that have been or are being friction stir welded 282
16.5 Typical microstructures of friction stir welded magnesium alloys 282
16.6 Properties of friction stir welded magnesium alloys 289
16.7 Weld defects of friction stir welded magnesium alloys 295
16.8 Applications of friction stir welded magnesium alloys 300
16.9 Future trends and sources of further information and advice 301
16.10 Acknowledgements 301
16.11 References 301

17 Laser welding of magnesium alloys 306
J. SHAN, Tsinghua University, China

17.1 Introduction 306
17.2 Character of the laser welding process and influence of laser welding parameters 307
17.3 Laser welding of magnesium alloys 318
17.4 Microstructure and properties of laser welding of magnesium alloys 322
17.5 Typical defects of laser welding of magnesium alloys 332
17.6 Outlook and future trends 346
17.7 References 347

18 Resistance spot welding of magnesium alloys 351
L. LIU, University of Waterloo, Canada, J. FENG, Harbin Institute of Technology, China and Y. ZHOU, University of Waterloo, Canada

18.1 Introduction 351
18.2 Fundamentals of resistance spot welding 351
18.3 Welding conditions: surface 354
18.4 Welding conditions: welding parameters 358
18.5 Nugget growth and microstructure 359
18.6 Welding of magnesium alloys to other alloys 362
18.7 Equipment for the welding of magnesium alloys 363
18.8 Future trends 364
18.9 References 365

19 Electromagnetic pulse welding of magnesium to aluminium sheets 367
S. KORE, Indian Institute of Technology, Guwahati, India and J. IMBERT, Y. ZHOU and M. WORSWICK, University of Waterloo, Canada

19.1 Introduction 367
19.2 Fundamental theory of electromagnetic welding 368
19.3 Equipment for electromagnetic welding 369
19.4 Welding technique and materials 372
19.5 Mechanical and metallurgical testing of welds 374

19.6 Safety guidelines while handling the electromagnetic welding setup 377
19.7 References 378

Index *380*

Contributor contact details

(* = main contact)

Chapters 1–7, 10, 11

Liming Liu
School of Material Science and Engineering
Dalian University of Technology
Key Laboratory of Liaoning Advanced Welding and Joining Technology
2 Linggong Road
Dalian City 116024
Liaoning Province
China
Email: liulm@dlut.edu.cn

Chapter 8

Takehiko Watanabe
Graduate School of Science and Technology
Faculty of Engineering
Niigata University
Ikarashi 2-nocho 8050
Niigata
Japan
Email: twatanab@eng.niigata-u.ac.jp

Chapter 9

Mathias Heger
Böllhoff Automation GmbH
Archimedesstrasse 1–4
33649 Bielefeld
Germany
Email: MHeger@boellhoff.com

And

M. Horstmann
Hella KGaA Hueck & Co.
Beckumer Strasse 130
59552 Lippstadt
Germany
Email: magnus.horstmann@hella.com

Chapter 12

Gang Song
School of Material Science and Engineering
Dalian University of Technology
Key Laboratory of Liaoning Advanced Welding and Joining Technology
2 Linggong Road
Dalian City 116024
Liaoning Province
China
Email: songgang@dlut.edu.cn

Chapter 13

Zhao Dong Zhang
School of Material Science and Engineering
Dalian University of Technology
Key Laboratory of Liaoning Advanced Welding and Joining Technology
2 Linggong Road
Dalian City 116024
Liaoning Province
China
Email: skyezzd@dlut.edu.cn

Chapter 14

Gang Song
School of Material Science and Engineering
Dalian University of Technology
Key Laboratory of Liaoning Advanced Welding and Joining Technology
2 Linggong Road
Dalian City 116024
Liaoning Province
China
Email: songgang@dlut.edu.cn

Chapter 15

Zhao Dong Zhang
School of Material Science and Engineering
Dalian University of Technology
Key Laboratory of Liaoning Advanced Welding and Joining Technology
2 Linggong Road
Dalian City 116024
Liaoning Province
China
Email: skyezzd@dlut.edu.cn

Chapter 16

Hua Zhang
School of Materials Science and Engineering
University of Science and Technology, Beijing
Xue Yuan Road 30
Beijing 100083
China
Email: zhhwhq@163.com

Chapter 17

Jiguo Shan
Department of Mechanical Engineering
Tsinghua University
Beijing 100084
China

and

Key Laboratory for Advanced Materials Processing Technology
Ministry of Education
Beijing 100084
China
Email: shanjg@mail.tsinghua.edu.cn

Chapter 18

Lei Liu
Centre for Advanced Materials Joining
University of Waterloo
Canada

and

J. Feng
State Key Laboratory of Advanced Welding Production Technology
Harbin Institute of Technology
China

and

Norman Y. Zhou*
Centre for Advanced Materials Joining
University of Waterloo
Canada
Email: nzhou@mecheng1.uwaterloo.ca

Chapter 19

Sachin Kore*
Department of Mechanical Engineering
Indian Institute of Technology Guwahati
North Guwahati
Guwahati 781039
Assam
India
Email: sdk@iitg.ac.in

Part I

General

1

Introduction to the welding and joining of magnesium

L. LIU, Dalian University of Technology, China

Abstract: As the lightest structural metal, the welding and joining of magnesium alloy has been studied with different methods. In this chapter, the background is introduced, and the main problems in the welding and joining of magnesium alloy are presented. The characteristics of Mg alloy welded joints under dynamic load, efficient gas metal arc welding of Mg alloys and dissimilar welding of Mg alloy to other metals are introduced.

Key words: welding and joining, magnesium alloy, dynamic load, dissimilar welding, welding efficiency.

1.1 Background

Magnesium, ranking eighth in the earth, is one of the most widely distributed elements and exists extensively in seawater and salt lakes. Magnesium alloy can be reused and recycled as an inexhaustible metal. As the lightest structural metal, it has many advantages, such as high specific strength and rigidity, high heat and electrical conductivity, which are close to those of aluminium (Al) alloys but much higher than engineering plastics, realizing the goal of lightening, energy saving and consumption reduction. Its characteristics, such as anti-knocking, anti-noise high conductivity, electromagnetic shielding and nontoxicity, make it of great potential in mechanical field, marine scope and aviation application, etc.[1,2] Due to the demands for energy saving and environment protection, magnesium is praised as a green engineering material and one of the most promising material categories in the twenty-first century. Relevant investigations and applications on magnesium alloys are in progress.

Because of the wide application of magnesium alloys, it is necessary to obtain a reliable joining process. Magnesium alloy components are joined by a variety of welding and joining methods including tungsten-arc inert gas (TIG), metal-arc inert gas (MAG), plasma *h* arc, electron beam, laser, friction and adhesive, besides friction stir explosion, stud, ultrasonic, spot welding and so on. For gas tungsten-arc filler welding processes of Mg alloys, many disadvantages appear, such as low welding speed, wide heat-affected zone (HAZ), high welding stress and significant evaporation; the tensile strength of the weld joint can reach 80–90% of the base metal by adjusting the welding parameters. This method can be applied in fixing casting defects and in lower demand fields.[3] High-energy beam welding methods, including laser, plasma *h* arc and electron beam, have characteristics such as high energy density, low power input and rapid cooling rate, which result in deep penetration, small HAZ and fine microstructures. With optimized parameters, fine welds can be achieved with no crack, no pores and satisfactory appearance, most of which have obtained tensile strengths close to the base metals.[4] Owing to beneficial interaction of the laser and arc, the combination of laser with TIG, called hybrid laser-TIG welding technique, can enhance the welding penetration, welding speed and quality of the weld, which makes this method fit for high-quality welding of Mg alloys.[5] Friction stir welding is also being focused upon and developed in the past few years, especially applied to the field of light alloy welding. The friction stir weld of Mg alloy has a high tensile strength, resulting from the less quadratic phase separation in the cooling process with a lower stirring temperature.[6] Finally, the other welding methods, such as adhesive, weld bonding, brazing, explosion and spot welding, have individual characters and advantages, which lead to their own application prospects of welding and joining of Mg alloys.

Although some progress was made in the last few years, several problems are still awaiting urgent solution in the welding process of Mg alloy, mainly present as increasing the fatigue strength of welded joint, developing efficient consumable electrode welding, dissimilar welding of Mg alloy to other metals and so on.

1.2 Characteristics of magnesium alloy welded joints under dynamic load

Comments about the Mg alloy weld dynamic load are receiving more attention with the application potential of Mg alloys in the fields of transportation. Actually, the dynamic performance of welding joint, including fatigue strength, impact ductility, bending strength, etc., is relatively low and is leading to the fact that Mg alloy is not a first choice in the fields of transportation. It is closely related to the welding process and to the properties of a base metal. Reports on the mechanism of fatigue crack of die cast of Mg alloys have been published, which revealed that cracks usually appeared in the surface of the material or along the pore in the sub-surface;[7] some illustrated that cracks grow on the basis of a-Mg and then extend between a-Mg and the eutectic,[8] and others said that the inhomogeneities of the secondary dendrite arm spacing and the grain sizes are the reasons affecting the fatigue properties of the Mg alloys.[9] As for the Mg alloy weld, factors influencing the fatigue strength are as follows: excess weld metal, recess and various welding defects, such as cracks, incomplete fusion, pores and slag inclusions, resulting in stress concentration and certain residual stress. When the stress concentration, slag inclusion and the residual tensile stress meet, the fatigue strength of the welded joint is significantly weakened. Some researches on the fatigue strength of the Mg alloy welded joint have already been published.

Tsujikawa, Somekawa and Higashi have pointed out that the fatigue joint efficiencies of AZ31 joint and AZ61 joint by TIG or friction stir welding are about 80% and 60%, respectively.[10] Fracture surfaces present brittle fatigue crack propagation, and moreover, the directions of crack propagation are influenced remarkably by the microstructures.

Kleinpeter, Rethmeier and Wohlfahrt have investigated the fatigue strength of the welded joints by metal inert gas (MIG), laser beam and electron beam.[11] Depending on the profiles of the weld seams, the highest fatigue strength (55% of the base metal strength) can be reached with electron beam welding without filler metal as well as with laser beam welding with filler metal. For laser beam welding without filler metal and MIG welding, the fatigue strength decreases to 50%, whereas tests with removed weld reinforcements show fatigue strength of 75% of the base metal strength.

Asahina, Katoh and Tokisue researched friction-welded joints of AZ31 magnesium alloy and showed that fatigue limit of the welded joint is 93.1% of the base metal in rotary bending tester and 95.8% of the base metal in repeated torsion fatigue tests.[12]

All these researches reveal that dynamic load properties of the Mg alloy welded joints still need further improving. However, investigations on the fatigue, impacting and bending properties are limited, and systematic research is urgent for more tests and corresponding solutions.

1.3 Efficient gas metal arc welding of magnesium alloys

Due to special physical and chemical characteristics of Mg alloys, there are many advantages of filler wire welding on Mg alloys, such as the compensation for the loss of evaporation of Mg element during welding, lowering the overburning of Mg elements and the sinking of weld, reduction of pores and cracks, decreasing the brittleness and sensitivity for stress corrosion of welded joint and allowing a certain space between the two welding sheets. The filler wire welding mainly consists of two categories: MIG welding and cold filler wire welding with arc, laser and electron beam heat source.

Metal inert gas welding is very popular in the field of non-ferrous metal welding. However, it was previously considered as not fit for Mg alloys. The boiling and melting temperatures of Mg alloys are relatively low; thus the demand for the welding input heat is restricted. It should make the Mg alloy wires melt completely but not boil. Thus, because splashing and overburning of the wires are the usual phenomena, it is rather difficult to obtain a continuous welding line with traditional gas metal-arc welding method. Besides, the filling process of Mg alloy wire as electrode is not very stable. Additionally, it is not easy to obtain the Mg alloy wire by conventional wire drawing methods such as Al alloy because of the hexagonal close-packed crystal structure and poor plasticity of Mg alloys. It is therefore necessary to develop a special wire-preparing technique for Mg alloy. So far, researches on gas metal arc welding of Mg alloy are focused on developing new power supplies, to make sure the wire is melted but not evaporated or splashed so that a continuous wire filling process is obtained. The only published paper succeeds in welding Mg alloy using a short arc with pulse superimposition or a triggered short arc.[13] The tensile strength and fatigue strength of the welded joint reach 80–100% and around 50% of the base metal, respectively.

Recently, investigations on cold filler wire welding of Mg alloys using TIG, laser or electron beam, have seen developments. A well-shaped weld can be attained with TIG filler wire welding, showing smaller HAZ, finer grains and higher tensile strength compared to the weld with TIG. As for the welding with small HAZ heat sources, such as laser and electron beam, higher demands for the wire filling process are asked for. However, it is difficult and costly to produce fine Mg alloy wires for laser welding; thus, such wires fit for industry applications are rather limited. On the other hand, wide wires need more powerful laser devices, lower welding speed and a smaller depth–width ratio. Subsequently, investigations on wires with different diameters and cross-section morphologies are focused on Mg alloys laser welding.

Wire components are also one of research contents in the filler wire welding. Both the kinds and the components of the wires will influence the welds' abilities. For the common AM and AZ series of Mg alloys, wires of the same series and the same grade as Mg alloy can be used[14] and, usually, wires of the same series but different grades with Mg alloy can be used to meet the strength demand of the welding seams. Furthermore, when welding Mg alloys containing no Al element, for example ZE series, wires containing Al element are usually employed, which is helpful in improving mechanical properties of the weld. If welding of cast Mg alloys is needed, AZ series of wires rich in Al element, such as AZ91 wire, are chosen. It has been proved that rare elements are good for welding microstructures; therefore, the addition of proper rare elements to welding wires is always an effective welding method. For example, with the wire containing Sb employed in the welding process, the weld improves in its welding strength, as Sb element works in grain refinement and dispersive distribution of eutectic phases.[15] Another example is that wires containing lanthanum increase the volume fraction of the low melting-point eutectic components, which helps heal the hot cracks during welding, and reduce the melting of the grain boundaries of the weld metal.[16]

1.4 Dissimilar welding of magnesium alloys to other metals

Mg alloys have important advantages, such as low weight and high specific strength, but also disadvantages, such as poor corrosion resistance. As an engineering material, wider applications of Mg alloy will meet the needs for dissimilar Mg alloy welding and dissimilar welding of Mg alloy to other metals like steel, Al, Cu and even nonmetals. The main difficulties in the welding process are the great difference in crystallographic features, physical and mechanical properties, dissolving into each other in liquid phase and separation from each other in the cooling process. Whether cracks can be avoided or not for the welding of the two partially matching metals depends on the crystallization condition, phase transition and stressing state; if the two welded materials react with each other, intermetallic compounds and precipitated supersaturated solid solution will decrease the mechanical properties of the weld. In addition, the corrosion of the dissimilar joint is always accelerated due to rather low corrosion potential of the Mg alloy. Up until now, Mg alloys are welded with other metals mainly using laser welding, laser-TIG hybrid welding, laser bond welding, diffusion welding, stir welding and so on.

Take the dissimilar fusion welding of Mg to Al alloy, for example. Hard and brittle intermetallic compounds Mg_3Al_2 and $Mg_{17}Al_{12}$ always appear, directly affecting service performances of the welded joint. Mg alloys are welded to Al alloys mainly using laser bond welding, diffusion welding, friction stir welding and so on. Among them, laser bond welding is a new hybrid welding combining laser fusion welding with adhesive bonding, joining Mg and Al together in the integration of chemical joining, mechanical joining and metallic joining.[17] Here, the adhesive helps the welding stress distribute uniformly, and on the other hand, welding improves the shear force of the adhesive. As a result, structural strengths of the weld are improved effectively. In the process of diffusion welding, an interlayer consisting of certain elements is employed, preventing or at least reducing the formation of intermetallics, and subsequently improving the structural strength of the joint significantly.[18] The friction stir welding makes the intermetallic interlayer thinner and improves mechanical properties of the weld.[19] As for the welding of Mg and steel, an interlayer can be introduced to improve the joining properties. Moreover, a coating deposition employed with arc-spraying technique act as a barrier to protect the whole structure from corrosion resulting from the great difference of corrosion potentials between the two metals.

In conclusion, various welding methods and processes of Mg alloys are comprehensively analyzed and discussed in this book. The pre- and post-treatments, welding quality evaluation and weld protection were also performed. The emphasis is to systematically show the present research status and developing trends in Mg alloy joining techniques. Academic communications and constructive suggestions will be appreciated.

1.5 References

1. Avedesian MM, Baker H (1999). *ASM Speciality Handbook – Magnesium and Magnesium Alloys*. Materials Park (OH): ASM International.
2. Xu H, Liu JG, Xie SS (2007). *Magnesium Alloy Fabrication and Processing Technology*. Beijing: Metallurgical Industry Press.
3. Liu LM, Dong CF (2006). Gas tungsten-arc filler welding of AZ31 magnesium alloy. *Mat Lett* **60**(17–18): 2194–7.
4. Cao X, Jahazi M, Immarigeon JP, Wallace W (2006). A review of laser welding techniques for magnesium alloys. *J Mater Process Technol* **171**(3): 188–204.

5. Liu LM, Song G, Zhu ML (2008). Low-power laser/arc hybrid welding behavior in AZ-based Mg alloys. *Metall Mater Trans A* **39A**(7): 1702–11.
6. Somasekharan AC, Murr LE (2004). Microstructures in friction-stir welded dissimilar magnesium alloys and magnesium alloys to 6061-T6 aluminum alloy. *Mater Charact* **52**(1): 49–64.
7. Mayer H, Papakyriacou M, Zettl B, Stanzl SE (2003). Influence of porosity on the fatigue limit of die cast magnesium and aluminium alloys. *Int J Fatigue* **25**(3): 245–56.
8. Nan ZY, Ishihara S, Goshima T (2004). Scanning probe microscope observations of fatigue processing magnesium alloy AZ31 near the fatigue limit. *Scr Mater* **50**(4): 429–34.
9. Horstemeyer MF, Yang N, Gall K (2004). High cycle fatigue of a die cast AZ91E-T4 magnesium alloy. *Acta Mater* **52**(5): 1327–36.
10. Tsujikawa M, Somekawa H, Higashi K (2004). Fatigue of welded magnesium alloy joints. *Mater Trans* **45**(2): 419–22.
11. Kleinpeter B, Rethmeier M, Wohlfahrt H (2005). Fatigue strength of welded wrought magnesium alloys. In: Kainer KU (ed.) *Magnesium: Proceedings of the 6th International Conference Magnesium Alloys and Their Applications*. Weinheim: Wiley-VCH Verlag, pp. 908–16.
12. Asahina T, Katoh K, Tokisue H (2001). Fatigue strength of friction welded joints of AZ31 magnesium alloy. *J Jpn Inst Light Met* **44**(3): 147–51.
13. Helmut W, Michael R, Belkacem B (2003). Metal-inert gas welding of magnesium alloys. *Weld Cut* **55**(2): 80–4.
14. Haferkamp H, Goede M, Bormann A, Cordini P (2001). Laser beam welding of magnesium alloys – new possibilities using filler wire and arc welding. *Proc LANE: Laser Assist Net Shape Eng* **3**: 333–8.
15. Dong CF, Liu LM, Gao HW, Liu D (2005). Effect of antimony on microstructure and performance of AZ31 magnesium alloy welded joint. *China Weld* **14**(1): 44–7.
16. Lukin VI, Dobrynina IS (1998). Weldability of cast magnesium alloys of the Mg–Zn–Zr system. *Svarochnoe Proizvodstvo* **45**(4): 6–8.
17. Liu LM, Wang HY, Zhang ZD (2007). The analysis of laser weld bonding of Al alloy to Mg alloy. *Scr Mater* **56**(6): 473–6.
18. Zhao LM, Zhang ZD (2008). Effect of Zn alloy interlayer on interface microstructure and strength of diffusion-bonded Mg–Al joints. *Scr Mater* **58**(4): 283–6.
19. Chen YC, Nakata K (2008). Friction stir lap joining aluminum and magnesium alloys. *Scr Mater* **58**(6): 433–6.

2

Welding metallurgy of magnesium alloys

L. LIU, Dalian University of Technology, China

Abstract: As light structural materials, Mg and its alloys have recently attracted more attention and welding plays an important role in exploiting the new fields of the Mg alloy applications. The weldability of Mg alloy and that of Mg alloy to other materials are discussed. The existing problems in welding Mg alloys are analyzed, as well as the characterization of welding Mg alloys to other metals.

Key words: magnesium alloy, weldability, other metals.

2.1 Introduction

Mg alloy, as a light metal, has specific physical and chemical characteristics that affect its welding property significantly, especially its boiling and melting temperatures, surface tension, corrosion potential and expansion coefficient, which will directly influence its welding process.

Table 2.1 illustrates the physical properties of Mg, Al and Fe. The density of Mg is 1.74 g/cm^3. With the same volume, Mg weighs only a quarter of steel and two-thirds the weight of Al. The melting point of Mg is 660 °C. The liquidus temperature of most Mg alloys is between 500 °C and 680 °C, and some melt at only 443 °C and others at 700–800 °C. The boiling temperature of Mg alloys at 1100–1107 °C is lower than that of the other structural materials; accordingly these alloys will be overburnt and the chemical components of the molten pool will be changed during welding. As Mg has a low surface tension, about 0.55 N/m, half of Al and one-third of Fe, and a high surface vapor pressure, splashing is likely to appear in the welding process, and weld shaping becomes difficult to control. Activating agents used in Al alloys, Ti alloys or steel welding perform badly in Mg alloys welding because of the low electrode potential of Mg alloys. So, it is necessary to investigate the mechanism of Mg alloy activating welding and the effect of activating elements. In addition, when Mg alloy is used together with other different alloys such as steel, the shielding technique should be put into use because of the low electrode potential of Mg alloy.

Mg alloy presents an average expansion coefficient between 18 °C and 399 °C at $1.6 \times 10^{-5}/°\text{F}$, almost equal to Al and twice that of steel. The thermal conductivity of pure Mg is 154 W/(m·k) and that of Mg alloys is around 70–110 W/(m·k). With low melting temperature, fusion heat and specific heat, Mg requires a smaller amount of heat to melt compared to aluminum and steel of the same volume, two-thirds and one-fifth, respectively. During the welding process, Mg undergoes a heavy deformation due to its high expansion coefficient and thermal conductivity.[1]

Table 2.1 Physical properties of Mg, Al and Fe

Parameters	Temperature (°C)	Mg	Al	Fe
Density (g/cm^3)	20	1.74	2.70	7.87
Melting temperature	–	651	660	1538
Boiling temperature	–	1107	2056	2735
Surface tension (10^{-3} N/m)	Melting point	559	914	1872
Specific heat (J/kg. K)	20	1022	900	444
Heat capacity (J/m^3. K)	20	1778	2430	3494
Thermal expansion rate (10^{-6}/K)	20	26.1	23.9	12.2
Thermal conductivity (W/m. K)	20–100	167	238	73.3
Electrical resistivity (10^{-8} Ω. M)	20	4.2	2.67	10.1
Young's modulus (10^{11} Pa)	20	0.443	0.757	1.90

Mg is oxidized rapidly when heated in the air. Subsequently, inert gas or welding flux must be used to prevent Mg from oxidizing at high temperatures. Once oxidized, magnesia with a rather high melting temperature, about 2800 °C, is formed, which is almost insoluble in liquid or in solid phases. Moreover, Mg will easily react with nitrogen, producing magnesium nitride, which is not stable and tends to dissolve when coexisting with water.

Mg has a hexagonal close packed (hcp) structure, which can cause Mg alloys to join with other materials in the form of solid solution, but instead, always by forming intermetallic compounds. For example, intermetallic compounds are usually formed during joining Mg alloy to Al alloy, which seriously affects the joining properties of the weld.[2–4] The joining of Mg alloy to steel is limited, as the two metals neither dissolve into each other nor produce intermetallics.[5] Therefore, it is difficult for Mg alloys to join with other metals successfully merely by a fusion welding method due to intermetallic formation or oxidation. Nowadays, due to the unique properties of Mg alloys and the intermetallics generated by the interaction of Mg alloys with other materials, the weldability of Mg alloys with other materials is being investigated comprehensively, which becomes particularly complicated. Some researchers have succeeded partly in welding Mg alloy and other metals using stir friction welding, diffusion welding and laser welding, etc.[6] However, it is far from practical.

2.2 Weldability of magnesium alloys

Welding defects always appear as a result of specific physical and chemical characteristics of an Mg alloy, mainly including oxidation and evaporation, overheated coarse grains, heat cracks, pores and thermal stress, and so on.[7–13]

1. Oxidation and evaporation: Mg alloy easily burns and evaporates in a fusion welding process with a high temperature owing to its low melting and boiling temperatures, only 649 °C and 1107 °C respectively.[14]

In the heating process, Mg element is apt to react with oxygen, producing magnesium oxide with a high melting temperature. The magnesium oxide will cover the molten pool and the weld groove, resulting in a bad weld shaping, and the formation of magnesium oxide slag inclusion seriously decreases the properties of the welded joint. Moreover, an Mg element tends to react with nitrogen and produce magnesium nitride slag inclusion, affecting the ductility of the joint.

To control the oxidation and evaporation of Mg alloy, a series of solutions are applied as follows: direct contact between Mg alloy and the air is avoided with gas shielding; lower heat input is preferred, including using pulse tungsten inert gas (TIG) welding method, properly swinging welding arc and choosing smaller welding heat input; and trying to elevate the boiling temperature by applying specific welding flux and alloying elements.

2 Overheated coarse grains: Due to its low melting temperature and high thermal conductivity, a heat source with a relatively higher power input is demanded, which will easily cause the overheat phenomenon and produce coarse grains, subsequently affecting the weld properties. Coarse grains are one of the main factors that affect weld properties.

3 Hot cracks: In the welding process, Mg alloy is easily deformed and thermal stress is generated, providing sufficient conditions for hot cracking, as Mg alloy has a high expansion coefficient of 2.61×10^{-5}/°C, twice that of steel of 1.13×10^{-5}/°C and almost equal to Al of 2.32×10^{-5}/°C. Moreover, Mg is apt to react with alloying elements such as Cu, Al and Ni, and produces eutectic phases with low melting temperatures. As a result, the span between solidus and liquidus of Mg alloy is widened. Among the eutectic alloys, the eutectic temperatures of Mg-Cu, Mg-Al and Mg-Ni are 480 °C, 430 °C and 508 °C, respectively. These eutectic phases with their low melting temperatures will form liquid films along the grain boundaries, resulting in the fact that the brittle temperature range of Mg alloy is widened and hot cracking forms because of stress.

4 Pores: Pores that are common in a welded joint are one of the main problems in the Mg alloy welding process. On the one hand, hydrogen dissolves completely in the heating process and is separated out while temperature decreases, resulting in the appearance of pores. On the other hand, many inherent small pores and shrinkage exist in the cast Mg alloys, which will subsequently concentrate and grow in the welding process, producing larger pores. This kind of pores will seriously affect the joint properties, especially the dynamic load. Accordingly, pores must be prevented and controlled by protecting the joint from air pollution and by optimizing welding process specifications.

5 Welding heat stress: Definitely, great heat stress will be generated in the heating and cooling process because Mg alloy has a high expansion coefficient. This stress will make the joint become deformed and simultaneously accelerate the generation of eutectic cracks, which will directly affect the quality and service performance of the joint structure.

All the defects mentioned above could occur in the Mg alloy welding process. Actually, the defects rising in the welding process of Mg alloys with different compositions do not vary greatly. Apart from welding cracks and pores, defects such as slag inclusion, incomplete penetration and overburning are usually observed too.

The weldability of Mg alloy varies with different grades. Generally, the weldability of wrought Mg alloy is better than that of cast Mg alloy. Table 2.2 illustrates the weldability of different Mg alloys, according to the crack sensitivity and type of weld effective coefficient.[14]

2.3 Weldability of magnesium alloys to other metals

The welding of Mg alloys embodies not only welding of different Mg alloys but also welding of Mg alloy to other metals. In the welding and joining process of Mg alloy to other metals, besides those described before, more

Table 2.2 Relative weldabilities of Mg alloys with common grades

Materials	Grade	Relative weldability
Cast Mg alloys	AM100A	B
	AZ63A	C
	AZ8IA	B
	AZ91AC	B
	AZ92A	B
	EK30A	B
	EK41A	B
	EZ33A	A
	HK31A	B
	HZ32A	C
	K1A	A
	QE22A	B
	ZE41A	C
	ZH62A	C
	ZK51A	D
	ZK61A	D
Wrought Mg alloys	AZ10A	A
	AZ31B,C	A
	AZ61A	B
	AZ80A	B
	HK31A	A
	HM21A	A
	HM31A	A
	ZE10A	A
	ZK21A	B

Note: A – very good; B – good; C – OK; D – poor.

problems may appear such as cold cracking, oxidation, evaporation and corrosion.

1 Cold cracking: Cold cracks are mainly those that occur after solidification when metals are fusion welded. When joining Mg alloy to other metals, hard, brittle intermetallic compounds are always generated with low shrinkage ratios. As a result, half-continuous cold cracks form along the boundary of melted Mg alloy and the intermetallics, in addition to the effect of the high expansion coefficient of Mg alloy. As intermetallic compounds always form continuous lamellar structures, under the action of external force those cold cracks are prone to expand and connect with each other, causing rupture in the end. All these problems are observed in the joining of Mg and Al alloy, Mg and Cu alloy,[15] as well as Mg and Zn alloy.[16] Some corresponding solutions are introduced such as reducing heat input, employing alloy interlayer, and using special welding methods such as stir friction welding, laser-arc hybrid welding and so on. However, these are not completely effective. Perfect ones are still underway and always present problems in Mg alloy welding investigations.
2 Oxidation and evaporation: When welding Mg alloy with other metals, oxidation appears not only in the molten pool of Mg alloy but also along the boundaries of Mg alloy and other metals. As the melting temperatures of other metals such as steel and Cu alloy are similar to or higher than the boiling temperature of Mg alloy, temperature in the molten pool easily reaches the boiling temperature of Mg alloy. Here, Mg atoms, especially those at the boundaries, are active, easy to be oxidized. These oxides will decrease the strength of the weld joint significantly. Moreover, oxidation cannot be prevented completely by increasing the flow of gas shield. Thus, employing an alloy interlayer is the principal solution of welding Mg alloy and other metals with high melting temperatures.

  The molten pool temperature in an Mg welding process with other metals is definitely higher than that in the single Mg alloy welding process, and the evaporation of Mg alloy is certainly more evident, resulting in the fact that pores and overburning are easier to appear. Reducing the heat input can solve the problem; however, at the same time the penetration and weld strength are decreased. Hence, special welding methods are suggested to realize the joining of Mg alloy and other metals.
3 Corrosion and protection: Mg alloy has a rather low corrosion potential and will be easily corroded in wet air. But metals extensively applied in the manufacturing industry, such as steel and Al alloys, are much more corrosion resistant. In the joints of Mg alloy with other metals, the corrosion of Mg alloy is accelerated not only with self-corrosion but also with galvanic corrosion due to the big corrosion potential difference. As corrosion proceeds, corrosion cracks form easily, and subsequently, the joint is destroyed. Evidently,

protection measures are especially important and necessary. Now, protection methods for Mg alloy mainly include micro-arc oxidation, chemical conversion film, ion plating and thermal spraying and so on. With regard to dissimilar joints, protection measurements are limited, as the two joining materials are significantly different in their physical and chemical properties. Pure aluminum coatings or certain composite coatings are effective to protect the joint of Mg alloy and other metals from corrosion.

On the whole, this chapter characterizes the weldability of Mg alloys and principal problems of welding Mg alloy and other metals. The effects of various alloying elements on the Mg alloy welding process were preliminarily investigated, but not yet systematically. Successful welding and joining of Mg alloys, especially to analyze the welding of Mg alloy compared with other metals, seems very important theoretically. Hence, further investigations on metallic welding of Mg alloys are urgently needed.

2.4 References

1. Cao X, Jahazi M, Immarigeon JP, Wallace W (2004). Pulsed CO_2 laser-TIG arc hybrid lap welding of magnesium alloy AZ31B. *J Mater Process Technol* **171**(3): 188–204.
2. Somasekharan AC, Murr LE (2004). Microstructures in friction-stir welded dissimilar magnesium alloys and magnesium alloys to 6061-T6 aluminum alloy. *Mater Charact* **52**(1): 49–64.
3. Liu LM, Liu XJ, Liu SH (2006). Microstructure of laser-TIG hybrid welds of dissimilar Mg alloy and Al alloy with Ce as interlayer. *Scripta Mater* **55**(5): 383–6.
4. Sato YS, Hwan S, Park C, Michiuchi M, Kokawa H (2004). Constitutional liquation during dissimilar friction stir welding of Al and Mg alloys. *Scripta Mater* **50**(9): 1233–6.
5. Liu LM, Zhao X (2008). Study on the weld joint of Mg alloy and steel by laser-GTA hybrid welding. *Mater Charact* **59**(9): 1279–84.
6. Yan JC, Xu ZW (2005). Microstructure characteristics and performance of dissimilar welds between magnesium alloy and aluminum formed by friction stirring. *Scripta Mater* **53**(5): 585–9.
7. Zhao LM, Zhang ZD (2008). Effect of Zn alloy interlayer on interface microstructure and strength of diffusion-bonded Mg–Al joints. *Scripta Mater* **58**(4): 283–6.
8. Liu LM, Wang HY, Zhang ZD (2007). The analysis of laser weld bonding of Al alloy to Mg alloy. *Scripta Mater* **56**(6): 473–6.
9. Sanders PG, Keske JS, Leong KH, Kornecki G (1999). High power Nd:YAG and CO_2 laser welding of magnesium. *J Laser Appl* **11**(2): 96–103.
10. Lehner C, Reinhart G (1999). Welding of die casted magnesium alloys for production machines. *J Laser Appl* **11**(5): 206–10.
11. Marya M, Edwards GR (2001). Factors controlling the magnesium weld morphology in deep penetration welding by a CO_2 laser. *J Mater Eng Perform* **10**(4): 435–43.

12. Liu LM, Song G, Liang GL, Wang JF (2005). Pore formation during hybrid laser-tungsten inert gas welding of magnesium alloy AZ31B-mechanism and remedy. *Mater Sci Eng A* **390**(1): 76–80.
13. Liu LM, Dong CF (2006). Gas tungsten-arc filler welding of AZ31 magnesium alloy. *Mater Lett* **60**(17–18): 2194–7.
14. Xu H, Liu JG, Xie SS (2007). *Mg Alloy Fabrication and Processing Technology.* Beijing: Metallurgical Industry Press.
15. Liu LM, Wang SX, Zhao LM (2008). Study on the dissimilar magnesium alloy and copper lap joint by TIG welding. *Mater Sci Eng A* **476**(1): 206–209.
16. Liu LM, Tan JH, Zhao LM, Liu XJ (2008). The relationship between microstructure and properties of Mg/Al brazed joints using Zn filler metal. *Mater Charact* **59**(4): 479–83.

3

Preparation for welding of magnesium alloys

L. LIU, Dalian University of Technology, China

Abstract: In this chapter, the preparation for Mg welding is introduced. Surface treatment is important for Mg welding, and lack of treatments may lead to defects. Typical processes of surface treatment are introduced. In welding with filler wires, the welding groove types are listed in the chapter. As the special characters of Mg, preheating and postweld treatments can influence the weld strength, the common methods are introduced.

Key words: magnesium alloy, surface treatment, groove, preheating, postweld treatments.

3.1 Introduction

Mg alloys are usually protected by oil coating, acid-pickled surface, or chromate conversion coating, but surface oxide films or contaminants will cause weld defects. Thus before welding, surfaces of Mg structures and welding wires should be cleaned to remove oxide film and hydride layers, grease/releasing agents and surface coatings. The groove types, preheating and postweld treatment methods are also important to Mg welding processes due to their specific characteristics.

3.2 Surface treatment of magnesium alloys

For corrosion protection, Mg and Mg alloys usually need oxidation treatment so that the surface is coated by chromate film. The film is a major obstacle in welding processes and it can result in some welding effects including cracking (non-fusion), porosity and slag, as shown in Fig. 3.1. The films on sheet surfaces and wires easily absorb moisture, which results in pores in the fusion zone. In filler wire welding, the film on the wires can lead to the formation of hydrogen in the droplets, resulting in an increased hydrogen content in the molten pool. In addition, the film may remain at the weld root and can also lead to pores when the heat input is low. Therefore, the film and oil on all surface and edges of the structures and wires must be completely removed prior to welding.

Different methods can be used to clean the surface according to the conditions of amount of oil and film on the structures to be welded. If the amount of oil is small, mechanical methods can be used with the help of stainless steel brushes. When the amount of oil is large, a combination of degreasing and abrasion methods can be used, which, in addition, result in good performance in removing oil and chromate film. Table 3.1 shows the chemical treatment methods before welding Mg alloys.[1]

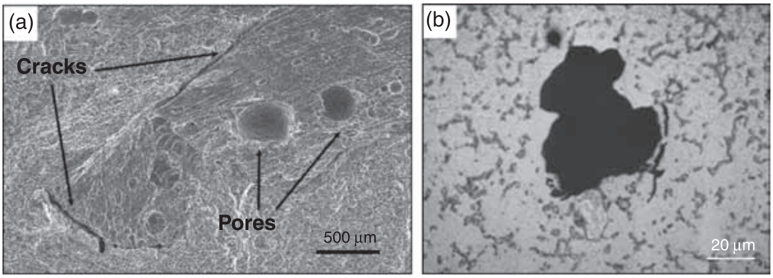

3.1 Defects of Mg alloys welding. (a) Cracks and pores in fracture, and (b) slag.

Table 3.1 Chemical pretreatment methods

Type	Component	Process	Use
Alkaline cleaning solution	Sodium carbonate, 84.9 g Caustic soda, 56.6 g Water, 3.8 dm^3 Temperature, 361–73K pH value ≥ 11	Immerse for 3–10 minutes, rinse with cold water and dry	For degreasing or removing chromate film
Bright cleaning solution	Chromic acid, 0.675 kg Ferric nitrate, 150 g Potassium fluoride, 14.2 g Water, 3.8 dm^3 Temperature, 289–311K	Immerse for 0.25–3 minutes, rinse with cold and warm water, and dry	For bright surface by removing chromate film after degreasing
Cleaning solution for spot welding	1. Concentrated sulfuric acid, 36.8 g Water, 3.8 dm^3 Temperature, 294–305K	Immerse for 0.25–1 minutes in (1), and immerse in (2) or (3) after rinsing with cold water.	For removing chromate film after degreasing
	2. Chromic acid, 0.675 kg Concentrated sulfuric acid, 2.0 g Water, 3.8 dm^3 Temperature, 294–305K	If in (2), immerse for 3 minutes, rinse with cold water and dry.	
	3. Chromic acid, 9.3 g Water, 3.8 dm^3 Temperature, 294–305K	If in (3), immerse for 0.5 minutes, rinse with cold water and dry.	
Chromic acid cleaning solution	Chromic acid, 0.675 kg Concentrated nitric acid, 75 g Water, 3.8 dm^3 Temperature, 294–305K	Immerse for 0.5–2 minutes in solution, keep for 5 seconds in air, rinse with cold or warm water and dry	For priming or surface prevention

Table 3.2 Pretreatment methods for wire

No.	Process	Component (g L^{-1})	Temperature (°C)	Time (minutes)
1	Degreasing	NaOH (10–25) Na_3PO_4 (40–60) Na_2PO_3 (20–30)	60–90	5–15
2	Flush with flowing warm water		50–90	4–5
3	Flush with flowing cold water		Room	2–3
4	Alkali treatment	NaOH (350–450)	MB8 70–80 MB3 60–65	2–3 5–6
5	Flush with flowing warm water		50–90	2–3
6	Flush with flowing cold water		Room	2–3
7	Chromic acid treatment	CrO_3 (150–250) SO_4 (<0.4)	Room	5–10
8	Flush with flowing cold water			2–3
9	Flush with flowing warm water		50–90	1–3
10	Dry		50–70	

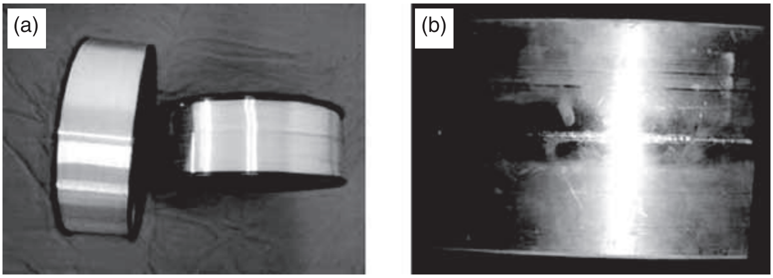

3.2 (a) Wires and (b) weld of Mg alloys. (Chen 2004)

The welding wire surface also needs chemical or mechanical cleaning before being used. In the mechanical method, the oxidation film can be removed by bit tools or brushes. In a chemical method, weld wire is usually immersed in the 20–25% nitric acid solutions for two minutes, then flushed with 50–90 °C water and finally dried. Some other methods are shown in Table 3.2. The cleaned wire should be used on the same day (within 10 days in dry weather). These pretreatment methods can be used to make a satisfactory weld, and Fig. 3.2 shows the wires and weld pretreated by the processes above.

3.3 Welding groove for magnesium alloys

Groove type is very important both in welding and in repairing welding. Table 3.3 shows the groove types in welding[2] and Fig. 3.3 shows the groove types

Table 3.3 Groove types for welding

No.	Joint type	Groove type	Thickness (*T*/mm)	Dimension					Welding method
				a/mm	*c*/mm	*b*/mm	*p*/mm	α	
1	Square groove butt joint	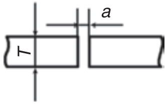	≤3.0	0–0.2	—	—	—	—	Manual or automatic tungsten arc welding
2	Corner joint	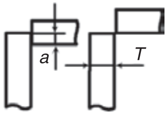	>1.0	0.2	—	—	—	—	Manual or automatic tungsten arc welding (with filling wire)
3	Lap joint	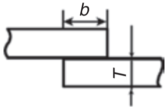	>1.0	—	—	3–4	—	—	Manual or automatic tungsten arc welding
4	Single V-groove butt joint	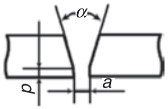	3–8	0.5–2.0	—	—	0.5–1.5	50°–70°	Manual or automatic tungsten arc welding
5	Double V-groove butt joint	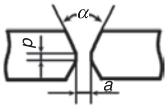	≥20	1.0–2.0	—	—	0.8–1.2	60°	Manual or automatic tungsten arc welding with filling wire

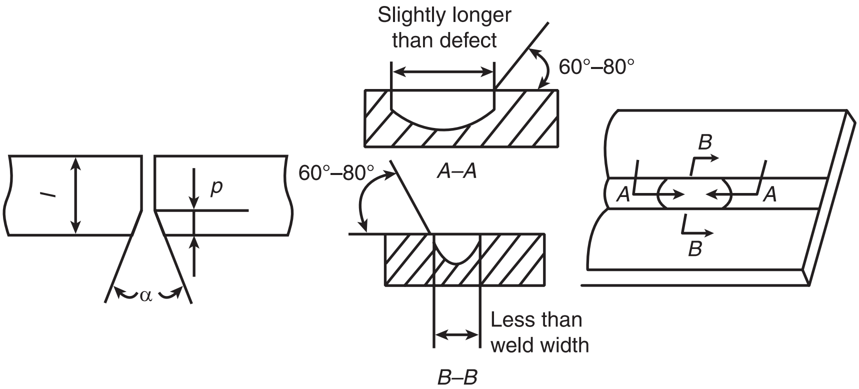

3.3 Groove types for repairing welding.

in repairing welding. When the magnesium sheet is less than 6 mm thick, ‘activating welding’ of Mg alloys can be used without groove.

3.4 Preheating and postweld treatments for magnesium alloys

There are often some defects in the castings, such as cracks, misruns or blowholes, and these defects have to be welded for repairing. In complex structures, especially in the structures with different thickness sections, the restraint on a weld can be high; therefore it is necessary to supply some preheating process to prevent weld cracking, especially in high-Zn Mg alloys. Local area preheating and entire preheating can be used in different conditions. In local area preheating, the torch can be used to heat a local area. In entire preheating, all the structures can be put into a furnace and be heated at a proper temperature. There are some considerations in preheating Mg alloys: first, the heating temperature must be lower than the maximum temperatures for various alloys; the temperatures are shown in Table 3.4.[3] Second, the structures require protection from the atmosphere during preheating, and argon shield is usually used in preheating process.

Castings made from alloys are usually heat-treated to T4 or T6 tempers. The weld metal freezes so rapidly that the grains in the bead metal become fine. The time required for complete solution of the second phase in the weld metal is shorter than the time required for the as-cast metal in the casting itself. Grains of the weld metal grow and the mechanical properties decline if heating is continued after solution is completed. Solution heat treating of the entire welded casting structures is not necessary if the casting that has been welded is in the as-cast condition before welding. It is necessary only to weld on castings that have already been raised to temperature to either T4 or T6 temper. After welding, castings and the weld metals can be put into the solution-heat-treated state in a

Table 3.4 Preheat and postweld treatments for castings

Alloy	Temper		Max preheat temperature (°C)	Postweld treatment	
	Before weld	After weld		Temperature (°C)	Time (hours)
AZ63A	T4	T4	380	385	0.5
	T4 or T6	T6	380	385	0.5
				+220	5
	T5	T5	260	220	5
AZ81A	T4	T4	400	415	0.5
AZ91C	T4	T4	400	415	0.5
	T4 or T6	T6	400	415	0.5
				+215	4
AZ92A	T4	T4	400	410	0.5
	T4 or T6	T6	400	410	0.5
				+260	4
AM100A	T6	T6	400	415	0.5
				+220	5
EK30A	T6	T6	260	200	16
EK41A	T4 or T6	T6	260	200	16
	T5	T5	260	200	16
EZ33A	F or T5	T5	260	345	2
				+215	5
HK31A	T4 or T6	T6	260	315	1
				+200	16
HZ32A	F or T5	T5	260	315	16
K1A	F	F	None	None	
QE21A	T4 or T6	T6	450	510	0.5–1
				+200	8
QE22A	T4 or T6	T6	260	530[a]	8
				+200	8
QH21A	T4 or T6	T6	450	510	0.5–1
				+200	16
ZE41A	F or T5	T5	315	330	2
				+175	16
ZH62A	F or T5	T5	315	330	2
				+175	16
ZK51A	F or T5	T5	315	330	2
				+175	16
ZK61A	F or T5	T5	315	150	48
	T4 or T6	T6	315	500	2–5
				+130	48

[a] Quench in water at 60–85°C before second heat treatment.

Note: T4, solution treatment; T6, solution treatment and artificial aging; F, as-cast condition.

short time at the heat-treating temperature, and the recommended procedures are shown in Table 3.4.

3.5 References

1. Chen Z (2004). *Mg Alloys*. Beijing: Chemical Industry Press.
2. Xu H, Liu J, Xie S (2007). *Mg Alloy Fabrication and Processing Technology*. Beijing: Metallurgical Industry Press.
3. American Society for Metals (1983). *Welding, Brazing and Soldering: Metal Handbook*, 9th edn, Vol. 6. Metals Park (OH): American Society for Metals.

4

Welding materials for magnesium alloys

L. LIU, Dalian University of Technology, China

Abstract: In this chapter, the welding material and its preparation methods for Mg welding are introduced. The hot extrusion process and hot pull process of magnesium welding materials are introduced in detail.

Key words: magnesium alloy, welding materials, hot extrusion process, hot pull process.

4.1 Introduction

Magnesium alloy welding materials have become one of the hot issues with the wide application of magnesium alloy parts in recent years. The welding materials are mainly used in gas tungsten arc welding and in gas metal arc welding processes as filler metal. The weldability of most magnesium alloys is good when the proper filler metal is employed. A filler metal with a wider freezing range than the base metal will provide good weldability and minimize weld cracking.

In the welding handbook published by the American Welding Society, four kinds of filler metals were recommended for various magnesium alloys. The composition of these magnesium alloy filler metals is shown in Table 4.1.[1] The recommended filler metals for various magnesium alloys are given in Table 4.2.[2]

ER AZ61A or ER AZ92A (Mg-Al-Zn) filler metal may be used to weld alloys of similar composition and ZK21A (Mg-Zn-Zr) alloy as well. ER AZ61A filler metal is generally preferred for welding wrought products of those alloys because of its low cracking tendencies. On the other hand, ER AZ92A filler metal shows less crack sensitivity for welding the cast Mg-Al-Zn and AM100A (Mg-Al) alloys. The deposited metal will respond to the precipitation heat treatments normally applied to the repaired castings. ER AZ101A filler metal may also be used to weld those casting alloys.

ER EZ33A (RE-Zn-Zr) filler metal is used to weld wrought and cast alloys designed for high-temperature service, either to themselves or each other. The welded joints will have good mechanical properties at elevated temperatures.

ER AZ92A filler metal is recommended for welding room temperature service wrought and cast alloys together or to one of the wrought or cast elevated service alloys. It will minimize weld cracking tendencies. ER EZ33A filler metal should not be used for welding aluminum-bearing magnesium alloys because of severe weld cracking problems.

Casting repairs should be made with a filler metal of the same composition as the base metal when good color match, minimum galvanic effects and good response to heat treatment are required.

Table 4.1 Composition of magnesium alloy welding wire

Composition (%)	ER AZ61A	ER AZ101A	ER AZ92A	ER EZ33A
Al	5.8–7.2	9.5–10.5	8.3–9.7	
Be	0.0002–0.0008	0.0002–0.0008	0.0002–0.0008	
Mn	0.15 Min.	0.13 Min.	0.15 Min.	
Zn	0.40–1.5	0.75–1.25	1.7–2.3	2.0–3.1
Zr				0.45–1.0
Re				2.5–4.0
Cu	0.05 Max.	0.05 Max.	0.05 Max.	
Fe	0.005 Max.	0.005 Max.	0.005 Max.	
Ni	0.005 Max.	0.005 Max.	0.005 Max.	
Si	0.05 Max.	0.05 Max.	0.05 Max.	
Other	0.30 Max.	0.30 Max.	0.30 Max.	
Mg	Bal.	Bal.	Bal.	Bal.

Table 4.2 Recommended filler metals for arc welding magnesium alloys

Alloys	Recommended filler metal				
	ER AZ61A	ER AZ92A	ER EZ33A	ER AZ101A	Base metal
Wrought					
AZ10A	X	X			
AZ31B	X	X			
AZ61A	X	X			
AZ80A	X	X			
ZK21A	X	X			
HK31A			X		
HM21A			X		
HM31A			X		
M1A					X
Cast					
AM100A		X		X	X
AZ63A		X		X	X
AZ81A		X		X	X
AZ91C		X		X	X
AZ92A		X		X	X
EK41A			X		X
EZ33A			X		X
HK31A			X		X
HZ32A			X		X
K1A			X		X
QH21A					X
ZE41A			X		X
ZH62A			X		X
ZK51A			X		X
ZK61A			X		X

For these and other unusual service requirements, the material supplier should be consulted for additional information. Table 4.3 shows the selected principle of filler metal for welding the two different kinds of magnesium alloys.[3]

The welding materials' selection principle of magnesium alloys has been introduced in some literature; however, the preparation method of magnesium alloy welding materials is less often reported. The preparation methods for welding materials of magnesium alloy will be introduced in this section. In summary, they mainly include:

1 Casting methods: The casting method can be used when low-volume filler wire is needed. A strip casting scrap can also be used as a filler wire. The casting filler wire can be used for casting welding and salvaging casting. But the casting scrap and casting wire must be selected carefully to ensure that there are no slag inclusion and rarefaction defects in them.
2 Drawing methods: For magnesium alloy, it is difficult to perform draw forming because the stress in the drawing process has a negative effect on the plastic deformation. But the product of draw forming has a high dimensional accuracy and surface roughness, and the drawing of wire and tube is easy to implement in a high-speed, continuous way; therefore, a high production efficiency can be obtained. The existing studies have shown that the wires of draw forming are stronger. Therefore, the research of magnesium alloy draw forming technology has attracted more attention in recent years. Japan Electric Industry Co. Ltd. prepared magnesium alloy wire using a draw forming process. Its tensile strength is up to 400 MPa and elongation is of ten per cent or more.[4] In addition, the AZ31, AZ61 and AZ80 drawing wires of good quality have been studied, which can also be used in cars, wheelchairs, etc., and to produce springs.
3 Hot extrusion methods: The conditions of magnesium alloy hot extrusion methods are not as harsh as rolling and forging. For coarse grains and uneven microstructure of magnesium alloy, it is difficult to be rolled and forged but can be extruded generally. Some oxide film impurities existing in the grain boundary of magnesium alloy may have little effect on the extrusion process, while it would have a strong effect on the casting and rolling performance. The extrusion methods may also improve the product's mechanical properties. In addition, the requirements of the extrusion process on the site are not that strict, and the extrusion speed range is wide. Typically, a lower extrusion temperature and slower extrusion speed can obtain high mechanical properties, and a high surface quality can be obtained under the high temperature and rapid extrusion process.

During a hot extrusion process of magnesium alloy, high-quality magnesium alloy extrusion products could be obtained by employing a special insulating device to hold the temperature of the ingot and die, and a special anti-friction material to ensure lubricity.

Table 4.3 Selection of magnesium alloy welding wire

	AM100	AZ10A	AZ31 AZ31C	AZ61A	AZ63A	AZ80A	AZ81A	AZ91C	AZ92A	EK41A	EZ33A HK31A	K1A HZ32A	LA141A	M1A MG1	QE22A	ZE10A	ZE41A	ZK21A	ZK51A ZK60A ZK61A
AM100	AZ92A AZ101	...	...	...	...	...	...	...	...	...	...	...	...	...	...	...	...	...	...
AZ10A	AZ92A	AZ61A AZ32A	...	...	...	...	...	...	...	...	...	...	...	...	...	...	...	...	...
AZ31B AZ31C	AZ92A	AZ61A AZ92A	AZ61A AZ92A	...	...	...	...	...	...	...	...	...	...	...	...	...	...	...	...
AZ61A	AZ92A	AZ61A AZ92A	AZ61A AZ92A	AZ61A AZ92A	...	...	...	...	...	...	...	...	...	...	...	...	...	...	...
AZ63A	×	×	×	×	AZ92A	...	...	...	...	...	...	...	...	...	...	...	...	...	...
AZ80A	AZ92A	AZ61A AZ92A	AZ61A AZ92A	AZ61A AZ92A	×	AZ61A AZ92A	...	...	...	...	...	...	...	...	...	...	...	...	...
AZ81A	AZ92A	AZ92A	AZ92A	AZ92A	×	AZ92A	AZ92A AZ101A	...	...	...	...	...	...	...	...	...	...	...	...
AZ81C	AZ92A	AZ92A	AZ92A	AZ92A	×	AZ92A	AZ92A	AZ92A AZ101A	...	...	...	...	...	...	...	...	...	...	...
AZ92A	AZ92A	AZ92A	AZ92A	AZ92A	×	AZ92A	AZ92A	AZ92A	AZ101A	...	...	...	...	...	...	...	...	...	...
EK41A	AZ92A	AZ92A	AZ92A	AZ92A	×	AZ92A	AZ92A	AZ92A	AZ92A	EZ33A	...	...	...	...	...	...	...	...	...
EZ33A HK31A	AZ92A	AZ92A	AZ92A	AZ92A	×	AZ92A	AZ92A	AZ92A	AZ92A	EZ33A	EZ33A	...	...	...	...	...	...	...	...
K1A HZ32A	AZ92A	AZ92A	AZ92A	AZ92A	×	AZ92A	AZ92A	AZ92A	AZ92A	EZ33A	EZ33A	EZ33A	...	...	...	...	...	...	...
M1A MG1	AZ92A	AZ61A AZ92A	AZ61A AZ92A	AZ61A AZ92A	×	AZ61A AZ92A	AZ92A	AZ92A	AZ92A	AZ92A	AZ92A	AZ92A	–	AZ61A AZ92A	–	...	...	...	...
ZE41A	–	–	–	–	×	–	–	–	–	EZ33A	EZ33A	EZ33A	–	–	EZ33A	–	EZ33A	...	...
ZK21A	AZ92A	AZ61A AZ92A	AZ61A AZ92A	AZ61 AZ92A	×	AZ61A AZ92A	AZ92A	AZ92A	AZ92A	AZ92A	AZ92A	AZ92A	–	AZ61A AZ92A	AZ92A	AZ61A AZ92A	–	AZ61A AZ92A	...
ZK51A ZK60A ZK61A	×	×	×	×	×	×	×	×	×	×	×	×	×	×	×	×	×	×	EZ33

Note: × Unweldable – no data.

High temperature and high extrusion ratio are the characteristics of hot extrusion for magnesium alloy. The high extrusion ratio causes grain refinement, resulting in the improvement of the mechanical properties of magnesium alloy.

In the following sections, a detailed description of the preparation technique for welding materials will be introduced, which includes the hot extrusion process and hot pull process.

4.2 Hot extrusion process of welding materials

The hot extrusion process includes the preparation and the extrusion of magnesium alloy ingots.

4.2.1 Preparation of magnesium alloy ingot

The first step in the preparation of magnesium alloy ingot is the melting of the magnesium alloy ingot.

A fusing agent is used to melt the magnesium alloy, which is composed of chloride and fluoride; the composition is shown in Table 4.4. The effects of the main composition of the fusing agent are as follows: $MgCl_2$ takes the role of adsorption of MgO and Mg_3N_2 inclusion. By combining with MgO to form a complex compound $MgCl_2 \cdot MgO$, the oxide inclusion can be removed. KCl can reduce the interfacial force and viscosity of the fusing agent and improve the spreadability of the fusing agent, making the fusing agent cover the magnesium alloy liquid uniformly. NaCl, by combining with the $MgCl_2 \cdot KCl$ to form the ternary system, reduces the melting point of the fusing agent. $BaCl_2$ increases the density of the fusing agent, making the magnesium alloy liquid and fusing agent separate, and increases the grain refinement level. CaF_2 increases the separating property of magnesium alloy liquid and fused slag, making the fused slag aggregate; then the fused slag on the surface can be removed easily.

Magnesium is very reactive, especially at high temperature; the magnesium alloy is oxidized easily, and the process of protecting the magnesium liquid from oxidation is the important factor in the melting of magnesium alloy. Furthermore, it may explode when the liquid magnesium alloy reacts with the water and oil under the high temperature; therefore, drying and degreasing of the melting tools

Table 4.4 Composition of fluxing agent wt%

Main composition					Impurity		
$MgCl_2$	KCl	$BaCl_2$	CaF_2	NaCl + $CaCl_2$	Insoluble	MgO	Water
38–46	32–40	5–8	3–5	8	1.5	1.5	3

is important for safety. The following indicate matter that need attention during the melting of magnesium alloy:

1 Drying and degreasing treatment of melting tools: The melting tools include the melting pot, stirring spoon, crucible tongs, shovel and ingot molds. These tools should be degreased with acetone or alcohol degreaser. All the tools which may come in contact with high-temperature magnesium alloy liquid must be treated with a degreasing substance.

2 Brushing the protective layer on the surface of the melting container and tools: Talcum powder is mixed with water-glass to form a paste. The mixture should be coated on the surface of melting tools such as the crucible, ingot mold and stirring rod which have to touch the liquid magnesium alloy. It has three purposes: (a) protection of tools from oxidation, (b) prevention of the liquid magnesium alloy from adhering to the tool surface, and (c) easy stripping. The coated protection layer should be dried to remove moisture because the presence of moisture may trigger an explosion.

3 Melting magnesium alloy: First, sprinkle a small amount of covering agent at the bottom of the crucible and put the metal into the crucible, and then sprinkle a certain amount of covering agent on the magnesium alloy metal. The covering agents need to be dried for one hour at a temperature of 120–150 °C before use. The role of a covering agent is mainly to prevent the liquid magnesium from oxidizing and burning. Finally, put the crucible with the magnesium alloy into the furnace heated to 700 °C and insulated until the magnesium alloy is completely melted.

4 The first mixing and deslagging: Using the stirrer, which has been dried, stir the magnesium alloy melting liquid, and then remove the slag and sprinkle covering agent on the surface of the magnesium alloy melting liquid. The slag, which is taken out from the crucible, should quickly be put into the sand box and covered with fine sand to prevent it from burning. The fine sand to be used should be pre-dried.

5 Stewing: The magnesium alloy liquid should be stewed for 20 minutes after the previous procedure. The role of stewing is to allow the molten slag to float from the magnesium alloy melting liquid to the surface.

6 The second mixing and deslagging: The procedure is the same as for the first mixing and deslagging. The purpose is to remove the oxide inclusions produced in the stewing process and to ensure that there are no oxide inclusions during the casting process.

7 Casting: After the second mixing and deslagging, the liquid magnesium alloy is poured into the ingot mold. Pay attention to the following in the casting process: (a) the mold should be preheated to 500–550 °C; (b) the magnesium alloy casting temperature should be about 700–750 °C; (c) the mold should be protected with argon to expel the air, to prevent the liquid magnesium alloy from oxidation; (d) the slag trap should be used to remove the slag. Figure 4.1 shows a flow diagram for the preparation of magnesium alloy ingots.

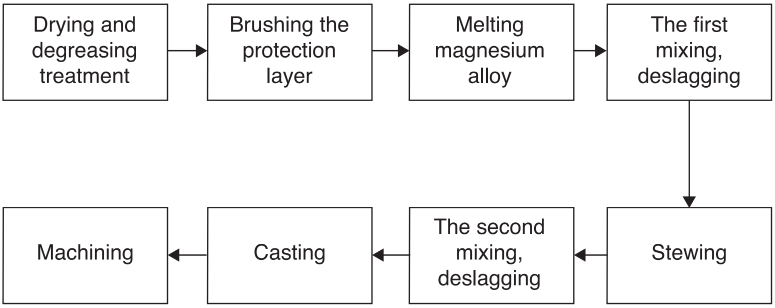
Drying and degreasing treatment
Brushing the protection layer
Melting magnesium alloy
The first mixing, deslagging
Stewing
The second mixing, deslagging
Casting
Machining

4.1 Flow diagram for melting of magnesium alloy.

The cast magnesium alloy ingot will be machined to obtain the appropriate size (2 mm less than the diameter of extrusion cylinder) and surface quality. The surface of the magnesium alloy ingot should be smooth, without inclusions, porosity and other defects, as shown in Fig. 4.2.

4.2.2 Extrusion of magnesium alloy ingot

Figure 4.3 shows the schematic diagram of a wire extrusion device for magnesium alloy, that is, the direct extrusion mode.[5] The device includes an extrusion shaft, extrusion mat, extrusion cylinder, extrusion die, cushion and the bed. The extrusion shaft, extrusion mat, extrusion cylinder and extrusion die should be made with hot die steel to ensure their high-temperature strength. The extrusion mat should match up with the extrusion cylinder and ensure smoothness to prevent the magnesium alloy from leaking back during the extrusion process. The heat-retaining part is needed to hold the temperature of the extrusion device.

4.2 Magnesium alloy ingot after machining.

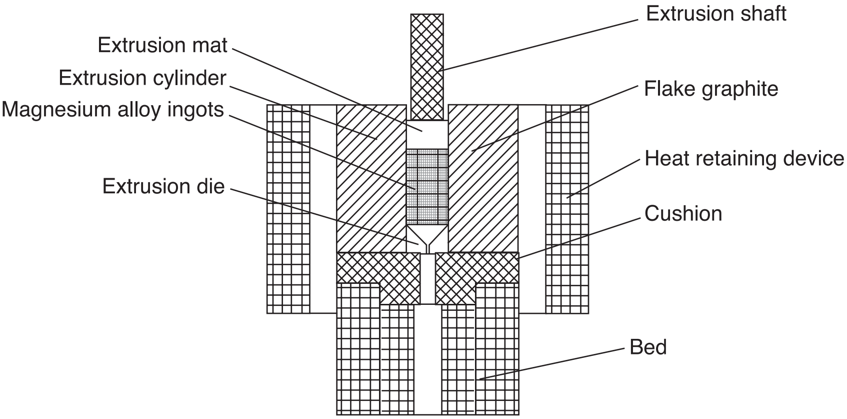

4.3 Schematic diagram of extrusion device for magnesium alloy welding materials.

Extrusion steps

Arrange the extrusion die, magnesium alloy ingots with outer pack flake graphite, and extrusion mat into the extrusion cylinder in an orderly fashion. Then, put the extrusion cylinder and cushion into the electrical furnace heated to 500–550 °C, holding for 1–1.5 hours to ensure temperature uniformity of the ingots and die. At the same time, the bed is preheated to 350–400 °C, the heat-retaining device is preheated to 400–450 °C and the temperature is held constant. Then, put the extrusion cylinder and cushion on the bed, install the heat retaining device outside and place the extrusion shaft on the extrusion mat. These devices are installed in the extrusion machine. Then, extrusion begins. A magnesium alloy wire arises from the extrusion die. The diameter of magnesium alloy wire depends on the diameter of the extrusion die. During the extrusion process, nitrogen is used to protect the extrusion die and magnesium alloy from oxidation. Figure 4.4 shows the flow diagram of the extrusion process of magnesium alloy ingots.

During the extrusion process, the following needs attention: the extrusion pressure and extrusion speed should be controlled carefully because excessive extrusion pressure can easily result in extrusion mold damage, and too little extrusion pressure would result in difficult formation of magnesium alloy wire.

Too fast an extrusion speed may result in magnesium alloy wire blow out because the deforming speed of magnesium alloy metal in the extrusion die makes the temperature rise under the friction and shear stress. In addition, the extrusion cylinder should maintain a temperature of 400–450 °C. This is because magnesium alloy has a high thermal conductivity. It is extremely sensitive to temperature changes, and the decrease of temperature may put strain on the extrusion and formation of the wire.

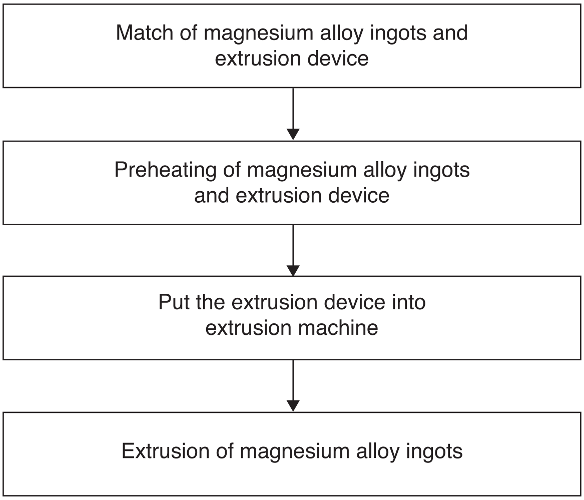
Match of magnesium alloy ingots and extrusion device
Preheating of magnesium alloy ingots and extrusion device
Put the extrusion device into extrusion machine
Extrusion of magnesium alloy ingots

4.4 Flow chart of extruding process for magnesium alloys.

4.2.3 The extrusion processing parameter

1 Preheated temperature of magnesium alloy ingots: Magnesium has a close-packed hexagonal structure. At room temperature, magnesium has only three slip systems, and its plastic deformation depends on the coordination of slipping and twinning deformation. When the temperature is lower than 250 °C or so, the plastic deformation includes the basal plane $\{0001\}<11\bar{2}0>$ slipping and $\{10\bar{1}2\}<10\bar{1}1>$ twinning, so the plastic deformability is weak. When the temperature is higher than 250 °C, the slipping of $\{10\bar{1}0\}$ prism plane $<10\bar{2}1>$ orientation comes into play. At the higher temperature, the slipping could occur on the $\{10\bar{1}1\}$ prism plane$<10\bar{2}1>$orientation. Figure 4.5 shows the slipping system of magnesium.

So, the plastic deformation of magnesium alloy occurs at high temperature. The appropriate deformation temperature range is 350–460 °C. The magnesium alloy ingots must be preheated before extrusion deformation. The preheated temperature is higher than the deformation temperature, that is, about 450–530 °C. To ensure the uniform temperature distribution of magnesium alloy ingots, one hour heat retaining is needed.

2 Preheating of extrusion die: When the high-temperature magnesium alloy ingots come in contact with the cold extrusion die, cracks easily appear. At the same time, the temperature of ingots decreases quickly, and the extrusion process would become difficult. So, the extrusion die should be preheated together with the magnesium alloy ingots.

3 Deformation rate: When the deformation rate of magnesium alloy ingots is high, the thermal effect of the deformation process will increase the temperature

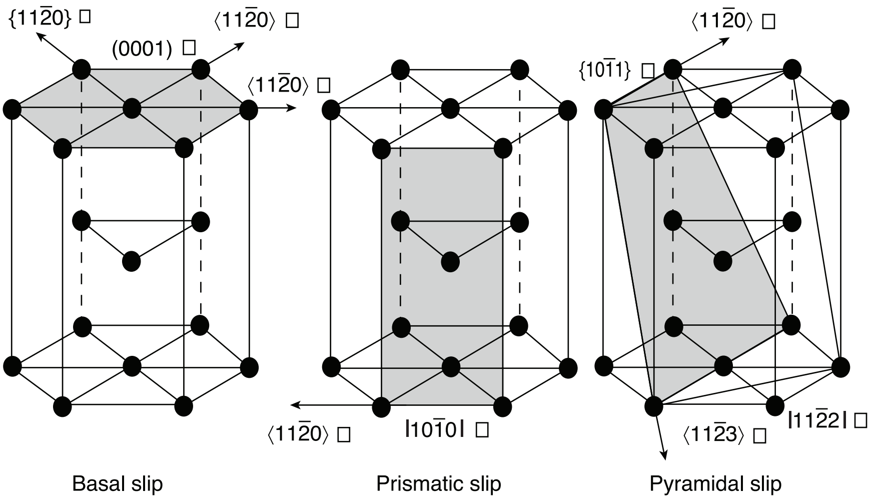

4.5 Slip systems of magnesium alloy.

of the extrusion billet, which would decrease the flow stress, and the required extrusion pressure will drop. But when the deformation rate is too high, the required extrusion pressure actually increases. This is due to deformation hardening of the metal in the hot extrusion process. The deformation hardening could be softened by the recrystallization process. However, it needs time to recrystallize. If the deformation rate is too fast, the softening effect of recrystallization will not take place and then the deformation resistance increases.

4 Lubricants: During the hot extrusion process of magnesium alloy welding wire, in order to reduce the deformation resistance, it is necessary to add the appropriate lubricant in the extrusion cylinder. As a result of the high temperature extrusion above 400 °C, graphite lubricant is selected. In addition, the presence of lubricants can also play a role in insulation and can improve the service life of the extrusion die.

4.3 Component design of welding materials

Because the boiling point of magnesium is lower than that of other elements in the process of magnesium alloy welding, it is easy to volatilize and segregate magnesium in the weld bath. Hence, it is very important to study the boiling point of magnesium alloys to determine the ideal alloy composition for engineering applications. There are many methods for measuring the boiling point. When the vapor pressure is greater than 1 torr (1 mmHg), direct measurement, phase transition or air current-carrying methods can be adopted. Analysis of these methods throws some light on the phase transition occurring in the boiling phenomenon. When it is boiling, the saturated vapor pressure of a liquid equals the atmospheric pressure. The saturated vapor pressure of the liquid can be determined from the temperature. Hence, for a certain atmospheric pressure, the boiling point can be defined via the relationship between the evaporation capacity and the temperature. To measure the boiling point, the following method can be used: keeping the pressure of the system constant, changing the temperature of a sample incrementally, and then measuring the corresponding change of the sample in terms of weight or other property. When a sudden change occurs, this is the boiling point (phase transition point).[6,7]

For measuring of the boiling point, the pressure of the system is set equal to the atmospheric pressure, which is a constant. Then, the weight change of the sample with incremental change in temperature is measured. The temperature at which the weight suddenly changes is the boiling point of the sample. This is termed the weight loss method. The influence of several common alloying elements, namely Al, Zn, Mn and La, on the boiling point of magnesium, has been investigated and compared.

Four different magnesium alloys were obtained, with 2 wt% Zn, Al, Mn and La added to pure magnesium. The experimental results indicated that the various additions had different influences on the boiling point of the magnesium alloys. Among the additions, Zn affected the boiling point of magnesium alloy most strongly, followed by Mn, Al and La. The present results indicate that the maximum boiling point of Mg-Zn alloy occurs at the proportion of 6 wt% Zn, as shown in Fig. 4.6.[8] It provides the foundation for the preparation of the high-boiling point magnesium alloy welding materials.[9]

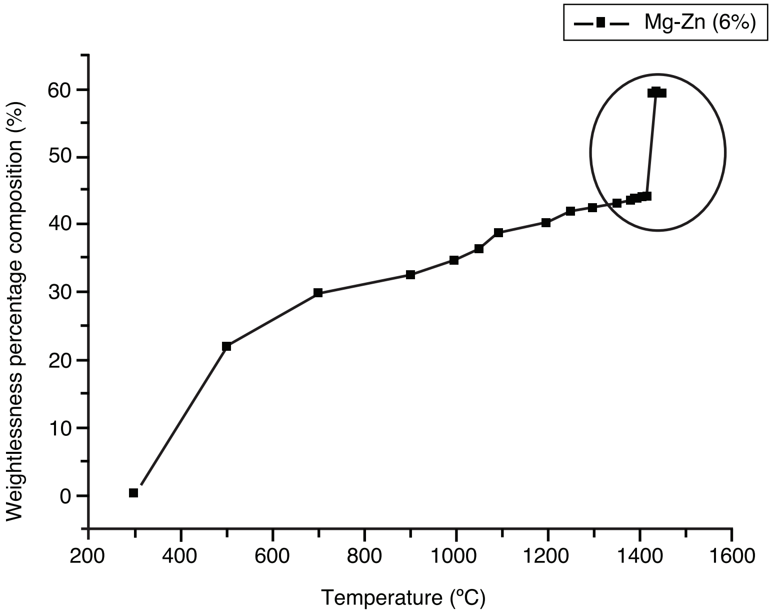

4.6 The boiling point of Mg-Zn with different compositions.

4.4 Hot pull process of welding materials

It is known that it becomes more and more difficult to extrude the magnesium alloy wire as the diameter of the wire becomes smaller and smaller. When the diameter of wire is smaller than 2.0 mm, the difficulty of extrusion increases rapidly. In addition, the 1.2–2.0 mm diameter magnesium alloy wire produced with the extrusion method is too soft to ensure the continuity of the wire-feeding process during welding.

To ease the production, increase the production efficiency and enhance the wire quality of the 1.2–2.0 mm diameter magnesium alloy wire, the hot pull process is used to produce 1.2–2.0 mm diameter magnesium alloy wire.

Figure 4.7 shows a hot pull device diagram. The thick wire is first preheated in the preheat furnace, and then passed through the wire drawing die and fixed on the wire drawing machine. The thick wire is pulled through the wire drawing die by the force of the wire drawing machine.

The process parameters of the hot pull process are described as follows:

1 Preheat temperature: When the temperature is higher than 250 °C, the plastic deformability of magnesium alloy would increase to a great degree. So, the preheat temperature of magnesium wire is selected in the range of 250–340 °C. When the temperature is higher than 340 °C, the magnesium alloy wire cannot be drawn due to oxidation.
2 Wire drawing die temperature: To avoid the shock chilling of thick wire by the wire drawing die, the wire drawing die should be preheated to the temperature near that of thick wire, usually 25 °C lower than the thick wire. This temperature difference would be compensated by the heat produced through friction and deformation of the magnesium wire during the hot pull process.

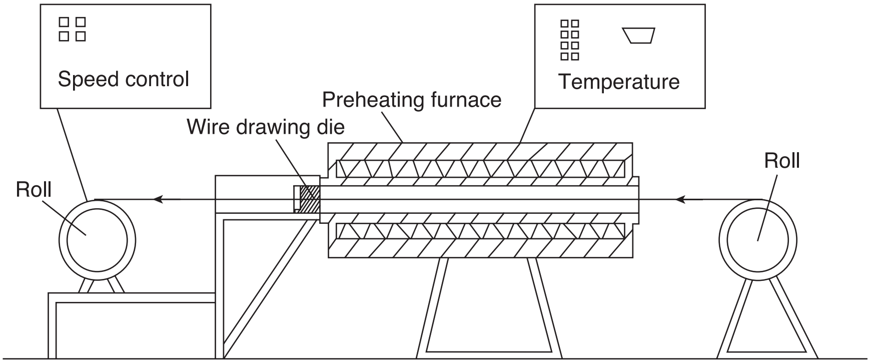

4.7 Hot pull equipment diagram.

3. Drawing speed: The magnesium wire is continually preheated during the hot pull process, so the drawing speed should hold sufficiently to ensure the preheat time.
4. Deformation quantity: Due to the low plasticity of magnesium alloy, the deformation quantity for each pass during the hot pull process should be lower than 20%.
5. Lubricants: During the hot pull process of magnesium alloy welding wire, in order to reduce the deformation resistance, it is necessary to add the appropriate lubricant to the wire drawing die. As a result of the hot pull above 250 °C, the gredag or molybdenum disulphide lubricant is selected. In addition, the lubricants should be cleared entirely after the hot pull process.

Magnesium alloy wires (<2.0 mm diameter) produced by the hot pull process have a better surface quality (sphericity or roundness) and straightness than those produced by the hot extrusion process.

4.5 Microstructure and strength of welding materials

The typical microstructure of magnesium alloy welding wire (AZ31, Φ3.0 mm, Φ1.6 mm) is shown in Fig. 4.8. It can be seen that the microstructure is composed of equiaxed grains, and it has been greatly refined compared with the as-cast microstructure. This is due to the dynamic recrystallization of magnesium alloy under the higher extrusion temperatures and grain refinement caused by the high extrusion ratio and high plastic deformation rate.

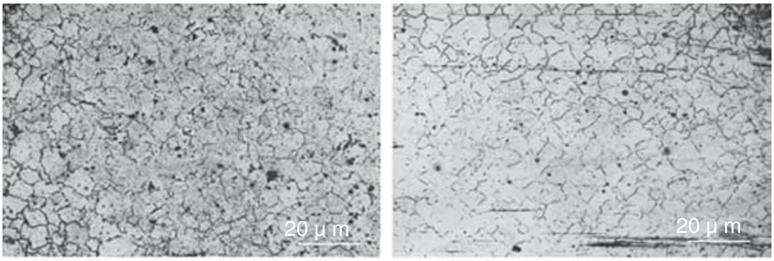

Φ3.0mm wire

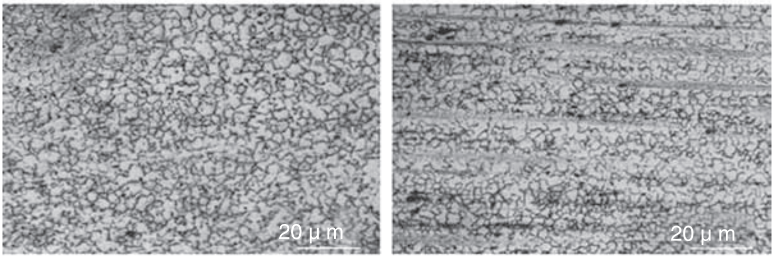

Φ1.6mm wire

4.8 Microstructure of magnesium alloy welding wire.

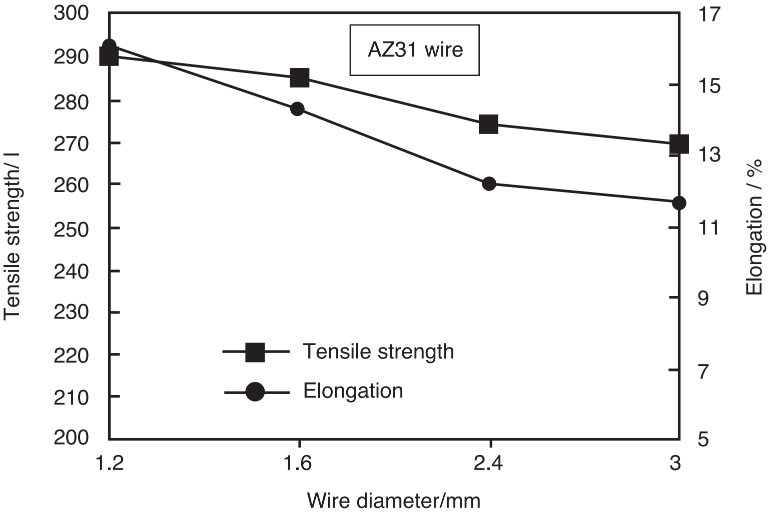

4.9 Ultimate tensile strength and elongation of welding wire.

The grain of magnesium alloy wire is refined greatly, leading to the increase of mechanical properties. Magnesium alloy welding wire has good tensile strength, good plasticity and high elongation. The tensile strength and elongation of different diameter wire (AZ31) are compared, as shown in Fig. 4.9, indicating that the smaller the diameter of the wire, the higher the tensile strength and elongation. The good tensile strength and plasticity of magnesium alloy wire will benefit the filler wire welding process.[10]

4.6 References

1. Kazuhiro N (2001). Weldability of magnesium alloys. *J Light Met Weld Constr* **39**(12): 26–35.
2. Avedesian MM, Baker H, editors (1999). *ASM Speciality Handbook Magnesium and Magnesium Alloys*. Ohio: ASM International.
3. Takahashi H, Oishi Y, Wakamatsu K, Kawabe N (2003). Tensile properties and bending formability of drawn magnesium alloy pipes. *Mater Sci Forum* **419–22**: 345–8.
4. Robert E (2001). Magnesium alloys and their applications. *Light Met Age* **6**: 54–8.
5. Chang-Fu D, Li-Ming L, Yu-Gang M (2004). Research of extruding stress in the process of extruding magnesium alloy welding wire. *J Plast Eng* **11**(3): 35–8, 42.
6. Lu YZ, Wang QD, Zeng XQ, Ding WJ, Zhai CQ, Zhu YP (1999). Effects of rare earths on the microstructure, properties and fracture behavior of Mg-Al alloys. *Mater Sci Eng A Struct Mater* **278**(1–2): 66–76.
7. Ying L, Chen WP, Zhang WW, Zhang DT, Li YY (2004). Effects of RE on microstructures and mechanical properties of hot-extruded AZ31 magnesium alloy. *J Rare Earths* **22**(4): 527–32.

8. Liu SH, Liu XJ, Liu B, Liu LM, Jin WZ, Hu XJ (2005). Effect of some alloying elements on boiling point of magnesium. *Mater Sci Tech* **21**(6): 735–8.
9. Dong C, Liu L, Gao H, LIU D (2005). Effect of antimony on microstructure and performance of AZ31 magnesium alloy welded joint. *China Weld* **14**(1): 44–7.
10. Dong C, Liu L-M, Zhao X (2005). Welding technology and microstructure of tungsten inert-gas welded magnesium alloy. *Trans China Weld Inst* **26**(2): 33–6.

5

Welding and joining of magnesium alloys to aluminum alloys

L. LIU, Dalian University of Technology, China

Abstract: Laser-TIG hybrid welding, diffusion bonding and laser weld bonding (LBW) of Mg to Al techniques are introduced in this chapter. The formations of Mg-Al intermetallics have a negative effect on the properties of joints. In LBW Mg-Al joint, the strength of the joint is about 80% of the Mg base metal.

Key words: Mg, Al, laser-TIG hybrid welding, diffusion bonding, laser weld bonding.

5.1 Introduction

With the rapid development of magnesium (Mg) alloys, the joining of Mg alloy to Al alloy has attracted more and more attention. Dissimilar metal welding is influenced by many factors. It is more difficult than the common welding process, especially for Mg and Al alloys. Joining processes, such as tungsten inert gas (TIG) welding, laser welding (Borrisutthekul, Miyashita and Mutoh, 2005), laser-TIG hybrid welding (Liu et al., 2005a; Liu, Liu and Liu, 2006), friction stir welding (FSW) (McLean et al., 2003; Sato et al., 2004; Somasekharan and Murr, 2004; Gerlich, Su and North, 2005; Yan and Xu, 2005; Chen and Nakata, 2008) and diffusion bonding (Liu, Tan and Liu, 2007; Mahendran, 2008; Wang et al., 2008; Zhao and Zhang, 2008), have been tried for joining Mg alloys to Al alloys (Liu, Liu and Liu, 2006). Mg-Al intermetallic compounds found in most of Mg-Al joints are known as crisp phases and have a negative effect on the properties of joints. Thus, it is hard to join Mg alloy to Al alloy by melted welding method only. In order to obtain joints with high strength between Mg and Al alloys, many new kinds of welding technologies should be used.

Friction stir welding is a solid-state joining process, and it has a high possibility of making high-quality dissimilar welds of Al and Mg alloys compared to fusion welding. Sato et al. (2004) previously preformed dissimilar FSW of Al alloy 1050 and Mg alloy AZ31, and the result showed that the irregular-shaped region contained a large number of intermetallic compounds, $Al_{12}Mg_{17}$. Kwon, Shigematsu and Saito (2008) investigated the dissimilar FSW between Mg and Al alloy plates with thicknesses of 2 μm. Chen and Nakata (2008) studied the friction stir lap joints of Al and Mg alloys.

Contact reaction brazing (CRB) is a method of brazing in which the joint is formed by means of low-melting phases formed by the eutectic reaction of the

Table 5.1 The main problem of welding Mg to Al alloy

Problems	Possible negative effect	Technical solution
Chemical activity of base metal	Difficult wetting by brazing filler metal	Halide brazing fluxes or vacuum brazing
Fast growth of oxide film		
Low solidus of base metals	Changes in structure and shape of brazed parts	Short holding time or low temperature filler metals
Joining temperature is close to solidus		
Formation of the intermetallic compounds of Mg/Al	Limited tensile-strength of the joint	Choose the correct parameters and filler metal

Source: Shapiro (2005).

dissimilar metals. This method is contamination-free because the joint can be achieved without the use of flux. Liu, Tan and Liu (2007) used the CRB to join AZ31B alloy and 6061 alloy plates by an economical and available zinc-based brazing alloy. The research showed that the inter-diffusion between Mg and Al substrate is impeded by the existence of a zinc-based brazing alloy, and hence the intermetallic compound of Mg and Al could be avoided. Wielage and Mücklich (2006) used the ultrasonic soldering to break the oxide layer. Furthermore, Li and Liang (2009) proved that the joints brazed by Mg-Al eutectic alloy had good erosion resistance, which shows that the Al-foil can easily be coated onto Mg, and the Al-coated Mg shows a much improved corrosion resistance.

Vacuum diffusion bonding is also used in the bonding of Mg/Al. Wang Juan, and Li (2008) investigated the microstructure at the interface of Mg/Al obtained by advanced vacuum bonding technology. Mahendran, Balasubramanian and Senthilvelan (2009) showed that the dominant parameters in diffusion bonding process were bonding temperature, bonding pressure and holding time. The main problems of welding Mg to Al alloys are shown in Table 5.1.

In this chapter, we shall introduce several new kinds of welding methods of Mg and Al alloys, which might be helpful to the researcher on this subject.

5.2 Hybrid laser-tungsten inert gas welding of magnesium and aluminum

Hybrid laser-TIG welding is an ideal process for Mg, as proved by our former work (Liu, Wang and Song, 2004). This high-speed welding process has realized the joining of Mg and Al alloys. However, cracking occurred in the most critical regions where the composition changed from Mg to Al (Liu et al., 2005b). Experiments were also performed with a laser only to lap join Mg and Al but some defects such as notching were found. Although notching is not a major problem in joining Mg and Al, there are better prospects in selecting the hybrid welding process than laser welding alone. Interlayer is always used in the dissimilar metal welding process. Ce is a kind of rare earth metal element, which can influence the microstructure of the laser-TIG hybrid welded Mg-Al joint to eliminate the cracks.

The optimized parameters for laser-TIG hybrid welding are: TIG current of 100 A, protective Ar gas flow of 7 L/min, laser current of 180 A, pulse duration of 3.2 ms, frequency of 39 Hz, a distance of 1.5 mm between laser and arc center (Dla) and welding speed of 1300 μm/min. The configuration of the laser-TIG welding system is shown in Fig. 5.1. Cerium foils of various thicknesses are manufactured. The strength of samples with cerium foils of different thicknesses as the interlayer is shown in Table 5.2. It can be seen that the addition of Ce interlayer improved the strength of the weld and that the strength varied according to the thickness of the cerium foil used as the interlayer.

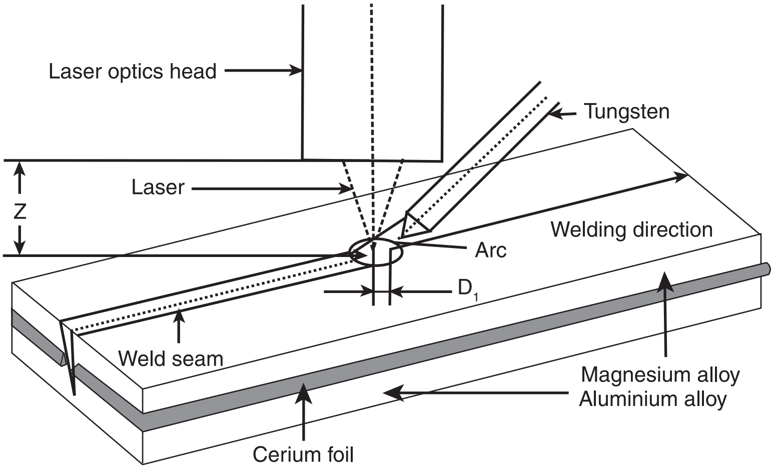

5.1 Configuration of the laser-TIG welding system.

Table 5.2 Strength of samples of Mg and Al joint with different thicknesses of cerium foils as interlayer

Sample group	Thickness of Ce (mm)	Shear load (kN)	Shear strength (MPa)
1	0.16	2.6	36.02
2	0.19	2.92	41.95
3	0.20	3.16	45.4
4	0.24	3.46	55.9
5	0.26	3.16	45.4

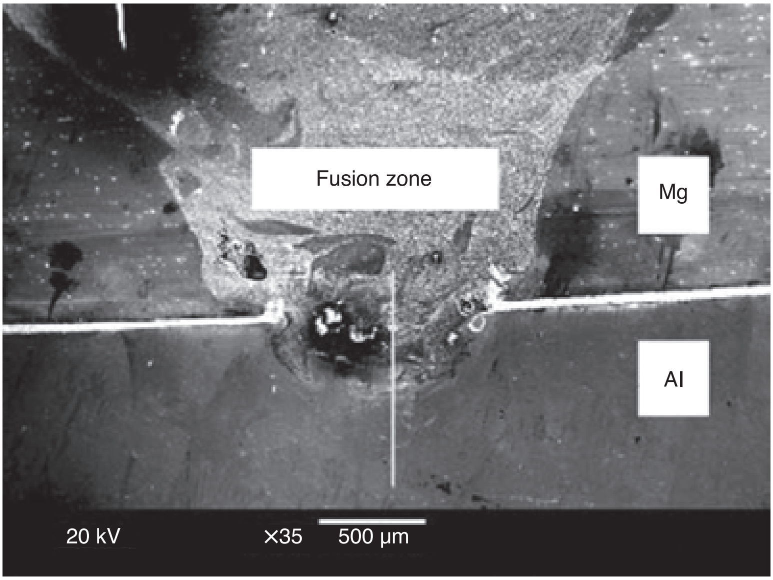

5.2 The SEM microstructure of Mg and Al lap joint.

The SEM microstructure of a Mg-Al lap joint made by hybrid welding with Ce as the interlayer is presented in Fig. 5.2. There are no macroscopic cracks in the joint, which always appear in the microstructure of Mg-Al joints made by the hybrid welding process. This indicates that the addition of Ce minimized the production of cracks.

The microstructure and composition of the middle of the fusion zone is shown in Fig. 5.3. The elemental analysis is conducted in the regions of the structure representing features. Because of the fineness of the microstructure after welding, the phases are very difficult to identify. The structure shown in Fig. 5.3(a) has countless little points dotted on the background consisting of 19 wt.% Al, 1.75 wt.% Ce and 64 wt.% Mg. According to the phase diagram of the ternary Al-Ce-Mg system (Grobner, Kevorkov and Schmid-Fetzer, 2002), the background is still estimated to be the as-eutectic structure after Ce is added to the Mg-$Mg_{17}Al_{12}$ eutectic phase. The structure represented in Fig. 5.3(b) has vortex flow patterns consisting of 84 wt.% Mg, 7.6 wt.% Al and a small amount of Ce, possibly close to the base material AZ31B. The structure represented in Fig. 5.3(c) shows typical oxide patterns consisting of 34 wt.% O, 29 wt.% Mg, 35 wt.% Al and 1.27 wt.% Ce. Because Ce is easily oxidized, some large areas of oxides may appear on the cross-section of Mg-Al joint with Ce as interlayer. However, it is not the main reason for cracks between Mg and Al during the welding process.

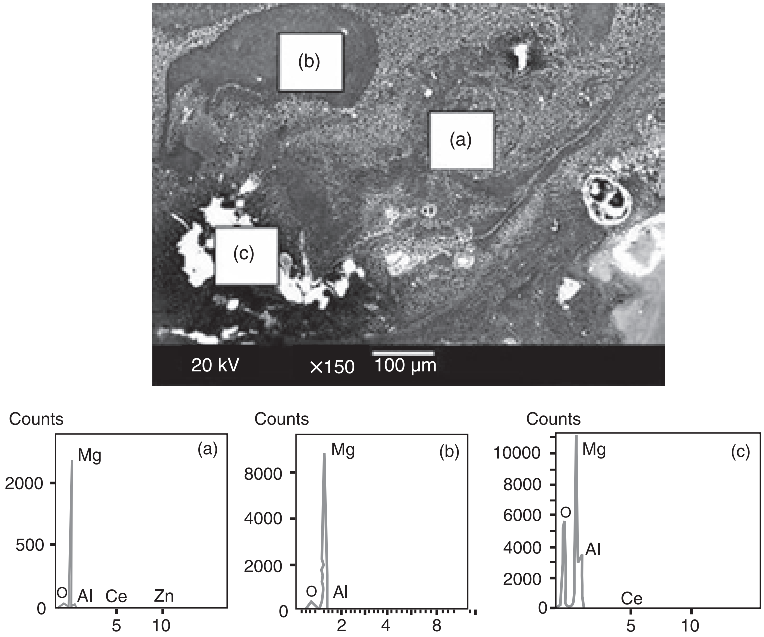

5.3 The microstructure and composition of the middle of the fusion zone.

Microstructures at the bottom of the fusion zone of the direct Mg-Al joint and that with added Ce are shown in Fig. 5.4(a) and (b), respectively. With different compositions of Mg and Al, the structure is very complicated, resembling frozen convection swirls. The microstructures at the bottom of the fusion zone of the direct joint are mainly composed of swirls, little dots and 'impurity phases.' The little dots are fine needles in different directions and disappear after adding Ce. Lots of vague impurity phases appear at the bottom of the fusion zone of the direct joint, much like dirt in the microstructure. After adding Ce, the microstructure becomes very clear without these impurity phases. The vague swirls of the black phase also change into the clear base phase dotted with little

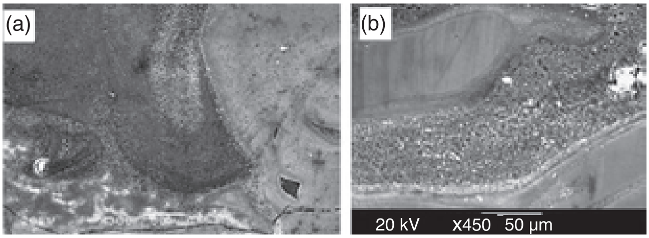

5.4 Microstructures at the bottom of weld pool in Mg/Al joint: (a) direct joint; (b) the joint with Ce.

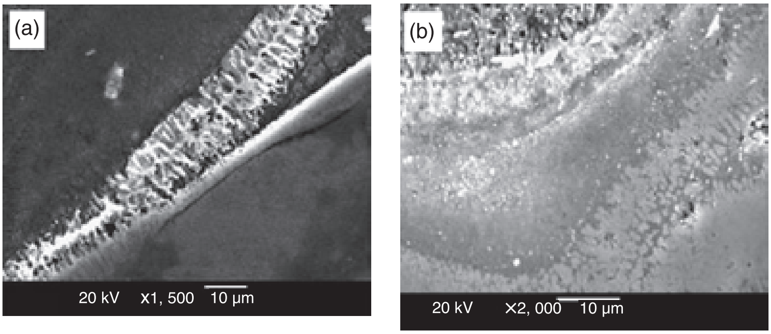

5.5 Interface in the Mg and Al joint: (a) direct joint; (b) the joint with Ce.

grains. Additionally, the interface of the two phases (the black phase dotted with little grains and the white phase in Fig. 5.4) changes from a rough edge to a smooth edge.

Figure 5.5(a) shows an interface between the Mg and Al direct joint made by the hybrid lap welding process. The microstructure looks like a 'spinal column', which is commonly known as a harmful microstructure with regard to strength. In Fig. 5.5(b), which shows the interface in the Mg-Al joint welded by the hybrid lap welding process with Ce as interlayer, three transitional sections are observed on the interface, although the microstructure cannot be seen clearly.

It can be concluded that the addition of Ce did not prevent the production of intermetallic compounds. How the change between the intermetallic compounds improved the strength will continue to be studied.

The EPMA image and distribution maps of major elements of hybrid welding of Ce added Mg-Al joint are presented in Plate I (in color section between pages 210 and 211). According to the distribution map of Ce in Plate I (b), Ce is not only distributed in the molten Mg but also at the interface of Mg and Al and in the molten or unmelted Al. Because the most critical regions are where the major composition changes from Mg to Al and the added Ce is distributed uniformly in these regions, it is very possible that Ce has an important influence on these most critical regions. From the distribution maps of Al and Mg in Plate I (c) and (d), it can be presumed that part of the molten Mg was formed in the fusion zone and moved downwards under the stirring of the laser and arc. In other words, the fusion zone in the hybrid welding of Mg-Al joint is mainly composed of the molten Mg, while only a small amount of Al is melted and makes waves in the molten Mg under the stirring of the laser and arc. It can be seen from the image that the microstructure pattern is consistent with the distribution of the elements, and the composition of the waves in the microstructure patterns is distinct from the base material. Fractography of the direct Mg-Al joint and that with added cerium is shown in Fig. 5.6 and Fig. 5.7. The fracture of the direct Mg-Al joint is

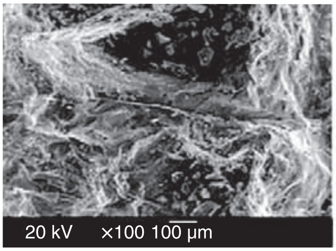

5.6 Fractography of Mg-Al direct joint.

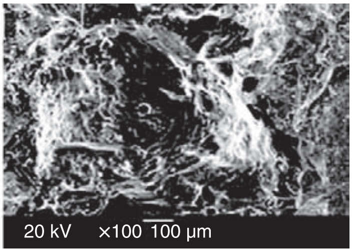

5.7 Fractography of the joint with Ce.

flatter than that with added Ce. Some dimples, indicated in Fig. 5.7 by arrows, rise in the fracture of the Mg-Al joint with added Ce, which indicates that the added Ce refines the microstructure of the fracture zone. But the strength of the laser-TIG Mg-Al joint with Ce as interlayer is still not appropriate and cannot be used in engineering production.

5.3 Diffusion-bonding magnesium to aluminum technology

5.3.1 Introduction

Joining dissimilar metals is very difficult, especially when the thermal conductivity of each is substantially different. Generally speaking, intersolubility is required in welding dissimilar metals. However, in some cases, a third metal which is soluble with the other two is needed to produce a successful joint. If the thermal expansion coefficients of dissimilar metals differ greatly, internal stresses will occur in the intermetallic zone during any temperature change of the weldment.

Diffusion bonding is often used in the dissimilar metal welding process. It can increase the strength of the joint by controlling the phase formation in the joint through restricting the reacting time and the interlayer composition. It is difficult to join Mg and Al alloys using the fusion welding technology, because of the formation of Mg-Al intermetallics. Although the thermal conductivity of Mg is close to that of

Al, the characteristics of the Mg-Al intermetallics, such as hardness and the thermal conductivity, are very different from those of Mg and Al. Thus, the interface between Mg and Al is the weak part of the joint. In the diffusion bonding of Mg and Al, an interlayer should be used and the reacting time should be controlled accurately.

5.3.2 Microstructure of diffusion-bonding Mg to Al joint

For Mg and Al alloys, Zn is a special element which exists in both the alloys. It can be used in the joining process as an interlayer. If the diffusion between Mg and Al takes a long time, there will be a large amount of Mg-Al intermetallics in the joint, which would have a negative effect on the strength of the joint. Therefore, the reacting time of diffusion bonding of Mg and Al should be very short. In order to understand the influence of Zn in the diffusion bonding of Mg and Al, the microstructure of the Mg-Al joint without Zn interlayer and with Zn-Ce interlayer are analyzed below.

Figure 5.8 shows the SEM images of interfacial structure of Mg-Al joints diffusion-bonded directly at 447 °C for 3 s. It can be seen that the interfacial

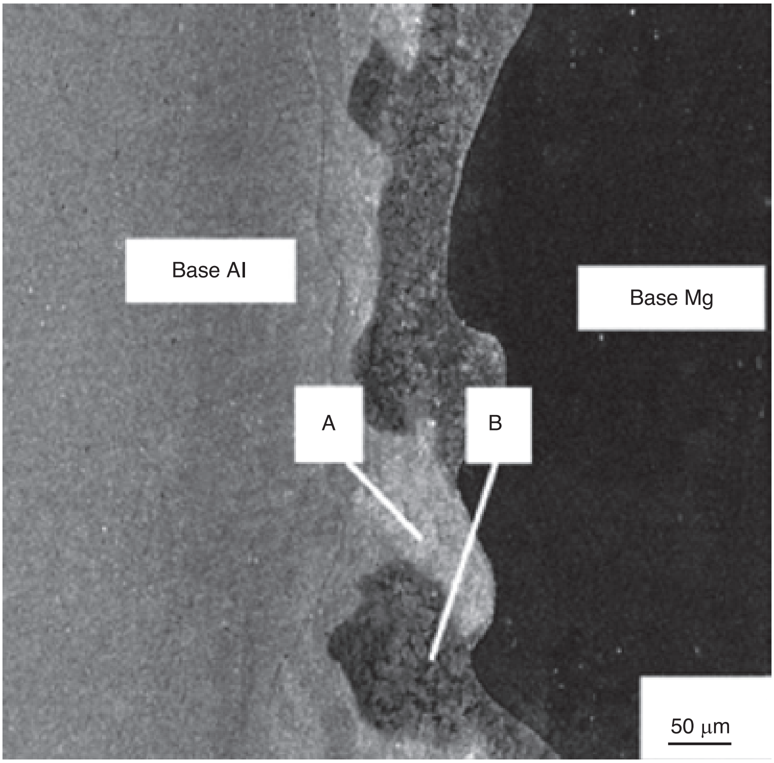

5.8 Interfacial microstructure of diffusion-bonded Mg-Al joint.

structure of Mg-Al joint consists of the hoar phase marked region A next to base Al and the dark eutectic phase marked region B next to base Mg. The narrowest part of region A exceeds 20 μm. The elemental analysis is conducted in regions A and B. Region A consists of 40.63 at.% Mg and 59.37 at.% Al. The stoichiometric proportion of Mg to Al is approximately 2:3. The selected area XRD has shown that region A is composed of Al_3Mg_2 compound. Region B is a eutectic zone composed of 68.97 at.% Mg and 31.03 at.% Al. Combining with the phase diagram of the binary Al-Mg systems, region B is estimated to consist of $Mg_{17}Al_{12}$ and Mg solid solution. The existence of these constituents in region B has also been identified by selected area XRD.

Shear strength tests are carried out on samples at the same joining conditions as the above joint. The maximum shear strength of Mg-Al joints using diffusion bonding directly is 41.3 MPa and this is not satisfactory. By XRD analysis, the fracture always occurs in the interface between base Al and intermetallic compound layer. To increase the strength of Mg-Al joint, Zn alloy interlayer is adopted. The interlayer is prepared by alloying zinc with Al and Ce. Adding Al to base Zn can make Al occupy the Zn crystal lattices and decreases the amount of base Mg into Zn interlayer, aiming to reduce Mg-Zn intermetallics. Addition of Ce attempts to improve the intermetallic patterns.

Figure 5.9 shows the SEM images of Mg-Al joints diffusion-bonded at 360 °C for 3 s with Zn alloy interlayer. It can be seen from Fig. 5.9(a) that there are many white second-phase particles (marked B) dispersed in the base of the bond region marked A, and near to side Al there is a thin second-phase layer with a thickness of about 1 μm which is marked C (the zone between the two black lines). Figure 5.9(b) is the high magnification of the bond region of the joint. It can be seen that the base of the bond region is a kind of single phase. The

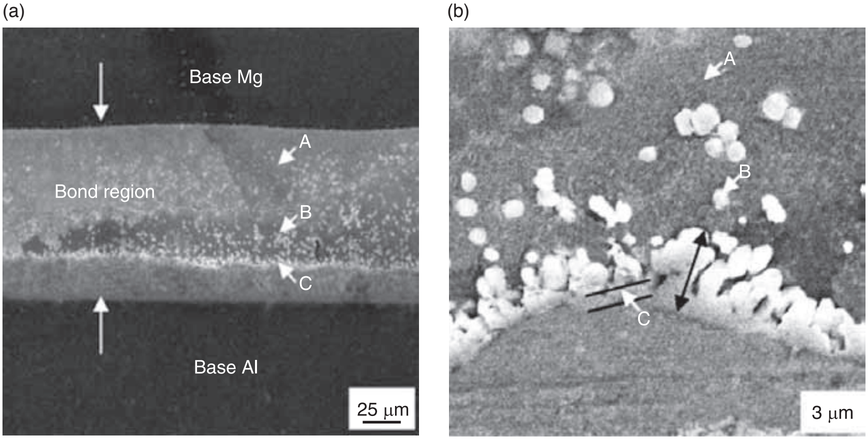

5.9 SEM images of Mg-Al joints diffusion-bonded with a Zn alloy interlayer at 360 °C for 3 s: (a) cross-section of the whole bond region, and (b) high magnification of the bond region of the joint.

average size of the second-phase particles is less than 1 μm. The second-phase thin layer and the second-phase particles precipitated on top of it combine and form a continuous layer of which the maximal thickness is less than 5 μm (indicated by black arrows).

Figure 5.10 shows a back-scattered electron image and elemental distributions of the cross-section of an Mg-Al joint diffusion-bonded with a Zn alloy interlayer. The bond region can be divided into three zones: 1, 2 and 3. The concentration profiles of major elements (Al, Mg, Zn, Ce) across the bond region marked with

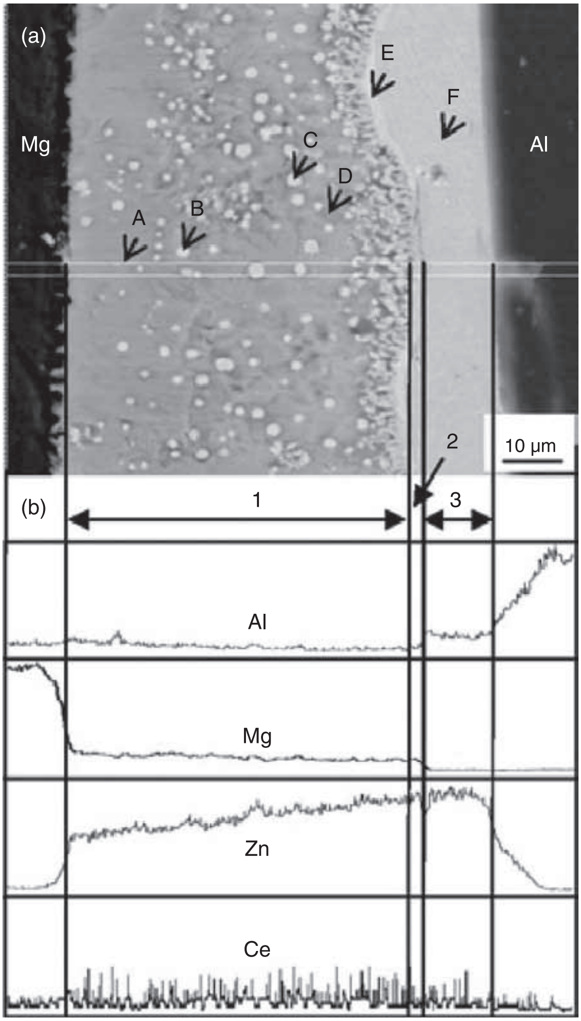

5.10 EPMA analysis results of bond region of Mg-Al diffusion bonded joint with a Zn alloy interlayer at 360 °C for 3 s: (a) back-scattered electron image; (b) elemental distributions.

white lines in Fig. 5.10(a) are shown in Fig. 5.10(b). Zn and Al elements diffuse from the interlayer to the base Mg. The concentration profile of Al is flat in zones 1 and 2, while there is an increase from zone 2 to zone 3. The concentration of Zn decreases gradually from zone 3 to zone 1. The distribution of Mg is similar to Al in zones 1 and 2, but there is almost no Mg in zone 3. The concentration profile of Ce fluctuates regularly in all zones, indicating that Ce is distributed dispersively in the bond region. In the heating process of diffusion bonding, the elements of contact surfaces of Mg-Zn begin to diffuse mutually. At a temperature approaching 360 °C, the low-melting eutectic liquid appears, which speeds up diffusion of elements from solid base into the liquid, and the liquid region starts widening continuously. And after that, zone 1 forms in the cooling process. At the same time, the elements in the liquid diffuse to the solid. As the element diffusion rate in solid is far lower than that in liquid and the contacting time between the liquid and the solid in this study is very short, the Mg elements can only diffuse to a close distance and form a thin second-phase layer, namely zone 2 in Fig. 5.10(b). The occurrence of zone 2 impedes the further inter-diffusion of Mg, Al and Zn; thus, there are almost no Mg elements in zone 3, and the contents of Al and Zn are relatively high. Noticeably, the second-phase particles precipitated on top of zone 2 (viz. the second-phase thin layer) are formed by element diffusion from the solid into the liquid, and they belong to zone 1.

5.3.3 Mechanical properties

Shear strength tests are carried out on samples of the Mg-Al joints diffusion-bonded with Zn alloy interlayer at the same joining conditions. The lowest value is 75 MPa and the highest is 83 MPa, which is twice that of the Mg-Al joints diffusion-bonded directly. For the bond region of dissimilar metal joints, the particle distribution of intermetallic compounds has no harmful effect on the joint performances; moreover, it strengthens the joints. However, once intermetallic compounds connect and their thickness is more than 5 μm, their high brittleness and internal stress and plasticity and strength of joints will obviously be decreased (Liu and Di, 1990). During the bonding of Mg-Al directly, once the eutectic liquid appears in the interface, a large number of Mg elements diffuse to base Al and form the intermetallic compounds. The study indicates that even if the heating rate is improved to decrease inter-diffusion of bases, the direct contact of Mg-Al cannot avoid a large number of Mg-Al intermetallic compounds, which exist as a layer or reticulation, and their thickness greatly exceeds 5 μm. So, the joint strength of the diffusion bonding of Mg-Al directly is unfavorable. By the addition of the Zn alloy interlayer between Mg and Al, the microstructure of bond zone of joints is improved greatly. Though intermetallics can be formed in the bond region, they precipitate dispersively, which can produce precipitation strength. The finer the second-phase size is, the more obvious the reinforcement effect will be (Hao et al., 2005). The thickness of the connective intermetallics in the bond region is less than 5 μm and has no effect on the mechanical characters of the joints. So the shear strength of joints is improved greatly by using the Zn alloy interlayer. By comparing interface structure and shear strength of diffusion bonding of Mg-Al with and without Zn alloy interlayer, it can be concluded that the direct contact of Mg-Al cannot avoid a large number of Mg-Al intermetallic compounds which lower the mechanical properties of the joints.

5.3.4 Welding mechanism

The diffusion bonding of Mg and Al is difficult in a common process. Diffusion bonding with a sound interlayer has been considered a feasible solution because the composition of interlayer could be adjusted flexibly to meet the requirements of phase constituent together with the mechanical properties of the joint. By the diffusion bonding of Mg and Al alloys using Zn-base interlayer containing Al and Ce, the intermetallic phases of the bonding zone change into dispersive particles and thin layers which improve joint strength greatly. Zn has a relatively low melting point, has the same crystal lattice with Mg and can form a solid solution with Al. A Zn-base interlayer of a different composition can be prefabricated onto the surface of Al alloy sample by hot dipping technique. In this way, the harmful effects of Al oxide film can be eliminated effectively. Additionally, a very short holding time is to be employed in the diffusion bonding experiments to avoid the excessive inter-diffusion between base Mg and Al alloys to form coarse Mg-Al intermetallics. The Zn interlayer would change the distribution and the formation of the intermetallics to an extent. It could be concluded that the interlayer must be used in the diffusion bonding of Mg and Al. If the content of the interlayer could change the formation and distribution of the intermetallics, the performance of the joint would be increased. Still, Zn interlayer is not the best interlayer for the diffusion-bonding of Mg and Al, and the composition of the interlayer should be studied.

5.4 Laser weld bonding magnesium to aluminum technology

5.4.1 Introduction of laser weld bonding technology

Laser weld bonding (LWB) technology is a new kind of welding technology. It is put forward as an alternative to adhesive bonding and laser welding. Laser welding has a small heat effect zone, which would have little effect on the adhesive bonding area. Otherwise, the adhesive in the fusion zone would be decompounded during the laser welding process, which would make little difference to the property of the joint. Thus, it could be said that laser welding and adhesive bonding would have little negative effect on each other. The excellent characteristics of laser welding and adhesive bonding are included in LWB technology. Still, adhesive bonding provided excellent stress distribution over large bonding areas, and welds improved the peel resistance of adhesives. Thus, the property of an LWB joint is better than that of laser welding and adhesive bonding alone. LWB technology is a new kind of hybrid bonding of metallurgy joining, mechanical joining and chemical joining. It is quite fit for the joining of dissimilar light metals.

LWB technology was first used to join Mg to Al alloy in 2006 (Liu, Wang and Song, 2007). The element distribution of LWB joint was analyzed in 2007 (Liu, Wang and Zhang, 2007). The different parts in LWB joint were explained in 2007 (Wang et al., 2007). Because of the addition of adhesive, the distribution of the Mg-Al intermetallics is changed, which is helpful for the property of the LWB Mg-Al joint. The strength of the joint is nearly 80% of Mg base metal.

The configuration of the LWB sample is shown in Fig. 5.11. In LWB Mg alloy to the Al alloy process, the Mg alloy is put on top of the Al alloy. The adhesive is in the middle of the Mg alloy and the Al alloy. Laser power is on top of the Mg alloy. The parameters of the laser welding are the main factors that affect the properties of the joints.

5.4.2 Microstructure of laser weld bonding Mg to Al joint

In LWB joint, the upside Mg alloy has melted completely, while the laser is operated in a conductive mode or a keyhole mode within the Al alloy. The sample with the keyhole welding mode in Al alloys is not of high quality. Thus, the microstructure of this kind of joint cannot be observed very clearly. The microstructure analyzed below is mainly about the samples with the conductive welding mode in Al alloys.

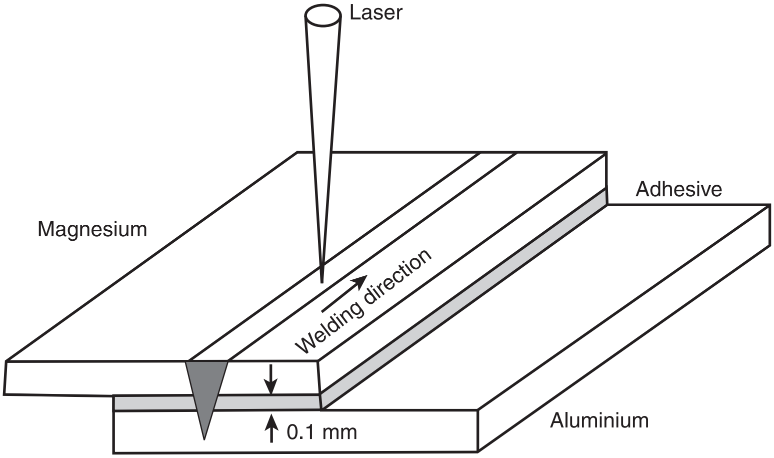

5.11 The configuration of the laser weld bonding sample.

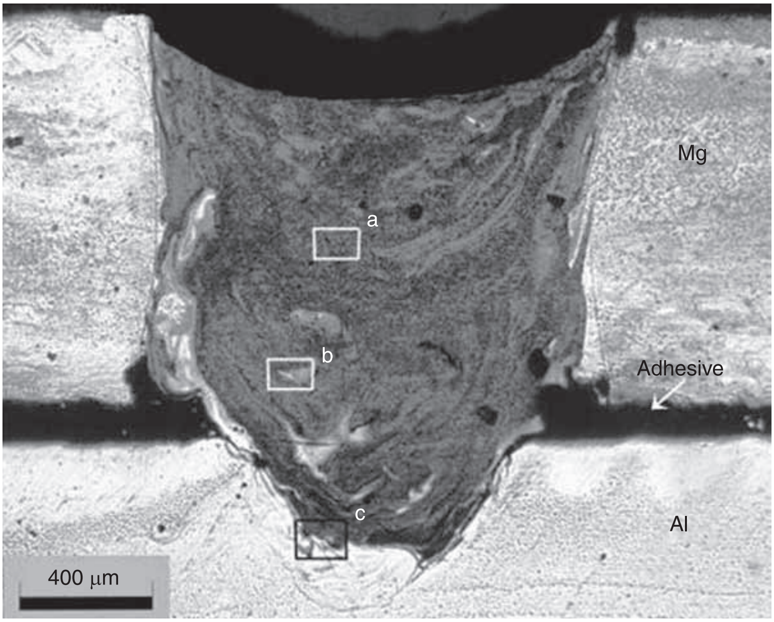

5.12 The transverse section of LWB joints.

The microstructure of the transverse section of LWB joint was examined by means of a scanning electronic microscope (SEM), as shown in Fig. 5.12. In the fusion zone, there is no obvious welding defect. The microstructures of the Mg fusion zone and Al fusion zone were examined separately.

The fusion zone of the Mg alloy is examined by SEM, as shown in Fig. 5.13, which is obtained from 'Part a' of Fig. 5.12. The grains in the fusion zone are refined with the effect of laser welding. There are few Mg-Al intermetallics in the Mg fusion zone, and there is no residual adhesive in the Mg fusion zone.

Figure 5.14 shows the SEM microstructure of 'Part b.' There are two obviously different phases in Part a. From the EDS analysis, Part A1 consists of 73.2 at.% of Mg and 26.8 at.% of Al, and Part A2 consists of 64.4 at.% of Mg and 35.6 at.% Al. The phases should be analyzed with the Mg-Al binary equilibrium phase diagram, as shown in Fig. 5.15. The percentage composition at Mg-$Mg_{17}Al_{12}$ eutectic point is 67 at.% of Mg and 33 at.% of Al. Thus, Part A1 should be Mg-$Mg_{17}Al_{12}$ eutectic phase with partially divorced eutectic morphology, and Part A2 should be Mg-$Mg_{17}Al_{12}$ hypereutectic phase. These two kinds of phases are well-joined.

The β-$Mg_{17}Al_{12}$ eutectic phase in Mg alloy is often found in the casting of AM60 alloy and extruded AZ91 alloy. The toughness of Mg alloys can be hampered by much rigid and crisp β-$Mg_{17}Al_{12}$ phase precipitated from grain

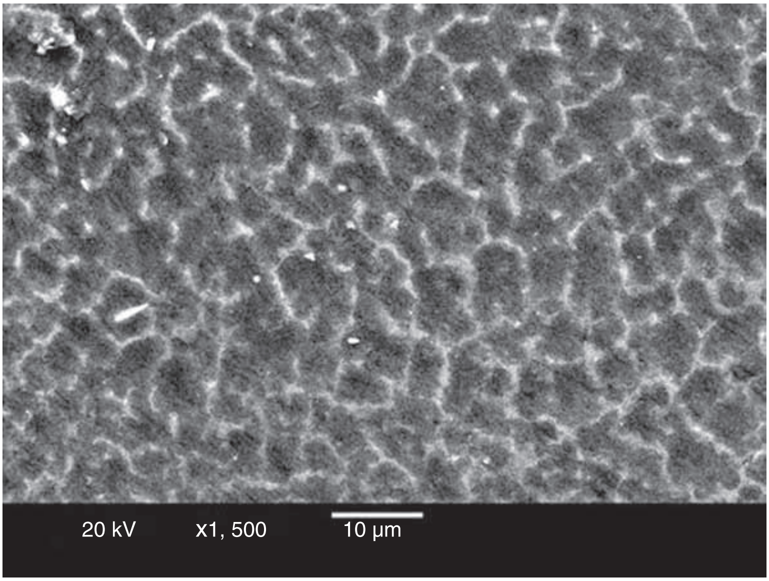

5.13 Microstructure of Mg fusion zone in the LWB Mg to Al joint.

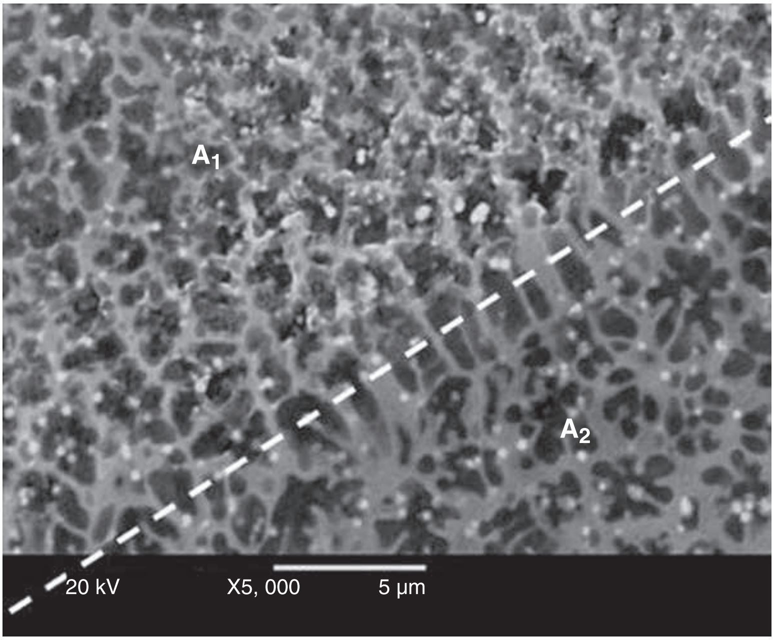

5.14 The microstructure of Mg-$Mg_{17}Al_{12}$ eutectic and hypereutectic phase.

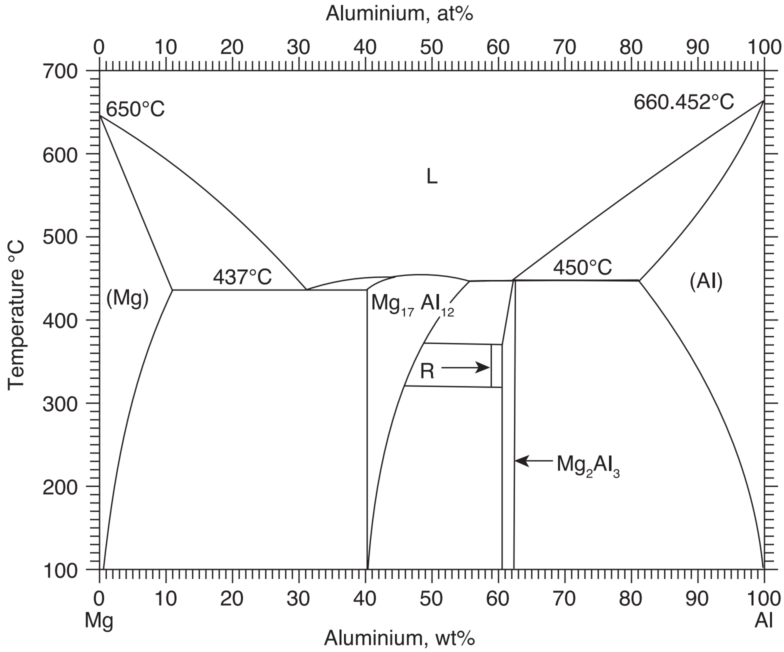

5.15 Mg-Al binary equilibrium phase diagram.

boundary in Mg-Al alloy with non-equilibrium solidification. When the percentage of the Al in the Mg alloy is between 6 and 32.3%, the Mg-Al phase is divorced eutectic. With the content of the Al element increasing, the Mg-Al phase in the Mg alloy is changed.

The Mg-Al interface in LWB fusion zone was analyzed by SEM, as shown in Fig. 5.16. The structures could be separated into three parts. The first part mainly consisted of the molten Mg alloy, the second part mainly consisted of the molten Al alloy and the last part was the Mg-Al intermetallic compounds layer which is connected by an imaginary line. EDS of the Mg and Al elements in the fusion zone is shown in Fig. 5.16. The concentrations of the Mg and Al elements are in echelonment. Based on the EDS of the Mg and Al elements, there is a Mg-Al intermetallic compound layer in the center of the figure. The Mg, Al and Mg-Al intermetallic compounds are joined without weld defect. The width of the intermetallic compounds layer is between 20 and 30 μm. But as can be seen from the whole Mg-Al interface, the intermetallic compound layer is not continuous and the width of the intermetallic compound layer is not the same. In the welding process, the gasification of the adhesive could affect the fusion zone. There is no stabilized state for the formation of the Mg-Al intermetallic compounds. Thus, under the action of adhesive, the intermetallic compounds could not form a long continuous layer.

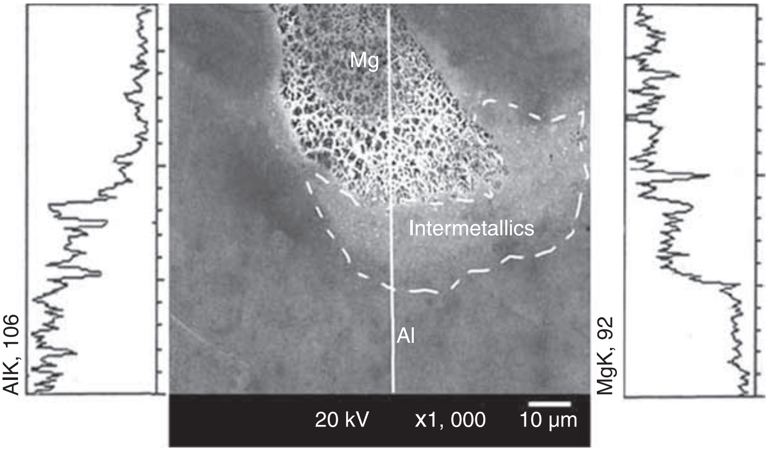

5.16 The microstructure of Mg-Al interface in LWB fusion zone.

5.4.3 Elements distribution in the fusion zone

The transverse section of the laser welding and LWB joints are examined by electron probe microanalyzer (EPMA), and the results are shown in Fig. 5.17. In a laser-welded joint, an intermetallic compound layer could be found at the bottom of the fusion zone, indicated by the arrows in Fig. 5.17(a) and 5.17(b). The thickness of the Mg-Al intermetallics is about 100 μm. In a laser welding process, only a little Al could be melted and the interface between the Mg-Al eutectic phase and the intermetallics would be a weak part of the joint. Figure 5.17(c) and 5.17(d) show the distributions of Mg and Al elements in the LWB joint. The results show that the content of Mg element at the bottom of LWB fusion zone is lower than that in the laser-welded joint. At the edge of the fusion zone, the concentration of the Al alloy in LWB joint is higher than that in laser-welded joint. Unlike the laser-welded joint, the Al element would come into the center of the fusion zone in the LWB joint. The different distributions of Mg and Al elements are induced by the adhesive decomposition and the fusion metal flowing. The thickness of the intermetallic layer which is not continuous in the LWB joint is about 50 μm. At the left of the fusion zone, there are nearly no Mg-Al intermetallics. Therefore, the effect of the intermetallic layer on the property of the LWB joint would be limited. It is known that epoxy resin adhesive is composed of C, O and H elements. The property of the joint would be directly influenced by the distribution of these three elements. Figure 5.17(e) and 5.17(f) show the distributions of C and O elements in the LWB joint. It can be seen that there are few C and O elements in the center of the LWB fusion zone. Thus, the adhesive in the fusion zone would have little effect on the properties of the LWB joint.

Figure 5.18 shows the secondary electron image of the laser-welded and LWB joints. The quantitative analysis of Mg and Al elements is done in seven different

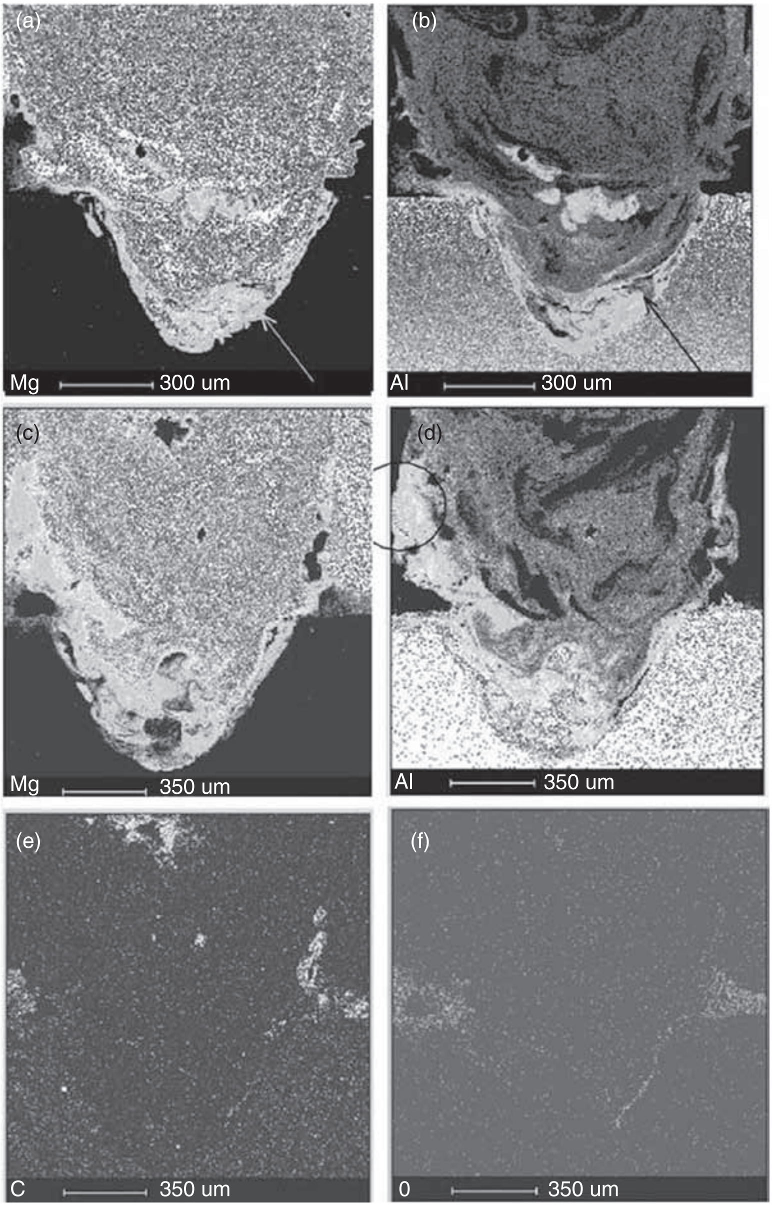

5.17 Transverse section EPMA analyses of the joint of laser welding and LWB. (a) Face scan of element Mg of laser welding joint, (b) face scan of element Al of laser welding joint, (c) face scan of element Mg of LWB joint, (d) face scan of element Al of LWB joint, (e) face scan of element C of LWB joint, and (f) face scan of element O of LWB joint.

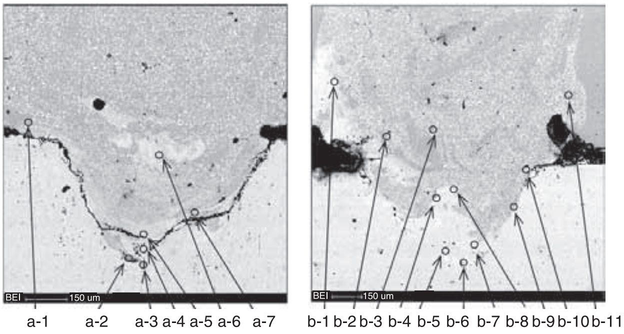

(a) (b)

5.18 Secondary electron images and quantitative analysis of laser welding and LWB joint: (a) secondary electron images of laser welding joint; (b) secondary electron images of LWB joint.

areas (a1–a7) of a laser-welded joint and in 11 different areas (b1–b11) of an LWB joint. The quantitative analysis area is a circular area with a 20 μm diameter. The percentage compositions of Mg and Al elements in these areas are shown in Table 5.3. According to the composition percentage of the Mg and Al elements, the components of the areas could be deduced as shown in Table 5.3. It shows that the areas (a2–a5) of laser welding joint are composed of intermetallic compounds with the formula of Mg_2Al_3 and $Mg_{17}Al_{12}$. These two kinds of intermetallic compounds can be found in the Mg-Al binary equilibrium phase diagram as shown in Fig. 5.15. However, the percentage composition of the areas (b2–b11) of LWB joint is not determined by the Al_3Mg_2 and $Mg_{17}Al_{12}$ intermetallic compound formulas. The region (b2–b11) should be composed of the mixture of intermetallic compounds and solid solution, resulting from the fact that the contents of the Al element in these regions are too low to form the intermetallic compounds. In the region b1, the $Mg_{17}Al_{12}$ intermetallic compounds which would reduce the strength of LWB joint are found at the edge of the fusion zone. However, the adhesive decomposition would depress the flowing of magnesium melt, which would decrease the contents of the Mg element at the bottom of the LWB weld pool. Thus, the content of intermetallic compounds in the LWB joint would be reduced in comparison with the laser-welded joints. In Fig. 5.18(a), it can be seen that at the bottom of the fusion zone, there are many serial micro-cracks, which will reduce the strength of the joint, while there is no obvious crack in Fig. 5.18(b).

5.4.4 Mechanical properties of laser weld bonding Mg to Al joint

In order to analyze the LWB joint, it is divided into two parts: the adhesive bonding only (part II) and the joining via the combination of laser welding and

Table 5.3 Quantitative analysis of Mg and Al elements about laser welding and LWB joints

Serial Number	Element	Percentage composition (%)	Whole number proportion (Mg:Al)	Inference composition	Serial number	Element	Percentage composition (%)	Whole number proportion (Mg:Al)	Inference composition
a-1	Mg	84.206	10:53	Mixture	b-1	Mg	56.779	17: 12.9	$Al_{12}Mg_{17}$
	Al	15.794				Al	43.221		
a-2	Mg	63.813	17:11	$Al_{12}Mg_{17}$	b-2	Mg	31.174	5:11	Mixture
	Al	36.187				Al	68.826		
a-3	Mg	39.398	2:3	Al_3Mg_2	b-3	Mg	98.586	70:1	Mg alloy
	Al	60.602				Al	1.414		
a-4	Mg	52.843	14:17	$Al_{12}Mg_{17}$	b-4	Mg	33.244	1:2	Mixture
	Al	47.157				Al	66.756		
a-5	Mg	54.401	14:17	$Al_{12}Mg_{17}$	b-5	Mg	14.637	5:29	Mixture
	Al	45.599				Al	85.363		
a-6	Mg	55.308	17:12	Al_3Mg_2	b-6	Mg	31.174	5:11	Mixture
	Al	44.692				Al	68.826		
a-7	Mg	68.869	10:22	Mixture	b-7	Mg	24.638	1:3	Mixture
	Al	31.131				Al	75.326		
					b-8	Mg	21.739	5:18	Mixture
						Al	78.261		
					b-9	Mg	22.372	5:18	Mixture
						Al	77.628		
					b-10	Mg	73.803	14:5	Mixture
						Al	26.197		
					b-11	Mg	26.784	1:3	Mixture
						Al	73.252		

Note: Mixture is the intermetallic compounds and the solid solution. The intermetallic compounds, such as $Al_{12}Mg_{17}$ and Al_3Mg_2, are the primary composition of the area.

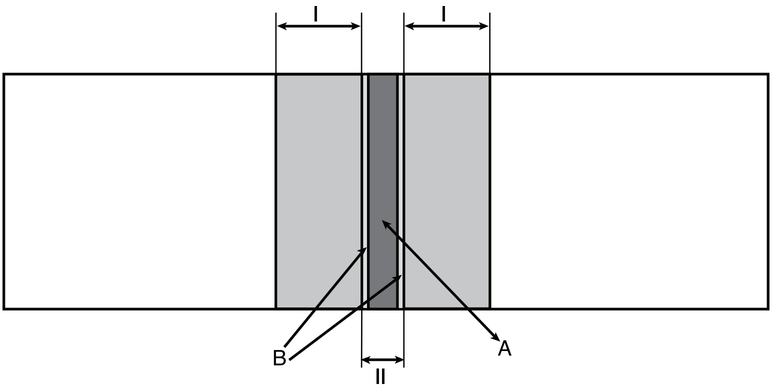

5.19 Different zones in the LWB joint.

adhesive bonding (part I), as shown in Fig. 5.19. In part II, region A in Fig. 5.19 is the fusion zone of the joint and region B is the heat effect zone in the joint. The adhesive in the region A would be fully decompounded during the laser welding process. The adhesive in region B would be partly decompounded. However, the area of the region B is very small and its effect on the mechanical property of the weld joint is limited.

During LWB, there is no effect of the laser process on the zone of adhesive bonding only, and the form of joining and joining forces in this zone would be the same as with adhesive bonding. The adhesive layer and metal are connected under the diffuse force or the mechanical force. Since the bonding performance will be improved by increasing the wetting ability of metals, the interfaces of specimens should be prepared well. In the present work, both the surface of the Al alloy and the surface of the Mg alloy were treated before coating with the adhesive.

In Fig. 5.19, the Mg alloy is observed to have melted completely by the effect of laser welding, while the laser operated in a conductive mode within the Al alloy. The zone of adhesive bonding is much wider than the zone where bonding is affected by the combination of laser welding and adhesive bonding. Thus, if the mechanical properties of this adhesive bonding area are low, then the mechanical properties of the total LWB joint would also be low.

It is very important to obtain consistent penetration between the Mg and Al alloys. During LWB, firstly the laser beam worked on the top Mg alloy sheet and then on the adhesive layer. After drilling through the adhesive layer, the power that worked on the Al alloy would be lower. The change of the laser power may have influenced the level of penetration. Table 5.4 shows the tensile shear strength of the joints. The LWB specimen shows the highest strength, which is better than that of laser welding and adhesive bonding. Good fusion is characterized by a joint that contains no weld flaws and little residual adhesive, and has a continuous level of penetration between the Al and Mg sheets.

Table 5.4 Tensile shear strength of the joints

Form of welding	Shear force (KN)	Fracture position
Laser welding	0.18	Joint between two plates
Adhesive bonding	4.19	The adhesive layer
LWB (sound joint)	5.79	The edge of the joint
LWB (bad joint)	3.87	Joint between two plates

In the tensile shear test of LWB joints, two kinds of fracture patterns were observed. Figure 5.20(a) shows fracture of the sample with the well joint, which fails at the edge of the welding joint shown in Fig. 5.17(b). Figure 5.20(b) shows the fracture of the sample with imperfect fusion. In this joint, the phenomenon of the discontinuous penetration between the Al and Mg sheets is evident. The sample with imperfect fusion failed at a lower tensile shear force than both the sample with favorable fusion and the sample that was joined by adhesive bonding only. So to get a higher quality LWB joint, there should be a proper joint.

The incomplete decompounded area is the most complex zone in the LWB joint. During LWB process, the power of the laser beam was not completely uniform. The power at the edge of the laser beam acting on the sample was less than that at the center of the beam, which resulted in the incomplete decomposition of the adhesive layer and the formation of an incomplete decompounded area. But the incomplete decompounded area is very small, which would only have a slight effect on the property of the joint.

5.4.5 Welding mechanism

Laser weld bonding is a new kind of welding technology, which was used to join Mg to Al alloy successfully. It causes a hybrid effect of metallurgy joining and mechanical joining. The microstructure in the LWB Mg to Al fusion zone is different from that in the laser welding joint because of the addition of the adhesive. The welding parameters in LWB processing are not easy to control and there are still a few welding defects in the fusion zone. The addition of the adhesive would change the distribution of the elements in the fusion zone and would influence the formation and the distribution of the intermetallics in the weld joint. Still, the adhesive would change the surface state of the Al alloy and would increase the laser absorptivity of the Al alloy to certain extent. Thus, the temperature difference between the Mg and Al fusion zone would be reduced, which would decrease the micro-cracks forming at the interface between the Mg and Al fusion zone (Liu and Wang, 2009). Therefore, the property of the laser-welded joint in the LWB process would be improved by the addition of the adhesive. The adhesive in the fusion zone should be wholly decompounded in the welding process, which could be controlled by regulating the laser welding parameters. The adhesion of Mg and Al

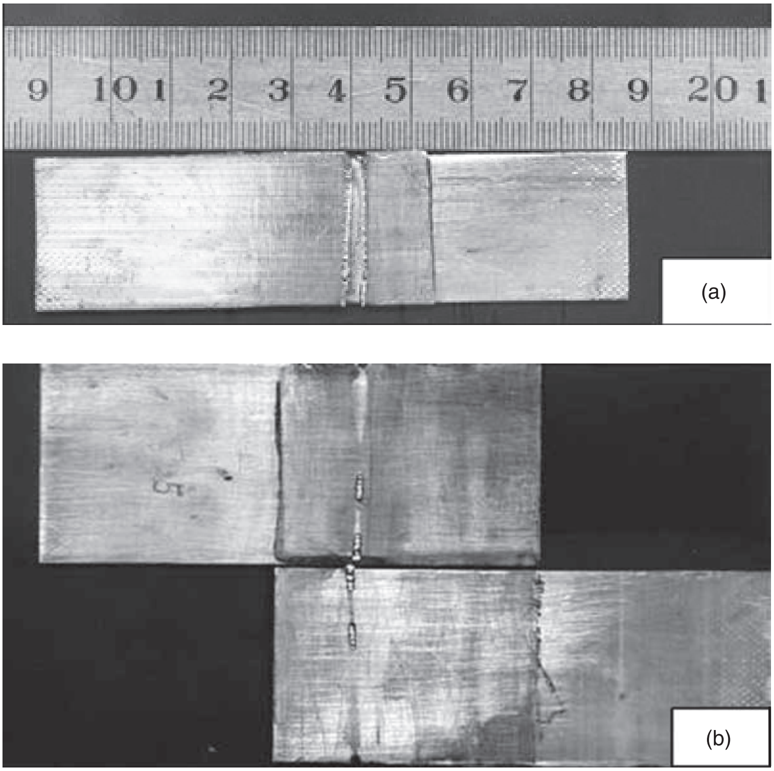

5.20 Fracture place of sample with (a) favorable fusion and (b) imperfect fusion.

is another factor for the property of the LWB joint, and a sound adhesion joint is very important. The mechanical property of the LWB joint would be better than that of the laser welding and adhesive bonding alone with the common effect of laser welding and the adhesive bonding.

5.5 Conclusion and future trends

The joining technology of Mg and Al has been improved with the development of welding technology itself. More and more new welding methods are tried to join the Mg and Al alloys. But the formation of the Mg-Al intermetallics has harmful effects on the joint property. In order to reduce the influence of the Mg-Al intermetallics, interlayers such as Ce and Zn are used in some welding processes. The addition of the interlayer changes the distribution of the Mg-Al intermetallics, decreases the formation of the Mg-Al intermetallics and improves the mechanical properties of the Mg-Al joints. However, the composition of the interlayer used in the Mg-Al joining process should be studied further. Laser weld bonding is used to join the Mg to Al successfully. The adhesive would be decompounded during the laser welding process, which would influence the Mg-Al intermetallics in the joint. The micro-cracks in the LWB Mg to Al joint are decreased by the effect of the adhesive. The LWB Mg-Al joint is of better quality than laser welding and adhesive bonding joints. However, if the LWB method is considered for commercial use, there are still many problems to be studied. Besides the welding technique introduced in this book, the fusion stir welding (FWS) is another welding method for the Mg to Al joining process. No matter what welding method is used to join the Mg to Al alloys, it should reduce the quantity of the Mg-Al intermetallics formation in the joint.

New kinds of Mg and Al alloys are continuously being developed. Alloys with good weldability will be developed by researchers. The use of Mg and Al alloys would still benefit the development of welding technology. It is believed that the joining technology of Mg and Al will be perfected in the near future.

5.6 References

Borrisutthekul, R., Miyashita, Y. and Mutoh, Y. (2005), 'Dissimilar material laser welding between magnesium alloy AZ31B and aluminum alloy A5052-O,' *Science Technology of Advanced Materials*, **6**, 199–204.

Chen, Y.C. and Nakata, K. (2008), 'Friction stir lap joining aluminum and magnesium alloys,' *Scripta Materialia*, **58**, 433–436.

Gerlich, A., Su, P. and North, T.H. (2005), 'Peak temperatures and microstructures in aluminium and magnesium alloy friction stir spot welds,' *Science and Technology of Welding and Joining*, **10**, 647–652.

Grobner, J., Kevorkov, D. and Schmid-Fetzer, R. (2002), 'Thermodynamic modeling of Al–Ce–Mg phase equilibria coupled with key experiments,' *Intermetallics*, **10**, 415–422.

Hao, S.Z., Gao, B., Wu, A.M., Zou, J.X., Qin, Y., Dong, C., An, J. and Guan, Q.F. (2005), 'Surface modification of steels and magnesium alloy by high current pulsed electron beam,' *Nuclear Instruments and Methods in Physics Research Section B*, **240**, 646–652.

Kwon, Y.J., Shigematsu, I. and Saito, N. (2008), 'Dissimilar friction stir welding between magnesium and aluminum alloys,' *Materials Letters*, **62**, 3827–3829.

Li, X.R. and Liang, W. (2009), 'Bonding of Mg and Al with Mg-Al eutectic alloy and its application in aluminum coating on magnesium,' *Journal of Alloys and Compounds*, **471**, 408–411.

Liu, L.M., Liu X.J. and Liu, S.H. (2006), 'Microstructure of laser-arc hybrid welds of dissimilar magnesium alloy and aluminium alloy with Ce as interlayer,' *Scripta Materialia*, **55**, 383–386.

Liu, L.M., Tan, J.H. and Liu, X.J. (2007), 'Reactive brazing of Al alloy to Mg alloy using zinc-based brazing alloy,' *Materials Letters*, **61**, 2373–2377.

Liu, L.M. and Wang, H.Y. (2009), 'The effect of the adhesive on the microcracks in the laser welded bonding Mg to Al joint,' *Materials Science and Engineering: A*, **507**, 22–28.

Liu, L.M., Wang, H. and Song, G. (2007), 'Microstructure characteristics and mechanical properties of laser weld bonding of magnesium alloy to aluminium alloy,' *Journal of Materials Science*, **42**, 565–572.

Liu, L.M., Wang, H.Y. and Zhang, Z.D. (2007c), 'The analysis of laser weld bonding of Al alloy to Mg alloy,' *Scripta Materialia*, **56**, 473–476.

Liu, L.M., Wang, J.F. and Song, G. (2004), 'Hybrid laser–TIG welding, laser beam welding and gas tungsten arc welding of AZ31B magnesium alloy,' *Materials Science and Engineering: A*, **381**, 129–133.

Liu, P., Li, Y.J., Geng, H.R. and Wang, J. (2005c), 'A study of phase constitution near the interface of Mg/Al vacuum diffusion bonding,' *Materials Letters*, **59**, 2001–2005.

Liu, X.J., Liu, L.M., Wang, H. and Song, G. (2005a), 'Microstructure of laser–TIG hybrid welding joint of dissimilar metals of Al and Mg,' *Transactions of the China Welding Institution*, **8**, 32–36.

Liu, X.J., Liu, L.M., Wang, H., Song, G. and Liu, S.H. (2005b), 'Microstructure of laser–TIG hybrid welding joint of dissimilar metals of Al and Mg,' *Transactions of the China Welding Institution*, **26**, 31–34.

Liu, Z.Q. and Di, B. (Ed.) (1990), *Welding of Dissimilar Materials*. Beijing: Scientific Press.

Mahendran, G. (2008), 'Developing diffusion bonding windows for joining AZ31B magnesium–AA2024,' *Journal of Material Design*. doi:10.1007/s11665-009-9531-6.

Mahendran, G., Balasubramanian, V. and Senthilvelan, T. (2009), 'Developing diffusion bonding windows for joining AZ31B magnesium–AA2024 aluminium alloys,' *Materials and Designs*, **30**, 1240–1244.

McLean, A.A., Powell, G.L.F., Brown, I.H. and Linton, V.M. (2003), 'Friction stir welding of magnesium alloy AZ31B to aluminium alloy 5083,' *Science and Technology of Welding and Joining*, **8**, 462–464.

Sato, Y.S., Park S.H.C., Michiuchi, M. and Kokawa, H. (2004), 'Constitutional liquation during dissimilar friction stir welding of Al and Mg alloys,' *Scripta Materialia*, **50**, 1233–1236.

Somasekharan, A.C. and Murr, L.E. (2004), 'Microstructures in friction-stir welded dissimilar magnesium alloys and magnesium alloys to 6061-T6 aluminum alloy,' *Materials Characterization*, **52**, 49–64.

Wang, H.Y., Liu, L.M., Zhu, M.L. and Wang, H. (2007), 'Laser weld bonding of A6061Al alloy to AZ31B Mg alloy,' *Science and Technology of Welding and Joining*, **12**, 261–265.

Wang, J., Li, Y.J., Liu, P. and Geng, H.R. (2008), 'Microstructure and XRD analysis in the interface zone of Mg/Al diffusion bonding,' *Journal of Materials Processing Technology*, **205**, 146–150.

Wielage, B. and Mücklich, S. (2006), 'Improving the soldering of magnesium alloys,' *International Brazing and Soldering Conference*, April, 24–26.

Yan, J.C. and Xu, Z.W. (2005), 'Microstructure characteristics and performance of dissimilar welds between magnesium alloy and aluminum formed by friction stirring,' *Scripta Materialia*, **53**, 585–589.

Zhao, L.M. and Zhang, Z.D. (2008), 'Effect of Zn alloy interlayer on interface microstructure and strength of diffusion-bonded Mg-Al joints,' *Scripta Materialia*, **58**, 283–286.

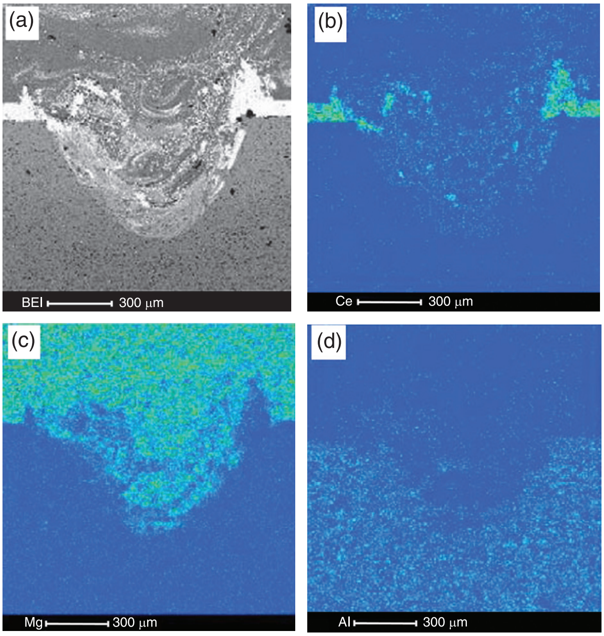

Plate I (a–d) EPMA image and distribution maps of major elements of hybrid welding of Mg-Al joint with added Ce.

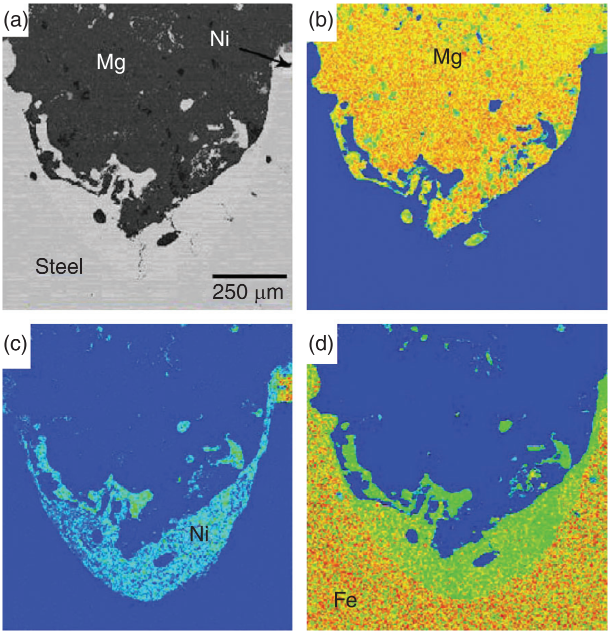

Plate II Distribution maps of (a) back scattered electron image; (b) Mg element; (c) Ni element and (d) Fe element.

6

The joining of magnesium alloy to steel

L. LIU, Dalian University of Technology, China

Abstract: The laser-TIG hybrid welding technique is used to join the Mg alloy to steel with Ni interlayer successfully, obviously better than without it. The addition of Ni into the joints changes the bonding mode, and the joint is achieved by the solid solution and intermetallic compound. The average shear strength of the Ni-added joint can reach 170.8 MPa, higher than that of a direct joint of 116.8 MPa.

Key words: magnesium alloy, steel, laser-TIG hybrid welding, interlayer.

6.1 Introduction

With the progress of modern science and technology, many components, including lots of nonferrous materials, need to react with the atmosphere of high or low temperature, corrosive, electromagnetic and radioactive environments. Materials that are selected should meet the needs of industrial production. Generally, one material used in industry cannot satisfy the various demands in practice. Therefore, not only a great number of similar materials are needed to be joined together but also a mass of dissimilar materials to be welded in modern constructive engineering. It will not only meet the demands of different circumstances on multiple properties of one part but can also save precious metals and costs, and surpass structural parts constructed with single materials in some cases. As welding of dissimilar materials attracts greater attention, it can be seen that its application to aerospace, petrol chemistry, boiler furnace of power plants, nuclear power, machines, electronic products, ship building and various other fields is increasing.[1–5]

Mg alloys are the lightest structural materials with some unique properties that steel does not possess, such as high specific strength, specific elastic modulus, damping capacity, low density and recyclability. They are called ‘Green materials of the 21st,[6] and are being introduced into aerospace, aviation, automobiles, personal computers (PCs), communication and appliances. Mg alloys have been used in automobiles in North America since the middle 1980s and their use has been increasing at the rate of 16.6% each year, of which casting components account for 70–80%, and so does the application of Mg alloys to automobiles worldwide. Other properties, such as good absorption of moisture, fluidity, machining property and shielding of interference of electromagnetic fields,[7–9] are suitable for the automotive development in lowering weight, enhancement of economy of fuels, low emission and higher safety. Consequently, it is imperative for North America, Europe, Japan and Korea to greatly increase their consumption of Mg alloys,[10–13] while welding as a key method, which can contribute to the forming of materials, optimizing structure and lowering costs, should be applied widely.

As is generally known, steels are dominant, and the most widely used metals in industry. It is an attractive option to join other materials to steel in order to obtain versatile properties in steel.[14] Due to similar uses of Mg alloys and steels, joining them together can lower weight and save materials. There will be an increasing demand in industry for the welding of the two materials in the near future, for example, in parts of spacecraft and their engines, which can lower the weight of aerospace materials so that their properties can be improved;[15,16] in automobiles, Mg alloys and steel have been used in manufacturing different parts of a vehicle, while the welding of the two materials has not been reported on. Thus, the welding of Mg alloys and steels has great significance, both theoretically and economically. The welding of the two materials is now being explored for the first time, along with theoretical and practical foundations. Due to great differences in the physical and chemical properties of Mg alloys and steels, welding has not been done yet. In addition, the erosion resistance of Mg alloys is not very high. The current chapter is mainly concentrating on the high-quality fusion welding between Mg alloy and steel.

6.2 Existing problems in the joining of magnesium alloys to steel

American researchers investigated the interface between Mg-Mn alloy and foundry ingot obtained by vacuum diffusion welding in 2003.[17] The specimen was subjected to grinding to reach 2 mm of surface roughness and was polished by the mixture of Cr_2O_3 and gasoline oil before they were put into the vacuum chamber. After 60 hours under 1000 K, they were not welded together, but a trace of interaction at the interface between the two was detected, and a weld bead was formed at the contact area of oxide film under conditions of 1000 K and 1.33 kPa–0.133 MPa. The author concluded that no transitional zone was directly formed between the two, while the joint of Mg-Mn alloy to steel was bonded by the phases of Mn/Fe. Japanese scholars studied the joints of Mg alloy and steel by friction stir welding (FSW), and they found that the two materials could be joined mechanically.[18]

Detailed physical and chemical properties of Mg and steel are described in Table 6.1.

1 Melting point: The larger the difference in the melting points of two metals, the more difficult it is for them to be welded together. The gap of melting temperature is 800–1000 °C between Mg alloys and steels. During welding, Mg alloys with lower liquidus would be melted first; in the meantime, the steel with higher liquidus would still be in solid state. Thus, the molten Mg

Table 6.1 Physical and chemical properties of Mg and steel

Metals	Steel	Mg
Density (ρ/g/cm)	7.87	1.74
Melting point (°C)	1539	650
Specific heat capacity (C/J/kg.k)	460	1078
Thermal conductivity (λ/w/m.k)	77	145
Coefficient of thermal expansion (a/10^{-6}k^{-1})	11.9	25.8
Conductivity (ρ/10^{-6}Ω.m)	9.7	4.46
Shrinkage %	10.6–11.7	3.97–4.2
Extra-nuclear electron	3	2
Lattice structure	bcc	Hexagonal
Lattice constant (10^{-16} m)	7.86	a = 3.0294, c = 5.2105
Periodic category	VIIA	IIA

alloy may be penetrated into the grain boundary of the overheat zone, causing structure property loss. However, the loss of Mg element is inevitable through evaporation, as the boiling point of Mg alloy is much lower than the liquidus of mild steel.

2 Coefficient of thermal expansion: The greater the difference in coefficient of thermal expansion (CTE), the harder the welding process becomes. The CTE of Mg-Al-Zn alloy is usually in the range of 23–32 × 10^{-6}/K and that of mild steels is in the range of 13–16 × 10^{-6}/K, which is 1.4–2 times greater than that of steel. The metal with a greater CTE would have heavier expansion or shrinkage during welding, resulting in different stress states on the sides of the bead. Hence, the micro-crack might occur at the interface between the weld bead and heat-affected zone, and so did the desquamation between the bead and base materials. If the weldment is subjected to the periodic thermal loop, the alternative stress is likely to result in fatigue flake of the bead from base materials. To lower the stress, an intermediate material with CTE between two dissimilar base materials should be selected.

3 Thermal conductivity and heat capacity: They are the items that affect the thermal loop, temperature field distribution (TFD) and crystallizing process, and could modify the TFD and the crystalline condition and thus the melt wettability on the surface of solid metal. Otherwise, the grain size can be coarsened and deteriorate the microstructure sequentially. Therefore, a powerful heat source should be used in the welding process and its location should be closer to the material with better thermal conductivity.

4 Electromagnetic property: The larger the difference in the dissimilar metal electromagnetism, the more difficult it is to carry on the welding, the more unstable the arc is and the more likely the welded joint forming is to fail. During the welding process, the arc deviates from its axial line under the

action of a magnetic field, causing excessive melting of the materials within the magnetic field and producing flaws in the base of the materials, caused by non-fusion owing to being diluted. In such cases, alternative current (AC) arc would be used.

5 Oxidizability: The stronger the metal oxidizability, the more difficult it is to conduct the welding process. At a high temperature, Mg is prone to oxidation and the oxidized products will be detrimental to the bonding of Mg alloys and steels, as the effect of galvanic cell often takes place in the boundary between the two materials. The brittle phase MgO usually leads to failure of the bead.

6 Unequivalent strength between base materials and weld seam: Powerful heat sources are often used in the welding process of dissimilar materials; thus, it is easy to cause evaporation and loss of elements, which then lead to a huge change of chemical composition in the weld seam, deterioration of microstructures and lowered strength of the seam, especially the welding of nonferrous alloys.

7 Solubility of dissimilar metals: Whether the welding of dissimilar metals can be carried out depends on the element interaction under the welding condition. When the type, constant of the crystal lattice, the atomic radius and the electronegativity between the two materials are fairly close, it would be easier for them to form a solid solution, which also implies that the wettability between them is favorable. In order to improve the performance of welding of dissimilar materials, intermediate elements can be selected as transitional layers that can form unlimited solid solutions with both base materials. It is noteworthy that Mg and Fe are not mutually completely soluble in liquid state. This means it is extremely easy for the bead to be stripped off the base materials after welding.

To sum up, it is clear that it is not possible to melt the Mg alloy and steel at the same time, and thus the butt joining of the two materials would be difficult.

6.3 Welding principles for the joining of magnesium alloys to steel

6.3.1 Welding method

The lap joining method was adopted by the hybrid laser-tungsten inert gas (TIG) welding technique, which is shown in Fig. 6.1. The sketch of the welding equipment is shown in the upper left corner of Fig. 6.1, and the photograph of weldment is shown in the upper right-hand corner.

In the experiment, the plates of Mg alloy and steel are AZ31B and Q235 mild steel, with a thickness of 2 and 1.2 mm, respectively. As it was hard for the welding process to be performed when the steel plate was on the Mg alloy plate, a method of placing the Mg alloy plate upon the steel plate was adopted.

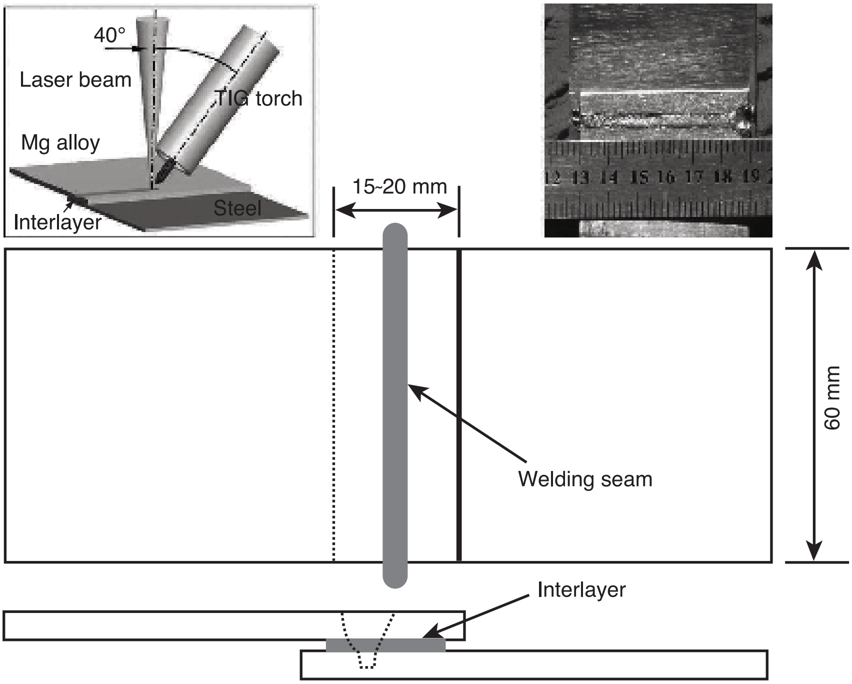

6.1 Schematic drawing of the test specimens.

The hybrid laser-TIG welding technique organically integrates the deep-penetrating characteristic of laser and the large heat input characteristic of arc, thus compensating the shortages of the respective laser and TIG welding technique.[19] The laser causes the spot of arc to be absorbed at the point where the laser beam converges, prompting the arc to remain steady at a high welding speed. In comparison with a single TIG source under the same parameters, the welding rate can be improved twice as much and welding efficiency can be enhanced greatly.

6.3.2 Principle of direct joining

In terms of Mg-Fe binary diagram, no interaction of the two elements happens at any given temperature. Otherwise, the chemical inertness of iron to pure liquid magnesium is remarkable. From the line analysis of Fig. 6.2(b), it can be seen that no interaction occurs at the interface between Mg and Fe elements. O elements are only shown on the side of the fusion zone (FZ), owing to the activity of the Mg atom; however, it is not clear how these O elements were formed: in the welding process, the sample preparation, or both.

By closer inspection (Fig. 6.3), gaps can be seen at the interface, indicating that they are not bonding well, which is closely related with the wettability of

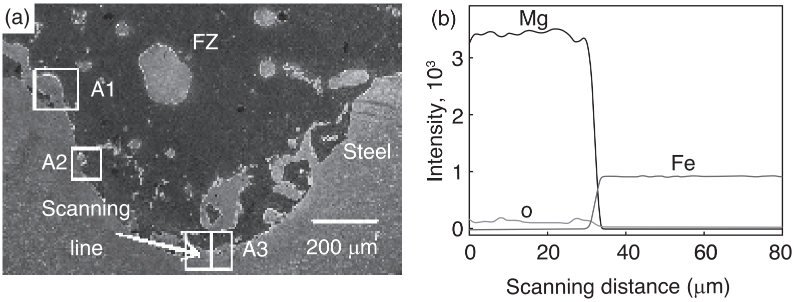

6.2 Cross-sectioned joint of direct joining (a) and line analysis (b) along the bottom of welding pool.

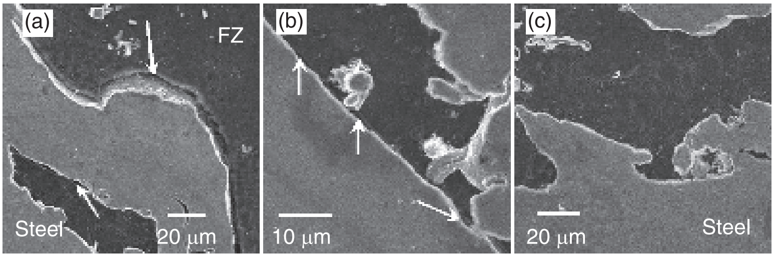

6.3 Interfacial microstructure: (a), (b) and (c) from region A1, A2, A3, respectively, of Fig. 6.2.

molten Mg alloy on the surface of steel sites during solidification. Nevertheless, it can also be observed that intimate joining was achieved at the bottom, suggesting that other factors may affect the bonding mode of Mg alloy and steel, for example, CTE of the two materials: CTE of Mg alloy in the present experiment is approximately double that of steel. The molten Mg alloy holds the bulges generated under the action of hybrid laser-TIG welding, thus not forming any gaps during the process of solidification.

6.3.3 Principle of interlayer into lap joint of the Mg alloy to the mild steel

The study found that the addition of Ni interlayer into the joint of Mg alloy/steel could form a transition layer (TL) between Fe and Ni, and the intermetallic compound (IMC) layer between Ni and Mg. As confirmed by the experiment, the TL between nickel and steel consisted of solid solution of Ni in Fe, and the interlayer between Mg alloy and Ni was composed of Mg_2Ni.

Note that the interface of Ni-added joints does not contain IMCs of Mg, Ni and Fe, but consisted of TLs between Mg and Ni and between Ni and Fe, in the form of Mg_2Ni intermediate phase and solid solution, respectively. Figure 6.4 shows

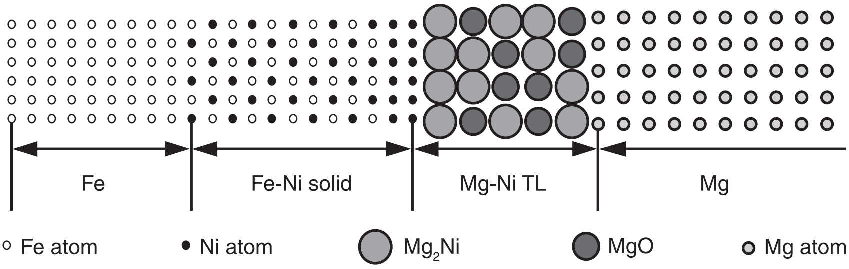

6.4 Schematic picture of Mg-Ni-Fe joint.

the joining mechanism of Mg alloy to steel by hybrid laser-TIG welding technique. The Mg atom radius is 0.16 nm, and both Fe and Ni atom radii are 0.124 nm; MgO lattice constant is 0.4212 nm and Mg_2Ni is 0.5205 nm.[20]

As shown in Fig. 6.4, in the welding process, due to the similarity in size of Fe and Ni atoms and the similar nature of Fe and Ni, the substitution reaction can occur after the melting of Fe and Ni, and Fe and Ni atoms form an exchangeable Fe-Ni solid solution layer. Thus, Fe and Ni were connected by solid solution. On the basis of the Mg-Fe binary phase diagram, no interaction of Fe and Mg occurred. While Mg-Ni IMC Mg_2Ni was confirmed by the experiment, the bonding between Mg and Ni was realized. However, it is inevitable for the joint to be oxidized, and the TL contains MgO and Mg_2Ni.

In summary, the addition of Ni into the joints changed the bonding mode and the joint was achieved by the solid solution and IMC.

6.4 Direct joining of magnesium alloys to mild steel

The quality of joint mechanical properties is one of the most effective ways to determine the quality of a welding method.

6.4.1 Effect of laser power on joint strength

Figure 6.5 shows the effect of laser power on the shear strength of a welded joint. It also illustrates that the shear strength increases at first and then decreases as the laser power increases, however. This proves that the improvement of laser power contributes to that of joint strength and the shear strengths of the joints gained at a higher laser power undergo little change.

When the laser power reached approximately 200 W, the strength of the joint was lower, only 25 MPa, while the maximum strength of 95 MPa was achieved at 400 W.

In the process of hybrid laser-TIG welding of the Mg alloy to the steel, the TIG arc acted on the upper surface of Mg alloy, melting the Mg plate but not the steel

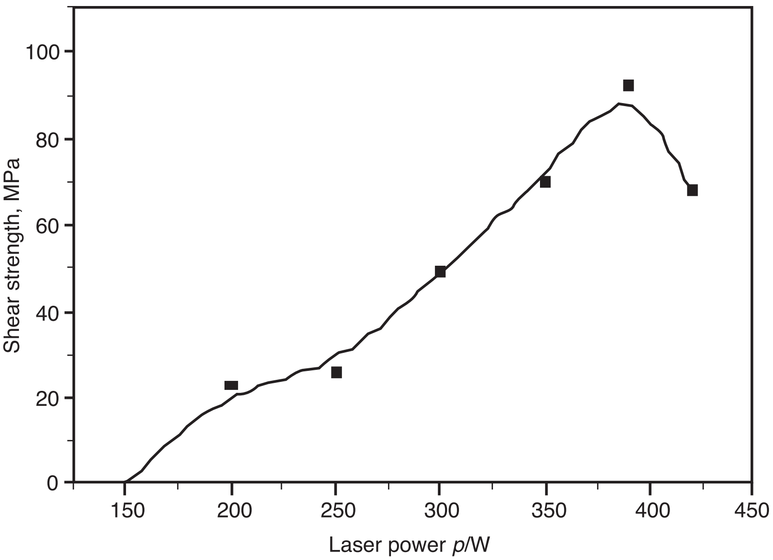

6.5 Effect of laser power on the strength of weld bead (defocus −3 mm, welding speed 750 mm/min, welding current 80 A).

plate. The steel plate was mainly melted by the laser beam; so, as long as the laser power is high enough, an effective joining between Mg alloy and steel can be achieved; but when the laser power was more than 450 W, lots of big holes were formed as a result of excessive evaporation of Mg, with a serious impact on the weld seam and reducing the quality and tensile strength of the welds.

6.4.2 Effect of welding speed on joint strength

Figure 6.6 shows the curves on penetration depth *h* and shear strength with different welding speeds. The curves show that with the increasing welding speed, the penetration depth on the plate decreases. It is well known that the larger heat input often contributes to a larger penetration depth. With the increase of welding speed, the heat input reduces, and so does the penetration on the plate.

Comparing the two curves in Fig. 6.6, it can be seen that the shear strength of the weld bead is closely related to the penetration depth inside steel. The strength increases with increasing penetration depth on steel and declines with decreasing depth.

6.4.3 Effect of defocus on joint strength

Figure 6.7 shows the relationship between the weld width *d* and joint strength. It can be seen that the weld width first decreases with the increasing defocusing distance, and then decreases. When the defocusing *D* of laser is approximately −2 mm, the laser spot on the steel plate surface is the smallest, whereas the laser

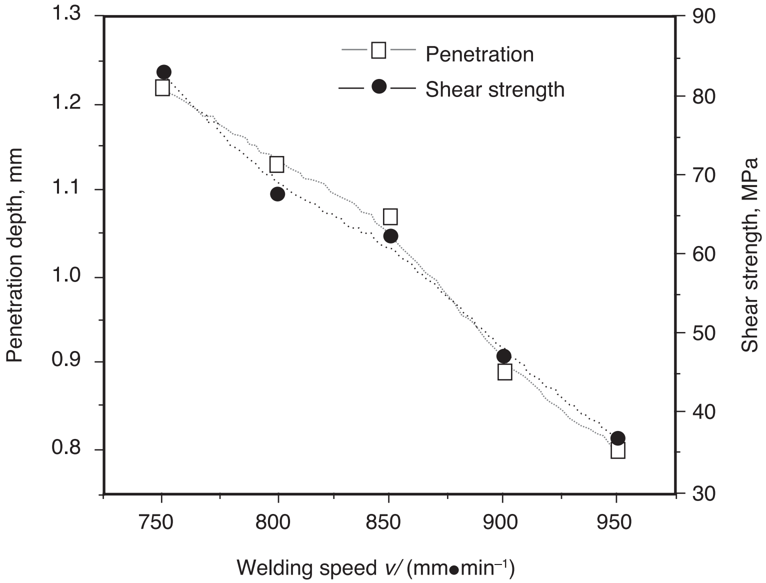

6.6 Effect of welding speed on top weld width and strength of weld bead (laser power 400 W, defocus −3 mm, welding current 80 A).

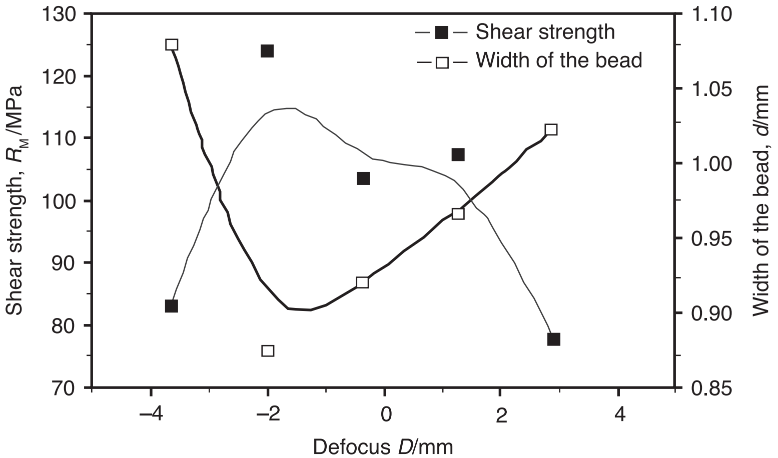

6.7 Effect of defocusing amount on strength and width of weld bead (laser power 400 W, welding speed 750 mm/min, current 80 A).

beam power density is the largest, causing an increase in penetration depth. With the increase or decrease of defocus, the laser spot on the surface gradually becomes larger, thus resulting in the reduction of weld penetration depth and an increase in the width. It is clear that the width of the seam is closely related to the defocus.

The shear strength of welded joint increases with increasing defocus at first, and then decreases, as shown in Fig. 6.7. When the defocusing D is -2 mm, the maximum shear strength is achieved. The reason is that when D is -2 mm, the laser beam is focused at its maximum power density on the surface of the steel plate, causing the plate to absorb most of the energy, which in turn increases the penetration depth and the joint strength. With the absolute increase in defocus, the focus of the laser beam deviated from the plate surface, causing a loss in laser energy. Consequently, the penetration depth was reduced and so was the shear strength.

To sum up, the laser defocus is correlating with the width of the weld. When the defocus is -2 mm, the depth-to-width ratio (DWR) of the seam is the largest, and the joint strength is the highest. When the defocus deviates from -2 mm, the DWR and joint strength decrease.

6.4.4 Effect of TIG current on joint strength

Figure 6.8 shows the curve for weld strength with different TIG currents. We can clearly see that the weld strength changed little with the increasing TIG currents, indicating that the TIG current has little effect on the weld strength. In the welding process, the weld width is correlated with the TIG welding current. An appropriate amount of current could reduce weld porosity and improve weld

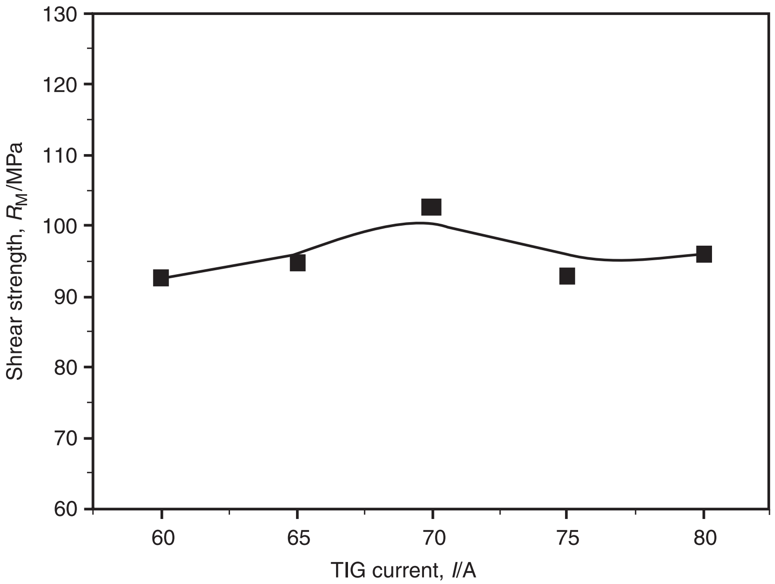

6.8 Effect of welding current on strength of weld bead (laser power 400 W, defocus -2 mm, welding speed 750 mm/min).

quality; however, the current can only melt Mg alloy and not the steel plate. It can be seen that the current could not directly impact the weld penetration depth with which the strength was closely related.

The best processing parameters were obtained through the above-mentioned trials, namely laser power of 400 W, volume of laser defocus of −2 mm, welding speed of 750 mm/min and TIG current of 70 A.

6.4.5 Characteristics of microstructure of direct joints

Figure 6.9 is the scanning electron microscope (SEM) image of a direct joint of Mg alloy and steel. During the welding process, some spatters occurred; thus, some big particles with the composition of Fe element were generated in the FZ, as shown in Fig. 6.9(a). As there is no interaction between Mg and Fe, the interfaces of Mg alloy and steel are distinct without a transitional zone. Due to a large difference in hardness, the sections of Mg alloy and steel in the prepared metallographic sample were not at the same level, as indicated by white arrows in Fig. 6.9(b–d). As indicated by black arrows in Fig. 6.9(b–d), a series of discrete gaps formed at the interface of Mg alloy and steel, suggesting that Mg alloy and steel are not bonded intimately enough in spite of some oxides[21] produced between them. Generally, the formation of the gaps

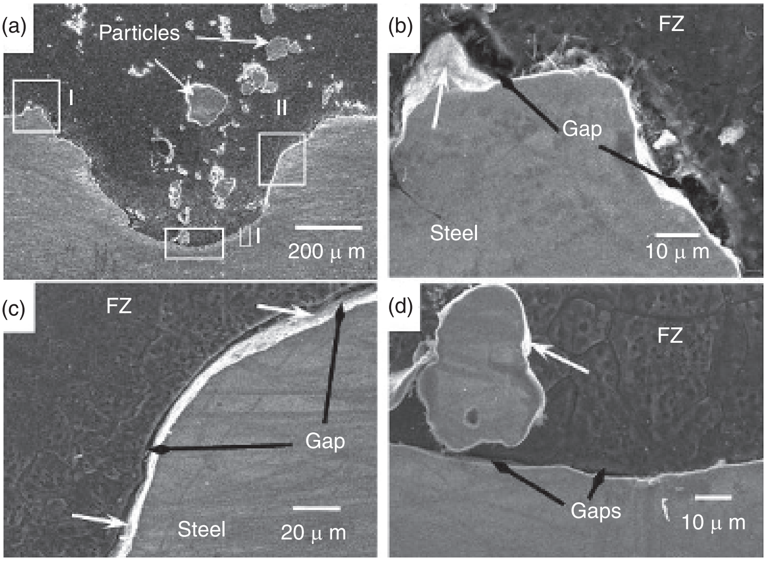

6.9 Microstructures of direct joint: (a) cross-section; (b), (c) and (d) from region I, II and III in (a) are interfacial structures of Mg alloy and steel.

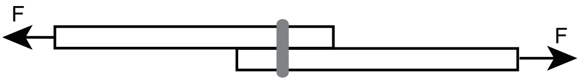

6.10 Sketch of sample in the tensile shear test.

between FZ and base materials is not favorable for the enhancement of joint mechanical properties.

6.4.6 Mechanical properties of direct joint

The joint strength test was carried out on the tester of a CSS-2205 electronic universal machine, and the sketch of the sample is shown in Fig. 6.10.

The clamped specimen was subjected to tensile testing at room temperature and traveling speed of 0.5 mm/min. The ultimate tensile force was recorded and then converted into the strength. The average of three specimens was taken as the value under this condition. It was found that the specimen failed at Mg alloy/steel interface. The average joint shear strength was 116.6 MPa.

6.5 Nickel-added joining of magnesium alloys to steel

6.5.1 Welding procedure

As the thickness of nickel interlayer, 100 microns, is very small compared to the thickness of base materials it has little effect on welding parameters after adding Ni interlayer; the laser power can be increased slightly to 450 W.

6.5.2 Characteristics of microstructure

Figure 6.11 shows the characteristics of a cross-sectioned joint with Ni interlayer. Some big particles distributed unevenly in the joints are exhibited by arrows, which may be ascribed to the stirring effect resulting from strong convection in the welding pool.

From Fig. 6.12(a) and (b), it can be seen that a new ribbon-shaped layer on the interface of the Mg alloy and the Ni interlayer was generated at the upper edge of the molten pool along the surface of the Ni interlayer, with distinct dendrites on top and compact lamellar structure at the bottom, as shown in Fig. 6.12(c). Figure 6.12(d) and (e) present the interface between Mg alloy and steel in the molten pool. A transitional layer between the dashed and the distinct white boundary was observed. Map analysis given in Plate II (b) (see color section between pages 210 and 211) shows that the layer did not contain an Mg element, indicating that Mg did not react with Ni or diffuse into the layer. However, this layer is not pure Ni interlayer any more, as is shown in Plate II (c). In light of the Fe element distribution in Plate II (d) and the Fe-Ni binary phase diagram, the transitional layer is a solid

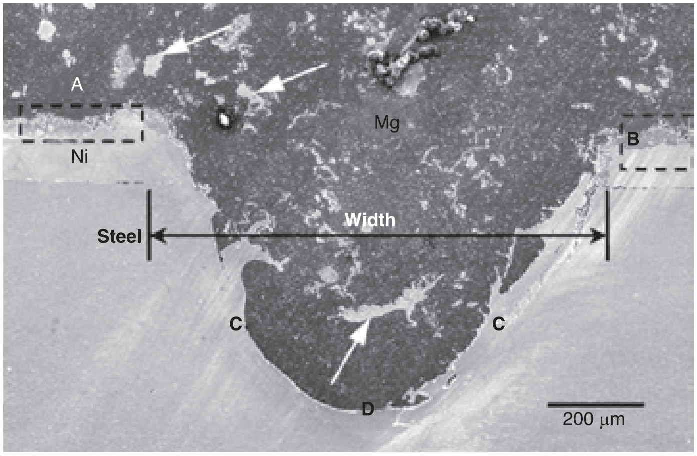

6.11 SEM microstructure of a joint with Ni interlayer.

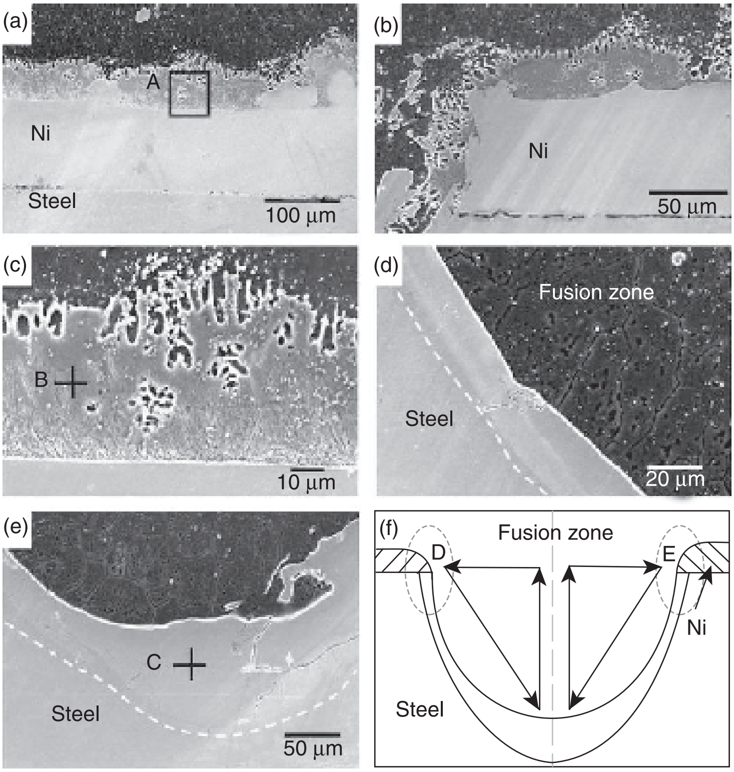

6.12 SEM images mainly from different locations in Fig. 6.11 and flow pattern in molten pool: (a), (b), (d) and (e) are from positions A–D of Fig. 6.11 and (c) area A in (a), and (f) sketch of flow pattern.

solution of Ni in Fe.[22,23] As the flow in the present experiment was intense and the compelling convection moved clockwise[24,25] from the centerline of the weld pool to the edges of the pool (Fig. 6.12(f)), the vortex was produced in the molten pool. Due to the action of the flow, the solid solution accumulated at the bottom of the pool formed the final morphology (Fig. 6.12(e)).

6.5.3 Distribution of Ni

Figure 6.13 is the X-ray diffraction (XRD) spectrum obtained from the fracture shown in Fig. 6.13(b). As the Ni interlayer is attached tightly to the Mg alloy and the fracture surface is very small, it is inevitable for Ni interlayer at the margins of fracture to be detected, as shown in Fig. 6.13(d). Some low-intensity peaks of a-Mg shown in Fig. 6.13 indicate that the fracture is composed of a majority of remelted Mg alloys. Combining with Fig. 6.12(d), (e) and energy dispersive spectrometer (EDS) analysis, the solid solution in the welding pool was the area between the distinct boundary and the broken line. The XRD pattern in Fig. 6.13 exhibits some new but weak peaks, suggesting that Mg_2Ni is distributed mainly at the interface of Mg alloy and Ni interlayer.

According to the EDS analysis, the composition of position B in Fig. 6.12(c) is 42.76 wt% Mg and 57.24 wt% Ni, indicating that the ribbon-shaped area in Fig. 6.12(a) and (b) is mainly composed of Mg_2Ni, in which Mg alloy and Ni interlayer were bonded successfully. Thus, the formation of the Mg_2Ni phase and the solid solution indicated the interaction of Ni with Fe and Mg elements, which occurred under the action of hybrid heat sources, and also suggested that metallurgical bonding occurred in the welding process.

6.5.4 Welded joint properties

The dimension of the specimen for tensile shear test is 80 × 10 mm. The results of the test are provided in Table 6.2, which indicate that the average shear

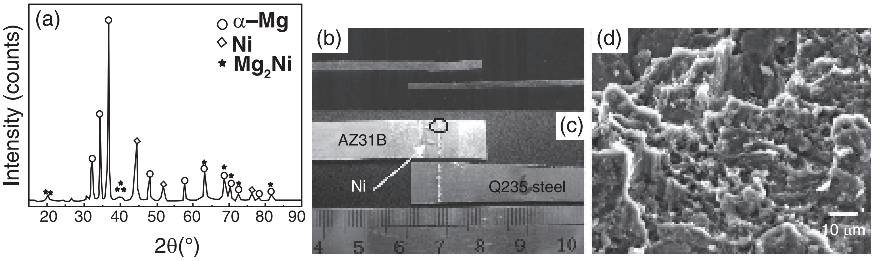

6.13 Interface between Mg alloy and Ni interface and fracture location: (a) XRD analysis; (b) transverse section of fracture of a specimen; (c) inside the joint; and (d) fracture surface from the Mg alloy side (circle region).

Table 6.2 Results of shear test

Names	Specimen 1	Specimen 2	Specimen 3	Specimen 4	Specimen 5	Average
Shear strength (MPa)	176	173	159	166	180	170.8

strength of the Ni-added joint can reach 170.8 MPa, higher than that of a direct joint (116.8 MPa).

6.6 Conclusion and future trends

Direct joining of magnesium alloy to steel can be realized with lower strength. From the above analysis, it can be concluded that although some oxides were found in the transverse sections, it is not sure how the O elements come into the FZ: through the welding process, sample preparation, or both. Consequently, the bonding mode of a direct joint is still mechanical and the shear strength of a joint is not high. With the addition of Ni interlayers, IMCs were detected at the Mg alloy/Ni interfaces. They are proof of metallurgical bonding; with the solution of Ni in Fe at the bottom of the melting pool, another metallurgical bonding between Ni interlayer and steel was completed. In contrast with the direct joining, metallurgical bonding was realized, which is a good sign for the bonding of Mg alloy and steel. In order to avoid the occurrence of galvanic cell erosion on the Mg alloy/steel joint, the whole structure should be shielded.

In the near future, joining Mg alloy to steel to achieve versatile properties in materials should be pursued in the welding of dissimilar materials.

6.7 References

1. Chinese Mechanical Engineering Society (2001). *Technology and Setup: Handbook of Welding*, Vol 1. Beijing China Machine Press.
2. Meng Q, Wang W, Wu Z (2005). *Welding Foundation of Metal Materials*. Beijing: Chemical Industry Press.
3. Li YJ, Wang J, Liu Q (2006). *Welding and Application of Nonferrous Alloy*. Beijing: Chemical Industry Press.
4. Liu ZQ, Di B (1990). *Dissimilar Materials Welding*. Beijing: Science.
5. Li YJ, Wang J, Liu P (2003). *Welding and Application of Dissimilar Materials with Poor Weldability*. Beijing: Chemical Industry Press.
6. Zeng RC, Ke W (2001). Recent development and application of magnesium alloys. *Acta Metallurgica Sinica* **37**(7): 673–85.
7. Cheng ZH (2004). *Mg Alloy*. Beijing: Chemical Industry Press.
8. Gu YX (1996). *Welding of Special Engineering Materials*. Liaoning: Liaoning Science & Technology.

9. America Welding Association (1991). *Welding Handbook: Metal and its Weldability,* Vol. 4, Beijing: China Machine Press.
10. Sato YS, Hwan S, Park C (2004). Constitutional liquation during dissimilar friction stir welding of Al and Mg alloys. *Scripta Mater* **50**(9): 1233–6.
11. Somasekharan AC, Murr LE (2004). Microstructure in friction stir welded dissimilar aluminum alloy. *Mater Charact* 52(1): 49–64.
12. Irving B (1992). Dissimilar metal welding paves the way to new venture. *Weld J* **71**(5): 27–33.
13. Aghion E (2001). The role of the Mg industry in protecting the environment. *J Mater Process Technol* **117**(3): 381–5.
14. Lilijas M (1995). 'Development of superaustenitic stainless steels' Paper presented at IIW-95 Annual Assembly, International Conference on Welding of Stainless Steels; June 12–13 1995; Stockholm, Sweden, Avesta Sheffield AB, R&D, S-77480 Avesta, Sweden.
15. Karlsson L (1995). Welding duplex and super duplex stainless steels. *Anti-Corrosion Meth Mater* **42**(6): 30–35.
16. LaBeouf BPS (1990). *Welding of Aluminum and its Alloy to Other Metals*. Beijing: China Astronautic Publishing House.
17. Pierre D, Viala JC, Peronnet M, Bosselet F, Bouix J (2003). Interface reactions between mild steel and liquid Mg-Mn alloys. *Mater Sci Eng A* **349**(1–2): 256–64.
18. Chen YC, Nakata K (2009). Effect of tool geometry on microstructure and mechanical properties of friction stir lap welded magnesium alloy and steel. Mater Design **30**(9): 3913–19.
19. Liu LM, Song G, Liang GL, Wang J (2005). Pore formation during hybrid laser-tungsten inert gas arc welding of magnesium alloy AZ31B: mechanism and remedy. *Mater Sci Eng A* **390**(1–2): 76–80.
20. Mezbahul-Islam M, Medraj M (2009). A critical thermodynamic assessment of the Mg-Ni, Ni-Y binary and Mg-Ni-Y ternary systems. *Comput Coupling Phase Diagr Thermochem* **33**(3): 478–86.
21. Liu LM, Zhao X (2008). Study on the weld joint of Mg alloy and steel by laser-GTA hybrid welding. *Mater Charact* **59**(9): 1279–84.
22. Kundu S, Chatterjee S (2006). Interfacial microstructure and mechanical properties of diffusion-bonded titanium–stainless steel joints using a nickel interlayer. *Mater Sci Eng A* **425**(1–2): 107–13.
23. Liu XB, Pang M, Guo J, Yu G (2008). Transmission electron microscopy characterization of laser welding cast Ni-based superalloy K418 turbo disk and alloy steel 42CrMo shaft. *J Alloys Comp* **461**(1–2): 648–53.
24. Yang XC (2002). Research on physical transfer process in a laser melting pool. *J Tianjin Polytech Univ* **21**(4): 1–7.
25. Liu JL, Liu C (1993). Melt flow in alloy melted pool under the action of laser. *J Chongqing Univ.* **16**(5): 109–23.

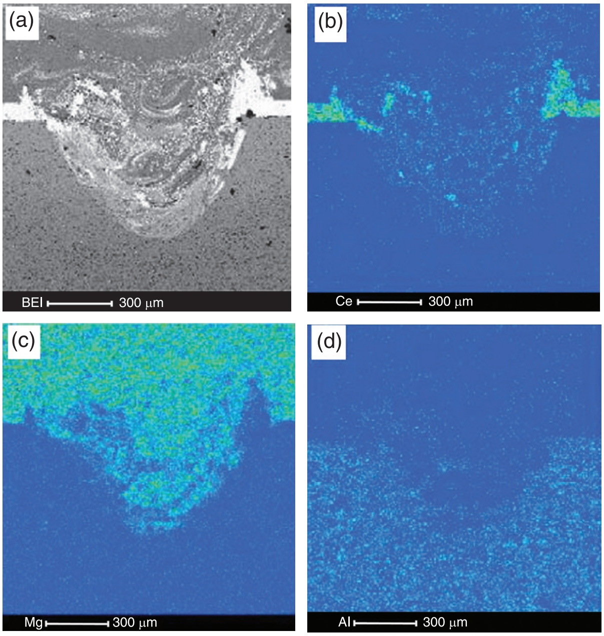

Plate I (a–d) EPMA image and distribution maps of major elements of hybrid welding of Mg-Al joint with added Ce.

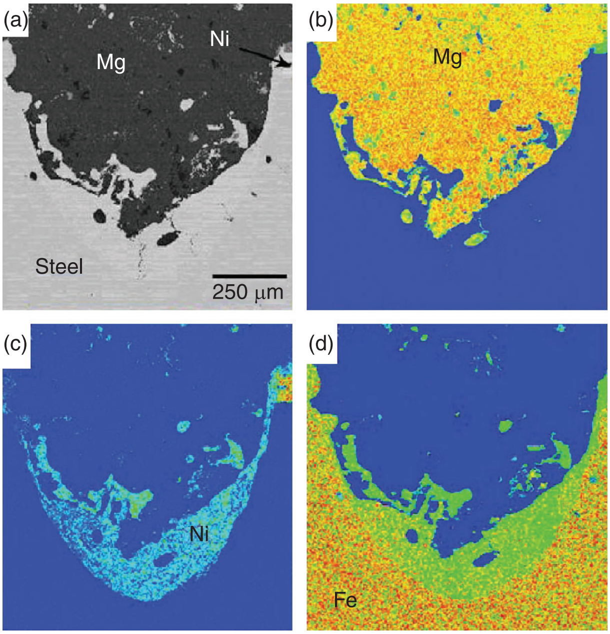

Plate II Distribution maps of (a) back scattered electron image; (b) Mg element; (c) Ni element and (d) Fe element.

7

Corrosion and protection of magnesium alloy welds

L. LIU, Dalian University of Technology, China

Abstract: In this chapter, the corrosion behaviors of magnesium alloy weldments are discussed, including Mg-Mg weldment, Mg-Al weldment and Mg-steel weldment. The application of arc spray technology on the Mg alloy weldment is shown. In addition, post-treatment technology of coating is introduced. Lastly, the chapter depicts the research trend of corrosion and protection of Mg alloy weldments.

Key words: magnesium alloy, weldment, corrosion, protection.

7.1 Introduction

Mg and its alloys are considered to be the most promising material categories of the twenty-first century.[1] Having densities 36% less than Al and 78% less than steel, Mg alloys have excellent strength/weight ratios.[2] In addition to their intrinsic characteristics of low density and high specific strength and stiffness, their high recyclability is attractive in reducing environmental burdens. Research findings on the welding of Mg alloys have been published in recent years. Mg alloys are welded with Mg alloys, Al alloys and steel, using various methods such as tungsten inert gas (TIG) welding, metal inert gas (MIG) welding, active flux welding, laser welding, electron beam welding, laser-TIG hybrid welding, laser bonding welding, plasma bonding welding and so on.[3–9]

It is evident that further applications of Mg alloy weldments are limited due to their poor corrosion resistance. With its extreme low corrosion potential, Mg alloy is always the most active metal, and a welding joint provides an electrically conductive connection in salt solution environments between Mg alloy and other metals, including Al alloys, steel and so on, resulting in severe galvanic corrosion and causing a deterrent to the use of Mg alloy in welding structural applications.[10] Besides, Mg alloy weldment, such as the fusion zone (FZ) and heat affected zone (HAZ), always undergoes microstructure and phase changes, making the corrosion performance of the weldment even more different in comparison to that of base metal.

Subsequently, research on corrosion mechanism and protection procedures of Mg alloy weldments is important and necessary. In this chapter, the corrosion behaviors and mechanisms of welds are discussed, including magnesium alloy weldments, brazing joint of magnesium alloy to Al alloy and the lap joints of AZ31 magnesium alloy to Q235 mild steel. In addition, several protection methods, such as arc spray and its post-treatments technology, are attempted to protect the Mg alloy weldments.

7.2 Corrosion characteristics of magnesium alloy weldment

7.2.1 Corrosion behaviors of laser-arc hybrid welded AZ91 magnesium sheet

Figure 7.1 displays the corroded macrostructures of a laser-arc hybrid welded AZ91 magnesium alloy joint detected by optical mirror before and after a two-hour salt spray test with 3.5% NaCl solution. The results show that localized corrosion has occurred over the whole surface area of weldment. The HAZ of the weldments exhibits the highest corrosion degree, with base zone (BZ) the second and FZ the lowest.

The polarization curves of weld joints in 3.5% NaCl saturated with $Mg(OH)_2$ solution are shown in Fig. 7.2. The polarization parameters measured from the polarization curves are given in Table 7.1. The results show apparent differences in the corrosion potential and the corrosion current density in the different zones of AZ91 alloy weld joint. For BZ, the corrosion potential is −1618 mV and current density is 4.744 $\mu A/cm^2$. For HAZ, the corrosion potential enhances by 6 mV, whereas corrosion density increases by 1.704 $\mu A/cm^2$, comparing with the BZ. For FZ, the corrosion potential is 13 mV higher than that of BZ and the

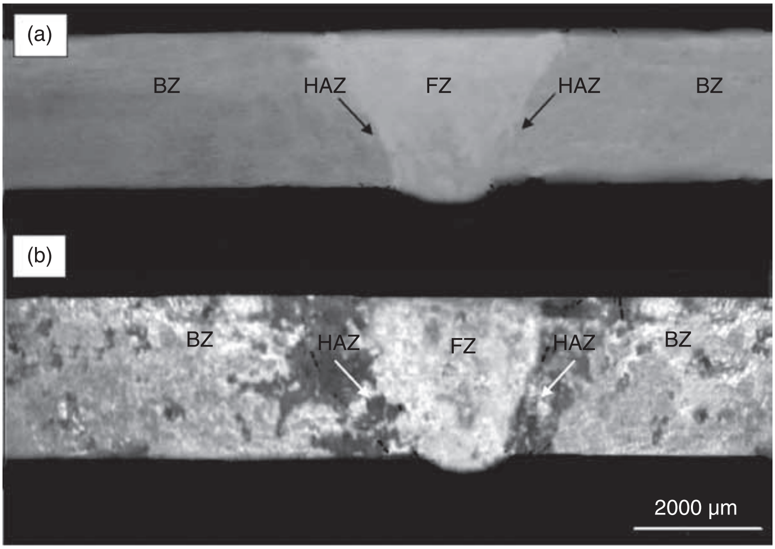

7.1 Cross-section macrostructure of the laser-arc hybrid welded AZ91 magnesium alloy joint: (a) before salt immersion test, and (b) after salt immersion test.

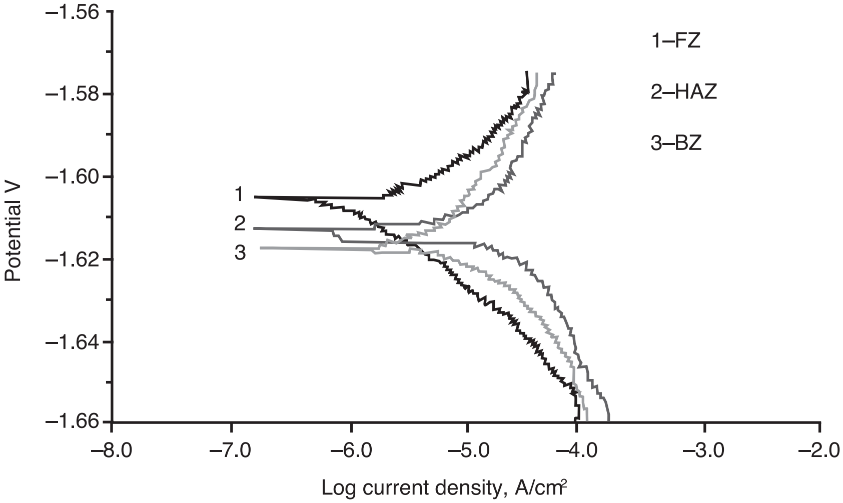

7.2 Polarization curves of laser-TIG hybrid welded AZ91 magnesium alloy in 3.5% NaCl saturated with $Mg(OH)_2$.

Table 7.1 E_{corr} and I_{corr} of different zones of AZ91

Zone	E_{corr} (mV)	I_{corr} (μA/cm²)
FZ	−1605	3.524
HAZ	−1612	6.448
BZ	−1618	4.744

current density is 1.22μA/cm² lower than that of BZ. The HAZ does not make a significant change in the corrosion potential but increases in corrosion current, compared to BZ. FZ has the lowest corrosion current density and the highest corrosion potential, meaning the highest corrosion resistance, whereas HAZ has the lowest. The differences of the potential among BZ, HAZ and FZ may induce galvanic corrosion, which could induce the pitting corrosion of the weld joint. The results of electrochemical tests are in accord with a salt spraying test.

The influence of microstructure on corrosion behavior of AZ91 can be understood from the interaction of the α-phase and β-phase, addition of elements and segregation of elements.[11–14] During the laser-arc hybrid welding, no other elements are added and harmful elements are not segregated, such as Fe element.

Grain size and interaction between the α-phase and β-phase play an important role in the corrosion behaviors of weld joints obtained by laser-arc hybrid technology. Song et al. have shown that the free corrosion potential of the β-phase (−1.3 V) is 0.3 V higher than that of the α-phase (−1.6 V) in sodium chloride solutions.[15,16] The β-phase has two different influences on the corrosion behaviors:

the β-phase can act as a galvanic cathode to accelerate corrosion and a corrosion barrier to hinder corrosion.

For the FZ, grains are very fine and the β-phase forms a continuous net over the α-Mg matrix, as shown in Fig. 7.3(a). During the corrosion process, β-phase particles do not readily fall out. Instead, many more α grains are completely separated by β-phase. The α-matrix corrodes much more easily due to the simultaneous corrosion of β-phase and α-matrix. With the increases of corrosion time, the α-matrix corrodes and falls out. The β-phase fraction forms a barrier resulting in a decrease of the corrosion rate. Finally, the corrosion susceptibility decreases.

For HAZ, grains grow and the isolated β fractions distribute unevenly, as shown in Fig. 7.3(b) and Fig. 7.4. The β fractions of some regions are more but

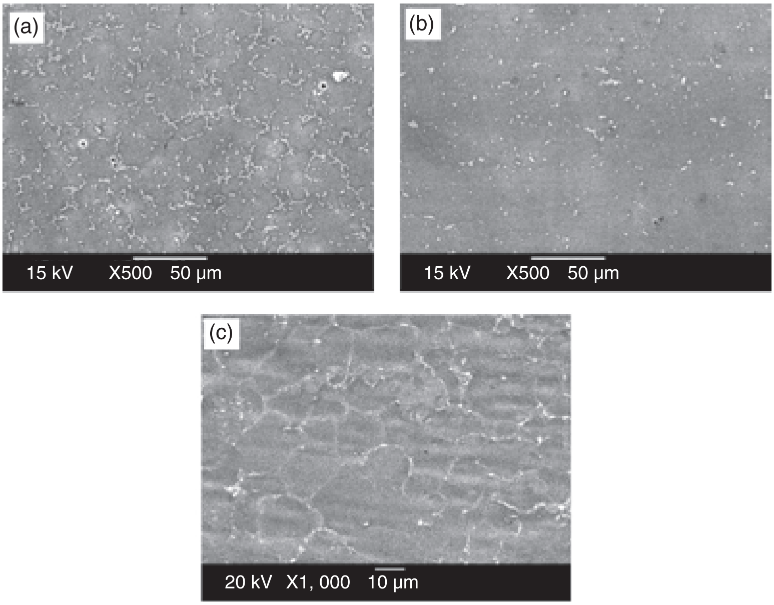

7.3 Microstructure of different zones in AZ91 magnesium alloy joint detected by scanning electron microscope: (a) FZ, (b) HAZ, and (c) BZ.

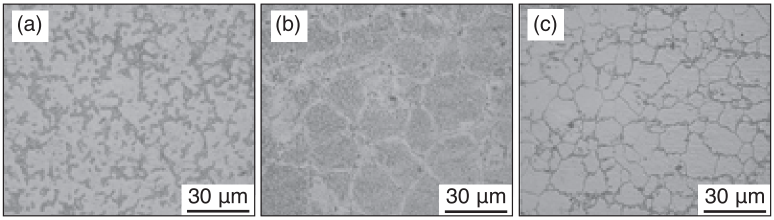

7.4 Magnification microstructure of different zones: (a) FZ, (b) BZ, and (c) HAZ.

those of some are less. The isolated β fractions do not form a continuous barrier to reduce the corrosion rate. At the beginning of corrosion, uneven β fractions cause micro-galvanic corrosion of the α-phase, resulting in accelerated corrosion of the adjacent α-phase. With the increase of the corrosion degree, the β fractions easily fall out by undermining. Therefore, the α-phase is not effectively blocked by this type of isolated β fraction or by the corrosion products deposited between the β-phase and the α-phase. The corrosion between the β-phase and the α-phase is accelerated without the barrier of β-phase. So the corrosion susceptibility of HAZ is enhanced.

In BZ, the grain is middle-sized compared to with that in FZ and HAZ, as can be seen in Fig. 7.3(c) and Fig. 7.4. The finest β fractions are homogeneously distributed along the grain boundary in BZ. The β-phase in BZ has a weaker barrier than that of FZ and makes a less active cathode to α-phase than that in HAZ.

In addition, the relations between microstructure and corrosion behavior of arc-welded AZ31B magnesium sheet are at present being investigated by G. Ben-Hamu.[17] Corrosion of friction stir welded magnesium alloy AM50 is being studied by Rong-Chang Zeng.[18] From all the above-mentioned data, the different zones of weld joint show different corrosion susceptibilities. In summary, the weld process affects both the microstructure and the corrosion behavior of magnesium alloy resulting in the different corrosion susceptibilities of BZ, HAZ and FZ.

7.2.2 Corrosion behaviors of the joints of magnesium alloy to dissimilar metals

Corrosion behaviors of lap joints of magnesium alloy to mild steel are investigated in this chapter. Figure 7.5 shows the SEM images of a cross-sectioned weld joint

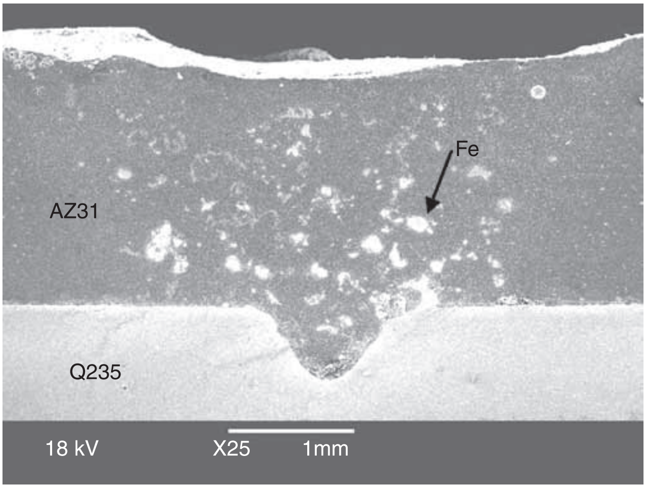

7.5 SEM images of cross-sectioned weld joint of AZ31 magnesium alloy to Q235 mild steel.

of AZ31 magnesium alloy to Q235 mild steel by laser-arc hybrid welding. Since some spatters occurred with the mixing effect in the laser-arc hybrid welding process, numerous big white particles in the weld pool are generated, as shown in Fig. 7.5. The white particles consist of Fe elements.[19] The concentrations of heavy metal impurities, such as iron, nickel and copper, can decrease the corrosion resistance of Mg alloy dramatically.[20]

Fe particles in the weld pool can increase the corrosion susceptibility significantly. At the same time, there is a wide difference in the electrochemical potentials of Mg and Fe. A welding joint provides an electrically conductive connection in salt solution environments between Mg alloy and steel. The severe galvanic corrosion between them is a deterrent to the use of Mg alloy in structural applications. Figure 7.6 shows the corrosion macrostructures of a weld joint in 3.5% NaCl saturated with $Mg(OH)_2$ for ten minutes. It is found that the weld joint suffers severe corrosion after a salt immersion test. The polarization curves of lap joints of magnesium alloy to mild steel and AZ31 base in 3.5% NaCl saturated with $Mg(OH)_2$ solution are shown in Fig. 7.7. It has been found that corrosion current density increases significantly. The results of electrochemical tests are in accord with the salt immersion test.

The corrosion characteristics of soldering joints of AZ31 magnesium alloy to 6013 aluminum alloy are being investigated by Bernhard Wielage, Silke Mucklich, and Thomas Grund. The research results show that intermetallic phases are formed in the soldered seam, as shown in Fig. 7.8. For the higher electrochemical potential of aluminum and filler materials, the corrosion current density of the soldered samples shows an increase of about one order of magnitude in comparison to bulk magnesium samples, as shown in Table 7.2.[21]

In summary, the corrosion rate of the joints of magnesium alloy to dissimilar metals can be accelerated by galvanic corrosion. Therefore, it is important to explore corrosion protection methods for the joints of magnesium alloy to other metals.

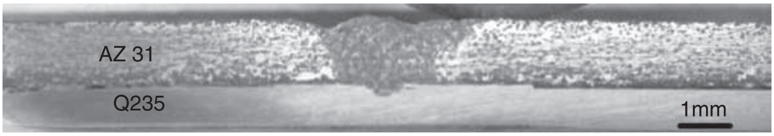

7.6 Corrosion macrostructures of a weld joint in 3.5% NaCl saturated with $Mg(OH)_2$ solution for ten minutes.

Table 7.2 Corrosion current densities and corrosion potentials of base materials and soldered joints measured in 3.5% NaCl solution[21]

	Corrosion current density (mA/cm^2)	Corrosion potential (mV)
Base materials (AZ31)	10 ± 2	−1380 ± 30
Soldered Joints (AZ31/6013)	273 ± 193	−1328 ± 62

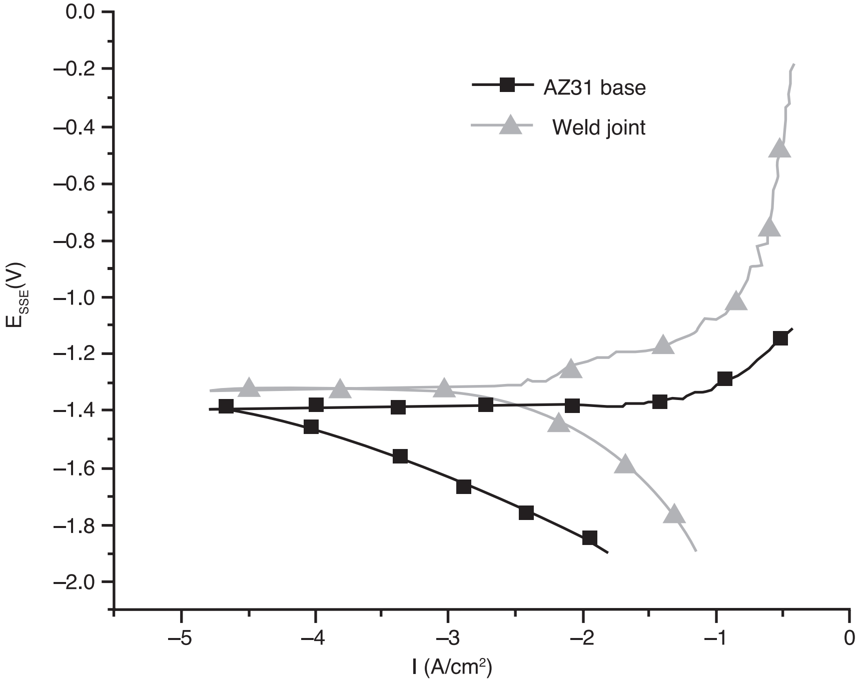

7.7 Polarization curves of low-power laser-TIG hybrid welded AZ31 magnesium alloy to mild steel in 3.5% NaCl saturated with $Mg(OH)_2$.

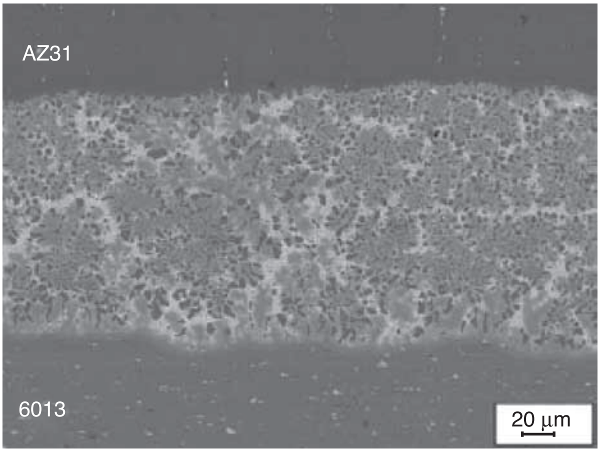

7.8 Microstructure of soldered joint between magnesium (upper side) and aluminium (lower side).[21]

7.3 Improvement in the corrosion resistance of magnesium alloy weldment

7.3.1 Arc spray technology

Arc spray is known to be one of the less expensive thermal spraying processes with an ability to produce dense coatings with a high rate of material deposition.[22] The technique is considered to be appropriate for improving the corrosion resistance of magnesium alloy weldments in view of its growing reputation as a simple, fast, economical, efficient technique to produce thick Al coatings on Mg alloy weldments.

Pure Al wires (wt% Al ≥ 99.7%) with a diameter of 2 mm are employed for the coating deposition. The selected parameters for arc spraying are as follows: spray distance of 150 mm, air pressure of 0.6 MPa, arc voltage of 28 V, arc current of 200 A. The samples are first shot blasted by Al_2O_3 particles with the average grain size of 0.6 mm. Figure 7.9 exhibits the interface morphologies of an arc-sprayed Al coating of magnesium alloy joints. The thickness of coating is about 800 μm. No cracks are detected in the coating/substrate interface, and good mechanical bonding can be obtained between Al coating and substrate.

Figure 7.10 exhibits the longitudinal section morphologies of the lap joints of AZ31 magnesium alloy to Q235 mild steel with arc-sprayed Al coating. The lap joints are completely covered by Al coating. The lap joint is separated from the

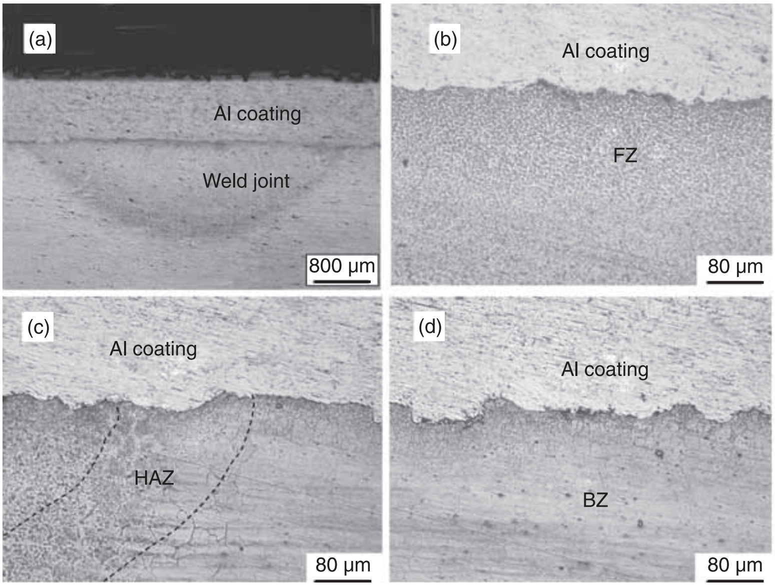

7.9 Cross section of an arc-sprayed Al coating on AZ31welded joint: (a) macrostructures of Al coating on AZ31welded joint; (b) interface pattern between Al coatings and FZ; (c) Al coatings and HAZ; and (d) interface pattern between Al coatings and BZ.

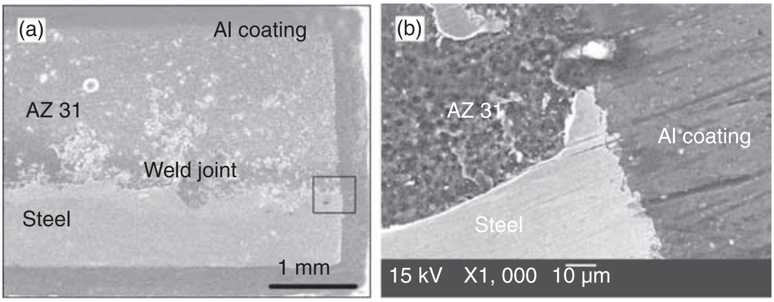

7.10 (a) Longitudinal section morphologies of the lap joints of AZ31 magnesium alloy to Q235 mild steel with arc-sprayed Al coating. (b) SEM microstructure of interface between weld joint and Al coating.

external environment by Al coating. Figure 7.10(b) shows the interface morphologies between arc-sprayed Al coating and lap joints of AZ31 magnesium alloy to Q235 mild steel. The weld joint and the Al coating show a good mechanical bonding at the interface, and no cracks are detected. The weld joint is protected by the arc-sprayed Al coating.

7.3.2 Post-treatment technology of arc spraying

The defects, such as porosity in coating, can greatly affect the bonding strength and mechanical property of formed parts, and make the penetration of aggressive species much easier, and subsequently affects the corrosion performances, so sealing treatment is of importance for arc spraying treatment. It is widely known that organic sealants, such as polyurethane- and epoxy-based sealants, have many technical and economic advantages for corrosion protection associated with barrier effects.[23,24] Three sealing treatments methods are attempted to improve the corrosion resistance of Al coating for magnesium alloy joints, mainly including epoxy resin sealing, hydrothermal sealing and micro-arc oxidation (MAO).

Epoxy resin sealing treatment

Epoxy resin sealing is a simple and effective sealing technology of Al coating. In our study, conventional epoxy resin and electrical conductive Al-rich epoxy resin-based paint are applied to the Al coating for improving the corrosion resistance of Al coating. Certain epoxy resins and polyamide firming agents (1:1 in weight) are used for conventional epoxy resin. Electricity conductive Al-rich epoxy resin-based paint is prepared by epoxy resin and polyamide firming agent (1:1 in weight) together with Al powder having a mean diameter of about 70 μm (200 mesh) and ophthalmic ester coupling agent 0.2% by weight.

Figure 7.11 shows the appearance of epoxy resin-sealed coating and the appearance of the Al-rich paint. An acceptable surface with small roughness and little glisten is obtained. Figure 7.12 represents optical images of the paint cross-sections. Al particles are discretely distributed, but certain defects, such as uneven particle concentrations and pores, can be observed in the paint. Few interstices either in the paint–coating interface or in the particle–resin interface are detected indicating a tight adhesion in the interface and a close integration in the paint, subsequently implying that Al powder has a good compatibility with epoxy resin.

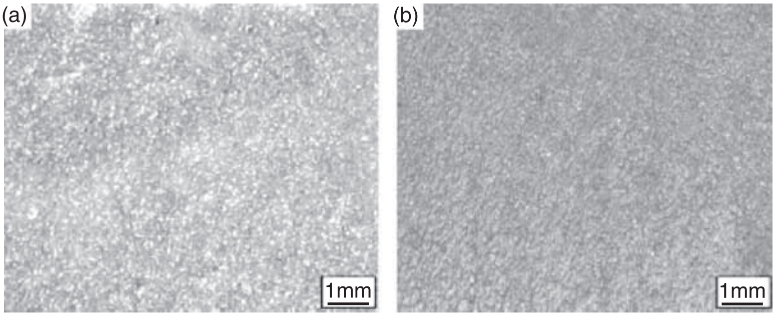

7.11 Appearance of (a) epoxy resin sealed coating, and (b) Al-rich paint.

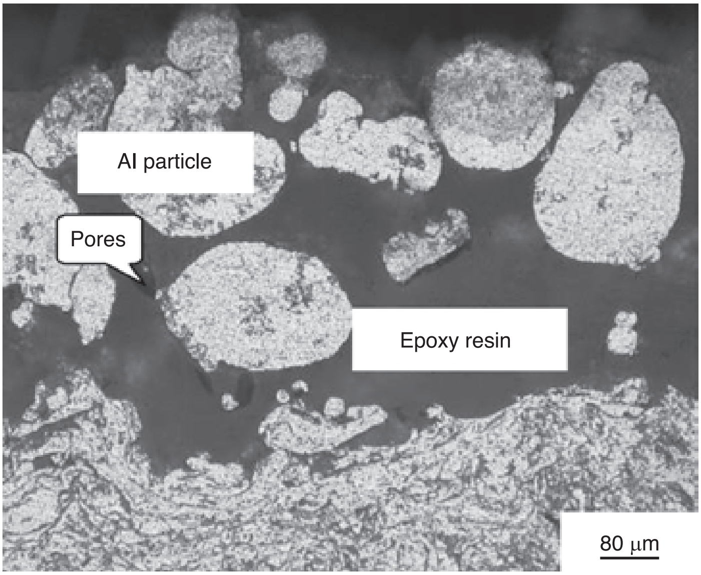

7.12 Cross section of the Al-rich epoxy resin based paint on the Al coating.

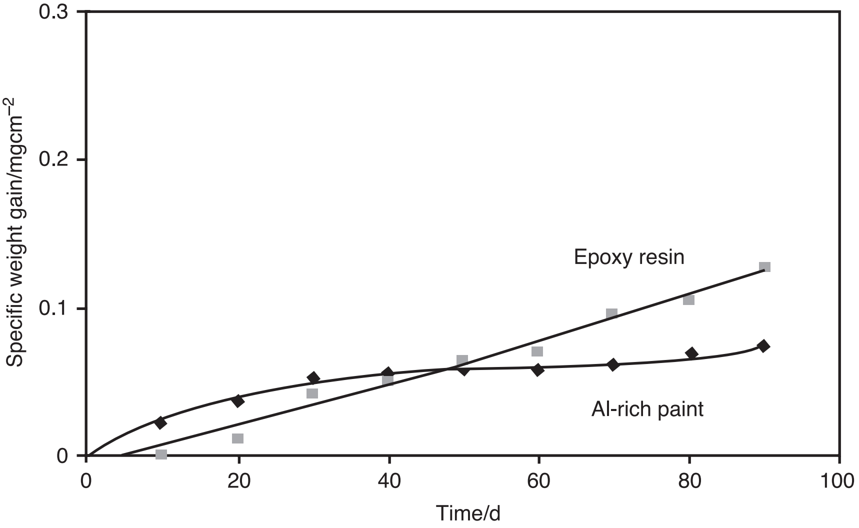

7.13 Corrosion kinetics of the epoxy resin- and paint-sealed coatings in SSIT.

Corrosion performances are evaluated with a salt immersion test in an aerated neutral 5 wt% NaCl solution at 25–28 °C for up to 90 days. The corrosion test shows that the two sealed coatings experience similar corrosion rates as can be seen in Fig. 7.13. The epoxy resin-sealed coating corrodes linearly and faster (faster because of blister and desquamation), while the paint-sealed coating corrodes more and more slowly. In other words, the addition of Al fillers arrests defects of the epoxy resin including blister and desquamation and, moreover, changes the linear corrosion rate into a slower and slower corrosion rate.

Hydrothermal sealing treatment

Hydrothermal sealing is an economic and effective post-treatment technology of Al coating. Figure 7.14 shows the surface morphologies of sealed and unsealed Al coating. There is no evident difference between the unsealed coating and the sealed coating, except that the hydrothermal sealing treatment (HST) coating is a little darker than the unsealed one.[25] Figure 7.15 shows the morphologies of the unsealed coating and the HTS coating. Some inherent pores appear in the top surface of the unsealed coating. After the HTS treatment, pores in the coating surface get smaller and fewer. Unlike the even pores in the anodic oxide film of aluminum, pores in the arc-sprayed coatings are uneven in shape and size, some of which are much bigger, and so they can only be plugged to a certain extent by HTS treatment. With the assistance of SEM–EDX analysis, both the unsealed coating and the HTS coating are compared in the content of Al

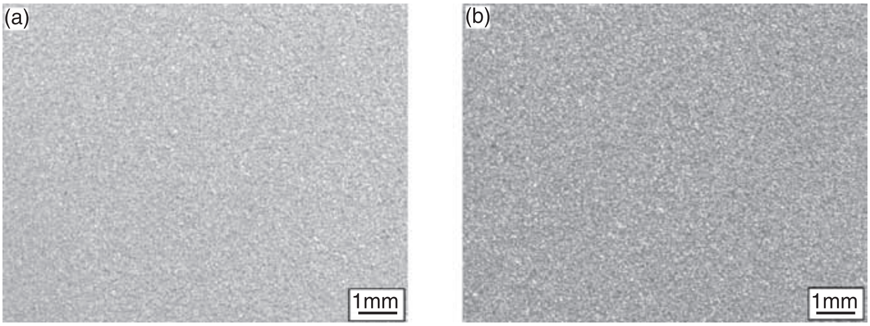

7.14 Appearance of the coatings: (a) the unsealed coating, and (b) the HTS coating.

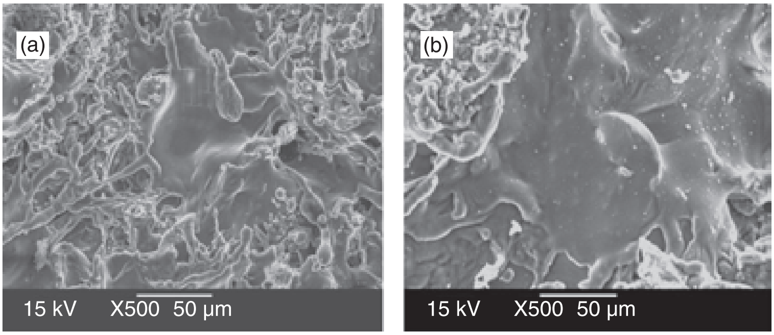

7.15 Morphologies of the coatings: (a) the unsealed coating, and (b) the HTS coating.

and O elements. On average, the HTS coating possesses an amount of O element more than twice as much as the unsealed coating. Corrosion performances of the unsealed coating and the sealed coating are evaluated and compared with the salt solution immersion test (SSIT). SSIT is conducted in an aerated neutral 5 wt% NaCl solution at 25 ± 2 °C for up to 90 days. The corrosion test shows that the corrosion resistance of Al coating is improved by HTS, as can be seen in Fig. 7.16.[25] The corrosion test shows that the two coatings undergo different corrosion rates. The unsealed coating suffers a more severe corrosion attack than sealed coating. Hydrothermal sealing can clearly improve the corrosion resistance of Al coating.

Micro-arc oxidation treatment

Recently, MAO has attracted more attention by virtue of its convenience and effectiveness to prepare oxide ceramic coatings with porous structures in the

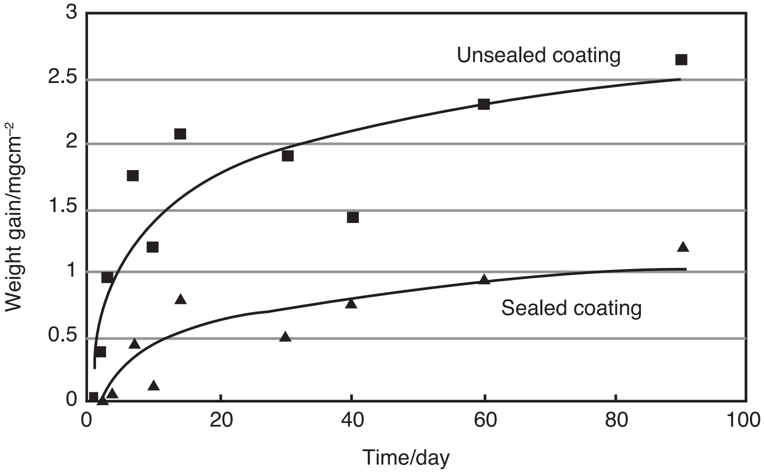

7.16 Corrosion kinetics of the coatings in SSIT.

surface of Ti, Al, Mg and their alloys.[26–28] Hence, it is attempted as a sealing treatment for thermal spraying coatings. The rough surface of the sprayed coating makes MAO treatment much easier, and simultaneously, MAO treatment makes the coating much more corrosion-resistant. In addition, arc-sprayed Al coating and MAO coating are both inherently corrosion-resistant, and evidently their combination will be equally effective.

Figure 7.17(a) shows the surface SEM images of Al coating with a MAO post-treatment. A coarse and porous surface is detected. The porous surface of the MAO coating can be traced back to the physical phenomena occurring during the coating process, as explained by Curran and Clyne.[29] Figure 7.17(b) is the XRD pattern of MAO coating on arc-sprayed aluminum coating. It is composed of α-Al_2O_3, γ-Al_2O_3 and θ-Al_2O_3. The oxide coating on arc-sprayed Al coating appears from plasma thermal chemical reactions in the discharging channels. The vicinal matter of the discharge channel is melted by the instantaneous several thousand degree high temperature in the discharging channels, and subsequently solidifies rapidly at surface–electrolyte interface, resulting in an amorphous Al_2O_3 phase (α-Al_2O_3, γ-Al_2O_3 and θ-Al_2O_3) within the ceramic coatings.

Al coating and MAO coating are performed in a salt solution of 5 wt% NaCl with pH 6.5. The electrochemical measurement is conducted using a conventional three electrodes electrochemical cell with a saturated calomel electrode as the reference, a Pt foil as the auxiliary electrode and the samples with an area of 1 cm^2 as working electrode. The corrosion test shows that corrosion current density of MAO coating decreases and the corrosion potential increases, showing a much improved corrosion resistance, as is to be seen in Fig. 7.18. MAO treatment technology is applied to the Al coating, improving its corrosion resistance.

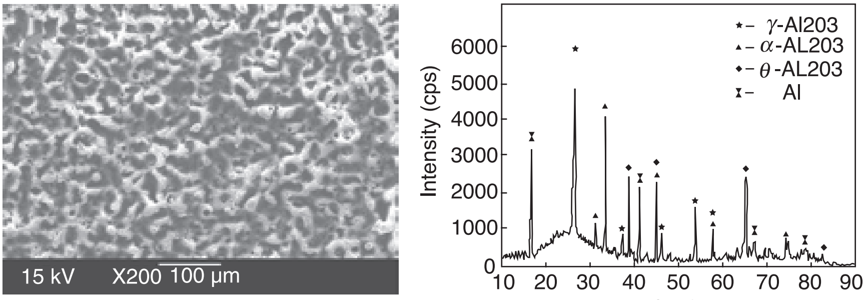

(a) (b)

7.17 (a) Surface images of MAO coating. (b) XRD pattern of MAO coating on arc-sprayed Al coating.

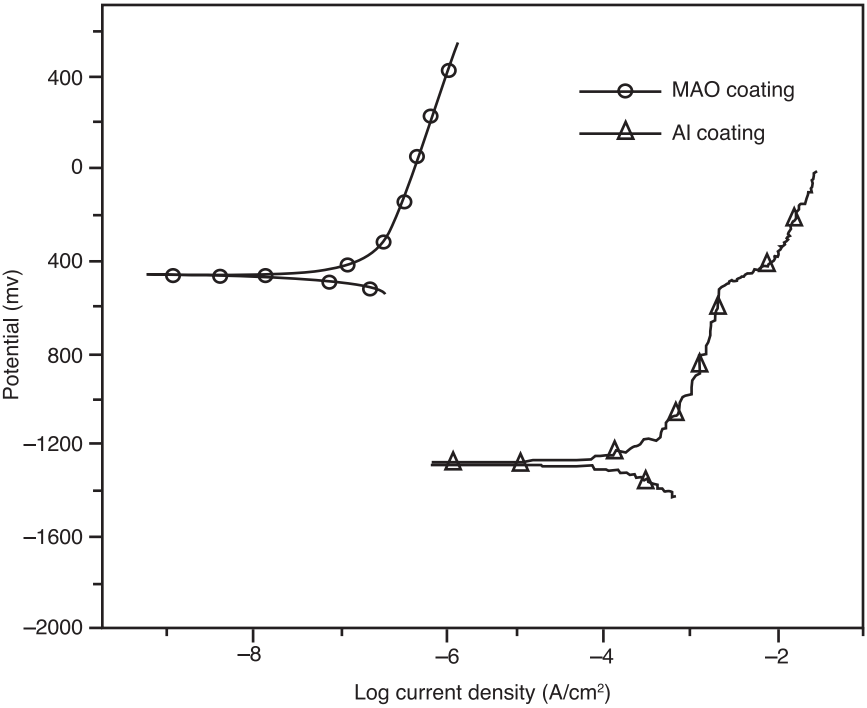

7.18 Polarization curves of arc-sprayed Al coating and MAO coating.

7.4 Conclusion and future trends

It was found in our previous study that the corrosion mechanisms of Mg alloy weldment become complicated due to the effect of welding process, the changes of microstructures, the differences in corrosion potential of dissimilar metal and so on. The different zones of Mg alloy weldments show differences in their corrosion susceptibility, which is due to different weld processes. In a word, corrosion of welded joints will reduce the service life of joints. Thermal spray technology is a highly efficient and a low-cost protection technology for Mg alloy weldments. At present, the research on the corrosion of magnesium alloy welded joints and their protection technology is still at an early stage. Further research on the corrosion mechanism of magnesium alloys and dissimilar metal welded joint and development of new protection technologies for magnesium alloy welded joint have become urgent.

7.5 References

1. Mordike BL, Ebert T (2001). Magnesium properties-application-potential. *Mater Sci Eng A* **302**(1): 37–45.
2. Lee K, Lee SH, Kim DH (1998). Effect of Y, Sr, and Nd additions on the microstructure and microfracture mechanism of squeeze-cast AZ91-X magnesium alloys. *Metall Mater Trans A*. **29**(4): 1221–35.
3. Munitz A, Cotler C, Stern A Kohn G (2001). Mechanical properties and microstructure of gas tungsten arc welded magnesium AZ91D plates. *Mater Sci Eng A* **302**(1): 68–73.
4. Sun Z, Pan D (2002). Comparative evaluation of tungsten inert gas and laser welding of AZ31 magnesium alloy. *Sci Technol Weld Join* **7**(6): 343–51.
5. Asahina T, Tokisue H (2001). Electron bean weldability of pure Mg and AZ31 Mg alloy. *Mater Trans* **42**(11): 2345–53.
6. Liu LM, Wang JF, Song G (2004). Hybrid laser-TIG welding, laser beam welding and gas tungsten arc welding of AZ31B magnesium alloy. *Mater Sci Eng A* **381**(1–2): 129–33.
7. Song G, Liu LM, Chi MS, Wang JF (2005). Investigations on laser-TIG hybrid welding of Mg alloys. *Mater Sci Forum* **488**–9: 371–6.
8. Cao X, Jahazi M, Immarigeon JP, Wallace W (2006). A review of laser welding techniques for Mg alloys. *J Mater Process Technol* **171**(2): 188–204.
9. Zhu TP, Chen ZW, Gao W (2006). Incipient melting in partially melted zone during arc welding of AZ91D magnesium alloy. *Mater Sci Eng A* **416**(1–2): 246–52.
10. Liu C, Chen DL, Bhole S, Cao X, Jahazi M (2009). Polishing-assisted galvanic corrosion in the dissimilar friction stir welded joint of AZ31 magnesium alloy to 2024 aluminum alloy. *Mater Charact* **60**(5): 370–6.
11. Bettles CJ (2003). The effect of gold additions on the ageing behaviour and creep properties of the magnesium alloy AZ91E. *Mater Sci Eng A* **348**(1–2): 280–8.
12. Zhang MX, Kelly PM (2003). Crystallography of Mg17Al12 precipitates in AZ91D alloy. *Scr Mater* **48**(5): 647–52.
13. Srinivasan A, Swaminathan J, Pillai UTS, Guguloth K, Pai BC (2008). Effect of combined addition of Si and Sb on the microstructure and creep properties of AZ91 magnesium alloy. *Mater Sci Eng A* **485**(1–2): 86–91.
14. Lunder O, Lein JE, Aune TK, Nisancioglu K (1989). The role of $Mg_{17}Al_{12}$ phase in the corrosion of AZ91. *Corrosion* **45**(9): 741–8.

15. Zhao MC, Liu M, Song GL, Atrens A (2008). Influence of the β-phase morphology on the corrosion of the Mg alloy AZ91. *Corrosion Sci* **50**(7): 1939–53.
16. Song GL, Atren A, Dargusch M (1998). Influence of microstructure on the corrosion of diecast AZ91D. *Corrosion Sci* **41**(2): 249–73.
17. Ben-Hamu G, Eliezer D, Cross CE, Böllinghaus T (2007). The relation between microstructure and corrosion behavior of GTA welded AZ31B magnesium sheet. *Mater Sci Eng A* **452–3**(15): 210–18.
18. Zeng RC, Chen J, Dietzel W, Zettler R, dos Santos JF, Nascimento ML, et al. (2009). Corrosion of friction stir welded magnesium alloy AM50. *Corrosion Sci* **51**(8): 1738–46.
19. Qi XD, Song G (2010). Interfacial structure of the joints between magnesium alloy and mild steel with nickel as interlayer by hybrid laser-TIG welding. *Mater Design* **31**: 605–9.
20. Cramer SD, Covino BS, Jr., editors (2003). 'Corrosion resistance of magnesium alloys.' In: *ASM handbook: Volume 13A – Corrosion: Fundamentals, Testing, and Protection*. ASM International, pp. 207–55.
21. Wielage B, Mücklich S, Grund T (2006). Corrosion behaviour of soldered joints of magnesium alloys and dissimilar materials. *Microchim Acta* **156**(1–2): 151–7.
22. Thorpe ML (1993). Thermal spray: industry in transition. *Adv Mater Process* **143**(5): 50–61.
23. Knuuttila J, Sorsa P, Mäntylä T, Knuuttila J, Sorsa P (1999). Sealing of thermal spray coatings by impregnation. *J Thermal Spray Technol* **8**(2): 249–57.
24. Ctibor P, Neufuss K, Zahalka F, Kolman B (2007). Plasma sprayed ceramic coatings without and with epoxy resin sealing treatment and their wear resistance. *Wear* **262**(9–10): 1274–80.
25. Liu LM, Wang Z, Song G (2010). Study on corrosion resistance properties of hydrothermal sealed arc sprayed aluminium coating. *Surf Eng*. Doi.10.1179/174329409X409459.
26. Yerokhin AL, Nie X, Leyland A, Matthews A, Dowey SJ (1999). Plasma electrolysis for surface engineering. *Surf Coat Technol* **122**(2–3): 73–93.
27. Xue WB, Deng ZW, Chen RY, Zhang TH (2003). Growth regularity of ceramic coatings formed by microarc oxidation on Al-Cu-Mg alloy. *Thin Solid Films* **372**(1–2): 114–17.
28. Han I, Choi JH, Zhao H, Baik HK, Lee IS (2007). Micro-arc oxidation in various concentration of KOH and structural change by different cut off potential. *Current Appl Phy*, **7**(suppl 1): e23–e27.
29. Curran JA, Clyne TW (2005). Thermo-physical properties of plasma electrolytic oxide coatings on aluminium. *Surf Coat Technol* **199**(2–3): 168–76.

Part II

Particular welding and joining techniques

8

Brazing and soldering of magnesium alloys

T. WATANABE, Niigata University, Japan

Abstract: The chapter first discusses the surface film property of magnesium and shows that the magnesium surface treated with hydrofluoric acid pickling is covered by a thin, protective film that results in improvement of the joinability. Then, the chapter describes the development of flux and filler metal for brazing the magnesium alloys, followed by presenting the flux-free ultrasonic brazing of magnesium alloy and reviewing soldering of the magnesium alloy.

Key words: surface film, brazing and soldering, flux, filler metal, ultrasonic brazing.

8.1 Surface preparation of magnesium alloys before joining

8.1.1 Surface film on magnesium

In the paper entitled 'The oxidation of metals at high temperatures,' presented to the *Journal of Institute of Metals*, Pilling and Bedworth[1] first correlated the porosity of a metal oxide with the specific density. The Pilling–Bedworth ratio, (P-B ratio) R, of a metal oxide is defined as the ratio of the volume of the metal oxide, which is produced by the reaction of metal and oxygen, to the consumed metal volume, given by the formula:

$$R = \frac{\text{V metal oxide produced}}{\text{V metal consumed}} = \frac{\text{Wd}}{\text{wD}} \qquad [8.1]$$

in which W = molecular weight of oxide, w = formula weight of metal, D = density of oxide and d = density of metal. Pilling and Bedworth realized that when R is less than 1, a metal oxide tends to be porous and non-protective because it cannot cover the whole metal surface. Later, researchers found that excessively large R, large compressive stresses are likely to exist in metal oxide, leading to buckling and spalling. In addition to R, factors such as the relative coefficients of thermal expansion and the adherence between metal oxide and metal should also be favorable in order to produce a protective oxide. Using the P-B ratio, the protective metal oxides are separated from the non-protective metal oxides. For example, since the P-B ratio of Al_2O_3/Al is 1.280 (i.e., larger than 1), aluminum oxide comes under the category of protective metal oxides and forms a thin protective film. On the other hand, since the P-B ratio of MgO/Mg is 0.806 (i.e., less than 1), magnesium oxide comes under the category of non-protective metal

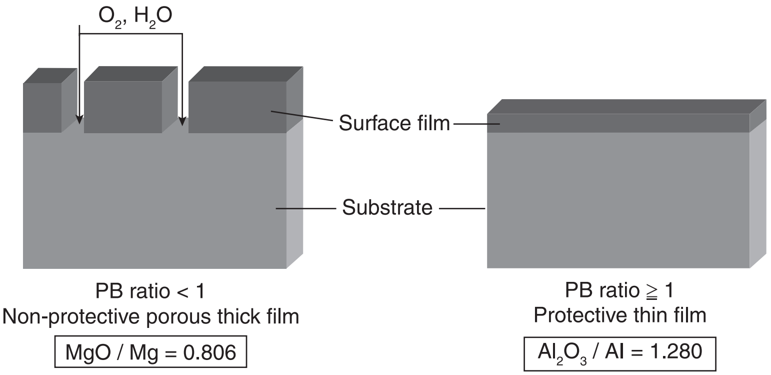

8.1 Schematic illustration for surface film on magnesium and aluminum.

oxides and forms an easy-to-develop, porous, thicker and non-protective film, as shown in Fig. 8.1.

Besides oxides of elemental metal, the P-B ratio can be applied to oxides of metal alloys, metal nitrides and other metal compounds such as metal fluorides.

8.1.2 Joinability of Al and Mg alloys

Studies on the ultrasonic weldability of Al and Mg alloys suggest that the Al alloy weldability is considerably superior to that of Mg alloy.[2,3] One of the main reasons for much of the difference in the weldability between Al and Mg alloys seems to be that the thickly developed Mg alloy oxide film on the faying surface deteriorates the weldability, as described in the previous section. This suggests that the weldability of Mg alloy can be improved by forming a thin film on the faying surface of Mg alloy. That is to say, if the faying surface of Mg alloys can be covered by the film with P-B ratio greater but not excessively greater than 1, then the surface film becomes thinner and the weldability in ultrasonic welding and brazing can be significantly improved.

Some surface films with the P-B ratio near to that of Al (1.280) were explored on the Mg metal compounds. Consequently, the fluoride of Mg (MgF_2/Mg) with the P-B ratio of 1.416[1] was found. The Mg alloy with faying surface covered by MgF_2 is expected to have a superior weldability.

8.1.3 Surface treatment of Mg alloy to improve the joinability

The surface of AZ31B Mg alloy was treated to investigate the effect of the surface treatments on the joinability in ultrasonic welding and the wettability in brazing.[4] The AZ31B-H24 specimen is 0.9 mm thick (Mg-2.7 mass%Al-0.9 mass%Zn) and the tensile strength is about 290 MPa.

Three kinds of surface treatments were employed on the faying surface. The first is wet polishing with emery paper of #400, the second is dry polishing with emery paper of #400 and the third is hydrofluoric acid (HF) pickling in which the faying surface is pickled in HF to make a fluoride film of MgF_2 on the surface after dry polishing with emery paper of #400.

X-ray photoelectron spectroscopy (XPS) analysis on the treated surfaces

Figure 8.2 shows the X-ray photoelectron spectroscopy (XPS) spectra of Mg2p photoelectron from the surfaces subjected to three kinds of surface treatments. The abscissa and ordinate indicate the binding energy of Mg2p photoelectron and the sputtering time of Ar ion to obtain depth profiles, respectively. The etching rate is about 0.168 nm/s. It is evident from Fig. 8.2(c) that the peak of MgF_2 is found on the treated surface by HF pickling, and the MgF_2 film covers the extreme outer surface of Mg alloy treated by HF pickling.

The thickness and compounds of the surface film on the Mg alloy processed with three kinds of surface treatments are summarized in Fig. 8.3. This reveals that the film on the surface wet-polished by emery paper is extremely thick (about 160 nm), and the film thickness on the dry-polished surface is about 30 nm. The surface processed with HF pickling treatment is covered by the protective and non-porous MgF_2 film, so that the total thickness of the surface films is very thin (about 12 nm).

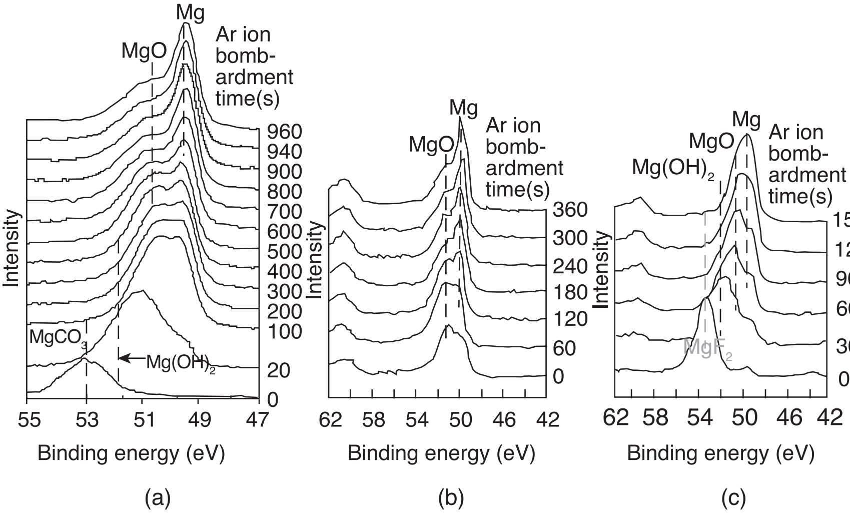

(a) (b) (c)

8.2 XPS spectra of Mg2p photoelectron from the surfaces subjected to various surface treatments: (a) wet polishing (b) dry polishing (c) HF pickling.

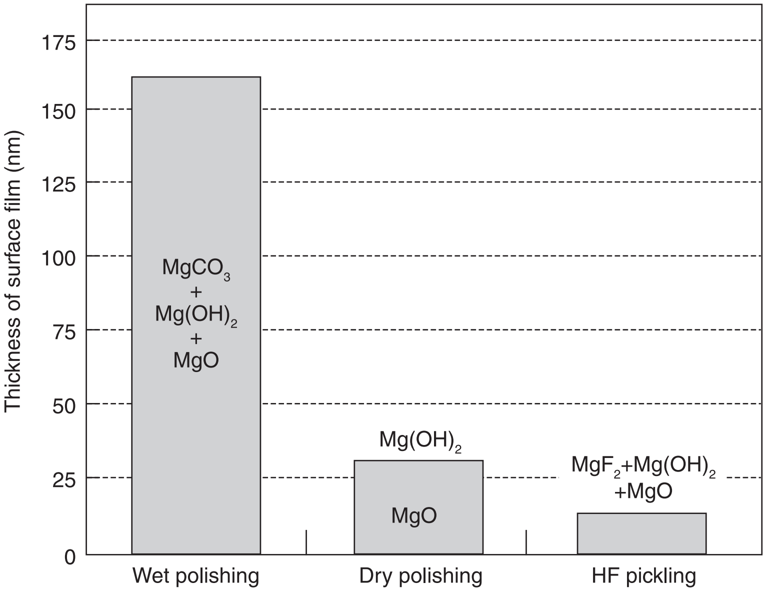

8.3 Thickness and components of the surface film of the specimen processed with three kinds of surface treatments.

Surface treatment and ultrasonic weldability

In this subsection, the Mg alloy specimens processed with three kinds of surface treatments were ultrasonically welded under the welding conditions of 1470 N clamping force and 2.0 seconds welding time. The strength of a joint was evaluated by the maximum cross-tensile load. Figure 8.4 shows the effect of the surface treatment for Mg alloy on the cross-tensile load of the ultrasonically welded joints. The joint strength seems to have a good correlation to the film thickness on the faying surface, as shown in Fig. 8.3. It is evident that the ultrasonic weldability of Mg alloy can be improved by decreasing the film thickness on the faying surface using HF pickling surface treatment.

Figure 8.5(a) shows the scanning electron microscope (SEM) fracture surface of the joint ultrasonically welded after HF pickling surface treatment. The schematic illustration of the fracture surface is shown in Fig. 8.5(b). Figure 8.5(c) shows the enlarged surface of the D region. Figure 8.5(d) exhibits the dimple pattern in the fracture surface of AZ31B base metal. Comparing the fracture surface of the D region in Fig. 8.5(b) with that of the base metal, the ductile fracture pattern with a dimple is observed in the D region. This means that the D region was well bonded and fractured ductilely. The B region in Fig. 8.5 was not a ductile region where MgF_2 compound was detected on the surface.

The optical micrographs around the ultrasonically welded interfaces under the conditions of 1470 N clamping force and 2.0 seconds welding time are shown in

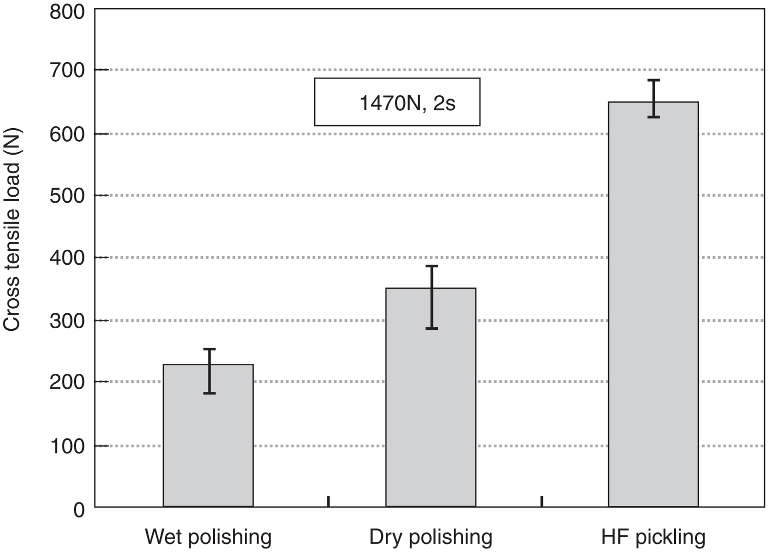

8.4 The effect of surface treatment on the strength of ultrasonic welds made under the conditions of 1470 N and 2 seconds.

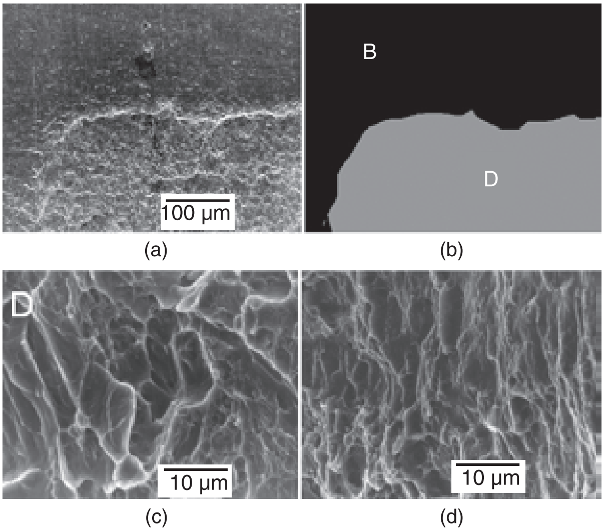

(a)

(b)

(c)

(d)

8.5 SEM photographs and schematic of the fracture surface of the weld with HF pickling treatment: (a) fracture surface, HF pickling; (b) schematic illustration of (a); (c) enlarged surface of region D; (d) AZ31B base metal.

Fig. 8.6. Figure 8.6(a) and (b) show the interfaces of the specimens processed with HF pickling and wet polishing, respectively. The bond interface line obviously remains in the weld of the specimen treated with wet-polishing, as shown in Fig. 8.6(b). However, the grain boundary migration across the weld

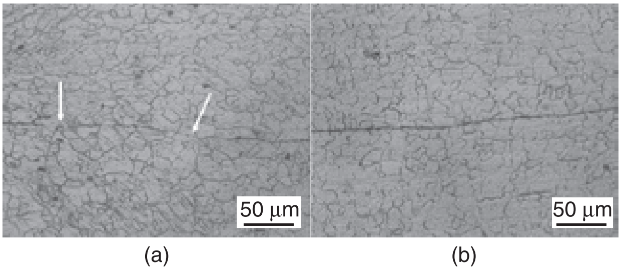

8.6 Micro-photographs around the ultrasonically welded interfaces of the specimens treated with (a) 1470N, 2s, HF pickling and (b) 1470N, 2s, wet polishing.

interface (arrows) is observed in the weld of the specimen treated with HF pickling, as shown in Fig. 8.6(a). This fact means that the bonding in the weld proceeds more quickly by HF pickling than that by wet polishing.

Surface treatment and wettability in brazing

The effect of the surface treatments of AZ31B plate on the wettability was evaluated with contact angle and spread area of solidified filler metal on the plate. The AZ31B surface was processed with the previous three treatment methods, and the flux of $CaCl_2$-LiCl-NaCl and the filler metal of 30 mass%Mg-64 mass% In-1 mass%Al, which were developed by the author,[5,6] were used to evaluate the wettability. The filler metal of about 0.05 g and the flux were put on the surface-treated AZ31B plate and were heated at 460 °C for 30 seconds in air, followed by measurement of the wettability.

The surfaces processed with wet-polishing and dry-polishing showed very poor wettability, and the surfaces could not be wetted by the filler metal. However, the surface treated with HF pickling showed good wettability, and the contact angle was about 60 °C. Figure 8.7 is the optical micrograph showing the solidified filler metal on the surfaces treated with dry polishing (a) and with HF pickling (b). It is obvious that the filler metal well spread on the AZ31B surface was treated with HF pickling.

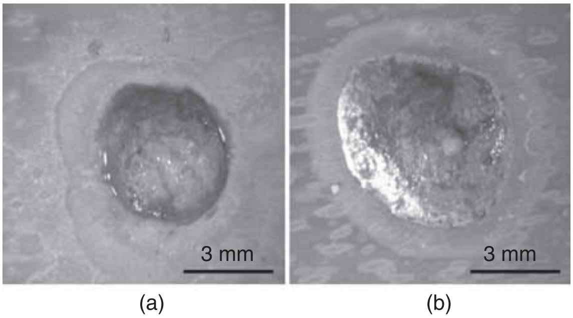

8.7 Photographs showing the brazing filler metal solidified on the surfaces treated with (a) dry polishing and (b) HF pickling.

Conclusively, the surface of Mg alloy treated with HF pickling was covered by a thin protective film, and it was revealed that the weldability, such as in ultrasonic welding, and wettability in brazing were successfully improved.

8.2 Brazing of magnesium alloys using flux and filler metal

8.2.1 Development of flux for brazing the magnesium alloys

Magnesium brazing is not simple, due to the high chemical activity among the structural metals.[5,6] A complex oxide film containing magnesium oxide and magnesium hydride is formed on the surface of the base metal when heated in air. This chemically stable film is not reduced either in conventional active gaseous atmosphere or in vacuum of up to 10^{-3} Pa. Consequently, the use of flux is inevitable in order to braze magnesium alloy. Table 8.1 summarizes a few practically used brazing fluxes.[7] The fluxes are based on halide salts of alkali and alkali earth metals with LiCl and/or NaF as active components.

This section describes some fluxes having suitable melting points that were newly developed by the author in order to braze a rolled magnesium alloy plate AZ31B. As previously mentioned, the Mg alloy surface is covered with films such as magnesium oxide, which is very stable and difficult to be reduced. For brazing the Mg alloy, the oxide film must be reduced using the fluxes. Fortunately, the Ellingham diagram[8] suggests that active ingredients containing Ca or Li elements have a great ability to reduce the magnesium oxide. On the basis of this suggestion, production of fluxes containing Ca and Li elements were tried referring to the $CaCl_2$-LiCl-KCl system phase diagram and $CaCl_2$-LiCl-NaCl system phase diagram shown in Fig. 8.8(a) and (b), respectively.

With reference to the phase diagrams, eight kinds of flux compositions were selected (Table 8.2), which were expected to have a melting point of about 450 °C. The circled numbers indicated in the phase diagrams in Fig. 8.8 mark the compositions of the selected fluxes. The capability of these fluxes to reduce the oxide was evaluated by the filler metal spread area on the AZ31B Mg alloy plate. The surface of the plate was treated by previously mentioned HF pickling. Approximately 50 mg of the filler metal (30.6%Mg-64.3%In-4.3%Zn-0.8%Al [mass%]) was set on the Mg alloy plate together with about 50 mg of flux. The spread area of the filler metal at 460 °C was measured to evaluate the ability of the flux.

Figure 8.9 shows the wetting test results for eight kinds of fluxes. Circled numbers 1–3 correspond to fluxes of the $CaCl_2$-LiCl-NaCl system, and circled numbers 4–6 correspond to fluxes of the $CaCl_2$-LiCl-KCl system. The maximum spread area was obtained with the circled number 5 flux (59.7%$CaCl_2$-18.5%LiCl-21.8%NaCl [mol%]). The circled numbers of 6 and 7 fluxes, which were composed of only LiCl and KCl, were used to examine the effect of $CaCl_2$ on the wetting.

Table 8.1 Composition and operational temperatures of magnesium brazing fluxes

Flux	Flux composition (mass%)												Temperatures (°C)	
	KCl	LiCl	NaCl	NaF	LiF	$CaCl_2$	$CdCl_2$	ZnF_2	$ZnCl_2$	Cryolite	Carnalite	ZnO	Melting	Brazing activity
F380Mg	Bal.	37	10	10	—	—	—	—	—	—	—	—	380	380–600
F530Mg	Bal.	23	21	3.5	10	—	—	—	—	—	—	—	530	540–600
F540Mg	Bal.	23	26	6	—	—	—	—	—	—	—	—	540	540–650
F390Mg	Bal.	30	—	—	—	—	15	10	10	—	—	—	390	420–600
F535Mg	Bal.	—	12	4	—	30	—	—	—	—	—	—	535	540–650
F400Mg	—	—	—	—	—	—	—	—	—	8	89	3	400	415–620
F450Mg	—	9	15	—	—	Bal.	—	—	—	—	—	—	450	450–650

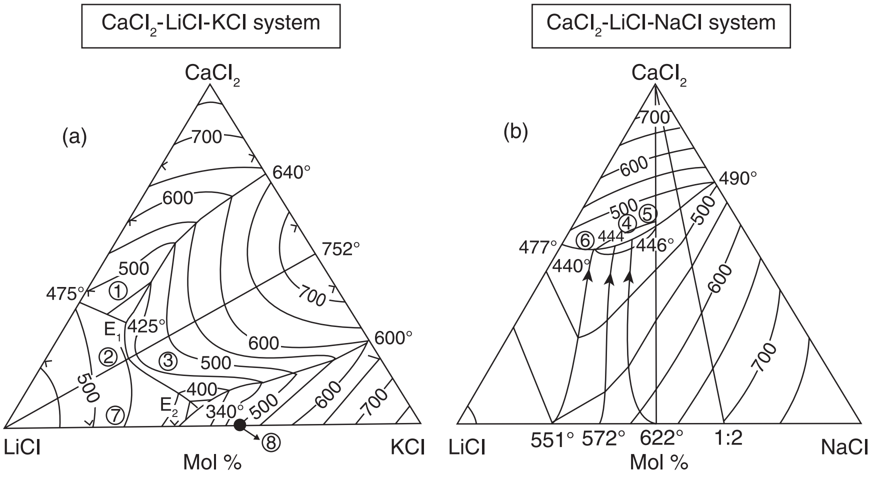

8.8 Equilibrium phase diagrams of $CaCl_2$-LiCl-KCl system and $CaCl_2$-LiCl-NaCl system. The circled numbers show the flux compositions examined in this work.

Table 8.2 Composition of fluxes examined in this work

	Flux composition (mol%)				Melting point
Flux	$CaCl_2$	LiCl	KCl	NaCl	°C
–	40.0	51.5	8.5	—	~450
α	20.0	64.8	15.2	—	~450
β	20.0	52.2	27.8	—	~450
χ	55.5	29.8	—	14.7	~450
δ	59.7	18.5	—	21.8	~450
ε	51.3	42.2	—	6.5	~450
φ	—	74.7	25.3	—	~450
γ	—	46.5	53.5	—	~450

As a result, it was shown that the fluxes without $CaCl_2$ also had the ability to wet filler metal.

Finally, the promising flux with the compositions of 60%$CaCl_2$-18%LiCl-22%NaCl (mol%) could be developed for brazing the rolled AZ31B Mg alloy.

8.2.2 Development of filler metal for brazing the magnesium alloys

This section describes the development of the new prospective filler metal for brazing the AZ31B alloy to attain the brazed joint with good mechanical

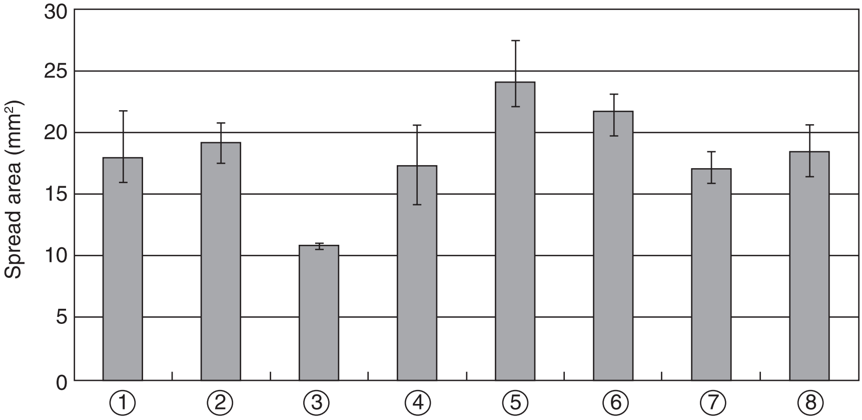

8.9 Spread area for eight kinds of fluxes examined in this work.

properties.[5,6] There has been a significant growth in the production and applications of structural magnesium alloys over the past two decades. The demand is driven primarily by the automotive and aerospace industries to reduce weight and fuel consumption. Table 8.3 presents the reportedly brazeable magnesium alloys.[9] Among the conventional forged magnesium alloys, the AZ31B alloy offers a good combination of strength, ductility, toughness, formability and weldability.[10] It seems to be necessary for the forged AZ31B alloy to be brazed in order to widen its application in many industries. Unfortunately, as the solidus of the forged AZ31B alloy is lower, the three commercial filler metals listed in Table 8.4[7] are not available for brazing the AZ31B alloy. On the other hand, some filler metals with a lower solidus are reported in Table 8.5.[7] Those filler metals can be used after appropriate testing of mechanical properties of brazed joints; however, it seems that the joints brazed using the filler metals with the lower solidus are poor in mechanical properties.

Table 8.3 Composition and melting temperatures of brazeable magnesium alloys

	Composition (mass%)							
ASTM alloy designation	Mg	Al	Zn	Mn	Zr	RE	Solidus °C	Liquidus °C
AZ10A	Bal.	1.2	0.4	0.2	—	—	632	643
AZ231B	Bal.	3.0	1.0	0.2	—	—	566	627
KIA	Bal.	—	—	—	0.7	—	649	650
MIA	Bal.	—	—	1.2	—	—	648	650
ZE10A	Bal.	—	1.2	—	—	0.17	593	646
ZK21A	Bal.	—	2.3	—	0.6	—	626	642

Table 8.4 Composition and melting temperatures of commercial brazing filler metals

AWS designation	Filler metal composition (mass%)						Solidus °C	Liquidus °C	Brazing range °C
	Mg	Al	Zn	Mn	Cu	Others			
BMg-1	Bal.	8.3–9.7	1.7–2.3	0.15–0.5	0.05	0.3	443	590	582–616
BMg-2a	Bal.	11–13	4.5–5.5	—	—	0.3	410	565	570–595
MC3	Bal.	8.3–9.7	1.6–2.4	0–0.1	0–0.25	<0.3Si	443	599	605–615

Table 8.5 Composition and melting temperatures of low-temperature brazing filler metals

Designation	Filler metal composition (mass%)					Solidus °C	Liquidus °C	Brazing range °C
	Mg	Al	Zn	Mn	Others			
GA432	Bal.	2	55	—	—	330	360	495–505
P430Mg	Bal.	0.7–1.0	13–15	0.1–0.5	0.3	380	430	550–560
P380Mg	Bal.	2.0–2.5	23–25	0.1–0.5	0.3	340	380	480–500
P435Mg	Bal.	25–27	1–1.5	0.1–0.3	—	435	520	520–560
P398Mg	Bal.	21–22	0.2–0.5	0.1–0.3	Cd 25–26	398	415	430–500

In-Mg-Zn system filler metals

This subsection describes a filler metal with a melting point lower than 480 °C. After surveying binary phase diagrams to find alloying elements suitable for brazing AZ31B Mg alloy, the elements of Mg, Cd, Pb and In were nominated as candidates for the filler metal because they make solid solutions with Mg, and intermetallic compounds are difficult to form with Mg. The elements of Mg and In were finally selected to produce the filler metal because Cd and Pb are harmful to human beings and the environment.

Figure 8.10 shows the equilibrium phase diagram for the Mg-In system. The diagram indicates that there is a peritectic point (circled) at the concentration of 58 mass% In, and the peritectic temperature is 484 °C. Six kinds of alloys were produced that consisted of approximately 65 mass% In and various amounts of Mg, and they contained Zn as a depressant to attain a melting point below 480 °C. The experimentally produced filler metals are listed in Table 8.6. The table shows the composition, liquidus, Vicker's hardness and the brazing temperature for the filler metals. The Al in the filler metal is attributed to the Mg alloy AZ31B being used as a raw material to make the filler metal.

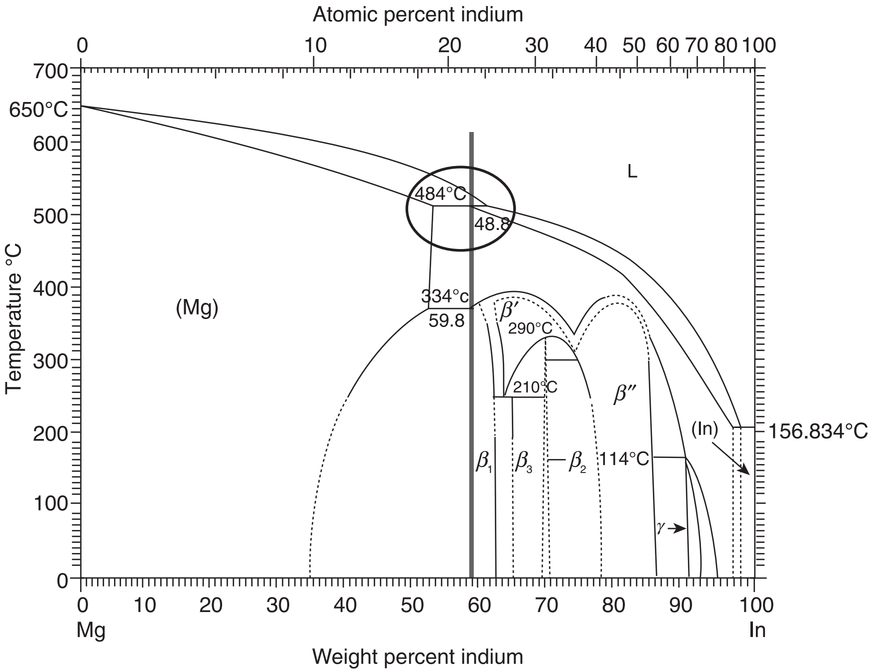

8.10 Equilibrium phase diagram of Mg-In system.

Table 8.6 Composition, hardness, liquidus and brazing temperature of new In-Mg-Zn system filler metals

Filler metal	Filler metal composition (mass%)				Hardness HV	Liquidus °C	Brazing temp. °C
	Mg	In	Zn	Al			
In-0Zn	34.5	64.5	0.2	0.8	110	476	490
In-1Zn	33.4	64.6	1.2	0.8	121	471	480
In-2Zn	32.8	64.2	2.2	0.8	132	467	480
In-4Zn	30.6	64.3	4.3	0.8	141	451	460
In-6Zn	27.8	65.1	6.4	0.7	155	449	460

The brazing procedure is described as follows. Rectangular specimens of 15 mm in width, 30 mm in length and a 0.9 mm thickness were crosswise lap-brazed. The brazing surface of the specimen was treated with HF pickling. It was painted with the circle number 5 flux, which showed the maximum spread area in the previous section, using about 50 mg of the specimen. Brazing filler metal was then put on the brazing surface, and the specimens were placed crosswise on a stainless steel stage plate for cross-tensile testing to evaluate the joint strength. Brazing was conducted at the temperature of approximately 10 °C higher than the liquidus of each filler metal, as reported in Table 8.6.

Figure 8.11 summarizes the cross-tensile load of the joints brazed using the new filler metals listed in Table 8.6. The strength of the joint brazed with In-0Zn filler metal, which contained a small amount of Zn, was the greatest. The brazed joint broke in the base metal in the strength test. Figure 8.12 shows the appearance of the joint broken in the base metal, which was brazed with In-0Zn filler metal. The strength of a brazed joint decreased as the Zn content increased in the filler metal. Figure 8.13 shows the cross-section of the joint brazed with In-4Zn filler

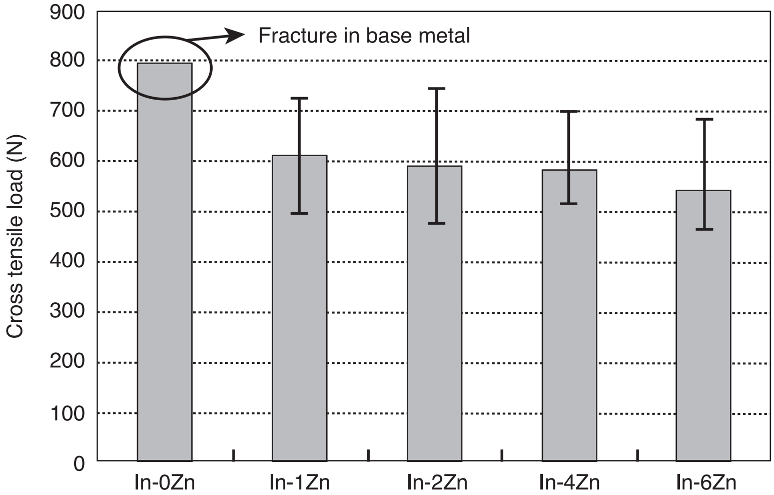

8.11 Strength of the joints brazed using new In-Mg-Zn filler metals.

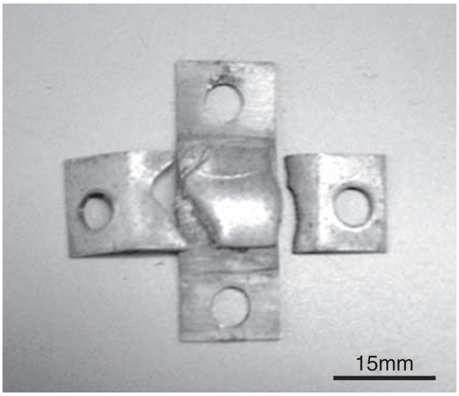

8.12 Appearance of the joint broken at the base metal after cross-tensile test.

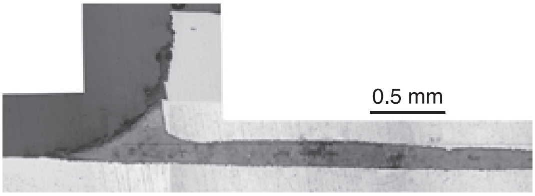

8.13 Cross-section of joint brazed with In-4Zn filler metal.

metal. The well-formed fillet is observed showing that the filler metal could wet the Mg alloy well.

Mg-Sn-In-Al system filler metals

In the previous section, the new In-Mg-Zn system filler metals were introduced. However, these filler metals contain a large amount of In, which is a rare metal and an expensive element, and involves a problem in cost. This section describes the Mg-Sn-In-Al system filler metals that contain a smaller amount of In.

In order to produce Mg-based filler metal, the eutectic point (circled) at the concentration of about 37 mass% Sn in the Mg-Sn phase diagram shown in Fig. 8.14 was considered. As the eutectic temperature was about 561 °C, In and Al

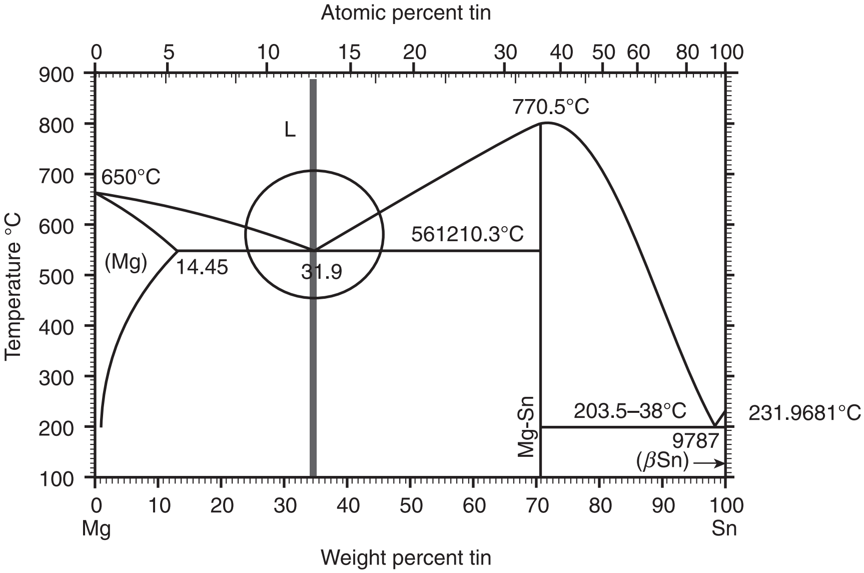

8.14 Equilibrium phase diagram of Mg-Sn system.

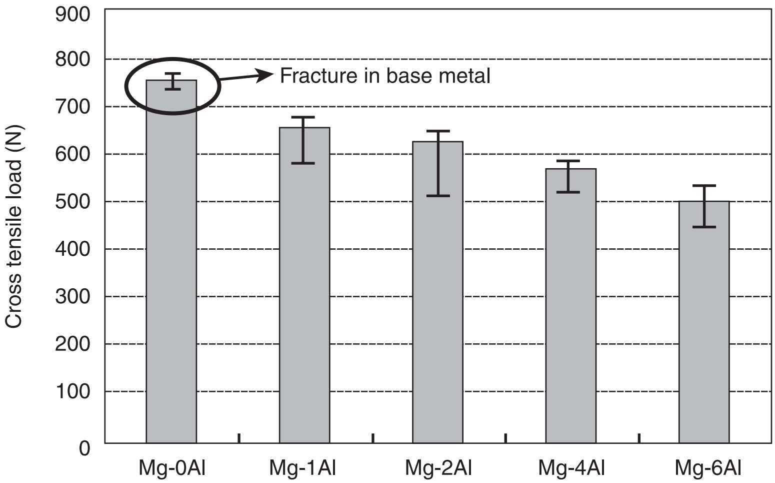

8.15 Strength of joints brazed using new Mg-Sn-In-Al filler metals.

were added as depressants to attain a melting point below 480 °C. The experimentally produced filler metals are summarized in Table 8.7. The table shows the composition, liquidus, Vicker's hardness and the brazing temperature for the filler metals. The added amount of In into the Mg-based alloy was limited to produce a solid solution with Mg.

The brazing procedure using the Mg-Sn-In-Al system filler metals is the same as that in the previous section. Figure 8.15 shows the cross-tensile load of the joints brazed using the Mg-Sn-In-Al system filler metals summarized in Table 8.7. The strength of the joint brazed with Mg-0Al filler metal was the greatest. The brazed joint broke in the base metal in the strength test. Figure 8.16 shows the appearance of the joint broken in the base metal and the fillet, which was well formed. The strength of the brazed joint decreased as the Al content increased in the filler metal.

Table 8.7 Composition, hardness, liquidus and brazing temperature of new Mg-Sn-In-Al system filler metals

	Filler metal composition (mass%)						
Filler metal	Mg	Sn	In	Al	Hardness HV	Liquidus °C	Brazing temp. °C
Mg-0Al	51	29	20	0	96	487	500
Mg-1Al	50.5	28.5	20	1	97	481	490
Mg-2Al	50	28.5	19.5	2	104	476	490
Mg-4Al	49	28	19	4	116	463	470
Mg-6Al	48	27	19	6	123	457	470

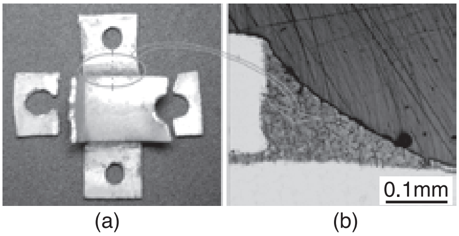

8.16 Appearance of joint broken in the base metal (a) and (b) fillet appearance.

In this section, new promising fluxes and filler metals for brazing the rolled AZ31B magnesium alloy plate at a temperature below 490 °C were presented.

8.3 Ultrasonic brazing of magnesium alloys with no flux

Flux is usually required to remove the oxide film on the faying surface for brazing the magnesium alloy in many cases, and a thorough rinsing is required after brazing.[11] Failure to completely remove all traces of flux from the brazed assembly will result in excess corrosion during use. To avoid a deterioration of the joint performances due to the corrosion, a flux-free joining process is needed. In this section, the author introduces flux-free ultrasonic brazing for magnesium alloy to avoid the problem.

8.3.1 The effect of temperature and applying time of ultrasonic vibration on brazing

The forged rods of AZ31B magnesium alloy with a 6 mm diameter were ultrasonically brazed in air with no flux. The faying surface was finished with the surface treatment of HF pickling before brazing. The filler metal equivalent to In-0Zn described in the previous section was used. The thickness was about 0.2 mm, and the solidus and liquidus temperatures were about 473 °C and 484 °C, respectively. Figure 8.17 shows a schematic of the apparatus for ultrasonic brazing of the AZ31B rods. The ultrasonic vibration with 19.5 kHz frequency and about 7.5 mm (p-p) amplitude was applied.

The effect of joining temperature (brazing temperature) on the tensile strength of the brazed joints is shown in Fig. 8.18. The brazing was conducted at the temperatures of 470 °C, 480 °C and 490 °C, keeping the applying time of ultrasonic vibration constant for 6 seconds. At the temperatures of 470 °C, 480 °C and 490 °C, the filler metal is in solid state, in solid and liquid coexisting state, and in molten state, respectively.

Brazing temperature at which the solid and liquid phases coexisted in filler metal could provide the maximum tensile strength. The joint efficiency was about 90%,

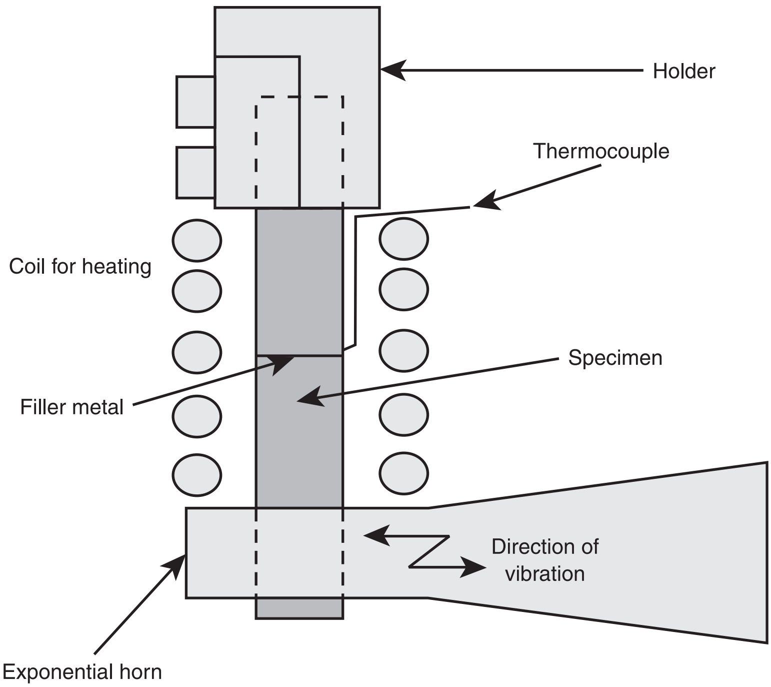

8.17 Schematic of apparatus for ultrasonic brazing.

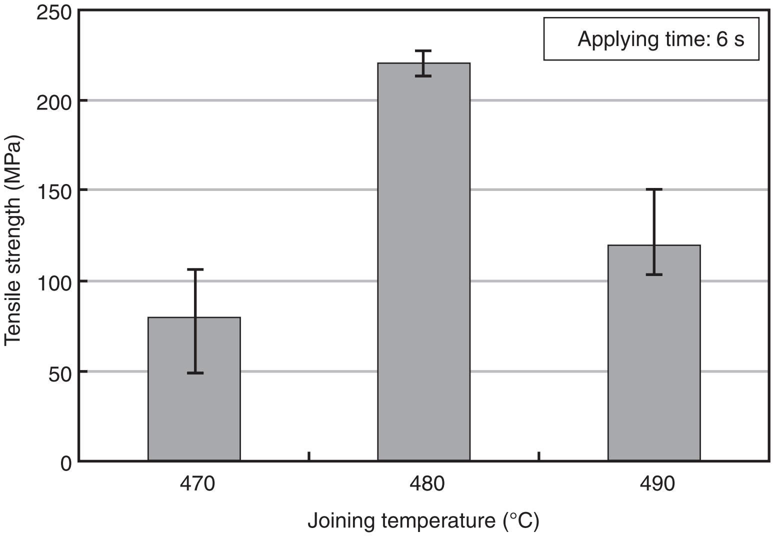

8.18 Relation between joining temperatures and the tensile strength of the brazed joints with applying ultrasonic vibration for 6.0 seconds.

and the joint strength was so large that the joint fractured both in the base metal and in the brazed layer, as seen in Fig. 8.19. Figure 8.20(a) shows the microstructure around the interface after heating to 480 °C. The filler metal consisted of two layers. One is the white-looking outside layer in liquid state and the other is the gray-looking inside layer that still remains in solid state. Figure 8.20(b) shows the brazed layer after applying ultrasonic vibration for 6 seconds. The gray-looking solid state layer in Fig. 8.20(a) changes to a molten state by applying ultrasonic vibration, and the molten filler metal is pushed out toward the outside of the brazed layer, followed by completing the brazing. It has been known that the interface temperature increases by 3–8 °C during the application of ultrasonic vibration.[11,12]

Figure 8.21 shows the effect of the applying time of ultrasonic vibration on the strength of the joints brazed at 480 °C. It is evident that the joint strength is zero when the ultrasonic vibration is not applied. This means that it is impossible to braze the magnesium alloy without applying ultrasonic vibration. The joint with

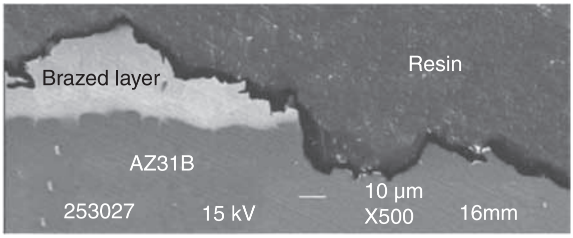

8.19 Microphotograph showing the fracture path in the joint brazed with applying ultrasonic vibration for 6.0 seconds at 480 °C.

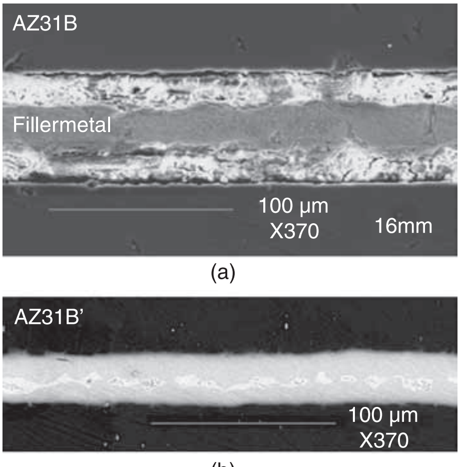

8.20 Microstructures of the brazed layer performed with applying time of ultrasonic vibration for 6.0 seconds at 480 °C. (a) Before applying vibration. (b) After applying vibration.

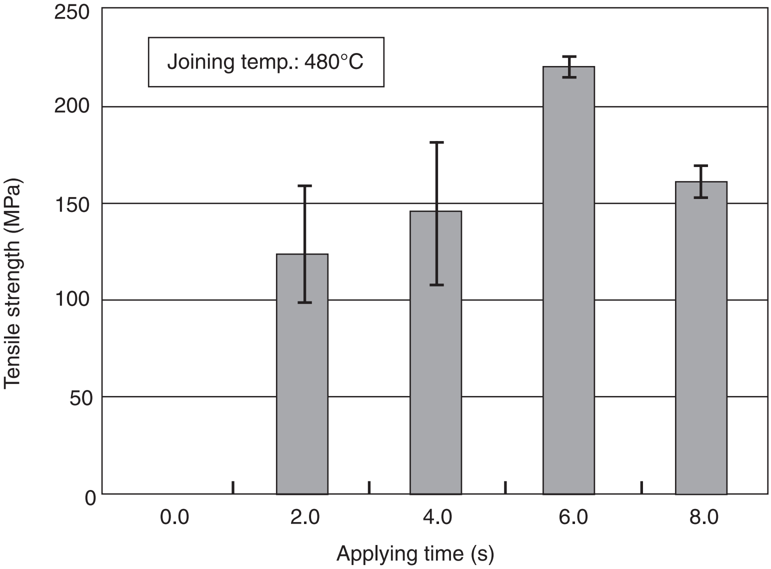

8.21 Relation between applying time of ultrasonic vibration and tensile strength of joints brazed at 480 °C.

the maximum tensile strength was attained under the applying time of ultrasonic vibration for 6 seconds.

The microstructures of the brazed layers with the various applying times of ultrasonic vibration are shown in Fig. 8.22. For the applying times of 2 and 4 seconds, the oxide films (arrows) obviously remained near the interface in the brazed layers and the fracture path ran along these oxide films. For the applying time of 8 seconds, defects, such as void, appeared in the brazed layer due to the lack of molten filler metal, resulting in a decrease in the joint strength.

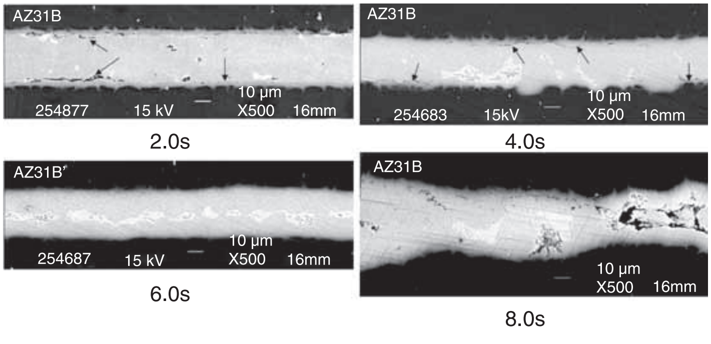
AZ31B
254877 15 kV 10 µm X500 16mm
2.0s
AZ31B
254683 15kV 10 µm X500 16mm
4.0s
AZ31B
254687 15 kV 10 µm X500 16mm
6.0s
AZ31B
10 µm X500 16mm
8.0s

8.22 Microstructures of the brazed layer performed with various applying times of ultrasonic vibration from 2.0 to 8.0 seconds at 480 °C. Arrows in the brazed layers of 2 and 4 seconds indicate the oxide films.

8.3.2 The bonding process in ultrasonic brazing of magnesium alloy

Figure 8.22 shows the brazed layer with applying time of ultrasonic vibration for 2.0–8.0 seconds, whereas the brazed layers with the short applying time of vibration of 0.5 s and 1.0 s are shown in Fig. 8.23, in order to investigate the oxide film behavior at the shorter applying time of vibration. Note that in the brazed layer with applying time of 0.5 s, a gray-looking non-melted region still remains at the center of the brazed layer; however, the oxide films (arrows) exist intermittendly in the white-looking melted region. This means that applying the ultrasonic vibration can break the oxide film and detach it from the interface in the brief time of 0.5 s. When the applying time of ultrasonic vibration is 1.0 s, the detached oxide film remains near the interface; however, the whole of the filler metal becomes molten and the bonded area of the interface expands. The detached oxide films are pushed out from the brazed layer and their number decreases with the applying time of ultrasonic vibration, allowing the brazing to make progress.

It has been known that a crack occurs in the surface oxide film of aluminum due to the difference in the thermal expansion coefficient between the aluminum substrate and the aluminum oxide film when the aluminum is heated.[13] The thermal expansion coefficients of Al and Al_2O_3 at 400 °C are about $26.5 \times 10^{-6}/°C$ and $10.4 \times 10^{-6}/°C$, respectively.[14] As the coefficients of Mg and MgO at 400 °C are about $28.9 \times 10^{-6}/°C$ and $12.2 \times 10^{-6}/°C$, respectively,[15] the crack also presumably occurs on the magnesium oxide film due to heating in the case of the AZ31B magnesium alloy. Figure 8.24(a) and (b) show the appearance of as-polished AZ31B surface with an emery paper and the surface appearance heated to 480 °C, respectively. It is obvious from the surface observation that many cracks (circled) were induced on the oxide film by heating. This fact suggests that the molten filler metal infiltrates the cracks, so that the oxide film is easily detached from the faying surface.

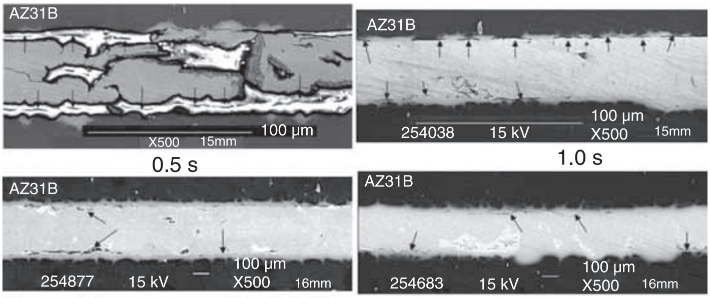

0.5 s

1.0 s

2.0 s

4.0 s

8.23 Microstructures of the brazed layer performed with applying time of ultrasonic vibration from 0.5 to 4.0 seconds at 480 °C. Arrows indicate the oxide films.

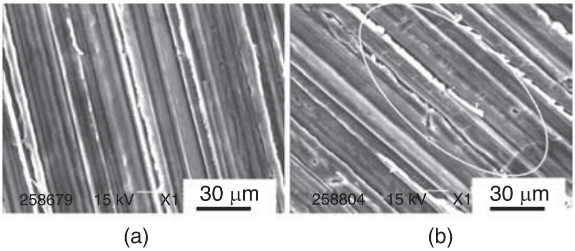

8.24 SEM photographs show the polished surface of AZ31B: (a) before heating and (b) after heating at 480°C.

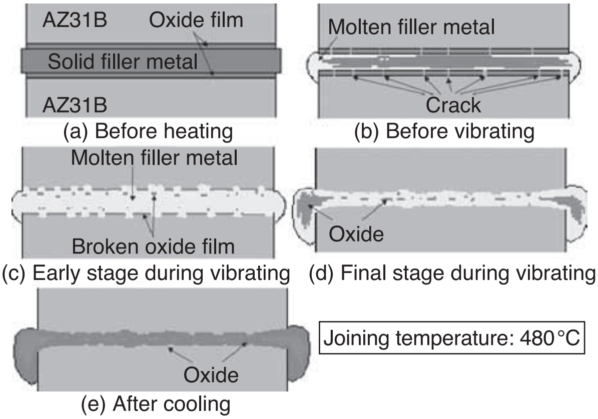

8.25 Schematic representation showing the ultrasonic brazing processes of magnesium alloy.

From the above experimental results, the mechanism of removing the oxide film from a faying surface in this ultrasonic brazing process is presumed as follows. First, a crack occurs in the oxide film on the faying surface after heating to brazing temperature due to the difference in thermal expansion characteristics between the substrate and the oxide film. Second, molten filler metal infiltrates the cracks and, in addition, the solid phase remaining in the filler metal rubs against the oxide film, resulting in breaking the oxide film and detaching it from the interface. Third, the broken and detached oxide films are pushed out toward the outside of the brazed layer by the flow motion of the molten filler metal. Figure 8.25 shows a schematic of the ultrasonic brazing process.

8.4 Soldering of magnesium alloys

This section presents a brief review on the soldering of magnesium alloys. It is said that no suitable flux is currently available to remove the oxide film on the surface to be soldered. Therefore, bare magnesium can be soldered only by abrasion and methods using ultrasonic vibration, which mechanically removes this film. When soldering by the abrasion (friction) methods, the solder sticks, soldering iron or other tool is rubbed on the magnesium surface under the molten solder to break up the oxide film.

Using the ultrasonic method, the molten solder is brought into contact with a hot solder vibrating at an ultrasonic speed; the cavitation effect caused by the vibration then removes the oxide film from the magnesium surface. After the magnesium surface is successfully precoated with solder, joining can be completed using a soldering iron, torch or hot plate. The flux-free soldering process using ultrasonic vibration, just like the ultrasonic brazing described in the section of 8.3.1, has been reported.[16,17]

Soldering of magnesium, however, is not normally recommended. This is because severe galvanic corrosion can result from contact of the magnesium base metal with the solder alloys used. Also, alloying between the base metal and the solder alloy results in brittle compounds being formed that weaken the joint. Therefore, soldering is seldom used with magnesium except for special situations such as making electrical contacts. Soldering should not be used to make joints in magnesium alloys that are subject to moderately high stress or that will be exposed to corrosive salt environment.

However, many kinds of solders for magnesium alloys have been well known from the necessity of soldering magnesium alloys. The solders for magnesium alloys are listed in Table 8.8.[10] The cadmium-base and tin-base solders can be used for soldering bare magnesium. Lead-base solders should not be used because the galvanic reaction that can occur in moist environments can be severe. The tin-zinc solders have lower melting temperatures and better wetting characteristics than the Sn-Zn-Cd solders, but they may form a joint with a low ductility. The high-cadmium solders produce the strongest and most ductile joints.

For the above-mentioned reasons, Wielage and Mucklich[18,19] developed new Mg-Zn-Al-based and Zn-Mg-Al-based solders that have low melting temperatures. The new solders are listed in Table 8.9. The researchers used

Table 8.8 Solders for magnesium

Solder composition (mass%)	Solidus (°C)	Liquidus (°C)
60Cd-30Zn-10Sn	157	288
90Cd-10Zn	265	299
72Sn-28Cd	177	243
91Sn-9Zn	199	199
60Sn-40Zn	199	341
70Sn-30Zn	199	311
50Sn-50Pb	183	216
80Sn-20Zn	199	270

Table 8.9 Composition and melting temperatures of new solders

Solder	Composition (mass%) Mg	Zn	Al	Solidus °C	Liquidus °C
Mg40Zn60	39	60	1	342	349
Mg45Zn55	45	55	—	342	347
Mg40Zn55Al5	40	55	5	338	343
Mg50Zn45Al5	50	45	5	338	345
Mg40Zn50Al10	40	51	9	338	433
Mg48Zn43Al9	48	43	9	340	348
ZnMg3Al1	3	96	1	338	400

ultrasonic equipment for soldering AZ31, AZ91 and AM50 magnesium alloys, and examined the soldered microstructure and the joint strength. Figure 8.26(a) shows the interfacial microstructure of AZ31 soldered with Mg48Zn43Al9. The base metal erosion is lower. Figure 8.26(b) shows the interfacial microstructure of AZ91 soldered with ZnMg3Al. It revealed that the ZnMg3Al solder rich in Zn eroded the base metal and the Zn element diffused into the base metal.

Table 8.10 lists the tensile strengths measured on different butt-soldered joints. The soldered joints were considerably more brittle because of the intermetallic compounds existing in the soldered layer. The statistical fluctuation of the strength was also high.

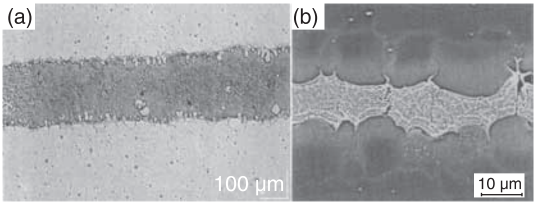

8.26 Microphotographs around the interfaces of the AZ31/AZ31 joint soldered with Mg48Zn43Al9 solder (a) and ZnMg3Al solder (b).

Table 8.10 Tensile strength of soldered joints

Base material/solder	Tensile strength of joint (MPa)
AZ31/ZnMg3Al	59.9 ± 9
AM50/ZnMg3Al	64 ± 18
AZ31/Mg48Zn43Al9	18 ± 8

It is reported that the solders of ZnMg3Al and Mg48Zn43Al9 are capable of soldering the magnesium and its alloys without flux. These low-melting solders allow soldering of high-magnesium alloys such as the cast alloy AZ91. Although the ZnMg3Al solder rich in Zn causes heavy base metal erosion, it provides the soldered joints with higher tensile strength. In contrast, the Mg48Zn43Al9 solder, which has a low-melting eutectic composition, provides the joints with lower strength, whereas the base metal erosion is small.

Recently, Liu and Wu[20] reported other solders for AZ31B magnesium alloy. They are Zn-based-Mg-Al and Mg-based-Zn-Al solders. It was found that the tensile shear strength of AZ31B joint soldered using Mg-based solder was higher than that soldered using Zn-based solder, and the joint rapidly cooled after soldering using Mg-based solder showed the highest tensile shear strength of about 80 MPa, which was about 63% of the AZ31B base metal tensile shear strength.

8.5 References

1. Pilling NB, Bedworth RE (1923). The oxidation of metals at high temperatures. *J Inst Met* **29**: 529–91.
2. Watanabe T, Yamashita S, Hiraishi M (2001). Effect of surface treatment on the ultrasonic weldability of AZ31B magnesium alloy plate. *J Japan Inst Light Metals* **51**: 521–7.
3. Hiraishi M, Watanabe T (2002). Effect of magnesium on ultrasonic weldability of Al-Mg alloy. *Quar J Japan Weld Soc* **20**: 552–8.
4. Watanabe T, Adachi H (2004). Effect of halogen surface treatment on the ultrasonic weldability and brazeability of magnesium alloys. *J Japan Inst Light Metals* **54**: 182–6.
5. Watanabe T, Komatsu S, Yanagisawa A (2004). Development of flux and filler metal for brazing magnesium alloy AZ31B. *Quar J Japan Weld Soc* **22**: 163–7.
6. Watanabe T, Komatsu S, Oohara K (2005). Development of flux and filler metal for brazing magnesium alloy AZ31B. *Weld J* **84**: 37S–40S.
7. Shapiro A (2005). Brazing magnesium alloys and magnesium matrix composites. *Weld J* **84**: 33–43.
8. Sano N (1996). Ellingham diagram and chemical potential diagram. *Bull ISIJ* **1**: 847–53.
9. AWS Committee on Brazing and Soldering (1991). *Brazing Handbook* edn. 4th, Miami, FL: AWS.
10. Oates WR (1996). *Welding Handbook*, 8th edn, Vol 3. Miami, FL: AWS.
11. Watanabe T (2009). Ultrasonic brazing and soldering of aluminum alloy and magnesium alloy. *J Japan Weld Eng Soc* **57**: 67–72.
12. Watanabe T, Tanaka Y, Yanagisawa A (1992). Soldering aluminum with the aid of ultrasonic vibration. *Quar J Japan Weld Soc* **10**: 470–6.
13. Kayashima M, Mushiro M (2000). Heat-induced cracking of anodic oxide films on aluminum. An in suit measurement of the cracking temperature. *Bull Tokyo Metropolitan Ind Technol Res Inst* 21–24.

14. Japan Institute for Metals (1974). *Metals Data Book*. Tokyo: Maruzen.
15. Kingery WD, Bowen HK, Uhlmann DR (1981). *Introduction to Ceramics* (translated by Komatsu W, Sata T, Moriyoshi Y, Kitazawa K, Uematsu K). New York: Wiley.
16. Wielage B, Mucklich S (2003). Flux-free soldering of magnesium materials. *Weld Cutt* **55**: 191–2.
17. Wielage B, Mucklich S (2006). Improving the soldering of magnesium alloys. *Weld J* **85**: 48–51.
18. Wielage B, Mucklich S (2007). A contribution to soldering of magnesium materials. *Prakt Metallogr* **40**: 232–41.
19. Wielage B, Mucklich S (2005). The influence of solder composition on the development of microstructures in magnesium solder joints. *Prakt Metallogr* **42**: 513–27.
20. Liu L, Wu Z (2010). Microstructure and interfacial reaction of soldering magnesium alloy AZ31B. *Mater Charact* **61**: 13–18.

9

Mechanical joining of magnesium alloys

M. HEGER, Böllhoff, Germany and
M. HORSTMANN, Hella KGaA Hueck & Co., Germany

Abstract: In comparison to thermal joining techniques such as welding and soldering, mechanical joining techniques are remarkable for the fact that materials or auxiliary materials to be joined do not have to be converted into a molten state. Thus, the mechanical strength of the connection is achieved by form or force lock instead of material closure. Usually an auxiliary joining element is used to create the joint. Due to the ability to assemble a wide range of different materials, mechanical joining techniques have been established in various branches of industry, especially the automotive industry.

Key words: mechanical joining, riveting, blind riveting, direct screwing, tapping screws, tack-setting, lock-ring bolt, clinching, hemming, flanging, self-piercing riveting, fastener, magnesium.

9.1 Introduction

In comparison with thermal joining techniques, such as welding and soldering, mechanical joining techniques are remarkable for the fact that materials or auxiliary materials to be joined do not have to be converted into a molten state. Thus, the mechanical strength of the connection is achieved by form or force lock instead of material closure. Usually an auxiliary joining element is used to create the joint. Due to the ability to assemble a wide range of materials, mechanical joining techniques have been established in various branches of industry, especially the automotive industry. Here, lightweight constructions based on an intelligent multi-material design have been successfully put into practice for several years. The aim of such lightweight constructions is the reduction of vehicle weight which leads to less exhaust emission. Although environmentally worth striving for, this aim is contrary to the increasing demands of customers with regard to the security and comfort of vehicles.

The existing concepts for lightweight constructions in the automotive industry are characterized by the efficient and load-compatible application of different materials. Because of their relative density and their mechanical properties, semi-finished products consisting of magnesium are becoming more and more important for future material concepts. Now, the increasing variety of materials leads to necessary requirements on the different joining technologies. Moreover, the joining techniques have to fulfill different criteria such as costs, joint properties, joint strengths, automation capability, etc.

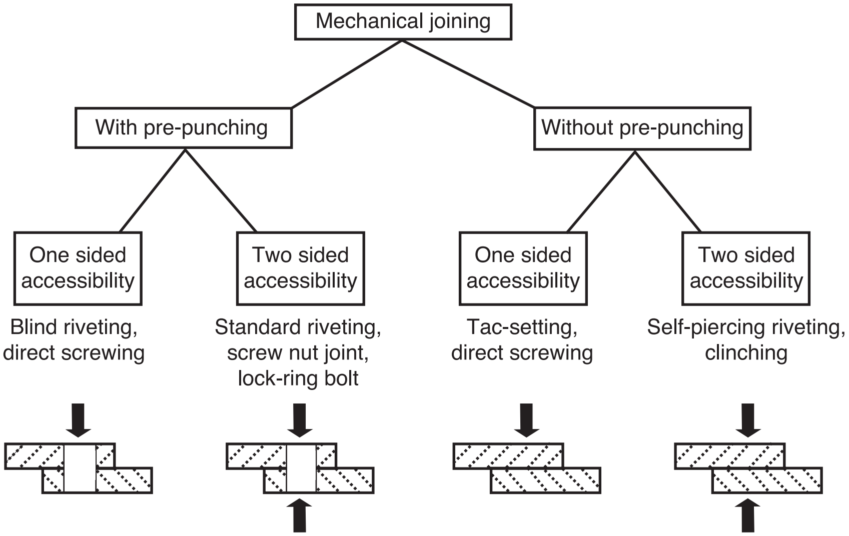

9.1 Classification of punctual mechanical joining techniques by criteria 'joining part preparation' and 'accessibility to the joining zone.'

All mechanical joining techniques mentioned in this chapter are specified in the fifth part of the DIN 8593 (2003). Here, 'joining by forming' is used as a general term for all production processes in which joining parts and/or auxiliary joining elements are locally or completely plastically deformed, and as a result, form locking connections with each other. In order to categorize mechanical joining techniques, the criteria 'joining part preparation' and 'accessibility to the joining zone' are appropriate.

Figure 9.1 gives an overview of the punctual mechanical joining techniques. For clarity, the following sections are structured according to this classification. The joining techniques listed are briefly described in the next section, and after that, the specialty of using magnesium is illustrated. At the end of the chapter, the linear hemming process and the combination of mechanical joining and adhesive bonding, the so-called hybrid joining, are detailed.

9.2 Technologies with pre-punching operation and one-sided accessibility

In this section, mechanical joining techniques are introduced, which only need accessibility from one side to the joining zone, but therefore a pre-punching or pre-drilling operation for the joining parts is required to execute the joining process. The two different techniques, blind riveting (also in combination with a functional element like a nut or a thread bolt), and direct screwing with thread forming screws are presented in this section.

9.2.1 Blind riveting

The joining technique blind riveting is especially characterized by the fact that only one-sided accessibility to the joining zone is required to produce a connection. This advantage and the high flexibility of this technique are the reasons why blind riveting often cannot be replaced by other joining techniques. One disadvantage of blind riveting is the higher preparation time compared to other mechanical joining techniques like self-piercing riveting or clinching, because a pre-punch operation is needed for the joining parts (Hahn and Klemens, 1996). DIN 14588 (2001) lists the exact terms of blind riveting. Normally, blind rivets consist of a rivet body and a mandrel which can be obtained in a pre-assembled state (see Fig. 9.2)

The rivet is processed by a setting tool. Besides manual converting machines, pneumatic hand setting tools or completely automated blind riveting machines are generally used in the industrial environment.

The blind rivet is inserted in the setting hole in order to be processed. Then, the mandrel is placed in the setting tool, and after the triggering, the clamping jaws in the setting tool grasp the mandrel and pull it supported on the rivet's head. The breakaway of the mandrel at a predetermined breaking point finishes the setting process. The geometrical design of the breaking point determines the maximum necessary setting force and, therefore, the required setting tool, too. During the setting process, the rivet body is plastically deformed regardless of the type of rivet used. The result is a form- and force-locked connection. This connection is permanent, that is, it can only be disassembled by the destruction of the blind rivet. Thereby, the substrates may or may not be damaged. The process steps of blind riveting and the most important terms of the joining system are shown in Fig. 9.3.

After finishing the setting process, the remaining mandrel normally stays force- and form-locked in the rivet's body. Additional terms describing the connection can be obtained from Fig. 9.4.

Besides different types of blind riveting, blind rivets can be produced out of different materials. Normally, blind rivets consist of a steel or aluminum body

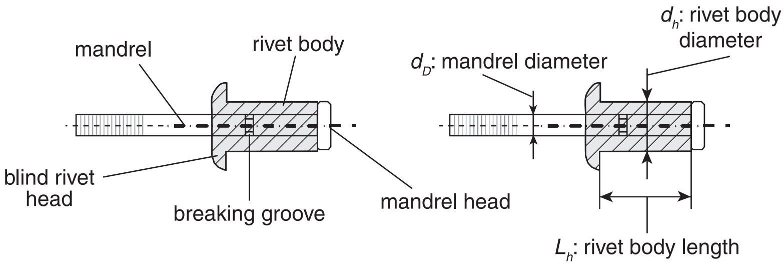

9.2 Design and terms of an unprocessed body folding blind rivet (Hahn and Heger 2008).

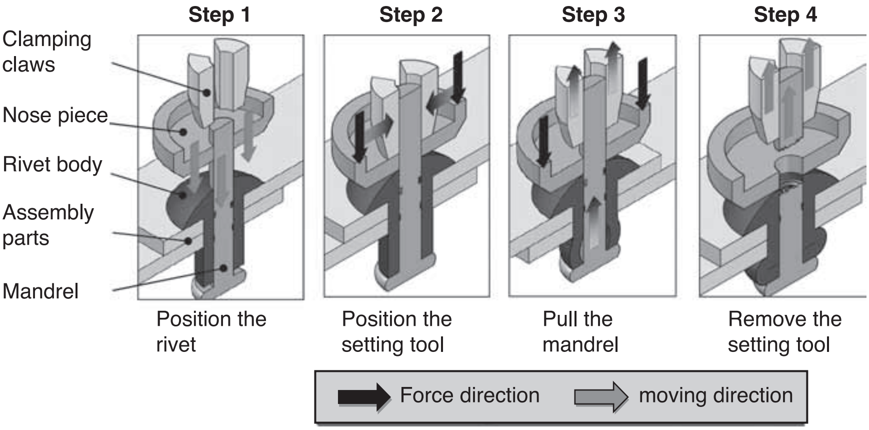

9.3 Process steps of blind riveting (Hahn and Heger 2008).

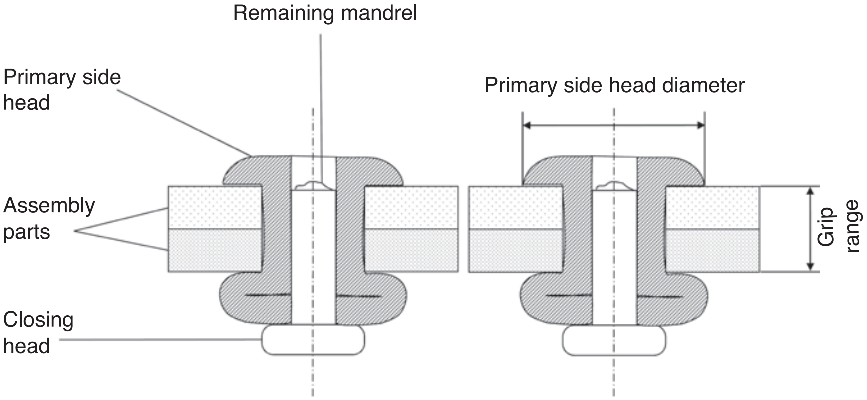

9.4 Design, terms and important dimensions of a blind riveting connection (Hahn and Heger 2008).

and a mandrel made of steel. But there also exist blind rivets made purely of aluminum or, for special applications, of titan. All blind rivets have in common that the material of the mandrel has a much higher strength than the material of the rivet body.

Hardly any other mechanical joining technique affects the magnesium substrates less than the blind riveting during the joining process. Because all holes are drilled or punched before the joining process starts, the corrosion protection of the components can be carried out before the blind rivet is inserted.

Joining partners or joining elements, which have a small potential difference to magnesium, have to be selected for the mechanical connection of magnesium and dissimilar materials in order to prevent a possible galvanic corrosion. Therefore,

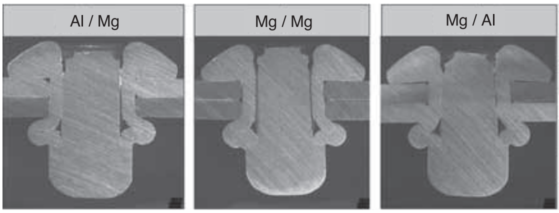

Material		Thickness
Mg-alloy	AZ31	1,5 mm
Al-alloy	AlMg0,8Si0,9	1.5 mm

Joining element	
Mandrel: Al, Body: Al	
d_h = 6 mm	3 mm

9.5 Joining element characteristics of body folding blind rivet connections (Heger 2010).

it is suggested that blind rivets with aluminum bodies be used. The reason for this is the difference in the electrochemical potential between magnesium and aluminum which is smaller than that between magnesium and steel.

In Fig. 9.5 and Fig. 9.6, the macroscopic samplings of two different types of blind rivets are illustrated. In each figure, three material combinations are shown: aluminum with magnesium, magnesium with magnesium and magnesium with aluminum. The blind rivet in Fig. 9.5 is a body folding blind rivet made of aluminum. This blind rivet is characterized by a high part of force closure within the connection. Moreover, the remaining mandrel covers the shear plane so that it can transmit the forces occurring from a tensile shear load and, thereby, increases the strength of the connection.

The rivet shown in Fig. 9.6 is a blind rivet with closed rivet body which is characterized by its leak-tightness. The connection gains additional tightness by the form-locked contact of the rivet body to the substrate at the side of the closing head.

9.2.2 Blind rivet nuts/blind rivet thread bolts

During blind riveting, the focus is on connecting two or more parts. In the joining techniques 'joining with blind rivet nuts' and 'joining with blind rivet thread bolts,' not only can components be connected but an attachment point like a nut body or a thread bolt can also be created. Because of the analogy of these two technologies, only the joining with blind rivet nuts is explained in the following sections. All

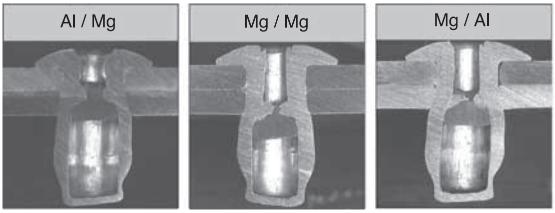

Material		Thickness
Mg-alloy	AZ31	1.5 mm
Al-alloy	AlMg0,8Si0,9	1.5 mm

Joining element	
Mandrel: Al, Body: Al	
d_h = 4 mm	3 mm

9.6 Joining element characteristics of blind rivet connections using blind rivets with closed rivet body (Heger 2010).

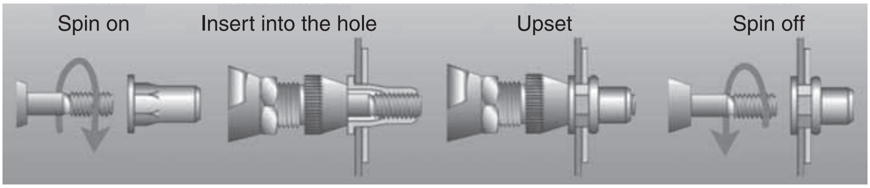

9.7 Process steps of processing a blind rivet nut (source: Böllhoff).

previous explanations for the blind riveting apply for the blind rivet nuts and thread bolts. It must be emphasized that all these elements can be processed manually, semi-automatically as well as fully automatically. The setting process of blind rivet nuts is slightly different because of the missing mandrel which is replaced by a modified setting tool. First, the nut is spun on the setting tool and then processed analogously to the blind riveting procedure. Finally, the setting process is finished with the spinning out of the nut from the setting tool (see Fig. 9.7).

Like blind rivets, blind rivet nuts can also be purchased in steel or aluminum. When using magnesium, an aluminum element should be preferred because of possible galvanic corrosion. Furthermore, blind rivet nuts with a closed body should be utilized to prevent the penetration of liquid media in the area of the screw thread (see Fig. 9.8).

9.2.3 Functional element Rivkle Elastic

Another element which is similar to the principle of blind riveting is Rivkle Elastic produced by Wilhelm Böllhoff GmbH & Co. KG. This joining element consists of a metallic nut and a metallic washer which are overmolded with a body of plastic (see Fig. 9.9). First of all, the Rivkle Elastic is inserted into the pre-manufactured hole of a substrate. In a second step, another component in form of a cover sheet and with a pre-manufactured hole is arranged above the joining element. By means of a screw, which is finally added, the nut is pulled up until it is closely connected to the washer. As the plastic body is closely connected to the nut, it is compressed during the setting process. Thereby a bead is created which guarantees the form lock of the joining element.

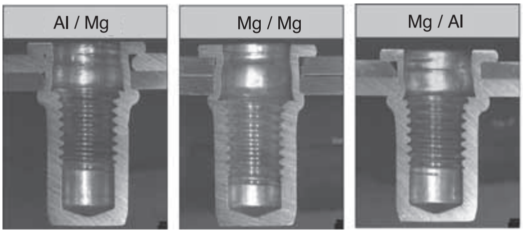

Material		Thickness
Mg-alloy	AZ31	1.5 mm
Al-alloy	AlMg0,8Si0,9	1.5 mm

Joining element
Body: Al, M5
3 mm

9.8 Joining element characteristics of blind rivet nut connections using blind rivet nuts with closed rivet body (Heger 2010).

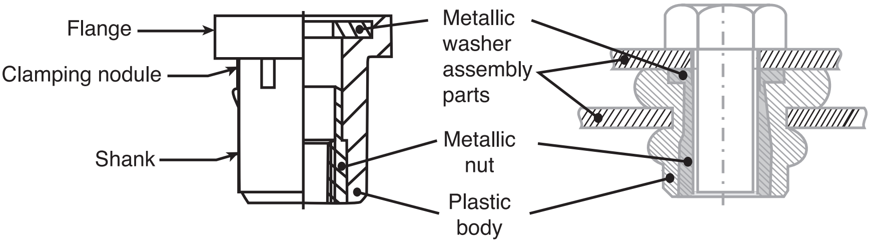

9.9 Functional element Rivkle Elastic in an unprocessed (left) and a processed (right) state (source: Böllhoff).

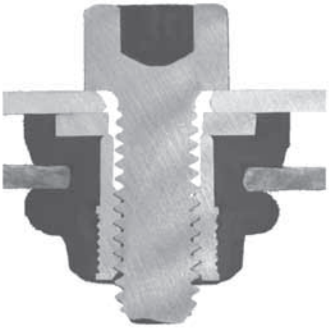

Material		Thickness
Mg-alloy	AZ31	1.5 mm
Al-alloy	AlMg3	1.5 mm

Joining element
RIVKLE Elastic, M5
5 mm

9.10 Joining element characteristic of a connection using the functional element Rivkle Elastic (Heger 2010).

The Rivkle Elastic is distinguished for its vibration-absorbing characteristics. Moreover, this element is especially suitable for joining of magnesium, due to the fact that the plastic body ensures a complete electrochemical isolation of other types of metal. Figure 9.10 shows an exemplary connection by means of Rivkle Elastic.

9.2.4 Direct screwing (thread-forming self-tapping screws)

In general, two essential process variants for the necessary joining part preparation are distinguished. One is the joining with hole- and thread-forming tapping screws which do not obligatorily require a pilot hole. A second process variant is the joining with thread-forming self-tapping screws which demand a pre-punch operation. Both the processes are described in this subsection.

The use of thread-forming self-tapping screws leads to a reduction in the process steps during the assembly, as the nut thread is shaped by the screw itself. Thread-forming self-tapping screws are often confused with thread-cutting self-tapping screws. The difference lies in swarf removal while cutting the thread as the thread-cutting screw is driven into the material, which does not apply to thread-forming screws. In the latter case, the substrate material is displaced downward into the groove of the thread. This results, for example, in a higher reliability toward self-loosening under vibration load because a form lock is produced via the thread-forming process. In comparison, the use of a conventional cut thread only leads to a force lock due to the frictional forces at the thread flanks.

Thread-forming self-tapping screws can be purchased in different variants of steel and aluminum and with various coatings. The processing of such screws is depicted in Fig. 9.11.

Firstly, the screw is positioned above the pre-punched hole and pressed against it with its tip. Then the screwing process is activated using a spindle speed which is constant throughout the complete process. The screw now forces its way into the material. At the same time, the forming of the thread takes place and the screw is turned tight till the screw head rests against the connected component. Last, the screw is prestressed with a defined torque.

When producing screw joints with thread-forming self-tapping screws, five influence factors are of special importance:

- Difference between screw and hole diameter (cover of the flanks)
- Thread surface and thread lubrication
- Relation of thread-forming torque and overtorque (the bigger the difference, the bigger the process latitude)
- Sufficient strength of the screws
- Five percent rule (configuration to an elongation at fracture of at least five percent)

Figure 9.12 shows an example of the application of a thread-forming self-tapping screw in a magnesium component. Here, one can see a screw connection of two high-pressure die castings made out of magnesium alloy AZ91D, which are combined as a reflector system for the headlight of the current BMW 5 series. By means of this system, the two functions ‘daytime running light’ and ‘position light’ are realized by one light bulb.

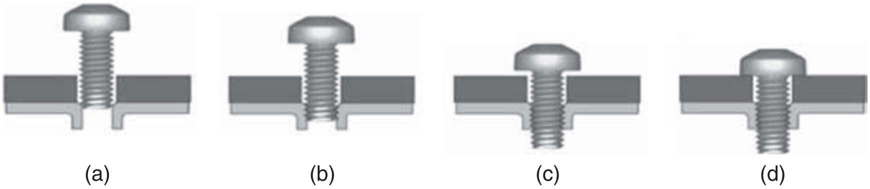

9.11 Process steps of processing thread-forming self-tapping screws in prepunched joining parts: (a) position, (b) thread formation, (c) screw in, and (d) tighten (source: Betzer).

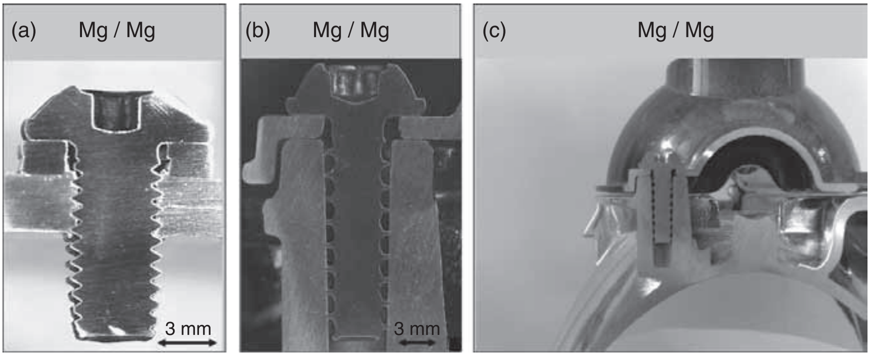

9.12 Joining element characteristics of screw connections using thread-forming self-tapping screws: (a) AZ31/AZ31 using aluminum screw Betzer Pentaform, (b) AZ91D/AZ91D using steel screw Ejot Delta PT, and (c) screw joint of piggyback reflector system within the headlamp of BMW 5 series (source: Hella KGaA/HDO GmbH).

9.3 Technologies with pre-punching operation and two-sided accessibility

In this section, mechanical joining techniques are introduced, which need accessibility from both sides to the joining zone. Also a pre-punched or pre-drilled hole is required to execute the joining process. Three different techniques are presented that all need additional joining elements to create the connection.

9.3.1 Conventional riveting

Conventional riveting is known as one of the oldest metal forming joining techniques which increasingly has been replaced by welding processes in the past 80 years. Nevertheless, this joining method shows various characteristics which make it indispensable in security-sensitive connections even today. This is true for steel constructions of buildings and commercial vehicles as well as for the aerospace industry, due to the fact that the joining technique is especially suitable under cyclic load. Even the most modern aeroplanes are still produced by conventional riveting of sheet metal structures with solid rivets. The simple production as well as the easy way of checking their quality by visual inspection are two important reasons which make this process still practicable today.

Conventional riveting allows the establishing of force- and form-locked connections by deforming a solid, semi-tubular or tubular rivet. The substrates need to be prepunched and are not deformed throughout the joining process. Similar to the process of blind riveting, these joints are also permanent.

The production of a conventional riveted connection takes place when inserting the rivet into the prepunched hole of the components which are to be connected

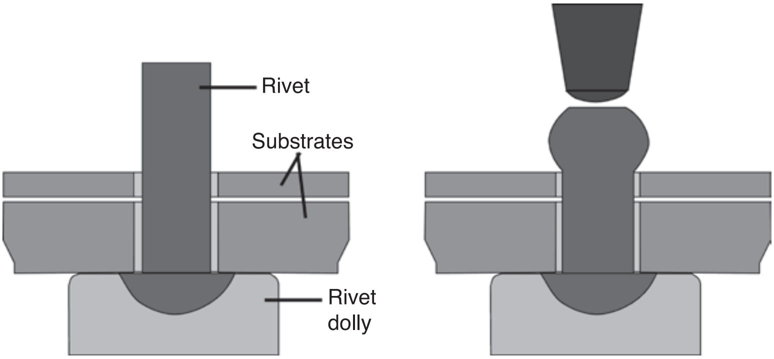

9.13 Process steps of conventional riveting using a solid rivet.

so that the rivet head lies flat against the above substrate. The connection is realized by deforming the opposite rivet shank into a closing head. The closing head can be formed through hammering, pressing, wobbling, rolling or blasting. The labeling of the rivets results from the upset form that the rivet head developed during production (universal, round, brazier, flat or countersunk rivet). Figure 9.13 shows an example of a conventional riveting procedure using a solid rivet.

Solid rivets can be produced out of different materials. The rivet material should consist of an alloy which is of the same type as the parts to be joined. But, the higher the stability of the rivet material, the more the necessary forming force will increase which is needed to form a closing head. Aluminum rivets with a diameter of 8 mm, for example, are still easily processable in a cold-forming process. Apart from solid rivets, there are different types of semi-tubular or tubular rivets which can be processed in a similar way.

Figure 9.14 shows an example of a conventional riveted magnesium connection using an aluminum solid rivet (AlMg5). The tensile shear strengths are comparable to those of blind riveted connections.

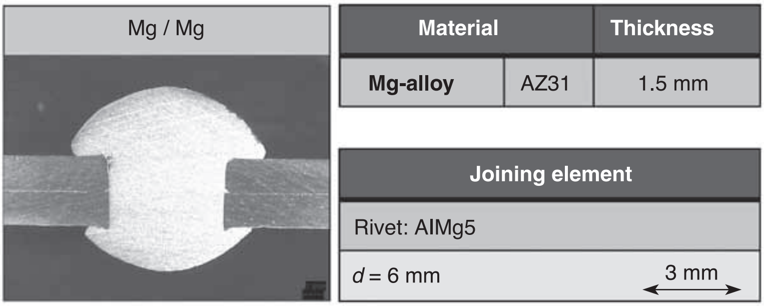

Material		Thickness
Mg-alloy	AZ31	1.5 mm

Joining element
Rivet: AlMg5
d = 6 mm

9.14 Joining element characteristic of a conventional riveting connection using a solid rivet.

9.3.2 Screw nut joint

A screw joint is a detachable connection of two or more joining parts which are connected by one or several threaded bolts (usually screws) with a male thread and parts with a female thread (usually nuts). A screw joint is a force-locked connection, that is, when turning a screw into a component, the applied moment is converted into an axial load, which induces a preload by tightening the screw. Additionally, a clamping force is generated when using nuts for connections where the screw is pushed through the prepunched holes. Both preload force and clamping force cause an elastic tensioning of the joining parts, and hence a storage of force. Thereby a frictional force is generated within the thread and the screw cannot loosen itself. This process is called self-locking. The dimension of the frictional force depends on the friction angle. The screw-and-nut joint is the best-known mechanical joint for connecting a prepunched magnesium component with any other component.

Due to the effect of galvanic corrosion, one should not use screws of steel, or alternatively, add coatings or use washers in order to prevent corrosion. The application of aluminum screws is possible (compare Fig. 9.15). Because of the high notch sensitivity, bigger screw diameters should be used. In order to prevent the nut thread from pulling out, the minimum length of thread engagement for light metal screw joints is of special significance.

According to Mordike and Wiesner (2005), the maximum surface pressure beneath the screw head or within the thread contact of magnesium components should not exceed 100 MPa in order to obviate improper plastic deformation which might lead to a relaxation of preload force.

9.3.3 Lock-ring bolts

The lock-ring bolt system consists of two components – a lock-ring and a bolt. The various lock-ring bolts are used for highly stressed connections. The bolt consists of a rivet head and a shank with a predetermined breaking point. The bolt is plugged into the prepunched pars, and the lock-ring is slipped over the bolt. The appropriate lock-ring has to be pressed into the grooves of the bolt shank by a setting tool. In this way, the ring is formed into the grooves of the bolt. Axial pressure is balanced by

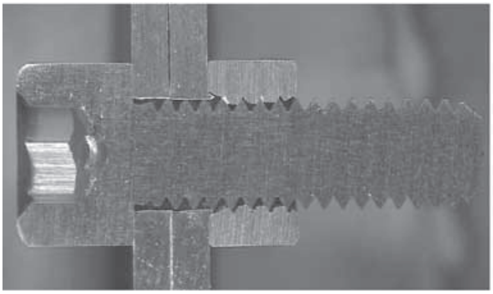

Material		Thickness
Mg-alloy	AZ31	1.5 mm

Joining element	
Screw: Al, Nut: Al	
M5	3 mm

9.15 Joining element characteristic of a screw nut joint.

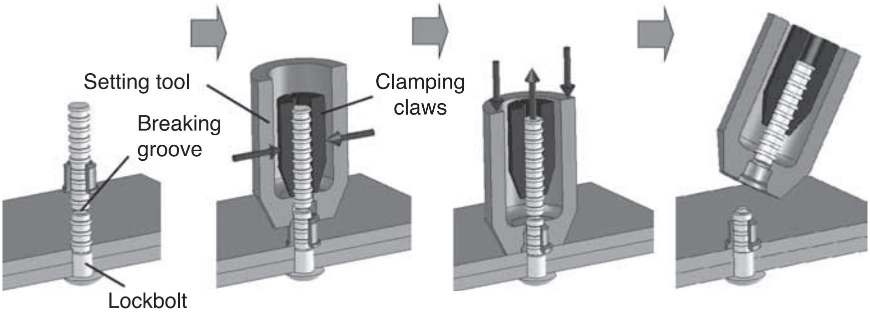

9.16 Process steps of processing a lock-ring bolt (source: LWF).

clamping of the bolt. With this, additional stress to the joining parts can be avoided. The process is shown in Fig. 9.16. The connection is force- and form-locked. The bolt is under pretension and is dimensioned against shear fracture.

Originally, lock-ring bolt connections were developed for aircraft and aeronautics but are used extensively in the fields of structural-steel erection, crane construction, railway vehicle construction, commercial vehicle construction and shipbuilding. In contrast to screws, the original preload of the connection is permanently retained. Therefore, lock-ring bolt connections are vibration-resistant. The parallel grooves of the bolts avoid a preload reduction, even in the case of vibration load. Lock-ring bolt connections are permanent. The only way to separate the joined parts is to destroy the lock-ring.

All materials that allow a manufacturing of a hole are able to be joined by lock-ring bolts. Thus, there are no special requirements for magnesium regarding formability or other properties. The material of the lock-ring bolt has to be adapted to the magnesium to attain an optimum strength and corrosion resistance. Lock-ring bolts made up of steel or aluminum are available with different coatings. As a result of the high-level strength, lock-ring bolt connections are suitable for parts with overall thicknesses of more than 3 mm.

9.4 Technologies without prepunching operation and one-sided accessibility

In this section, mechanical joining techniques are introduced, which only need accessibility from one side to the joining zone and no premanufactured hole. This clearly has advantages in terms of process times, costs and positioning accuracy. The two joining techniques, tack-setting and direct screwing by using hole- and thread-forming tapping screws, are depicted in the following subsections.

9.4.1 Tack-setting

During the process of tack-setting, a nail-like fastening element is inserted with high velocity into the materials to be joined. Its advantages are the one-sided

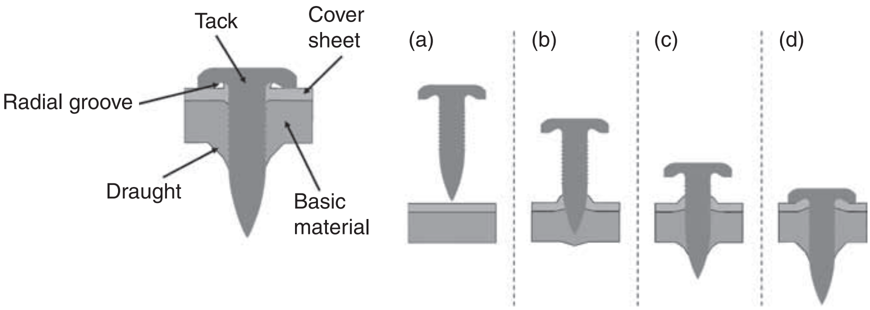

9.17 Terms of a tack-setting connection and process steps of tack-setting: (a) positioning, (b) entering, (c) penetration, and (d) fixing (source: Böllhoff).

access to the joining zone, the short process time and the possibility of connecting different materials. Thus, the flexibility of this technology with regard to the usage of various materials allows the connection of super high strength steels and also of magnesium alloys. The steps of the setting process can be described as follows: First of all, the element is positioned above the joining zone by the setting tool. After activating the joining process, the tack is accelerated up to 30 m/s by the pneumatically driven setting tool. When the element enters into the substrate, the material is displaced by the element. Thereby the typical rim hole is shaped around the base material. Parts of the base material rise up along the tack against the joining direction and, after finishing the setting process, remain in the provided radial groove of the tack. The setting process is finished when the head of the tack sits solidly on the cover sheet (cf. Fig. 9.17). Apart from the high force lock, the connection forms an additional form lock at the shank knurl of the tack due to the flow of the substrate materials. There are manual and fully automated setting tools available which can be used for tack-setting technology.

Especially when working with magnesium alloys it is important to use the magnesium component as cover sheet. Magnesium alloys are not suited as basic material because of the high deformation of the material and the visible cracks that appear during the shaping of the rim hole. Moreover, the joining zone should be of a very stiff design. The softer the joining zone, the more likely it is that cracks will appear underneath the set head of a magnesium cover sheet. Figure 9.18 shows a connection realized with a special aluminum tack. It was produced in order to minimize the electrochemical potential between the additional joining element and the substrates used.

9.4.2 Direct screwing (hole- and thread-forming tapping screws)

Direct screwing with hole- and thread-forming tapping screws means that a screw which connects two or more components is inserted without the necessity of a

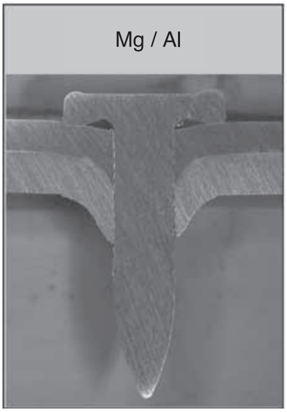

Material		Thickness
Mg-alloy	AZ31	1.5 mm
Al-alloy	AlMg3	2.0 mm

Joining element	
Tac: Al	
d = 4 mm	3 mm ⟷

9.18 Joining element characteristic of a tack-setting connection (source: Heger 2010).

prepunched hole. There are two different variants of this technology that have to be distinguished. According to one variant, only the upper joining part is prepunched. The lower joining part is attached to the upper one by direct screwing. The second variant is an advancement of this first technology. Here, both joining parts are joined without a premanufactured hole. This second variant is preferred in the automotive industry because of the fact that there is no need of a cost-intensive prepunch operation. Moreover, this variant makes the positioning above the joining zone much easier. Thus, process time and process costs are minimized.

In this manner, two different kinds of screws are used in industrial applications: flow drill screws (FDS) and cold-forming screws.

Flow drill screws

The flow drill screw (FDS) is especially developed for such a type of joining process. One characteristic of the screw is the particular tip whose geometric design makes the joining possible (cf. Fig. 9.19).

At the beginning of the setting process, the element is set into rotation. As soon as the nominal rotation speed is reached, the screw is positioned on the joining part by an aligned axial feed force. Due to the frictional heat which is generated during this process, the material partially plasticizes. Now the screw can penetrate the material. Moreover, a rim hole is formed and expands according to and also against the feed force. Depending on the material and the process parameters, the dimension of the rim hole constitutes around the triple size of the joining part thickness. In the following phase, the cylindrical part of the screw forms the core hole based on the rim hole. Finally, the thread is formed by a non-cutting grooving and the screw is tightened by a defined tightening torque. As the joining zone cools down, the rim

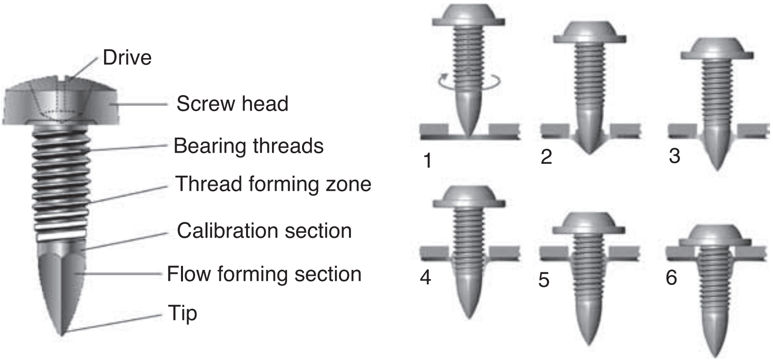

9.19 Functional sections of a flow forming screw and process steps of flow drill screwing with a pre-punched joining part at one side. (1) Heating the shield metal. (2) Penetration of the material with the conical tip of the screw. (3) Formation of the cylindrical passage. (4) Non-cutting tapping of dimensionally accurate nut threads. (5) Screwing through. (6) Tightening the screw with the set torque (source: EJOT).

hole contracts and covers the thread of the screw free from play. Thus, the connection gets a higher loosening torque which adds to the leak tightness of the joint. In contrast to most of the other mechanical joining techniques, the FDS can be unscrewed and replaced by another screw (Meschut 2007; DVS 2241–1).

In the following paragraphs, the two different process variants are demonstrated. Figure 9.20 shows a flow drill screwing joint where the upper joining part is pre-punched. As said before, the length of the formed thread is dependent on the overall sheet thickness. Moreover, Fig. 9.20 shows that a direct screwing with magnesium results in good joining element characteristics due to the locally induced frictional heat which supports the high deformation in the thread zone. Heating is already part of the process and does not have to be additionally induced. Re-screwable magnesium joints with outstanding strength characteristics can therefore be manufactured.

Exemplary results of a flow drill screwing without a prepunched hole are shown in Fig. 9.21. Here, the quality criteria which can be derived from the macro grinding are fulfilled too. A slight gap between the joining sheets cannot be

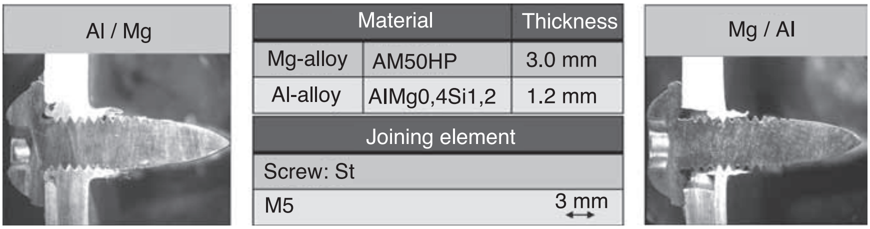

Material		Thickness
Mg-alloy	AM50HP	3.0 mm
Al-alloy	AlMg0,4Si1,2	1.2 mm
Joining element		
Screw: St		
M5		

9.20 Joining element characteristics of flow drill screwing connections with a prepunched joining part at one side (source: Bruedgam et al. 2003).

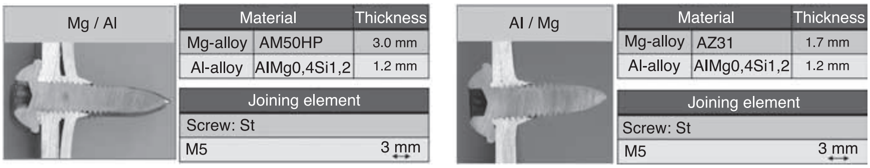

9.21 Joining element characteristics of flow drill screwing connections without pre-punching (source: Bruedgam et al. 2003).

completely obviated due to the thick magnesium sheet in the magnesium/aluminum connection. This formation of a gap can be regarded as noncritical as it does not reduce the strength of this joint. Finally, one can say that the technology flow drill screwing is appropriate when joining magnesium alloys.

Cold-forming screws

When using cold-forming screws, in comparison to FDS, the substrate material is not plasticized by heat. Here, the substrate material is plastically deformed by the geometry of the screw tip and the resulting surface pressure. After positioning the screw, the screw tip forms a hole into the joining part. As soon as the screw tip penetrates the substrate material, the threads form and pull the screw into the sheet. The rim hole is shaped into the sheet via the thread geometry of the screw. Throughout the process of screwing, the thread is formed into the rim hole by its non-cutting tapping, into which the screw is turned in further. The spindle is stopped when the favored tightening torque is reached (Fig. 9.22). In comparison to the process of flow drill screwing, the process mentioned here does only include a low frictional heat. Therefore, this process is suitable for magnesium materials to only a limited extent. The appropriateness of this process depends on the considered alloy as well as the thickness of the unpunched joining parts.

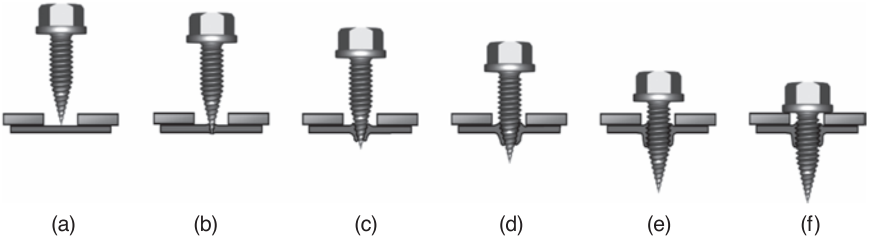

9.22 Process steps of processing a cold forming screw with a prepunched joining part at one side: (a) position, (b) form hole, (c) form rim, (d) form thread, (e) screw in, and (f) tighten (source: Betzer).

9.5 Technologies without prepunching operation and two-sided accessibility

The technologies described in this section are processes where the joining components are mechanically deformed to a considerable degree. As the ductility of magnesium alloys at room temperature is quite low, possible ways of improving those material properties are addressed here. A marked improvement in the characteristics of the joining components can be achieved by either locally heating the components or by accelerating the joining processes described below. A complete listing of all options can be found in Horstmann (2008). In practice, after considering costs, operational safety, process stability and process time, in particular, the method of heating by induction has been established. The acceleration of the setting process is generally realized by the use of accelerated masses driven by pressurized air.

9.5.1 Self-piercing riveting with semi-tubular rivet

In the past, the automotive industry has been consistently initiating innovative technologies for forming and joining processes. Modern and sustainable auto bodies built with new materials have been made possible by the advancements in joining technology. Having been developed for an aluminum body-in-white, semi-tubular, self-piercing rivets have also been proven successful in steel, aluminum, magnesium and plastic composite construction elements and are now an integral part of vehicles of every kind. High flexibility with regard to the multitude of materials used in composite construction is one of the key benefits which gives joining technology its outstanding status. During self-piercing riveting with semi-tubular rivets, two or more joining components are being connected with a joining element in a force and form locking manner. This process is executed without a prepunched hole and with two-sided accessibility. The main terms as well as an overview of the riveting process can be seen in Fig. 9.23.

The tool consisting of blank holder, punch and die is positioned over the joining zone. The die can vary in contour, size and depth depending on the joining task.

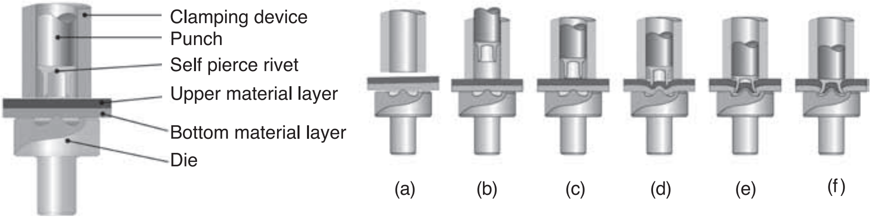

9.23 Terms and process steps of self-piercing riveting using a semi-tubular rivet: (a) positioning, (b) holding, (c) piercing, (d) stamping, (e) forming, and (f) setting (source: Böllhoff).

The stamping mechanism holding the riveting element is encased within a blank holder which fixes the components by pressing them with a predefined force. After triggering the setting process, the riveting element is pressed into the upper layer of material and punches it through. This cutting process is encouraged by the geometry of the cutting edge of the rivet. As the rivet meets the sheet metal facing the die, a radially directed flow process of the metal initiates. This deforms the joining element, causing it to wedge itself into the lower sheet metal without punching it through. In a final step, the joint is compressed in order to achieve a gap-free form- and force-locked joint. After reaching the maximum punch force or the preadjusted feed of the punch, the stamping mechanism is returned to its home position.

The main factors determining the quality of self-piercing riveting joints are a sufficient undercut of the joining element within the material facing the die as well as a gap-free joint of the rivet head to the material facing the punch.

With regard to the processability of magnesium at room temperature, it is necessary to differentiate between different formations of the materials used in the joining process. Magnesium can generally be used as the material facing the punch, as that layer is merely punched through without being deformed too much. Depending on the thickness of the sheet metal and composition of the alloy, however, fissures below the snap head may occur. If magnesium is used as the material facing the die, the locally occurring deformation can be limited by choosing an extra small die. The joinability is limited, however, as external fissures of the snap head are frequently observed.

Figure 9.24 shows a joint set at room temperature. The material is a further developed variant of the AZ31 alloy used within the research project 'Mobil mit Magnesium' (Heger 2010). The alloy is characterized by an increased ductility and achieves a very good result at room temperature.

As described above, the joinability of magnesium alloys can be greatly improved by either locally heating the components or by accelerating the joining process. Considering costs, process time, installation space and operational safety, heating by induction has proven to be the best method of those described above.

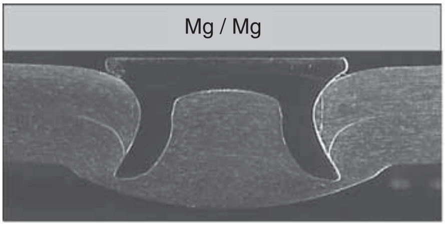

Material		Thickness
Mg-alloy	AZ31	1.5 mm

Joining element
SPR C5 × 5H2 CSR ← 3 mm →

9.24 Joining element characteristic of a self-piercing riveting connection using a semi-tubular rivet at room temperature (source: Heger 2010).

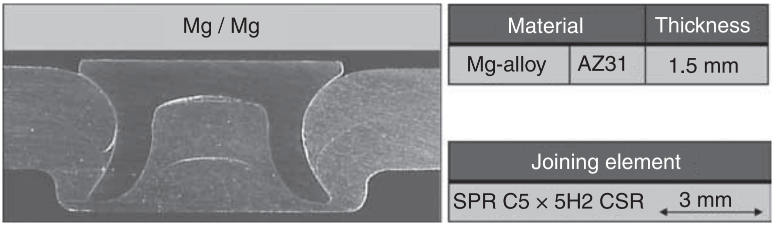

9.25 Joining element characteristic of a thermally supported self-piercing riveting connection using a semi-tubular rivet (source: Heger 2010).

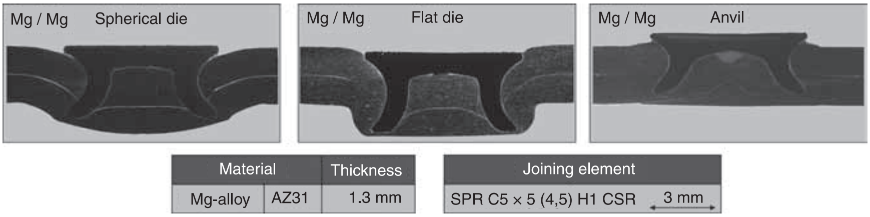

9.26 Joining element characteristics of self-piercing riveting connections using a semi-tubular rivet within an accelerated setting process at room temperature; left: spherical die, center: flat die, right: anvil (source: Horstmann 2008).

Figure 9.25 shows a monotype join of AZ31. Increasing the ductility by heating allows for a standard anvil/die used with conventional punch rivets.

Another possibility of increasing the joinability of magnesium alloys is by increasing the setting speed. This causes the joining components to heat locally upon penetration of the rivet and results in a gap-free joint which conforms to all specifications (cf. Fig. 9.26).

9.5.2 Flanging

Flanging is a process similar to self-piercing riveting with semi-tubular rivets but differs in the setting process and the characteristics of the joining element. Contrary to punch riveting with semi-tubular rivets, the hollow punch rivet is punched through all joining materials in one step. The element is deformed only slightly during this step. After removing the slug formed by the punching process, the protruding rivet is stamped with a flanging punch in a second step. This forms a force- and form-fitting joint as shown in Fig. 9.27. Figure 9.28 shows typical joints achieved by flanging.

The joints show no gap between the joining elements or the setting head and the element facing the punch. The resulting undercuts responsible for the form-fit and the stability of the joint are entirely comparable to the results achieved by punch riveting.

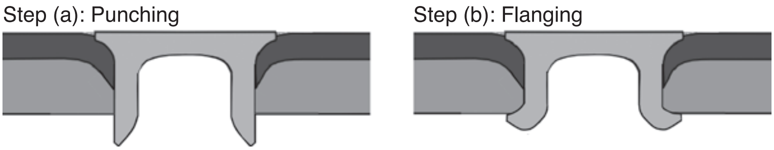

9.27 Process steps of flanging: (a) punching, and (b) flanging (source: Böllhoff).

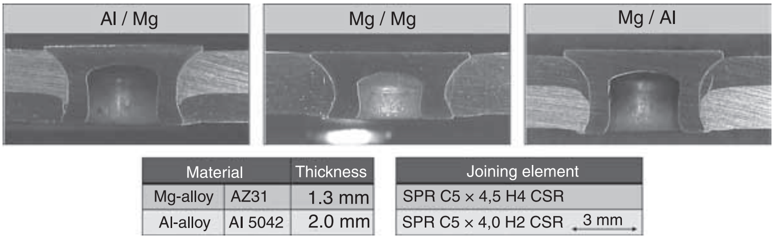

Material		Thickness
Mg-alloy	AZ31	1.3 mm
Al-alloy	Al 5042	2.0 mm

Joining element
SPR C5 × 4,5 H4 CSR
SPR C5 × 4,0 H2 CSR

9.28 Joining element characteristics of flanging connections (source: Heger 2010).

9.5.3 Self-piercing riveting with solid rivet

Basically, the self-piercing riveting process with solid rivet is a cold-forming operation used to fasten two or more sheets of material by driving a solid rivet through the sheets. Joining parts are directly and permanently connected by form or force lock without premanufacturing a hole. The rivet itself is not deformed. The solid rivet produces the necessary hole itself while punching a small slug out of all joining parts. The sheets need to have two-sided accessibility for joining. Transmission of connection strength between joined parts is given exclusively by the rivet. As there is no requirement for predrilled holes in the sheet materials, the process eliminates the need for exact alignment between components and between components and rivet setting machinery.

While the setting tool moves to the joining spot, the rivet will be fed into the blank holder and vertically positioned to the surface of the joining parts. The blank holder fixes the parts before joining and serves a guiding and centering function for the rivet during the beginning of the joining process. The punch presses the rivet through the sheets. In this way, the solid rivet acts like a single-use punching tool. The pieces punched out are removed through the die. The ring-shaped die has a small offset at its inner diameter, which causes the material of the die-sided sheet to flow into the ring groove of the solid rivet. A complete filling of the ring groove provides the best mechanical properties of the joint, because of the undercut of the sheet material within the groove. Thereby the connection is established. The self-piercing riveting procedure using a solid rivet is pictured in Fig. 9.29.

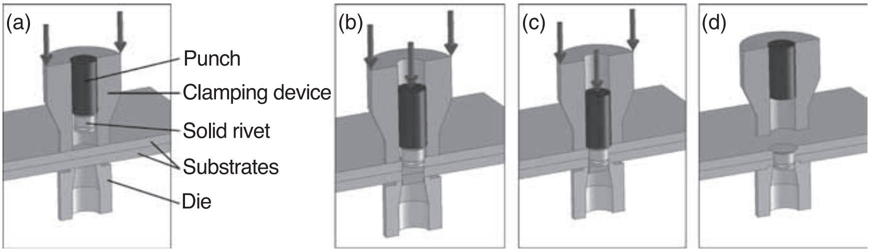

9.29 Process steps of self-piercing riveting using a solid rivet (source: LWF).

The length of the solid self-piercing rivet has to be aligned to the overall thickness of the joining zone. If this is done correctly, both sides of the joint are flushed with the surfaces of the joining parts. When joining materials of different thicknesses, the thicker sheet should be placed on the die side of the joint. The use of multi-application solid rivets offers the additional possibility to cover certain thickness variations of the parts. In this case, several ring grooves can be found on the rivet.

The material of the rivet needs to have a higher tensile strength and hardness than the material of the joining parts, because the punching is effected by the cutting edge of the rivet. Typical materials of the punch rivets are mild stainless steel as well as aluminum, but most of the rivets are heat-treated steels. To avoid electrochemical corrosion, the rivet manufacturers offer different coatings for their rivets especially in combination with aluminum substrates.

Compared to thermal joining techniques and also to self-piercing riveting with semi-tubular rivet, an important advantage of using solid pierce rivets is the high dimensional stability. The joining parts are only deformed locally while the die-sided material flows in the ring groove of the rivet. Because of its simple technology and reduced surface damage around the joining spot, especially on coated and painted parts, this connection is an economical alternative to resistance spot welding. This also applies to magnesium sheets. Due to the lower demand for deformability, it is more advantageous to place the magnesium sheet on the punch side of the joint. Depending on sheet thickness, alloy composition, joining temperature and tools that are used, good joining element characteristics can also be achieved by having magnesium on the die side of the joint (cf. Fig. 9.30).

9.5.4 Clinching

The technology of clinching is different from the other mechanical joining techniques as there is no use of an additional joining element to create the joint. Clinch technology can be divided into cutting and non-cutting processes. Besides dividing clinch systems according to their cutting ratio, they could also be classified according to their joining kinematics. Here, single-stage and multi-

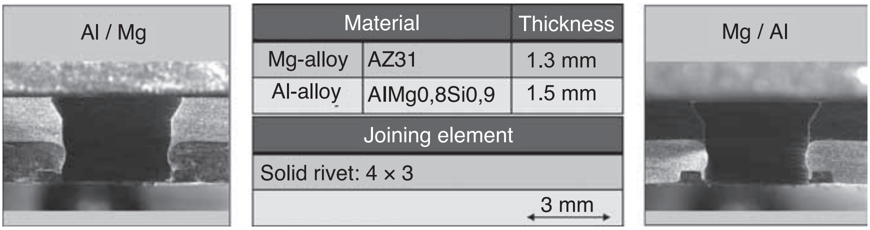

Material		Thickness
Mg-alloy	AZ31	1.3 mm
Al-alloy	AlMg0,8Si0,9	1.5 mm

Joining element
Solid rivet: 4 × 3

9.30 Joining element characteristics of self-piercing riveting connections using a solid rivet.

stage clinch processes are known. Owing to many advantages, such as quick process times and the good automation capability, mostly non-cutting round clinch processes manufactured in a single action are used in industrial applications. For joining magnesium, cutting clinch processes can be excluded, because they lead to an exposed cutting edge. This is not very positive for protection against corrosion. Therefore, only the single-stage, non-cutting clinching process is described in the following paragraphs.

Normally the clinch tool consists of a punch, a blank holder and a die (cf. Fig. 9.31). A distinction is made between different types of dies. The die can be one massive part with a cavity and a ring groove (closing die), or it can have moving die blades that are clamped together by springs (split die). These die blades enable expansion of the diameter and allow an outward flow of metal to create a form- and force-closed permanent interlocking. The blank holder fixes the joining parts before the punch is pressed into them and prevents distortion of the parts while joining is in progress.

The clinching procedure is done as follows. To start with, the parts to be joined are positioned between the punch and the die. Then a blank holder fixes the parts and presses them together without leaving any gaps. Now the actual joining process takes place. In a first step, the substrates are deep-drawn into the die. When the substrates reach the bottom of the die, a compression process is activated. Thereby a material flow is caused in radial directions due to high surface pressures. Along the way, a characteristic undercut is formed (cf. Fig. 9.31).

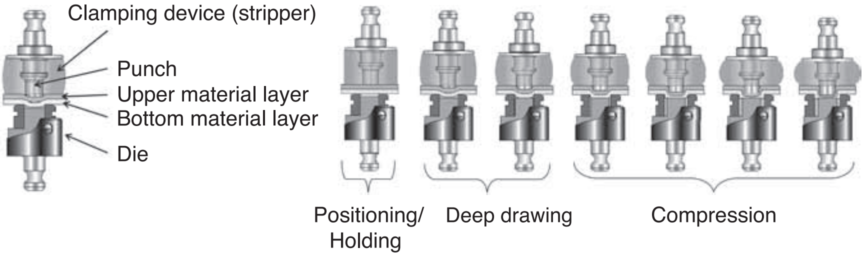

9.31 Process steps of clinching using a split die (source: Böllhoff).

Values which determine the quality of a clinch joint are the residual bottom thickness, neck thickness and the dimension of undercut. While the neck thickness has an influence on the maximum shear stress, the generated undercut affects the properties in head and peel tests. Because of form and force closure, clinch connections should be preferentially loaded with shear stress. Head and peel tests of clinch joints show much lower possible loads. Torsional stress should be generally avoided for single-spot connections, such as clinch connections.

Because the technology of clinching creates a connection without adding an additional joining element, the materials to be joined have to be malleable. As a result of the necessary plastic deformation of the substrates, clinching of most of the magnesium alloys at room temperature is difficult to realize. The material tears apart in neck- and bottom-areas of the clinch joint. With an unmodified standard joining process, commercially available clinching systems achieve no sustainable connections (Hahn et al. 2001). Alternatively, however, special clinching processes are available that take into account the poor forming properties of magnesium alloys. These processes, for example punch clinching, are listed in Bruedgam et al. (2003) and can be executed at room temperature. In general, the created connections show much worse mechanical properties than connections which were conventionally manufactured at high substrate temperatures. An example of a joining element characteristic of a special clinching process is given in Fig. 9.32.

For common magnesium alloys, the deformation escalates at a temperature of above 225 °C, resulting from the thermal activation of additional slip systems in the lattice structure. Preheating of magnesium substrates leads to a broad extension of deformation and, thus, offers the chance to realize a high-quality clinch joint. The heating of the substrates before or during the clinching process can be performed by different heating concepts (Huebner 2005; Neugebauer et al. 2005; Hahn et al. 2009). Compared to other heating principles, one of the most efficient methods is the electromagnetic induction which has already been mentioned for the self-piercing riveting with semi-tubular rivet. Figure 9.33 displays characteristic joining elements of alloy AZ31 (sheet thickness: 2 mm each) which were created at different substrate temperatures.

While the punch-sided disposition of magnesium leads to better mechanical properties for the self-piercing riveting, it is the other way around for

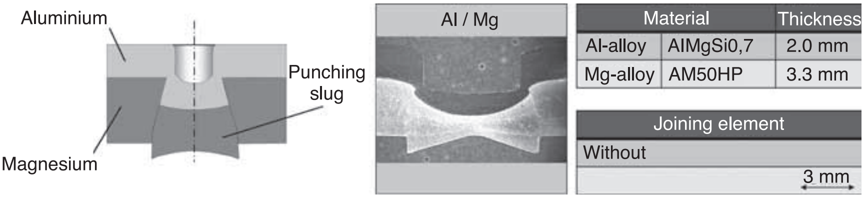

Material		Thickness
Al-alloy	AlMgSi0,7	2.0 mm
Mg-alloy	AM50HP	3.3 mm

Joining element
Without

9.32 Terms and joining element characteristic of a punch clinching connection (source: Bruedgam et al. 2003).

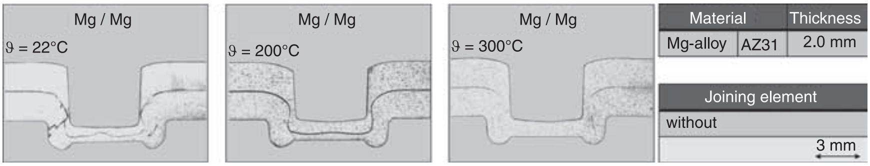

9.33 Joining element characteristics of clinch connections using a closed die manufactured at different substrate temperatures.

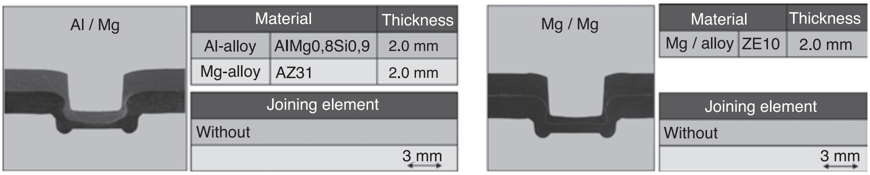

9.34 Joining element characteristics of clinch connections using a closed die manufactured with a high (>100 m/s) setting velocity (source: Hahn et al. 2009).

the clinching process. The magnesium part should be arranged on the die-side during clinching.

In the same way as described for self-piercing riveting with a semi-tubular rivet, the malleability of magnesium in the clinching process can be significantly improved not only by heating of the substrates but also by accelerating the setting process to achieve extremely high deformation rates.

Hahn et al. (2009) exemplarily show a clinch joint, which has been successfully realized with an accelerated setting velocity of above 100 m/s. Figure 9.34 shows joining element characteristics of joints produced by such method.

9.6 Linear technology: hemming

In many industries, hemming is profitably used for joining thin metal sheets. The process of hemming is used to join two components by folding the edge of one over the other to create a mechanical interlock. Often the operation is deployed in combination with adhesive bonding to achieve a sealing of the fold and thus an improvement of the corrosion protection of the joining area as well as an improvement of the mechanical properties. Typical applications in the automotive industry are opening parts, for example, doors, hoods, sliding doors or tailgates, at which the flange of an outer panel is bent over the inner panel. With this technology sheets of different materials can be manufactured economically in small quantities.

The hemming operation is usually a three-step process: flanging, prehemming and hemming. Flanging takes place during the drawing operation and consists of bending the sheet edge up to around 90 °C. Prehemming is done after the inner part is placed on the outer part and increases the angle of the sheet bend to around

135 °C to prepare for the next operation. Finally, the hemming tool folds the outer part over the inner part.

There are two main industrial hemming technologies, i.e. the classical hemming process, also known as tabletop hemming, and the roll-hemming process. The former is used in hemming units situated around the opening part. Hemming tools simultaneously assemble the opening part. The advantage of this method is the velocity at which it can be carried out, thus forwarding a very short cycle time. The latter uses a roller guided by a handling robot along the hemming line. The inclination of the robot head changes between the pre-hemming and hemming operations. The roller, which freely rotates around its revolution axis, progressively prehems and then hems the flanged edge of the opening part. The advantage of this method is the use of relatively light equipment. This method is very economical, if not taking the investment of the robot into account. The main drawbacks are the high cycle time and the hemming difficulties of parts with complex geometries. Finally, time is also shorter than for classical hemming because the programmer only modifies the roller trajectory in the problem area. Figure 9.35 illustrates the procedure for roller hemming and bonding using three hemming steps as an example.

Hemming of magnesium alloys is only difficult to realize because of the necessary procedural plastic deformation of the substrates. The material tears at the joining seam. Without modification of the joining process no adequate connections are achievable using the conventional or roller hemming process. This is rooted in a minor deformation of magnesium compared to steel and aluminum at room temperature. The anisotropic deformation characteristics of the hexagonal lattice structure of magnesium have a negative effect on the deformability, especially under multi-axial load.

For common magnesium alloys, a sufficient plastic malleability and, thus, a crack-free deformation is ensured at temperatures above 225 °C, resulting from the thermal activation of additional slip systems in the lattice structure. According to this, preheating of the folded edge can lead to a broad deformation of the material and thus offers the chance to realize a high-quality joint. The heating of

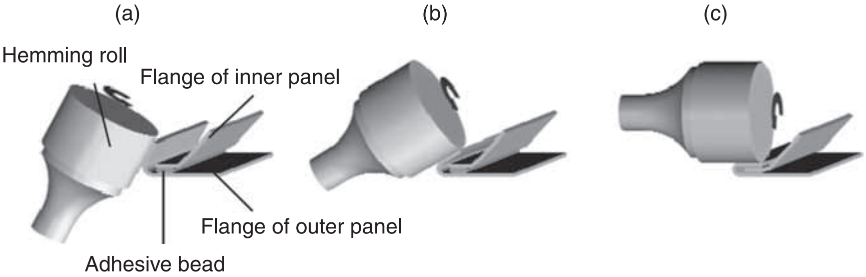

9.35 Process sequence of roller hemming and bonding: (a) first prehemming, (b) second prehemming, and (c) final hemming (source: LWF).

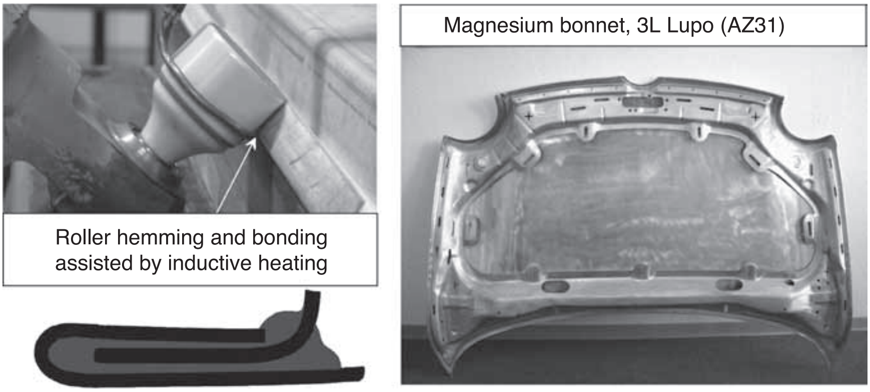
Roller hemming and bonding assisted by inductive heating
Magnesium bonnet, 3L Lupo (AZ31)

9.36 Magnesium sheet roller hemming using the example of a magnesium demonstrator bonnet (3L Lupo).

the substrates before or during the joining process can be performed by different heating concepts like hot air or inductive heating.

Using the example of a magnesium bonnet, Fig. 9.36 shows thermally supported magnesium sheet hemming, in which crack-free folded and mechanically bonded joints are produced in combination with an applied adhesive.

As a result of the high temperatures of more than 225 °C and the high degrees of deformation during a magnesium hemming process, high demands are also made on the applied surface coating system. Against the background of corrosion protection a delamination or burning of the coating layer must be avoided.

Due to the thermally supported process to deform the magnesium substrate, up to now a combination of roller hemming and adhesive bonding has not been possible from what is known so far, because the adhesive already shows a chemical reaction in the first prehemming step, when the material is heated to 225 °C. This leads to an insufficient deformation and wetting ability of the adhesive at the final hemming step, as the common curing temperatures of hot-curing systems in the automotive industry only reach values up to 180 °C. If the adhesive is exposed to such a high temperature, this can lead to an abrupt curing which has a harmful effect on the properties of the adhesive. In order to avoid precuring during the thermally supported prefolding steps, adhesives must be used whose reaction kinetics have been adapted to the process.

9.7 References

Bruedgam, S. et al. (2003). *Fügesystemoptimierungen zur Herstellung von Mischbauweisen aus Kombinationen der Werkstoffe Stahl, Aluminium, Magnesium und Kunststoff*. Paderborn, final report BMBf-project 03N3077D1.
DIN 8593 (2003). *Manufacturing Processes Joining*. Berlin: Beuth.
DIN 14588, 2001. *Blind Rivets – Terminology and Definitions*. Berlin: Beuth.

DVS 2241–1 (2003). Direktverschraubung von Formteilen aus Kunststoffen. *In: DVS, Taschenbuch DVS – Merkblätter und – Richtlinien Mechanisches Fügen*. Düsseldorf: DVS-Media, 147–154.

Hahn, O. and Heger, M. (2008). *Ermittlung des Einflusses von verbleibender Klemmkraft auf die Schwingfestigkeit von hochfesten Blindnietverbindungen*. Hannover: Europäische Forschungsgesellschaft für Blechverarbeitung e.V. (EFB), EFB research report no. 281.

Hahn, O. and Klemens, U. (1996). *Fügen durch Umformen, Nieten und Durchsetzfügen – Innovative Verbindungsverfahren für die Praxis (Dokumentation 707)*. Düsseldorf: Verlag und Vertriebsgesellschaft Stahlanwendung GmbH.

Hahn, O., Kurzok, J.R., and Amedick, J. (2001). Mechanisches Fügen von Leichtbau-Werkstoffen – Vorwärmen schafft neue Potenziale. *Aluminium Kurier News* **1**: 10–12.

Hahn, O. et al. (2009). Development of innovative technologies for joining magnesium alloys and dissimilar materials. *In*: K.U. Kainer, ed. *Magnesium – 8th international conference on Magnesium Alloys and their Applications*. Weinheim: Wiley, 1302–1307.

Heger, M. (2010). *Mobil mit Magnesium – Teilprojekt: Grundsatzuntersuchungen zu Füge- und Montagetechniken*. final report BMBf-project 03X3012. Bielefeld: Forschungszentrum Jülich.

Horstmann, M. (2008). *Entwicklung umformtechnischer Fügeprozesse für das Verbinden von Magnesiumhalbzeugen*. Paderborn: Shaker.

Huebner, S. (2005). *Clinchen moderner Blechwerkstoffe*. Hanover: PZH.

Meschut, G. (2007). Mechanical and hybrid joining. *In*: H.E. Friedrich and B.L. Mordike, eds. *Magnesium Technology – Metallurgy, Design Data, Applications*. Berlin: Springer, 374–397.

Mordike, B.L. and Wiesner, P. (2005). *Fügen von Magnesiumwerkstoffen*. Düsseldorf: DVS-Verlag.

Neugebauer, R., Dietrich, S., and Kraus, C. (2005). Matrizenloses Clinchverfahren verkürzt Prozesszeiten beim temperierten Fügen von Magnesiumbauteilen. *In*: O. Hahn, ed. *Mechanisches Fügen und Kleben – 12. Paderborner Symposium Fügetechnik*. Paderborn: Shaker, 100–110.

10

Adhesive bonding of magnesium alloys

L. LIU, Dalian University of Technology, China

Abstract: In this chapter, the research and progress in adhesive bonding of magnesium alloys and the typical processes of adhesive bonding are introduced. Surface treatment is very important for adhesive bonding of Mg, especially in bonding of Mg to other metals due to the corrosion behaviors. Some surface treatments that have recently been researched are introduced, and the treatments, instead of chromating pretreatments, are the highlights. The adhesives used for Mg are listed in the chapter. Finally, the applications of adhesive bonding of Mg are introduced.

Key words: magnesium alloy, adhesive bonding, surface treatments, corrosion.

10.1 Introduction

Adhesive bonding is the process of uniting materials with the aid of an adhesive, a substance capable of holding such materials together by surface attachment,[1] and is suitable for any shape and size of the magnesium alloy materials. Smooth joint surfaces are advantages of adhesively jointed structures, and large-area connection can also be achieved by adhesive bonding. Magnesium alloys and almost any other materials such as metal, plastic, ceramics, cork and rubber can be joined by adhesives after proper surface treatments, so that they are suitable for aircraft applications. Attention needs to be paid to corrosion issues for magnesium alloy's adhesive bonding because of the low potential of magnesium; however, it can be protected by a layer of nonconductive adhesive that can isolate it from air. Therefore, adhesive bonding is suitable for joining magnesium and other metals. The adhesive can also provide uniform distribution of stress and large stress-bearing areas. The basic processes of adhesive bonding include surface treatments, adhesive application, assembly and cure.

10.2 Surface treatments of magnesium alloys

The material surface should be pretreated before application of the adhesive in order to form a satisfactory structure, and good surface treatments are necessary if good environmental or thermal durability is needed. Commonly used methods of surface treatments include degreasing methods, abrasion methods and chemical methods, and the typical pretreatment process is shown in Fig. 10.1. The degreasing and abrasion methods are all applicable and the chemical methods can provide strength and long-term durability bonds and are easily put into operation.

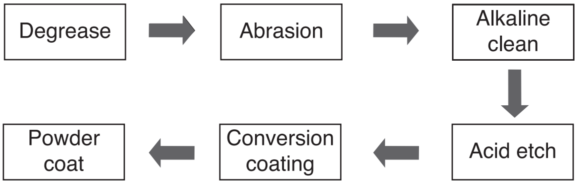

10.1 Typical pre-treatment and powder coating process.

The degreasing method is the process of removing oil from a surface with an organic solvent, which includes vapor degreasing, spraying, immersion and ultrasonic scrubbing. Under normal circumstances, clean acetone is used to brush or wipe the magnesium surfaces with a clean brush or cloth. If the surface needs finer treatment, aerosol spray may be suitable. After this process, vapor degreasing can be used for further treatments, and currently, trichloroethylene is favored for vapor degreasing.

For many materials, light abrasion of the surfaces can allow better performance when a highly polished adherent is used; so, abrasion methods are useful. If the surfaces require simple treatment, the surfaces to be bonded can be treated using a suitable abrasive cloth, wire brush or waterproof abrasive paper. When the surface requires a more vigorous abrasion, air- or water-borne grit blasting is the suitable method. After abrasion methods are applied, a soft brush or a clean and dry compressed air blast must be used to ensure that the surface is completely free from loose and loosely bound particles.

As a chemically active natural metal, magnesium alloy needs careful surface treatment. In adhesive bonding of magnesium alloy, some by-products may be produced at the interface due to the potential reaction between adhesive and the metal, which could result in poor cohesive properties. For this reason, some chemical or anodic treatments are necessary after degreasing and abrasion, and such treatments result in the formation of thin inorganic chemical films on the magnesium surface to improve the cohesive properties. Due to the active nature of magnesium and its alloys, corrosion prevention must be considered in surface treatments. The key to surface treatment is to apply sufficient thickness of coating to prevent corrosion, but the coating must not be so thick that it will affect the bonding performance. Alkaline detergent solution[2] (ASTM D2651, Method A) is commonly used in the following way in magnesium treatments:

- Degrease (use caution, as contaminants, such as metal particles, oils, etc., may pose fire or explosion hazard)
- Immerse for 10 minutes at 60–71 °C (140–160 °F) in an alkaline detergent solution as follows:

Sodium metasilicate	2.5 pbw
Trisodium pyrophosphate	1.1 pbw
Sodium hydroxide	1.1 pbw

Nacconal NR or equivalent	0.3 pbw
Water	95 pbw

- Rinse thoroughly
- Dry at not over 60 °C (140 °F)

It is generally believed that a suitable pretreatment must be applied prior to bonding in order to achieve a durable adhesive bonded joint. In addition, extensive environmental durability testing is required to establish confidence in the adhesive bonding for long-term performance. The durability of a bonded joint is based on adhesive properties, the adherent and interfaces between them. Adhesive-bonded joint failure usually occurs at the interfaces after long-term exposure to the corrosive environment. For untreated magnesium alloys, the oxide on the adherent surface is usually the weakest link in a long-term corrosive environment and the oxide will lead to a failure when stress is loaded. A conversion coating before adhesive bonding can stabilize the oxide for suitable corrosion prevention to arrest the oxide influence. The technologies for corrosion protection are keys to wider applications of magnesium.

Conversion coatings are generally divided into two categories: chrome and non-chrome. Chrome conversion coatings have long been known for significant corrosion protection due to the formation of a 'self-healing' protective layer. The chrome conversion method uses hot chromic acid[2] (ASTM D2651, Method B), as follows:

- Immerse for 10 minutes at 71–87.8 °C (140–190 °F) in the following solution:

Chromic acid (CrO_3)	1 pbw
Water	4 pbw

- Rinse thoroughly
- Dry at not over 60 °C (140 °F)

This method can be combined with the alkaline detergent solution method (ASTM D2651, Method A) to improve bond strengths. The hot chromic acid solution method should follow the alkaline detergent method, with a water rinse in between.

Chrome systems are detrimental to the environment and are subject to the European End-Of-Life Vehicle Directive (2000/53/EC), and their application should be reduced and eventually eliminated. Chromating pretreatments generally show the best results regarding strength and durability, whereas chrome-free alternatives require further optimization.[3] Bonding strength of conversion coating on AZ31B and AZ91D magnesium alloys has been researched, and the conversion coating includes chromate conversion coating, manganese conversion coating, tin conversion coating and $Mg(OH)_2$ coating, the latter being chromate-free.[4] $Mg(OH)_2$ coating can show higher tensile shear strength than chromate conversion coating in a tensile shear strength test with epoxy resin; manganese conversion coating and tin conversion coating show about equal tensile shear strength to chromate conversion coating in tensile shear strength test with modified silicone resin; tin conversion coating showed higher tensile shear strength than chromate conversion coating in a tensile shear strength test with modified silicone resin – phenol-formaldehyde resin. Therefore, some chromate-free conversion coatings can be applied as surface treatment for Mg-Mg adhesive bonding.

Galvanic corrosion is a wide concern in magnesium applications, especially in complex structural parts with other adjacent metals. As an (electrochemically) active metal used for structural applications, Mg will corrode when being joined with other metal parts in the presence of an electrolyte. Some methods are used to solve this problem, such as insulating components from the environment with either protective coatings or insulating washers as spacers. Some researches have been done on conversion coatings in conjunction with a spray powder coat for pretreatment of Mg-Al adhesive bonding.[5] A group of tests were conducted as reported in Table 10.1.[5] The tensile shear strength results and the samples before and after corrosion testing are shown in Fig. 10.2[5] and Fig. 10.3,[5] respectively.

Table 10.1 Group pre-treatment/coating/adhesive combinations[5]

Group ID	Conversion coating	Powder coat	Adhesive
A	Chromium VI	Epoxy/Polyester primer	1K epoxy
B	Chromium VI	Epoxy/Polyester primer	2K epoxy
C	Organometallic Ti/Zr	Epoxy/Polyester primer	1K epoxy
D	Organometallic Ti/Zr	Epoxy/Polyester primer	2K epoxy
E	Ti/Zr fluoronate	Epoxy/Polyester primer	1K epoxy
F	Ti/Zr fluoronate	Epoxy/Polyester primer	2K epoxy
G	Ti/Zr fluoronate	Epoxy	1K epoxy
H	Ti/Zr fluoronate	Epoxy	2K epoxy

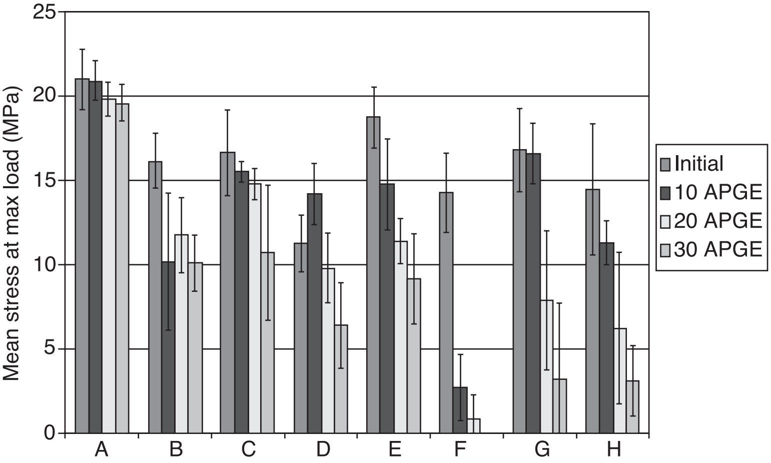

10.2 Mean lap-shear peak stress before and after corrosion testing.[5]

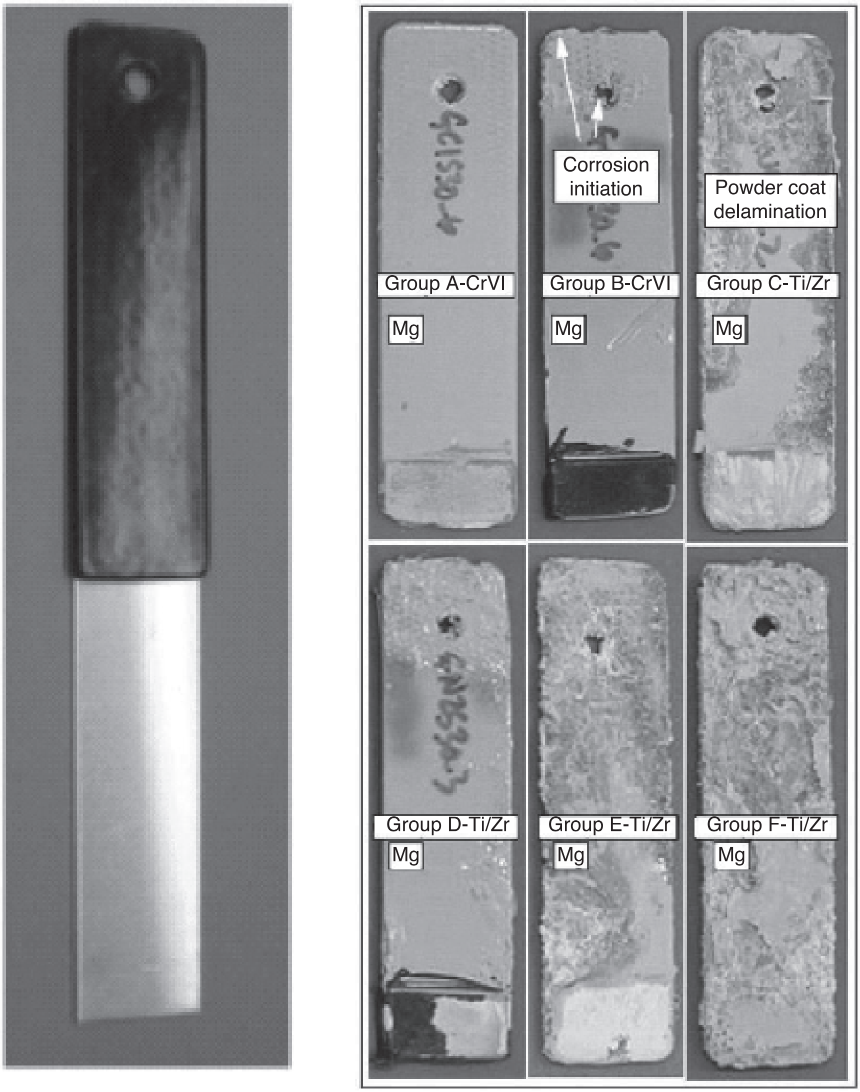

10.3 Lap-shear samples.[5]

The results show inconsistent performance of the Ti/Zr conversion coatings compared to the hexavalent chromium systems, and the lap shear data after corrosion exposure can only provide very limited indication of durability performance. Therefore, the non-chrome conversion coatings cannot show better performance than the traditional hexavalent chromium pretreatments. This technology needs more in-depth research.

10.3 Adhesive for the bonding of magnesium alloys

After thorough surface treatment, structural adhesive is applied to the faying surfaces of the metal parts to be joined, and it is important that the adhesive is evenly coated. A variety of adhesives can be used in adhesive bonding of magnesium if proper corrosion protection is applied. Adhesives used in bonding of magnesium include epoxy-phenolics, polyurethanes, silicones, cyanoacrylates, polyvinyl acetate, etc., and some adhesives with their characteristics are shown in Table 10.2.[6]

10.4 Cure for the bonding of magnesium alloys

Some adhesives must be cured in an adequate time in order to improve the strength after the adhesives are applied. The room temperature-curing adhesives usually require several hours, and heat-curing adhesives are often cured in minutes. In the curing period, the assembly must be supported under some pressure. Due to the chemically active nature of magnesium and magnesium alloys, inert atmosphere is needed for heat curing in order to avoid oxidation.

In the actual operation, a suitable temperature and pressure should be chosen to achieve the best result, and the exact conditions depend on the properties of the specific adhesive. Curing temperatures range from room temperature up to about 350 °C, but because of the low-melting points of magnesium and its intermetallic phases, a high-curing temperature adhesive should be avoided.

10.5 Applications of the bonding of magnesium alloys

Adhesive bonding is a high-potential technology, especially for joints of mixed materials due to almost no restrictions on the material combinations. Therefore, adhesive bonding of Mg alloys has been used in automotive applications. Magnesium door inner panel has been used by Ford Motor Co.,[5] as shown in Fig. 10.4 and Fig. 10.5.

Adhesive bonding between magnesium alloys and polypropylene (PP sheet) has also been researched as a potential application[7] because polypropylene is also a lightweight material and usually used for automotive purposes. Suitable chemical pre-treatments are done to the surfaces of both magnesium and PP sheets prior to bonding, and satisfactory joints are achieved, because the PP–adhesive interface significantly increases. Failed joints of peel tests show that a little PP is present on the peeling region.

The effect of mixing 1 wt.%SiO_2 particles into the adhesive is also researched. The adhesive bonding strength is higher than that of the base metal of PP sheet after the SiO_2 particles are added, as shown in Fig. 10.6.[7] The appearance of the adhesive layer containing SiO_2 is shown in Fig. 10.7.[7] The increase in bonding strength is due to the bonding between PP and the adhesive layer interface taking

Table 10.2 Characteristics of various adhesives used for bonding magnesium[6]

General type of composition	Curing conditions					Adhesive thickness		Shear strength at 20°C (70°F)	
	Temperature		Time	Pressure					
	°C	°F	min	MPa	psi	mm	in.	MPa	psi
Phenol formaldehyde plus polyvinyl formal powder[a]	130	270	32	0.3–3.4	50–500	0.08–0.15	0.003–0.006	11–18	1600–2600
Phenolic rubber-base resin[a]	160	325	20	1.4	200	0.08–0.15	0.003–0.006	15–18	2200–2600
Phenolic synthetic rubber-base plus thermosetting resin[a]	175 175	350 350	40 60	0.05–0.8 0.7	7–45 100	0.13–0.50 0.13–0.50	0.005–0.020 0.005–0.020	7–17 14–20	1000–2500 2100–2900
Ethoxyline resin-liquid, powder or stick used as solder	200	390	60	Contact	Contact	0.03–0.15	0.001–0.006	10–15	1500–2200
Ethoxyline resin, two liquid	20	68	24 h	Contact	Contact	0.03–0.15	0.001–0.006	10–15	1500–2200
Epoxy-type resin paste plus liquid activator	95	200	60	Contact	Contact	0.08–0.13	0.003–0.005	<20	<3000
Rubber base	200	400	8	1.4	200	0.25–0.38 (tape)	0.010–0.015 (tape)	12–16	1700–2300

(*Continued*)

Table 10.2 Continued

General type of composition	Curing conditions					Adhesive thickness		Shear strength at 20°C (70°F)	
	Temperature		Time	Pressure					
	°C	°F	min	MPa	psi	mm	in.	MPa	psi
Vinyl phenolic	150	300	8 preheat	Varied	Varied	0.10–0.30	0.004–0.012	7–12	1000–1700
	135–200	275–400	70.4	Varied	Varied	0.10–0.30	0.004–0.012	7–12	1000–1700
Epoxy-type resin	95	200	45	Contact	Contact	0.50–0.75 (tape)	0.020–0.030 (tape)	8–12	1200–1700
	95	200	45	0.1	14	0.50–0.75 (tape)	0.020–0.030 (tape)	8–12	1400–1700
Phenolic	150	300	15	0.2	2.8	0.50–1.00	0.002–0.004	<16	<2400
Modified epoxy resin	175	350	60	Contact	Contact	0.06–0.13	0.0025–0.005	19–30	2700–4300
Epoxy-phenolic (high-temperature type)	115	240	15–30	0.02–0.2	3–25	0.30–0.75 (tape)	0.012–0.030 (tape)	5–16 (at 68–260°C)	700–2300 (at 70–500)
	165	330	30	0.02–0.2	3–25	0.30–0.75 (tape)	0.012–0.030 (tape)	5–16 (at 68–260°C)	700–2300 (at 70–500)

Note: [a]Known to meet USAF specification.

10.4 Magnesium alloy door inner panel by Ford Motor Co.[5]

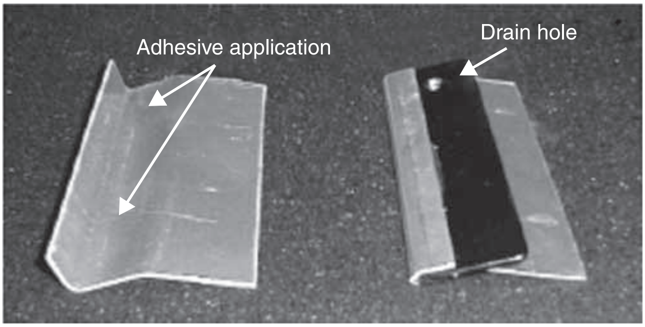

10.5 Adhesive bonding in magnesium automotive parts.[5]

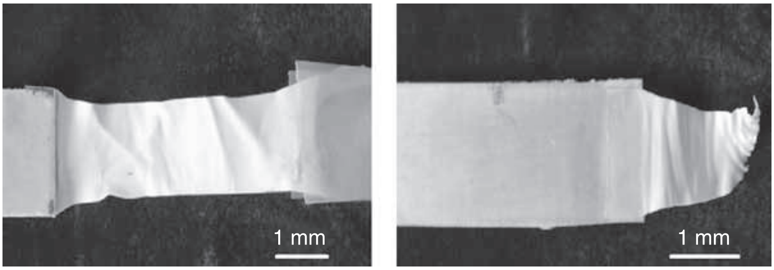

10.6 Specimens with SiO_2 doped after the tensile test.[7]

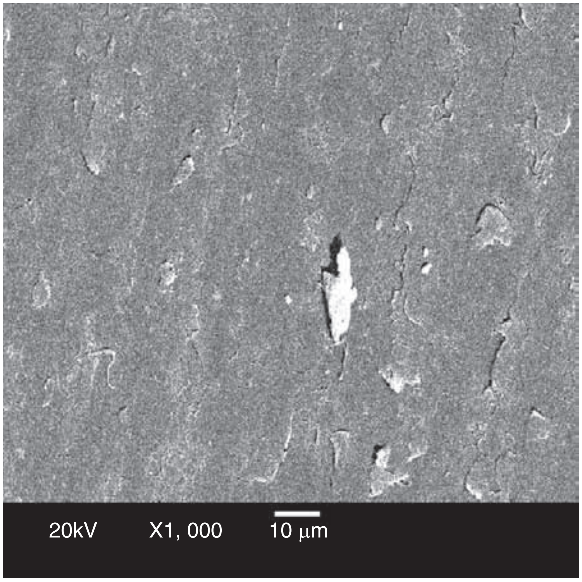

10.7 Micrograph of adhesive layer containing SiO_2 reinforcement.[7]

place by diffusion and mechanical interaction, and the bonding between the magnesium and adhesive is mainly the result of coordinative bond forces.

10.6 Future trends

Adhesive bonding technology can be used in magnesium alloys, and there is a clear trend toward the application of Mg in vehicle manufacture. Adhesive bonding of magnesium and other materials, such as Al, Fe and Cu, will be used in wider applications because welding of magnesium to these materials is relatively difficult. Moreover, the corrosion problems of magnesium alloy-bonding joints must also be investigated further.

10.7 References

1. ASTM D 907-82 (1984). *Standard Definition of Terms Relating to Adhesive. Vol 15, 06-Adhesive.* Philadelphia, PA: American Society of Testing Materials.
2. Snogren RC (1974). *Handbook of Surface Preparation.* New York: Palmerton Publishing Co.
3. Kötting G (2000). Mechanisches Fügen & Kleben. 7th Paderborner Symposium Fügetechnik, Germany, 147–64.
4. Sekiguchi M, Otani C, Takaya M (2006). Effect of conversion coatings on bond strength of magnesium alloy adhesive joints. *J Japan Inst Light Metals* **56**(3): 156–61.

5. Bretz GT, Lazarz KA, Hill DJ, Blanchard PJ (2004). Adhesive bonding and corrosion protection of a die cast magnesium automotive door. *Magnes Technol* 113–19.
6. Avedesian MM, Baker H (1999). *ASM Specialty Handbook: Magnesium and Magnesium Alloys*. Ohio: ASM International Materials Park.
7. Liu LM, Xie L (2007). Adhesive bonding between Mg alloys and polypropylene. *Mater Technol* **22**(2): 76–80.

11

Gas-tungsten arc welding of magnesium alloys

L. LIU, Dalian University of Technology, China

Abstract: This chapter discusses weld shapes, microstructures, mechanical property and the hardness of the gas tungsten arc welding (GTAW) of magnesium alloy joint with and without filler wire. The investigations show that excellent welded joints can be obtained both by GTAW and GTAW with filler wire. The investigations also show that the heat-affected zone is the weak part of the joint and the addition of the filler wire can increase the strength of the joint.

Key words: gas tungsten arc welding, gas tungsten arc welding with filler wire, heat-affected zone, microstructure.

11.1 Introduction

Because of the characteristics of low density, high ratio rigidity and specific strength, good damping and recycle (Hiraga et al. 2001; Lin et al. 2001; Munitz et al. 2001; Liu et al. 2002), magnesium alloys are considered as green engineering material (Huang et al. 2000), having a widely applied prospect in the fields of the automotive industry, motor vehicle industry and aviation (Draugelates et al. 2000; Schubert and Joaquin 2001; Su et al. 2001). With the increasing application of magnesium alloy structural components, the issues of magnesium alloy welding need to be resolved. Weld defects of oxidation and heating – crack and over wide heat-affected zone (HAZ) – during welding readily occur due to magnesium alloy's low melting point, high expansion coefficient and conductive coefficient, and it is hard to get high-quality joints matching base metals (Toshikatsu et al. 1994; Gu 1996; Asahina et al. 1999). Gas tungsten arc welding (GTAW) is an arc welding method which is based on tungsten or tungsten alloys (thorium tungsten, cerium tungsten, etc.) as electrodes, using argon as a protective gas, also known as tungsten-arc inert gas (TIG) welding, which is currently the most common magnesium alloy welding method.

The principle of GTAW or GTAFW (gas tungsten arc filler welding) is shown in Fig. 11.1. The tungsten electrode has been gripped by the electrode clip, sticking out a certain length from the torch nozzle; the arc is produced between the bottom of tungsten electrode and base metal; the inert gas flowing through the tungsten electrode is used to protect electrode, arc and weld pool from atmosphere infringement. When filling metal into the weld pool (as shown in Fig. 11.1), the filler wire is manually or automatically fed from the front of the arc using a certain speed.

The gas tungsten arc welding method is widely used because of its economical and practical characteristics. In the process of GTAW, it may or may not fill the welding wire. The magnesium alloy GTAW method is similar to that of the welding

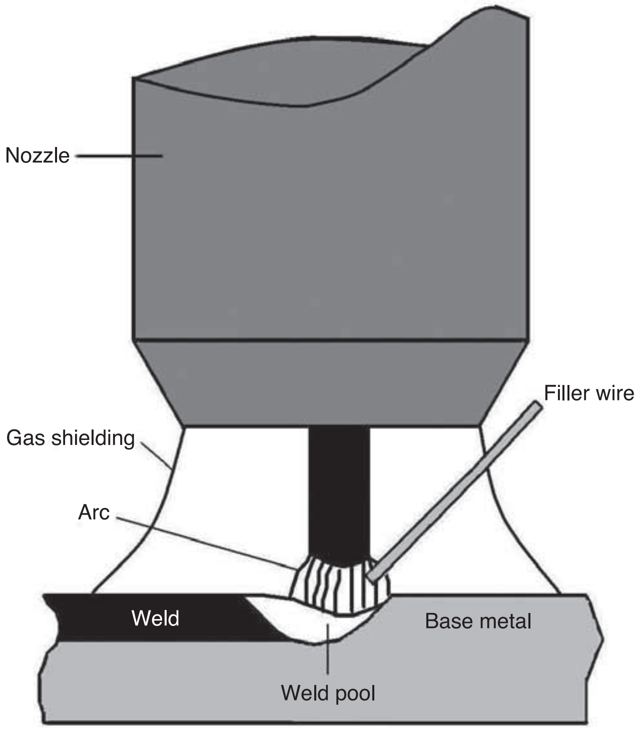

11.1 Principle of GTAW.

of aluminum alloy, in which alternating currents (AC) or direct current electrode positive (DCEP) is mostly used. In the AC and DCEP process, when the base metal is negative (–), the positive ions would bombard the base metal surface, which would evaporate and remove the oxide film on the magnesium alloy's surface. For the DCEP welding process, the welding penetration is shallow. The AC welding can obtain high penetration and small electrode consumption, so it is used more widely (Yang and Lin 2003).

At present, GTAW is applied in all industrial sectors but it is especially suitable for high-quality welding. GTAW would play a major role in the acceptance of magnesium for high-quality welding and structural applications as more research on the GTAW of magnesium alloys is being performed.

11.2 Gas-tungsten arc welding of magnesium alloys without filling wire

11.2.1 Preparing for welding

When it is necessary to feed materials, we can usually choose the same composition as the base metal; in some conditions, we can also use different feeding materials. Before welding, the surface of the wire and base metal must be cleaned carefully. The usual methods are machine cleaning and chemical cleaning to remove oil, rust and so on (Yang and Lin 2003).

11.2.2 Macrograph of weld joint

The effect of heat input on the molding of welds for Mg-based alloys was obvious (Liu et al. 2004) due to their characteristics of low melting point, high thermal conductive coefficient, high linear expansion coefficient and heat expansion coefficient. The macrostructure photographs of joints under different heat input conditions are shown in Fig. 11.2. From Fig. 11.2, it can be seen that heat input has a certain effect on the joint geometry, which mainly reflects the weld penetration and width. When the heat input is high (corresponding to weld speed of 7 mm/s), excessive penetration appears. The bigger the weld width, the more significant the deformation is (Fig. 11.2a). It also causes overheating, even burning through. With the increase of welding speed, the weld penetration becomes smaller (Fig. 11.2b), and the ripples start to appear on the surface, improving the appearance of the weld. When the welding speed is up to 9 mm/s, regular ripples appear, and there is no obvious excessive penetration, resulting in a perfect appearance (Fig. 11.2c). With the welding speed increasing further, irregular ripples appear, the appearance of the weld deteriorates, and the defects of incomplete penetration and undercut appear (Fig. 11.2d).

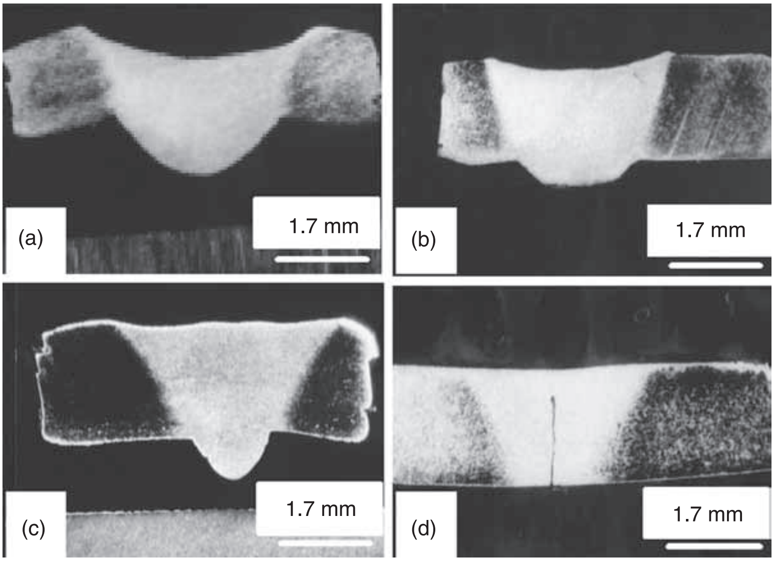

11.2 Macrophotographs of weld joint under different welding speeds (AZ31B, $t = 1.7$ mm): (a) 7 mm/s, (b) 8 mm/s, (c) 9 mm/s, and (d) 10 mm/s.

11.2.3 Microstructure observation and analysis of weld joint

To further investigate the effect of heat input on the quality of a welding joint, microstructure observation on a welded joint was carried out and the results are shown in Fig. 11.3. The joint consists of fusion zone (FZ) and HAZ. Due to the effect of the heat recycle process and the material of base metal (Toshikatsu and Tokisue 1995; Miao et al. 2003a), the crystal grains in FZ are fine, while the crystal grains in the HAZ are remarkably coarser. In Fig. 11.3, it is also found that heat input has an effect on the grain size of weld zone and the width of HAZ. With the decrease in the heat input, the grain size of the weld zone becomes bigger, while the width of HAZ becomes smaller. When the heat input is 77.1 J/mm, the grain size in the weld bead and HAZ is large and the area of HAZ is wide (Fig. 11.3a). With the increase of welding speed, the heat input decreases, the grain size in FZ and HAZ becomes fine, and the HAZ becomes narrow (Fig. 11.3b). When the heat input is 60 J/mm, the grain size in weld zone becomes finer (Fig. 11.3c). As the heat input further decreases due to higher welding speed, the wobble and the effect area of the arc are enhanced, which causes the width of HAZ to increase slightly (Fig. 11.3d).

Based on the above analysis, it has been found that the microstructure of magnesium alloy joints is sensitive to heat input. The relation between the heat input and the width of HAZ and grain size is shown in Fig. 11.4. Researchers are of the opinion that when the heat input is large, the liquid metal in the molten pool will stay at a high temperature for a long time; the cooling rate is slow, and the

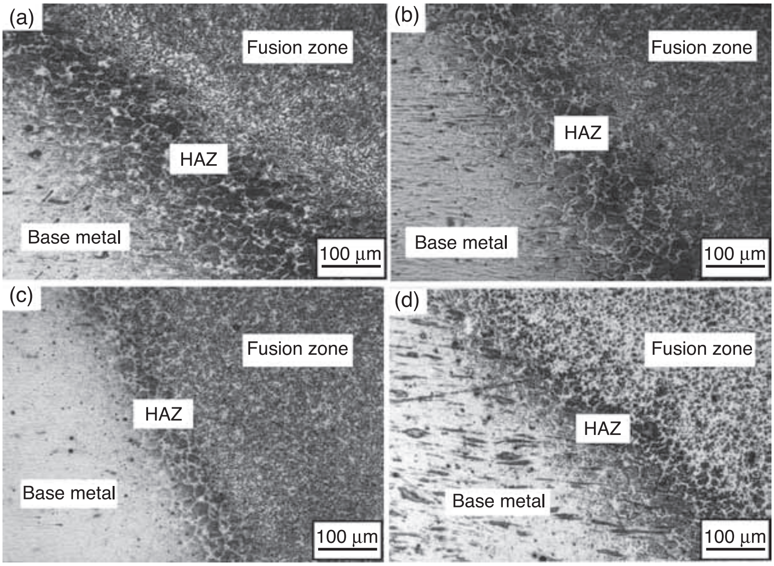

11.3 Microstructure of weld joints affected by heat input (AZ31B, $t = 1.7$ mm): (a) 77.1 J/mm, (b) 67. 5 J/mm, (c) 60 J/mm, and (d) 54 J/mm.

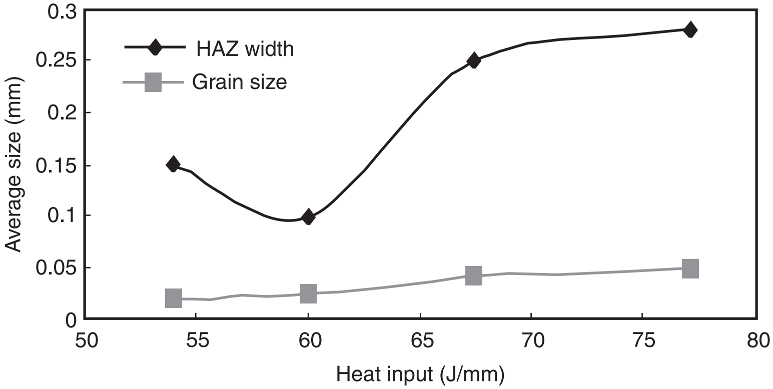

11.4 Relation of heat input, HAZ width and grain size (AZ31B, $t = 1.7$ mm).

overheating of joints is significant, causing the grain in the weld zone to grow and the HAZ to widen. The fine crystal grains in FZ can enhance the joint properties, while the coarse grains in the HAZ have the opposite effect on the mechanical properties of magnesium alloy joints. The HAZ is a dangerous zone in the joint fracture. Therefore, it is suggested that the strong current, the high welding speed and less heat input in the process of penetration are the keys to improving the quality of joints and inhibiting the inferior function of HAZ (Yang and Lin 2003; Liu et al. 2006; Wang et al. 2006).

For further analysis, the grain evolution mechanism of the weld, the HAZ of the magnesium alloy welding process and the microstructure of the weld joint are observed after being magnified as shown in Fig. 11.5.

From Fig. 11.5(a) it can be seen that the grain in the base metal is a fibrous structure which comes from rolling deformation. Figure 11.5(b), shows an obvious fusion line between the weld seam and the HAZ. The HAZ is a typical overheating microstructure, with large coarse grains. The weld zone has finer grains than that in the base metal and the HAZ. It is a typical casting quench microstructure consisting of small equiaxed grains.

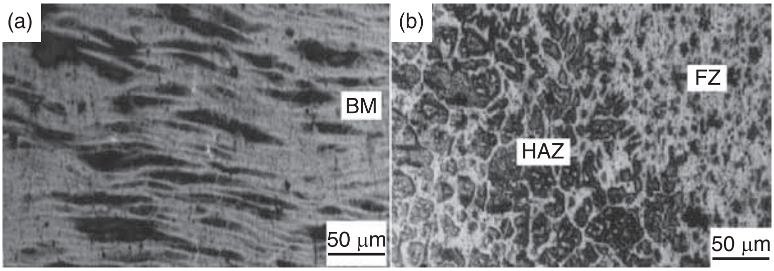

11.5 Microstructures of weld joint (AZ31B, $t = 1.7$ mm): (a) base metal, and (b) FZ/HAZ.

The microstructure mentioned above is primarily related to the physical properties of magnesium alloy and the thermal cycle process of GTAW. In the welding process, the base metal absorbs a lot of heat while melting, then freezes quickly due to the large thermal conductivity (154 W/(m k)), resulting in grain refinement of the weld area, and therefore leading to the formation of small equiaxed grains in the weld area. In addition, the stirring of the weld pool induced by the pulse arc also promotes equiaxed weld formation. Coarse grains in the wide HAZ is because of the low melting point (usually in the range of 500–680 °C) and high thermal conductivity of magnesium alloy. The HAZ quickly becomes overheated. Grains of the base metal obtained after rolling deformation will grow rapidly under the heat effect, which also is the reason for coarse grains in the HAZ (Miao 2004).

11.2.4 Mechanical properties of weld joints

Tensile properties

Specimens used here are AZ31B wrought magnesium alloy with a thickness of 2.5 mm. The tensile specimens were machined as standard style, as shown in Fig. 11.6. The result is shown in Table 11.1: the tensile strength of the weld joints is a little lower than that of the base metal, about 88% of the base metal strength.

Table 11.1 Tensile properties of specimen

Specimen	Tensile strength (MPa)	Elongation (%)	Fracture location
T specimen	222	5.33	Weld interface
V specimen	237	8.33	Center
H specimen	248	6.67	Center

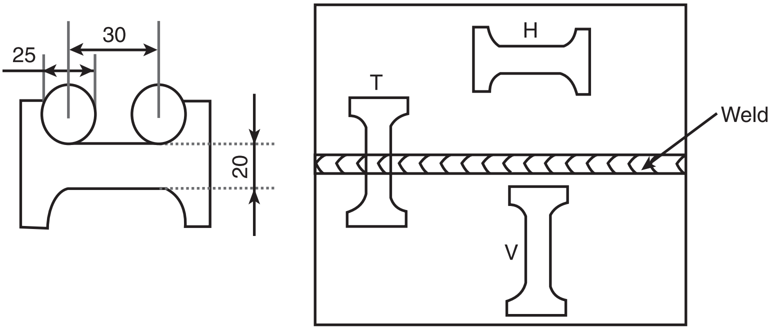

11.6 Size and position of tensile specimen (AZ31B, $t = 1.7$ mm).

The rupture occurred in the HAZ. The elongation of weld joints is less than that of the base metal, which may be related to the welding heat cycle process and the original state of the base metal. The base metal is obtained by the rolling deformation, which has a high strength and plasticity. The HAZ has coarse grains due to overheating in the welding process, inducing lower strength and plasticity in the HAZ (Miao 2004).

Figure 11.7 shows the relationship between heat input and the strength of magnesium alloy GTAW joints. The results show that the effect of heat input on tensile strength and elongation of joints is evident. With the decrease of heat input, the tensile strength and elongation of joints are enhanced. For example, when the heat input is 77.1 J/mm, efficiency (joining coefficient, Φ) is 0.36, and when the heat input is 67.5 J/mm, Φ is 0.60. When the heat input is 60 J/mm, the tensile strength and elongation of joints reach the maximum values ($\Phi = 0.94$). Hereafter, with the further decrease of heat input, incomplete penetration occurs, and the mechanical properties of the weld decrease ($\Phi = 0.24$).

The tensile test shows that the fracture location of samples lies in the HAZ, and for the base metals it lies in the middle of the samples, which is related to the coarse grains in the HAZ and the stress centralization of joints. The analysis shows there are some factors affecting the mechanical properties of joints. First, the change of heat input affects the grain size in weld zone and the width of the HAZ. When the heat input increases, the holding time at the high temperature of the molten pool in liquid state is prolonged, and the growth of grains is significant, which obstructs the increase of mechanical properties of joints; when the heat input drops too far, the holding time at high temperature of the molten pool in liquid state becomes very short. Thus, the welding molten pool has not enough time to form, and easily cause defects of the incomplete penetration and undercut,

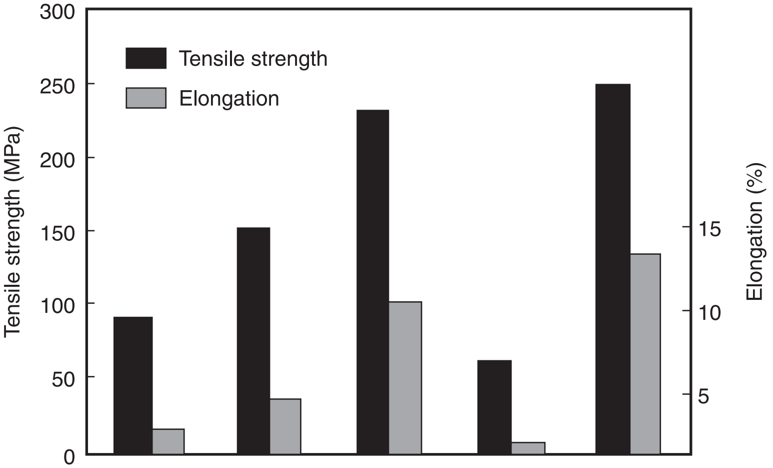

11.7 Relation between tensile strength and elongation.

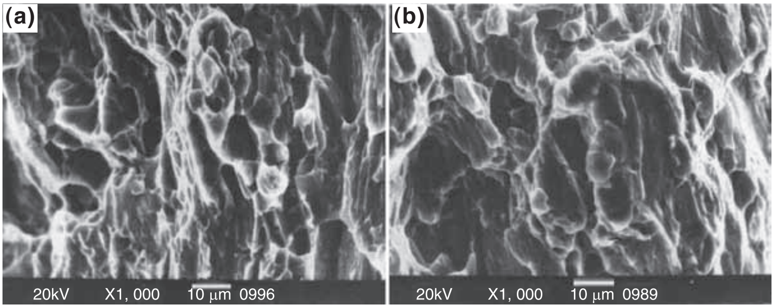

11.8 SEM images of the tensile fractures (AZ31B, *t* = 1.7 mm): (a) base metal, and (b) Mg joint.

which also decrease the mechanical properties of joints. Second, the change of heat input affects the appearance of joints. With increasing heat input, the excessive penetration and weld width enlarge remarkably; the stress convergence also increases. Third, due to the low boiling point of Mg (1100 °C), with increasing heat input, the time of the molten pool in liquid state is prolonged, which makes the oxidation and evaporation of Mg element significant (Gu 1996; Miao et al. 2003b). The tensile fracture of GTAW for magnesium alloy shows the rough surface, but no obvious necking before fracture from the macrograph. It is a ductile–brittle mixed fracture. The base metal fractures at an angle of about 45 ° to the tensile force, which shows a shear-mode fracture type. To better understand the mechanism of joint fracture, the SEM morphology of fracture is analyzed and the results can been seen in Fig. 11.8.

It shows that the weld joint is connected to the part of the brittle fracture in Fig. 11.8(a), which is composed of cleavage fracture and plastic pit fracture. The fracture of the base metal is mainly composed of a number of plastic pits shown in Fig. 11.8(b), which reflects the characteristics of plastic fracture (Miao 2004).

Hardness testing

The effect of heat input on the hardness of the joints was investigated. Table 11.2 lists the average hardness of joints under different heat inputs, and Fig. 11.10 shows the hardness of typical joints. It can be seen from Table 11.2 and Fig. 11.10

Table 11.2 Average hardness of different positions on weld joints

Heat input (J/mm)	FZ	HAZ	Base metal
77.1	42.37	41.19	54.73
67.5	47.19	43.84	46.36
60.0	54.57	49.09	50.92
54.0	58.09	53.45	54.40

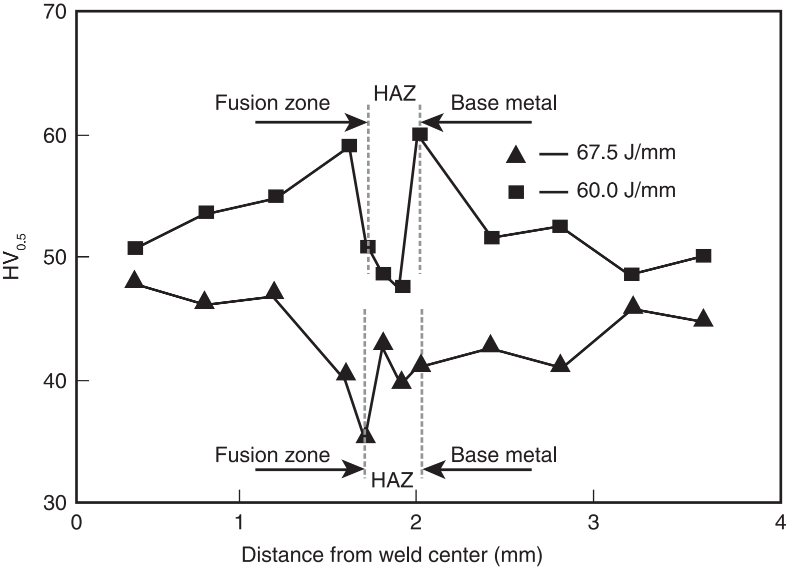

11.9 Hardness distributions of weld joint (AZ31B, $t = 2.0$ mm).

that, except for the sample with the highest heat input, the hardness of FZ is slightly higher than that of the base metal, but the difference is not obvious. Compared with the hardness of base metal, the hardness of HAZ will decline slightly. The less the heat input is, the higher the hardness (Fig. 11.9). It is known that the change caused by the joint rigidity has some relation to the grain size of weld joints. Nakata et al. (2001) investigated the relation between grain size and hardness in magnesium alloy welds. The results showed that the hardness of joints is inversely proportional to the square root of grain sizes. Therefore, with the decrease of heat input, the grain size in the weld zone decreases and the hardness increases. The grain size in the HAZ is coarse, thus the hardness is low. When the heat input is 77.1 J/mm, the hardness of FZ and HAZ decreases, because the grain grows significanty. In addition Miao et al. 2003 showed that the content of Mg and other elements in the FZ is different from that of the base metal due to the evaporation of Mg during the welding process. The content of Mg in the FZ is lower than that in the base metal, while the contents of Al and Zn are higher than those in the base metal. The increase of contents of Al and Zn increases the hardness of FZ (Gu 1996), especially Al.

11.3 Gas tungsten arc filler welding of magnesium alloys

Until recently, the welding of magnesium alloys, such as gas tungsten arc (GTA), laser and laser-GTA hybrid welding, has been investigated widely (Munitz et al.

2001; Liu et al. 2003). For utility and economy purposes, GTAW has been used extensively and some research on GTAW has been reported. Researchers (Asahina and Tokisue 1995; Asahina et al. 1999) have investigated some characteristics of TIG-welded joints of AZ31 magnesium alloy and solidification crack sensitivity of TIG-welded AZ31 magnesium alloy. However, the effect of filler wire on microstructure and performance of joint has not been included in the research.

Based on the former research on GTAW magnesium alloy (without filler wire), coarse grains in HAZ always become the weakness during the tensile test, which proves to be hampering the performance of GTAW joints (Munitz et al. 2001; Miao et al. 2003). The present study adopted an automatic gas tungsten arc filler (GTAF) process to weld AZ31 magnesium alloy plates and examined the effect of filler wire on microstructure and performance of welded joint in particular.

11.3.1 Welding parameters for the GTAFW of magnesium alloy

The preparation of welding for GTAFW is the same as for GTAW of magnesium alloy. Magnesium alloy welding parameters, such as welding current, speed, arc length, wire feeding speed, shielding gas and so on, have a great impact on the weld shape. The study found that use of filler wire can broaden the range of welding parameters for GTAW magnesium alloys, as shown in Fig. 11.10. Without filler wire welding, the weld specifications are relatively narrow, as shown in the zone which is enclosed by dotted lines in Fig. 11.10(A) (Miao et al. 2003). Using the filler wire in the welding process, as the welding current and

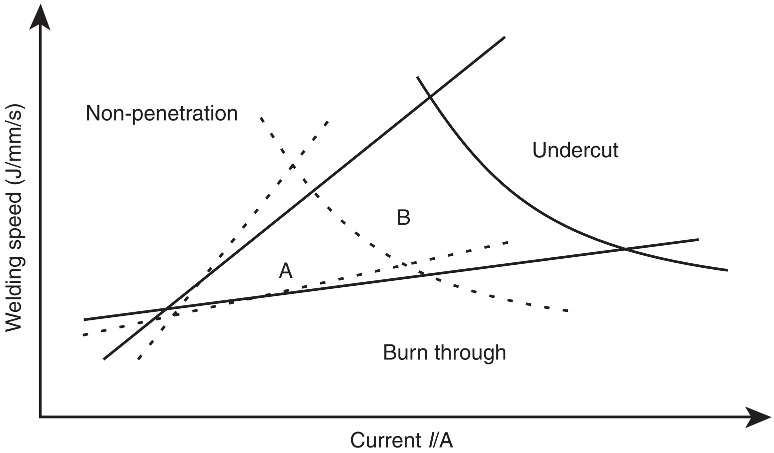

11.10 Normative interval of welding process parameters (AZ31B, $t = 2.5$ mm).

welding speed can be increased without producing undercut and depression defects, the range of welding parameters can be broadened, as shown in the zone enclosed by solid lines in Fig. 11.10(B).

In addition, in the auto-fill wire GTAW process, it is most important to maintain the electrode and filler wire in the correct place to cooperate with each other. Wire should be fed at a very small angle with the work piece into the welding arc. The weld quality obtained by forward-wire filler method (wire-guided gun in front of the welding torch along the moving direction) is better than that by after-wire filler. This is because the wire can always fit accurately into the pool when it is positioned in front of the welding torch; even a slight deviation of wire can provide sufficient energy to melt it (Dong 2005).

11.3.2 The effect of welding parameters on weld shape

Initially, bead-on-plate GTAF welds were made on 5 mm thick AZ31 magnesium alloy to study the effect of welding parameters on depth of penetration and width of weld. Because current, welding speed and arc length in GTAFW act in the same way as GTAW, only the effect of wire feed rate on the appearance of weld was noted as shown in Fig. 11.11. It was found that depth of penetration decreased with the increase of wire feed rate, which is caused by the energy consumption of filler wire. At the same time, the width of the welded joint showed little variation or reduction (Liu and Dong 2006). Then the welding process was investigated by

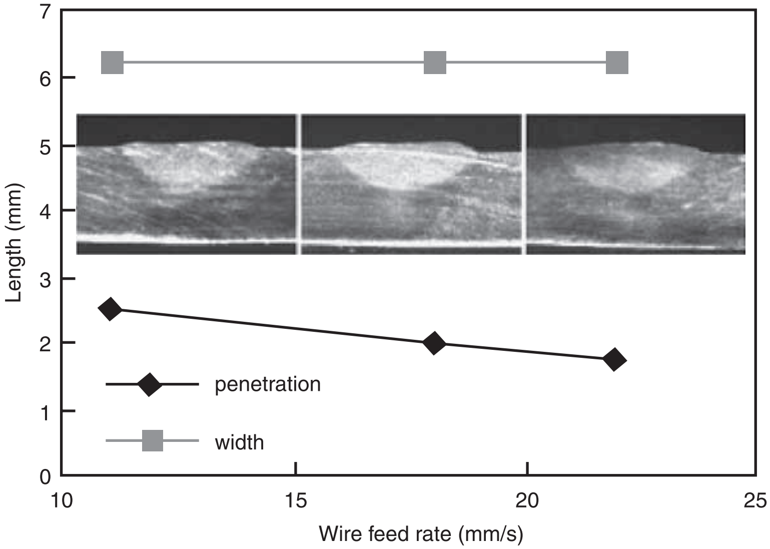

11.11 Effect of wire feed rate on depth of penetration and width of weld. Macro sections are also presented in the figure at three wire feed rates of 11, 18 and 22 mm/s (AZ31, $t = 5$ mm).

optimizing specific experiments on butted 2.5 mm thick plates. Macro sections are also presented in the figure at three feed rates of 11, 18 and 22 mm/s.

11.3.3 Macro-morphology of GTAF-welded joint

Figure 11.12 shows the contrast in appearance between GTAF and GTA butt-welded joints at proper welding parameters. It was found that the GTAF-welded joint held a humping appearance compared with the GTA-welded joint. Despite the humping bead, the macro section of the GTAF-welded joint is similar to that of the GTA-welded joint (Liu and Dong 2006).

11.3.4 Microstructure of GTAF-welded joint

Figure 11.13 shows the microstructure of GTAF-welded joints. In Fig. 11.13(a) the microstructure in the FZ presents finer equiaxed grains with intergranular $Mg_{17}Al_{12}$ precipitates (b phase), which is more apparent in Fig. 11.13(b). The reason for the formation of a finer microstructure was that the rapid cooling induced by good thermal conductivity and low thermal capacity of magnesium has hampered the growth of grains in the FZ. But compared with that of the GTA-welded joint (without filler wire) (Miao et al. 2003), grain size in the FZ of the GTAF-welded joint is bigger, which may be caused by the high heat input and the longer cooling time of the molten pool. There are some etch pits, induced by small precipitated inclusions at FZ and at HAZ as shown in Fig. 11.13(b) and (c) (Tsujikawa et al. 2004). In Fig. 11.13(c), grains in the HAZ reveal a little

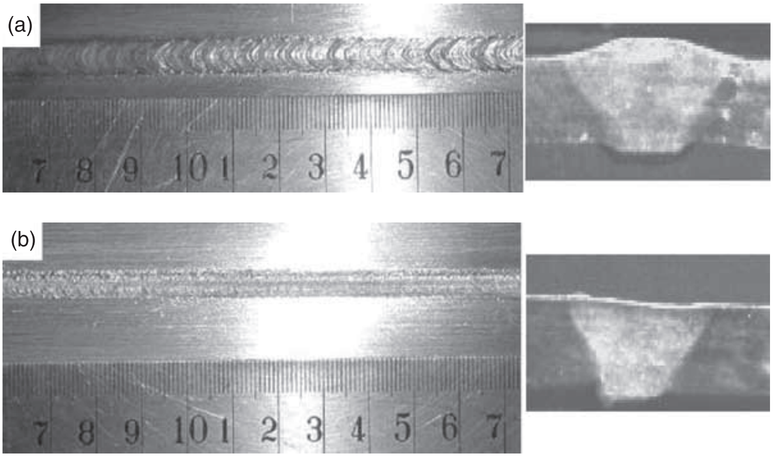

11.12 Appearance contrast between (a) GTAF- and (b) GTA-welded joints. (a) Current: 98 A; welding speed: 10 mm/s; arc length: 0.5 mm; wire feed rate: 30 mm/s. (b) Current: 85 A; welding speed: 10 mm/s; arc length: 0.5 mm.

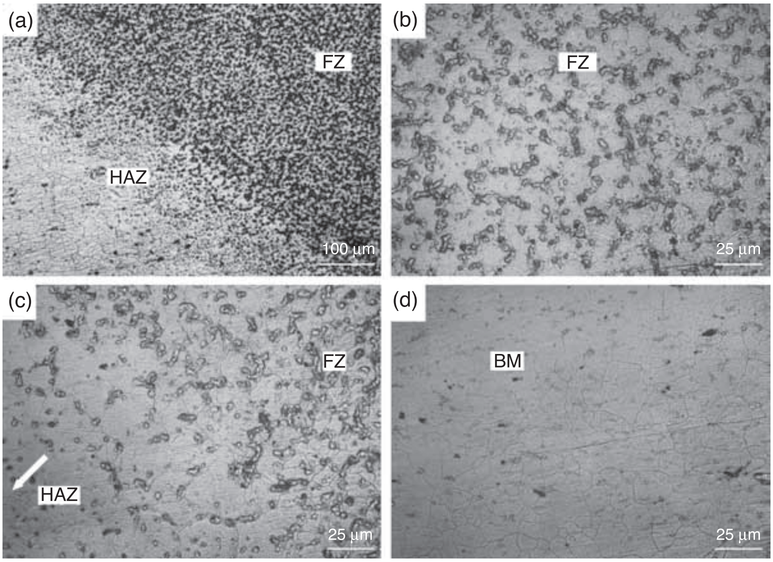

11.13 Microstructure of GTAF-welded joint at transition zone: (a) HAZ/FZ, (b) FZ, (c) HAZ/FZ, and (d) BM.

growth, and no severe overheated microstructure was found compared with the microstructure of base metal shown in Fig. 11.13(d). This is because the filler wire reduced the degree of overheating in the molten pool, which has changed the thermal cycle in the HAZ. The equiaxed grains in the base metal were caused by recrystallization during hot-extrusion (Chen 1991; Dong 2005; Liu et al. 2007). The microstructure of the GTA-welded joint (without filler wire) revealed a HAZ.

Because the coarse grains in the HAZ of GTA-welded joint (Fig. 11.14) always lead to fracture in a tensile test, grain size in the base metal, HAZ and FZ of the GTAF-welded joint has been measured by using optical microscopy in contrast to that of GTAW, as shown in Fig. 11.15. It was found that the grain size in the HAZ of GTAF-welded joint held a small variety with a low peak compared with that of GTAW. This is mainly because the feeding of wire decreased the degree of overheating in the molten pool and even reduced the energy transfer from FZ to HAZ. The uniform grains in the HAZ of GTAF-welded joint should improve the strength of welded joint.

11.3.5 Mechanical properties of GTAF-welded joints

Tensile properties

The tensile properties of magnesium alloy base metal and weld joints have been tested, and the geometry size and location of tensile specimens are shown in

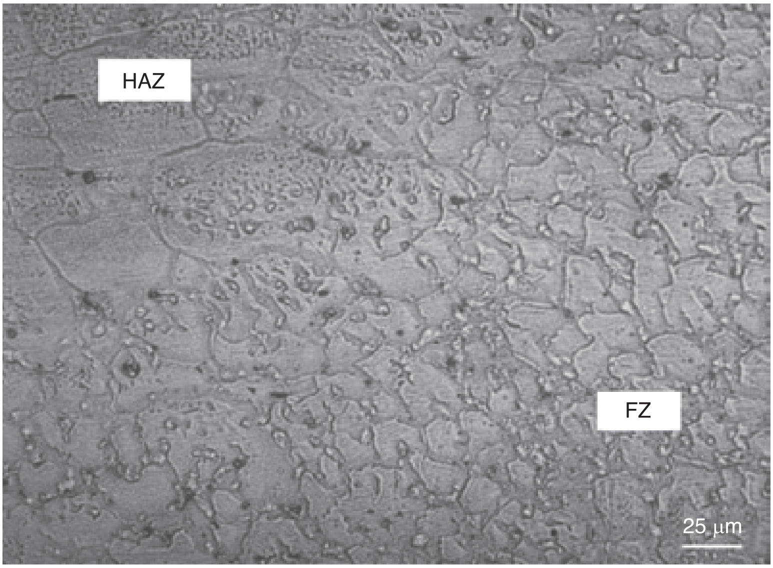

11.14 Microstructure of transition zone in GTA-welded joint (without filler wire).

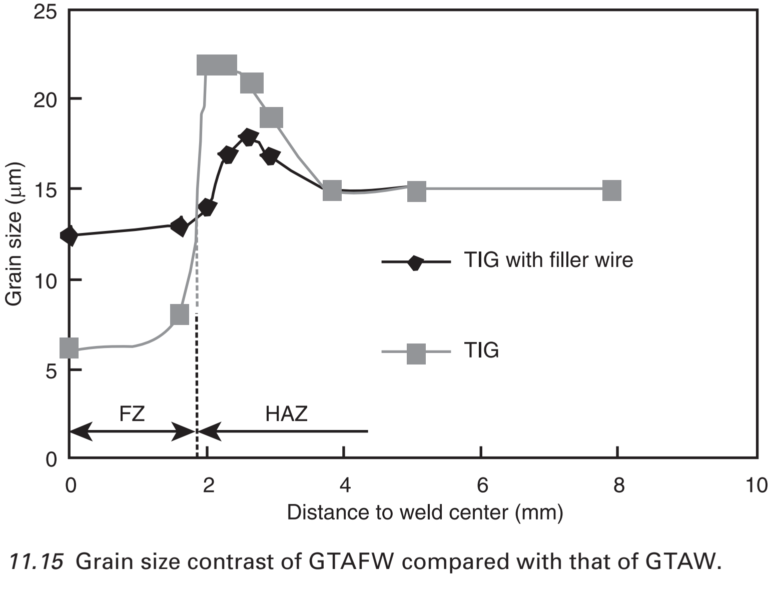

11.15 Grain size contrast of GTAFW compared with that of GTAW.

Fig. 11.16. The results are shown in Table 11.3 – the strength of horizontal and vertical tensile specimens for the base metal are larger than that of the T specimen. The strength value is about 260 MPa, while the T-weld sample strength is lower than the base metal, which is about 93.5% of the base metal strength.

Table 11.3 Tensile properties of specimens (AZ31B, $t = 2.5$ mm)

Specimen	Tensile strength (MPa)	Fracture location
T Specimen	243	Welding seam
V Specimen	259	Center
H Specimen	260	Center

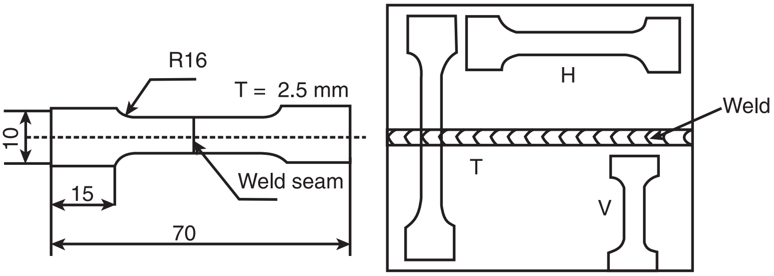

11.16 Geometry size and location of tensile specimens.

The difference of microstructure in the HAZ between GTAF- and GTA-welded joint may also change the location of fracture in a tensile test. To approve the presumption, tensile specimens were tested at room temperature. The tensile test indicated that the ultimate tensile strength (UTS) of the GTAF-welded joint was about 94% of the base metal, which is higher than that of a GTA-welded joint. The UTS of the latter can attain 90% of the base metal only. In the GTAW of magnesium alloy, the HAZ proved to be the weakness where the fracture occurred. But the HAZ was not the weakness in GTAF-welded joints. For the GTAFW of magnesium, fracture always occurs in the FZ of a welded joint, which is initiated at the weld root and propagated vertically through the FZ. Figure 11.17 shows the SEM fractography of the specimens welded by GTAF. The fracture surface is characterized by mixture fracture. Some dimples can be found on the fracture surface, as well as the cleavage feature (Dong 2005a, 2005b).

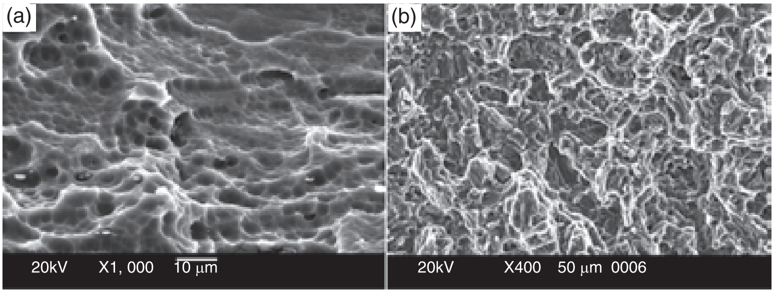

11.17 (a) and (b) SEM fractograph of GTAF-welded joint (AZ31B, $t = 2.5$ mm).

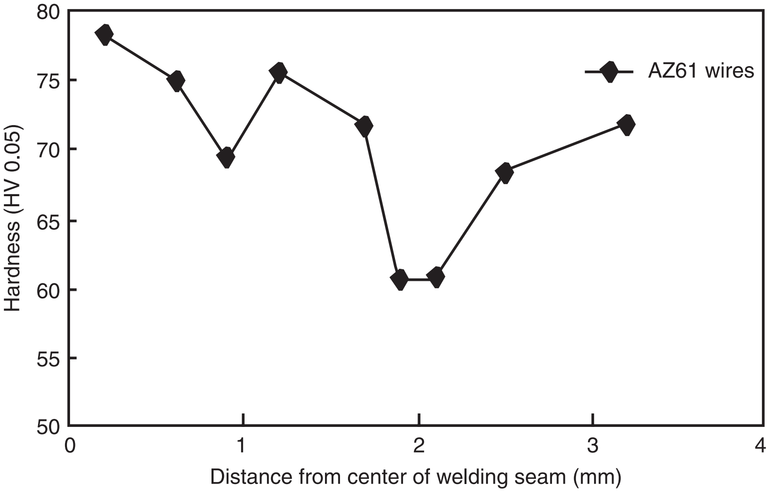

11.18 Hardness analysis of weld joint (AZ31B, $t = 2.5\,\text{mm}$).

Hardness testing

The micro-hardness of the GTAF-welded joint was tested, and the hardness distribution along with the weld joint cross section is shown in Fig. 11.18. Studies have shown that the hardness of a magnesium alloy weld joint is inversely proportional to the square root of its average grain diameter. The filler wire weld joint hardness of the weld area has improved, which is due to its grain refinement in the weld zone. While the hardness of the HAZ is the highest, it also reflects the characteristics of its larger grains (Dong 2005).

11.4 References

Asahina, T. and Tokisue, H., 1995. Some characteristics of TIG welded joints of AZ31 magnesium alloy. *Journal of Japan Institute of Light Metals*, **45**(2): 70–75.

Asahina, T., Tokisue, H., and Katoh, K., 1999. Solidification crack sensitivity of TIG welded AZ31 magnesium alloy. *Journal of Japan Institute of Light Metals*, **49**(12): 595–599.

Chen, B.L., 1991. *Theory of welding metallurgy*. Beijing: Tsinghua University Press.

Dong, C., 2005. *Magnesium alloy gas tungsten arc filling welding process and microstructure analysis*. Dalian: Dalian University of Technology.

Dong, C., Liu, L., and Tian, X., 2005a. Welding technology and microstructure of tungsten inert-gas welded magnesium alloy. *Transaction of the China Welding Institution*, **26**(2): 33–36.

Dong, C., et al., 2005b. Effect of antimony on microstructure and performance of AZ31 magnesium alloy welded joint. *China Welding*, **14**(1): 44–47.

Draugelates, U., et al., 2000. Welding of magnesium alloys by means non-vacuum electron beam welding. *Welding and Cutting*, **52**(4): 62–67.

Gu, Y., 1996. *Particular engineering materials welding*. Shenyang: Science and Technology Press.

Hiraga, H., Inoue, T., Kamado S., and Yo, K., 2001. Effect of shielding gas and laser wavelength in laser welding of magnesium alloy sheet. *Yosetsu Gakkai Ronbunshu*, **19**(4): 591–599.

Huang, X., Zhou, H., and He, Z., 2000. Research and development on ignition proof magnesium alloys. *The Chinese Journal of Nonferrous Metals*, **10**(1): 797–801.

Lin, G., Peng, D., and Zhang, H., 2001. Influence of chemical composition on corrosion resistance of AZ91D magnesium alloy ingots. *The Chinese Journal of Nonferrous Metals*, **11**(1): 79–82.

Liu, L. and Dong, C., 2006. Gas tungsten-arc filler welding of AZ31 magnesium alloy. *Materials Letters*, **60**(17–18): 2194–2197.

Liu, L., Dong, C., and Song, G., 2007. Extrude-curving forming process of magnesium alloy thick plate coated with steel plate. *Journal of Materials Processing Technology*, **182**: 163–166.

Liu, L., Wang, J.F., and Song, G., 2004. Hybrid laser-TIG welding, laser beam welding and gas tungsten arc welding of AZ31B magnesium alloy. *Materials Science and Engineering A*, **381**(1–2): 129–133.

Liu, L., et al., 2004. Effect of heat input on microstructure and properties of welded joint in magnesium alloy AZ31B. *Transactions of Nonferrous Metals Society of China*, **14**(1): 88–92.

Liu, L., et al., 2006. Infrared measurement and numerical simulation of AZ31 magnesium alloy welding temperature field. *Science in China, Series E: Technological Sciences*, **36**(1): 29–38.

Liu, Y., et al., 2002. Microstructure and properties of AZ80 magnesium alloy prepared by hot extrusion from recycled machined chips. *The Chinese Journal of Nonferrous Metals*, **12**(5): 882–885.

Miao, Y., 2004. *Welding process and arc control of magnesium alloy sheet*. Dalian: Dalian University of Technology.

Miao, Y., et al., 2003a. Adaptive arc length control for magnesium alloy sheets TIG welding. *Transaction of the China Welding Institution*, **24**(6): 33–36.

Miao, Y., et al., 2003b. Microstructure feature analysis of fusion welded joint of wrought Mg-alloy. *Transaction of the China Welding Institution*, **24**(2): 63–66.

Munitz, A., Colter, C., Stern, A., and Kohn, G., 2001. Mechanical properties and microstructure of gas tungsten arc welded magnesium AZ91D plates. *Materials Science and Engineer*, **302**(1): 68–73.

Nakata, K., et al., 2001. Weld ability of friction stir welding of AZ91D magnesium alloy thixo molded sheet. *Journal of Japan Institute of Light Metals*, **51**(10): 528–533.

Schubert, G. and Joaquin, A., 2001. Electron beam process delivers consistent welds. *Welding Journal*, **80**(6): 53–57.

Su, S.F., et al., 2002. Electron beam welding behavior in Mg-Al base alloys. *Metallurgical and Materials Transactions A*, **33**(5): 1461–1473.

Toshikatsu, A., Michinori, O., and Hiroshi, T., 1994. Mechanical properties of electron beam welded joints of AZ80 magnesium alloy. *Journal of Japan Institute of Light Metals*, **44**(4): 210–215.

Toshikatsu, A. and Tokisue, H., 1995. Some characteristics of TIG welded joints of AZ31 magnesium alloy. *Journal of Japan Institute of Light Metals*, **45**(2): 70–75.

Tsujikawa, M., et al., 2004. Fatigue of welded magnesium alloy joints. *Materials Transactions*, **45**(2): 419–422.

Wang, S.X., Song, G., and Liu, L., 2006. Analysis of the organization performance of magnesium alloy TIG and AC pulsed TIG. *Transaction of the China Welding Institution*, **27**(9): 63–66.

Yang, C.L. and Lin, S.B., 2003. *Electric arc welding basis*. Harbin: Harbin Institute of Technology Press.

12

Metal inert gas welding of magnesium alloys

G. SONG, Dalian University of Technology, China

Abstract: In this chapter, direct current (DC) pulsed metal inert gas (MIG) welding and alternating current (AC) pulsed MIG welding methods are developed by adding a pulse rework current and negative current based on traditional DC pulsed MIG welding. AZ31B plates are welded in these two separate processes. The microstructure, mechanical properties and hardness are investigated by metal phase microscopy, scanning electron microscope, tensile testing machine and hardness instrument after welding. The detachment of droplets and arc shape is documented with a high-speed camera.

Key words: magnesium alloy, MIG welding, current waveform, mechanical property, microstructure.

12.1 Introduction

What is MIG welding? MIG welding (metal inert gas welding) is a method of arc welding. Recently, the literature regarding the welding process of Mg alloys has increased rapidly, mainly focusing on arc welding,[1,2] laser beam welding,[3–5] electron beam welding,[6] diffusion welding[7,8] and friction stir welding. However, as the vaporization point (1100 °C) of Mg is low, there is always some sag on the top surface of weld bead and loss of alloying elements in the fusion zone (FZ).[9] Gas tungsten-arc filler welding of AZ31B has been studied and found to be a remedy for the lost composition.[10] MIG welding, as a kind of consumable electrode welding method, could make up for the lost alloying elements and has a better gap-bridging ability. MIG welding is simpler to operate and more efficient compared with other methods. It is also fit for welding thick plates compared with tungsten inert gas welding and gas tungsten-arc filler welding.

Due to its low melting point (650 °C) and low vaporization point (1100 °C), difficulties (particularly spattering) frequently arise during MIG welding. A crucial factor in MIG welding is the energy input into the filler wire, which must be regulated to ensure that the filler wire melts completely but does not vaporize. Just a few reports on MIG welding of Mg alloys can be found in literature. Wohlfahrt and Rethmeier in Germany obtained the weld beads of Mg alloys using a triggered short arc in 2003. The tensile strength of AZ31 weld beads is 81–93% higher than that of the base metal. The fatigue strength is 50–75% higher than that of the base metal.[11–13] Ueyama and Nakata[14] in Japan also obtained the weld beads of the Mg alloys using pulsed MIG welding in 2004. The tensile strength of the welds is about 91% higher than that of the base metal.[14]

However, spattering and welding stability are still the main problems in MIG welding of Mg alloy.

As the energy input into the filler wire must be accurate, the parameter range for MIG welding of Mg is narrow. The parameters should change properly with different diameters of filler wire or different wire speed, and even with different thickness of base metal. If the MIG welding of Mg can be realized satisfactorily, there must be a power source whose parameters of wire speed, base current and time, pulse current and time, base voltage and pulse voltage can be changed separately, not linked. Otherwise, the power source may not give one proper parameter for MIG welding of Mg.

This chapter will mainly present two kinds of technology for MIG welding namely pulsed MIG welding and alternating current (AC) MIG welding, respectively, containing welding parameters, FZ characteristics, mechanical properties and droplet transition characteristics.

12.2 Pulsed metal inert gas welding for magnesium alloys

Pulsed MIG welding is a kind of MIG welding with a base current and a high pulse current immediately afterwards. The main parameters for pulsed MIG welding are base current, base current time, pulse current and pulse current time. A pulse rework current was added in our experiment. The pulsed MIG welding process for Mg alloys will be introduced, and the microstructures and mechanical properties of welded joints and the droplet transition mechanism will also be discussed.

As the heat input into filler wire is critical to the weld bead formation in the pulsed MIG welding process of Mg alloys, the welding parameters, such as pulse rework current, welding speed and pulse frequency, were investigated to study their effects on the weld bead formation, including the weld width and surface appearance. Welding experiments were performed on the AZ31B alloy plate with dimensions 300 × 130 × 3.5 mm. The extruded magnesium filler wire with a diameter of 1.6 mm was used.

Figure 12.1 shows the effect of the pulse rework current on the bead formation. With the increase of pulse rework current, the weld width increases a little. When it is between 140 and 170 A, the stable welding process can be realized and the appearance is satisfactory. When pulse rework current is less than 80 A, the continuous welding cannot be realized because the wires cannot be melted sufficiently. When it is larger than 180 A, a lot of spattering occurs and some hot cracks arise on the bead, as shown in Fig. 12.2.

Figure 12.3 shows the effect of welding speed on joint formation. With the increase of welding speed, the weld width decreases sharply. The welding speed would reach a big scale when the wire speed and base current match it. However, when welding speed surpasses 1400 mm/min, it is hard to find other parameters

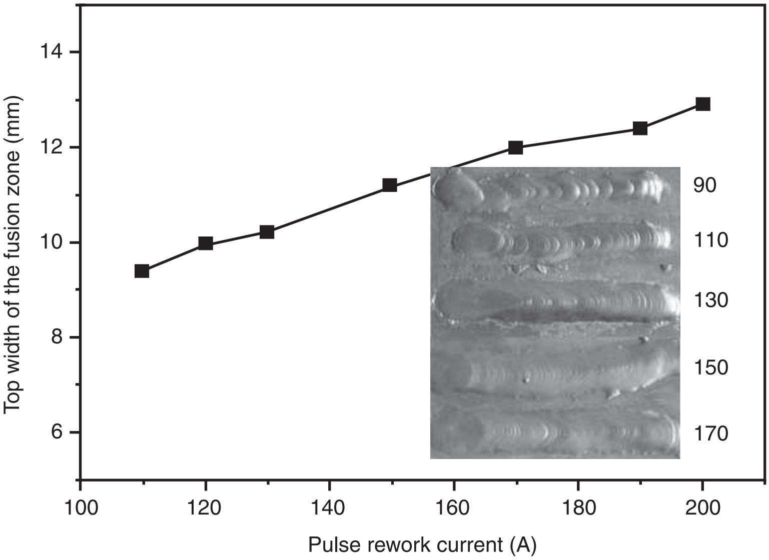

12.1 The relationship between weld width and pulse rework current (base current: 50 A; wire speed: 7.2 m/min; welding speed: 900 mm/min; pulse frequency: 65 Hz).

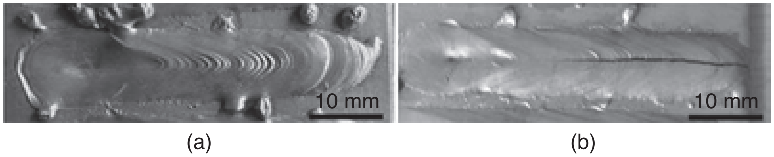

(a) (b)

12.2 Spatters (a) and hot cracking (b). In (a) the pulse rework current is 185 A. In (b) the pulse rework current is 195 A.

to match it, and the appearance of weld bead deteriorates. When the welding speed is less than 400 mm/min, there is a burning phenomenon on the weld bead in the welding process.

Figure 12.4 shows the effect of pulse frequency on joint formation. With the increase of pulse frequency, both the effective current and voltage decrease, so the weld width also decreases. When the frequency is less than 30 Hz, a wider weld bead can still be gained. When it is higher than 90 Hz, the noise of the welding is unbearable. Between 65 and 75 Hz, the welding procedure is much better and a good appearance of weld can be obtained.

Considerable research has been carried out into the optimization of MIG welding parameters of AZ31B Mg alloys. When all the parameters match, the welding procedure can be continuous and stable. As the pulse rework current increases, the welding speed and wire speed should also increase. When the pulse current is up to a certain value, a droplet can easily be detached from the

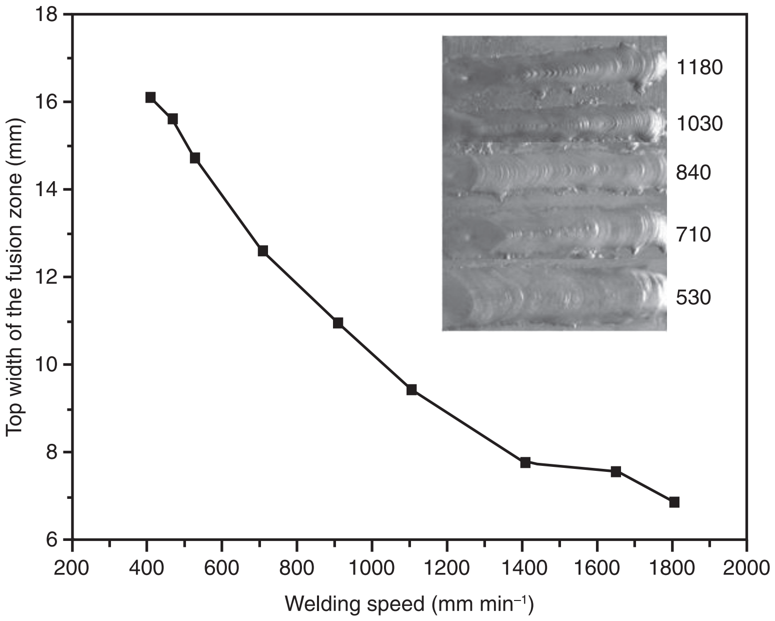

12.3 The relationship between weld width and welding speed (base current: 50 A; wire speed: 7.2 m/min; pulse rework current: 165 A; pulse frequency: 65 Hz).

wire end. The pulse rework current should not be too high or too low, for if that happens, the MIG welding process would not be realized and a lot of spattering would occur.

Typical appearance of AZ31B Mg alloy butt joint welded by a pulsed MIG welding process with optimized parameters are shown in Fig. 12.5. Continuous joints without cracks, inclusions and surface pores were obtained. AZ31B alloy plates and the extruded AZ31 Mg wire with a diameter of 1.6 mm were used.

Figure 12.6 shows the microstructures of the base metal and the weld beads. Figure 12.6(a) shows the microstructure of the base metal. It presents equal-axis crystals whose size is not uniform, because the base metal is a wrought Mg alloy by heat treatment, and the fine crystals distribute around the strip large crystals. The grain size is about 10–30 µm, and the average grain size is about 20 µm.

From Fig. 12.6(b), it is observed that the amount of precipitates (β-Mg17Al12) increases from base metal to heat-affected zone (HAZ) to FZ. The amount of precipitates changes slowly, and we cannot see an obvious boundary between the two different zones. The precipitates in the FZ and HAZ are dispersive. These characteristics give some benefits to the properties of the joints, and they are related to heat recycling and resolidification. Figure 12.6(b) also shows that the width of HAZ increases from top to bottom along the fusion boundary. The width is 100–160 µm, and the average width is about 130 µm. The grain size in HAZ is

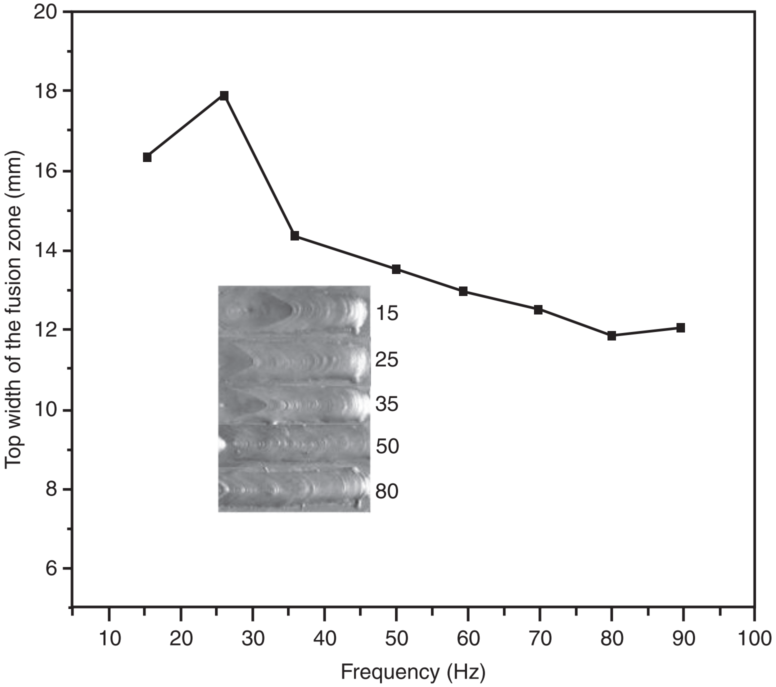

12.4 The relationship between weld width and pulse frequency (base current: 50 A; wire speed: 7.2 m/min; pulse rework current: 165 A; welding speed: 900 mm/min).

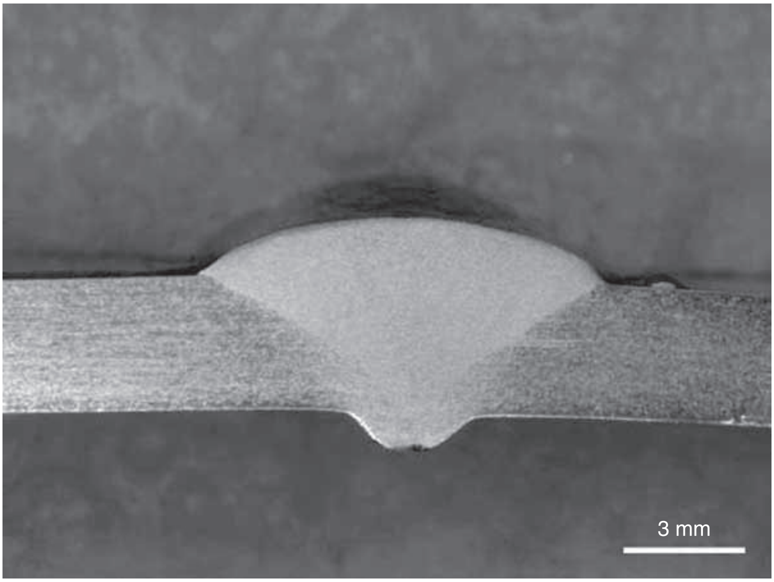

12.5 Appearance of weld bead.

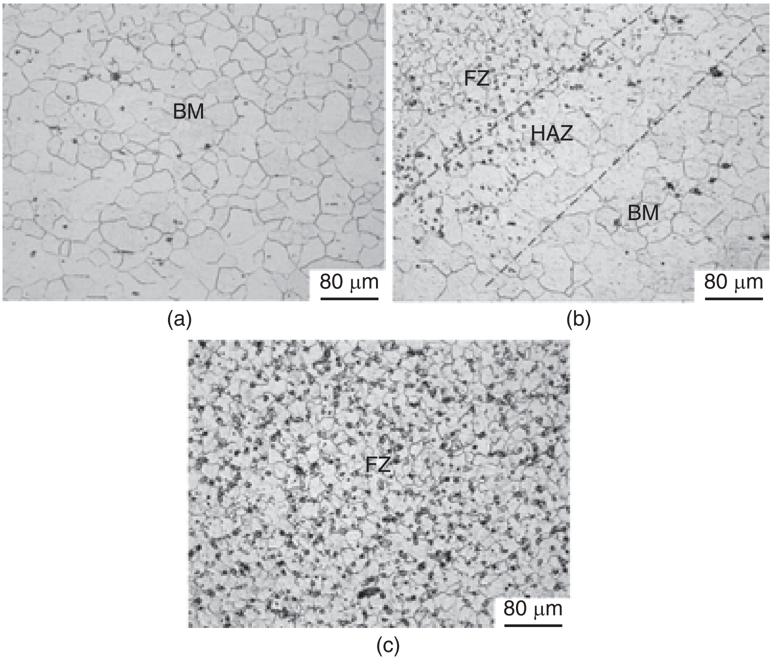

12.6 Microstructures of weld beads and base metal observed by OM: etched by picric acid: (a) base metal; (b) part of weld bead; (c) fusion zone.

also not uniform like the base metal, about 20–50 μm, and the average grain size is about 35 μm. The grain size in this zone did not grow too large compared with the base metal. This characteristic is beneficial for the HAZ. The grain size in the HAZ is larger than the base metal due to the intensive heat and the high temperature it experiences during welding.

It is found in Fig. 12.6(c) that the microstructure in FZ presents finer equiaxed grains with intergranular β-Mg17Al12 precipitates. The microstructures of the weld beads observed by scanning electron microscopy (SEM) are presented in Fig. 12.7. Figure 12.7 shows that the precipitates are almost granular and all of these precipitates always appear at the grain boundary. The reason for the formation of a finer microstructure is that the rapid cooling induced by good thermal conductivity and low thermal capacity of Mg has hampered the growth of grains in FZ. The distribution of grains within the FZ is uniform, and their average size is about 13 μm. These characteristics also benefit the properties of the weld beads.[15,16]

The tensile test indicates that the ultimate tensile strength (UTS) of weld beads is at least 94% higher than that of base metal (even reaches 97%), and the average elongation could get up to 11%.

Figure 12.8 shows the high-speed photographs of drop detachment in the welding process with the optimized parameters. The time between the two images is 14.58 ms. As it is shown in Fig. 12.8, the diameter of the drop is larger than that of the wire

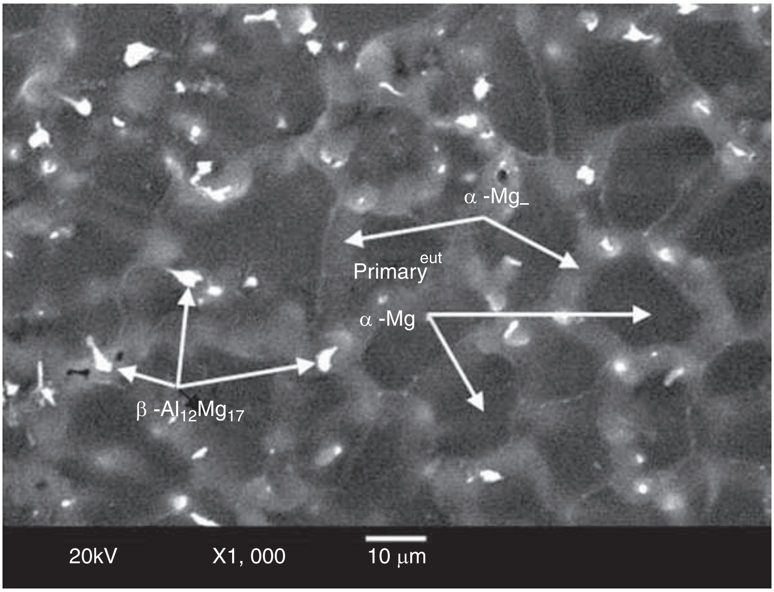

12.7 Microstructures of weld beads observed by SEM: etched by hydrochloric acid.

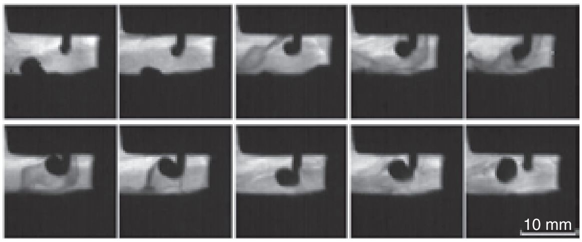

12.8 Drop detachment of pulsed MIG welding. Parameters are base current: 50A; base current time: 10.1 ms; pulse rework current: 165 A; pulse rework time: 4.0 ms; pulse current: 247 A; pulse current: 1.3 ms; wire speed: 7.0 m/min; welding speed: 700 mm/min; pulse frequency: 65 Hz; and diameter of filler wire: 1.6 mm.

and the drop detachment is performed in globular transfer mode. Although it belongs to globular transfer, it can still form continuous butt joints with little spattering.

Figure 12.9 shows the forces on the drop when it is detaching from the wire end in a flat position. As shown in Fig. 12.9, there are various forces such as surface tension (F_d), gravity (F_g), electromagnetic force (F_m), plasma stream force (F_d) and spot force (F_s) acting on the drop when it hangs from the end of wire. The electromagnetic force, gravity and plasma stream force accelerate the drop detachment; meanwhile, the surface tension and spot force restrain the drop detachment. Moreover, the cathode spot force is always larger than the anode spot

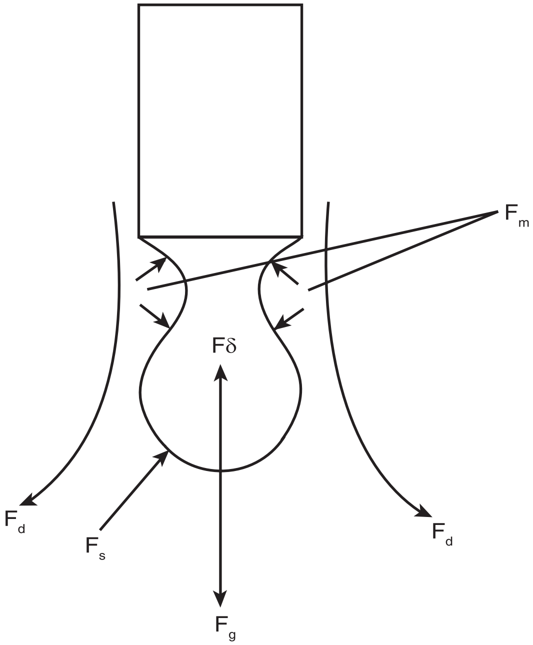

12.9 The forces on the drop when it detaches from the wire.

force. Only when the drop grows to a certain size, it can detach from the end of the filler wire with the help of beneficial forces (electromagnetic force, plasma stream force, etc.).

The most important factor for the change in droplet diameter is the pulse current. As the pulse current increases, the electromagnetic force and plasma stream force increase too, which would cause the droplet diameter to become smaller and the periodicity of drop transition to become shorter. The periodicity of current is about 15.38 ms. When the pulse current is among 240–270, 260–290 and 290–310 A, the periodicity is approximately 90–120, 60–90 and 44–70 ms, respectively. In order to improve the drop detachment, the pulse current should be at least 310 A. However, the base current and pulse rework current should be matched with the pulse current. If the filler wire is heated to boiling temperature, an irregular and disturbed drop detachment would occur, which would result in great spatter formation. But if the energy input into filler wire is relatively low, it is also impossible to warrant a secure drop detachment.[12]

12.3 Alternating current metal inert gas welding for magnesium alloys

A novel AC pulsed MIG welding process attracted interest after 1994.[17] There are two advantages of AC MIG welding compared with conventional direct current

(DC) pulsed MIG welding. It is all known that AC MIG welding is the ideal process to deal with a magnetic blow problem in backing welding with a groove.[18] AC MIG welding is also fit for welding thin plates, as it is a more flexible process for heat input control in comparison with DC pulsed MIG welding. The heat input can be controlled via adaptive control of electrode negative (EN) proportion.[19,20] In relation to AC MIG welding, significant work has been done in the field of aluminum and steel, but no published literature concerning magnesium alloys has been reported. However, the characteristics of AC MIG welding are advantageous for welding magnesium.

The process of AC MIG welding for Mg alloys includes both a positive current and a negative current. A negative part of current is added compared with the previous pulsed MIG welding. Except those parameters in pulsed MIG welding, negative current and negative current time are included. The characteristics of arc and droplet transition, the microstructure and mechanical properties will be discussed below.

Welding experiments are performed on AZ31B alloy plate with the dimension of 300 × 100 × 3 mm. The extruded AZ31 magnesium wires with a diameter of 1.6 mm are used as filler wire. A special current waveform is designed to guarantee the accurate energy input into the filler wire. Figure 12.10 shows the schematic diagram of the designed current waveform. Figure 12.11 shows the arc change with the special current waveform. A cycle is defined as a period from the beginning of a pulse to the end of the base time just before the next pulse. Morphological variation of the arc with both polarities (EN and electrode positive [EP]) was obtained using a high-speed video camera operating at 1820 frames

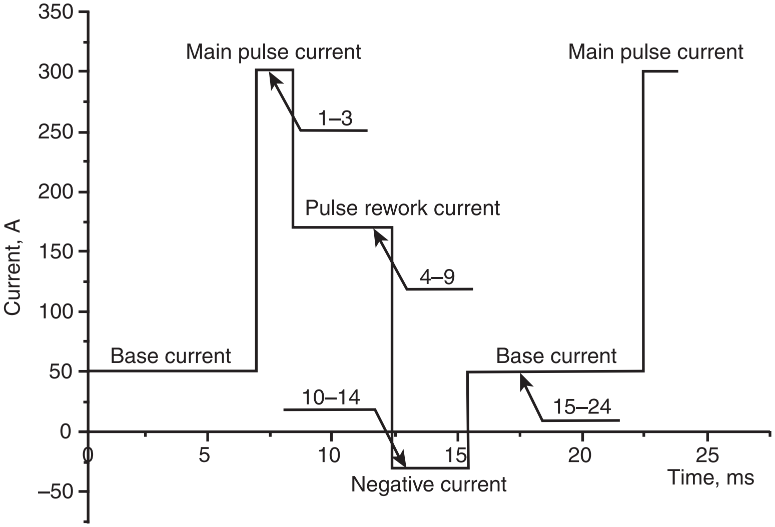

12.10 Schematic diagram of the designed current waveform.

per second. We can see from Fig. 12.11 that the arc is very stable. The aim of Fig. 12.11 is mainly focused on arc shape. There is a current immediately after the main pulse current, which is called 'Pulse rework current.' So, the pulse time includes two parts: the time of main pulse current and the time of pulse rework current. For the addition of pulse rework current, the main pulse current could be increased while the other parameters are constant. The existing pulse rework current keeps the arc stable.[21,22]

There are two roles for the EN polarity. First, supposing that the total energy input for welding is constant and a negative wave is added, the main pulse current can be increased with the other parameters as constants. Second, the current and

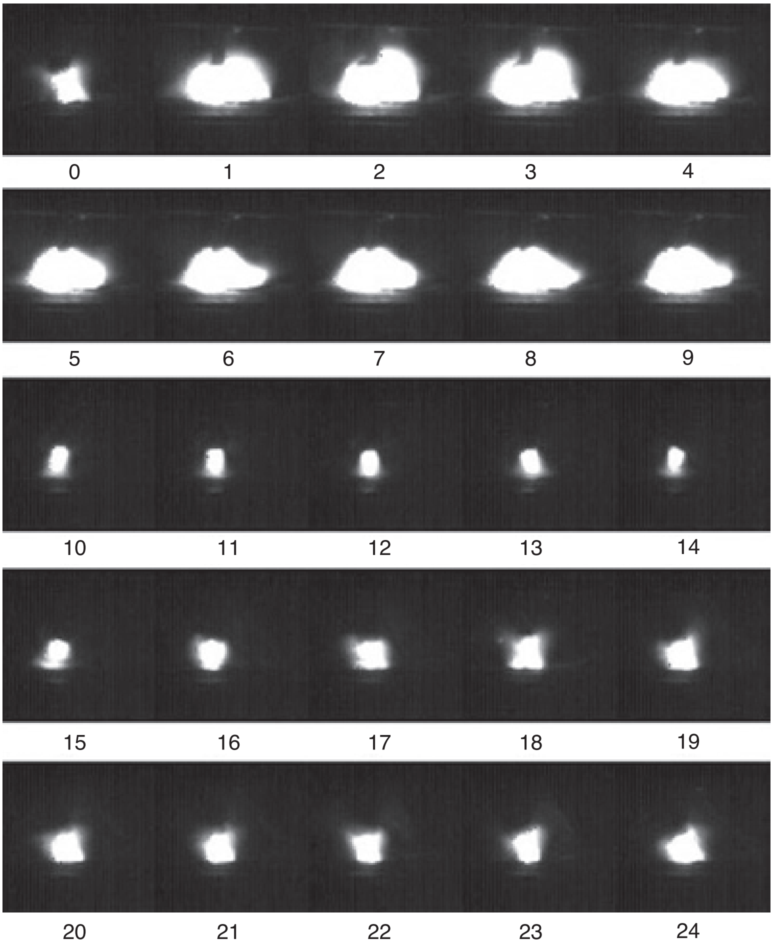

12.11 Morphological change of the arc with the special current waveform.

duration of EN polarity can be set to control the energy input to the wire. That means it can control the distribution of heat to wire and base metal. We know that the heat produced at the cathode area is more than in the anode area in MIG welding. In EN duration, the wire gets more arc heat, and arc heat is effectively used to melt the wire. On the other hand, in EP duration, arc heat is not as effective for wire melting, and the base metal gets more arc heat. The base metal can also be cleaned during the EP duration (oxide film broken). This characteristic of AC MIG can control the distribution of heat to wire and base metal.[23,24]

All parameters can be changed separately to give an accurate energy input into filler wire, especially with an EN polarity. The main pulse current becomes much bigger, and it is beneficial for the droplet detachment. Both of them are important for MIG welding of Mg.

The arc photographs of different forms of metal transfer are obtained using a high-speed video camera operating at 1072 frames per second. Figure 12.12 gives the arc photographs of different metal transfer forms in different parameters. It can be observed from Fig. 12.12 that there are two kinds of metal transfer forms, namely globular transfer and shot transfer. Figure 12.13 shows the typical weld appearance of these two different metal transfer forms. When a droplet hangs from the end of a wire, there are various forces such as surface tension, gravity, electromagnetic force, plasma stream force and spot force acting on the droplet. The electromagnetic force, gravity and plasma stream force accelerate the droplet detachment; meanwhile, the surface tension and spot force restrain the droplet detachment.

It is shown in Fig. 12.12 that when there is a globular transfer, the droplet grows larger in size. Only when the droplet grows to a certain extent, it can detach from the end of filler wire with the help of beneficial forces (electromagnetic force and plasma stream force). The periodicity of current is about 15.4 ms. The periodicity of drop transfer ranges from 46.1 to 169.2 ms and is generated from many experiments. So, when each drop transfers, about 3–11 pulse current periods

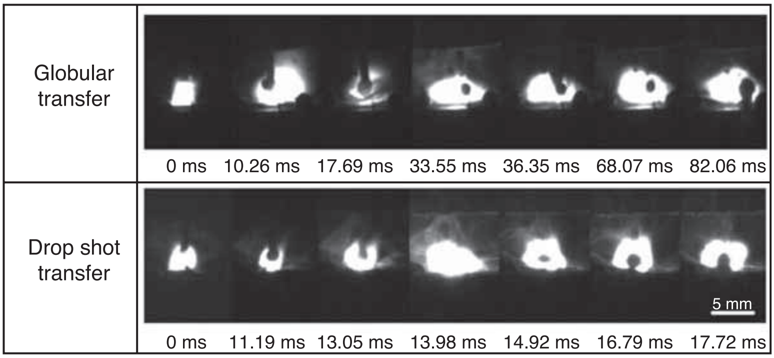

12.12 The arc of different forms of metal transfer.

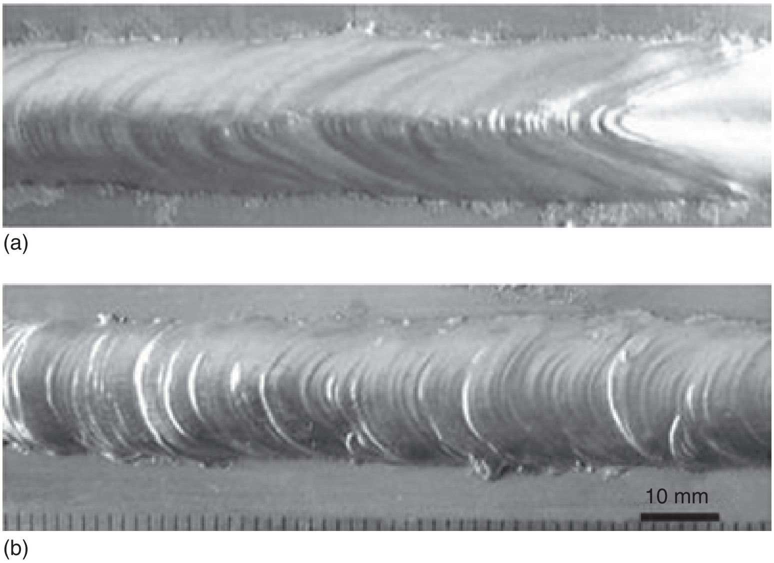

12.13 The appearance of weld beads under different forms of metal transfer: (a) globular transfer; (b) drop shot transfer.

have passed. The higher the drop transfer frequency, the smaller is the size of a drop.

As the main pulse current increases, the electromagnetic force and plasma stream force increase too. When the main pulse current is increased to a certain value, the forces that are beneficial for the droplet detachment will become large enough to change the transfer form. The periodicity of drop shot transfer is between 15.9 and 28.9 ms. So, when each drop transfers, one to two pulse current periods have passed. The arc of drop shot transfer form is more stable than that of globular transfer form, and globular transfer form is more prone to spatter than drop shot transfer form.[25]

Figure 12.13(a) shows the weld appearance obtained by globular transfer. The ripples of weld beads are wide. However, the ripples of weld beads obtained by drop shot transfer, as shown in Fig. 12.13(b), are fine. Table 12.1 reports the range of parameters for different metal transfers generalized from many experiments. The most important factor for the change of transfer form is the main pulse current. When the pulse current is less than 300 A, a globular transfer occurs, and when it is more than 350 A, a drop shot transfer occurs.[26] While the current is in the range of 300–350 A, both globular and drop shot transfers may take place.

If the parameters do not match each other, the arc will become unstable, and also much more spattering will occur. Figure 12.14(a) shows the arc with mismatched parameters. It can be seen that the arc shape is not regular and there is some spattering to be seen in the picture. Figure 12.14(b) shows weld appearance with some spattering.

Table 12.1 The range of parameters for different metal transfers

	Main pulse current (A)	Main pulse voltage (V)	Mean current (A)	Mean voltage (V)	Droplet morphology
Globular transfer	<300–330	18–26	90–130	18–25	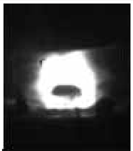
Drop shot transfer	>320–350	≥27	110–180	21–26	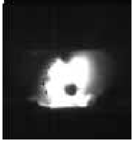

(a) The arc of some spatter under mismatched parameters

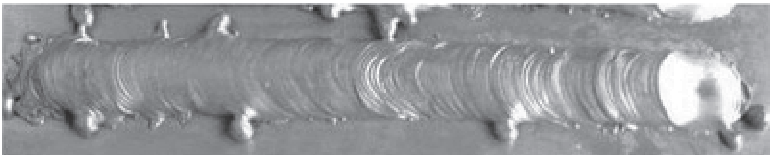

(b) The weld appearance with some spatter

12.14 The arc and weld appearance with some mismatched spattering and parameters. (a) The arc of some spattering under mismatched parameters. (b) The weld appearance with some spattering.

Figure 12.15(a) and (b) show the weld appearance of butt joint and lap joint with 3 mm plates, respectively, and all the parameters are listed in Table 12.2. Even if the welding speed reaches 1000 mm/min, the welding penetration is still too big for butt joint under the condition of drop shot transfer. One important reason is that the weld becomes wide while using a big diameter filler wire, causing it readily to form weld sag. If the welding speed is larger than 1200 mm/min, then the weld appearance will become poor and there will be more spattering. In order to get proper penetration, globular transfer is employed to get the butt joint with 3-mm thick base metal. Drop shot transfer is used to get the lap

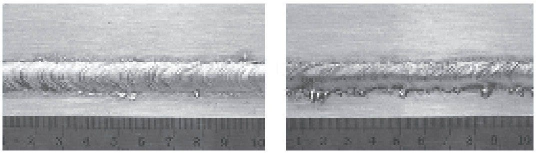
(a) (b)

12.15 The weld appearance of AC MIG welding with 3-mm thick plates. (a) The top appearance of butt joint; (b) the top appearance of lap joint.

Table 12.2 Parameter plates with different thickness

Parameter	Value		
Diameter of filler wire (mm)	1.6 mm	1.6 mm	1.6 mm
Thickness of plates (mm)	5 (butt joint)	3 (butt joint)	3 (lap joint)
Wire speed (m/min)	7.25	5.5	7.0
Welding speed (mm/min)	800	800	800
Mean current (A)	175	103	118
Mean voltage (V)	24.2	22.3	21.7

joint with 3-mm thick base metal. It can be observed from Fig. 12.15(a) that the ripples of the butt joint are wide, but uniform and with almost no spattering. It obviously belongs to globular transfer. However, it can be observed from Fig. 12.15(b) that the ripples of the lap joint are fine, with no surface pores and cracks, but on the lower side of the weld bead, some spattering is visible along the weld toe. It belongs to drop shot transfer.

Drop shot transfer is used to obtain the butt joint of plates with 5 mm thickness and 2.4 mm space between the two plates. The weld appearance of butt joints with 5 mm thick plate is shown in Fig. 12.16. Note that the bead is the result of drop shot transfer and presents a good appearance. There are no surface pores or cracks but uniform ripples.

The formula of welding heat input is as follows:

$$Q = UI\,\mu/v \qquad [12.1]$$

where Q is heat input, U is arc voltage, I is welding current, μ is effective coefficient and v is welding speed. The value of μ is between 0.7 and 0.8 for MIG welding, and the assumption value is 0.75. We can see from Table 12.2 that for the butt joint of 5 mm thick plates, the mean current is 175 A and the mean voltage is 24.2 V. So, its heat input is 2.38 kJ/cm. For the butt joint of 3 mm thick plates, the mean current is 103 A and the mean voltage is 22.3 V. So, its heat input is 1.22 kJ/cm, indicating that when the thickness of plates is increased, the heat

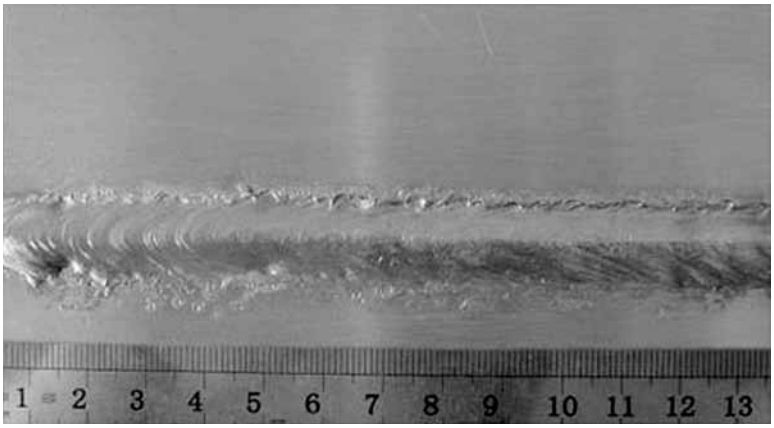

12.16 Weld appearance of AC MIG welding with 5 mm thick plates.

input will also be increased. It is equivalent to the increase in the thickness of the lap joint compared to the butt joint of the same plates. For the lap joint of 3 mm thick plates, the mean current is 118 A, the mean voltage is 21.7 V and the heat input is 1.44 kJ/cm. The heat input for the lap joint is larger than that for the butt joint of the same thick plates. As the thickness of plates is increased, the heat input should be increased accordingly.

We can get the relationship between wire speed and heat input through the regulation of wire feed speed. Table 12.3 shows the minimum energy input needed for a different wire speed. If the energy input is less than the limit inferior, the wire cannot melt enough and the welding procedure will become unstable.

According to Eq. 12.1 and Table 12.2, it can be assumed that when the wire speed is 6.5, 7.0, 7.5 and 8.0 m/min, the minimum heat input is 1.21, 1.35, 1.42 and 1.50 kJ/cm, respectively. So, it is observed that as the wire speed increases, the heat input increases correspondingly.

The macroscopic cross-sections of weld beads are shown in Fig. 12.17. It can be seen that the microstructures within weld beads are uniform and flawless. There are no pores, cracks and inclusions in the weld bead. Figure 12.18 shows

Table 12.3 Parameters for different wire speed

Parameter	Value			
Diameter of filler wire (mm)	1.6 mm	1.6 mm	1.6 mm	1.6 mm
Wire speed (m/min)	6.5	7.0	7.5	8.0
Welding speed (mm/min)	800	800	800	800
Mean current (A)	106	117	121	130
Mean voltage (V)	20.2	20.5	20.8	20.5

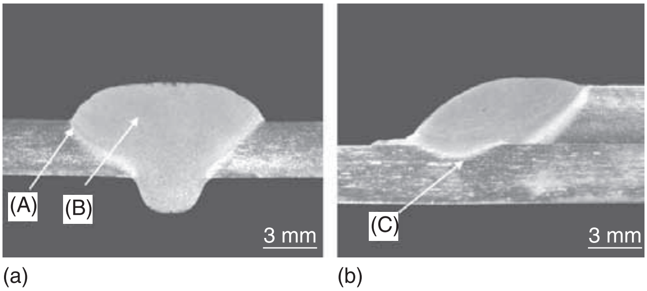

12.17 Macrostructures of weld beads. (a) Macrostructure of butt joint. (b) Macrostructure of lap joint. Parameters for (a) are wire speed: 5.5 m/min; welding speed: 800 mm/min; and main pulse current: 286 A. Parameters for (b) are wire speed: 7.0 m/min; welding speed: 800 mm/min; and main pulse current: 414 A.

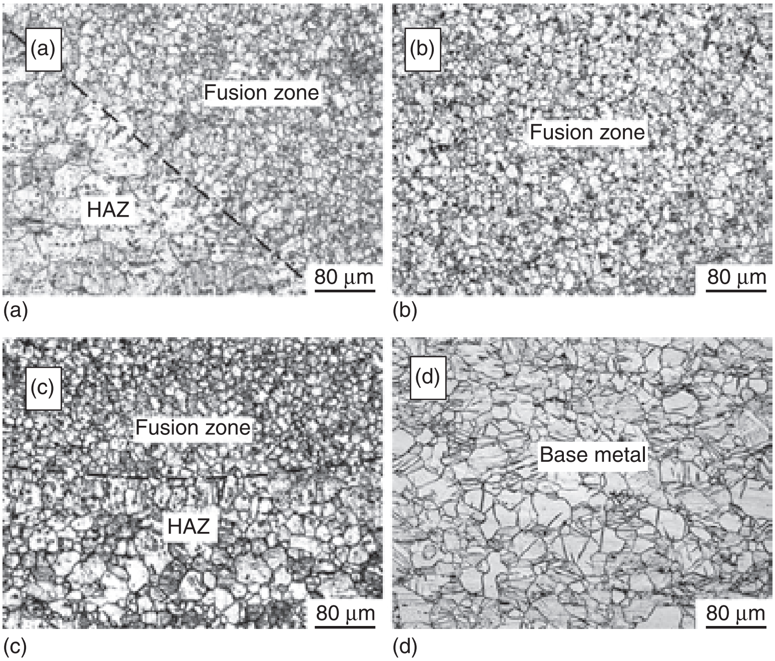

12.18 Microstructures of weld beads and base metal by OM. (a) Fusion boundary of butt joint. (b) Fusion zone of butt joint. (c) Fusion boundary of lap joint. (d) Base metal.

the microstructure of the base metal and the weld beads by optical microscope (OM). Figure 12.18(a), (b) and (c) present the magnification of the areas A, B and C in Fig. 12.17, respectively. Figure 12.18(d) shows the microstructure of base metal. It can be observed from Fig. 12.18 that the microstructure in FZ presents fine equiaxed grains with precipitates.[27–29] The grain size in FZ is finer and more uniform than in the base metal. The grain size in HAZ is larger than that of the base metal, but their coarsening is not significant. These characterizations can benefit the properties of the weld beads.[30,31]

Butt joints are obtained with globular transfer form. The UTS of weld beads is at least 92% of base metal, and even increases to 95%. The fracture of base metal is due to cleavage fracture. However, the fracture of weld bead is related to quasi-cleavage fracture.[32]

12.4 Future trends

The experiments show that both pulsed MIG and AC MIG methods can be used to weld magnesium alloy. However, the range of welding parameters is too small, especially for pulsed MIG. A crucial factor in MIG welding of magnesium alloy is still how to control the energy input into the filler wire. It is urgent to find a novel power supply method of MIG welding to solve the above problems. If a new MIG welding method of Mg alloy can be realized easily and successfully, then the use of the welding structure of magnesium alloy will increase in industrial production.

12.5 References

1. Liu LM, Cai DH, Zhang ZD (2007). Gas tungsten arc welding of magnesium alloy using activated flux-coated wire. *Scr Mater* **57**: 695–8.
2. Liang GL, Zhou G, Yuan SQ (2009). Study on the temperature measurement of AZ31B magnesium alloy in gas tungsten arc welding. *Mater Sci Eng A* **499**: 93–6.
3. Wang JF, Liu LM, Song G (2004). Microstructure character of YAG laser welding AZ31B Mg alloy. *Trans China Weld Inst* **25**(3): 15–18.
4. Abderrazak K, Salem WB, Mhiri H, Lepalec G, Autric M (2008). CO_2 and diode laser welding of AZ31 magnesium alloy. *Opt Laser Technol* **40**: 581–8.
5. Chi CT, Chao CG, Liu TF, Wang CC (2008). Texture characterisation of hexagonal metals magnesium AZ91 alloy welded by laser processing. *Vacuum* **82**: 1177–82.
6. Zhang B, Yuan SQ, Wang XH (2008). Characterization on electron beam welds and parameters for AZ31B-F extrusive plates. *Rare Met* **27**: 393–9.
7. Jiang JB, Zhang ZD (2008). The study on the plasma arc weld bonding process of magnesium alloy. *J Alloy Compd* **466**: 368–72.
8. Zhao LM, Zhang ZD (2008). Effect of Zn alloy interlayer on interface microstructure and strength of diffusion-bonded Mg–Al joints. *Scr Mater* **58**(4): 283–6.
9. Asahina T, Tokisue H (1995). Some characteristics of TIG welded joints of AZ31 magnesium alloy. *J Jpn Inst Light Met* **45**(2): 70–75.
10. Liu LM, Dong CF (2006). Gas tungsten-arc filler welding of AZ31 magnesium alloy. *Mater Lett* **60**: 2194–7.
11. Rethmeier M, Wiesner S (2001). Characteristic features of MIG welding of magnesium alloys. *Z Metallkd* **92**(3): 281–5.

12. Wohlfahrt H, Rethmeier M, Bouaifi B, Schütz M (2003). Metal-inert gas welding of magnesium alloys. *Weld Cutt* **55**(2): 80–4.
13. Rethmeier M, Kleinpeter B, Wohlfahrt H (2004). MIG welding of magnesium alloys metallographic aspects. *Weld World* **48**(4): 28–33.
14. Ueyama T, Nakata K (2004). Pulsed MIG welding of magnesium alloy. Kei Kinzoku Yosetsu **42**: 203–13.
15. Dahle AK, Lee YC, Nave MD, Scheffer PL, St.John DH (2001). Development of the as-cast microstructure in magnesium–aluminium alloys. *J Light Metals* **1**: 61–72.
16. Barbagallo S, Laukli HI, Lohne O, Cerri E (2004). The study on the plasma arc weld bonding process of magnesium alloy. *J Alloys Compd* **378**: 226–32.
17. Schiedermakyer M (1997). Improving the reliability of inverter based welding machines. *Weld J* **76**(2): 51–2.
18. Jennings CH, White AB (1941). Arc blow. *Weld J* **20**: s427–36.
19. Tong H, Era T, Ueyama T (2002). Development of adaptive control system for alternating current pulsed metal inert gas welding parameters. *Sci Technol Weld Join* **7**(6): 408–12.
20. Tong H, Ueyama T, Harada S, Ushio M (2001). Quality and productivity improvement in aluminum alloy thin sheet welding using alternating current pulsed metal inert gas welding system. *Sci Technol Weld Join* **6**(4): 203–8.
21. Ghosh PK, Dorn L, Hübner M, Goyal VK (2007). Arc characteristics and behaviour of metal transfer in pulsed current GMA welding of aluminium alloy. *J Mater Process Technol* **194**: 163–75.
22. Ghosh PK, Dorn L, Kulkarni S, Hofmann F (2009). Arc characteristics and behaviour of metal transfer in pulsed current GMA welding of stainless steel. *J Mater Process Technol* **209**: 1262–74.
23. Ueyama T, Tong H, Harada S, Passmore R, Ushhio M (2005). AC pulsed GMAW improves sheet metal joining. *Weld J* **84**(2): 40–6.
24. Kumar R, Dilthey U, Dwivedi DK, Ghosh PK (2009). Thin sheet welding of Al 6082 alloy by AC pulse-GMA and AC wave pulse-GMA welding. *Mater Design* **30**: 306–13.
25. Suban M, Tušek J (2003). Studies on softening of heat-affected zone of pulsed-current GMA welded Al–Zn–Mg alloy. *J Mater Process Technol* **143**: 430–7.
26. Praveena P, Kangb MJ, Yarlagadda PKDV (2008). Drop transfer mode prediction in pulse GMAW of aluminum using statistical model. *J Mater Process Technol* **201**: 502–6.
27. Yakubtsov IA, Diak BJ, Sager CA, Bhattacharya B, MacDonald WD, Niewczas M (2008). Effects of heat treatment on microstructure and tensile deformation of Mg AZ80 alloy at room temperature. *Mater Sci Eng A* **496**: 247–55.
28. Nave MD, Dahle AK, St.John DH (2000). CRC for alloy and solidification technology. Proceedings of 2nd International conference on 'Eutectic Growth Morphologies in Mg-Aluminium Alloy' pp. 1502–6. Brisbane, Australia, The University of Queensland, paper 4072.
29. Marya M, Edwards GR (2002). Factors controlling the magnesium weld morphology in deep penetration welding by a CO_2 laser. *Sci Technol Weld Join* **7**: 286–93.

30. Liu LM, Miao YG, Song G (2004). Effect of heat input on microstructure and properties of welded joint in magnesium alloy. *Chinese J Nonferrous Metals* **14**(1): 1–5.
31. Liu LM, Liu XJ, Liu SH (2006). Microstructure of laser-TIG hybrid welds of dissimilar Mg alloy and Al alloy with Ce as interlayer. *Scr Mater* **55**: 383–6.
32. Lü YZ, Wang QD, Ding WJ, Zeng XQ, Zhu YP (2000). Dissimilar friction stir welding between magnesium and aluminum alloys. *Mater Lett* **44**: 265–8.

13

Variable polarity plasma arc welding of magnesium alloys

Z.D. ZHANG, Dalian University of Technology, China

Abstract: In this chapter, VP-PAW and VP-PAWB behaviors of the AZ-based Mg alloys are analyzed respectively, in terms of welding parameters, fusion-zone characteristics, mechanical properties, welding temperature fields and the behavior of arc plasma. Besides, a novel welding method, plasma arc weld bonding process which combines plasma arc welding with bonding, is put forward in detail.

Key words: magnesium alloy, plasma arc welding, microstructure, mechanical property.

13.1 Introduction

Variable polarity plasma arc welding (VP-PAW) is an arc welding process that produces coalescence of metal by heating with a constricted arc between an electrode and the workpiece (transferred arc) or between the electrode and a constricting nozzle (nontransferred arc). Plasma arc is a special form of arc, which is constricted by the external conditions such as the use of a plasma arc welding (PAW) gun nozzle. The cross-section of arc column is limited, so that the temperature of the arc column and the energy density increases, the gas ionizes more fully, and plasma flow also significantly increases.[1,2] The plasma arc is the high-temperature, high-degree ionized and high-energy density arc, which is compressed from free arc between the cathode and anode. Moreover, VP-PAW is especially suitable to weld the structural components that are relatively thick and difficult to be welded on the back side.[3,4] The VP-PAW is the use of PAW as a source of heat, and its principle is presented in Fig. 13.1.

VP-PAW offers significant advantages over conventional gas tungsten arc welding (GTAW) in terms of penetration depth, joint preparation and thermal distortion.[5,6] Although its energy is less dense than that of laser beam welding (LBW) and electron beam welding (EBW),[7] VP-PAW is more cost-effective and more tolerant of joint preparation. VP-PAW technique has the characteristics of asymmetrical square alternating-current waveform and keyhole mode. VP-PAW integrates technical advantages of variable polarity GTAW and PAW, and its technical performance is better than that of GTAW and gas metal arc welding (GMAW).[8] Characteristic parameters (e.g., current frequency, peak values of variable-polarity current, duty cycle, etc.) of the VP-PAW process can be easily adjusted to satisfy the need of cathode cleaning and keyhole mode welding for

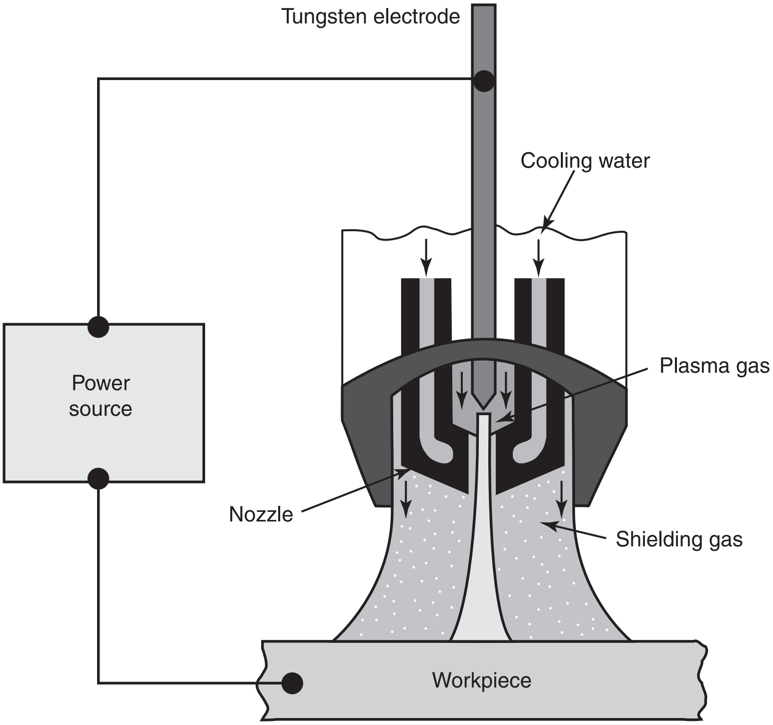

13.1 The schematic diagram of VP-PAW process.

Mg and Al alloys.[9] Because of these distinct attributes, VP-PAW has found applications in the welding of aluminum alloy and structural steels in the manufacture of automobiles, airplanes, rockets, and space shuttle, and possibly on welding in space.[6,10] Adhesive joints were found to increase structural applications in various fields, especially for high-performance composites. The properties of variable polarity plasma arc weld bonding (VP-PAWB) joint could be improved because it combined the VP-PAW and adhesive bonding process. In comparison with mechanical fasteners, VP-PAWB process could offer the following benefits: high static strength, improved fatigue strength, elimination of sealing operations, improved corrosion resistance, elimination of the shop noise of riveting and excellent acoustical properties.[11–16]

In this chapter, VP-PAW and VP-PAWB behaviors of the AZ-based magnesium alloys are introduced in terms of welding parameters, fusion zone characteristics, mechanical properties, welding temperature fields and the behavior of arc plasma. Furthermore, a novel welding method, the plasma arc weld bonding process, which combines PAW with bonding, is put forward in detail.

13.2 Variable polarity plasma arc welding of magnesium alloys

By adjusting the welding parameters, a fine welding seam is obtained, as shown in Fig. 13.2(a) and (b). The tensile strength of the welding joint is 90% of the base metal.

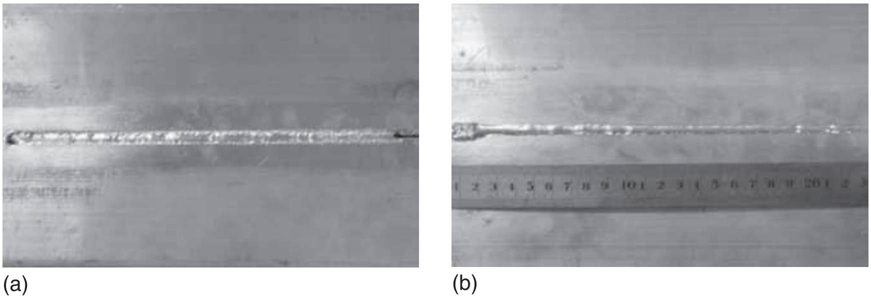
(a) (b)

13.2 Variable polarity plasma arc welding appearance of magnesium alloy AZ31 with 5 mm thickness. (a) The face of variable polarity plasma arc welding joint. (b) The back side of a variable polarity plasma arc welding joint.

13.2.1 Alternating current electrode negative time to cycle ratio (M_k)

M_k is a ratio between the alternating current electrode negative (ACEN) and the cycle, as shown in Fig. 13.3.

$$M_k = t_{ACEN}/(t_{ACEN} + t_{ACEP}) = t_{ACEN}/T, \qquad [13.1]$$

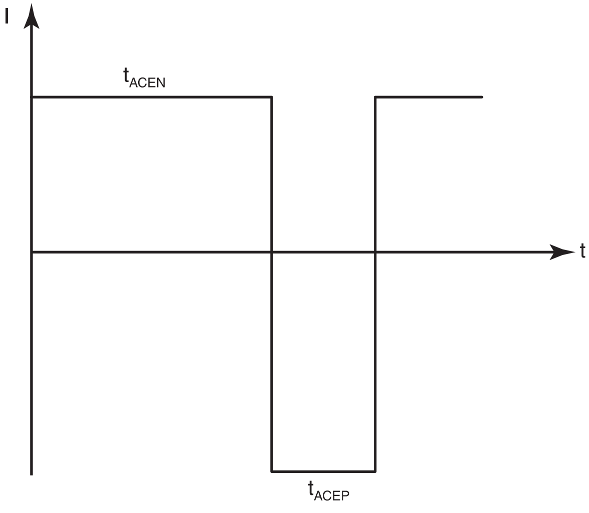

13.3 Schematic of variable polarity current waveform.

where T is the current cycle time, t_{ACEN} is the ACEN time in one cycle time and t_{ACEP} is the alternating current electrode positive (ACEP) time in one cycle time.

M_k increases from 0.6 to 1.0 within the same cycle, that is, the welding current frequency is not changed. As shown in Fig. 13.4, the butt welding of magnesium alloy with a thickness of 5 mm is carried out under the matched welding parameters. After welding, the welding appearance and the tungsten electrode burning loss are investigated, as shown in Fig. 13.4 and Fig. 13.5. The failure loads of welding joints with different M_k are evaluated, and the result is shown in Fig. 13.6.

From Fig. 13.4, it is observed that the welding width reduced with the increase in M_k. From Fig. 13.5, it is observed that the tungsten electrode burning loss reduced with the increase in M_k. From Fig. 13.6, it can be seen that with the increase in M_k, welding width was reduced and the tensile strength of the welding joint was increased. The highest tensile strength of the welding joint is obtained as $M_k = 0.9$, which is 95% of the base metal.

The reasons for the above are described as follows. When M_k increased, in one cycle, ACEP decreased, whereas the alternating current workpiece positive increased. Thus, the catelectrode clean effect was reduced, thereby decreasing the

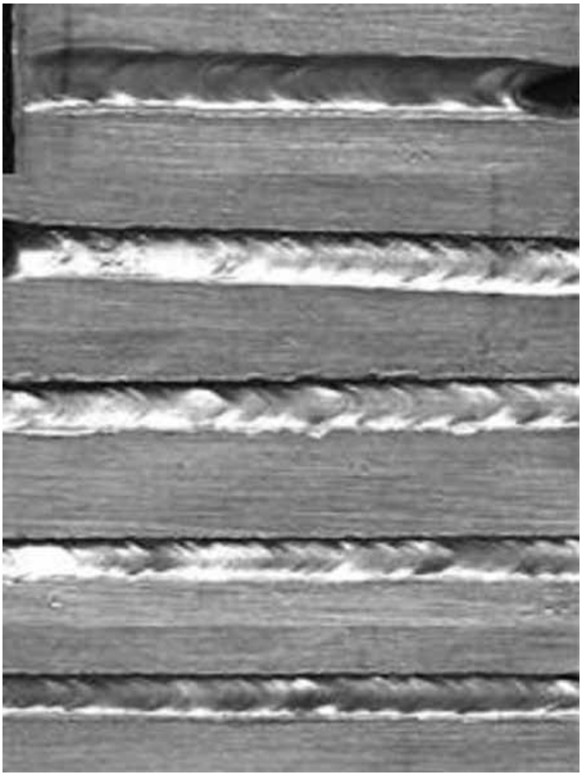

13.4 Effect of different M_k on weld appearance.

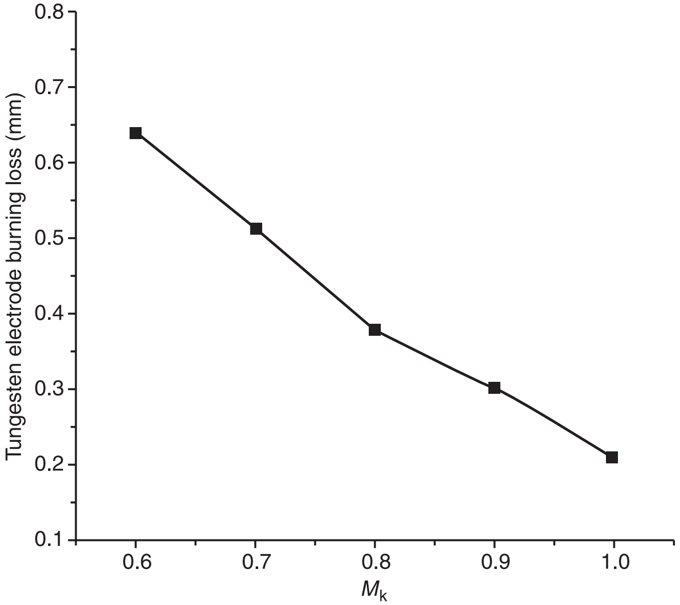

13.5 Comparison of the melting loss of tungsten (diameter 4 mm; current 80 A; time 300 s).

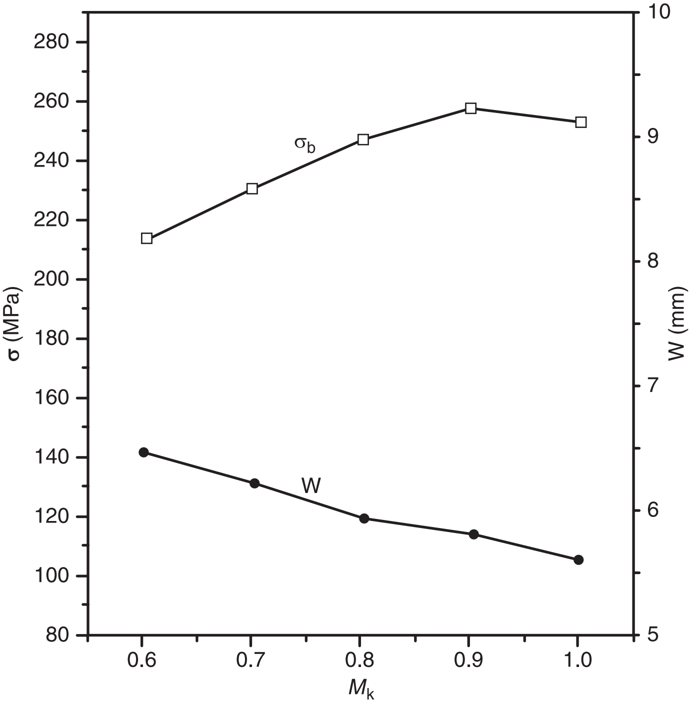

13.6 Effect of different M_k on joint dimension and strength.

welding width and tungsten electrode burning loss. The distribution of arc energy in one cycle is affected by the change in M_k. If M_k is too big, there is almost no catelectrode clean stage. The presence of the oxide on the surface of the welding joint reduces the weldability. The welding process is unsteady and results in a lot of welding defects, thus decreasing the tensile strength of the welding joint.

13.2.2 Effect of welding parameters on the welding process

In the PAW process, when the nozzle structure is determined, the welding current (I), the welding speed (V) and the plasma gas flow rate (Q) should be matched with each other in order to get a steady VP-PAW process.^{6} In the VP-PAW process of magnesium alloy, the matching connection among the welding current, the plasma gas flow rate and the welding speed with the keyhole mode is shown in Fig. 13.7. (The upper sideline shows that the welding joint is formed without cut, and the under sideline shows that the welding joint is formed with the steady keyhole mode.) The nozzle structure is shown in Fig. 13.8.

From Fig. 13.7, it is known that the plasma gas flow rate plays an important role in the VP-PAW process. The matched welding parameter range is quite small when the plasma gas flow rate is 2 or 4 L/min, and the matched welding parameters range is quite big when the plasma gas flow rate is 3 L/min.

The effect of welding current on welding width has been investigated, and the results are shown in Fig. 13.9(a). If the welding current increases too much, then the keyhole becomes unsteady. A discontinuous welding seam will be formed (even

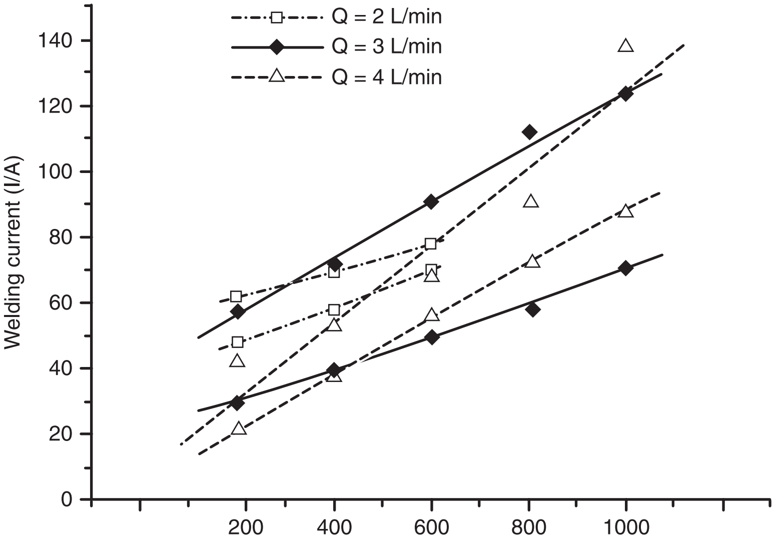

13.7 Processing parameters of VP-PAW on AZ31B magnesium alloy.

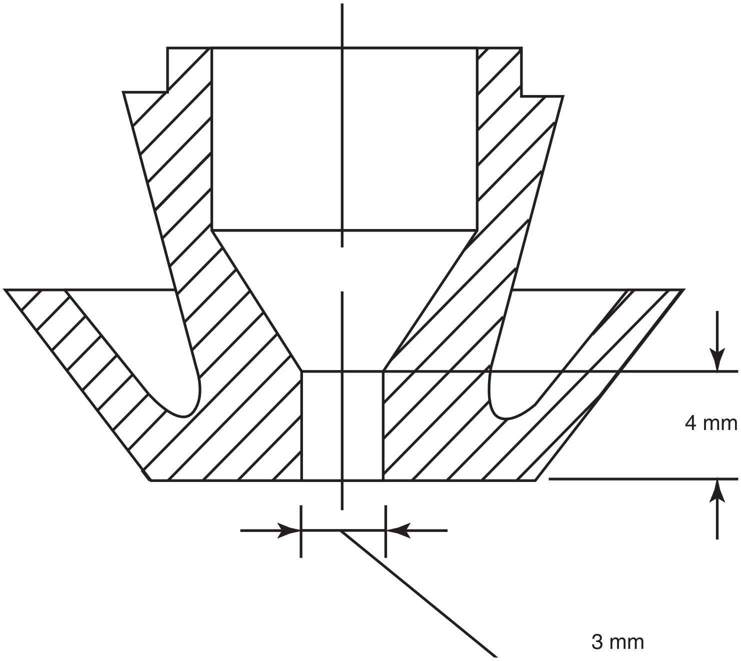

13.8 The structure of the nozzle.

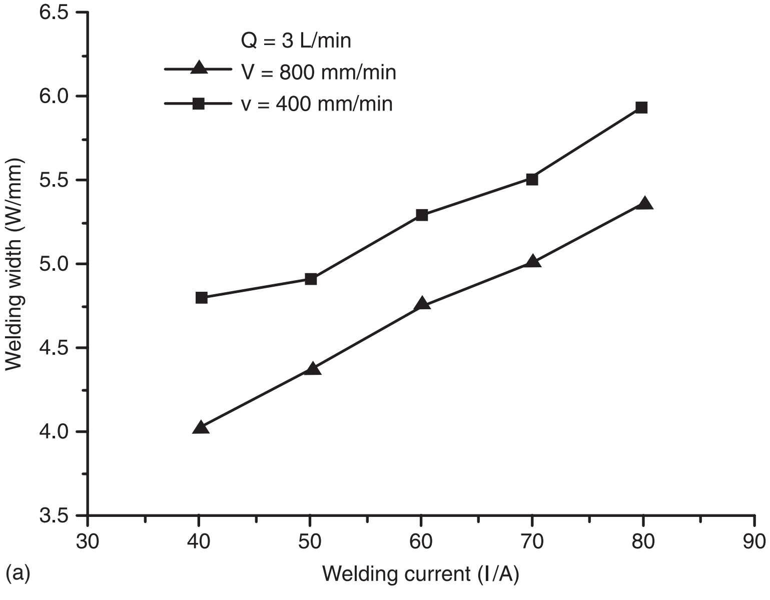

13.9 Effect of different currents and speeds on welding width. (a) Effect of different welding currents on weld. (b) Effect of different welding speeds on weld.

Continued overleaf

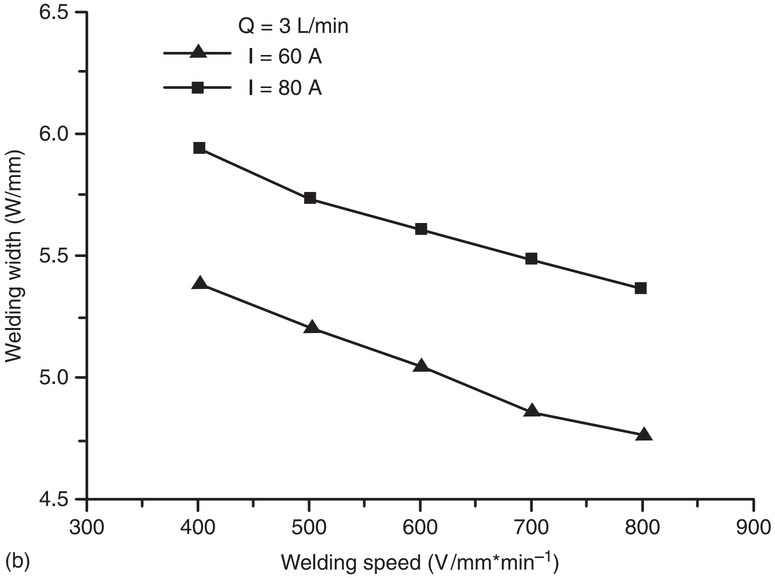

13.9 Continued.

burning through or being cut), and the welding repetition will be reduced. With a definite welding current and plasma gas flow rate, the welding process is affected by adjusting the welding speed. As shown in Fig. 13.9(b), the welding width reduces with the increase of the welding speed. If the welding speed is too high, the keyhole would be unstable and even disappear, resulting in poor welding appearance.

13.2.3 Effect of catelectrode clean t_{ACEP} on the mechanical property of welding joint

When the other welding parameters are the same, the tensile strength of the welding joint, the welding width and the catelectrode clean area are investigated with different catelectrode clean t_{ACEP}, as shown in Fig. 13.10.

From Fig. 13.10, it is seen that with the increase of clean time, the catelectrode clean effect is enhanced. The width (*C*) of clean area (including welding width *W*) increased greatly, and the surface of the welding joint became brighter. The tensile strength increased first and then reduced with the increase of the clean time. It is at its highest when the clean time is 3 ms. The main reason is that when the clean time is shorter, the increase of clean time could enhance the clean effect by clearing the oxide on the surface of welding joint, resulting in an increase in the tensile strength of the welding joint. If the clean time increased too much, the clean area would increase, resulting in the jumping of the plasma arc. This causes an increase of welding width.

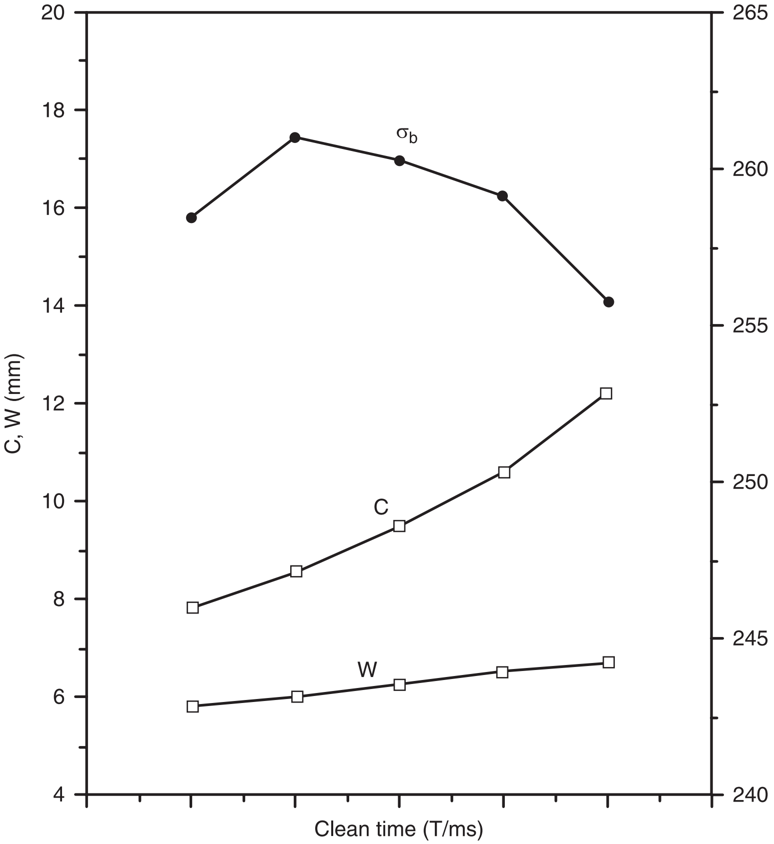

13.10 Effect of variations in clean time on joint dimension and strength.

In the welding process of the magnesium alloy and aluminum alloy, the decrease of the tungsten electrode burning loss and the increase of the welding quality are contrary to the enhancement of the clean effect. Although increasing the clean time could wipe off the oxide effectively, the tungsten electrode burning loss increases, and the welding width and the size of the heat-affected zone (HAZ) also increases, resulting in the reduction of the welding quality. Therefore, in the actual welding process of magnesium alloy, it is better not to increase the clean time as long as possible. On the contrary, under the proper clean time condition, the clean time should be reduced. This increases the alternating current workpiece positive time, resulting in reduction of the tungsten electrode burning loss and an increase in the penetration depth.

When the other welding parameters are the same, the catelectrode clean time is changed by adjusting the square wave current frequency. Therefore, on the basis of the above experiments, it is known that the change of the current frequency has an important effect on the welding appearance and the mechanical property. From Fig. 13.10, it is obvious that the tensile strength could get the highest value by changing the current frequency.

13.2.4 Variable polarity plasma arc welding of magnesium alloy with lap joint

Welding characters

A good lap joint of magnesium alloy with 2.5 mm thickness is found in keyhole PAW mode. One-side welding with back formation is obtained. The welding appearance is shown in Fig. 13.11.

From Fig. 13.11, it is observed that the welding appearance is uniform and continuous without filler rod, and the back-face formation of welding joint is also uniform and no flash exists.

A good lap joint could be obtained without groove and sheet backing in the keyhole mode VP-PAW process. When the plasma arc acts on the surface of magnesium alloy, the base metal in the upper board melts and forms a molten pool. Then, the plasma arc melts the lower board to form a keyhole with the plasma arc force, as shown in Fig. 13.12.

The energy of plasma arc is absorbed through the welding keyhole. The heat quantity is transferred from the metal around the keyhole, resulting in molten metal. At the same time, the keyhole and the metal around the keyhole run with the plasma arc, and the keyhole is filled with molten metal to form the welding seam.

The plasma arc has higher energy density and arc force, which is suitable to weld the medium plate. With the plasma arc, double plates are all penetrated and melt sufficiently, resulting in reduction of the bugs and residual stress.

In the keyhole mode VP-PAW process, the welding current could be adjusted to a bigger area. In this welding parameter, arc length plays an important role.

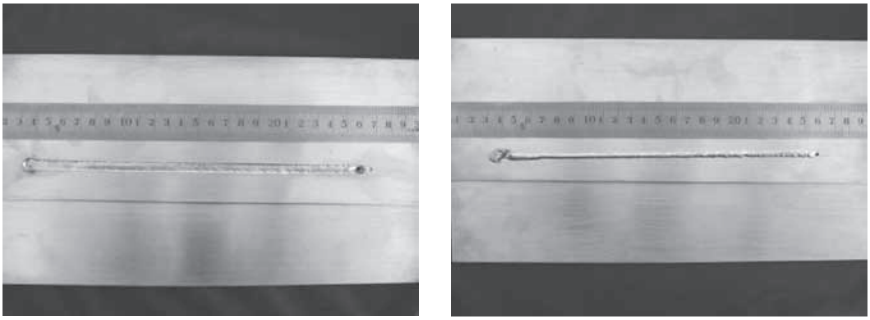
(a) (b)

13.11 Welding appearance of magnesium alloy. (a) Front face formation of welding joint. (b) Back face formation of welding joint.

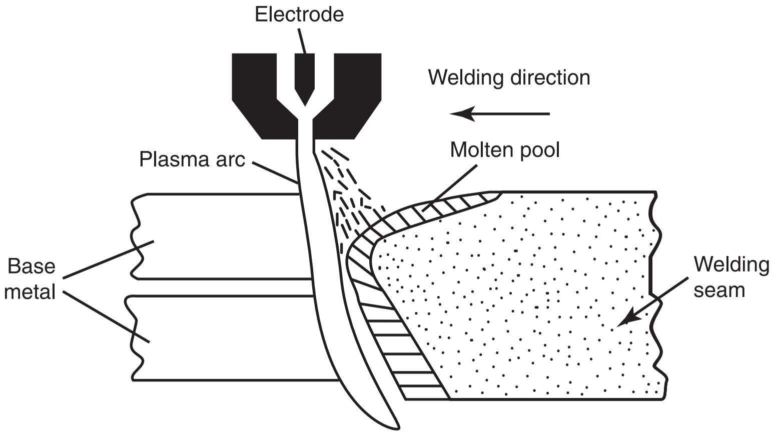

13.12 Schematic diagram of VP-PAW.

Changing the distance between the nozzle and the workpiece, namely arc length change, would have a great effect on the pressure in the keyhole and the welding appearance under the effect of arc force, surface tension and self-gravity. The shorter the arc length, the larger is the plasma arc force effect on the molten pool. The melted metal in the upper molten pool is likely to flow to the back side, and the welding width is narrow. However, it is easy to form the undercut and the spatter. If the arc length is longer, the arc force and the penetrating power reduce. The lower magnesium plate could not be penetrated and the welding seam is not easy to form. It has been found that the proper arc length is about 1–2 mm.

Mechanical properties of welding joints

The result of the tensile shear test of the keyhole mode variable polarity plasma arc (continues) welding of magnesium alloy joint is reported in Table 13.1. The schematic of a test specimen is shown in Fig. 13.13.

In the test, because of the presence of the eccentric moment, the plastic deformation of the workpiece would occur in order to reduce the eccentric

Table 13.1 Results of tensile test for magnesium alloy produced by VPPA welding

	Fail area (S/mm^2)	Fail load (F/kN)	Fail position
	55	7.54	Heat-affected zone
1	53	7.49	Heat-affected zone
	53	7.24	Heat-affected zone
	58	7.28	Heat-affected zone
2	55	7.34	Heat-affected zone
	50	7.15	Heat-affected zone

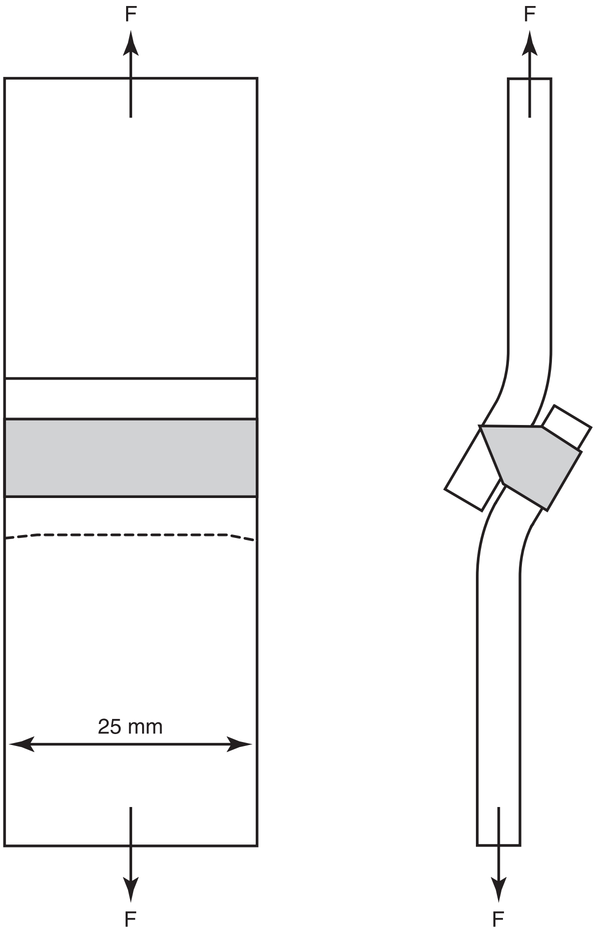

13.13 Schematic diagram of the test specimens.

moment. Therefore, there is not only shear stress but also tensile stress. The results show that the welding joint easily failed at upper part of welding seam, and the average failure load is above 7.34 kN. With the keyhole mode variable polarity plasma arc (continues) welding process, a good welding joint is obtained. It is helpful to promote the application of magnesium alloy structure.

The microhardness could reflect the microstructure of the welding joint, as shown in Fig. 13.14. It is found that the microhardness of the welding seam is higher than that of the base metal, and the microhardness in the upper part of the welding seam is higher than that in the lower part of the welding seam.

The grains in the molten pool are fine compared with the base metal, resulting in the increase of microhardness. The grains in the lower plate grow by the caudal plasma arc, and are bigger than the grains in the upper plate. Therefore, hardness was reduced in the lower plate.

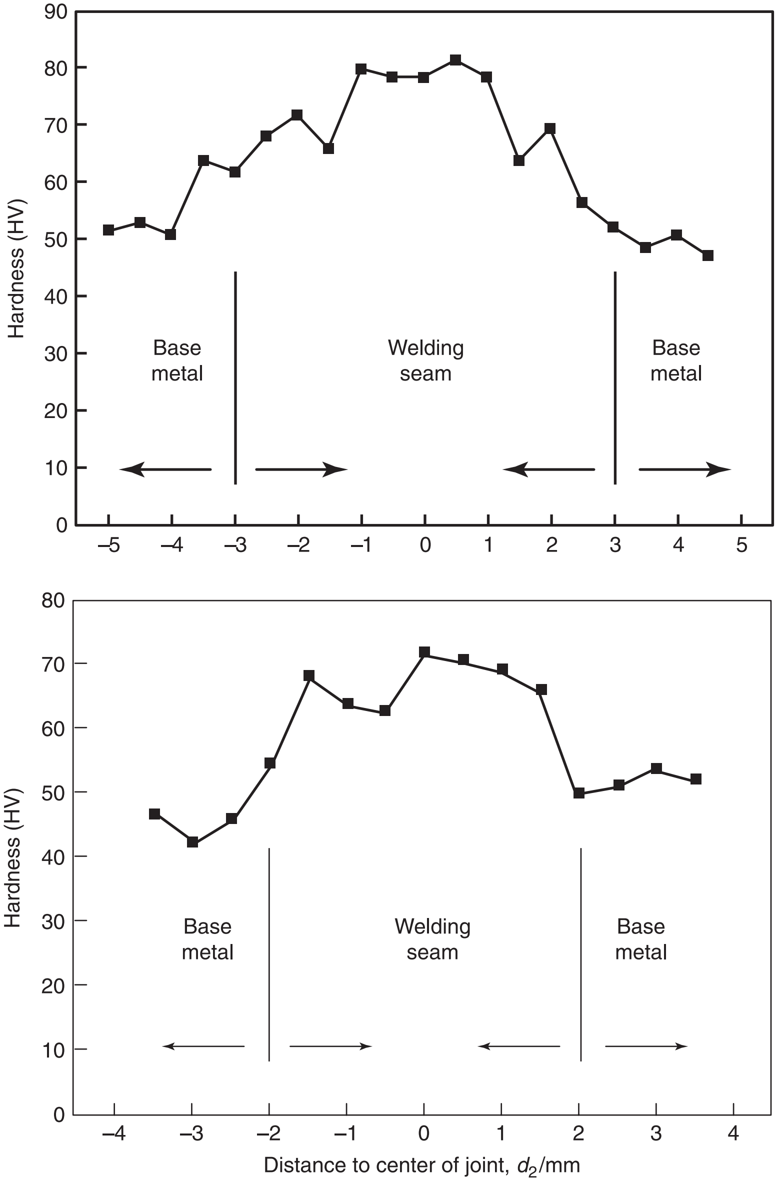

13.14 Distribution of hardness in the joint.

Microstructure of welding joints

The cross-section of the welding seam is prepared to observe the microstructure. The macrostructure and microstructure of a welding joint are shown in Fig. 13.15 and Fig. 13.16, respectively.

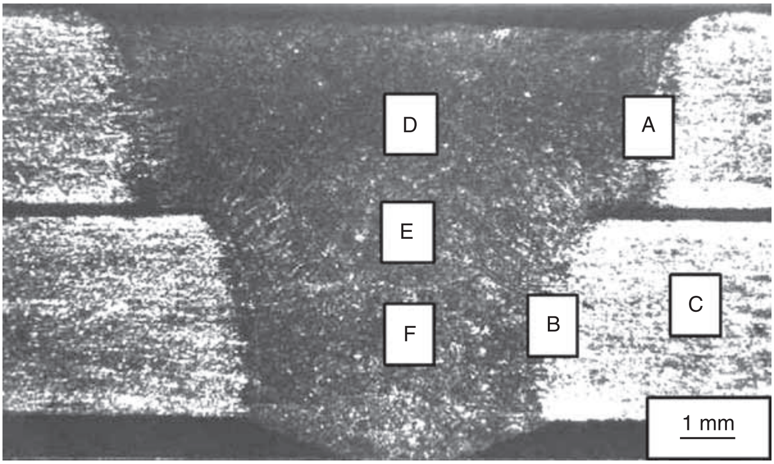

13.15 Weld pool shape of magnesium alloy produced by VP-PAW.

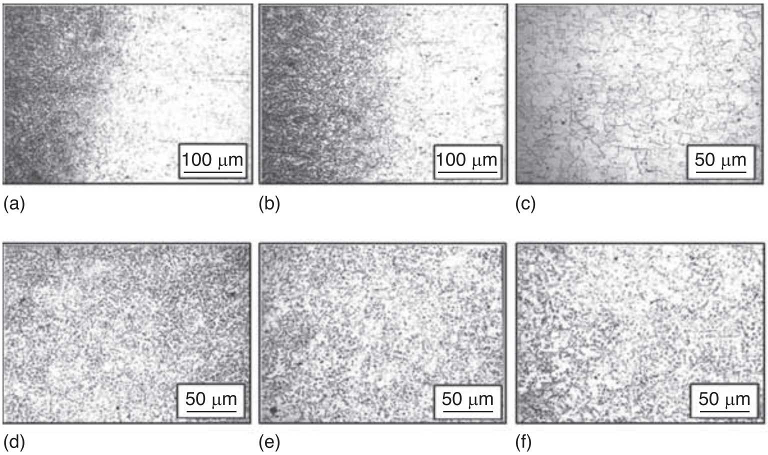

13.16 The microstructure produced by AZ31B weld. (a) Microstructure in area A. (b) Microstructure in area B. (c) Microstructure in area C. (d) Microstructure in area D. (e) Microstructure in area E. (f) Microstructure in area F.

From Fig. 13.15, it is observed that the welding joint is 'T' shaped. The welding width in the upper plate is about 7.3 mm and in the lower plate it is about 4 mm. The excessive penetration of the welding joint is smaller, and there are no pores and cracks. The upper plate is closer to the heat source, so by the effect of the plasma arc, the quantity of melted metal is higher and the welding width is bigger. The lower plate is melted when the upper plate is penetrated, and the welding width is smaller.

Figure 13.16(a) and (b) is the transition zone in the upper plate and lower plate respectively, and Fig. 13.16(c) is the base metal. From Fig. 13.16, it is observed that the heat effect zone is not visible. At the edge of the molten pool, little columnar crystals are growing into the center of the molten pool. Figure 13.16(d), (e) and (f) show the change of microstructure along the penetration depth. The fusion zone is composed of finer isometric crystals without cracks and pores. The grain size in the lower plate is larger than that in the upper plate. Because of the ability of the caudal plasma arc to sustain heat, grains in the lower molten pool grow further.

13.3 Variable polarity plasma arc weld bonding of magnesium alloys

13.3.1 Introduction of plasma arc weld bonding of Mg alloys

The VP-PAWB process has been referred to as a new welding method to join Mg alloy. The lap joint was made by the VP-PAW process when an adhesive layer existed in the interface of the Mg alloy sheets. The performance of the welding joint could be enhanced due to the characteristics of the adhesive layer such as excellent fatigue and good energy absorption.[12] Moreover, it had a great advantage on the joining of dissimilar alloy of Al to Mg alloy. Although many reports were published about the spot weld-bonded process[16,17] and continuous laser weld-bonded process,[18,19] there have been few articles published about the VP-PAWB process.

13.3.2 Investigation of the keyhole mode variable polarity plasma arc weld bonding technique

The base material used in this investigation was extruded AZ31B plate (250 mm × 100 mm × 2.5 mm). The adhesive used in this experiment was a structural epoxy adhesive with shear strength at room temperature on electrogalvanized steel (EZG) of about 20 MPa, decomposing into carbon monoxide, carbon dioxide and/or low molecular weight hydrocarbons above 230 °C. The specimens were lap joined with an adhesive interlayer of 0.1 mm in thickness in the overlap area.

Figure 13.17 shows the weld bead surfaces of the no-keyhole mode VP-PAWB process, keyhole mode PAWB process and keyhole mode VP-PAWB process. It shows the characteristics of the three welding techniques. The effects of the keyhole mode and variable polarity power were observed. Figure 13.17(a) and (b) show the weld bead surfaces of the no-keyhole mode VP-PAWB process. It was observed that the welding seam was discontinuous and contained a lot of pores (Fig. 13.17a), and could not even form the welding seam (Fig. 13.17b). Figure 13.17(c) and (d) show the weld bead surfaces of the keyhole mode PAWB

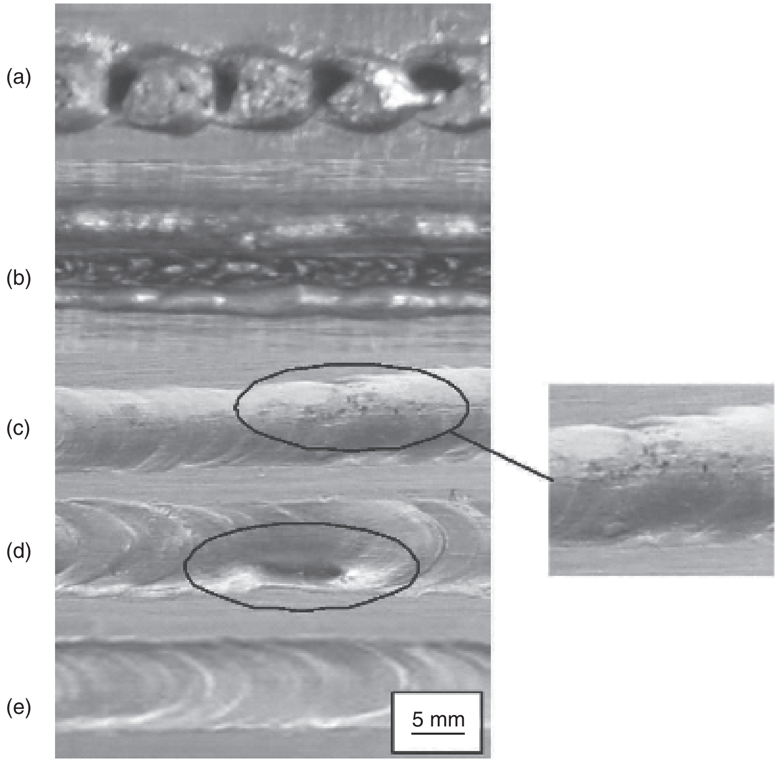

13.17 Weld bead surface of thermal conduction VP-PAWB process (a and b), keyhole mode PAWB process (c and d) and keyhole mode VP-PAWB process (e).

process. It was observed that the welding seam was formed, but there were a lot of inclusions (Fig. 13.17c), even undercut (Fig. 13.17d) on the weld bead surface. Figure 13.17(e) shows the weld bead surface of the keyhole mode VP-PAWB process. It was observed that a smooth welding joint was formed, and there were no inclusions or undercuts on the surface of the welding seam.[20]

During the welding process, the adhesive was decomposed, and its decomposed products were carbon monoxide, carbon dioxide and/or low molecular weight hydrocarbons. During the no-keyhole mode VP-PAWB process, no keyhole was formed. The decomposed adhesive products only escaped upward from the molten pool, which interrupted the welding seam. During the keyhole mode PAWB process, the decomposed adhesive products could escape downward from the molten pool with the plasma arc. However, a few of these products remained in the welding seam and then formed inclusions. But for the keyhole mode VP-PAWB process, under the effect of the cleaning of the cathode, the inclusions in the molten pool of the welding joint disappeared. It was concluded that keyhole mode and the variable polarity power were helpful to release the decomposed adhesive products and clean the inclusions in the molten pool; in other words, the keyhole mode and variable polarity power were helpful in obtaining a defect-free joint.

13.3.3 Pore behavior investigation

Porosity of VP-PAWB joint

In the VP-PAWB process, because of the addition of adhesive, it was easy to form a lot of pores in molten pool. Figure 13.18(b) shows the cross-section of a VP-PAWB joint. It was observed that there were a large number of pores, and most of the pores were distributed in the upper part of the VP-PAWB joint. Four large elliptical pores with major axis of about 3 mm grew from the upper part to the lower part of the VP-PAWB joint. Some smaller elliptical pores with a 1 mm major axis and circular pores with a 0.3 mm diameter were distributed around the large elliptical pores. The inner wall of these regular-shaped pores was smooth. Figure 13.18(a) shows some anomalous (irregular) pores at the edge of the upper molten pool, such as asteroid and polygonal pores. The inner wall of the anomalous pores was rugged. The micropores with diameters of about 10 mm were also observed at the edge of bottom molten pool, as shown in Fig. 13.18(c). It was observed that the porosity was easy to achieve during the VP-PAWB process. During the process, the presence of the adhesive layer had an effect on the formation of the pores in the welding joint. The adhesive combusted and gasified acutely under the effect of the plasma arc. A number of decomposition products, such as gas and low molecular weight hydrocarbons, were produced, which could result in the formation of a number pores in the welding joint.[21]

The elements on the inner wall of pores were analyzed by electron probe microanalysis (EPMA), and the results are reported in Table 13.2. It was found that the elements on the inner wall of all pores were mainly Mg, C and O elements. On the inner wall of bigger elliptical pores (shown as Fig. 13.18b), C and O content was up to 10% and 16.5%, respectively. The C and O content on the inner wall of micropores (as shown in Fig. 13.18c) was up to 6.5% and 8.9%,

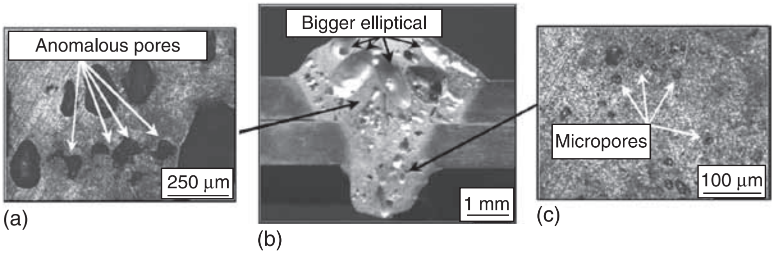

13.18 Cross-section of VP-PAWB joint (a), the anomalous pores, (b) bigger elliptical pores and (c) micropores.

Table 13.2 Results of an EPMA analysis of the element on profile of macropores in Fig. 13.18(b) and micropores in Fig. 13.18(c) and anomalous pores in Fig. 13.18(a)

	Mg	O	C	Al	Zn	Cl	K
Macropore	70.347	16.502	10.058	2.592	0.500	—	—
Micropore	82.756	8.905	6.521	1.248	0.476	0.053	0.041
Anomalous pore	0.245	1.165	96.75	—	1.84	—	—

respectively, and the C content on the inwall of anomalously shaped pores (as shown in Fig. 13.18a) was up to 96.75%. It was concluded that the formation of the pores had a close relationship with the content of C and O elements. In addition, the decomposed products of the adhesive were known to be carbon monoxide, carbon dioxide and/or low molecular weight hydrocarbons. Therefore, the C and O elements on the inner wall of pores would come from the adhesive, and the decomposition of the adhesive was the reason for the porosity of the VP-PAWB joint. On the basis of the molecular rate between C and O, the gases in bigger elliptical pores and micropores were composed of CO and CO_2, and the molecular ratio was about 2:3. The gases in the anomalous pores were considered to consist of the low molecular weight hydrocarbons based on the C element content.

Effect of welding parameters on the pores

During the VP-PAWB process, the decomposition of the adhesive was inevitable due to the effect of the plasma arc. The larger the area of decomposed adhesive layer, the more products were decomposed. The width of decomposition adhesive layer was proportional to the molten width (L) at the bottom of the upper sheet. Therefore, decreasing the molten width was considered as one method to reduce the amount of pores. For example, with the increase of the flow rate of plasma gas, the constriction of the plasma arc was increased, and so the molten width could be reduced. Furthermore, increasing the heat input could increase the cooling time of the molten pool, which was helpful for the releasing of pores. Therefore, increasing the welding current and decreasing the welding speed was considered another method to reduce the amount of pores in a VP-PAWB joint. Analyzing the effect of the parameters on the pores' behavior and matching them were the keys to avoid porosity in the VP-PAWB joint.

Flow rate of plasma gas

With different flow rates of plasma gas, the pore behavior and the change of the molten width were investigated, as shown in Fig. 13.19. It was found that the molten width decreased with the increase in the flow rate of plasma gas. The size

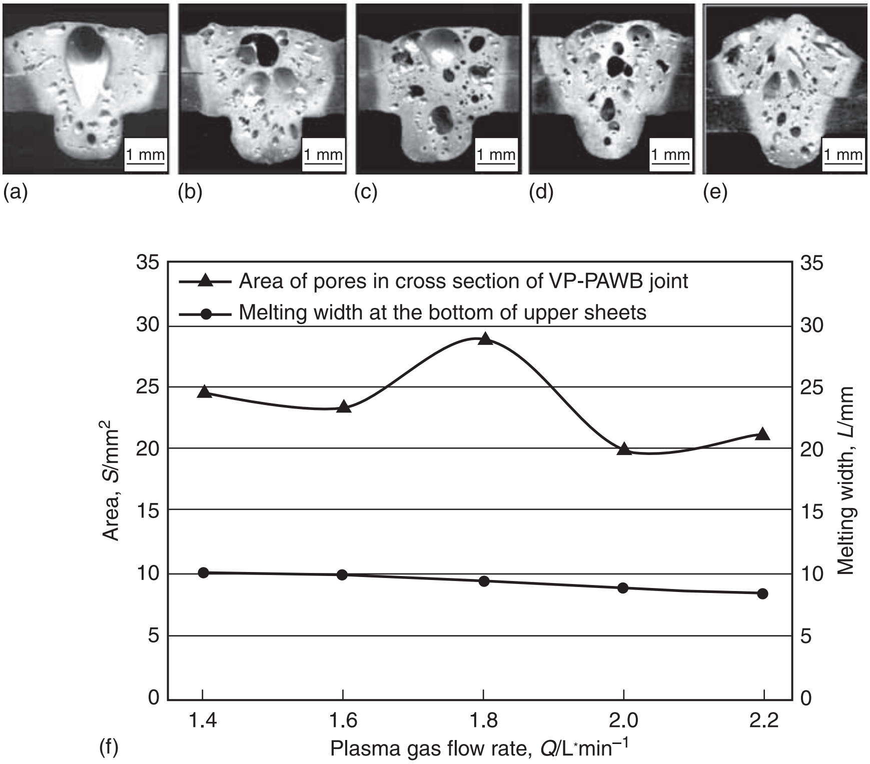

13.19 Cross-section of VP-PAWB joint with different flow rates of plasma gas. (a) 1.4 l/min; (b) 1.6 l/min; (c) 1.8 l/min; (d) 2.0 l/min; (e) 2.2 l/min; and (f) pores area and *L* with different flow rates of plasma gas.

of the pores reduced, and the shape of pores was changed to slender. However, the amount of pores increased, but the total area of pores in cross-section of VP-PAWB joints hardly changed. With the increase of the flow rate of plasma gas, the plasma arc constricted and the arc force increased. It could reduce the molten width and increase the stirring in the molten pool. The bigger pores broke up into smaller pores. Therefore, it was concluded that the flow rate of plasma gas mainly affects the shape and size of the pores but does not greatly affect the total amount of pores in VP-PAWB joint.

Welding current

Figure 13.20 shows the pore behavior and change of the molten width with different welding currents. With the increase of the welding current, the molten width increased. The amount of the pores reduced. The small pores coalesced into the big pores; then, the pores moved to the upper part of VP-PAWB joint and

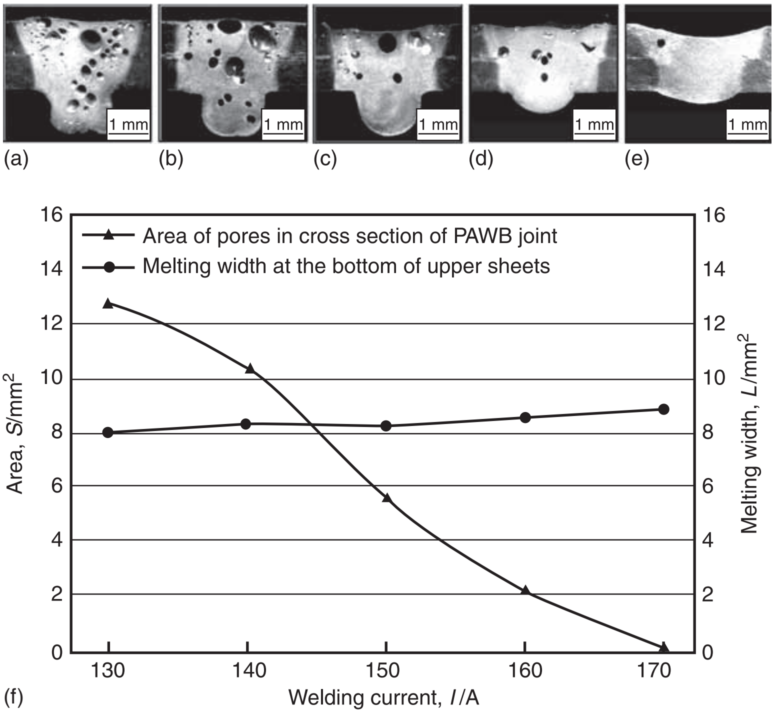

13.20 Cross-section of VP-PAWB joint with different welding currents. (a) 130 A; (b) 140 A; (c) 150 A; (d) 160 A; (e) 170 A; and (f) pores area and *L* with different welding currents.

were eventually released from the VP-PAWB joint. The total area of the pores in cross-section of VP-PAWB joints reduced rapidly. With the increase of the welding current, the heat input increased. Although the molten width increased, the solidification time of the molten pool also increased. It made the escape of gas easier. Therefore, it was concluded that the welding current influenced the size, amount and distribution of the pores. With the increase of welding current, the total amount of the pores decreased.

Welding speed

With different welding speeds, pore behavior and the change of the molten width were observed, as shown in Fig. 13.21. It was found that with the decrease of the welding speed, the molten width increased. The total area of pores in a cross-section of a VP-PAWB joint reduced quickly. The effect of the welding speed on pore behavior was opposite to the welding current. With the decrease of welding speed, not only the heat input and the molten width increased but so did the solidification time of the molten pool. The increase of welding current made it

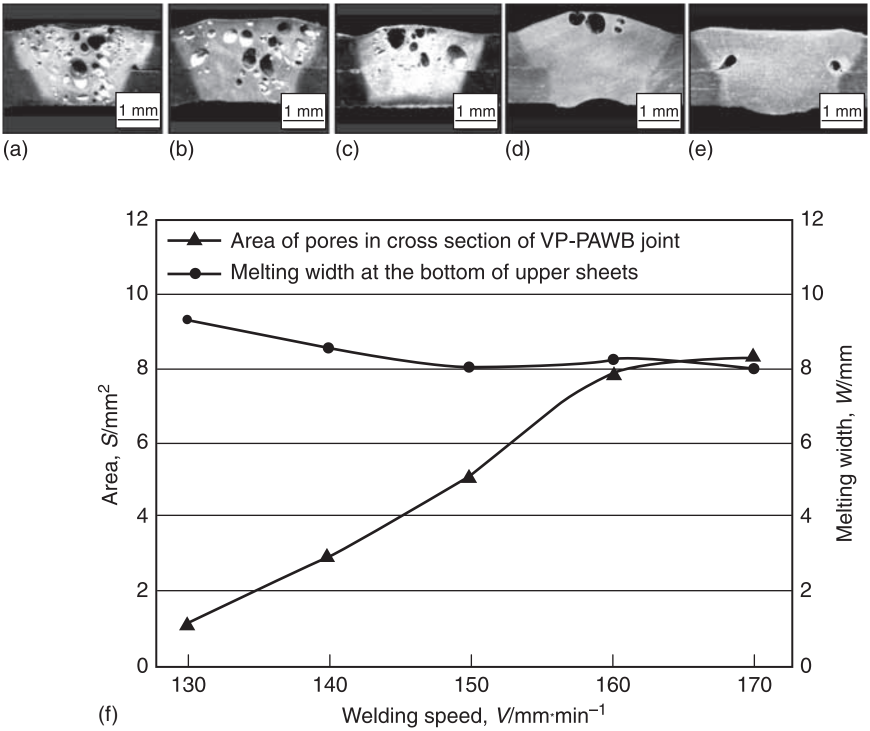

13.21 Cross-section of welding joint with different welding speeds. (a) 425 mm/min; (b) 400 mm/min; (c) 375 mm/min; (d) 350 mm/min; (e) 325 mm/min; and (f) pores area and *L* with different welding speeds.

easier for gases to be released. It was concluded that the welding speed influenced the size, amount and distribution of the pores. With the decrease of welding speed, the total amount of pores decreased.

The remedy for eliminating pores

In the VP-PAWB process, the decomposition of adhesive at both sides of welding seam was considered the main cause for the porosity of a VP-PAWB joint. It was obvious that the adhesive in the area of instant welding seam decomposed completely because of the high temperature of plasma arc during the VP-PAWB process. Under the effect of the arc force, most of the decomposition products were released from the molten pool along the keyhole with the plasma arc, but only a few decomposition products could follow the melted metal from the molten pool. During the VP-PAWB process, however, the adhesive at both sides of the welding seam also decomposed and produced products such as CO and CO_2. During the solidification process of the molten pool, CO and CO_2 could remain in the molten pool along the interface between the specimens, as shown in

Fig. 13.21(e). If there was not enough time for the gases to be released from the molten pool, the gases would later form pores. Thus, the decomposition of adhesive on both sides of the welding seam was considered the main cause for the porosity of the VP-PAWB joint.

During VP-PAWB process, the decomposition of adhesive was inevitable. From previous experiments, it was known that the flow rate of plasma gas hardly affected the total amount of pores in the VP-PAWB joint. However, with the increase of the welding current or the decrease of the welding speed, the total amount of pores in the VP-PAWB joint decreased quickly.

In the VP-PAWB process, the heat input J (kJ/m) could be expressed as:

$$J = \frac{P}{V} = \frac{UI}{V} \qquad [13.2]$$

where P is the power of plasma arc (kW), U is the output voltage (V), I is the output current and V is the welding speed (m/s).

On the basis of the previous experiments, the relationship between the total area of the pores in a cross-section of the VP-PAWB joint and the heat input was established, as shown in Fig. 13.22. It was observed that with the increase of the heat input, the total area of the pores was reduced quickly. The total area of the pores in a cross-section of a VP-PAWB joint showed a linear relation to the heat input. The function of the relationship between the total area of the pores and heat input could be expressed as a simple equation:

$$S = 43.023 - 0.1151J, \qquad [13.3]$$

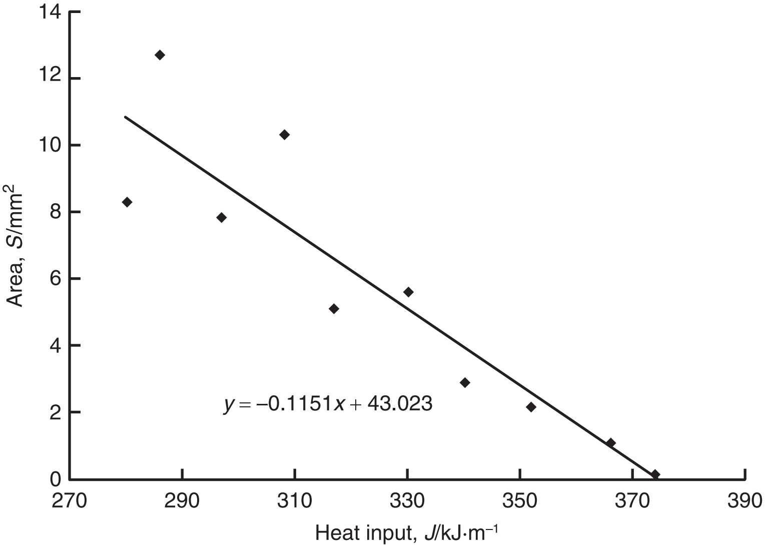

13.22 Relationship between the total area of the pores and the heat input.

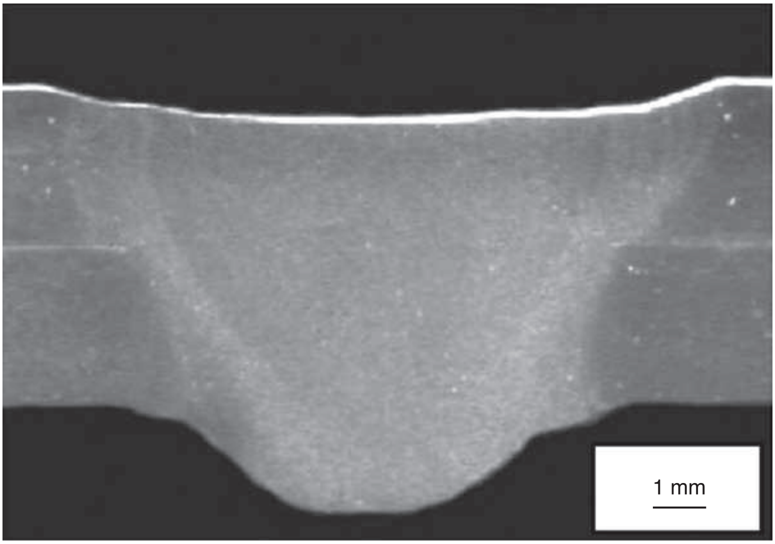

13.23 Cross-section of welding joint by the optimal welding parameters.

where S is the total area of the pores (mm^2) in the cross-section of the VP-PAWB joint and J is the heat input (kJ/m). On the basis of this equation, it can be concluded that there will be no pores when J is 373.79 kJ/m.

In the experiment, under the condition of forming a good welding seam, the welding parameters were chosen on the basis of Eq. (13.2) and Eq. (13.3). Figure 13.23 shows the cross-section of the welding joint, making it clear that there were no pores in the welding joint.

13.3.4 Welding joint morphology and microstructure

The VP-PAWB process was used to join Mg alloy successfully with the proper welding parameters. The morphology of a welding seam is shown in Fig. 13.24. It was observed that lustrous surfaces without splash and one-side welding with back formation were obtained.[21,22]

Figure 13.25 shows the transverse section of the VP-PAWB joint. It was observed that the molten pool of the VP-PAWB joint looked as ‘T’ shape, which was wider in the upper sheet and narrower in the bottom sheet. The adhesive layer disappeared and no pores or inclusions remained in the VP-PAWB joint. The melted metal of upper molten pool moved downward and extruded the adhesive to both sides, as shown in A zone of Fig. 13.25. In this zone, the adhesive layer's thickness was reduced but did not disappear. Figure 13.25 also shows the different zones of the VP-PAWB joint such as the fusion zone, the transition zone and the base metal zone. It was observed that the fusion zones B and C in Fig. 13.25 were composed of refined equiaxed grains, and the grain size was about

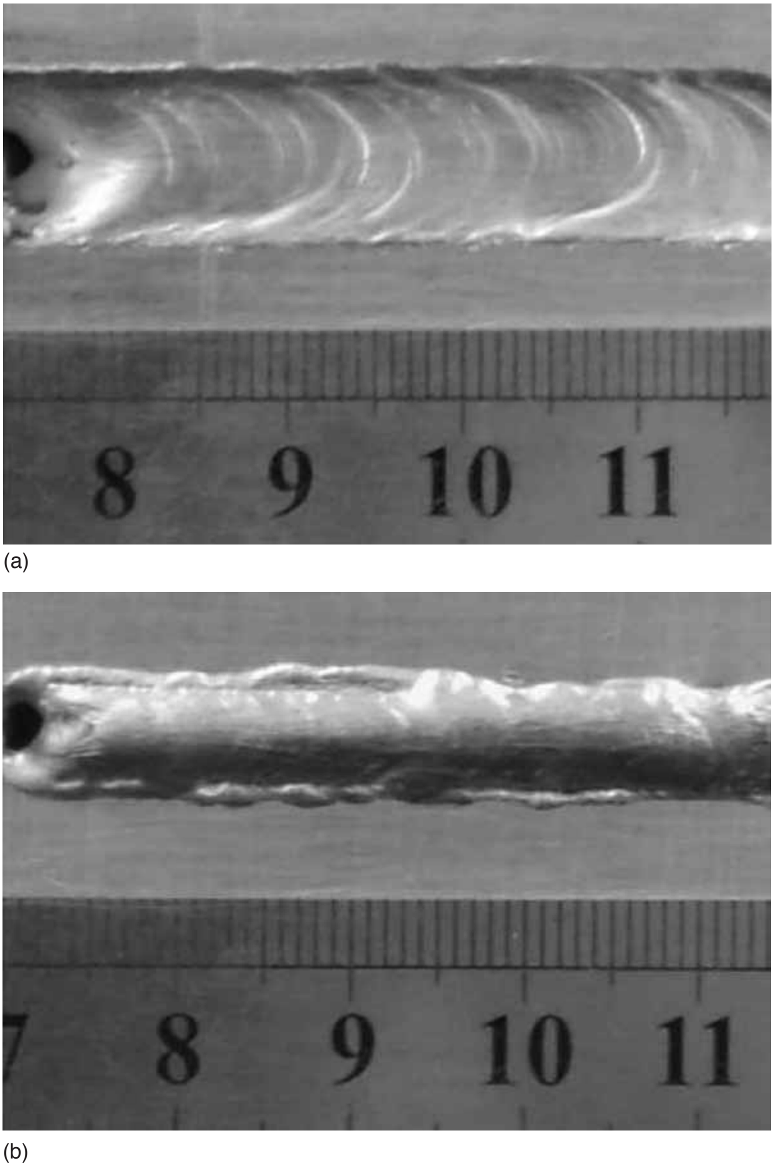

13.24 Morphology of the VP-PAWB joint. (a) Front face formation of welding joint. (b) Back face formation of welding joint.

10 and 20 mm, respectively. The grain size of the B zone was smaller than that of the base metal (F zone in Fig. 13.25), and the grain size of zone C was the same as that of the base metal. The HAZ was evident, as shown in zones D and E in Fig. 13.25. The sizes of the HAZ grains in the upper sheet and the bottom sheet were about 40 and 30 mm, respectively.

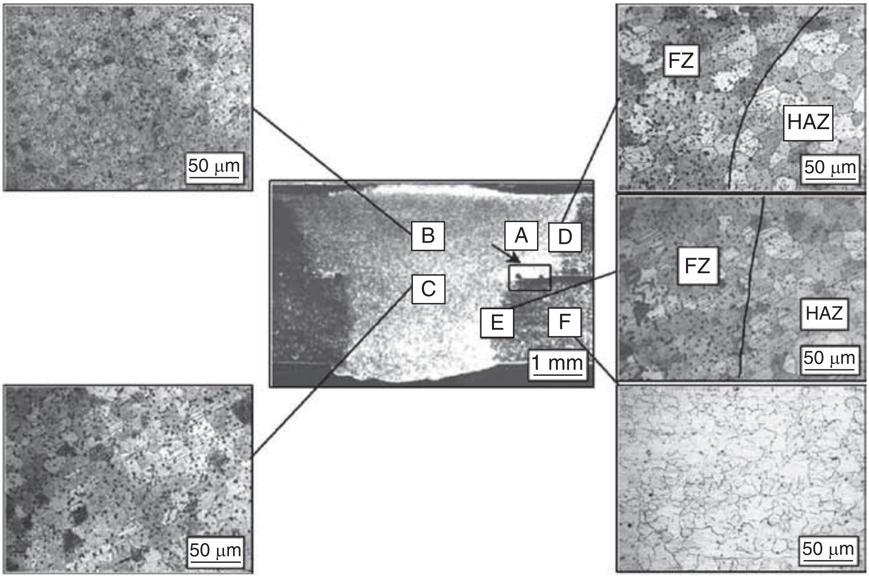

13.25 The weld pool shape and microstructure of the VP-PAWB joint.

Figure 13.26 shows the transverse section of the VP-PAW joint as compared with the VP-PAWB joint. The molten pool of the VP-PAW joint was also 'T' shaped, and was wider in the upper sheet and narrower in the bottom sheet, but the difference of the fusion width between the upper sheet and the bottom sheet was not evident. The melted metal of the upper molten pool did not

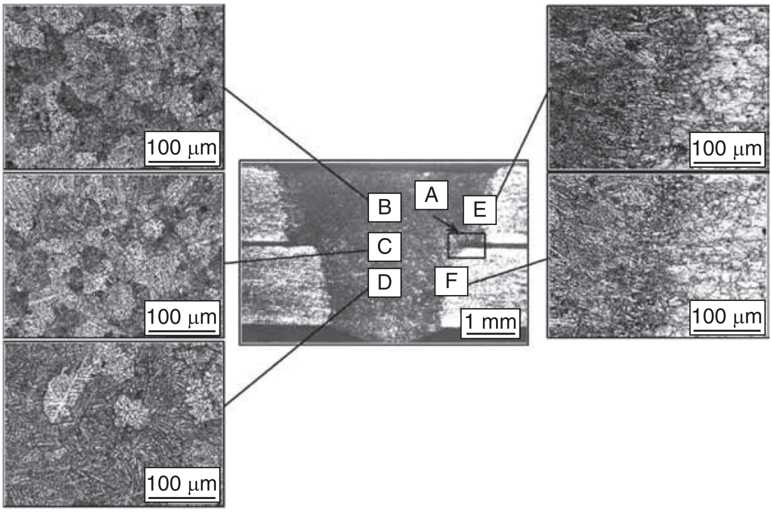

13.26 The weld pool shape and microstructure of the VP-PAW joint.

move downward, as shown in A zone of Fig. 13.26. The microstructures of the VP-PAW joint are also shown in Fig. 13.26. It was observed that the fusion zones B and C in Fig. 13.26 were composed of coarse equiaxed grains, and the grain sizes were about 120 and 100 μm, respectively. The fusion zone D in this figure was mainly composed of columnar crystals and a few of the coarse equiaxed grains. Zones E and F in this figure show the transition zone in the upper sheet and the bottom sheet. The HAZ was clearly visible and the fusion zone close to the fusion line was composed of the columnar crystals. The sizes of the HAZ grains in the upper sheet and the bottom sheet were about 70 and 50 μm, respectively.

As mentioned above, a welding joint without pores and inclusions can be obtained by the VP-PAWB process. Because of the higher heat input of the plasma arc, the quantity of the melted metal of the VP-PAWB joint and the cooling time of the molten pool were increased as compared with the VP-PAW joint. It is known that the higher heat input would increase the fusion width and promote the grain growth of the fusion zone and the HAZ. However, Fig. 13.25 and Fig. 13.26 show that the upper sheet fusion width of the VP-PAWB joint was wider; that is, the difference of the fusion width between the upper sheet and the bottom sheet of the VP-PAWB joint was more evident than the VP-PAW joint. Because of the presence of the adhesive layer, the growing tendency of the HAZ grains in the VP-PAWB joint was smaller than that in the VP-PAW joint, and the grain growth of the HAZ was proportioned in the VP-PAWB joint and disproportioned in the VP-PAW joint. As for the fusion zone of the welding joint, it was found that the grains in the fusion zone of the VP-PAWB joint were refined, and the zone was composed of equiaxed grains without columnar crystals. The grains in the fusion zone of the VP-PAW joint were coarse, and the zone was composed of the coarse equiaxed grains in the center and columnar crystals at its edge. The finer grains of the upper molten pool of the VP-PAWB joint can be seen in zones B and C of Fig. 13.25, as opposed to the VP-PAW joint. In the VP-PAWB process, the adhesive would be decomposed and would form a lot of gases under the thermal effect of the plasma arc. The gases stirred the molten pool metal, which hindered the growth of grains in the fusion zone and formed the columnar crystals. This was considered the reason for the refining of the grains in the fusion zone. The adhesive layer was distributed in the interface of the sheets and greatly influenced the upper molten pool metal. It resulted in more refinement of the grains in the upper molten pool.

13.3.5 Distribution measurement of elements

The distribution of elements in the transverse section of the VP-PAWB joint was investigated by the EPMA, and the results are shown in Plate IV (in colour section between pages 210 and 211). It is well known that epoxy resin adhesive or its decomposed products mainly consist of C, O and H elements, so the distribution of the adhesive or its decomposed products could be indicated by observing the distribution of C, O and H elements. Plate IV(a), (b) and (c) show the distributions of C, O and Mg elements, respectively, in zone A of Fig. 13.25. It was observed that there were a lot of C and O elements, which existed consistently in the interface of the specimens and disappeared in welding seam. This proved that the adhesive layer still existed at both sides of the welding seam and disappeared in the welding seam after welding. Plate IV(d), (e) and (f) show the distributions of C, O and Mg elements, respectively, in zone B of Fig. 13.25. It was observed that there were almost no C and O elements in the fusion zone of VP-PAWB joint. This proved that the adhesive layer in the fusion zone is broken down completely under the thermal effect of the plasma arc; that is, no adhesive or decomposed products remained in the welding joint after welding.

13.3.6 Mechanical property measure

Table 13.3 shows the failure load of the keyhole mode VP-PAWB joint, keyhole mode VP-PAW joint and adhesive bonding joint in a tensile shear test. The average failure load of the keyhole mode VP-PAWB joint, the keyhole mode VP-PAW joint and adhesive bonding joint was 6.24, 4.46 and 4.27 kN, respectively. The keyhole mode VP-PAWB joints showed the highest failure load, and most of the specimens failed at HAZ of the upper sheet. Under the combined effect of the welding seam and the adhesive layer, the mechanical property of the welding joint improved. When the keyhole mode VP-PAWB joint worked under tensile shear force, the load was resisted by the adhesive layer and welding seam together. The adhesive layer distributed the load to the whole specimen and the welding seam improved the stability of the adhesive layer. In this process, if no welding seam occurs, the adhesive will slip quickly, and as a result, the property of the joint will be low. If there is no adhesive layer, because of the stress concentration, the welding joint will fracture under a lower force.

However, during the keyhole mode VP-PAWB process, a part of the adhesive layer on both sides of the welding seam was partially decomposed or gasified as a result of the welding heat. In that area, the adhesive layer was not replaced by the welding seam. The adhesive layer was destroyed and the property was decreased.

Table 13.3 Results of tensile shearing test of the keyhole mode VP-PAW joint, adhesive bonding joint and keyhole mode VP-PAWB joint

	Failure load (F/kN)			Average failure load (F/kN)
Keyhole mode VPPAW joint	4.53	4.5	4.34	4.46
Adhesive bonding joint	4.32	3.96	4.53	4.27
Keyhole mode VPPAWB joint	6.45	5.76	6.5	6.24

It was inevitable in the welding process. How to reduce the area of the useless adhesive layer was important for enhancing the property of the keyhole mode VP-PAWB joint. At present, the better conduction plate and higher welding speed were mainly used to achieve this purpose.

13.3.7 Arc behavior observations

Figure 13.27 shows the arc shape of VP-PAW and VP-PAWB in two current cycles. Each current cycle is composed of ACEN and ACEP stages. It was found that the arc shape of the VP-PAW process is concentrated in ACEN stage and divergent in the ACEP stage. The arc mainly acts on the welding seam in the ACEN stage and on both sides of the seam in the ACEP stage. In contrast, the arc shape of the VP-PAWB process is concentrated not only in the ACEN stage but also in the ACEP stage. The arc mainly acts on the welding seam both in ACEN stage and the ACEP stage.[23]

During the VP-PAWB process, the adhesive in the welding zone is decomposed due to the arc. The arc behavior will be affected by the adhesive decomposition products. However, it has been found that the arc shape in the VP-PAWB process is no different compared with that in the VP-PAW process in the ACEN stage. As is known, the arc is concentrated in the ACEN stage, and thus the arc force is strong. A high-pressure zone is formatted in the arc stream, as shown in Fig. 13.28(a). Under the effect of the arc force, a number of adhesive decomposition products escape downward through the keyhole. Therefore, adhesive decomposition products hardly affect the arc shape in the ACEN stage. However, in the ACEP stage, the high-pressure zone in the arc stream disappears on account of the alternating current polarity. A number of adhesive decomposition products move to the center of the arc stream, as illustrated in Fig. 13.28(b). The ionization atmosphere is composed of argon and the decomposition products of adhesive. The arc shape is constricted by the mixed ionization atmosphere. At the time of the experiment, it was not clear how the decomposition products of

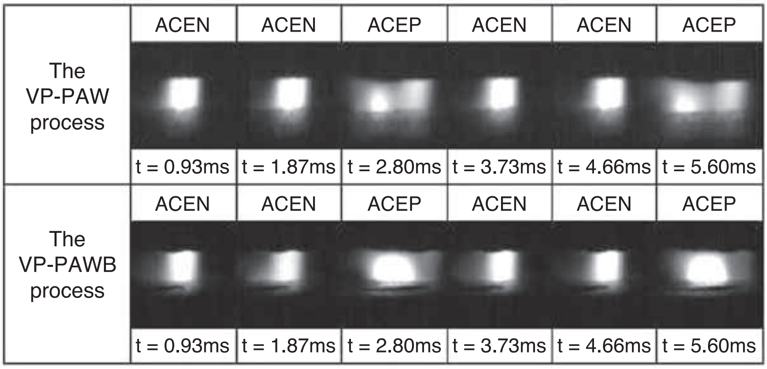

13.27 Arc behavior of VP-PAW and VP-PAWB process.

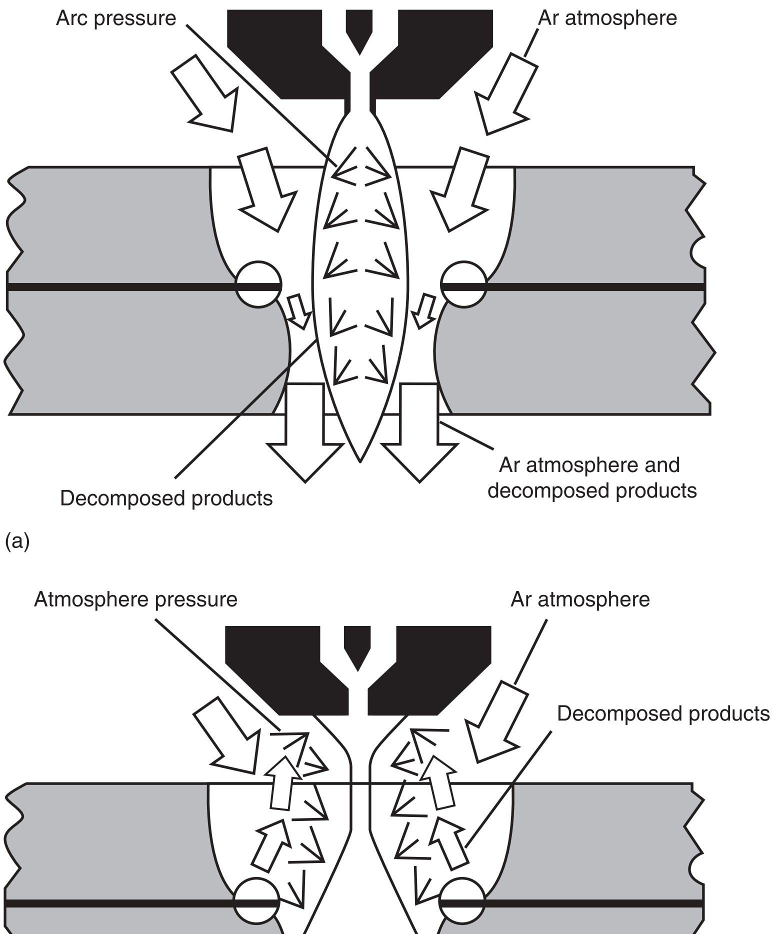

13.28 Ionization atmosphere in ACEN stage (a) and in ACEP stage (b) during VP-PAWB process.

adhesive would affect the arc behavior. It was thought that the addition of CO_2 in the ionization atmosphere was the main reason for the different arc shape in the ACEP stage between VP-PAW and VP-PAWB processes. The properties of arc welding were improved when CO_2 was added to the pure argon shield gas.[24] Figure 13.29 shows physical properties of argon and CO_2, which were calculated under the assumption of local thermodynamic equilibrium (LTE), using methods mentioned in the literature.[25,26] The most important characteristics of CO_2 were

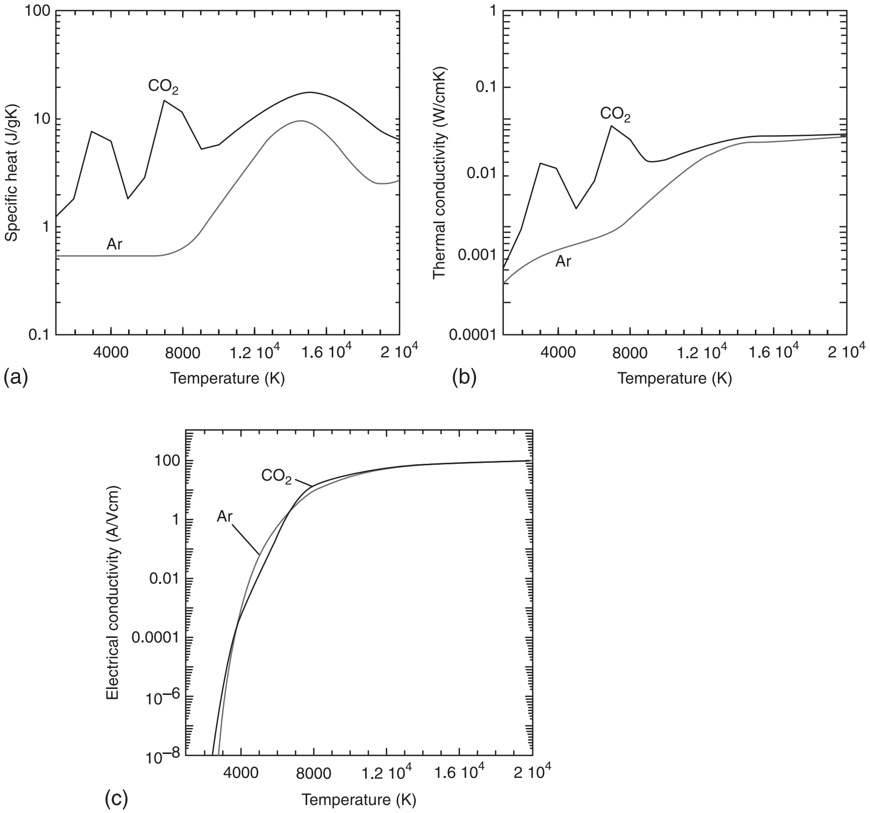

13.29 Physical properties of argon and CO_2 at atmospheric pressure. (a) Specific heat. (b) Thermal conductivity. (c) Electrical conductivity.

its high specific heat and thermal conductivity at lower temperatures. Besides, the electric conductivity of CO_2 was the same as that of argon. Increasing the specific heat and thermal conductivity of the shielding gas will lead to arc constriction, because it facilitates the heat transfer in the arc fringes, thereby localizing the arc current path to the arc axis area. The increase in arc current density will result in an increase in the magnetic field strength and therefore the cooling of the arc column by the cathode jet. The net effect of this cooling is in fact an increase in the on-axis temperature because of the consequent arc constriction. It is known as the thermal pinch effect.

13.4 Conclusion and future trends

Through the PAW process, Mg alloy could be joined effectively, whatever the butt joint or the lap joint. On the basis of the characteristics of the PAW process, thin or thick sheet of Mg alloy could be joined effectively and one-sided welding with back formation could be achieved. Moreover, with the increasing focus on the hybrid welding process, the plasma arc weld bonding process of Mg alloy was recommended. From the above observations, it was found that Mg alloy was welded successfully by using the plasma arc weld bonding process. The presence of adhesive alloy had several advantages for the welding process. It was concluded that PAW was helpful to improve the connection of Mg alloy, and Mg alloy would be more widely available.

13.5 References

1. Raymond T, Slatter E (1988). The plasma advantage in automated welding. *Weld J* **9**: 55–7.
2. Martikainen JK, Moisio TJI (1993). Investigation of the effect of welding parameters on weld quality of plasma arc keyhole welding of structural steels. *Weld J* **7**: s329–40.
3. Wang HX, Yang CL, Wei YH, Lin SB, Shen HY (2006). Study of keyhole closure and analysis of microstructure and mechanical performance of weld joints for variable polarity vertical up plasma arc welding process. *Sci Technol Weld Join* **11**(3): 315–25.
4. Wang HX, Yang CL, Wei YH, Shen HY (2006). Establishment of stable keyhole pool during variable polarity vertical-up plasma arc welding process. *Chin J Mech Eng* **42**(12): 59–64.
5. Craig E (1988). The plasma arc welding: a review. *Weld J* **67**(2): 19–25.
6. Tomsic M, Barhorst S (1984). Keyhole plasma arc welding of aluminum with variable polarity power. *Weld J* **63**(2): 25–32.
7. O'Brien RL, editor (1991). *Welding Handbook, 8th ed. Vol 2. Welding Processes*. Miami, FL: American Welding Society, p. 786.
8. Dong CL, Wu L, Shao YC (2000). The history and state-of-the-art of keyhole mode plasma arc welding. *Chin J Mech Eng* **11**(5): 577–81.
9. Chen KX, Li HQ, Li CX (2004). Progress in variable polarity plasma arc welding. *Trans China Weld Inst* **25**(1): 124–8.
10. Nunes AC, Bayless EO, Jones CS (1984). Variable polarity plasma arc welding on the space shuttle external tank. *Weld J* **63**(9): 27–35.
11. Darwish SM, Ghanya AA (2000). Critical assessment of weld-bonded technologies. *J Mater Process Technol* **105**(3): 221–9.
12. Wang PC, Chishholm SK, Banas G, Lawrence VL (1995). The role of failure mode, resistance spot weld and adhesive on the fatigue behavior of weld-bonded aluminum. *Weld J* **74**: 41–7.
13. Darwish SM, Niazi A, Ghanya A, Kassem ME (1990). Improving electrical conductivity of structural epoxy resin adhesives. *Int J Adhes Adhes* **11**(1): 37–41.
14. Kilik S, Davies R, Darwish SM (1990). Thermal conductivity of epoxy resin adhesives. *Int J Adhes Adhes* **19**(4): 219–23.
15. Chang B, Shi Y, Dong S (1998). Comparative studies on stresses in weld-bonded, spot-welded and adhesive-bonded joints. *J Mater Process Technol* **87**(1): 230–6.
16. Darwish S, Al-Abbas R, Sadek MM (1991). Design rational of bonded, double containment joints with dissimilar materials. *Int J Adhes Adhes* **11**(2): 65–70.

17. Pocius AV (2002). *Adhesion and Adhesives Technology: An Introduction*, 2nd ed. Cincinnati, OH: Hanser Gardner.
18. Liu L, Wang H, Song G (2007). Microstructure characteristics and mechanical properties of laser weld bonding of magnesium alloy to aluminum alloy. *J Mater Sci* **42**(2): 565–72.
19. Wang HY, Liu L, Meili Z, Wang H (2007). Laser weld bonding of A6061Al alloy to AZ31B Mg alloy. *Sci Technol Weld Join* **12**(3): 261–5.
20. Liu LM, Jiang JB (2008). Keyhole mode variable polarity plasma arc weld bonding of Mg alloy. *Mater Res Innov* **12**(3): 147–50.
21. Liu L, Jiang J (2009). Formation and disappearance of pores in plasma arc weld bonding process of magnesium alloy. *Mater Trans* **50**(7): 1649–54.
22. Liu L, Jiang J (2009). The effect of adhesive layer on variable polarity plasma arc weld bonding process of magnesium alloy. *J Mater Process Technol* **209**(6): 2864–70.
23. Jiang J, Zhang Z (2008). The study on the plasma arc weld bonding process of magnesium alloy. *J Alloys Compd* **466**(1/2): 368–72.
24. Lu S, Fujii H, Nogi K (2004). Marangoni convection and weld shape variations in Ar–O_2 and Ar–CO_2 shielded GTA welding. *Mater Sci Eng A* **380**(1/2): 290–7.
25. Murphy AB (1995). Transport-coefficients of air, argon-air, nitrogen-air, and oxygen-air plasmas. *Plasma Chem Plasma Process* **15**(2): 279–307.
26. Murphy AB (1997). Transport coefficients of helium and argon-helium plasmas. *IEEE Trans Plasma Sci* **25**(5): 809–14.

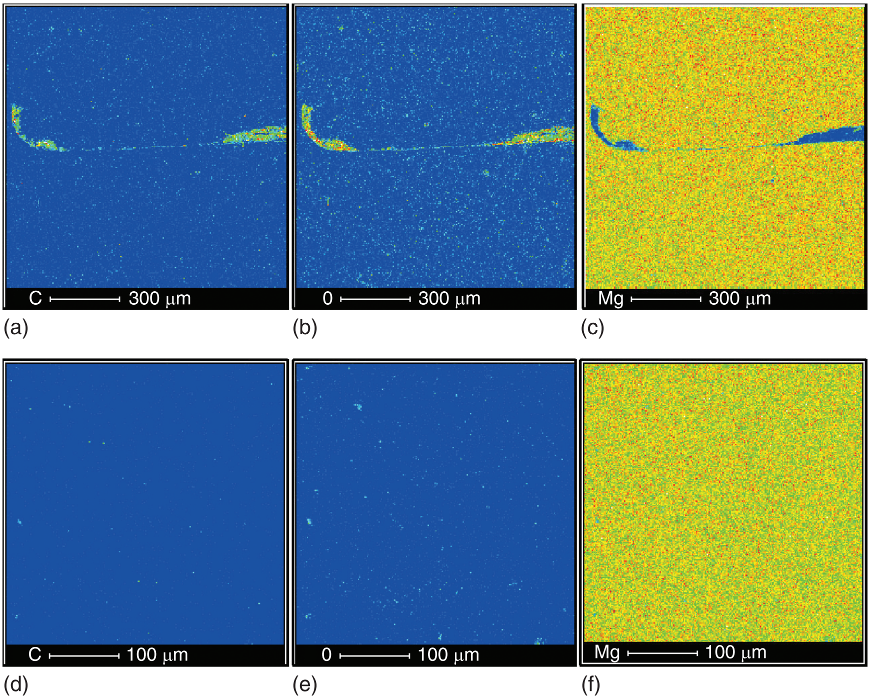

Plate IV (a)–(f) Transverse section EPMA analyses of the VP-PAWB joint.

14

Hybrid laser-arc welding of magnesium alloys

G. SONG, Dalian University of Technology, China

Abstract: In this chapter, the research and progress in laser/arc hybrid welding of magnesium alloys will be critically reviewed. Low-power laser/arc hybrid welding processes of magnesium alloys, with and without filler metal in detail, including the welding technology, microstructure, mechanical properties and so on, are introduced. Some applications of low-power laser/arc hybrid process in magnesium alloy products are discussed. Lastly, the chapter depicts the existing problems in hybrid welding of magnesium alloys and views the developing trend of the hybrid welding process.

Key words: magnesium alloy, laser/arc hybrid welding, filler wire, microstructure, mechanical property.

14.1 Introduction

The laser/arc hybrid welding process was propounded by W. Steen of the Imperial College of Science and Technology in the 1970s.[1,2] A diagram of the hybrid welding process is shown in Fig. 14.1.[2] It combines the heat sources with different physical properties and thermal transmission mechanisms to work together. It not only combines the advantages of laser welding and arc welding but also eliminates their defects.

The advantages of the hybrid welding process over laser welding are the following:[3]

- Higher process stability
- Higher bridgeability
- Deeper penetration
- Greater ductility
- Lower capital investment costs because of savings in laser energy

The advantages of the hybrid welding process over arc welding are the following:[3]

- Higher welding speeds
- Deeper penetrations at higher welding speeds
- Lower thermal input
- Higher tensile strength
- Narrower weld joints

Recently, researchers all over the world have been paying attention to the hybrid welding process and have developed hybrid welding with more hybrid modes such as laser-metal inert gas (MIG),[4,5] laser-plasma[6] and laser-double arc[7] hybrid welding processes. The investigations show that the hybrid welding

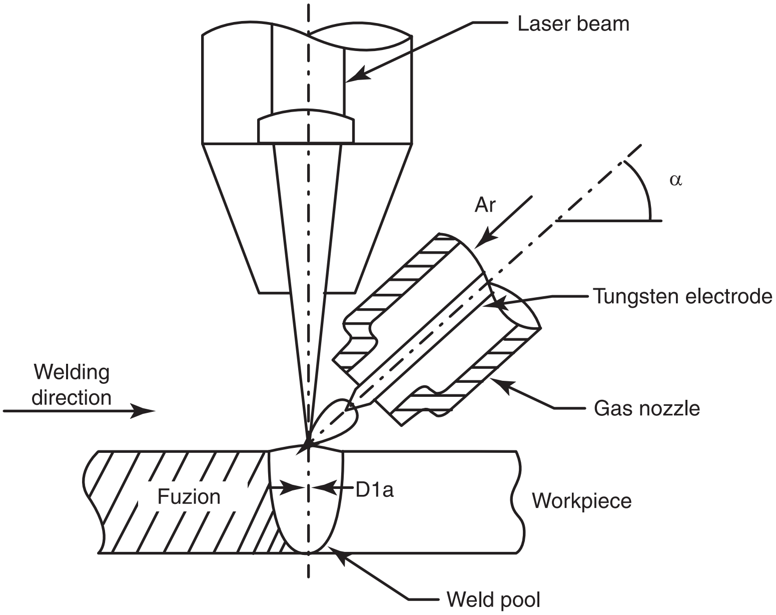

14.1 Hybrid laser-tungsten inert gas (TIG) welding.[2]

process is suitable for welding steel, aluminum, titanium alloy and other alloys.[8–10] It has been applied in the manufacturing of ships and automobiles.[3,11]

In this chapter, research and progress in laser/arc hybrid welding of magnesium alloys will be critically reviewed. Section 14.2 and Section 14.3 introduce low-power laser-arc hybrid welding processes of magnesium alloys, with and without filler metal, in detail, including the welding technology, microstructure, mechanical properties and so on. Section 14.4 introduces some applications of low-power laser/arc hybrid welding processes in the manufacture of magnesium alloy products. Section 14.5 depicts the existing problems in hybrid welding of magnesium alloys and views the developing trend of the hybrid welding process.

14.2 Low-power laser/arc hybrid welding of magnesium

In the research of welding magnesium alloys, the Institute of Welding Technology at Dalian University of Technology propounds the low-power laser/arc hybrid welding technique. Liu et al.[12] explain that when low-power laser beam is coupled with tungsten inert gas (TIG) arc, the weld penetration of hybrid welding is two times deeper than that of TIG welding and the weld joint shows good mechanical properties.

14.2.1 Morphology of the welded seam

Figure 14.2[12] shows the weld appearance and macro-sections of the TIG welding, laser welding and hybrid welding processes. The welded seam by laser welding alone is narrow without any defects (Fig. 14.2a) and that by TIG welding alone is wide with a low depth-to-width ratio (Fig. 14.2b), while in hybrid welding, the depth-to-width ratio is larger and the welded seam appears wavy (Fig 14.2c). The penetration of the hybrid welding seam is the deepest – four times deeper than that of laser welding and two times deeper than that of TIG welding under the same conditions, which proves the synergic characteristics of low-power laser/arc hybrid welding.

Figure 14.3[13] shows the typical appearance of magnesium alloy joints of AZ31 to AZ31 and AZ31 to AZ91 welded by laser-TIG hybrid welding process. Continuous weld seams without crack and surface pores are obtained. It is observed that the similar joint of AZ31 to AZ31 takes on ripples just like scale, but the dissimilar joints of AZ31 to AZ61 and AZ91 are smooth.

Figure 14.4[13] shows the macroscopic cross-sections of dissimilar welds. There is a large heat-affected zone (HAZ) at the side of AZ61 and AZ91 but narrow HAZ at the side of AZ31. This is attributed to the difference in magnesium alloys' surface tension and thermoconductivity with the increase in Al content.

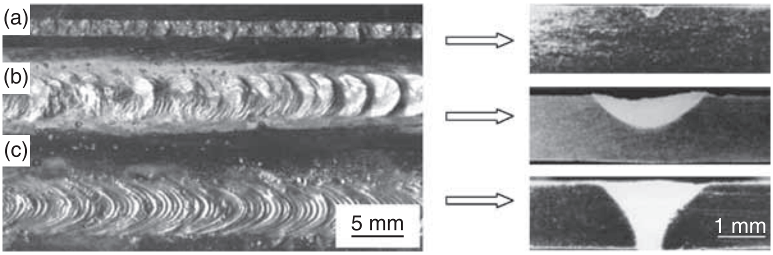

14.2 Comparison of welded joints and macro-sections.[12] (a) Laser welding. (b) TIG welding. (c) Hybrid welding. (I_{arc} = 100 A; P_{laser} = 400 W; h = 1.5 mm; f_d = −1.0 mm; D_{LA} = 1 mm; V = 1500 mm/min).

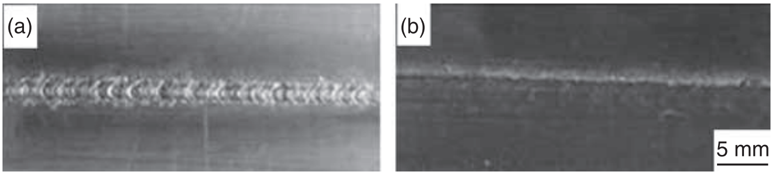

14.3 The appearance of joints of AZ31 to AZ31 and AZ31 to AZ91.[13] (a) AZ31 to AZ31. (b) AZ31 to AZ91.

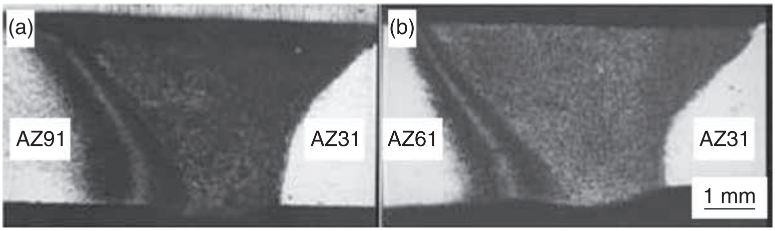

14.4 Cross-section of laser-TIG hybrid-welded magnesium alloys.[13] (a) Dissimilar weld of AZ91 to AZ31. (b) Dissimilar weld of AZ61 to AZ31.

14.2.2 Influences of welding parameters

Arc power

Figure 14.5[14] shows the effect of arc power on the weld penetration in hybrid welding, in which the laser power is constant at 300 W. The penetration of a hybrid welding joint is much deeper than the sum of TIG welding and laser welding, even two times deeper than the sum when arc power increases to a specific value. The value of arc power increases with the increase of welding speed. The intensifying effect of hybrid welding penetration is more noticeable at a higher welding speed. When the laser power is less than 500 W, the hybrid welding effect is good when the arc power is two times higher than the laser power.

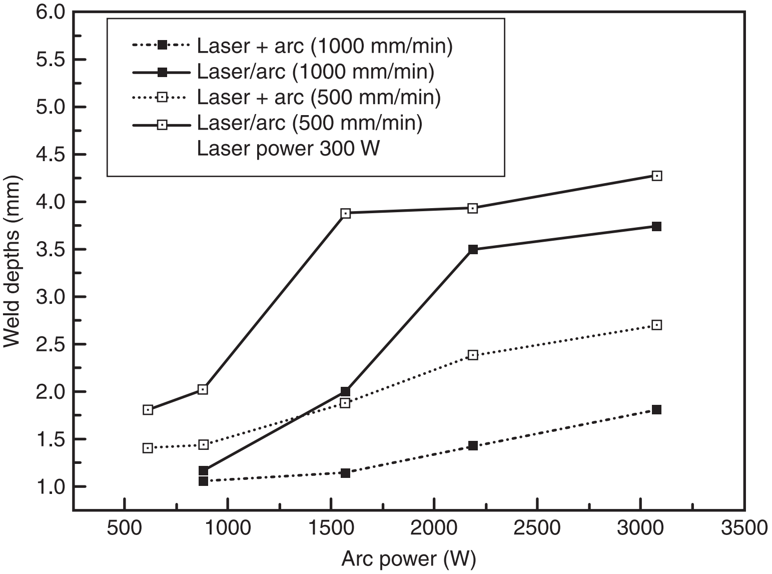

14.5 The variation of weld depths as a function of arc power in AZ31B.[14]

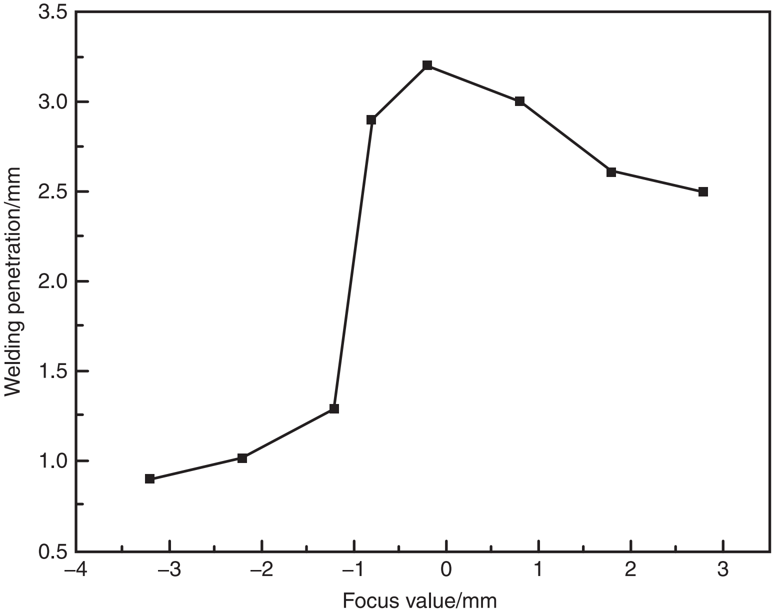

14.6 The influence of focus value on welding penetration.[15] (P = 400 W; f_d = –0.8 mm; I = 100 A; h = 2 mm; D_{LA} = 2.0 mm; V = 1200 mm/min; argon = 10 l/min).

Defocusing value

Figure 14.6[15] shows the effect of defocusing value on the weld penetration in hybrid welding. The defocusing value means the position of laser focus relative to the surface of the workpiece, which influences the power density of the laser beam affecting the surface of base metal and the flow of the molten pool. When the defocusing value is within the range of –0.8 to 0.8 mm, the penetration of the hybrid welding joint is deepest and the formation of the weld seam is best. When it exceeds –1.2 mm, the cross-section of hybrid weld seam is the same as that of TIG welding and the effect the of laser beam on the weld penetration disappears. Therefore, it is important to give preference to the suitable defocusing value in low-power laser/arc hybrid welding process.

Welding speed

Figure 14.7[15] shows the effect of welding speed on the weld seam. With the increase of the welding speed, both the weld width and penetration decrease sharply. This is because the thermal input to base metal decreases for the increase in welding speed. In low-power laser/arc hybrid welding of magnesium alloys, the welding arc is still stable at a high welding speed, even at 1500–2000 mm/min.

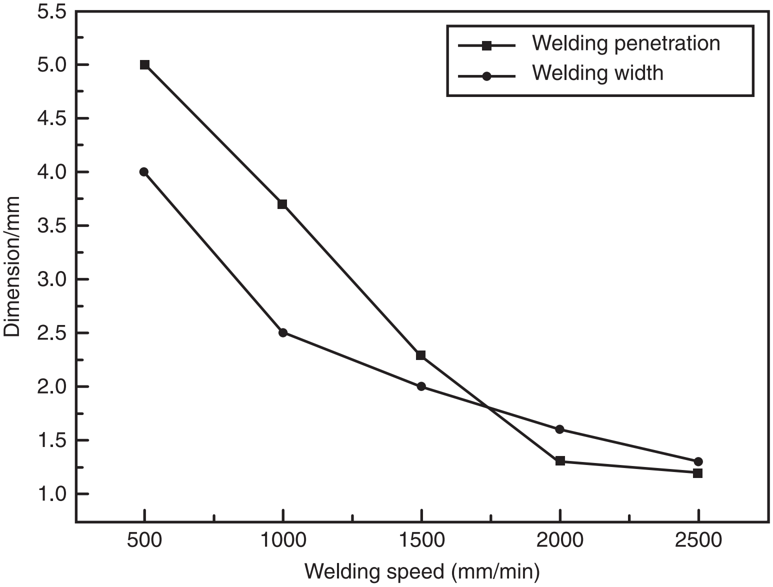

14.7 The influence of welding speed on welding quality.[15] (I = 120 A; P = 300 W).

Distance between laser and arc (D_{LA})

Figure 14.8[15] shows the effect of D_{LA} on the formation of the weld seam and penetration. D_{LA} is the distance between laser beam and tungsten electrode, which is the most important parameter to affect the interaction between laser beam and arc plasma. It is observed that the weld penetration increases remarkably with the decrease of D_{LA}, but the penetration decreases when D_{LA} is less than 0.5 mm. When D_{LA} is too short, the tungsten electrode will be burnt by the laser beam and it will worsen the instability of arc plasma and induce the defects such as spattering and tungsten inclusion. Therefore, in low-power laser/arc hybrid welding of magnesium alloys, D_{LA} is preferred between 1.0 and 1.5 mm.[15]

Combining the effects of welding parameters on weld joints, the optimal hybrid welding parameters for magnesium alloy are listed in Table 14.1.[14]

Table 14.1 The optimal hybrid welding parameters for magnesium alloy[14]

Parameters	P_{arc}/P_{laser}	Defocusing value	Arc length (mm)	Welding speed (mm/min)	D_{LA} (mm)
Value	2	–1.0	1.0	1000	1.5

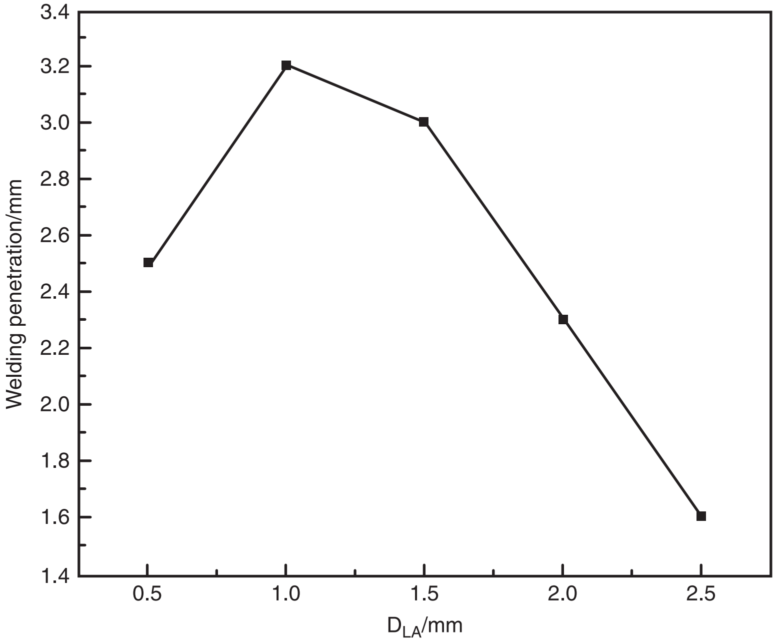

14.8 The influence of D_{LA} on weld penetration.[15] (P = 400 W; I = 100 A; V = 1500 mm/min; f_d = –0.8 mm).

14.2.3 Microstructure

Figure 14.9[12] shows the microstructure of a hybrid welding joint. As is shown in Fig. 14.9(a), the microstructure of the base metal AZ31B is equiaxed grain. The transition region between the HAZ and the welded zone is revealed in Fig. 14.9(b), in which the fusion line is marked by the arrow. It can be seen that the microstructure in the transition region is homogeneous and that it combines well with the other two adjacent zones.[12]

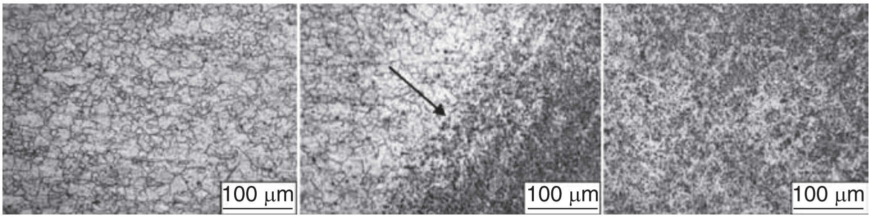

14.9 Microstructure of welded joint by hybrid welding.[12] (P = 400 W; V = 850 mm/min; I_{arc} = 100 A; f_d = –1 mm; D_{LA} = 1 mm).

Due to welding thermal cycles, the crystal grains in the HAZ become uniform and the crystals do not grow noticeably. For the high speeds of welding and heat transmission of magnesium alloys, there is a cast quenching structure in the fusion zone (FZ) (Fig. 14.9c), which is made up of exiguous equiaxed grains. When welded by TIG, the crystal grain in HAZ is large (Fig. 14.10), so it harms the welded seam.

Figure 14.11[13] shows the microstructures of AZ31, AZ61 and AZ91. The fibered microstructure is found in AZ31 base metal. The AZ61 Mg alloy shows equiaxed structure and the average grain size is about 30–50 μm. The microstructure of AZ91 is composed of a primary phase and some $Mg_{17}Al_{12}$ (β phase) distributing along the grain boundary.

The microstructures of AZ31 to AZ61 and AZ31 to AZ91 are similar. Figure 14.12 shows the typical microstructure of a dissimilar joint of AZ31 to AZ91.[13] Figure 14.12(a) shows a large HAZ at the side of AZ91 in dissimilar joints, in which no grain coarsening is found. A cellular solidification structure

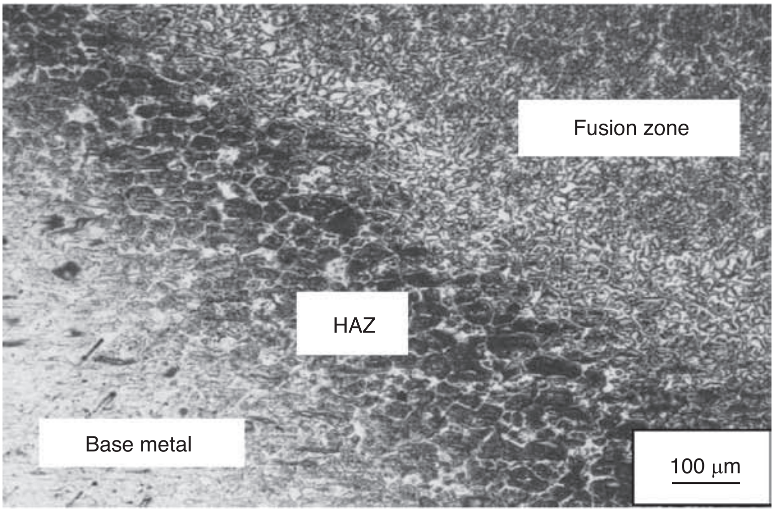

14.10 Microstructure of welded joint by TIG.[12] (I_{arc} = 60 A; V = 500 mm/min).

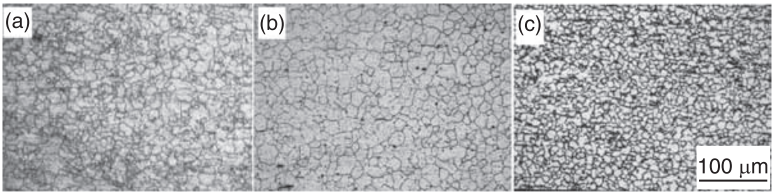

14.11 Microstructure of magnesium alloys AZ31, AZ61 and AZ91.[13] (a) AZ31. (b) AZ61. (c) AZ91.

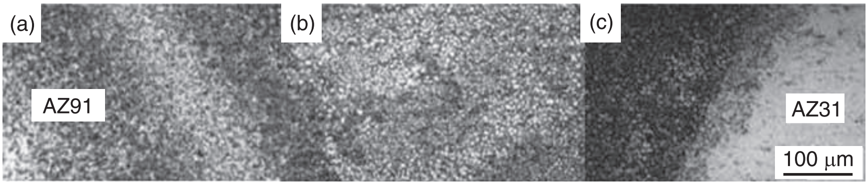

14.12 (a)-(c) The microstructure of AZ91 to AZ31 joint.[13]

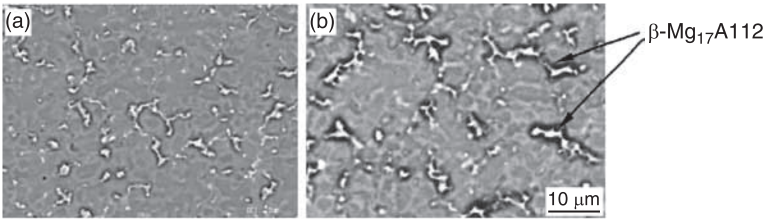

14.13 The back scattering electron image of weld metal.[13] (a) Dissimilar weld of AZ61 to AZ31. (b) Dissimilar weld of AZ91 to AZ31.

can be observed in the FZ, which shows a more globular grain shape, as shown in Fig. 14.12(b). The rapid cooling during laser-TIG hybrid welding leads to a significant grain refinement compared to the initial structure shown in Fig. 14.12(c). Moreover, Fig. 14.12(c) shows the HAZ at the side of AZ31 in dissimilar joints, which is narrow. Figure 14.13[13] shows the back scattering electron image of AZ31 to AZ61 and AZ91 weld fusion. There is abundant β phase at the boundary of grain, which is composed of 75.02wt% Mg and 20.35wt% Al by electron microprobe analysis (EPMA).

To observe the element distribution in the weld metal, the main elements, such as Mg, Al, Zn and O, are analyzed using EPMA, and the results are shown in Plate V (in colour section between pages 210 and 211).[15] Distribution of Al and Zn represent enrichment at the crystal boundary, especially as white spots marked by arrows. The white spot is a kind of Mg-Al-Zn intermediate compound. Moreover, the O content within weld metal is very high, which mainly distributes around the white spot. In overlap welding, argon gas cannot provide effective shielding to prevent O between the sheets from invading the welding area. Both Mg and Al are active elements, which will be readily oxidized.

14.2.4 Mechanical properties

Table 14.2[16] shows the results of the tensile tests, in which the joint efficiency is defined as the ratio of the joint tensile strength to the base metal. The tensile strength of hybrid welding joint is higher than that of TIG welding. The strength of AZ31B in similar joints of hybrid welding can approach or even exceed that of

Table 14.2 Selected data obtained from the base metal and as-welded tensile specimens of Mg alloys produced by hybrid welding and TIG welding[16]

Materials	Welding style	Welding process	Tensile strength (MPa)	Joint efficiency (%)	Fracture position
AZ31B	Base	—	253	—	—
AZ61	Base	—	295	—	—
AZ91D	Base	—	325	—	—
AZ31B	Similar	Laser/arc	250	99	BM
AZ31B	Similar	Laser/arc	248	98	BM
AZ31B	Similar	Laser/arc	253	100	BM
AZ31B	Similar	TIG	236	93	HAZ
AZ31B	Similar	TIG	241	95	HAZ
AZ31B	Similar	TIG	234	92	HAZ
AZ31B–AZ61	Dissimilar	Laser/arc	255	101	BM(AZ31B)
AZ31B–AZ61	Dissimilar	Laser/arc	259	102	BM(AZ31B)
AZ31B–AZ61	Dissimilar	Laser/arc	257	102	BM(AZ31B)
AZ31B–AZ91D	Dissimilar	Laser/arc	261	103	FZ
AZ31B–AZ91D	Dissimilar	Laser/arc	259	102	FZ
AZ31B–AZ91D	Dissimilar	Laser/arc	254	100	FZ
AZ61–AZ91D	Dissimilar	Laser/arc	252	85	FZ
AZ61–AZ91D	Dissimilar	Laser/arc	234	79	FZ
AZ61–AZ91D	Dissimilar	Laser/arc	237	80	FZ

the base metal, which are fractured most in base metal owing to the narrow HAZ and grain refinement in FZ. Moreover, the tensile specimens of AZ31B to AZ61 joints are fractured at the side of AZ31B base metal, while that of AZ31B to AZ91D and AZ61 to AZ91D are fractured at the weld FZ. Moreover, the impact ductility of hybrid welding joint attains 113% of that of base metal, much higher than that of TIG welding.

Figure 14.14[17] shows the results of fatigue test of AZ31B joints and base metal. It was observed that the fatigue property of AZ31B welded by laser-arc hybrid welding is higher than that of base metal at different stress levels, as well as that of the strengthened joint. The fatigue property of AZ31B welded by TIG is evidently lower than that of AZ31B welded by laser-arc hybrid welding process and base metal. On the basis of the curve of strength-cycle number (S-N), the cycle number of the joint welded by laser-arc hybrid welding is 128% of the base metal at a stress level of 140 MPa, 120% at a stress level of 110 MPa and 100% at a stress level of 80 MPa, while the cycle number of the joint welded by TIG is only 71% of the base metal at a stress level of 140 MPa, 83% at a stress level of 110 MPa and less than 72% at a stress level of 80 MPa. This is because, comparing with TIG welding of magnesium alloys, the HAZ is narrow and the crystal grains are exiguous in hybrid welding. Moreover, the defects, such as gas porosities and cracks, can be avoided effectively in hybrid welding.

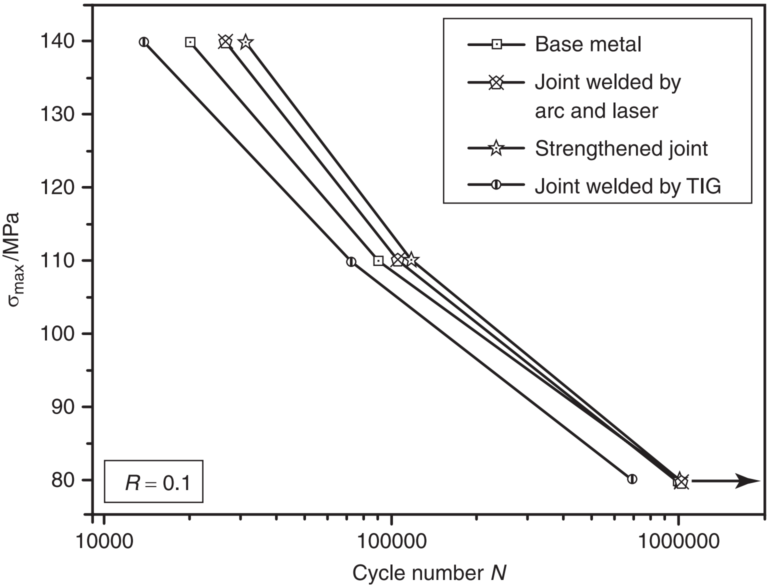

14.14 The tensile results of the welded joints.[17]

Measurements of the microhardness are conducted to detect submicroscopic changes in the structure, especially in the HAZ. The results are used to evaluate the influence of the laser-TIG welding process on the mechanical properties of the joints. The hardness in the FZ and HAZ of AZ61 and AZ91 shows a larger change relative to the base metal due to the existing β phase, while no change occurs relative to AZ31, which are shown in Fig. 14.15–Fig. 14.17.[18]

Figure 14.18 and Fig. 14.19 show the hardness of both dissimilar joints.[13] It is found that the hardness in weld zone is noticeably higher than that of each base metal in both dissimilar joints, which fluctuates due to the existence of β phase

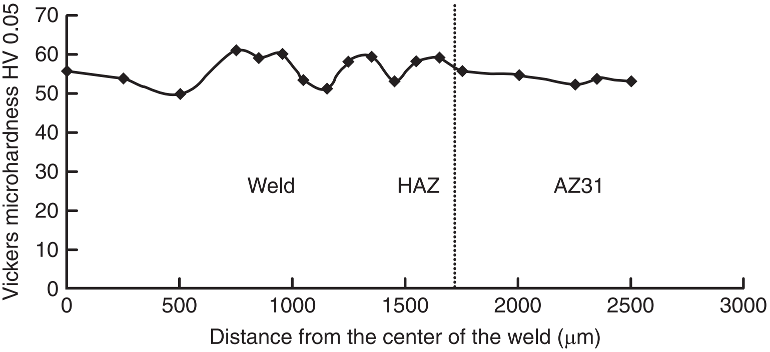

14.15 Hardness profile across weld in AZ31.[18]

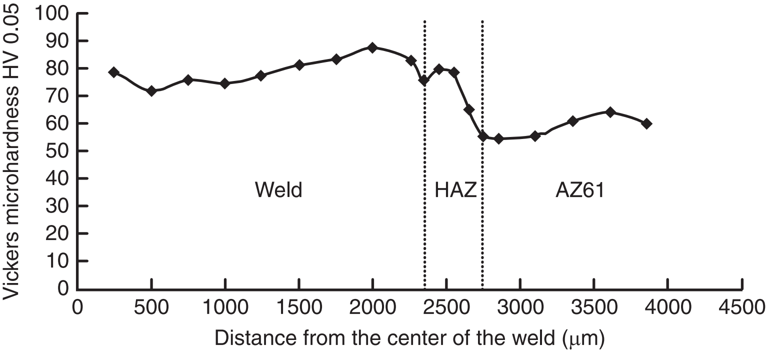

14.16 Hardness profile across weld in AZ61.[18]

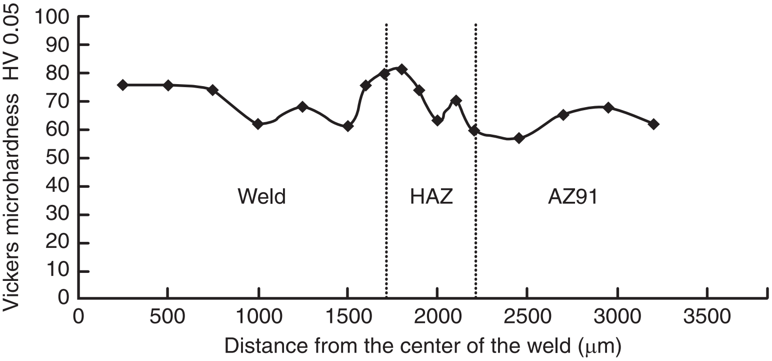

14.17 Hardness profile across weld in AZ91.[18]

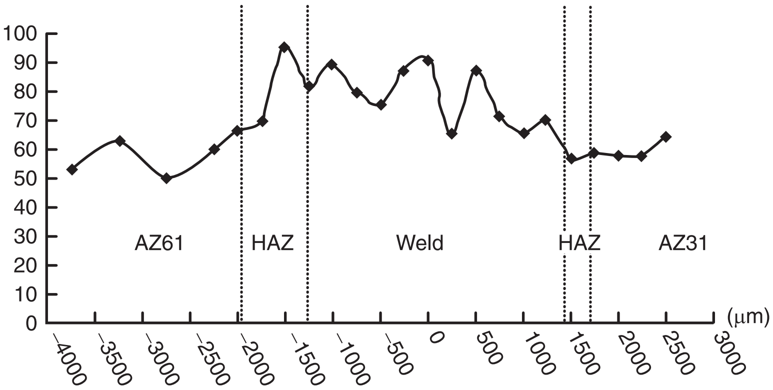

14.18 Hardness profile in the weld of AZ61 to AZ31.[13] Laser power: 400 W; TIG current: 100 A; welding speed: 1000 mm/min.

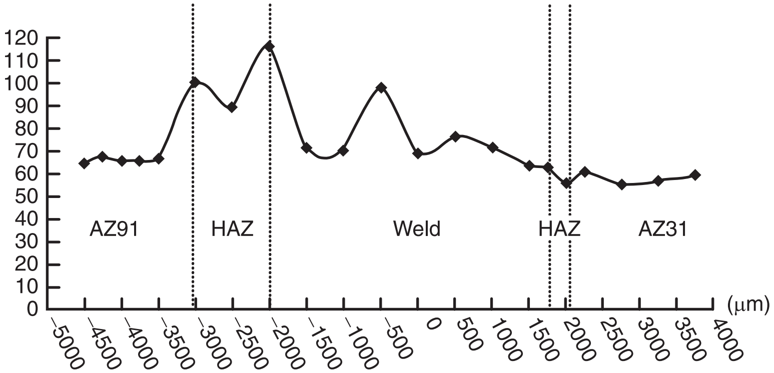

14.19 Hardness profile in the weld of AZ91 to AZ31.[13] Laser power: 400 W; arc current: 100 A; welding speed: 1000 mm/min.

($Mg_{17}Al_{12}$) distributed along the boundary of grain. Moreover, the HAZ hardness augmentation at the side of AZ61 and AZ91 is found in both dissimilar joints, while that at the side of AZ31 is without change compared to AZ31B base metal.

14.2.5 Porosity

One of the major concerns during the high-speed welding of magnesium alloys is the presence of porosity in the weld metal that can deteriorate mechanical properties. Figure 14.20[19] shows the top-face of a hybrid welding joint treated by a milling machine. Lots of pores are found in the weld metal and most of them appear from the center of the weld metal arranged in line. The cross-section of pores is shown in Fig. 14.21,[19] from which it is observed that the wall of pores is not smooth and some reactants accumulate. The dimension of pores is more than 0.5 mm, most of which often distribute in the under-part of weld metal.

The element profile of pore is analyzed by EMPA. The contents of O and N in pores are excessive, which are up to 24.8% and 9.4%, respectively. It can be

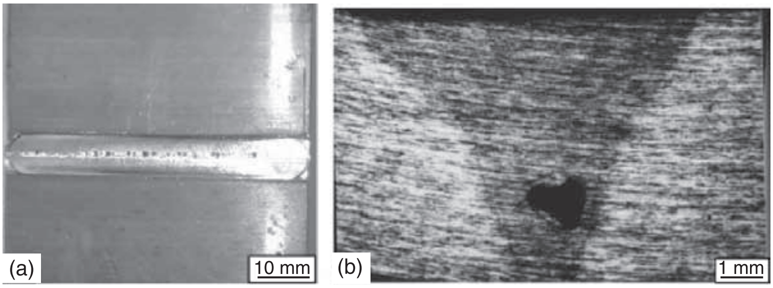

14.20 Macrographs of AZ31B weld joint.[19] (a) Top view of weld. (b) Cross-section of weld.

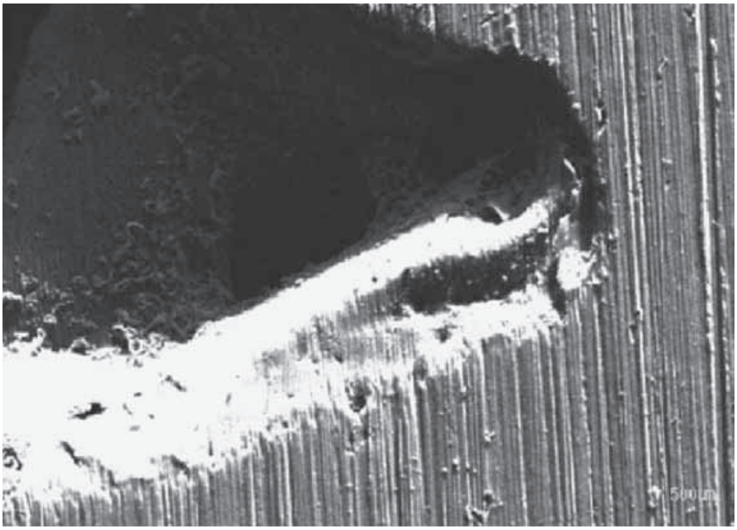

*Ratio [Correction = ZAF1]

No.	ELE.	Crystal	W.L. (A)	PKI – BGI	STD(I)	I–Ratio	WT(%)	Mol (%)	ELE.
1	Mg Ka	RAP	9.8300	91284.24	3178.43	3.8425	63.359	51.762	Mg
2	N Ka	PBST	31.6000	62.60	29.83	2.0348	24.852	35.230	N
3	O Ka	RAP	23.6200	27.33	41.75	0.6560	9.435	11.710	O
4	Al Ka	RAP	8.3333	483.60	3725.88	0.1288	1.830	0.878	Al
5	Zn Ka	RAP	12.2540	83.43	703.22	0.1186	0.890	0.270	Zn
6	Mn Ka	LIF	2.1018	13.29	633.54	0.0210	0.135	0.049	Mn
Total							100.000		

14.21 The element distribution in pore by EMPA.[19]

safely concluded that the air enters into the molten pool during the welding process. Magnesium is so active that it can readily react with oxygen and nitrogen at a high temperature, resulting in the formation of oxide and nitride.

The pore formation is analyzed in Fig. 14.22.[19] During laser-TIG hybrid welding, the molten pool is shielded by argon gas through TIG torch alone. When the workpiece plate is thin enough (less than 1.2 mm), the size of molten pool is small, with a diameter of about 2 mm, especially at a high welding speed. Under this condition, the molten pool can be shielded effectively using TIG torch alone. When the thickness of plate exceeds 1.2 mm, such as 2.5 or 5 mm, with the increase of weld current, the diameter of molten pool is commonly between 5 and 8 mm. It is found that shielding gas through TIG torch does not satisfy the practical demand. Figure 14.22(a) shows that the molten pool consisted of air-intruded area, keyhole area and argon gas-shielded area. If the laser beam is not shielded by argon, the air easily enters the molten pool and forms pores. During the welding process there is a film on the air-intruded area, which produces color in the dark area but the color is shiny in an argon gas-shielding area. It can be concluded that the area containing air is the main source of gas that results in the formation of pores. Moreover, during

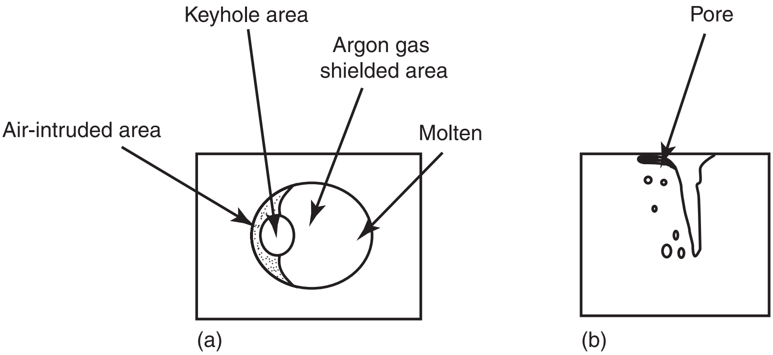

14.22 (a) and (b): Pore formation sketch map.[19]

welding, the laser beam first gets into contact with the air, possibly engulfing the air and even the shielding gas into the bottom of the molten pool, leading to the formation of pores in a line. This is caused by a laser-TIG welding process with a high welding speed and a high cooling rate in weld metal, which does not allow the air enough time to overflow, and so it remains in the weld.

Figure 14.23[19] shows the weld surface by hybrid laser-TIG welding, which utilizes coaxial shielding gas of laser beam and different TIG currents.

In this experiment, the formation of the weld surface is worse and darker when TIG current is lower than 120 A with other parameters as constant. While the current is over 120 A, the formation of the weld surface begins to level up. All this points to the fact that adding laser coaxial shielding gas has a strong effect on arc, and the direction of adding shielding gas can prevent the arc from rooting to the laser impinge spot, which partly leads to arc instability. Only when the arc current is great enough and the stiffness of the arc is strong enough, the arc can be rooted to the laser impingement spot. It is found that there are various threshold values under various welding conditions. Using the coaxial shielding gas, a great arc current is needed to get high-quality joints.

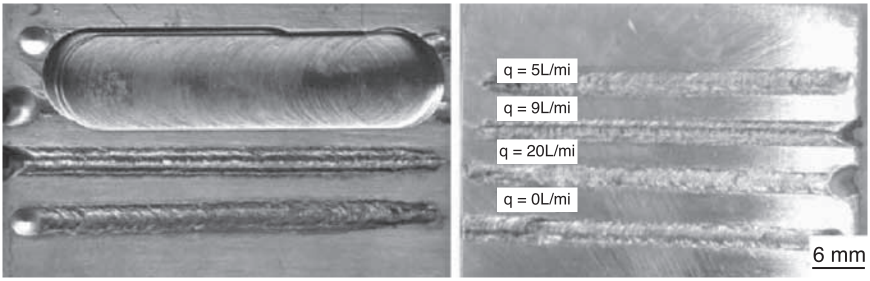

14.23 The amount of pores in weld metal using laser coaxial shielding.[19]

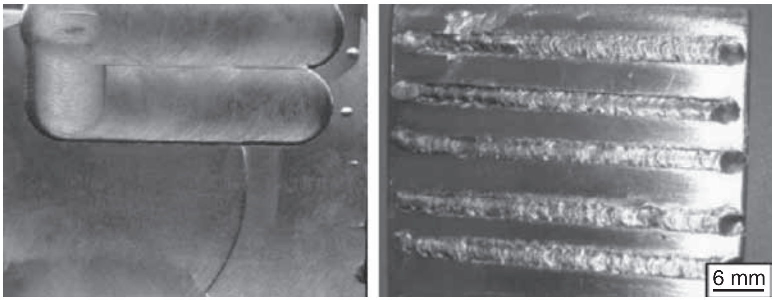

14.24 The amount of pores in weld metal using laser lateral shielding.[19]

Figure 14.23[19] shows the pore amount of the weld metal after adding coaxial shielding gas. It has been found that the pore amount with shielding is evidently less than that without shielding, and the formation of weld deteriorates with the increase in the flow rate of laser shielding gas. Moreover, as the shielding gas is not optimal, a channel and surface pores appear. The flow rate of laser shielding gas also has a strong effect on weld arc stability.

Figure 14.24[19] shows the pore amount of the weld with lateral shielding gas. The weld is continuous and bright. The pores have been restrained.

From the above-mentioned fact, it is evident that low-power laser-TIG hybrid welding process is fit to weld magnesium alloy. The high quality weld joint can be obtained at a much higher speed than with TIG welding. The mechanical properties of weld joints are closer to that of the base metal. Moreover, the energy loss and welding cost are reduced due to the use of low-power laser. It provides an efficient way for the practical manufacturing of magnesium alloys.

14.3 Hybrid welding process with filler metal

The use of filler metal provides many advantages[20] because it can

- compensate for metal loss due to vaporization
- reduce burn-up and weld drop-through
- reduce porosity
- control seam compositions to reduce susceptibility to FZ brittleness or stress from corrosion cracking, or to avoid weld cracks
- promote process stability
- lower the sensitivity to joint gaps and lead to a slightly wider FZ.

Liu and Dong[21] studied TIG welding of magnesium alloy with filler wires. The tensile strength of a TIG weld joint with a filler metal is about 90% of base metal, but the welding speed is only 600 mm/min.

In this section, the filler wire is used in a low-power laser/arc hybrid welding process to weld magnesium alloy. The welding process is introduced in detail.

14.3.1 Welding mode

Figure 14.25 shows the feeding modes of filler wires in low-power laser/arc hybrid welding processes. In front-feeding mode, the filler wire is in front of the molten pool and is melted by TIG arc, then the filler metal is mixed into molten pool under the action of laser and TIG arc. In back-feeding mode, the laser beam and TIG arc are mainly used to heat the base metal. The filler wire is melted by the edge of the TIG arc and the thermal conduction of the molten pool.

Figure 14.26 shows the weld appearance of two hybrid welding modes. With the assistance of laser beam, the welding speed of the hybrid welding process is 50% higher than TIG welding. It has been found that the weld formations of the two welding modes are good, but the welding penetration of back-feeding mode

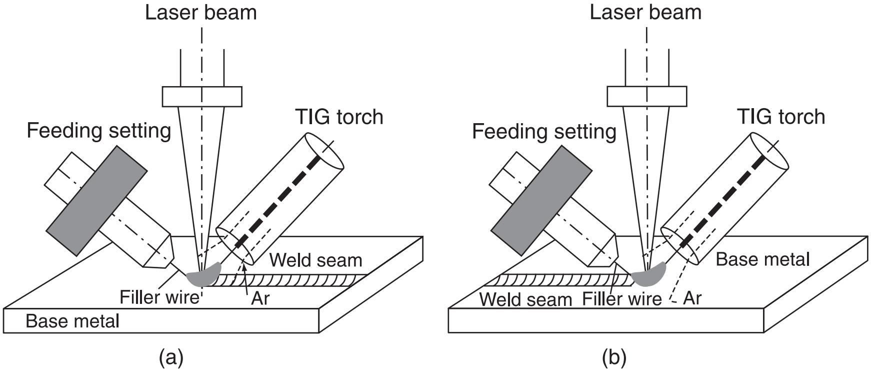

14.25 The hybrid welding process with different feeding modes of filler wire. (a) Front-teeding mode. (b) Back-feeding mode.

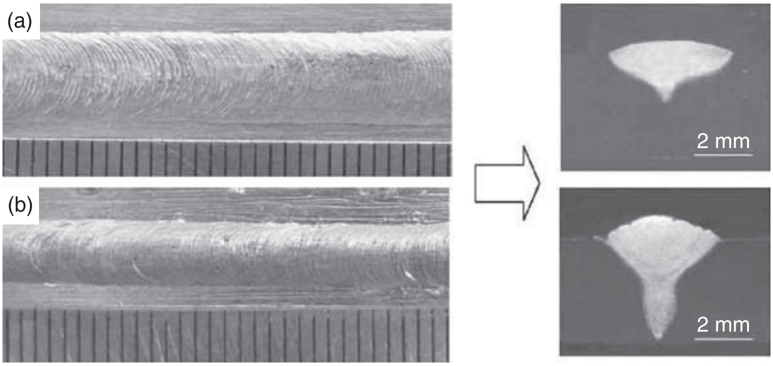

14.26 The appearance of hybrid welding joints with filler wire. (a) Front-feeding mode. (b) Back-feeding mode. Laser power: 350 W; arc current: 120 A; welding speed: 800 mm/min; feeding speed of filler wire: 1.5 m/min.

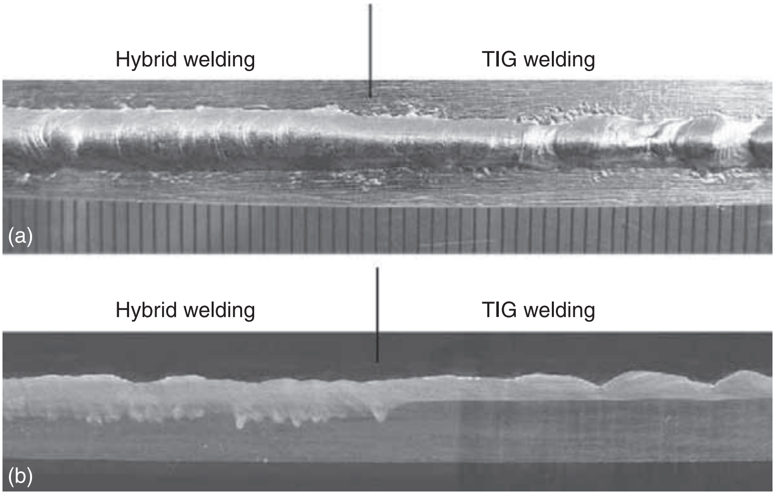

14.27 Comparison of weld joints with back-feeding filler wire. (a) Weld appearance. (b) Weld penetration. Laser power: 350 W; arc current: 100 A; welding speed: 1000 mm/min; feeding speed of filler wire: 1.5 m/min.

is about two times deeper and the weld width is narrower than that in front-feeding mode. This is induced by different heating effects. In front-feeding mode, the energy of the laser beam and TIG arc is mostly used to melt the filler wire and reheat the droplet. So the welding is wide and it is insufficient to get deep penetration. In back-feeding mode, the effect of filler wire on the laser beam is weak and the hybrid effect between the laser beam and TIG arc is significant; so, the welding penetration is deeper in this mode than in the former.

Figure 14.27 shows the contrast between a TIG welding joint and a hybrid welding joint with back-feeding mode of filler wire. The weld seam of TIG welding is narrow and discontinuous. The penetration is also shallow. Under the action of laser pulses, the formation of hybrid welding joint is continuous, without welding defects. There is enough reinforcement on the front surface of the weld joint and the welding penetration is much deeper than TIG welding. It indicates that laser pulses can stabilize and intensify arc plasma in the welding process with back-feeding mode of filler wire.

14.3.2 Welding parameters

The effects of welding speed, arc current and arc length are similar to that of TIG welding with filler metal. With the increase of arc current and the decrease of welding speed, both the welding penetration and joint width increase. The arc length has an optimal value to achieve the best welding penetration and joint width. Shorter or longer arc length than the optimal value will induce the decrease of welding penetration.

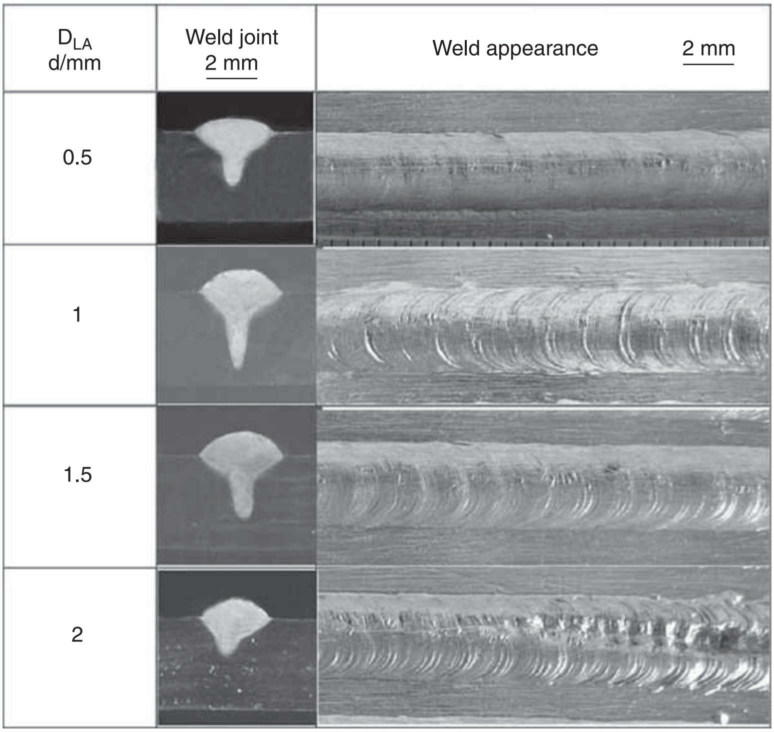

14.28 The influence of D_{LA} on weld formation. Laser power: 350 W; arc current: 120 A; welding speed: 800 mm/min; feeding speed of filler wire: 1.5 m/min.

In the hybrid welding process, the distance between the laser beam and the tungsten electrode (D_{LA}) is an important factor to influence the welding capability. Figure 14.28 shows the influence of D_{LA} on welding penetration and joint width. It is evident that the welding penetration is deep when the D_{LA} is about 1.0 mm. In this case, the assistance effect of laser beam on arc plasma is the best. When the D_{LA} is larger than 1.5 mm, the assistance effect of the laser beam weakens because the laser beam cannot act on the center of the arc plasma and the molten pool. Moreover, the distance between the filler wire and arc plasma is too large, and therefore not effective for the melting of filler wire and weld formation.

The distance between the filler wire and the laser beam is usually kept between 0 and 0.5 mm to avoid spattering induced by the action of laser beam on filler wire.

14.3.3 Welding defects

Figure 14.29 shows the welding defects under unsuitable parameters. The defects are usually induced by the improper feeding speed of filler wire and the distance

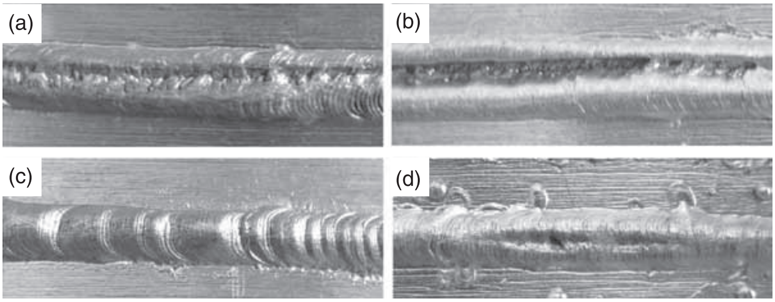

14.29 Common defects in the hybrid welding process with back-feeding filler wire. (a) Nick. (b) Division of molten pool. (c) Globular transfer. (d) Spattering and nick.

between filler wire and heat resource. The defects shown in Fig. 14.29(a), (b) and (d) are induced by insufficient melting of filler wire when the feeding speed of the filler wire is too high or the distance between filler wire and heat source is large. The insufficient melting of filler wire will extend to the laser beam, which not only induces spattering but also distorts the weld formation. When the filler wire is fed insufficiently, there will be a large droplet at the tip of the filler wire and the filler metal will be fed in a globular transfer mode. In this case, the weld seam is discontinuous and bumpy, as is shown in Fig. 14.29(c). So, in a hybrid welding process with a back-feeding mode of filler wire, the feeding speed of filler wire and the distance between filler wire and laser beam should be set appropriately.

14.3.4 Weld microstructure

Figure 14.30 shows the typical microstructure of a hybrid welding joint with back-feeding mode of filler wire. Figure 14.30(b) shows that the microstructure of base metal is composed of equiaxed grains and that the sizes of grains are non-uniform. The HAZ is narrow and the fusion line is clear in Fig. 14.30(a) and (c). During the hybrid welding process, the grains in FZ and HAZ become uniform and the HAZ coarsens.

14.3.5 Tensile strength

The average tensile strength of a hybrid welding joint is about 246 MPa, about 95% of base metal (260 MPa). It is higher than that of a TIG welding joint with filler metal (90% of base metal), as mentioned in the study by Liu and Dong.[21] The weld joint fails at the HAZ, and it is induced by the microstructure of the HAZ, in which the grains are the coarsest.

Figure 14.31 shows the scanned photograph of a fracture of a hybrid welding joint. We can see that there are lots of dimples in the fracture, while a

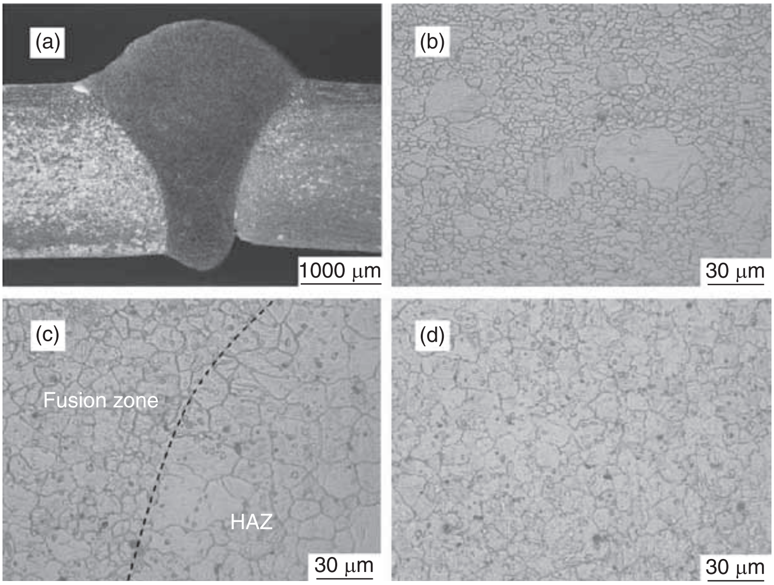

14.30 Microstructure of hybrid welding joint with back-feeding filler wire. (a) Weld joint. (b) Base metal. (c) Heat-affected zone. (d) Fusion zone. Laser power: 350 W; arc current: 100 A; welding speed: 800 mm/min; feeding speed of filler wire: 1.5 m/min.

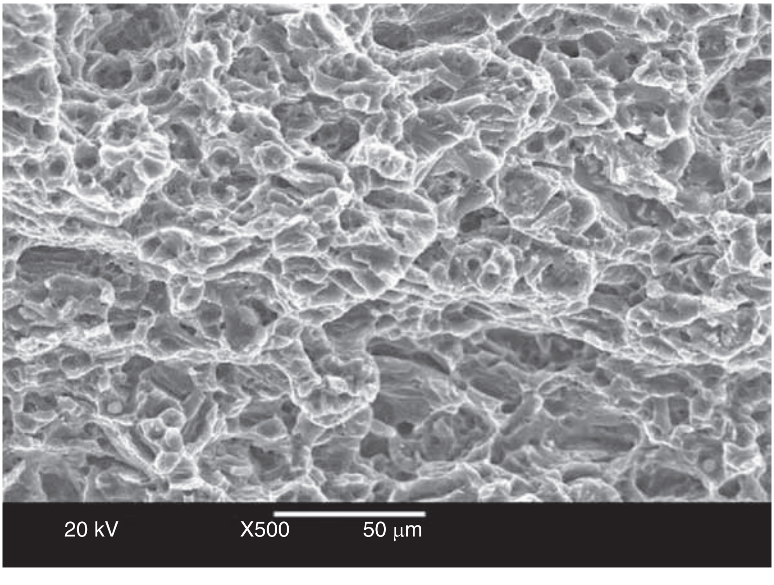

14.31 Scanned photograph of fracture of hybrid welding joint.

quasi-cleavage fracture of short and coarse tearing ridges can also be observed, which demonstrates that the weld bead has a good tensile strength and ductility.

From the above-mentioned facts, it can be deduced that with the assistance of a laser beam, the welding speed of the hybrid welding process is 50% higher than TIG welding. The microstructure and the tensile strength of the weld joint prove that the low-power laser/arc hybrid welding process with back-feeding mode of filler wire can obtain joints with high quality and efficiency.

14.4 Practical application

Laser/arc hybrid welding joints of magnesium alloy have the same capability as the base metal under both steady loads and dynamic loads. They have been successfully applied in the bicycle and automotive industries. Samples and products for magnesium alloy bicycle and autocycle are shown in Fig. 14.32 and Fig. 14.33. Batch production of these magnesium alloy products has been achieved. A low-power laser/arc hybrid welding process has shown excellent economic and social performances.

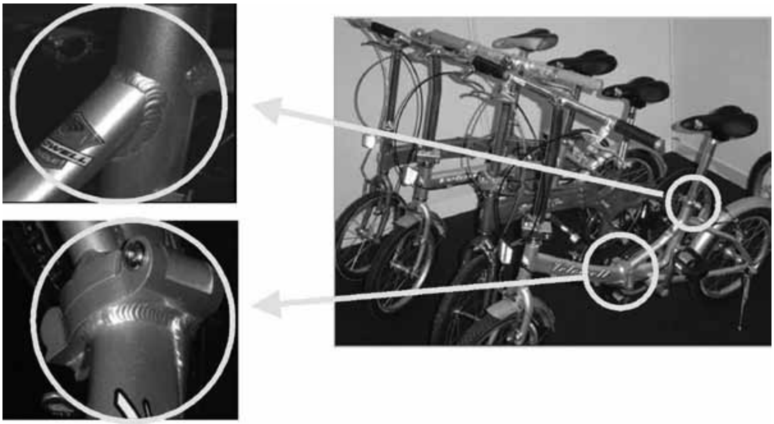

14.32 Products for magnesium alloy bicycle.

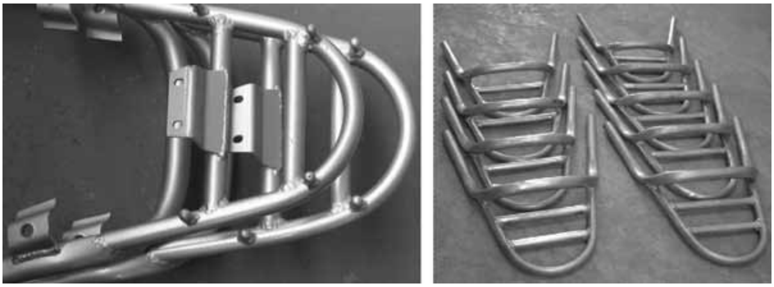

14.33 Products for magnesium alloy autocycle.

14.5 Conclusion and future trends

The low-power laser/arc hybrid welding processes have successfully been applied to weld magnesium alloys at high speeds. The hybrid weld joint has deep penetration and excellent mechanical properties under both dynamic and steady loads, which will expand its application in industry. However, the laser-MIG hybrid welding process of magnesium alloy has not been realized to solve problems resulting from the physical properties of magnesium. So, it is necessary to further develop the laser/MIG hybrid welding processes to meet the need to join thick magnesium plates.

14.6 References

1. Steen WM, Eboo M (1979). Arc augmented laser welding. *Metal Construct* **11**(7): 332–5.
2. Steen WM (1980). Arc augmented laser processing of materials. *J Appl Phys* **51**(11): 5636–41.
3. Graf T, Staufer H (2003). Laser hybrid welding drives VW improvements. *Weld J* **82**(1): 42–8.
4. Gao M, Zeng X, Yan J, Hu QW (2008). Microstructure characteristics of laser-MIG *hybrid welded mild steel. Appl Surf Sci* **254**(18): 5715–21.
5. Kim YP, Alam N, Bang HS (2006). Observation of hybrid (cw Nd:YAG laser+MIG) welding phenomenon in AA5083 butt joints with different gap condition. *Sci Technol Weld Join* **11**(3): 295–307.
6. Vitek JM, David SA, Richey MW, Biffin J, Blundell N, Page CJ (2001). Weld pool shape prediction in plasma augmented laser welded steel. *Sci Technol Weld Join* **6**(5): 305–14.
7. Dilthey U, Keller H (2001). Prospects in laser-GMA hybrid welding of steel. *Proceedings of the 1st International WLT-Conference on Lasers in Manufacturing*, June 2001, Munich pp. 453–65.
8. Swanson PT, Page CJ, Read E, Wu HZ (2007). Plasma augmented laser welding of 6 mm steel plate. *Sci Technol Weld Join* **12**(2): 153–60.
9. Cui L, Kutusna M, Simizu T, Horio K (2009). Fiber laser-GMA hybrid welding of commercially pure titanium. *Mater Design* **30**(1): 109–14.
10. Casalino G (2007). Statistical analysis of MIG-laser CO_2 hybrid welding of Al-Mg alloy. *J Mater Process Technol* **191**(1–3): 106–10.
11. Page CJ, Devermann T, Biffin J, Blundell N (2002). Plasma augmented laser welding and *its applications. Sci Technol Weld Join* **7**(1): 1–10.
12. Liu L, Hao X, Song G (2006). A new laser-arc hybrid welding technique based on energy conservation. *Mater Trans* **47**(6): 1611–14.
13. Liu LM, Song G, Chi MS (2005). Laser-tungsten inert gas hybrid welding of dissimilar AZ based magnesium alloys. *Maters Sci Technol* **21**(9): 1078–82.
14. Song G (2006). Research on low-power laser-tungsten inert gas (TIG) hybrid welding technology of Mg alloy. PhD thesis, Dalian University of Technology, Dalian, 2006.

15. Song G, Liu LM, Wang PC (2006). Overlap welding of magnesium AZ31B sheets using laser-arc hybrid welding process. *Mater Sci Eng A* **429**(1-2): 312–19.
16. Hao XF, Song G (2007). Low-power YAG laser-arc hybrid welding of AZ-based Mg alloy. *Rare Metals* **26**: 67–72.
17. Song G, Liu LM, Chi MS (2005). Laser-TIG hybrid weldability of AZ-based magnesium alloys. *Proceedings of International Conference on Advanced Welding and Joining Technology*, October 20–23, Dalian, pp. B69–B74.
18. Song G, Liu LM, Chi MS, Wang JF (2005). Investigations on laser-TIG hybrid welding of magnesium alloys. *Mater Sci Forum* **488–9**: 371–6.
19. Liu LM, Song G, Liang GL, Wang JF (2005). Pore formation during hybrid laser-tungsten inert gas arc welding of magnesium alloy AZ31B-mechanism and remedy. *Mater Sci Eng A* **390**(1–2): 76–80.
20. Cao X, Jahazi M, Immarigeon JP, Wallace W (2006). A review of laser welding techniques *for magnesium alloys*. *J Mater Process Technol* **171**(2): 188–204.
21. Liu LM, Dong CF (2006). Gas tungsten-arc filler welding of AZ31 magnesium alloy. *Mater Lett* **60**(17–18): 2194–7.

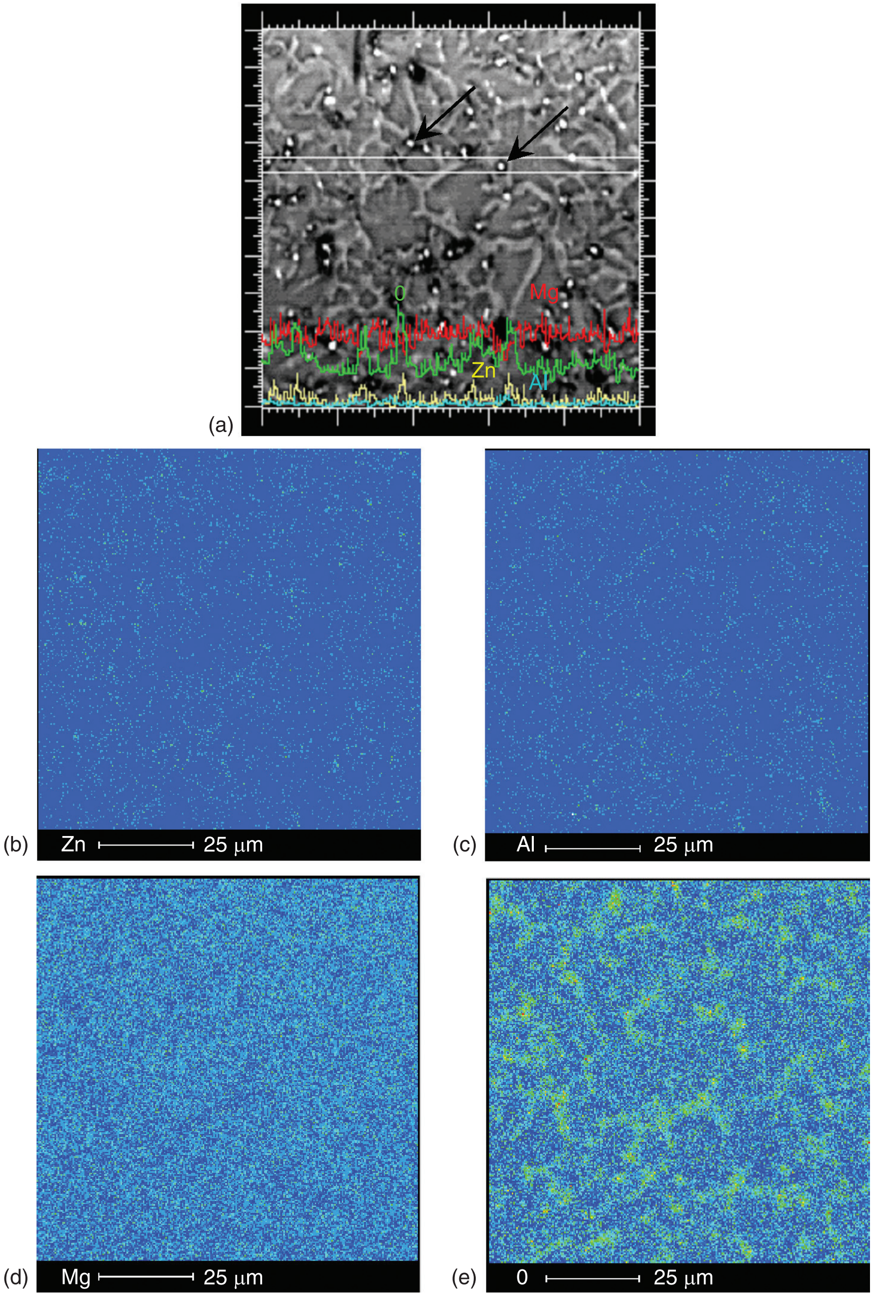

Plate V (a)–(e) EPMA patterns obtained from AZ31B after hybrid overlaps welding.

15

Activating flux tungsten inert gas welding of magnesium alloys

Z.D. ZHANG, Dalian University of Technology, China

Abstract: The activating flux tungsten inert gas welding process can obviously increase the welding penetration of Mg alloy. The mechanisms of activating welding of Mg alloys are discussed with different activating fluxes. The influences of the welding parameters on the penetration of activating welding of Mg alloys joint are analyzed separately. The tensile strengths of welded joint are all about 93% of the base metal.

Key words: magnesium alloy, A-TIG, activating flux, welding arc, welding pool.

15.1 Introduction

Magnesium-based alloys are finding extensive application prospects in the transport industry to decrease the weight of vehicles and prevent contamination during welding, which is a vital step in the production process. The development of an efficient welding process for magnesium requires cosmetic welds at low heat inputs so as to avoid excessive grain growth.[1] High-quality cosmetic welds with smooth weld ripple can be obtained by using alternating current tungsten inert gas (ACTIG) welding that allows fragmentation of refractory oxides during the half cycle when the base becomes an electron-emitting cathode (EP, positive electrode period). However, high penetrations are generated only in the electrode-negative cycle of current (EN period), when the base metal receives the impinging electron. This implies that the average weld penetrations in ACTIG welding remain low. Thus, efforts are made to improve weld penetrations required for a given job. Actually, an improvement in penetration capability in welding has long been a subject of interest for many processes. One of the most notable examples is the application of activating flux in tungsten inert gas (TIG) welding (A-TIG welding). This technique was invented in the 1960s by researchers at the Paton Electric Welding Institute in Ukraine.[2]

When using an activating flux, a thin layer of the flux is deposited on the surface of the joint before welding, using a brush or a dispenser such as a spray. Using activating flux for steels, significant increases in penetration capability of up to 300% have been reported in comparison with the conventional TIG welding process.[3–8] The use of activating flux has also been demonstrated to increase penetration capability substantially in plasma arc welding of steels.[3] A study on laser welding of steels using activating flux indicated that the effect of activating flux on the weld penetration depends on laser welding parameters, that is, penetration increases substantially only when laser welding is performed in the conductive mode.[9] Although activating flux is known to increase the penetration capability in TIG and plasma welding of various steels such as carbon steels and stainless steels, data on Mg alloy welding with activating flux are still limited.[10–13] Such data are important to determine whether the penetration improvement function of the activating flux on Mg alloys can be as effective as that on steels. Although a commonly agreed mechanism for this phenomenon is still being sought, the study of the activating flux on Mg alloy will provide an in-depth understanding of the mechanism for the penetration improvement function of the activating flux.

15.2 Welding mechanism

Several mechanisms for the augmented penetration observed in A-TIG welding have been suggested.[14–16] The relative importance of each mechanism is a function of the chemical composition of the flux and base metal, as well as the process parameters. Although not entirely resolved, the mechanism of arc constriction that raises the current density and creates welds with greater depth-to-width ratios has often been used. Because the flux also chemically interacts with the molten material, a surface tension contribution that originates a Marangoni flow has also been proposed.

For activating welding of Mg alloy, the arc images of TIG welding, both with and without oxide fluxes, were obtained with a high-speed camera and stored in a computer with a frame grabber. The schematic representation of the specimen used in the TIG/A-TIG welding trials is shown in Fig. 15.1. Figure 15.2 shows the arc images of welding magnesium alloy with and without oxide fluxes under the standard welding conditions. For ACTIG welding, it includes EN (negative electrode period) cycle and EP (positive electrode period) cycle. From Fig. 15.2, it can be observed that the arc shape of TIG welding with the use of oxide fluxes is not very different from that produced without flux. The views for EN period

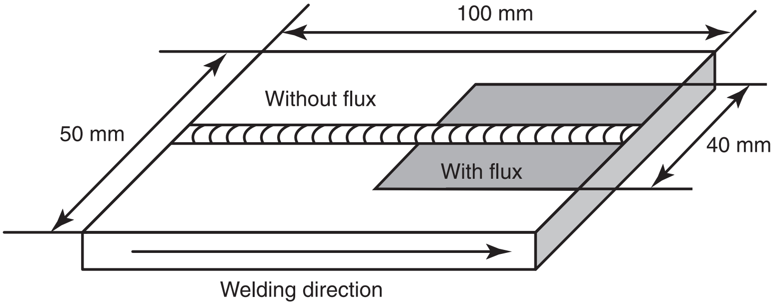

15.1 Schematic representation of the specimen used in the TIG/A-TIG welding trials.

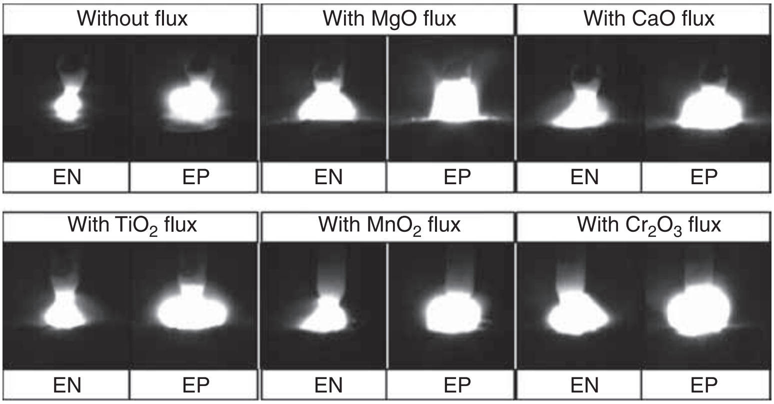

15.2 Arc image of ACTIG welding of Mg alloy with and without oxide fluxes.

suggest that the arc was dispersed when oxide fluxes were present, and the views for EP period suggest that the arc had expanded slightly. The dispersed arc and the expanded arc indicated that the oxide fluxes were vaporized and decomposed into arc. However, the process of electron attachment occurs only in the outer region of the arc for temperatures below 1000 K.[17] Current densities are dominated in the central region of the arc where the electron densities are four to five orders higher in magnitude. The process of electron attachment at the edge of the arc to form negative ions may be too weak to cause arc constriction and affect the electron densities in the central region of the arc in the present process.

In order to study the effect of flux on the weld arc, observations were made when TIG simulation was carried out on a plate with flux applied only on one side. The video showed an asymmetric arc that deviated toward the flux-free side. Figure 15.3 shows the welding configuration. Figure 15.4 shows the images of arc plasma. From Fig. 15.4, it can be observed that the arc deflected to the side of the plate without flux. According to the mechanism of arc electric conduction, the current will pass through the zone where the electric resistance is lowest to form the loop current. The oxide

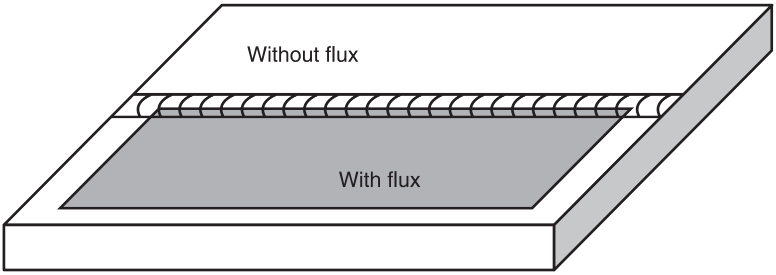

15.3 Welding configuration.

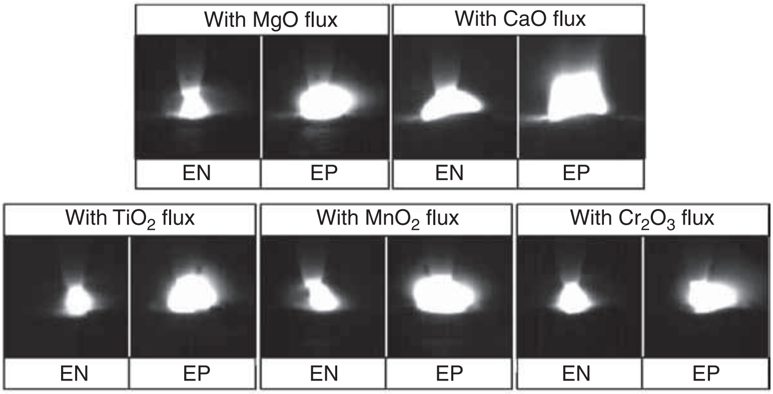

15.4 Arc image of ACTIG welding of Mg alloy with oxide fluxes applied only on one side.

flux, which is usually a metal oxide, covered the surface of the workpiece. This layer will act as an insulation barrier to the arc current. Under the effect of elevated temperature and electromagnetic (Lorentz) forces of arc, the oxide fluxes will enter into the weld arc or the weld pool in response to the physical or chemical property. It will change the component of the weld arc or weld pool, further changing the resistance of conducting channel, which is made up of weld arc, oxide flux layer and weld pool. So, the arcs will deflect to the side without flux where the electric resistance is lower.

The role of flux in increasing weld penetration is obviously very complex, and hence it is not possible to give a complete analysis of all effects or a simple dominant physical mechanism to explain these effects. There are several mechanisms that influence the penetration characteristics, such as Marangoni flow due to surface tension gradient, electromagnetic (Lorentz) forces due to the magnetic field and direction of current, buoyancy forces due to temperature-dependent density differences, and aerodynamic forces due to pressure differences in arc column. At different levels, these mechanisms interact with the flow direction (Fig. 15.5). The change to an inward Marangoni flow and the increase of electromagnetic forces will benefit the increase of weld penetration. The oxide fluxes coated on the surface of welding metal first melt under the high temperature of arc and then decompose into atom. The active element on the surface of the molten pool alters the surface tension gradient from negative to positive and therefore changes the direction of melt flow from outward to inward.

To highlight the comparative importance of different penetration enhancement mechanisms, an yttrium aluminum garnet (YAG) welding laser with a defocused beam was used in place of the arc. The flux is applied only on one side of the joint, as shown in Fig. 15.6. For comparison, TiO_2, $CdCl_2$ and AlF_3 were used as fluxes. The result (see Fig. 15.7) showed that the weld pools with $CdCl_2$ flux and AlF_3 flux were symmetric, but the weld pool with TiO_2 flux became asymmetric. The penetration was very shallow on the flux side when the TiO_2 flux was used. The

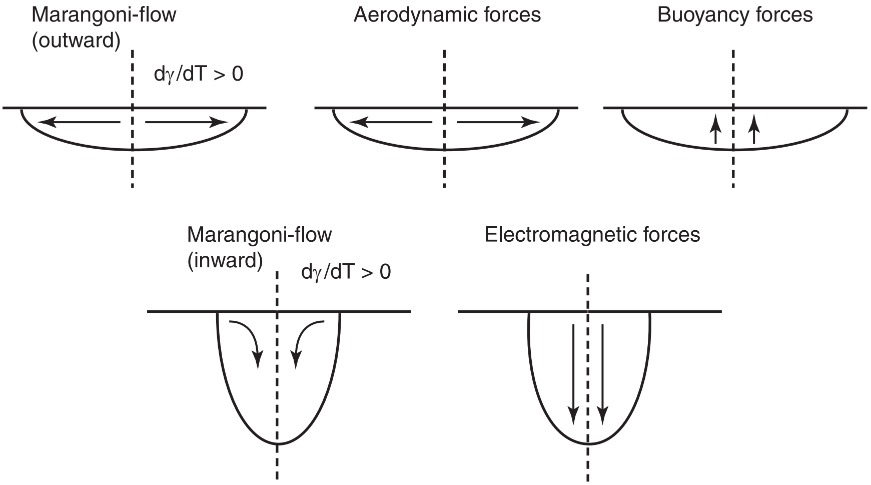

15.5 Different mechanisms affecting the penetration characteristics in TIG welding.

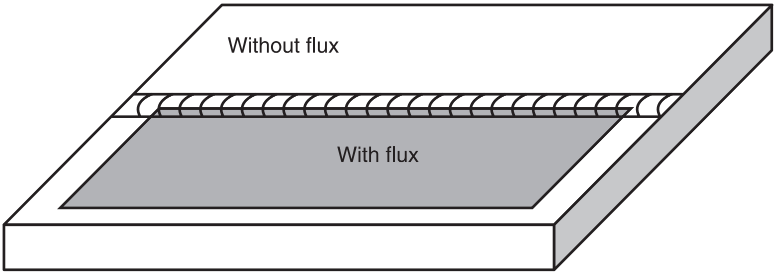

15.6 Welding configuration.

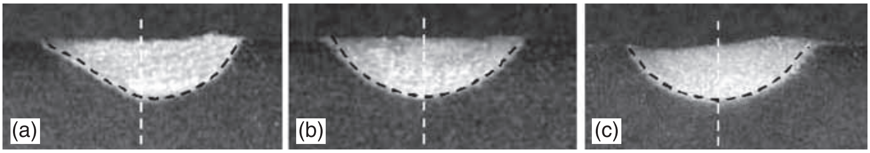

15.7 The effects of the fluxes on the weld shape. (a) With TiO_2 flux. (b) With $CdCl_2$ flux. (c) With AlF_3 flux.

fluid flow appears to be preferentially oriented toward the flux-free side, as schematically presented in Fig. 15.7(a).

The surface tension modifications by the applied flux can help explain the results seen with the defocused laser beam. It shows that the surface tension value increases continuously from one side to the other. Whereas on the free side, the surface tension follows the natural behavior of the metal, the behavior inversion

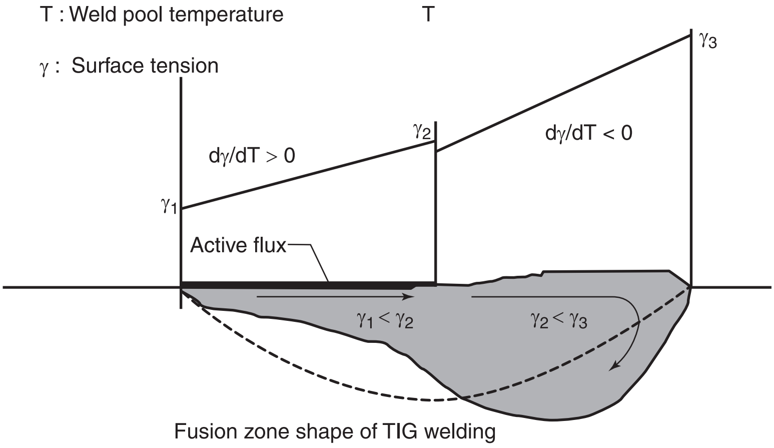

15.8 The effects of the fluxes on the weld shape.

occurs on the flux side with continuous surface tension reduction from the center to the free-surface boundary, as shown in Fig. 15.8. It implies that the applied flux modifies the surface tension temperature coefficients from negative to positive.

Although it cannot be determined whether changing the oxygen content changes the direction of melt flow from outward to inward, it can be used as a kind of mechanism for increasing weld penetration.

In addition, the oxide fluxes will act as an insulation barrier to the arc current. The flux should be melted so that the electric current can penetrate the flux to the weld pool and workpiece. The arc electric resistance will be increased by the insulating effect of the flux. In the experiment, some slag can be seen on the surface of the weld seam welded with oxide flux. It indicated that some oxides do not evaporate to allow arc current to enter the weld pool, and some oxides dissolve into the molten pool. This can also explain the phenomenon of the arc diameter reduction; the unmelted oxide divided the current pathway into a separated zone. For a given current, the current density will be increased in the zone where the flux had been molten and evaporated, leading to increased electromagnetic (Lorentz) forces and aerodynamic forces in the weld pool, resulting in strong convective downward flow in to the weld pool and an increased weld penetration. So, the thermal stability of oxide should be considered, and the undecomposed oxide acts as an insulation barrier to increase the arc pressure on the weld metal.

15.3 Welding parameters

In this section, the influence of the welding conditions on the bead shape of ACTIG welds, both with and without activating flux, was studied, including welding speed, welding current, arc length, shielding gas flowrate and the thickness of activating flux. For the activating flux, oxide, chloride and fluoride were selected.

15.3.1 Effect of welding current

Figure 15.9[18] shows the cross-sections of a group of Mg alloy welds produced with and without activating flux at various current levels. Figure 15.10 shows the effect of welding current on the weld penetration with and without activating flux.

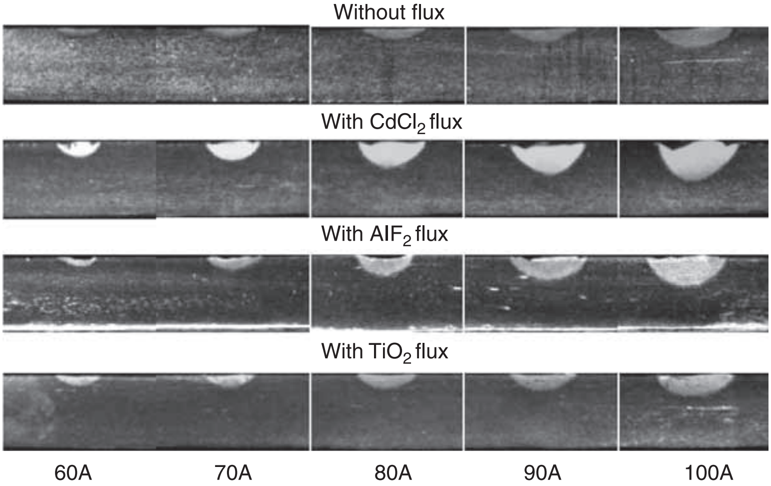

15.9 Cross-sectional macrographs for ACTIG welding of Mg alloy with and without $CdCl_2$, AlF_3 and TiO_2 activating flux at various current levels (welding speed: 360 mm/min; Ar shielding gas flowrate: 10 l/min; arc length: 1 mm).

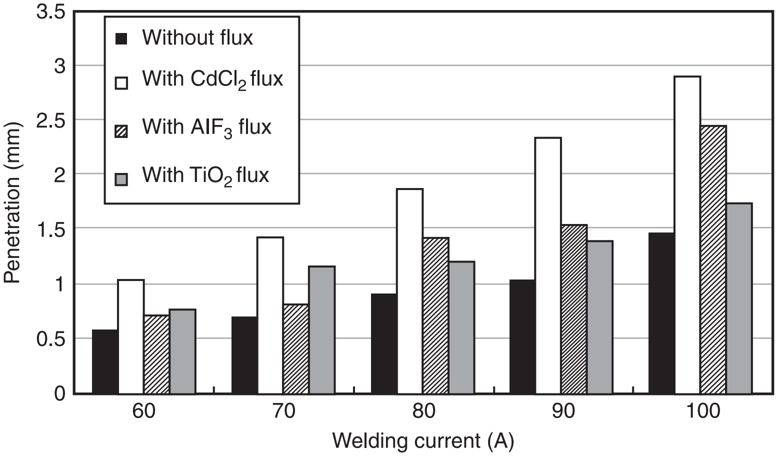

15.10 Effect of welding current in ACTIG welding of Mg alloy with $CdCl_2$, AlF_3 and TiO_2 activating flux and without flux (welding speed: 360 mm/min; Ar shielding gas flowrate: 10 l/min; arc length: 1 mm).

The results show that at all welding current levels, penetration capability increases on applying all three activating fluxes ($CdCl_2$, AlF_3 and TiO_2). The penetration percentage (penetration with activating flux to penetration without activating flux) increase varies from about 117% (with TiO_2 flux) to 227% (with $CdCl_2$flux) at various welding currents, with the different current welds achieving a greater percentage increase. For the $CdCl_2$ flux, a greater penetration percentage increase is achieved when the welding current is 90 A (227%). For the AlF_3 flux, a greater penetration percentage increase is attained under 100 A welding current (167%). For the TiO_2 flux, a greater penetration percentage increase is attained under 70 A welding current (167%). By increasing the welding current, the weld penetration percentage both with and without activating flux increased. It was also found that the weld bead width had few changes with and without activating flux at all welding current levels. In the TIG welding, the current density increases with the increase in welding current. So, the arc cross-sectional area increases, thus increasing the temperature of the arc center and then the penetration. Besides, the capability of activating flux increasing the penetration percentage becomes slow with the increase in welding current.

15.3.2 Effect of arc length

Arc length is critical in determining the arc energy density during TIG welding. For the TIG welding of Mg alloy, the arc length has more impact on the weld penetration and weld surface shape. In the present workpiece, the effect of arc length in ACTIG welding of Mg alloy with activating flux was studied, and four arc lengths were used, namely 0.5, 1.0, 1.5 and 2.0 mm. Figure 15.11 shows the penetration depth versus arc length with different activating fluxes ($CdCl_2$, AlF_3 and TiO_2). It can be clearly seen that in both normal welding and welding with activating flux, when the arc length is 1 mm, the penetration percentages achieve the greatest value, which is 204% with $CdCl_2$ flux, as opposed to 155% with AlF_3 flux and 131% with TiO_2 flux. This is mainly ascribed to the efficiency of the thermal conduction of the welding arc. Generally, during shorter arc (length) welding, the heat of the arc is more readily transferred into the workpiece than diffused to the surrounding environment. The motion speed of the electron in arc is slower when the arc length is too short, such as 0.5 mm, than that with a suitable arc length due to the decrease in welding voltage. This can also be demonstrated by the measured temperature distribution of the TIG welding arc. Moreover, for both short and long arc lengths, the penetration depth increases when activating flux is used. It seems that the effectiveness of the flux is more or less the same at both short and long arc lengths. It should be mentioned that although a shorter arc length can produce a deeper penetration, an excessively short arc length may not be practical because a very small change in arc length could dramatically affect the arc stability. This could be more pronounced when welding over a long distance, as keeping the arc length consistent for a long-distance weld would be difficult and time-consuming.

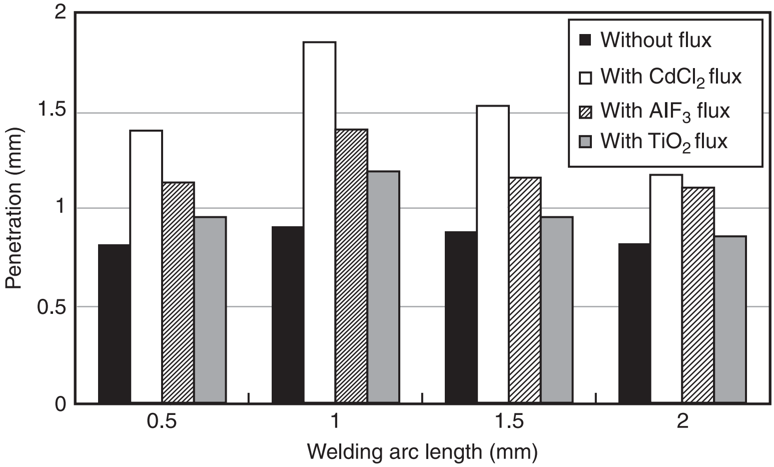

15.11 Effect of welding arc length in ACTIG welding of Mg alloy without flux and with $CdCl_2$, AlF_3 and TiO_2 activating flux (welding current: 80 A; welding speed: 360 mm/min; Ar shielding gas flowrate: 10 l/min).

15.3.3 Effect of shielding gas flowrate

In the TIG welding of Mg alloy, Ar gas was commonly used for shielding gas. In the present chapter, the effect of Ar gas flowrate on ACTIG activating flux welding of Mg alloy was evaluated. Ar gas flowrate changed from 5 to 15 l/min, with an interval of 2.5 l/min. Figure 15.12 shows the effect of Ar shielding gas flowrate on the penetration for ACTIG welding with and without activating flux. It is evident that for welding without activating flux, penetration capability increases with the increase of Ar shielding gas flowrate. The effect of Ar shielding gas flowrate on the penetration depth is different when a different activating flux is used (as different as the activating flux). When the $CdCl_2$ flux and the AlF_3 flux are used, the lower Ar shielding gas flowrate welds achieve a greater increase in penetration percentage, that is, 316% and 162% respectively. When the TiO_2 fluxes are used, the great increase in penetration percentage capability achieved under the larger Ar shielding gas flowrate is about 148%. This indicates that the effect of $CdCl_2$ and AlF_3 fluxes on weld penetration in ACTIG welding of Mg alloy is closely related to the temperature of the weld arc and the gaseous particle. The heat of the arc results from the dissipation of the electrical energy into a resistive medium. This heat also measures the kinetic energy of gaseous particles. The gaseous atoms release electrons and molecules to dissociate into other neutral atoms and/or lighter molecules, before splitting into cations, anions and free electrons. Anions and electrons are attracted to the anode, whereas cations prefer the vicinity of the cathode. In TIG welding, cations are mainly generated by the thermal ionization of metal vapors from the electrodes. With ionic fluxes, like

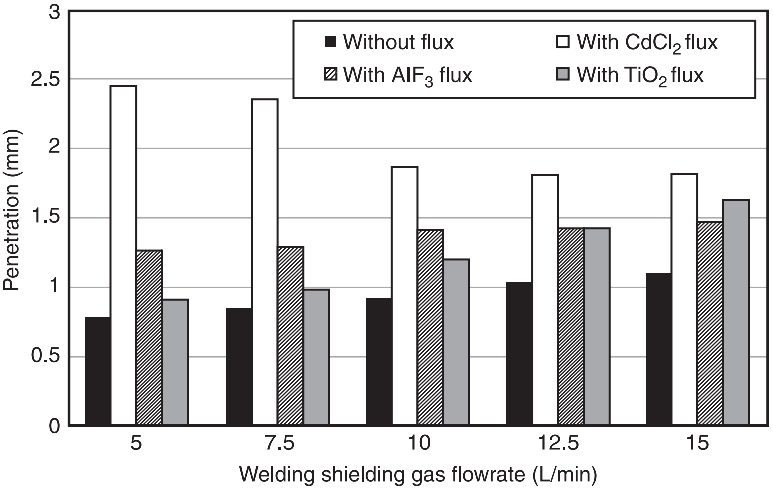

15.12 Effect of welding shielding gas flowrate in ACTIG welding of Mg alloy without flux and with $CdCl_2$, AlF_3 and TiO_2 activating flux (welding current: 80 A; welding speed: 360 mm/min; arc length: 1 mm).

$CdCl_2$, it will influence the metal vapors of the base metal and the gaseous species in the arc.

15.3.4 Effect of welding speed

In the development of modern welding technology, the welding speed is an important welding parameter that marks the welding efficiency. The welding efficiency of TIG welding will be enhanced with the use of activating flux, that is, when the same thickness is achieved in the welding plate, the welding speed of A-TIG welding is higher than that in TIG welding process. In the present study, the effect of welding speed on ACTIG welding of Mg alloy, with and without activating flux, was investigated. Welding speed changed from 300 to 480 mm/min, with an interval of 60 mm/min. Figure 15.13 shows the effect of welding speed on the penetration for ACTIG welding with and without activating flux. The result shows that with the lower welding speed, penetration capability increases on applying the activating flux. The great increase in penetration percentage is achieved when the welding speed is the slowest (300 mm/min), that is, 260% with $CdCl_2$ flux, 188% with AlF_3flux and 137% with TiO_2 flux. The welding speed mainly affects the heat input of TIG welding. For the ACTIG welding of Mg alloy, the heat input is the one of main factors to influence the welding penetration. When the welding speed is slow, the holding time of the molten pool will be prolonged. This is beneficial for the flowing of molten pool metal. It may include a different mechanism in activating flux, thus increasing penetration.

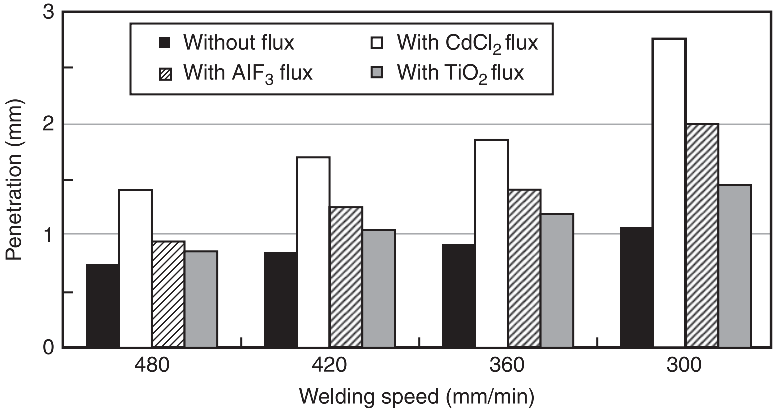

15.13 Effect of welding speed in ACTIG welding of Mg alloy without flux and with $CdCl_2$, AlF_3 and TiO_2 activating flux (welding current: 80 A, Ar shielding gas flowrate: 10 l/min; arc length 1 mm).

15.3.5 Effect of flux thickness

It should be mentioned that results for the effects of welding current, welding arc length, welding shielding gas flowrate and welding speed in the previous sections were all obtained using a thin layer of flux. To demonstrate the effect of flux thickness, both thin and thick layers of fluxes were studied in detail. However, uniform manual pasting of the flux on the Mg alloy surface is difficult. In general, it is easier to achieve a uniform thickness with a thin layer of flux than with a thick layer of flux. The electronic balance was used to weigh the welding plate with and without activating flux. The pasting quantity in the unit area was computed by the difference between the weights divided by the pasting area. Figure 15.14[19] shows the tendency of welding penetrations with and without different thicknesses of the activating fluxes. The results indicate that the flux thickness plays a different role for the different fluxes in determining the penetration capability. For the $CdCl_2$ flux, the increase in penetration is evident with the increasing flux thickness, up to the highest value. The highest increase could be in the range of 200–300%. The capability of increasing penetration is best with $CdCl_2$ than with TiO_2 and AlF_3. This is most probably due to the decomposition of the activating flux during welding. The melting point of $CdCl_2$ is lower than Mg alloy, and even lower than AlF_3 and TiO_2. $CdCl_2$ will decompose more easily than AlF_3 and TiO_2 at a high temperature, and consequently release the energy of their atomic bonding (ionic, covalent or both). Furthermore, more flux will result in greater interaction between the flux and the arc, which will enhance the arc's function. Obviously, the greater the quantity of activating flux applied, the more energy is released from the flux and thus the deeper is the weld penetration produced. But excessive flux in the surface of welding plates could not adhere and they will be blown off. So, the

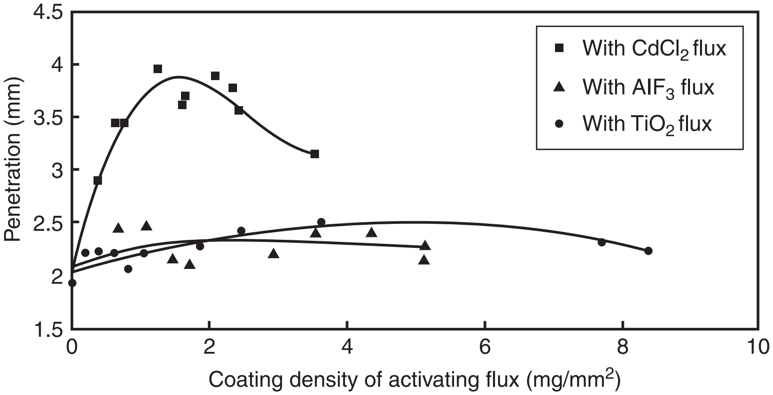

15.14 Effect of coating density of activating flux in ACTIG welding of Mg alloy with $CdCl_2$, AlF_3 and TiO_2 activating flux (welding current: 80 A; welding speed: 360 mm/min; Ar shielding gas flow rate: 10 l/min; arc length: 1 mm).

quantity of flux that could function has a top limit. For the TiO_2 flux and the AlF_3 flux, the increase in penetration is gentle with the increase of flux thickness, and the highest increase of TiO_2 flux could be 160% and for AlF_3 flux could be 150%. The melting point of AlF_3 and TiO_2 flux is higher than Mg alloy. The mechanics of increasing penetration with AlF_3 and TiO_2 flux will be different from $CdCl_2$ flux, and they will result in an interaction between the flux and the molten pool. However, it is noted that the penetration changed with the flux thickness presenting a problem, particularly when applying a thick layer of flux. If the flux cannot be uniformly applied, the penetration will also vary along the welds. It should be pointed out that a large variation in penetration is unacceptable in many applications. In fact, the change in penetration may raise issues of quality control. For instance, a large variation in penetration may produce a lack of fusion in the weld back bead. Therefore, uniformly activating the flux layer is the critical factor in producing a consistent weld penetration. In this aspect, the AlF_3 and the TiO_2 fluxes are better than the $CdCl_2$ flux; furthermore, the $CdCl_2$ flux is toxic.

The effects of the activating fluxes are dependent on welding parameters. Significant improvement of penetration occurred when ACTIG welding was carried out with the correct fluxes and parameters. For the range of parameters studied, when the single $CdCl_2$, AlF_3 and TiO_2 activating fluxes were used, the highest penetration improvements achievable for ACTIG welding of Mg alloy were 320%, 240% and 200%, respectively. Table 15.1[20] shows the appropriate welding parameters in TIG welding of magnesium alloy.

Figure 15.15 shows weld bead surfaces produced with and without activating flux, in which three single fluxes of $CdCl_2$, AlF_3 and TiO_2 were used. It can be observed that the weld produced without flux has a lustrous surface with good

Table 15.1 Welding parameters in A-TIG welding of magnesium alloy

Parameters	Values
Welding current	60–100 A
Arc length	1–2 mm
Welding speed	360–480 mm/min
Flow rate of argon	7–12 l/min
Electrode diameter	2.4 mm
Thickness of flux	1.5–4 mg/mm^2

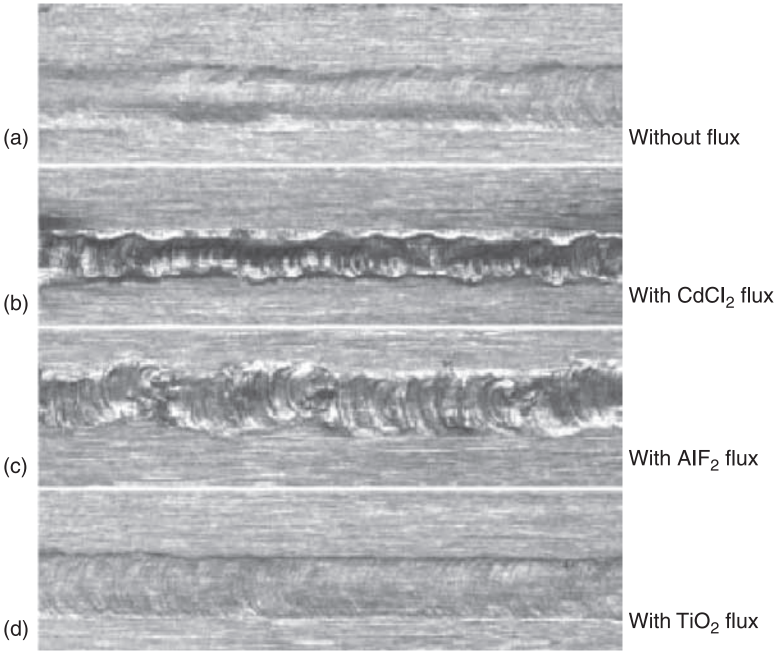

15.15 Comparison of weld penetration during ACTIG welding of Mg alloy with and without activating flux (welding current: 60 A; welding speed: 600 mm/min; Ar shielding gas flowrate: 10 l/min; arc length: 1 mm).

shielding, whereas the weld produced with $CdCl_2$ and AlF_3 activating flux appears to be rough. However, the surface appears to be better with TiO_2 activating flux than without activating flux. The weld bead surface formation was determined by the flow of the molten metal in the molten pool. The type of flow of the molten metal is related to the Marangoni convection in the welding pool.

Because the better surface appearance could be obtained with the oxide fluxes, the different oxide fluxes were studied to examine the weld bead morphology, microstructure and mechanical properties of TIG welds, which would be more suitable for the practical application of activating welding for magnesium alloy.

Figure 15.16[21] shows the weld bead surfaces of the welds made without flux and with various oxide fluxes in the standard welding condition. Figure 15.16(a) shows the results of the welds without flux, which produced a satisfactory appearance of weld, and the zone of cathodically disrupted refractory surface oxide can be seen at the sides. Figure 15.16(b) shows that a depression with a lustrous surface was produced with use of MgO flux. Figure 15.16(c) shows the satisfactory surface appearance of TIG flux magnesium alloy welds obtained with the use of CaO flux. Figure 15.16(d) shows that some slag and non-uniform surface were produced with the use of the TiO_2 flux. Figure 15.16(e) shows that few slags and smooth surfaces were produced with the use of MnO_2 flux. Figure 15.16(f) shows the result of Cr_2O_3 flux, which produced excessive slag.

Figure 15.17 shows the cross-section of TIG welds produced without flux and with various oxide fluxes in the 5 mm thick magnesium alloy in the standard

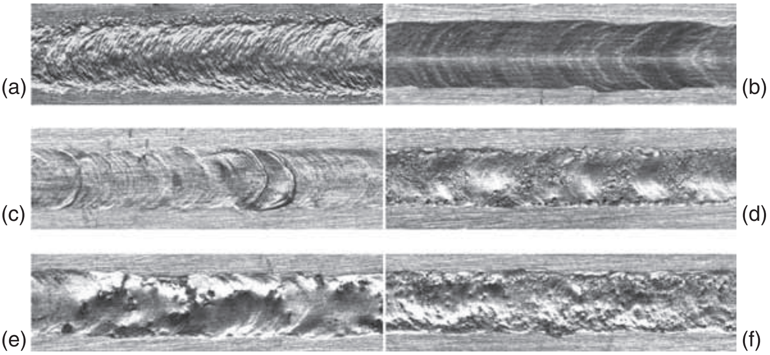

15.16 Effect of activating fluxes on surface appearance. (a) Without flux. (b) MgO flux. (c) CaO flux. (d) TiO_2 flux. (e) MnO_2 flux. (f) Cr_2O_3 flux.

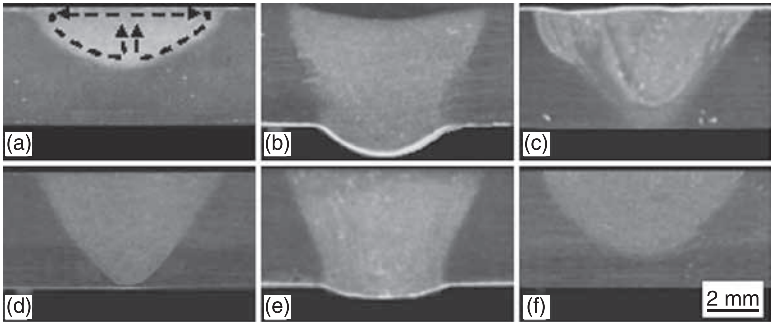

15.17 Effect of activating fluxes on weld morphology (a) without flux; (b) MgO flux; (c) CaO flux; (d) TiO2 flux; (e) MnO2 flux; (f) Cr2O3 flux.

welding condition. There was a significant variation in the penetration and bead width of the welds. The result distinctly shows that the five oxide fluxes can all increase the penetration of the ACTIG welding of Mg alloy, whereas the increasing of penetration capability is different. It should be mentioned that the MgO and MnO_2 fluxes can give full weld penetration. According to the work of Heiple and Roper (1992), the direction of fluid flow can affect the weld morphology.[22] For magnesium alloy, the surface tension will decrease with the increase of temperature, so the surface tension will be the greatest at the edge of the weld pool and the lowest in the hottest part of the weld pool near the center under the arc. The surface tension gradient therefore produces fluid flow outward from the center of the weld pool surface, as indicated in Fig. 15.17(a), resulting in a relatively wide and shallow weld bead. The addition of suitable surface active elements to molten metals can dramatically change the temperature dependence of the surface tension. For TIG flux welding, the surface tension is highest near the center (hotter) region of the weld pool. Fluid flow will be inward along the surface of the weld pool toward the center and then down, and will tend to increase the weld penetration and decrease the weld width. Figure 15.17(b) through (f) shows that the weld penetration increased when the oxide fluxes were used. However, the weld width did not decrease. Not all oxide fluxes can provide surface active elements to change the surface tension properties of the molten weld pool.

15.4 Microstructure of welding joints

An optical micrograph illustrating the crystal grain size of a weld seam is shown in Fig. 15.18. The as-weld fusion zone without flux exhibited a fine crystal grain structure (Fig. 15.18a). The grain size in the weld seam is about 20 mm on average. However, the as-weld fusion zone with oxide flux exhibited a rather large crystal grain size in the weld interior (Fig. 15.18b–f). Figure 15.18(b) shows grains of about 20–40 μm in size that were produced with use of the MgO flux. Figure 15.18(c) shows non-uniform grain sizes that were obtained with use of the CaO flux and the size of grains was 15–60 μm. Figure 15.18(d) shows that large sizes of grain were produced with use of the TiO_2 flux, about 50 mm on an average. Figure 15.18(e) shows that grains of about 60 mm in size, on an average, were produced with use of the MnO_2 flux. Figure 15.18(f) shows the effect of the Cr_2O_3 flux, which produced excessive grain size, with the size of grain reaching 100 μm.

Figure 15.19 shows the secondary electron images of a weld seam with and without flux, and the element content of some zone (as indicated by the white cross piece) also analyzed with energy dispersive spectroscopy (EDS). The results of EDS analysis are summarized in Table 15.2. Figure 15.19(a) shows the secondary electron images of a weld seam without flux, with some white dots and black pits inside the grain and sometimes in the grain boundary. The black pit is formed from the white dot, etched and pulled out. The EDS analysis indicated

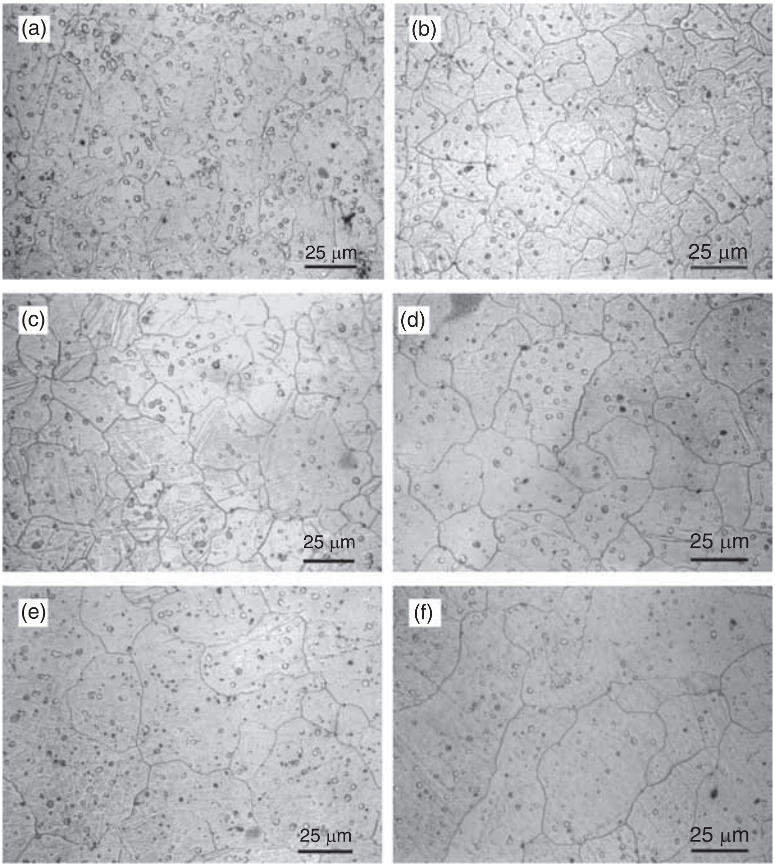

15.18 Optical macrostructure of TIG welded Mg-AZ31B alloy with and without oxide fluxes. (a) Without flux. (b) MgO flux. (c) CaO flux. (d) TiO_2 flux. (e) MnO_2 flux. (f) Cr_2O_3 flux.

that the white dot contains up to 12.65 wt.% and 13.05 wt.% of Al and Zn, respectively, as reported in Table 15.2, while the black pit contains 100 wt.% Mg. This phase was predominantly composed of Al and Zn and was identified as the Mg_{17} $(Al,Zn)_{12}$ phase by X-ray diffraction, as shown in Fig. 15.20. In the weld seam of welded oxide fluxes, the white pit, which was indicated as Mg_{17} $(Al,Zn)_{12}$ phase, can also be observed. During the TIG welding process, the solidifying process of the metal in the weld seam is a non-equilibrium process, and β-$Al_{12}Mg_{17}$ could appear under the rapid cooling rate.

Welded with oxide fluxes, these were shown in Fig. 15.19(b–f), and these particles were analyzed by EDS; the results are also listed in Table 15.2. Figure 15.19(b) shows the pattern of the particle in the weld seam using MgO flux. It can be seen that the particle was about 50 mm in size and contains up to 56.76 wt.%

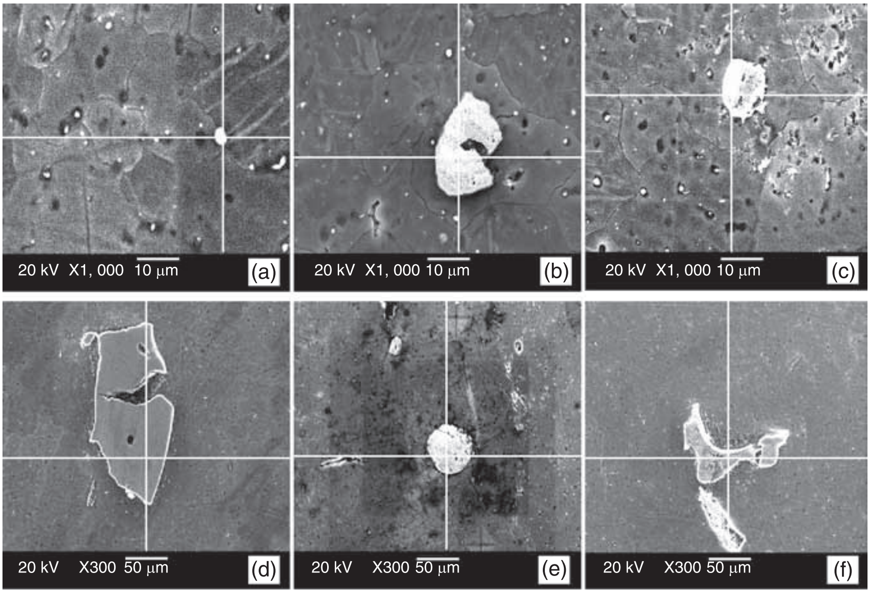

15.19 Secondary electron images in the weld seam of GTA weld with and without oxide fluxes. (a) Without flux. (b) MgO flux. (c) CaO flux. (d) TiO_2 flux. (e) MnO_2 flux. (f) Cr_2O_3 flux.

Table 15.2 EDS analysis in the weld seam of GTA weld with and without flux

Without flux		MgO flux		CaO flux		TiO_2 flux		MnO_2 flux		Cr_2O_3 flux	
Element	wt%	Element	wt%	Element	wt%	Element	wt%	Element	wt%	Element	wt%
Mg	82.05	Mg	56.76	Mg	21.14	Mg	9.53	Mg	23.09	Mg	29.70
Al	12.59	—	—	Ca	18.86	Ti	24.50	Mn	28.08	Cr	35.89
Zn	5.36	O	43.24	O	60.00	O	65.97	O	48.83	O	34.41
Total	100	Total	100	Total	100	Total	100	Total	100	Total	100

and 43.24 wt.% of Mg and O, respectively. Figure 15.19(c) shows the pattern of the particle in the weld seam using CaO flux, and the particle was about 50 μm in size, which contains up to 18.86 wt.% and 60.00 wt.% of Ca and O, respectively. Figure 15.19(d) represents the pattern of the particle in the weld seam using TiO_2 flux. It shows that the particle was about 100 μm in size and contains up to 24.50 wt.% and 65.97 wt.% of Ti and O, respectively. Figure 15.19(e) shows the pattern of the particle in the weld seam using MnO_2 flux. It can be seen that the particle was about 50 μm in size and contains up to 28.08 wt.% and 48.83 wt.% of Mn and O, respectively. Figure 15.19(f) shows the pattern of the particle in the weld seam

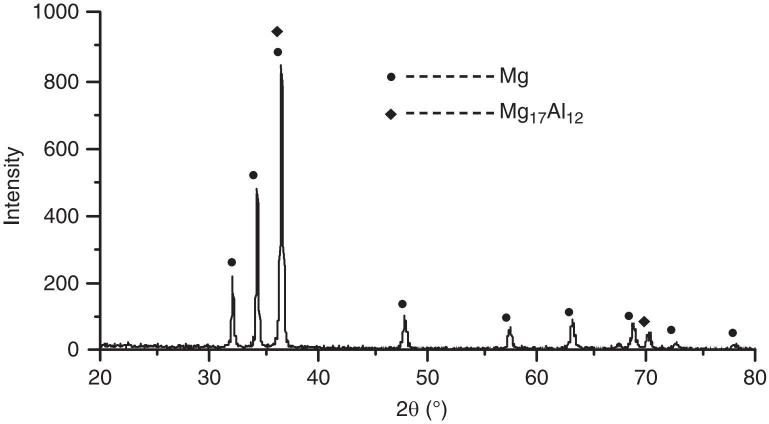

15.20 XRD analysis of the fusion zone TIG welding of magnesium alloy.

using Cr_2O_3 flux. The particle had an irregular shape and contains up to 35.89 wt.% and 34.41 wt.% of Cr and O, respectively. These results show that a possible Marangoni fluid flow in the surface of welding pool brought the activating flux particles into the molten pool.

Lu et al.[23] reported that an optimum depth-to-width ratio is reached when the oxygen content in the weld is in the range of 70 to 300 ppm when the oxide flux is used in the TIG welding of steel. From the results of Table 15.2, the oxygen element in the weld seam accumulated in the oxide particle which was trapped in the weld seam. If the content of oxygen was analyzed with oxygen/nitrogen analyzer, which Lu et al. have used, it would include the content of trapped oxide because of the non-uniform distribution of oxygen content in the welded seam. In this experiment, the content of oxygen in the weld seam was analyzed with EPMA quantitative analysis. The cross-sections of welds made with and without oxide fluxes were used to detect about 10–20 points in each cross-section. Then, the average value of oxygen content in the weld seam without considering the trapped oxide was indicated in Table 15.3, including the oxygen contents of the parent material and in the melted material of the welds made using the fluxes studied. All welds gave a substantial increase in the oxygen content of the melted material when compared with the oxygen content of the parent material. The oxygen content of the welds made without flux is not very different from those produced with a flux. However, if the oxygen contents of trapped oxide were considered, the oxygen content of the welds made without flux will be lower than of those produced with oxide flux. For the Marangoni effect, it is the surface active elements in the surface of molten metal and not the oxide that can change the Marangoni fluid flow of the weld pool. The oxide flux coating on the weld metal will decompose and then dissolve into the molten weld pool. Welds that have the best penetration are those made using MgO, CaO and MnO_2 fluxes, which have

Table 15.3 Oxygen contents in the base metal and in the melted materials using different fluxes (%)

Base metal	No flux	MgO flux	CaO flux	TiO_2 flux	MnO_2 flux	Cr_2O_3 flux
0.176	0.287	0.268	0.277	0.238	0.325	0.215

relatively higher oxygen content (0.268%, 0.277% and 0.325%, respectively) among those produced with flux. Welds that have the lowest penetration are those made using Cr_2O_3, which has a relatively lower oxygen content (215%) among those produced with flux. It is hard to say whether penetration will be or will not be correlated with the oxygen content. In the case of magnesium, no active species so far have been proposed, as verified by different researchers, by inoculating steels with surface active species.

15.5 Mechanical properties

The strength of the base material and weld, with and without oxide fluxes, is shown in Fig. 15.21. The results show that base material properties are considerably higher than those of weld metals, and weld metal properties without flux are higher than those with oxide fluxes.

The base metal used is wrought Mg alloy, which has higher properties than the as-cast metal because of strain strengthening. So, the tensile strengths of the TIG welded joint without flux are lower than that of the base metal, that is, about 96%

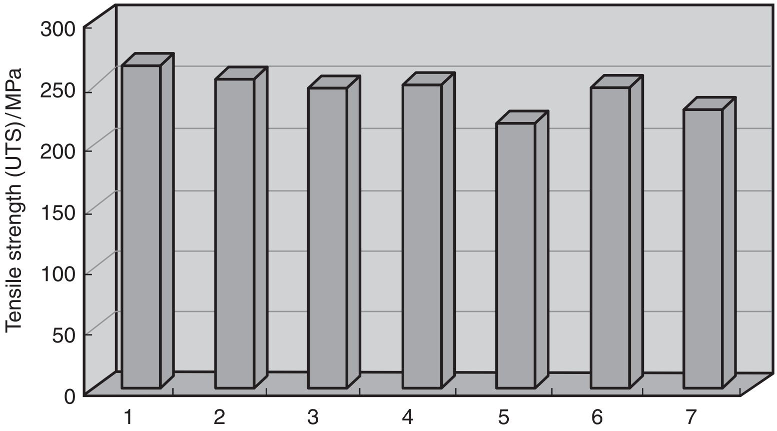

15.21 Room temperature tensile test results. 1 – base metal; 2 – without flux; 3 – with MgO flux; 4 – with CaO flux; 5 – with TiO_2 flux; 6 – with MnO_2 flux; 7 – with Cr_2O_3 flux.

of the base metal. The results in Fig. 15.21 show that the grains with oxide fluxes are all larger than those without flux in the weld seam. The results in Fig. 15.19 show that there are trapped oxides in the weld seam when the oxide fluxes are used. These all decreased the tensile strength of the TIG welded joint with oxide flux. After the tensile test, it can be seen that the specimens without flux fracture in the heat-affected zone (HAZ) and the specimens with oxide fluxes all fracture in the weld seam. Especially when the TiO_2 and Cr_2O_3 fluxes are used, the tensile strengths of welded joints are only about 81% and 86% of the base metal, respectively. When the MgO, CaO and MnO_2 fluxes were used, the tensile strengths of welded joint are all about 93% of the base metal. Generally, the HAZ is a dangerous zone of the welded joint fracture in the TIG welding of Mg alloy. So, the specimens without flux fracture in the HAZ. When the oxide fluxes were used, the weld penetration increased the weld penetration twofold or threefold without flux. More metals were melted, and more heat input was needed. For magnesium alloy, because of the high specific heat capacity and heat conductivity of magnesium alloys, weld penetration could not increase unless the scale of heat input was large enough to compensate for the heat loss with the introduction of flux. It needs higher energy density of the welding heat source, and thereby the high degree of energy concentration during TIG fluxes' welding process.

15.6 Future trends

The experiments show that an A-TIG welding process can double the increase in welding penetration. The use of fluxes does not increase the costs of TIG welding, so it is a low-cost, high-efficiency welding process. The A-TIG welding of magnesium alloy does not decrease the strength compared with the strength of TIG welding. A-TIG welding, serving as a replacement for TIG welding, could have wide application prospects.

15.7 References

1. Asahina T, Tokisue H (1995). Some characteristics of TIG welded joints of AZ31 magnesium alloy. *J Japan Inst Light Metals* **45**(2): 70–5.
2. Gurevich SM, Zamkov VN, Kushmienko NA (1965). Improving the penetration of titanium alloys when they are welded by argon tungsten arc process. *Avtom Svarka* **18**(9): 1–5.
3. Lucas W, Howse D (1996). Flux-increasing the performance and productivity of the TIG and plasma process. *Weld Metal Fabricat* **64**(1): 11–17.
4. Anderson PCJ, Wiktorowicz R (1996). Improving productivity with ATIG welding. *Weld Metal Fabricat* **64**(3): 108–9.
5. Paskell T, Lundin C, Castner H (1997). GTAW flux increases weld-joint penetration. *Weld J* **76**(4): 57–62.
6. Middel W, den Ouden G (1999). Additive assisted through the arc sensing during gas tungsten arc welding. *Sci Technol Weld Join* **4**(6): 335–9.

7. Howse DS, Lucas W (2005). Investigation into arc constriction by active fluxes for tungsten inert gas welding. *Sci Technol Weld Join* **5**(3): 189–93.
8. Tanaka M, Shimizu T, Terasaki T, Ushio M, Koshi-Ishi F, Yang C-L (2000). Effects of activating flux on arc phenomena in gas tungsten arc welding. *Sci Technol Weld Join* **5**(6): 397–402.
9. Kuo M, Sun Z, Pan D (2001). Laser welding with activating flux. *Sci Technol Weld Join* **6**(1): 17–22.
10. Marya M, Edwards GR (2002). Interaction between impurities and welding variables in determining GTA weld shape. *Weld J* **81**(12): s291–8.
11. Marya M (2002). Theoretical and experimental assessment of chloride effects in the A-TIG welding of magnesium. *Weld World* **46**(7–8): 7–21.
12. Zhang, Z-D, Liu L-M, Wang L (2004). Activating flux for arc welding of magnesium alloy. *Trans China Weld Inst* **25**(4): 55–8.
13. Lin SB, Yang CL, He WB, Dai HB, Zhu Q (2005). Effects of fluxes with single component on weld depth in A-TIG welding of magnesium alloy. *Trans Nonferrous Metals Soc China* **15**(2): 56–9.
14. Perry N, Marry S, Soutif E (1998). Study and development of flux enhanced GTA penetrations in a commercial grade titanium. *Proceedings of 5th International Conference on Trends I Welding Research (ASM/AWS)*, June 1–5, Pine Mountain, GA, pp. 520–5.
15. Rodrigues A, Loureiro A (2005). Effect of shielding gas and activating flux on weld bead geometry in tungsten inert gas welding of austenitic stainless steels. *Sci Technol Weld Join* **10**(6): 760–5.
16. Lowke JJ, Tanake M, Ushio M (2005). Mechanisms giving increased weld depth due to a flux. *J Phys D: Appl Phys* **38**(18): 3438–45.
17. Gurevich SM, Zamkov VN (1973). *Titanium Science and Technology*. New York/London: Plenum Press.
18. Zhang ZD, Liu LM, Shen Y, Wang L (2005). Welding of magnesium alloys with activating flux. *Sci Technol Weld Join* **10**(6): 737–43.
19. Liu LM, Zhang ZD, Shen Y, Wang L (2006). Effects of activating fluxes on TIG welding of magnesium alloy. *Acta Metallurgica Sinica* **42**(4): 399–404.
20. Zhang ZD, Liu LM, Shen Y, Wang L (2008). Mechanical properties and microstructures of a magnesium alloy gas tungsten arc welded with a cadmium chloride flux. *Mater Charact* **59**(1): 40–6.
21. Liu LM, Zhang ZD, Song G, Wang L (2007). Mechanism and microstructure of oxide fluxes for gas tungsten arc welding of magnesium alloy. *Metallurg Mater Trans A* **38**(3): 649–58.
22. Heiple CR, Roper JR (1992). Mechanism for minor element effect on GTA zone geometry. *Weld J* **61**(4): 97–102.
23. Lu SP, Hidetoshi F, Hiroyuki S, Kiyoshi N (2003). Mechanism and optimization of oxide fluxes for deep penetration in gas tungsten arc welding. *Metallurg Mater Trans A* **34**(9): 1901–7.

16

Friction stir welding of magnesium alloys

H. ZHANG, University of Science and Technology, Beijing, China

Abstract: In this chapter, the current state of understanding and development of friction stir welding of magnesium is reviewed, including the microstructure evolution, properties, the relationship between the joint and the welding parameters and welding tools, weld defects, typical applications and research prospects.

Key words: friction stir welding, microstructure, properties, weld defects.

16.1 Introduction

The challenge of significant weight reduction of vehicles in the automobile industry, especially in the context of significant fuel savings, recyclability and emission reduction, has promoted a focus on both aluminum and magnesium alloy substitutions and structural innovations.[1–3] Magnesium alloys, normally produced by casting, may find significant applications in the automotive and aerospace industries with rapid growth, particularly in die-cast vehicle components, because of their better mass-equivalent properties. They are used for manufacture of lightweight parts that operate at high speeds.[4] When Mg alloys are used for the construction of a structure, welding and joining procedures are required. However, conventional fusion welding for Mg alloys often produces some porosities in the weld metal, which weaken the mechanical properties. The production of a defect-free weld requires complete elimination of the surface oxide layer. On the other hand, solid-state friction stir welding (FSW) does not result in solute loss by evaporation or segregation during solidification, resulting in homogeneous distribution of solutes in the weld.[5] Also, many magnesium alloys in the cast condition contain porosity that can be healed during FSW.

FSW was invented at The Welding Institute (TWI) in the UK in 1991 as a solid-state joining technique, and it was initially applied to aluminum alloys. The basic concept of FSW is remarkably simple. A non-consumable rotating tool with a specially designed pin and shoulder is inserted into the abutting edges of sheets or plates to be joined and traversed along the line of joint (Fig. 16.1). The tool serves two primary functions: heating of the workpiece, and movement of material to produce the joint. The heating is accomplished by friction between the tool and the workpiece and the plastic deformation of the workpiece. The localized heating softens the material around the pin, and a combination of tool rotation and translation leads to the movement of material from the front of the pin to the back of the pin. As a result of this process, a joint is produced in 'solid state.' Because

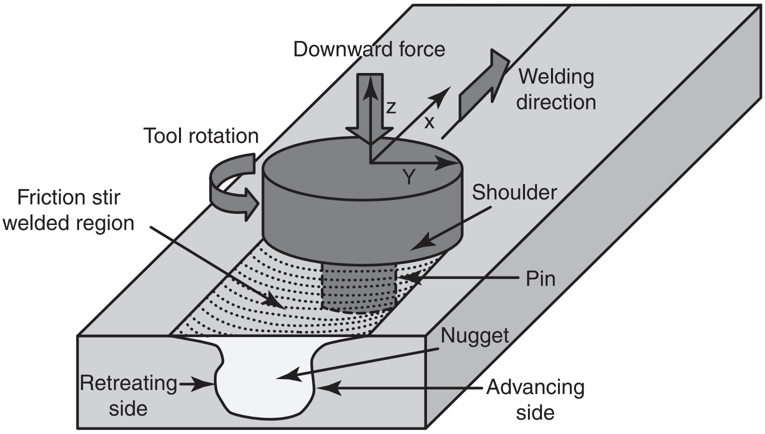

16.1 Schematic drawing of friction stir welding.

of the various geometrical features of the tool, the material movement around the pin can be quite complex. During the FSW process, the material undergoes intense plastic deformation at an elevated temperature, resulting in the generation of fine and equiaxed recrystallized grains. The fine microstructure in friction stir welds produces good mechanical properties.[6]

FSW is considered to be the most significant development in metal joining in a decade and is a green technology due to its energy efficiency, environment friendliness and versatility. As compared to the conventional welding methods, FSW consumes considerably less energy. No cover gas or flux is used, thereby making the process environmentally friendly. The joining does not involve any use of filler metal, and therefore, any aluminum or magnesium alloy can be joined without concern for the compatibility of composition, which is an issue in fusion welding. When desired, dissimilar magnesium alloys and aluminum can be joined with equal ease.[7–17] In contrast to the traditional friction welding, which is usually performed on small axisymmetric parts that can be rotated and pushed against each other to form a joint, FSW can be applied to various types of joints such as butt joints, lap joints, T-butt joints and fillet joints, as shown in Fig. 16.2. FSW has many advantages, including the following:[18–22]

- solid phase process, therefore no problems with hot cracking, porosity, etc.
- low distortion
- no filler wire or shielding gas requirement
- no fume, no spatter, no UV radiation, therefore environmentally friendly
- uses machine tool technology, therefore easy to automate, and reduces need for skilled welders
- can work in any position
- good mechanical properties
- energy efficient.

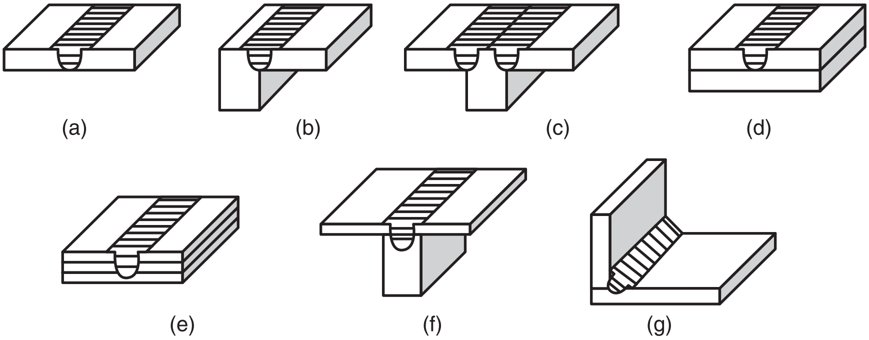

16.2 Joint configurations for friction stir welding: (a) square butt, (b) edge butt, (c) T butt joint, (d) lap joint, (e) multiple lap joint, (f) T lap joint, and (g) fillet joint.

Indeed, the first studies in this field have shown that the joint efficiency of magnesium friction stir welds is typically very high (80–100%). In other words, FSW has very good potential for the joining of magnesium alloys.[3] In this chapter, the current state of understanding and development of the FSW of magnesium is reviewed, including the microstructure evolution, properties, the relationship between the joint and the welding parameters and welding tools, weld defects, typical applications and research prospects.

16.2 Welding parameters and procedures

The welding speed, the tool rotational speed, the vertical pressure on the tool and the tilt angle of the tool are the main independent variables that are used to control the FSW process. The rotation of tool results in stirring and mixing of material around the rotating pin, and the translation of the tool moves the stirred material from the front to the back of the pin and finishes the welding process. The heat generation rate, temperature field, cooling rate, x-direction force, torque and power depend on these variables. The effects of several of the independent variables on the peak temperature will be discussed in this section.

16.2.1 The welding speed and the rotation speed

During friction stir welding procedure, the welding temperature will increase with the increase of the rational speed, and decrease with the increase of the welding speed, as shown in Fig. 16.3. Peak temperature also increases with increase in the axial pressure. Higher tool rotation rates generate higher temperature because of higher friction heating and result in more intense stirring and mixing of material. However, it should be noted that frictional coupling of the tool surface with the workpiece is going to govern the heating. So, a monotonic increase in heating

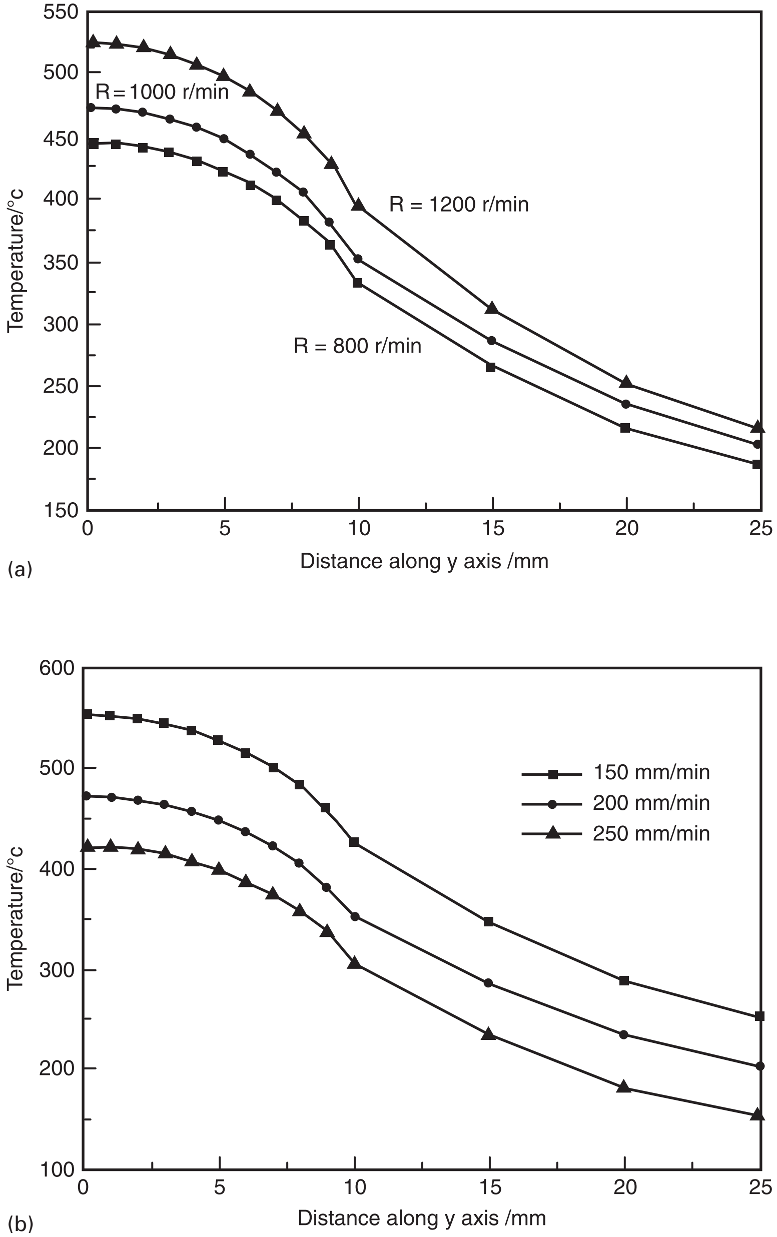

16.3 Temperature distributions in the transverse direction at different parameters (AZ31 magnesium): (a) welding speed is 200 mm/min and (b) rotation speed is 1000 r/min.

with an increasing tool rotation rate is not expected as the coefficient of friction at the interface will change with an increasing tool rotation rate.

The quality of FSW welds of magnesium alloys is highly sensitive to tool rotation rate and traverse speed. The tensile strength of the friction stir welded increased with the higher rotation speed and then decreased, as shown in Fig. 16.4.

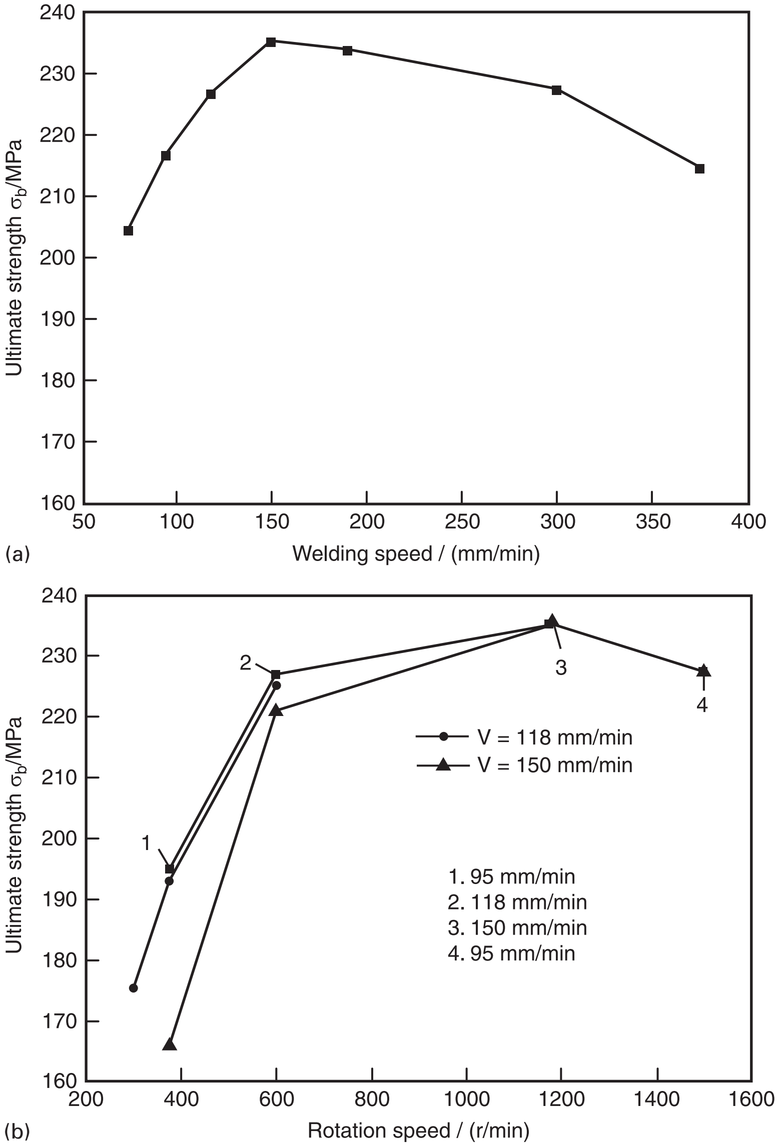

16.4 Relationship between the welding parameters and the ultimate strength (AZ31 magnesium alloy): (a) with the welding speed and (b) with the rotation speed.

The author has worked on 2.5- and 5-mm thick AZ31 magnesium alloys, and the joints were well formed with lower distortion.[22] For 2.5-mm thick AZ31 magnesium alloy, the joint strength without any treatment after welding can reach to 93% of that of base metal. The best welding parameters are welding speed of 95 mm/min and rotation speed of 1180 r/min. For 5 mm thick magnesium alloy, the joint strength nearly equals that of base metal. The best welding parameters are a welding speed of 150 mm/min and rotation speed of 800 r/min. The fracture locations were on a thermo-mechanically affected zone (TMAZ). Small pores were formed rapidly when using unreasonable parameters, and these small pores were growing, gathering and eventually fracturing at the disturbance of external force during tensile tests.

The area of the porosity was measured and its variation with welding speed is shown in Fig. 16.5.[23] The maximum overall porosity area was observed at a welding speed of 120 mm/min.

16.2.2 Tilt angle

In addition to the tool rotation rate and traverse speed, another important process parameter is the angle of spindle or tool tilt with respect to the workpiece surface. A suitable tilt of the spindle in the trailing direction ensures that the shoulder of the tool holds the stirred material by a threaded pin and moves material efficiently from the front to the back of the pin. The general tile angle is 2°–5°.

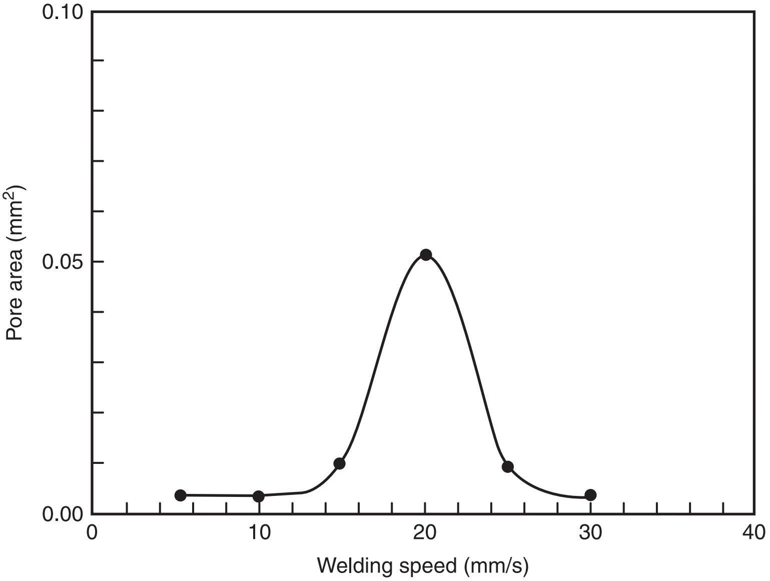

16.5 Effect of welding speed on pore area in stir zone.

16.2.3 Welding pressure

Generally, the welding pressure changes with the insertion depth. So, the insertion depth of the pin into the workpieces (also called target depth) is important for producing sound welds with smooth tool shoulders. The insertion depth of the pin is associated with the pin height. When the insertion depth is too shallow, the shoulder of the tool does not contact the original workpiece surface. Thus, the rotating shoulder cannot move the stirred material efficiently from the front to the back of the pin, resulting in generation of welds with an inner channel or a surface groove. When the insertion depth is too deep, the shoulder of the tool plunges into the workpiece, creating excessive flash. In this case, a significantly concave weld is produced, leading to local thinning of the welded plates.[6]

Excessive x-direction force can be an important indicator of potential for tool erosion and, in extreme cases, tool breakage. Axial pressure also affects the quality of the weld. Very high pressures lead to overheating and thinning of the joint, whereas very low pressures lead to insufficient heating and voids. Power requirement also increases with the increase in axial pressure.[4]

At the same welding rate (the welding speed is 200 mm/min and the rotation speed is 1000 r/min), the welds at different welding pressures are shown in Fig. 16.6. When the welding pressure is relatively lower, a pore is formed at the bottom, while with a suitable welding pressure, the weld is good and there is full penetration. It shows that increasing the welding pressure is effective for weld formation. This is because the temperature during FSW, defining the amount of the superplastic materials and the temperature, is greatly dependent on the welding pressure.

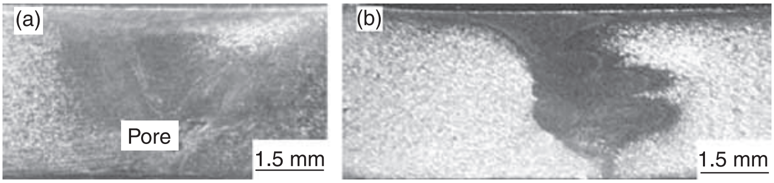

16.6 Friction stir weld with welding speed 200 mm/min and rotation speed 1000 r/min at different welding pressures: (a) relatively lower welding pressure; (b) relatively higher welding pressure.

16.3 Welding tools and equipment

Tool geometry influences heat generation, plastic flow, power required and uniformity of the welded joint. The shoulder generates most of the heat and prevents the plasticized material from escaping from the workpiece, while both the shoulder and the tool pin affect the material flow. The FSW tool requires the following important characteristics: a shape as simple as possible to reduce the cost, and sufficient stirring effect to produce sound welds similar to an ordinary tool for aluminum and magnesium alloys. With conventional aluminum alloys, tools made of tool steels give good results, but with the softer alloys, such as magnesium, these tools may be effective with other tool materials.[6,24–27]

In recent years, several new features have been introduced in the design of tools. Several tools designed at TWI are reported in Table 16.1. The Whorl and MX-Triflute have smaller pin volumes than the tools with cylindrical pins.[28,29] The tapered threads in the Whorl design induce a vertical component of velocity that facilitates plastic flow. The flute in the MX-Triflute also increases the interfacial area between the tool and the workpiece, leading to increased heat generation rates, softening and flow of material. Consequently, more intense stirring reduces both the traversing force for the forward tool motion and the welding torque.

Clearly, different materials and different thicknesses will require different pin profiles. The variations in tool design are infinite, and combinations of shoulder diameter, shoulder profile, pin length, diameter and profile are all important parameters in determining the speed of welding and the quality of the finished weld. Another important parameter in the determination of the suitability of a tool for a particular application is the tool material itself. Welding is carried out at around 70–90% of the material melting point. So, it is important that the tool material should have sufficient strength at this temperature; otherwise, the tool can twist and break. The prior research investigation was carried out to select proper FSW tool parameters to weld AZ31B magnesium alloy. The joints fabricated by high carbon steel tools with threaded pin profile and shoulder diameter of 18 mm exhibited superior tensile properties compared to their counterparts.[27]

The effect of tool geometry on microstructure and mechanical properties of friction stir lap welded AZ31 Mg alloy (top sheet) and steel (zinc-coated steel and brushed finish steel) sheets was studied by Chen and Nakata.[25] Tools with two different probe lengths were used in their study. The research results showed that

Table 16.1 A selection of tools designed at TWI

Tool	Cylindrical	Whorl™	MX triflute™	Flared triflute™	A-skew™	Re-stir™
Schematics	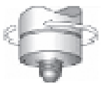	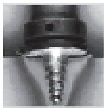	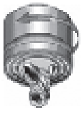	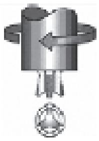	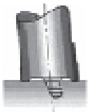	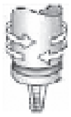
Tool pin shape	Cylindrical with threads	Tapered with threads	Threaded, tapered with three flutes	Tri-flute with flute ends flared out	Inclined cylindrical with threads	Tapered with threads
Ratio of pin volume to cylindrical pin volume	1	0.4	0.3	0.3	1	0.4
Swept volume to pin volume ratio	1.1	1.8	2.6	2.6	Depends on pin angle	1.8
Rotary reversal	No	No	No	No	No	Yes
Application	Butt welding; fails in lap welding	Butt welding with lower welding torque	Butt welding with further lower welding torque	Lap welding with lower thinning of upper plate	Lap welding with lower thinning of upper plate	When minimum asymmetry in weld property is desired

the microstructure at the joining interface, the failure loads and the fracture locations of the joints varied significantly with the probe length.[25]

16.4 Materials that have been or are being friction stir welded

Recently, research on FSW of magnesium alloys, including AZ (Mg-Al-Zn) and AM (Mg-Al-Mn) alloys, has been reported.[2,3,5,7,23,30–48] It has been found that in AZ alloys, FSW joints have better mechanical properties than those of gas tungsten arc welded joints. FSW studies have been recently reported on AM50, AM60, AZ91 AZ61 and AZ31.

16.5 Typical microstructures of friction stir welded magnesium alloys

Generally, as in FSW magnesium alloys, three microstructural zones are identified in FSW magnesium alloys, namely weld nugget, heat-affected zone (HAZ) and TMAZ.[2,3,32,33,49] The weld nugget with a basin or elliptical shape was characterized by fine recrystallized grains. However, Zhang et al.[50] reported that the stirred zone can be divided into two sub-zones, crown and weld nugget, in FSW hot-rolled AZ31B, as shown in Fig. 16.7. The crown, located at the center and upper side of

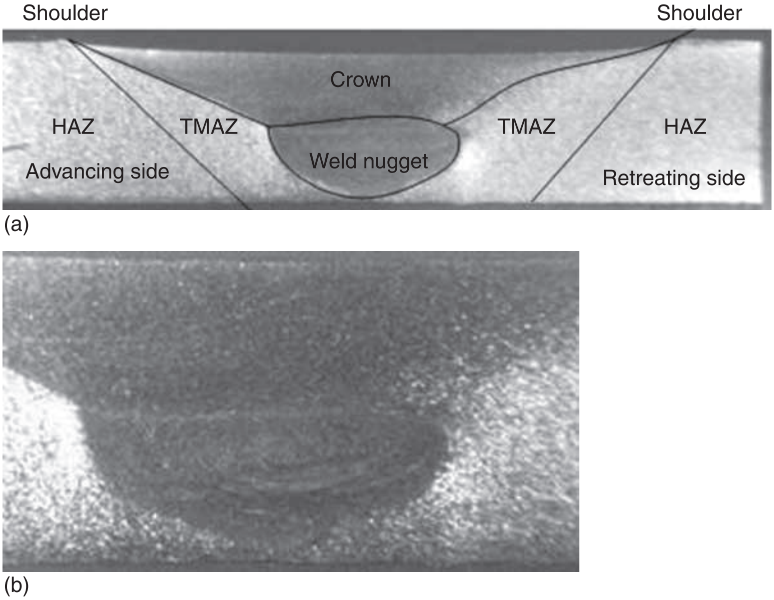

16.7 Macrograph of friction stir welded AZ31 magnesium alloy on transverse section (80 mm/min; 800 r/min): (a) typical zones and (b) local magnified view of the weld nugget.

the stirred zone, was characterized by partial dynamic recrystallization (DR), and deformation layers were observed throughout the grains. In the weld nugget, full DR and grain growth had occurred, and no deformation structure, such as twins and deformation layer, was observed. The microstructural changes in various zones have a significant effect on post-weld mechanical properties. Therefore, the microstructural evolution during FSW has been studied by a number of researchers.[14,38,40,41,43,45,47,51–54]

16.5.1 Nugget zone

Microstructural examinations of magnesium friction stir welds have shown that the material in the stir zone (SZ) typically exhibits an equiaxed grain structure, which is commonly referred to as being 'recrystallized.'[33,35,55]

In order to describe clearly the characterization of the onion rings in the weld nugget, the transverse section was intercepted at the welding speed of nearly zero. The specimen was near the keyhole, where the superplastic material was stirred only by the probe rotation. The macrostructure of the weld nugget is shown in Fig. 16.8. The magnified microstructure of Fig. 16.8 is shown in Fig. 16.9. Figure 16.9(a)–Fig. 16.9(d) illustrated microstructure variations from advancing side (AS) to retreating side (RS). It can be seen that there are onion rings, caused by the welding tool stirring, and great plastic formation occurred in the onion rings. The onion rings were more regular at RS than those at AS, and the gap between the rings was smaller in the top part than in the bottom part; that means, the gap increased along the thickness direction from top to bottom. The gap between the onion rings was determined by the welding rate, the times of the rotation speed per millimeter (r/mm). The onion ring gap decreased with the increase of the welding rate. The temperature was higher near the adjacent zones of onion rings and the deformation began in those zones. Material flow bands were clear and the microstructures underwent DR; so, the grains were steadier in these zones, as shown in Fig. 16.9(a)–Fig. 16.9(d). The grains in the center of the weld nugget were fine and uniform, and the temperature was highest in this zone; so, the DR process was effective. The grain boundaries were difficult to be etched, as shown in Fig. 16.9(e).

The grain structure evolution was shown to be a very complex process including several stages. Far ahead of the tool, the material first experienced pronounced

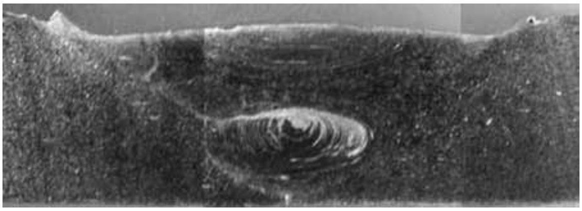

16.8 Onion rings in the weld nugget.

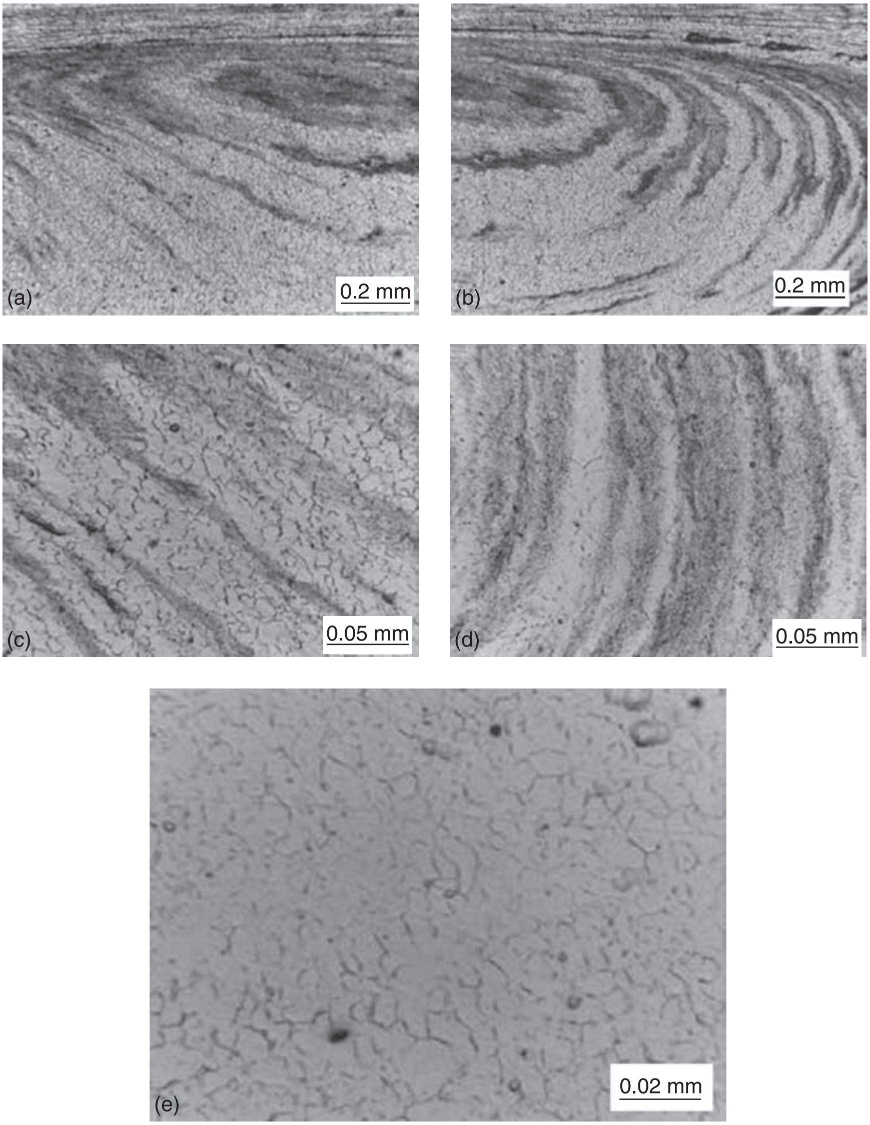

16.9 Microstructures of the weld nugget: (a) onion rings on the advancing side; (b) onion rings on the retreating side; (c) magnified view of advancing side; (d) magnified view of the onion rings; (e) magnified view of recrystallized grains.

{1012} twinning. Then, approaching the tool, the microstructural development was governed by the geometrical effects of strain and presumably by the limited, discontinuous recrystallization. Directly near the tool, the grain structure evolution was closely linked with the texture development. Formation of a very strong texture led to texture-induced grain convergence, thus increasing the grain size and LAB (low-angle boundary) fraction.[3] With the increase in the shoulder diameter from 18 to 24 mm, the grains in the SZ increased remarkably and the grains in the TMAZ exhibited a slight increase.[34]

16.5.2 Thermo-mechanically affected zone

TMAZ experiences both temperature variation and deformation during FSW. A typical micrograph of TMAZ is shown in Fig. 16.10. The TMAZ is characterized by a highly deformed structure. The parent metal's elongated grains were deformed in an upward flowing pattern around the nugget zone. Although the TMAZ underwent plastic deformation, recrystallization did not occur in this zone due to insufficient deformation strain.

Figure 16.10(a) was at an AS while Fig. 16.10(b) at a RS. In Fig. 16.10(a), three different zones are indicated by 'A,' 'B' and 'C,' respectively. The material had undergone larger deformation in TMAZ (indicated by 'C' in Fig. 16.10a), and the long "pancake" grains were broken into small, short and coarse grains. The grain boundary direction was unequal, as shown in the region indicated by 'C' in Fig. 16.10(b). There were obvious onion rings in the weld nugget, and the grains were uniform and fine, as shown in the region indicated by 'B' in Fig. 16.10(a). On the top of the weld nugget was another DR zone (DRZ), but the DRZ was not completed as the weld nugget, and the materials were affected by both the shoulder and the probe, while in the weld nugget, the material moved around the probe and had undergone a sufficient DR process; so, the microstructure was steadier than that of 'A' regions in Fig. 16.10.

The boundaries between the weld nugget, TMAZ and another DRZ were obvious, and this can be explained by the material flow during FSW. The materials around the probe rotated anti-clockwise and moved from AS to RS on the cross-section surface, and the materials in the upper part moved upward and formed another DRZ, and between these two zones was the TMAZ, as shown in Fig. 16.10(b). On the boundary of the weld nugget, different onion rings moved around the same center of a circle, and the deformation was regular.

In TMAZ near the weld nugget, the flow band was regular. The flat pancake grains were elongated by the friction between superplastic materials and underwent incomplete DR, and some grains were broken into uniform equiaxed grains in deformed flow bands, as shown in Fig. 16.11. In the whole TMAZ, the flow bands were not continuous and broken into short deformation bands, and between those bands, the grain was partly smaller than that of the base metal.

16.5.3 Heat-affected zone

Beyond the TMAZ, there is an HAZ. This zone experiences a thermal cycle but does not undergo any plastic deformation. The HAZ as a zone experiences

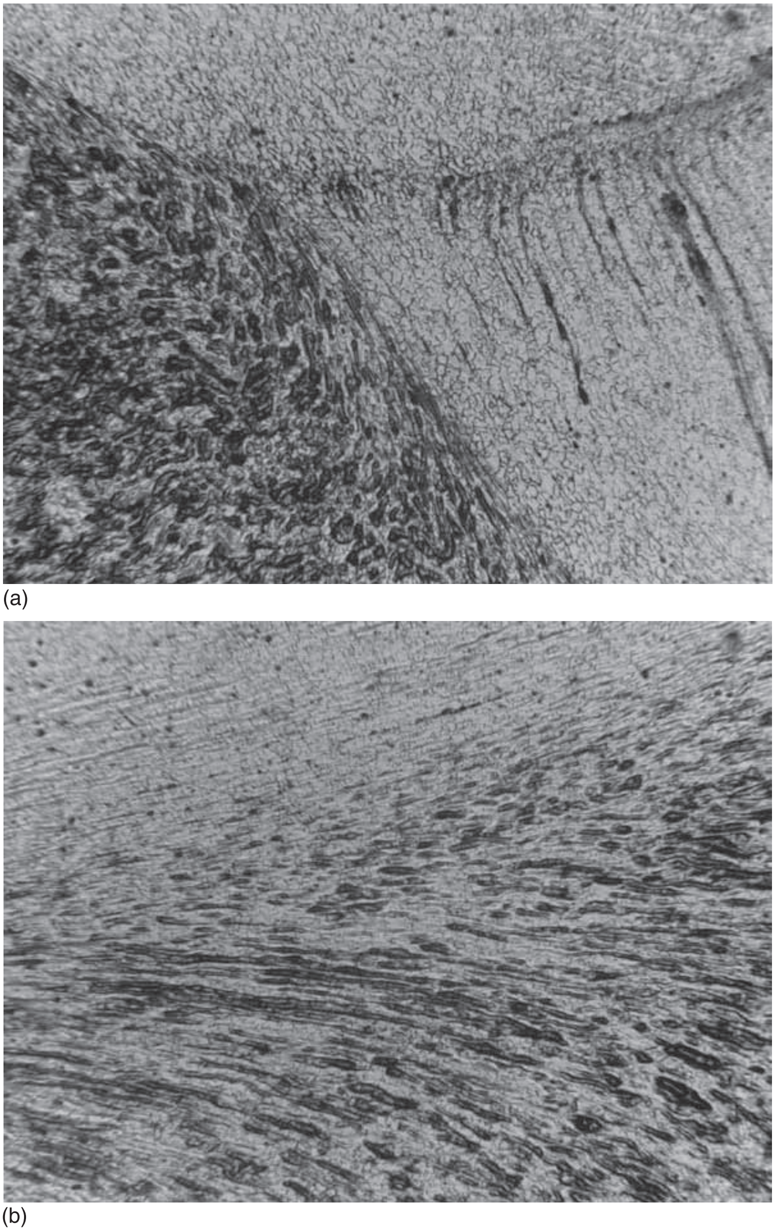

16.10 Microstructures of the zone along line of TMAZ, weld nugget and crown: (a) on the advancing side, and (b) on the retreating side.

a temperature rise above 250 °C for a heat-treatable AZ31 magnesium alloy.[56] The HAZ retains the same grain structure as the parent material. However, the thermal exposure above 250 °C has a significant effect on the precipitate structure.

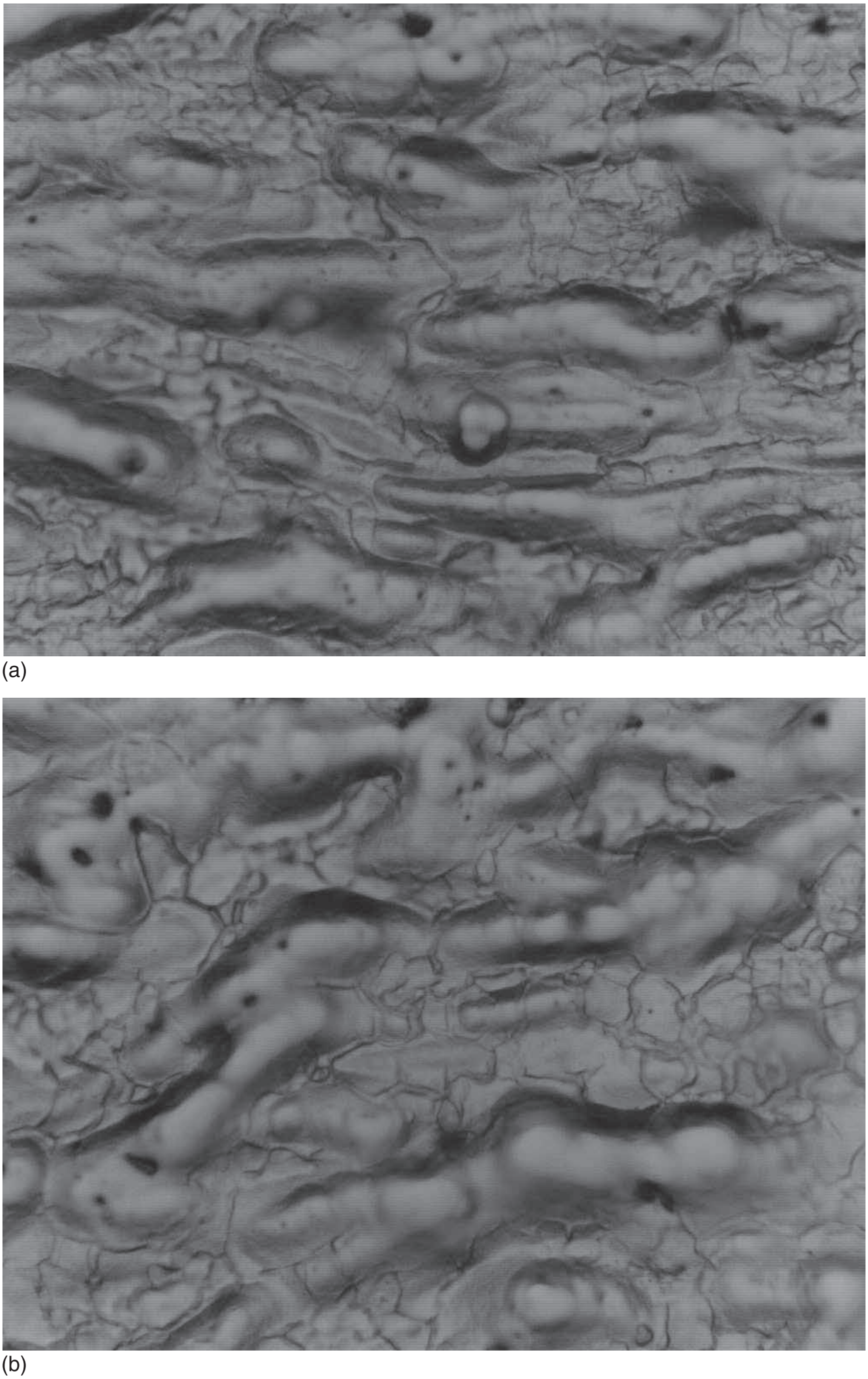

16.11 Microstructure of the TMAZ: (a) on the advancing side, and (b) on the retreating side.

16.5.4 Mechanism of microstructure evolution

During each rotation of the tool, the metal in front of the tool was heated by friction and the forward motion extruded the metal to the back of the tool. If this happens, then there will be a cavity at the back. Therefore, the materials were stirred and filled the cavity. The formation of the onion rings was due to the process of friction heating produced by the rotation of the tool, and the forward movement extruded the metal around the RS of the tool. At the center of the weld, the deformation was greatest and the DR was complete. In the TMAZ, the grain was elongated and heated, but the DR was not strong enough. When the welding speed was zero, the materials only rotated around the probe and did not move forward towards the weld; near the keyhole, the onion rings were clear and the gaps between those onion rings varied. The heat and mechanical processes affected the formation of different zones in the friction stir welded A31 magnesium alloy because they affect the production and movement of material flow.

The nucleus of recrystallization was produced in those zones that had undergone large deformation, and polygonization during the reversion process assists the preparation for the nucleus of recrystallization. The cellular structure changed into sub-grains after polygonization, and some sub-grains grew into the nucleus of recrystallization. During FSW, the materials underwent great deformation in the conditions that produce sub-grains in the weld nugget and the crystallization was complete, but in TMAZ, the deformation was smaller than that of the weld nugget and only some grains were recrystallized.

The superplastic deformation was not a free process, that is, dependent on its boundary grains, and the grains around it also formed adaptive distortion to retain the joint of the grains and the continuum of the whole metal. The grain bit vector was different, so the choice of direction of the slip system was different, and under the applied pressure, the sub-shear stress value between the slip systems differed greatly. Not all the grains formed superplastic deformation, and only those grains with the advantage of bit vector and the biggest choice of direction factor will undergo superplastic deformation with the increase of applied pressure. The dislocation source started to move due to the superplastic deformation of some grains, but the slip systems can go through the grain boundaries because of the grain bit vector; slip systems differ, so the dislocations cannot extend to another grain, and the dislocations were hindered in grain boundaries and formed a flat-face dislocation clog group. Each grain was enclosed by other grains, the superplastic deformation was not isolated and free, and those grains had to adapt to each other, otherwise it would be difficult to deform during the FSW. A simple model of the microstructure evolution on the weld nugget is presented in Fig. 16.12.

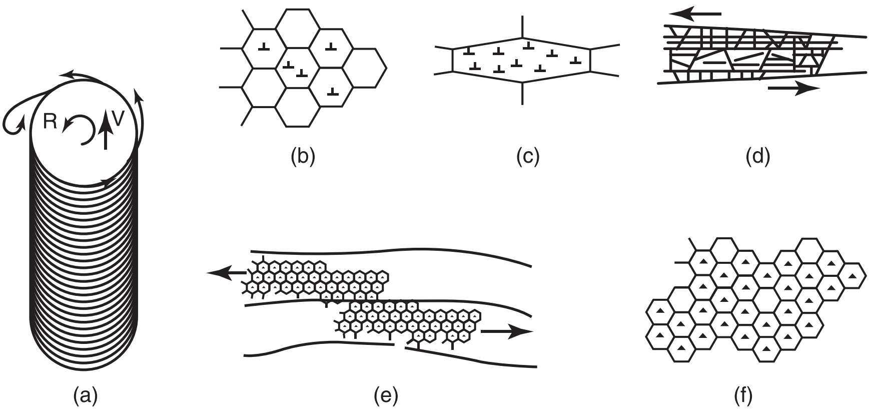

16.12(a)–(f) Simple model of the microstructure evolution on the weld nugget.

16.6 Properties of friction stir welded magnesium alloys

16.6.1 Tensile properties

FSW resulted in an improvement in tensile properties of cast magnesium alloys such as AZ91, whereas a reduction in tensile properties was observed in wrought magnesium alloys such as AZ31B-H24 and AZ61. There have been many research projects on the tensile properties of friction stir welded magnesium.[2,5,23,33,34,40,43,44,49,57–60]

The work of Srinivasan et al. shows that FSW of AZ61 alloy can give joints with efficiency levels close to 95% under optimized welding conditions.[30] The hardness of the weld nugget does not differ much from the parent region; however, fracture location in the tensile tests suggests that the TMAZ/HAZ region is the weakest zone in the joint.[30,57]

Figure 16.13 shows a typical tensile fracture location of the friction stir welded joints of AZ31 alloy. The friction stir welds failed at the boundary between the SZ and TMAZ at the AS. The failure of the samples was basically 45 ° shear fracture, which could be due to the formation of texture by the shear deformation resulting from the rotation of the pin and tool shoulder in that region.[22]

Fracture locations are observed to be about 5–8 mm from the weld centerline measured at the top surface of the specimens. At a low rotational speed of 500 r/min, failure occurs closer (5–6 mm from the weld centerline) to the weld nugget than at a higher rotational speed of 1000 r/min (6–8 mm from weld centerline). The lower rotational speed creates a smaller weld zone due to the lower heat input, and the boundary between the TMAZ and the weld nugget (i.e., the fracture location) thus shifts closer to the weld centerline.[2]

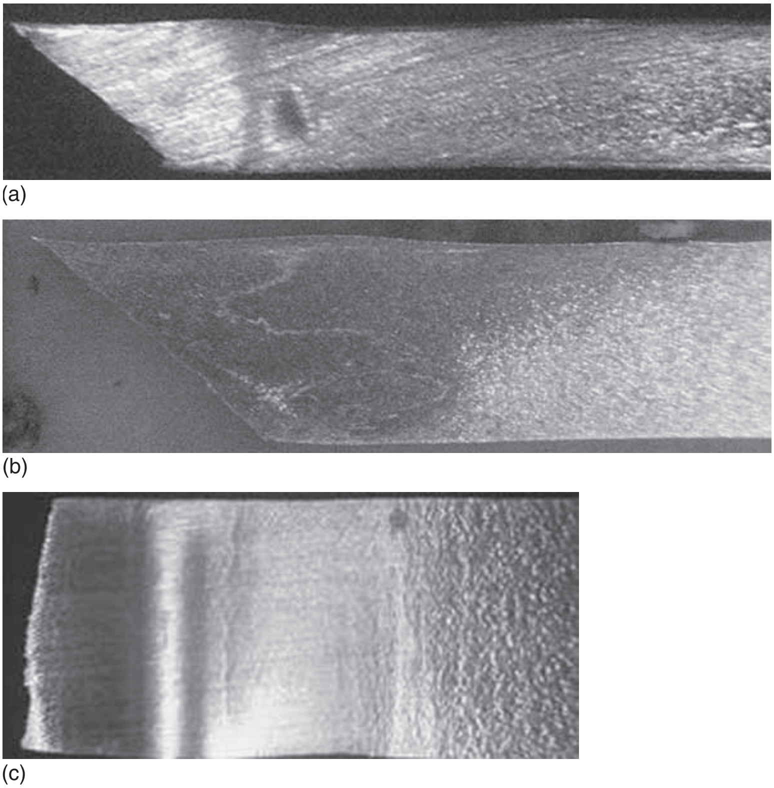

16.13 Fracture location of no. 3 specimen: fracture is on advancing side. (a) Transverse section; (b) 'S' shape faying surface; (c) top surface.

In the paper of Park et al., microstructural evolution of Mg alloy AZ61 during FSW and the relationship between microstructure and mechanical properties in the friction stir weld were examined.[5] FSW produced an SZ with a recrystallized grain structure and a high density of dislocations. Additionally, FSW led to the formation of a recrystallized grain structure with a high density of dislocations just outside the SZ. Microstructural observations showed that the friction stir weld had fairly uniform distributions of grain size and dislocation density. Such microstructure distribution caused the homogeneous Vickers hardness profile of the weld. Besides grain size and dislocation density, crystallographic orientation distribution strongly affected tensile properties of the homogeneous hard friction stir weld of Mg alloy AZ61.

When the welding parameters were not suitable, the tensile strength was relatively lower and the fracture location was along the interface between the weld nugget and the TMAZ, as shown in Fig. 16.14.

So, there are two typical fracture mechanisms on FSW of AZ31 magnesium. The first fracture failed at the TMAZ/HAZ boundary. The second fracture was

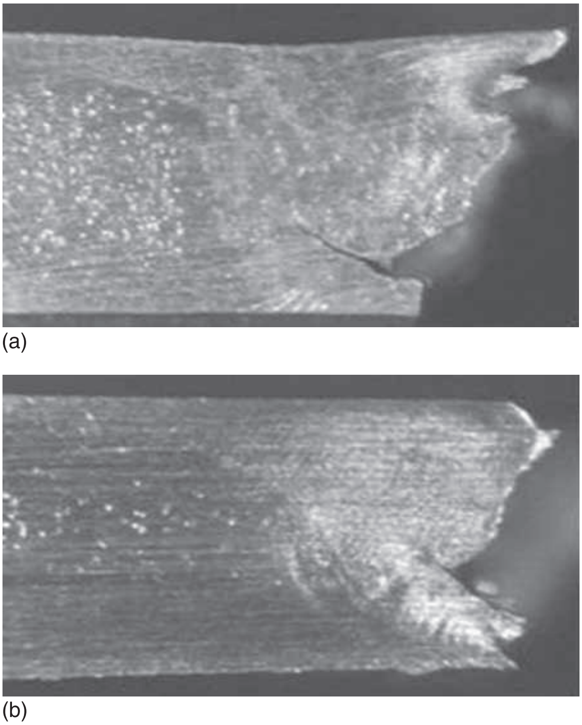

16.14 The crack in cross-section of friction stir welds (5 mm in thickness) with the welding parameters: (a) $R = 1000$ r/min, $V = 150$ mm/min, and (b) R = 1000 r/min, $V = 500$ mm/min.

extended along the weld nugget. Both of these fractures occurred at the AS, as shown in Fig. 16.15.

16.6.2 Fatigue properties

Compared to the as-cast parent material, the friction stir processing (FSP) sample exhibited significantly enhanced fatigue properties, with the fatigue strength being increased approximately from 45 to 95 MPa and the fracture mode being changed from a quasi-cleavage fracture to a dimple fracture. The improvement was attributed to refinement of grains, elimination of porosities and coarse β networks, and precipitation of fine β particles.[37]

16.6.3 Corrosion properties

Despite favorable properties and positive outcomes in the processing, magnesium alloys still suffer from their inherent poor corrosion resistance, and for many applications, surface treatments are necessary for meeting the demands.[30]

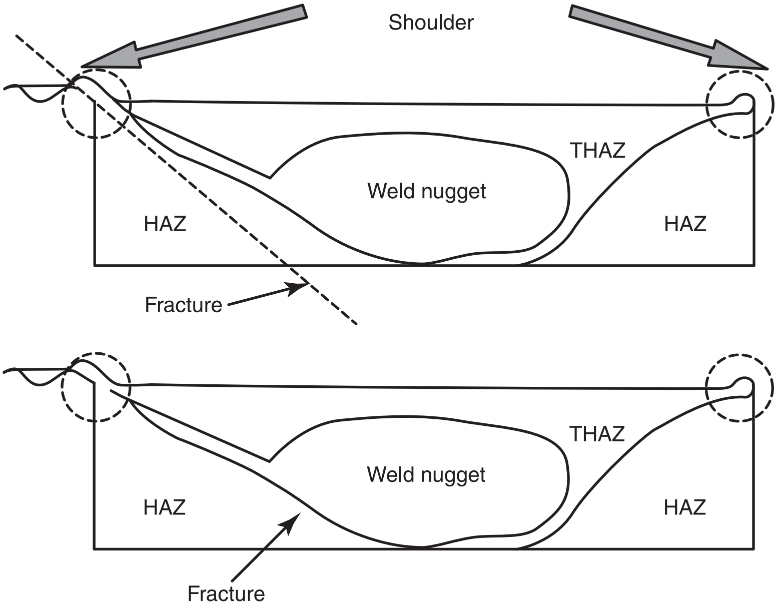

16.15 Two typical fracture modes of friction stir welds.

Consequently, considerable attention has been focused on the corrosion behavior of magnesium alloy. A few investigations on the corrosion and stress corrosion cracking (SCC) behavior of magnesium alloy weldments are underway.[61,62]

The reason for the poor corrosion resistance of magnesium and its alloys results primarily from two mechanisms: oxide films forming on the surface are not perfect and protective, and galvanic or bimetallic corrosion can be caused by impurities and secondary phases when associated most notably with iron, nickel and copper. It is well known that iron is detrimental for magnesium alloys in their ability to resist corrosion. Thus, there is a tolerance limit for the iron content in magnesium alloys. This tolerance limit depends on the level of manganese present.

Recently, a variety of studies on the corrosion behavior of magnesium alloys were undertaken. Nevertheless, research on corrosion of friction stir welded magnesium alloys is limited in the literature. Magnesium alloys have also been demonstrated as having a lower wear and corrosion resistance than most other friction stir welded light alloys. Kannan et al. found that the friction stir welded magnesium alloy AZ31 exhibited a higher SCC susceptibility than the base material.[46] At the same time, the SZ or weld nugget exhibited a higher and more uniform pitting corrosion resistance than the base material. Zeng et al. found that the weld nuggets of friction stir welded AM50A and AZ90D alloys had poor corrosion resistance, and suggested that embedded iron contaminants from wear of the tool could be responsible for the poor corrosion properties of the welds.[36]

The work of Zeng et al. showed that the corrosion rates varied across the different friction stir weld zones.[36] They were found to be higher in the base material than in the weld. Similarly, TMAZ was found to be more susceptible to corrosion attack than the HAZ of the joint. The corrosion resistance of the various zones increased in the order BM (base metal), TMAZ, HAZ and SZ.

The work of Srinivasan et al. showed that both the parent alloy and the friction stir weld specimens exhibited SCC in ASTMD1384 solution, but the friction stir weld nugget had a higher susceptibility to SCC in this weldment.[30]

In the paper of Liu et al., the polished surfaces of the SZ in the dissimilar friction stir welded 2024-T3Al/AZ31B-H24 Mg joints using a water-based and a non-water-based liquid as polishing solution were evaluated.[7] It was found that the water-based polishing solution induced the galvanic corrosion attack more readily than the non-water-based polishing solution during the polishing process. The predominant locations of the corrosion attack were observed in the narrow regions of AZ31 alloy adjacent to Al2024 areas, where there was a low ratio of anode-to-cathode surface area. The corrosion was basically due to the establishment of a strong galvanic coupling between Mg and Al alloys in the dissimilar friction stir weld joints. The low micro-hardness value in the corroded region was attributed to the formation of the porous magnesium hydroxide layer with micro-cracks.

A macrograph of an FSW AZ31 Mg sample exposed to a salt spray test is shown in Fig. 16.16. The base material region shows severe corrosion, whereas the weld metal region shows a significant improvement in corrosion resistance. Figure 16.17(a) and (b) show the scanning electron microscope (SEM)

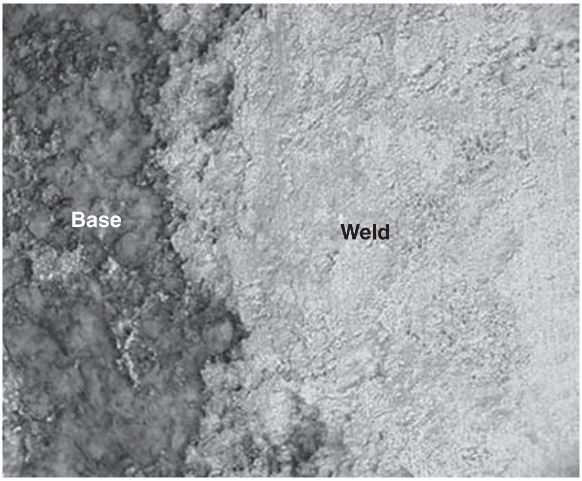

16.16 Macrograph of FSW AZ31 Mg sample exposed to salt spray test.

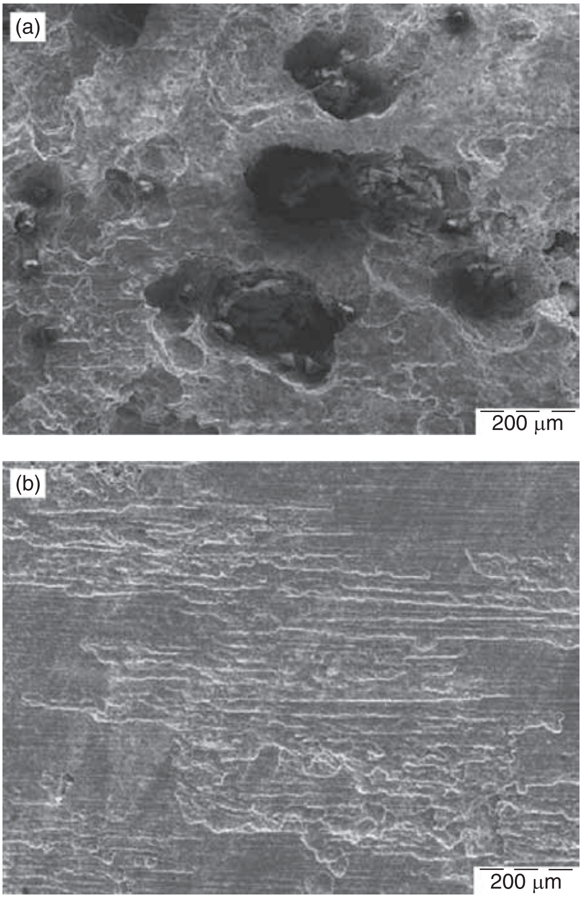

16.17 SEM micrographs of (a) base material and (b) SZ of FSW AZ31 Mg sample exposed to salt spray test.

micrographs pertaining to the base region and SZ from the salt spray test samples, respectively. The base region exhibited large pits, whereas the SZ showed no such pitting morphology. A large reduction in thickness was also observed in the base region as compared to the weld metal. This further confirms the higher corrosion resistance of the SZ as compared to the base material, which can be attributed to the fine distribution of secondary phase particles and the fine grain size found in this region.[46]

16.6.4 Other mechanical properties

The hardness of the SZ is generally higher than that of the base materials due to refined grain structure in the SZ. Variation in hardness with grain size was

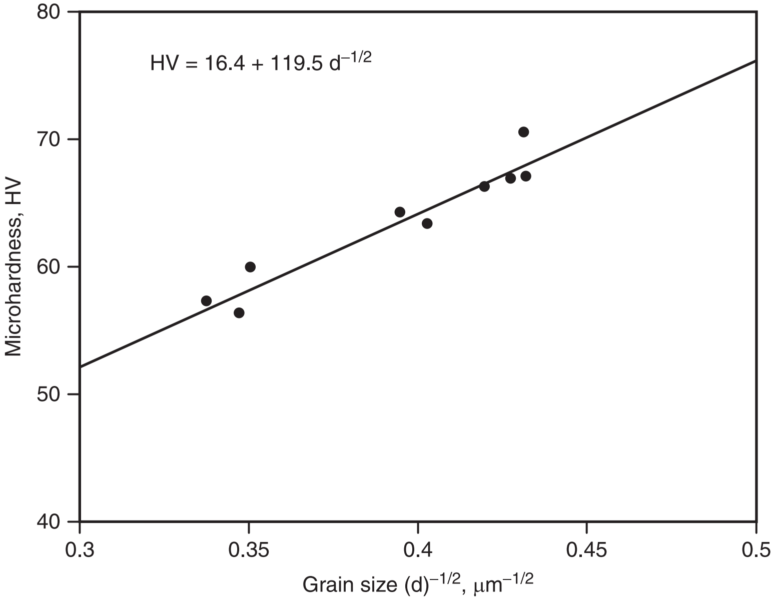

16.18 A typical plot of the Hall–Petch type relationship for the friction stir welded sample (1000 r/min, 240 mm/min).

identified to follow the Hall–Petch relationship, that is, hardness increases with decreasing grain size. However, a reduction in hardness was revealed in the SZ of FSW hot-rolled AZ31B-H24 due to coarsening of grains.[38]

The hardness values and grain sizes were taken at the center and both sides of the weld nugget at distances of 5, 10, 15 and 20 mm. It was seen that the Hall–Petch type linear relationship is followed and can be written as HV = 16.4 + 119.5d – 1/2, where d is the grain size (see Fig. 16.18). The relationship showed a strong grain size dependence on the hardness in the FSW AZ31B-H24 alloy. The grain boundaries thus become the main obstacle to the slip of dislocations, and the materials with a smaller grain size would have higher hardness or strength and would impose more restriction to the dislocation movement.[2]

16.7 Weld defects of friction stir welded magnesium alloys

In the fast development and application of the FSW process, it has been observed that welding defects may be formed during FSW when inappropriate welding parameters or technological conditions are used, and defects as such groove, cavity and kissing bond have a significant influence on the mechanical properties of the joints.[63]

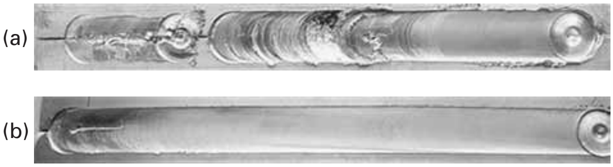

16.19 Two typical defects of friction stir welded AZ31 magnesium.

Figure 16.19(a) shows a weld with a 'rough surface appearance,' together with 'excessive side flash.' Figure 16.19(b) shows a poor weld with a large surface groove at the start. If a surface void was developed at the start of a weld, it gradually disappeared as the weld progressed. Also, when the traverse speed was too slow, it was possible to develop a surface void toward the end of a previously sound weld.

If the welding parameters used are appropriate, then usually no defects are formed when using friction stir welded AZ31 magnesium alloy. But in order to understand the relationship between the welding parameters and the potential defects, a lower welding pressure than normal value was used in all the specimens. In the current experimental conditions, pores and insufficient penetration at the bottom of the weld occur, so the zone near the weld root was magnified to study the defects. As shown in Fig. 16.20, the welding direction is out of paper and rotation is anti-clockwise; on the left is AS and on the right is RS. The white arrow is directed to the welding line at the bottom of the weld.

The experimental results showed that pores were produced in the friction stir weld when the welding speed increased to 200 mm/min with the constant rotation speed of 1000 r/min. The pore first occurred near the welding line at a relatively low welding speed but moved into AS and the upper part of the weld with the increase in the welding speed. The faster the welding speed, the larger the size of the pore.

When the welding tool moved forward along the welding line, many micro-pores were left behind, and each micro-pore was filled by the tool at the same time. The FSW, in other words, is a procedure that both generates and eliminates micro-pores, as shown in Fig. 16.21. The width of a micro-pore is about equal to the welding rate v_{rate}, and the welding tool movement distance per revolution is indicated as l. The length of a micro-pore is about the diameter of the shoulder and its thickness is equal to that of the base metal. The volume of the micro-pore is indicated as V, which is relative to the base metal thickness δ, welding rate v_{rate} and the radius of the shoulder.

The radii of the shoulder and the pin are indicated as $r_{shoulder}$ and r_{pin}, respectively. The welding proceeds from right to left and the rotation is anti-clockwise. v_W and v_R are the welding speed and the rotation speed, respectively, and P is the welding pressure, as shown in Fig. 16.22.

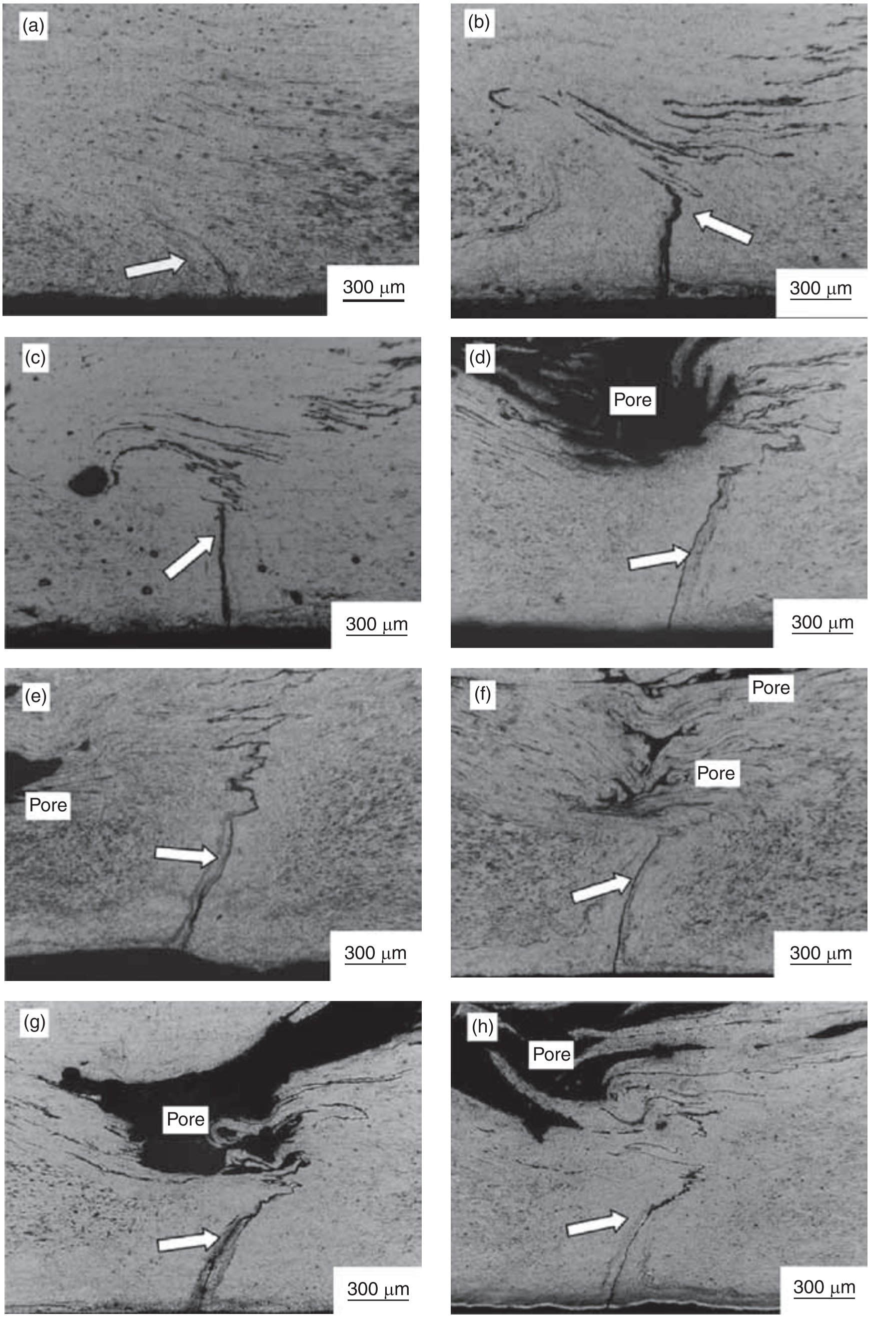

16.20 The defects in friction stir weld at different welding speeds: the welding speed in (a)–(h) is 40, 120, 150, 200, 250, 300, 400 and 600 mm/min, respectively. The white arrow points to the welding line at the bottom of the weld.

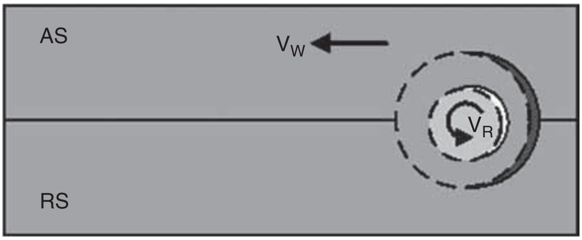

16.21 The micro-pore produced during friction stir welding.

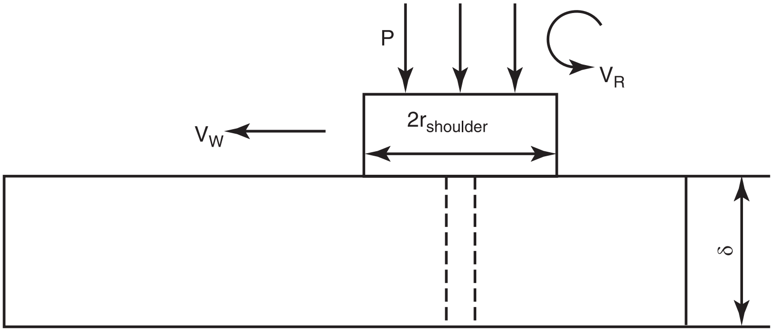

16.22 Schematic figure of micro-pore fill procedure.

Assume that the volume of press-in metal into micro-pore per second caused by the shoulder is marked by s, when the welding pressure P and the rotation speed v_R were kept at a constant value. The time effect of the shoulder on the micro-pore is indicated as t, then

$$t = \frac{r_{shoulder}}{v_W} \qquad [16.1]$$

If the micro-pore was completely filled, the fill metal must be equal to the volume of the micro-pore. If the fill time is t_1, then

$$V = st_1 \quad \text{or} \quad t_1 = \frac{V}{s} \qquad [16.2]$$

In fact, the only time that the shoulder plays effect is when less than completely filled, the micro-pore can successfully disappear.

$$t \geq t_1 \qquad [16.3]$$

Combining Eq. (16.1) and Eq. (16.2) results in the following equation:

$$\frac{r_{shoulder}}{v_W} \geq \frac{V}{s} \qquad [16.4]$$

The s is dependent on the welding pressure P and the rotation speed v_R; when the other welding parameters are kept at the same value, the volume of press-in metal will increase with the increase of the rotation speed, that is

$$s \propto v_R.$$

The friction force under the shoulder will increase with the speed of the welding pressure, relative to the momentum theory $m(v - v_0) = Ft$; the press-in speed increases with the welding pressure, so the volume of press-in metal is directly proportional to the welding pressure,

$$s \propto P.$$

Then, the relationship between s and P and the rotation speed v_R can be indicated as.

$$s = kPv_R. \qquad [16.5]$$

In Eq. (16.5), k is the proportion factor and is related with the properties of the metal and temperature.

Eq. (16.4) combined with Eq. (16.5) results in either of the following equations:

$$\frac{Pv_R}{v_W} \geq \frac{V}{kr_{shoulder}} \quad \text{or} \quad P \cdot r_{rate} \geq \frac{V}{kr_{shoulder}}. \qquad [16.6]$$

If the pin effect was taken into account, then the conditions for complete penetration changed into

$$P \cdot r_{rate} \geq \frac{V}{k(r_{shoulder} - r_{pin})}. \qquad [16.7]$$

Equation (16.7) gives the essential conditions for a defect-free weld. If the welding tool is constant, then the Eq. (16.7) can be simplified into

$$P \cdot r_{rate} \geq \alpha. \qquad [16.8]$$

When the welding pressure and the rotation speed are kept at a constant value, the welding speed must be less, and the formation of pores can be avoided. When the welding speed is kept at certain value, the welding pressure and rotation speed must be higher than a specific value, and defects can be avoided. These three welding parameters are dependent on one another, and only by using the relationship of Eq. (16.7), a defect-free weld can be obtained. It provides a simple method for choosing suitable welding parameters. For different materials, α will be different, but there must be a specific value of α for each material.

One advantage of the fine-element method (FEM) model is its ability to predict void formation, because the arbitrary Langrangian–Eulerian formulation allows for large material deformation and for the grid to track the material so that separation can occur between the workpiece and the tool. Figure 16.23 shows

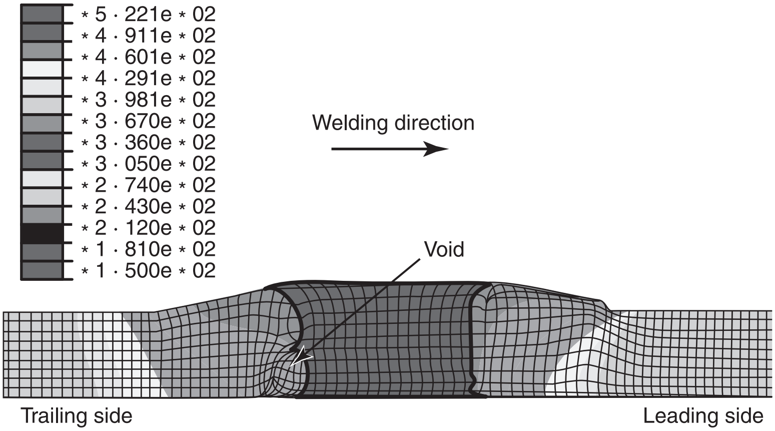

16.23 Void formation at the lower advancing side due to incomplete filling modeled using ALE formulation of FEM.

void formation at the lower AS, near the trailing edge of the pin/workpiece interface, due to incomplete deposition of plastic material.

Therefore, the friction stir repair welding was utilized to remove such a groove defect, and the focus was on the mechanical properties and microstructural characteristics of the repair joints so as to obtain an optimum repair welding process. In the paper of Liu et al., the base metal used was a 2219 aluminum alloy plate of 7.5 mm thick.[64] The experimental results indicated that the groove defect could be removed by friction stir repair welding, and the offset repair welding process was superior to the symmetrical repair welding process. In the symmetrical repair welding process, a large number of fine cavity defects and an obvious aggregation of hard-brittle phase Al2Cu occur; accordingly, the mechanical properties of the repair joint were weakened, and the fracture feature of the repair joint is partly brittle and partly plastic. A good quality repair joint can be obtained by the offset repair welding process, and the repair joint will be fractured near the interface between the weld nugget zone and TMAZ.[64]

16.8 Applications of friction stir welded magnesium alloys

The use of magnesium alloys in the automobile industry encompasses the manufacturing of a wide range of parts such as steering wheels, steering column parts, instrument panels, seats, gear boxes, air intake systems, stretchers, gearbox housings, tank covers, etc. Future developments will include the manufacture of large body parts, cylinder blocks, door frames and petrol tank covers.[65] With the development of research into the effect of FSW on magnesium alloy, FSW shows great potential for application in these fields.

16.9 Future trends and sources of further information and advice

Magnesium is the lightest of all metals used as the basis for constructional alloys. It is this property that resulted in automobile manufacturers replacing denser materials – not only steels, cast irons and copper base alloys but even aluminum alloys by magnesium-based alloys. Reducing the weight of car components as a result in part of new legislation for limiting carbon emissions has triggered renewed interest in magnesium. A wider use of magnesium-based alloys necessitates several parallel programs, one of which is joining problems. Although much research has been done on FSW of various magnesium alloys, and some useful results have been reported, the application of FSW on magnesium is still far less than that of aluminum alloy. More work has to be done to improve the FSW application of magnesium alloys, including the development of higher mechanical properties and suitable parameters.

The main research institutes include the following:

- China FSW Center: http://www.sfswt.com/
- AWS: http://www.sws.org/w/a
- TWI: http://www.twi.co.uk/
- IIW: http://www.iiw-iis.org/.

16.10 Acknowledgments

I am grateful to the authors whose works I have made use of in this chapter. Some of the author's research was supported by the National High Technology Development Foundation of China.

16.11 References

1. Esparza JA, Davis WC, Trillo EA, Murr LE (2002). Friction-stir welding of magnesium alloy AZ31B. *J Mater Sci Lett* **21**(12): 917–20.
2. Afrin N, Chen DL, Cao X, Jahazi M (2008). Microstructure and tensile properties of friction stir welded AZ31B magnesium alloy. *Mater Sci Eng A* **472**(1–2): 179–86.
3. Suhuddin UFHR, Mironov S, Sato YS, Kokawa H, Lee CW (2009). Grain structure evolution during friction-stir welding of AZ31 magnesium alloy. *Acta Mater* **57**(18): 5406–18.
4. Nandan R, DebRoy T, Bhadeshia HKDH (2008). Recent advances in friction-stir welding – process, weldment structure and properties. *Prog Mater Sci* **53**(6): 980–1023.
5. Park SHC, Sato YS, Kokawa H (2003). Effect of micro-texture on fracture location in friction stir weld of Mg alloy AZ61 during tensile test. *Scripta Mater* **49**(2): 161–6.
6. Mishra RS, Ma ZY (2005). Friction stir welding and processing. *Mater Sci Eng R* **50**(1–2): 1–78.

7. Liu C, Chen DL, Bhole S, Cao X, Jahazi M (2009). Polishing-assisted galvanic corrosion in the dissimilar friction stir welded joint of AZ31 magnesium alloy to 2024 aluminum alloy. *Mater Charact* **60**(5): 370–6.
8. Kwon YJ, Shigematsu I, Saito N (2008). Dissimilar friction stir welding between magnesium and aluminum alloys. *Mater Lett* **62**(23): 3827–9.
9. Chen YC, Nakata K (2008). Friction stir lap joining aluminum and magnesium alloys. *Scripta Mater* **58**(6): 433–6.
10. Kostka A, Coelho RS, Santos J, Pyzalla AR (2009). Microstructure of friction stir welding of aluminium alloy to magnesium alloy. *Scripta Mater* **60**(11): 953–6.
11. Scialpi A, Giorgi MD, De Filippis LAC, Nobile R, Panella FW (2008). Mechanical analysis of ultra-thin friction stir welding joined sheets with dissimilar and similar materials. *Mater Des* **29**(5): 928–36.
12. Aonuma M, Nakata K (2009). Effect of alloying elements on interface microstructure of Mg–Al–Zn magnesium alloys and titanium joint by friction stir welding. *Mater Sci Eng B* **161**(1–3): 46–9.
13. Zadeh A, Saeid T, Sazgari B (2008). Microstructural and mechanical properties of friction stir welded aluminum/copper lap joints. *J Alloys Compd* **460**(1–2): 535–8.
14. Somasekharan AC, Murr LE (2004). Microstructures in friction-stir welded dissimilar magnesium alloys and magnesium alloys to 6061-T6 aluminum alloy. *Mater Charact* **52**(1): 49–64.
15. Yutaka SS, Seung HCP, Masato M, Hiroyuki K (2004). Constitutional liquation during dissimilar friction stir welding of Al and Mg alloys. *Scripta Mater* **50**(9): 1233–6.
16. Yan JC, Xu ZW, Li ZY, Li L, Yang SQ (2005). Microstructure characteristics and performance of dissimilar welds between magnesium alloy and aluminum formed by friction stirring. *Scripta Mater* **53**(5): 585–9.
17. Thomas WM, Nicholas ED (1997). Friction stir welding for the transportation industries. *Mater Des* **16**(4/6): 269–73.
18. Davis CJ, Thomas WM (1996). Friction stir process welds aluminum alloys. *Weld J* **75**(3): 41–5.
19. Colligan K (1999). Material flow behavior during friction stir welding of aluminum. *Weld J Suppl* **78**(7): S229–37.
20. Yutaka SS, Hiroyuki K (1999). Microstructural evolution of 6063 aluminum during friction stir welding. *Metall Mater Trans A* **30A**: 2429–37.
21. Friction stir welding – the state of the art. Copyright TWI, PRAD No: 7417.01/99/1012.03.
22. Zhang H. Study on friction stir welding procedures of magnesium alloy and joint formation mechanism [D]. HeiLongJiang, China: Harbin Institute of Technology.
23. Cao X, Jahazi M (2009). Effect of welding speed on the quality of friction stir welded butt joints of a magnesium alloy. *Mater Des* **30**(6): 2033–42.
24. Boz M, Adem K (2004). The influence of stirrer geometry on bonding and mechanical properties in friction stir welding process. *Mater Des* **25**(4): 343–7.
25. Chen YC, Nakata K (2009). Effect of tool geometry on microstructure and mechanical properties of friction stir lap welded magnesium alloy and steel. *Mater Des* **30**(9): 3913–9.

26. Leal RM, Leitão C, Loureiro A, Rodrigues DM, Vilaça P (2008). Material flow in heterogeneous friction stir welding of thin aluminium sheets: Effect of shoulder geometry. *Mater Sci Eng A* **498**(1–2): 384–91.
27. Padmanaban G, Balasubramanian V (2009). Selection of FSW tool pin profile, shoulder diameter and material for joining AZ31B magnesium alloy – an experimental approach. *Mater Des* **30**(7): 2647–56.
28. Thomas WM, Johnson KI, Wiesner CS (2003). Friction stir welding–recent developments in tool and process technologies. *Adv Eng Mater* **5**: 485–90.
29. Thomas WM (2003). Friction stir welding – recent developments. *Mater Sci Forum* **426–32**: 229–36.
30. Srinivasan PB, Zettler R, Blawert C, Dietzel W (2009). A study on the effect of plasma electrolytic oxidation on the stress corrosion cracking behaviour of a wrought AZ61 magnesium alloy and its friction stir weldment. *Mater Charact.* **60**(5): 389–96.
31. Du XH, Wu BL (2008). Using friction stir processing to produce ultrafine-grained microstructure in AZ61 magnesium alloy. *Trans Nonferrous Metals Soc China* **18**(3): 562–5.
32. Woo W, Choo H, Prime MB, Feng Z, Clausen B (2008). Microstructure, texture and residual stress in a friction-stir-processed AZ31B magnesium alloy. *Acta Mater* **56**(8): 1701–11.
33. Dobriyal RP, Dhindaw BK, Muthukumaran S, Mukherjee SK (2008). Microstructure and properties of friction stir butt-welded AE42 magnesium alloy. *Mater Sci Eng A* **477**(1–2): 243–9.
34. Yang J, Xiao BL, Wang D, Ma ZY (2010). Effects of heat input on tensile properties and fracture behavior of friction stir welded Mg–3Al–1Zn alloy. *Mater Sci Eng A* **527**(3): 708–14.
35. Feng AH, Ma ZY (2009). Microstructural evolution of cast Mg–Al–Zn during friction stir processing and subsequent aging. *Acta Mater* **57**(14): 4248–60.
36. Zeng RC, Chen J, Dietzel W, Zettler R, Santos JF, Nascimento ML, et al. (2009). Corrosion of friction stir welded magnesium alloy AM50. *Corros Sci.* **51**(8): 1738–46.
37. Ni DR, Wang D, Feng AH, Yao G, Ma ZY (2009). Enhancing the high-cycle fatigue strength of Mg–9Al–1Zn casting by friction stir processing. *Scripta Mater.* **61**(6): 568–71.
38. Zhang DT, Suzuki M, Maruyama K (2005). Microstructural evolution of a heat-resistant magnesium alloy due to friction stir welding. *Scripta Mater* **52**(9): 899–903.
39. Darras BM, Khraisheh MK, Abu-Farha FK, Omar MA (2007). Friction stir processing of commercial AZ31 magnesium alloy. *J Mater Process Technol* **191**(1–3): 77–81.
40. Afrin N, Chen DL, Cao X, Jahazi M (2008). Microstructure and tensile properties of friction stir welded AZ31B magnesium alloy. *Mater Sci Eng A* **472**(1–2): 179–86.
41. Wang XH, Kuaishe W (2006). Microstructure and properties of friction stir butt-welded AZ31 magnesium alloy. *Mater Sci Eng A* **431**(1–2): 114–17.
42. Cavaliere P, De Marco PP (2007). Friction stir processing of AM60B magnesium alloy sheets. *Mater Sci Eng A* **462**(1–2): 393–7.

43. Chang CI, Du XH, Huang JC (2007). Achieving ultrafine grain size in Mg–Al–Zn alloy by friction stir processing. *Scripta Mater* **57**(3): 209–12.
44. Xie GM, Ma ZY, Geng L (2008). Effect of microstructural evolution on mechanical properties of friction stir welded ZK60 alloy. *Mater Sci Eng A* **486**(1–2): 49–55.
45. Xie GM, Ma ZY, Geng L, Chen RS (2007). Microstructural evolution and mechanical properties of friction stir welded Mg–Zn–Y–Zr alloy. *Mater Sci Eng A* **471**(1–2): 63–8.
46. Kannan MB, Dietzel W, Zeng R, Zettler R, Santos JF (2007). A study on the SCC susceptibility of friction stir welded AZ31 Mg sheet. *Mater Sci Eng* A **460–1**(15): 243–50.
47. Zhang DT, Suzuki M, Maruyama K (2006). Study on the texture of a friction stir welded Mg-Al-Ca alloy. *Acta Metallurgica Sinica (English Letters)* **19**(5): 335–40.
48. Zhang H, Lin SB, Wu L, Feng JC (2004). Microstructural evolution characters of friction stir welded AZ31 magnesium alloy. *Rare Metal* **23**(4): 340–6.
49. Ma ZY, Pilchak AL, Juhas MC, Williams JC (2008). Microstructural refinement and property enhancement of cast light alloys via friction stir processing. *Scripta Mater* **58**(5): 361–6.
50. Zhang H, Lin SB, Wu L, Feng JC (2004). Microstructural studies in friction stir welded AZ31 magnesium. *Acta Metallurgica Sinica* **17**(5): 747–53.
51. Chang CI, Lee CJ, Huang JC (2004). Relationship between grain size and Zener–Holloman parameter during friction stir processing in AZ31 Mg alloys. *Scripta Mater* **51**(6): 509–14.
52. Du XH, Wu BL (2008). Using friction stir processing to produce ultrafine-grained microstructure in AZ61 magnesium alloy. *Trans Nonferrous Metals Soc China* **18**(3): 562–5.
53. Lee WB, Lee Y, Kim MK, Yoon J, Kim YJ, Yoen YM, et al. (2006) Microstructures and wear property of friction stir welded AZ91 Mg/SiC particle reinforced composite. *Compos Sci Technol* **66**(11–12): 1513–20.
54. Chang CI, Du XH, Huang JC (2008). Producing nanograined microstructure in Mg–Al–Zn alloy by two-step friction stir processing. *Scripta Mater* **59**(3): 356–9.
55. Lin SB, Zhang H, Wu L, Feng JC (2003). Using friction stir welding to join AZ31 magnesium. *China Weld* **12**(2): 137–41.
56. Zhang H, Huang JH, Lin SB, Wu L, Zhang JG (2006). Temperature simulation of the preheating period in friction stir welding based on finite element method. *Proc Inst Mech Eng: J Eng Manufacture* **220**(B7): 1097–1106.
57. Afrin N, Chen DL, Cao X, Jahazi M (2007). Strain hardening behavior of a friction stir welded magnesium alloy. *Scripta Mater* **57**(1): 1004–7.
58. Balasubramanian V (2008). Relationship between base metal properties and friction stir welding process parameters. *Mater Sci Eng A* **480**(1–2): 397–403.
59. Woo W, Choo H, Brown DW, Liaw PK, Feng Z (2006). Texture variation and its influence on the tensile behavior of a friction-stir processed magnesium alloy. *Scripta Mater* **54**(11): 1859–64.
60. Gharacheh MA, Kokabi AH, Daneshi GH, Shalchi B, Sarrafi R (2006). The influence of the ratio of 'rotational speed/traverse speed' (w/v) on mechanical properties of AZ31 friction stir welds. *Int J Mach Tools Manufacture* **46**(15): 1983–7.

61. Kannan MB, Dietzel W, Zeng R, Zettler R (2007). A study on the SCC susceptibility of friction stir welded AZ31 Mg sheet. *Mater Sci Eng A* **460–1**: 243–50.
62. Kannan MB, Dietzel W, Blawert C, Riekehr S, Kocak M (2007). Stress corrosion cracking behavior of Nd:YAG laser butt welded AZ31 Mg sheet. *Mater Sci Eng A* **444**: 220–6.
63. Zhang H, Lin SB, Wu L, Feng JC, Ma SL (2006). Defects formation procedure and mathematic model for defect-free friction stir weld of AZ31 magnesium alloy. *Mater Des* **27**(9): 805–9.
64. Liu HJ, Zhang HJ (2009). Repair welding process of friction stir welding groove defect. *Trans Nonferrous Metals Soc China* **19**(3): 563–7.
65. Mordike BL, Ebert T (2001). Magnesium: properties–applications–potential. *Mater Sci Eng A* **302**(1): 37–45.

17

Laser welding of magnesium alloys

J. SHAN, Tsinghua University, China

Abstract: Magnesium alloys have been increasingly applied in many fields which depend upon efficient welding technologies. As a high energy density thermal source, laser welding can reduce many welding defects compared with conventional welding methods. This chapter introduces the character of the laser welding process, the influence of laser welding parameters and the laser weldability of magnesium alloys. Based on these, it introduces some typical kinds of magnesium alloy (such as AZ31B), for example, to analyze the microstructure and mechanical properties of laser weld, which further explain the typical welding problems of magnesium alloys. The main defects of the different magnesium alloys in laser welding are discussed, and then the reasons for each defect formation, the factors affecting the defects and the prevention of defects are analyzed.

Key words: laser welding, magnesium alloys, microstructure, mechanical properties, defects.

17.1 Introduction

This chapter includes five sections: character of the laser welding process and influence of laser welding parameters; laser weldability of magnesium alloys; microstructure and properties of laser welding of magnesium alloys; typical defects of laser welding of magnesium alloys; and outlook and future trends.

The first section analyzes interaction between laser and materials at first, then introduces the formation of keyhole in laser welding and the three modes of laser welding, and finally analyzes the influence of welding parameters on weld shape and welding mode. The second section introduces the physical and chemical properties of magnesium alloy, then discusses the advantage of laser welding over other welding methods, and finally analyzes the laser weldability of magnesium alloy and the advantage of laser welding of magnesium alloy based on these properties. The third section describes types (such as AZ31B, AM50, ZE41A and so on), components (such as Mg-Al-Zn, Mg-Mn, Mg-Zr and so on) and process methods (such as wrought, sand cast and die cast) of commercial magnesium alloys, then selects some typical kinds of magnesium alloys, such as AZ31B wrought magnesium alloy, and finally analyzes the microstructure and the mechanical properties (such as hardness, tensile strength and ductility) of laser weld, especially the fracture mechanism and crack origin of welded joints based on strength test experiments. The fourth section introduces some typical kinds of defect of laser welding of magnesium alloy (such as porosity, crack, oxide inclusions and loss of alloying elements). It also introduces the main welding defects of magnesium alloys under different processes, emphasizes the reasons for the saging of molten pool (which is one of the main defects of laser welding of wrought magnesium alloys and prevention methods); the reasons for porosity formation (which is the main defect of laser welding of die cast magnesium alloys); the factors causing porosity; and prevention methods. The fifth section discusses likely future trends and gives a description of sources of further information and advice on the laser welding of magnesium alloys.

17.2 Character of the laser welding process and influence of laser welding parameters

17.2.1 Physical process of laser welding

Laser beam irradiates on the surface of the material and interacts with it. The energy of the laser beam is partially reflected by the surface of the material, and partially absorbed by the material. The rest of the energy is transmitted by the material. This process is shown in Eq. 17.1.[1]

$$E_0 = E_r + E_a + E_s \tag{17.1}$$

In Eq. 17.1, E_0 is the total energy of the laser beam, E_r is the partial energy reflected by the surface of the material, E_a is the partial energy absorbed by the material and E_s is the partial energy transmitted by the material. Most of the energy of the laser beam is absorbed several micrometers deep into the surface of the metal, and the surface changes the absorbed energy to heat, which is transferred into the material by heat conduction.[1–4] This partial energy can be used in laser welding.

When the laser beam vertically irradiates the surface of metal, the laser absorptivity of the metal can be calculated as in Eq. 17.2[5] and Eq. 17.3.[5]

$$A = 0.365(\rho/\lambda)^{1/2} - 0.0667(\rho/\lambda) + 0.006(\rho/\lambda)^{3/2} \tag{17.2}$$

$$\rho = \rho_{20}\,(1 + K_\rho T) \tag{17.3}$$

In Eq. 17.2, A is the ratio of the laser absorptivity of the solid metal, ρ is electrical resistivity of the metal and λ is the wavelength of the laser. In Eq. 17.3, ρ is electrical resistivity of the metal, ρ_{20} is the electrical resistivity of the metal at room temperature, K_ρ is the ratio of electrical resistivity changing with temperature and T is the temperature of the metal.

According to Eq. 17.2 and Eq. 17.3, we can conclude that the laser absorptivity of the solid metal increases when the electrical resistivity of the metal increases; it increases when the temperature of the metal increases, and decreases when the wavelength of the laser beam increases. So, the absorption ratio changes with various materials and wavelengths of laser, as shown in Fig. 17.1.[6]

The laser absorptivity of the solid metal is much slower than that of room temperature changing to the melting temperature of the metal. The absorption ratio increases rapidly to 50–60% once the metal begins to melt. When the temperature

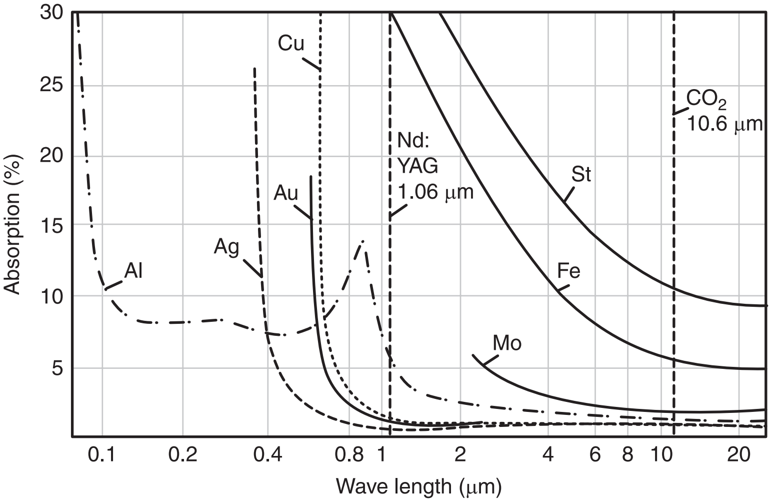

17.1 Absorption of a number of metals as a function of laser radiation wavelength.

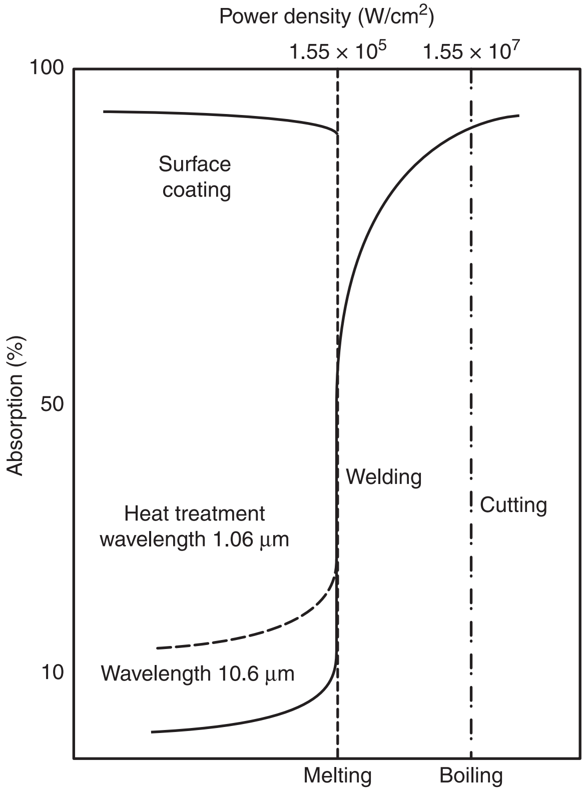

17.2 Absorption of metals as a function of temperature.[8]

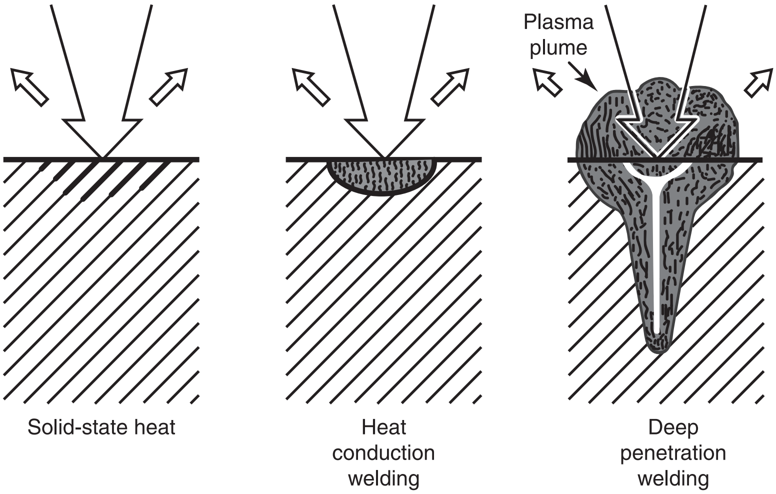

17.3 Various processes in different power density laser radiations.[1]

gets close to boiling point, the absorption ratio can exceed up to 90%.[7] These observations are illustrated in Fig. 17.2. Different power densities of the laser beam's irradiation on the metal can result in different physical processes, which are shown in Fig. 17.3[1]:

1 When the laser power density $I < 10^4$ W/cm^2, the laser energy absorbed by the metal results in the rise of its temperature, but the metal always remains solid.[1] The process can be used for heat treatment of metallic parts.
2 When the laser power density $I > 10^4$ W/cm^2 and $I < 10^6$ W/cm^2, the laser energy absorbed by the metal results in the melting of the metal surface, and the heat is conducted into the interior of metal, resulting in the melting of the interior of the metal. The molten pool remains shallow and evaporation of the metal is not likely. This process is usually applied for the heat conduction mode of laser welding and surface coating and alloying.
3 When the laser power density $I > 10^6$ W/cm^2 and $I < 10^7$ W/cm^2, the laser energy absorbed by metal results in the rapid rise in the temperature of the metal and reaches boiling point in a very short time (10^{-6}–10^{-8} s). A small amount of metal evaporates from the molten pool, which results in the pressure recoiling toward the molten pool. The recoil pressure pushes the liquid metal aside and then a keyhole forms. Metal evaporates continuously from the keyhole wall because of the high temperature, and the keyhole fills with metallic vapor and shielding gas. After the keyhole formation (the keyhole resembles a black body), the laser beam forms multiple reflections on the keyhole wall, which increases the absorption ratio further. The keyhole wall absorbs the laser and conducts the heat into the metal, which results in the melting of the surrounding metal and forms a molten pool around the

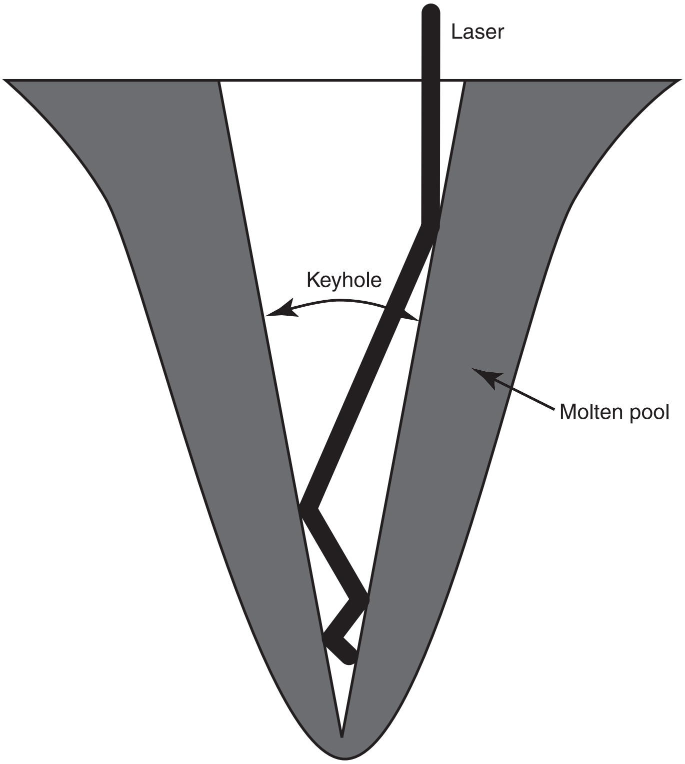

17.4 Laser multiple reflection on the surface of the keyhole.[5]

keyhole.[1–4,9,11] This process is used for the deep penetration mode of laser welding, which is illustrated in Fig. 17.4.

4 When the laser power density $I > 10^7$ W/cm^2, the metal evaporates significantly. This process is used for cutting. 'Cutting' means laser cutting, which is a similar processing method to laser welding, not one of the modes of laser welding.

Heat conduction mode and deep penetration mode are both stable processes; however, the depth of deep penetration mode is much more than that of the heat conduction mode. As a result, deep penetration mode is the preferred process.

In deep penetration welding, free electrons of metallic vapor from the molten pool surface and the keyhole wall, and shielding gas are accelerated by absorbing laser energy. Accelerated free electrons collide with metallic vapor and shielding gas and ionize them. The number of free electrons increases very rapidly and forms compact laser-induced plasma, which is shown in Fig. 17.5. The compact laser-induced plasma sits above the molten pool and can shield laser significantly. The laser-induced plasma partially absorbs laser energy; however, the laser-induced plasma also refracts and scatters laser significantly, which shows that the laser cannot focus on the surface of the workpiece.[5] The two factors result

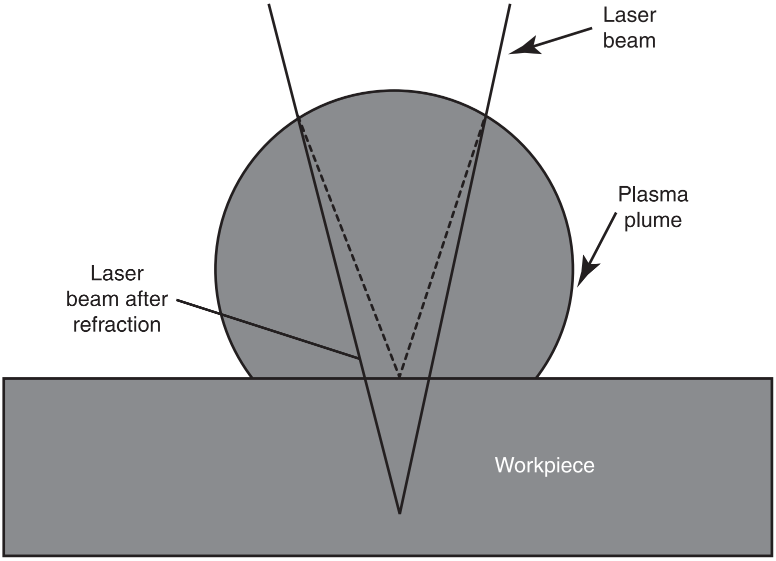

17.5 Influence of plasma.[5]

in a decrease in laser power density; hence, the heat conduction mode and deep penetration mode alternate, the welding process becomes very unstable and the weld formation weakens. Shielding gas is usually used to blow down the laser-induced plasma in order to avoid its effect; it also can protect the molten pool at the same time.

In CO_2 laser welding of wrought magnesium alloy AZ31B, heat conduction mode, deep penetration mode and the mix mode can all be present. The determinant is power density instead of heat input. When the power density is lower than the critical value (900 W for AZ31B),[12] the welding mode cannot keep the deep penetration mode even if the heat input is very high (Fig. 17.6). In Fig. 17.6, P is deep penetration mode, U is unstable mode and H is heat conduction mode, as illustrated in Fig. 17.7–Fig. 17.13.

17.2.2 Laser welding parameters

In the laser welding process, laser beam, power, welding speed, focal position, and kind and flow of shielding gas have an important influence on the weld quality.

Character of laser beam

The character of a laser beam consists of wavelength, spot size, divergent angle and so on. Under the same welding conditions, the depth of the molten pool of the

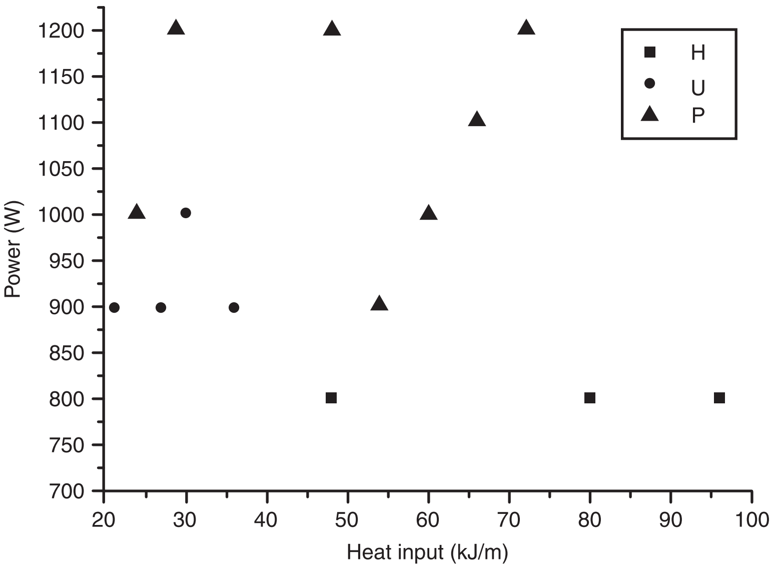

17.6 Influences of heat input and laser power on welding mode. H: heat conduction mode, U: unstable mode, P: deep penetration mode.[12]

short wavelength laser (such as Nd:YAG) is more than that of long wavelength laser (such as CO_2). First, the absorption ratio of short wavelength laser by magnesium alloy is higher than that of long wavelength laser, which can decrease the critical power of deep penetration mode and is favorable for the formation of deep penetration mode. Second, the tendency of plasma formation of short wavelength laser is smaller than that of long wavelength laser, which reduces the shield of short wavelength laser. The spot size affects the weld quality through power density. The smaller the spot size, the higher the power density becomes, and the more easily deep penetration mode is obtained. The laser beam divergence angle has an effect on laser transmission – the smaller the divergent angle, the better the laser transmission. In addition, the mode and polarization of laser beam also have an effect on weld quality.

Laser power

Laser power is one of the most important parameters in the welding process. With the increase in the laser power, the welding mode transforms the heat induction mode into unstable mode and then into deep penetration mode, and thus the width and depth of the molten pool increase. In addition, the change of depth is more obvious than that of width. This is illustrated in Fig. 17.7.

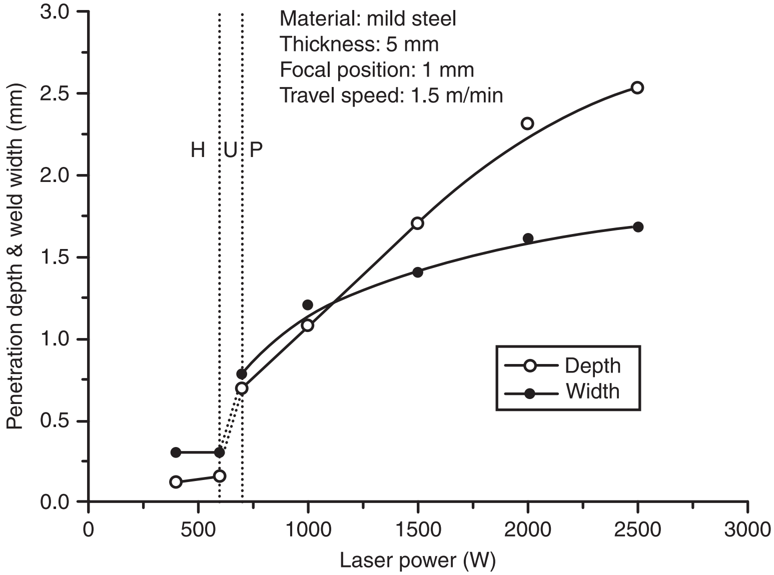

17.7 Depth and width of welding seam as a function of laser power.[7]

Welding speed

When welding speed increases, heat input decreases, and the width and depth of the molten pool decreases, as shown in Fig. 17.8. Welding speed also has an effect on the welding mode, which is similar to power. With the increase of the welding speed, the welding mode transforms deep penetration mode into unstable mode and then into heat induction mode.

Focal position

Focal position means the distance between the laser focus and the surface of the workpiece. This is illustrated in Fig. 17.9.

Focal position has an effect on the welding mode through changing power density. With the increase of the absolute value of D_f, the welding mode transforms deep penetration mode into unstable mode and then into heat induction mode. The depth of the molten pool decreases rapidly, however, as the width increases. In deep penetration mode, the depth achieves the maximum when D_f is about 0.5–1.5 mm, as shown in Fig. 17.10. This is because the reflection of the laser on the keyhole wall is favored by multiple reflection and absorption by the keyhole wall when D_f is about 0.5–1.5 mm. Focal position affects the power density through changing the spot size (Fig. 17.11), which is the reason why the focal position affects the welding mode, depth and width of the molten pool. Equation 17.4 expresses the relationship between focal position and spot size, and Eq. 17.5[5] reflects the relationship between focal position and power density.

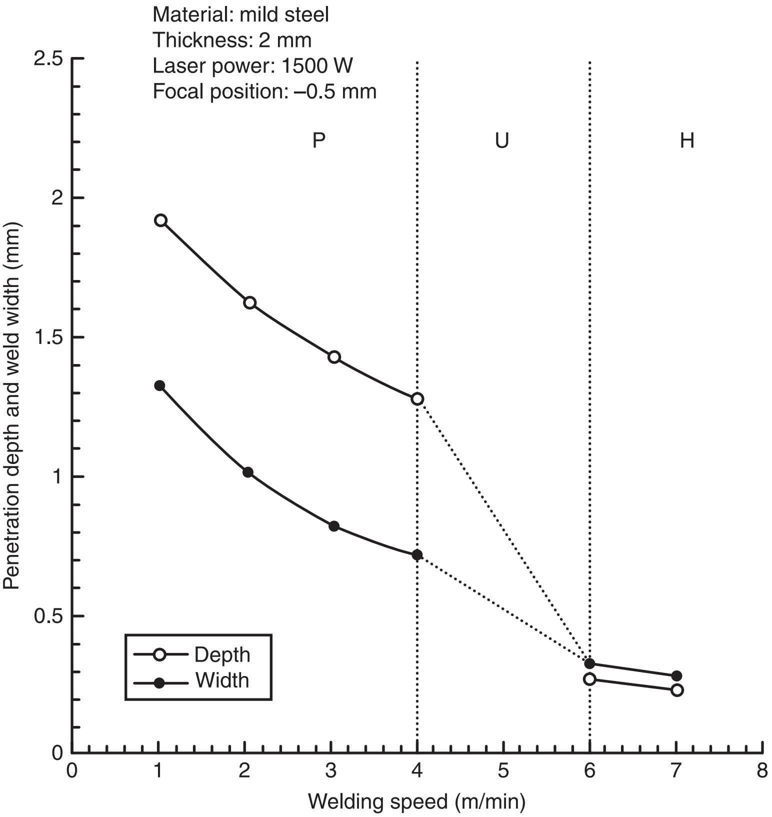

17.8 Depth and width of welding seam as a function of welding speed.[7]

$$I(r, z) = \frac{P}{\pi r_z^2} \tag{17.4}$$

$$r_z^2 = r_0^2\left[1 + \left(\frac{\lambda D_f}{\pi r_0^2}\right)^2\right] \tag{17.5}$$

In Eq. 17.4 and Eq. 17.5, $I(r, z)$ is the power density on the surface of the workpiece, P is power, r_z is spot size, r_0 is focus size, D_f is focal position and λ is wavelength of laser.

Complex influence of several factors

Heat input is the main factor that affects the welding mode and weld shape. When power and focal position both change, the regulation of welding mode also changes, as shown in Fig. 17.12. If the power is lower than the critical value, deep penetration mode is not possible. Similarly, when welding speed and focal position both change,

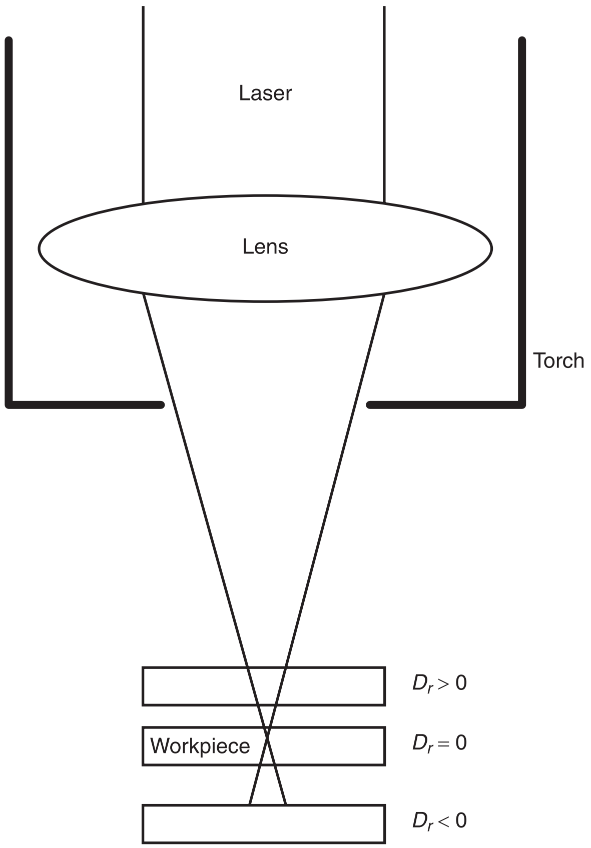

17.9 Sketch of focal position.

the regulation of welding mode changing with welding speed and focal position is shown in Fig. 17.13. If the speed is higher than the critical value it prevents deep penetration mode.

However, when power and welding speed both change, even if the heat input is kept constant, welding conditions (the combination of high power and high speed is termed strong conditions, and the combination of low power and low speed is termed weak conditions) that effect the weld shape will change. Rise in power enlarges the zone of plasma as well as the area of molten pool heated by the plasma and also increases the loss of energy. These result in increase in width, and a decrease in depth and the ratio of depth to width, as shown in Table 17.1.[12]

Shielding gas

It is well known that magnesium is highly susceptible to oxidation, and therefore thorough protection from the atmosphere is required. This is achieved by using

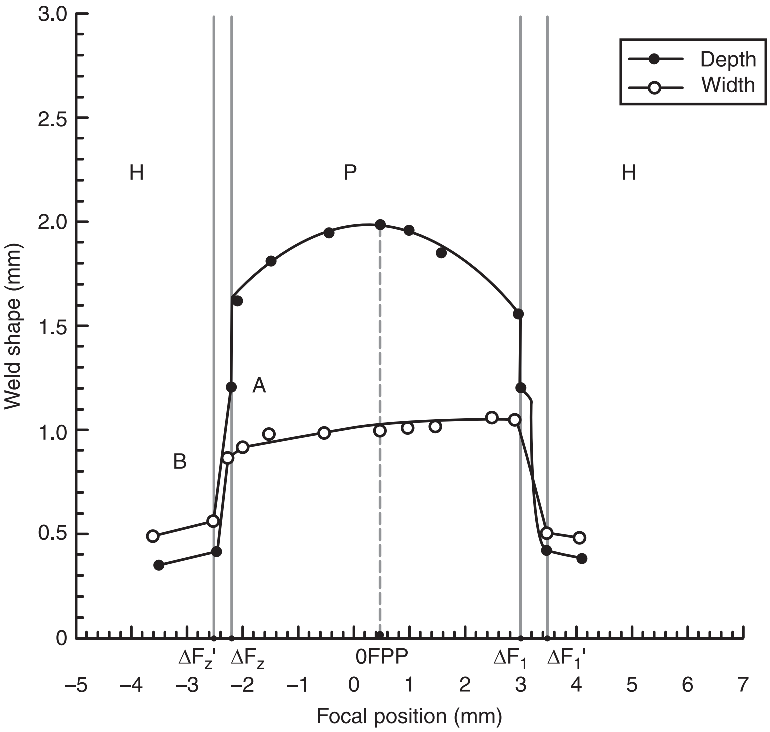

17.10 Depth and mode as a function of focal position.[7]

inert gases. Good shielding can avoid burning or porosity and protects the optics from metal slag (cinders). The shielding gas also influences the formation of the plasma. Shielding gas absorbs laser energy and becomes ionized, and then laser-induced plasma forms.

Conventional shielding gas in laser welding includes He, Ar and N_2; sometimes CO_2 may be used. Helium, with its high ionization potential of 24.5 eV and good thermal conductivity, has a high plasma formation threshold.[13] Thus, little plasma is produced using helium as shielding gas. However, helium is expensive. Therefore, for the protection of the molten pool and the blowing down of plasma, Ar is selected as shielding gas during welding of active metal, N_2 is selected as shielding

Table 17.1 Influence of welding parameter combination on weld shape parameter[12]

Welding conditions	Power (W)	Speed (m/min)	Heat input (J/mm)	Width of weld (mm)	Depth of weld (mm)	Width/ depth
Weak	1500	1.5	60	2.8	2.7	1.04
medium	2000	2.0	60	2.9	2.5	1.16
Strong	2400	2.5	58	3.0	2.5	1.20

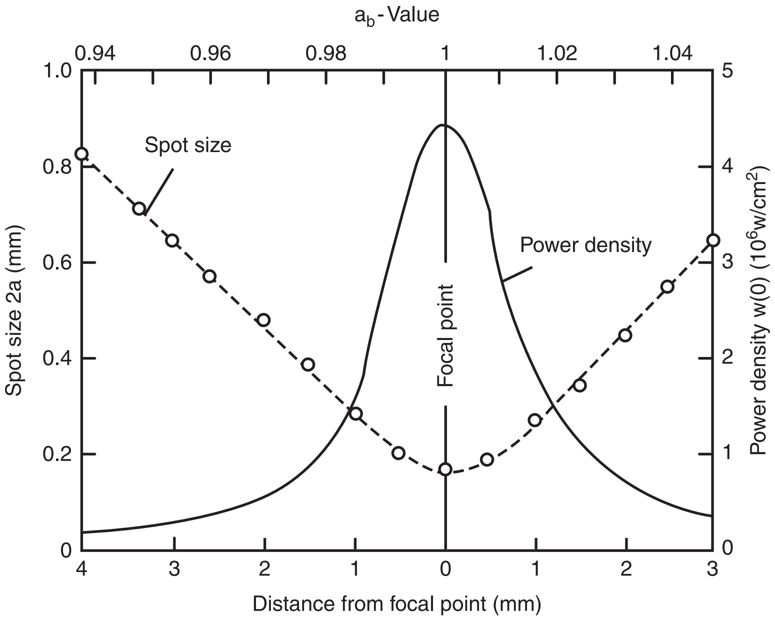

17.11 Relationship between focal position and spot size as well as power density.[7]

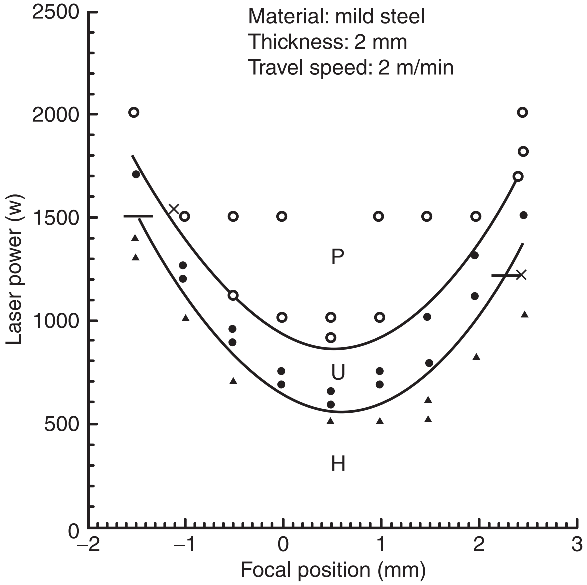

17.12 Mode transition curve determined by laser power and focal position.[7]

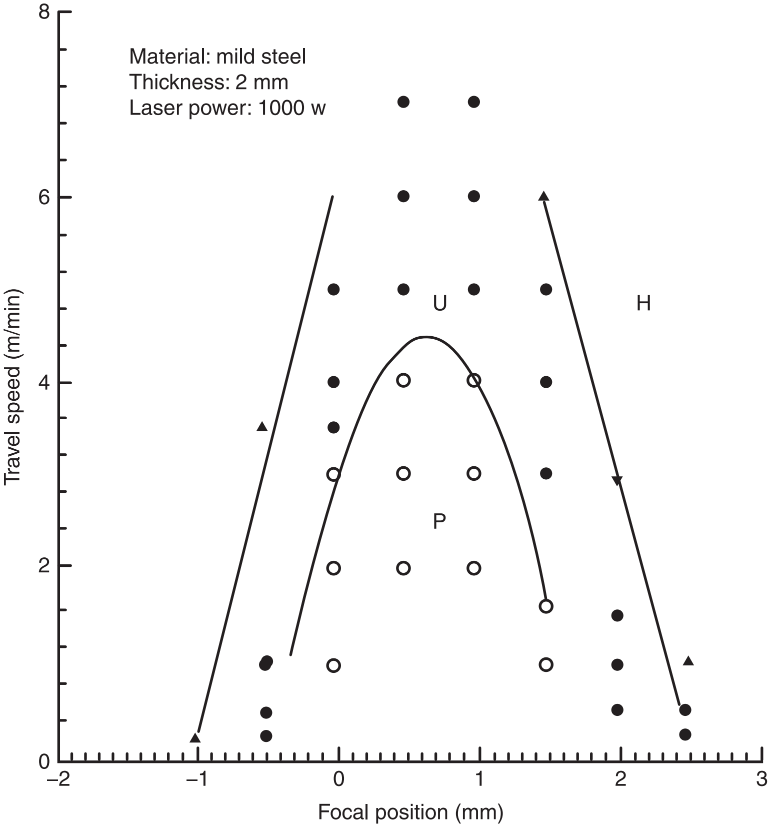

17.13 Mode transition curve determined by welding speed and focal position.[7]

gas during welding of stainless steel and CO_2 is selected as shielding gas during welding of carbon steel to reduce porosity. In addition, proper flow, direction (along the welding direction or against the welding direction) and the angle with the horizontal plane of shielding gas can blow down plasma effectively.

Molten magnesium alloys have a strong tendency to sag or even drop-through due to low viscosity and surface tension. Thus, copper or stainless steel backing is usually employed during laser welding. When shielding gas is used as a backing system, the sag can be reduced, the process window can be extended to lower welding speeds and a better root surface quality can be obtained.[13]

17.3 Laser welding of magnesium alloys

In all metals and alloys applied in structure materials, magnesium alloys have the lowest density. The density of pure magnesium is 1.738 g/cm^3 at 20 °C and most of magnesium alloys have a little higher density of 1.75–1.85 g/cm^3. The density of Mg-Li alloy, which is the lightest metal applied in structure materials, is only 1.30–1.65 g/cm^3.[14] Compared to other metals applied in structure materials, magnesium alloys have some advantages, such as high specific strength, anti-vibration, electromagnetic shielding, anti-radiation and good mechanical properties. Magnesium alloys thus have potential application in aerospace, automobile and other fields that have stringent requirements regarding weight.[9,15–22]

Wide application of magnesium alloys in various fields needs the development of related processing technologies, and welding is necessary for the manufacture of casting and wrought magnesium alloys parts and the repairing of casting defects. Welding problems, such as joining magnesium alloys to themselves and joining magnesium to steel or aluminum, have received more and more attention in recent years.[9,13,23–26]

17.3.1 Weldability of magnesium alloys

A series of special physical and chemical properties of magnesium element (Table 17.2), such as low melting and boiling points and lively chemical properties, determine the weldability of magnesium alloys as reflected by the following:

- Magnesium alloys, with composition of magnesium and other elements (such as Cu, Al, Ni), have a wide crystal temperature range and high hot cracking sensitivity. Mg-Cu alloy's eutectic temperature is 480 °C and its crystal temperature achieves 100 °C; Mg-Al alloy's eutectic temperature is 430 °C; Mg-Ni alloy's eutectic temperature is 508 °C; Mg-Zn-Zr alloy, for example M18 and M22 alloys, has a crystal temperature that ranges up to 100 °C, and some magnesium alloys' crystal temperature even achieves 130 °C.[13,14,22,27–31]

Table 17.2 Physical properties of Mg, Al, Fe[17]

	Mg	Al	Fe
Ionization energy (eV)	7.6	6	7.8
Specific heat capacity (J/kg/K)	1360	1080	795
Latent heat of fusion (J/kg)	3.7×10^5	4×10^5	2.7×10^5
Melting point (°C)	650	660	1536
Boiling point (°C)	1090	2520	2860
Viscosity (kg/m/s)	0.00125	0.0013	0.0055
Surface tension (N/m)	0.559	0.914	1.872
Thermal conductivity (W/m/K)	78	94.03	38
Thermal diffusivity (m^2/s)	3.73×10^{-5}	3.65×10^{-5}	6.80×10^{-6}
Thermal expansion coefficient (1/K)	25×10^{-6}	24×10^{-6}	10×10^{-6}
Density (kg/m^3)	1590	2385	7015
Elastic modulus (N/m^3)	4.47×10^{10}	7.06×10^{10}	21×10^{10}
Resistivity (Ω m)	0.274	0.2425	1.386
Vapor pressure (Pa)	360	10^{-6}	2.3

In addition, when Al content exceeds 1.5%, Mg-Al-Zn alloys have a high sensitivity to stress corrosion cracking; when Zn content exceeds one percent, Mg-Al-Zn alloys become sensitive to hot cracking.[9]

- Magnesium alloys have active chemical properties and are easy to form inclusions in welding. The affinity of Mg and O is very high and easy to form MgO at high temperature. MgO, which exists as fine lamellar solid inclusions in molten pools, affects weld shaping and decreases weld properties. Mg can react with atmospheric N_2 and form Mg_3N_2 in molten pools, and these Mg_3N_2 inclusions further reduce weld plasticity.[9,15,22,24,32]
- Surface tension of liquid magnesium alloys is low, which leads to violent fluid flow occuring in the molten pool, thereby collapsing the molten pool.[8–10,12,20]
- Magnesium alloys have a high expansion coefficient, about twice that of steel and 1.2 times that of aluminum, which causes the occurrence of stress during welding process and lead to deformation and hot cracking.[9,13,22,24,32]
- Magnesium alloys have a low boiling point (about 1100 °C) and high vapor pressure. Evaporation leads to the loss of Mg, the instability of molten pools and spattering.[13,22,24,32]
- Hydrogen has a high solubility in the melting state of magnesium, but with decrease in temperature, the solubility decreases acutely. If a large amount of hydrogen cannot escape in time, it will be retained in the weld and form porosity.[13,15,22,24,32]

In a word, weld defects, such as hot cracking, porosity and collapse of the molten pool, often occur during welding of magnesium alloys. Compared with steel and aluminum alloys, the usual structural materials, magnesium alloys do not weld successfully.

17.3.2 Laser welding advantages of magnesium alloys

To solve the welding problems of magnesium alloys, research has been done in many countries. At present, research mainly focuses on the following welding methods: arc welding, electron beam welding, laser welding, laser-arc hybrid welding and friction stir welding (FSW).[9,15]

Arc welding (including TIG and MIG) is a conventional method for welding magnesium alloys. Adding metal to a molten pool by wire filling can change the chemical composition and microstructure of the weld, and the properties of weld also can be improved.[33] Using alternating current or direct current reverse polarity in arc welding can eliminate oxide film on the surface of magnesium alloys by cathode cleaning.[24] Shortage of arc welding leads to low power density and high heat input. High heat input can cause loss of alloy element, a larger fusion zone and heat-affected zone (HAZ), deterioration of the base metal and serious residual stress and deformation of the weld.[13] In addition, defects, such as porosity and hot cracking, will occur in the weld of arc welding.[24]

Electron beam welding has high energy density and low heat input; therefore a high depth:width ratio, narrow HAZ and good quality weld can be obtained.[15,34] Vacuum is beneficial to protect active alloy elements such as magnesium. However, in the process of vacuum electron beam welding, magnesium with high vapor pressure will evaporate and lead to loss of alloy elements and pollution of the vacuum chamber. Non-vacuum electron beam welding can prevent this problem,[35] but the loss of electron energy is significant. When the work distance gets longer it becomes impossible to process the non-vacuum electron beam welding.

Laser-arc hybrid welding makes full use of the interaction between laser and arc and can solve some problems existing in the welding methods of a single heat source, improve laser absorption of solid state magnesium alloys and enhance arc stability.[24,36,37] This method can ensure deep penetration and good weld formation in high welding speeds and wide gap conditions, and can decrease porosity and hot cracking sensitivity.[38,39] However, hybrid welding has many parameters which are complex to adjust and control. Furthermore, addition of arc causes a wide HAZ, large deformation and various other defects because of much higher heat input.

Friction stir welding is a method of solid state welding which heats base metals over the plasticity temperature range using heat produced by friction between the stir head and the base metal. At the same time, the pressure from the stirring head forces the plastic flow of base metal to form atomic bonding between base metals. Because base metal does not melt during welding, hot cracking, porosity and the loss of alloy elements, which usually appear in the fusion welding, do not often occur.[40–47] However, FSW only adapts to simple structure or shape, and it is difficult to weld complex structures or in concealed positions.[40–47]

Laser welding, which is a high energy density, high efficiency and precise joining method, has received wide attention. Compared to other methods, laser welding has the following advantages in magnesium alloy welding:[1–3,9,13,14,24,25,32,48,49]

- High power density, low heat input, narrow fusion zone and HAZ, depth: width ratio of weld up to 10:1, little deformation in thick plate welding.
- Little weld stress and deformation can decrease hot cracking sensitivity.
- High welding speed, high cooling ratio, fine weld structure, good welded joint properties.
- Little weld pool volume can alleviate the problem of weld pool collapse because of low surface tension of liquid magnesium.
- Laser beam can process metal accurately for small spot diameter. Optical system or fiber is used to transport laser, lenses are used to focus laser, and remote non-contact welding can be realized. Automatic welding and precise control, once realized and combined with computers and manipulators could even be able to weld complex 3D parts.
- Laser beams are not affected by electromagnetic fields and do not need a complex vacuum chamber.

Laser welding can alleviate the problems in magnesium alloys' welding (e.g., high stress and deformation), but weld defects, such as collapse of keyholes, loss of alloy elements, porosity and hot cracking, also appear possible.

17.4 Microstructure and properties of laser welding of magnesium alloys

The major alloy elements are Mn, Al, Zn, Zr and rare earth. According to this, magnesium alloys can be classified by alloy element into Mg-Mn, Mg-Al-Mn, Mg-Al-Zn, Mg-Zr, Mg-Zn-Zr, Mg-RE-Zr and so on.[13,15] In addition, magnesium alloys can also be classified by process methods into wrought magnesium alloys and cast magnesium alloys. The detail is shown in Fig. 17.14.[15]

Magnesium alloys manufactured by different processes have different weldabilities, and the microstructure and the properties of laser weld also differ. At present, laser welding is mainly applied on wrought magnesium alloys, because porosity is a severe problem in the laser welding of cast magnesium alloys, especially die cast magnesium alloys. In this section, some typical magnesium

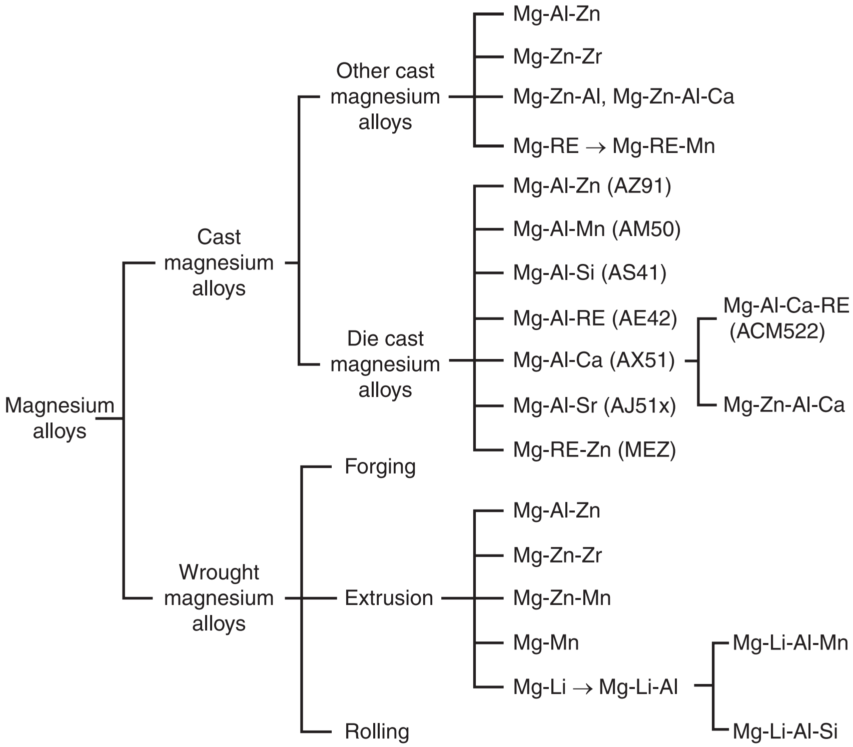

17.14 Classification of magnesium alloys.[15]

alloys (such as AZ31B) are used as examples to analyze the microstructure and the mechanical properties of laser weld.

17.4.1 Microstructure of laser welds

Figure 17.15 is the microstructure of a CO_2 laser weld of AZ31B wrought magnesium alloy. From Fig. 17.15, we can deduce that the microstructure includes two phases: the dark dendrite phase and the interdendritic light phase. The components of the two phases are measured by energy dispersive X-ray spectroscopy (EDS) and the result is shown in Table 17.3. The ratio of Al in the dark phase is 1.06 at.% and in the light phase is 4.53 at.%. Combining the Al-Mg phase diagram,[50] note that the dark phase and the light phase are both α-Mg (Al solid solution in Mg). The dark phase solidifies first because of its high melting temperature; the light phase solidifies last in the grain boundary where the concentration of Al is higher than in the dark phase. Because the solidification rate of laser weld is very high, Al atoms in the grain boundary cannot precipitate, and so the light phase forms. The result of X-ray diffraction (XRD) is shown in Fig. 17.16, which proves that the weld is α-Mg. The grain size is less than 10 μm.

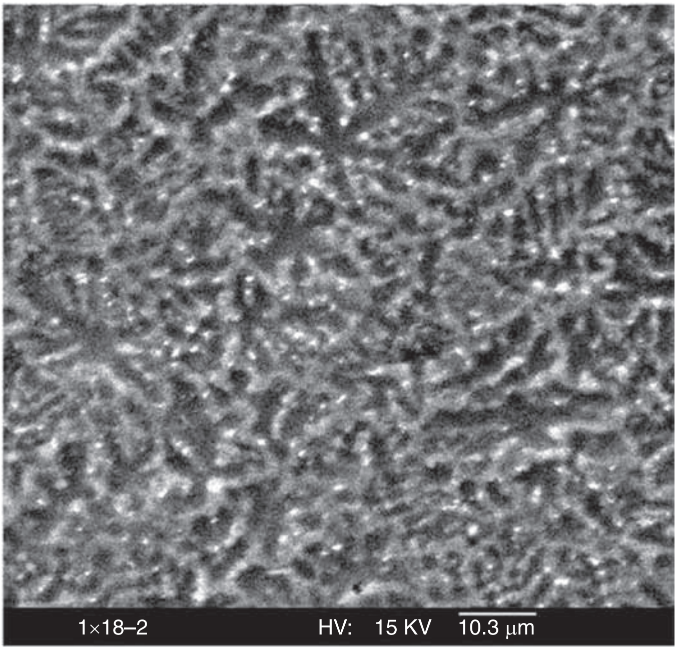

17.15 The microstructure of the center of the weld (SEM, secondary electrons). Power: 2300 W, speed: 2800 mm/min, shielding gas: Ar.

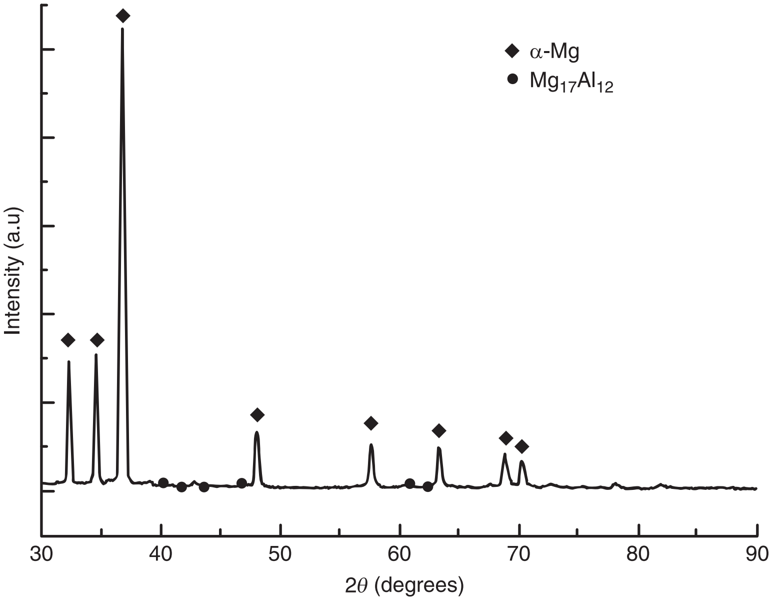

17.16 XRD analysis of weld.

It has been found that the shapes of microstructures in different zones of the weld differ greatly. In the width direction of weld, equiaxed grains are present in the center and column grains in the partially melted zone. A significant grain coarsening is not obvious in the HAZ (Fig. 17.17).

In the center of the molten pool, the moving rate (R) of the solid–liquid interface is very high (close to welding speed), whereas the temperature gradient (T_L) in the front of the interface is low. According to solidification principles, equiaxed grain will form in the center of a weld. However, in a partially melted zone, if R is small and T_L is large, then column grain will form. In addition, no significant grain coarsening is obvious in the HAZ. This is because the heat input of laser welding is small and the thermal conductivity of magnesium is effective; the HAZ stays very briefly in high temperature and grains have no time to grow.

Table 17.3 Components of weld (at.%)

	Dark dendrite phase	Interdendritic light phase
Mg	92.14	91.20
Al	1.06	4.53
Zn	0.39	0.88
O	6.24	3.32

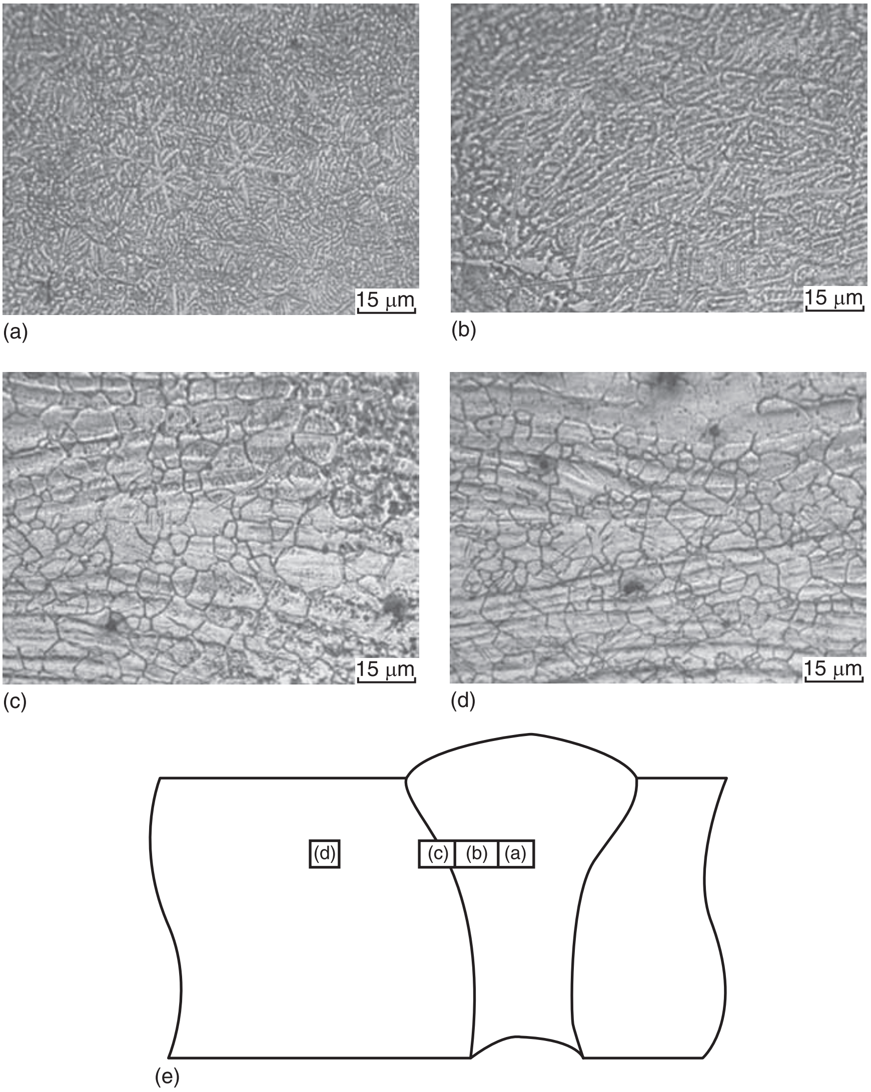

(a) (b) (c) (d) (e)

17.17 Microstructure of different zones in width direction of weld: (a) center of weld; (b) fusion zone; (c) HAZ; (d) base metal; and (e) distribution of (a)–(d) in welding joint.

In the depth direction of the center of the weld, it is found that the shapes of the microstructures in different zones of the weld are all equiaxed grains. However, the grains differ in size. Grains at the bottom of the weld are the smallest, those on top are medium size and those in the center are the largest (Fig. 17.18).

This is due to different cooling conditions in different zones. At the bottom of the weld, heat can be lost by convection with backside shielding gas and heat

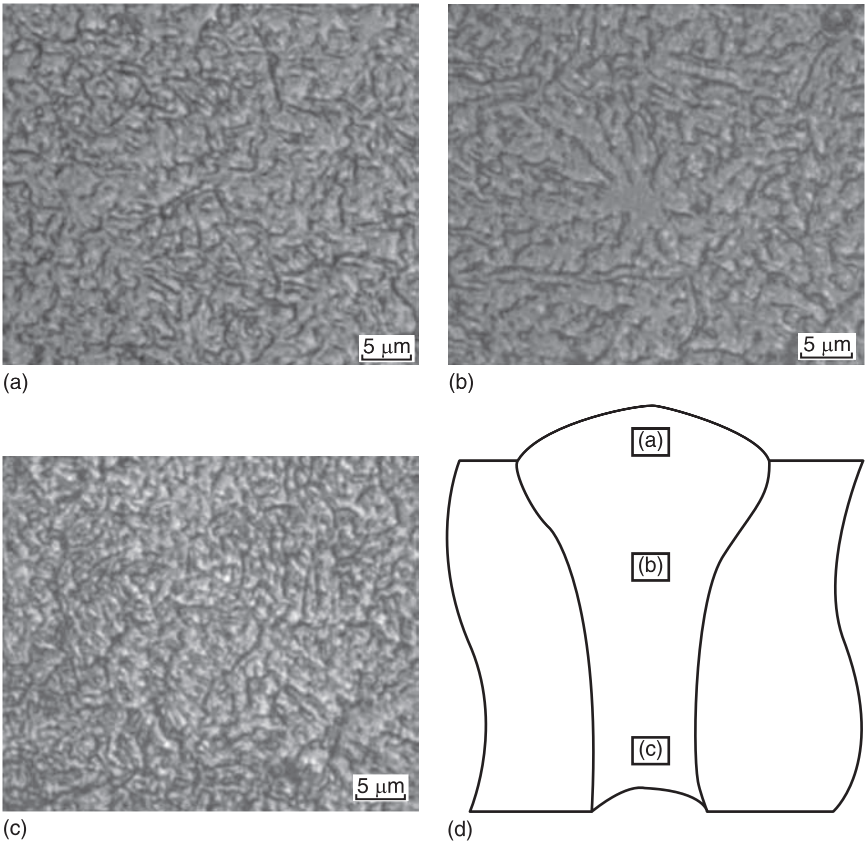

17.18 Microstructure of different zones in depth direction of weld: (a) top of the weld; (b) center of the weld; (c) bottom of the weld; (d) distribution of (a)–(c) in welding seam.

conduction to the backing plate and base metal. Its cooling condition is the best and the solidification rate is the highest, so the grain size is the smallest. On the top of the weld, its cooling condition is similar to that of the bottom, except for heat conduction to the backing plate. Hence, its grain size increases a little, so its solidification rate is the smallest and its grain size is the largest.

Cao has researched the microstructure of 2.5 kW CW Nd:YAG laser weld of 2 mm ZE41A-T5 sand casting magnesium alloy (Fig. 17.19).[54] From Fig. 17.19, we can infer that the fusion zone has a width of approximately 0.8–1.3 mm and the grains in fusion zone are very fine. The rapid cooling experienced during laser welding leads to a significant grain refinement in the fusion zone.[51,52] The partially melted zone is rather narrow, only several grains wide. No significant grain coarsening in the HAZ has been observed.

Heat is rapidly extracted from the molten fusion zone by the surrounding base material. Grains usually grow epitaxially from the FZ–HAZ interface. At the

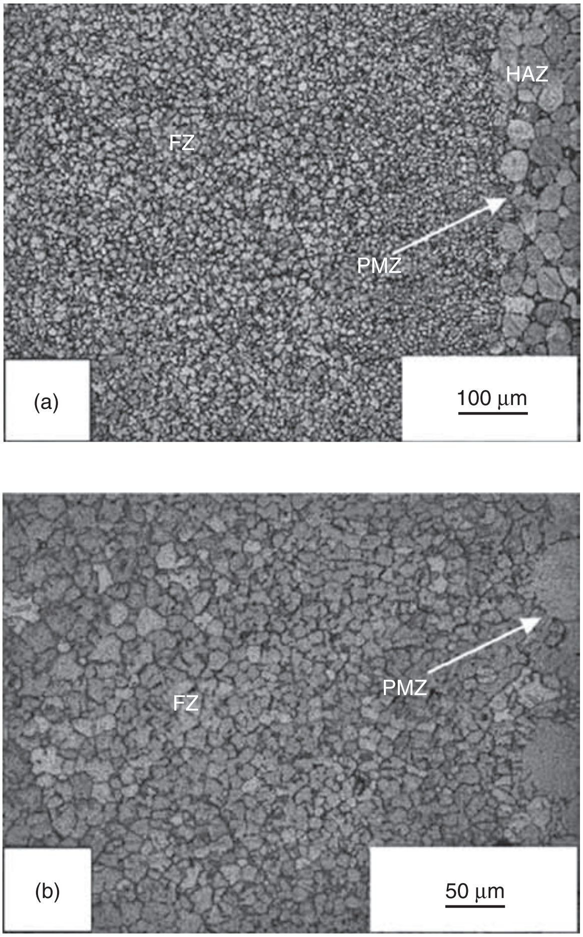

17.19 Optical micrographs of weld of 2 mm ZE41A-T5 sand casting magnesium alloy: (a) near the interface between the FZ and HAZ, and (b) close-up view of (a); laser: 2.5 kW CW Nd:YAG.[54]

fusion boundary, where a relatively large thermal gradient and small growth rate are established, the microstructure is predominantly cellular.[53] Fine equiaxed grains in the fusion zone formed by cellular growth were also observed.

17.4.2 Mechanical properties of welds

Microhardness

Microhardness can synthetically display the elasticity, plasticity and strength of materials. On measuring the hardness distribution in the weld (Fig. 17.20), the result shows that softening takes place in a particular zone. The reason is that after melting and solidification, the strengthening effect of the base metal due to the cold work is lost.

In the depth direction of the weld, the microhardness of the zone is measured near the axis. It is found that the average microhardness at the bottom of the weld is the highest, the average microhardness on the top of the weld is medium and the average microhardness in the center of the weld is the lowest. This is in keeping with the

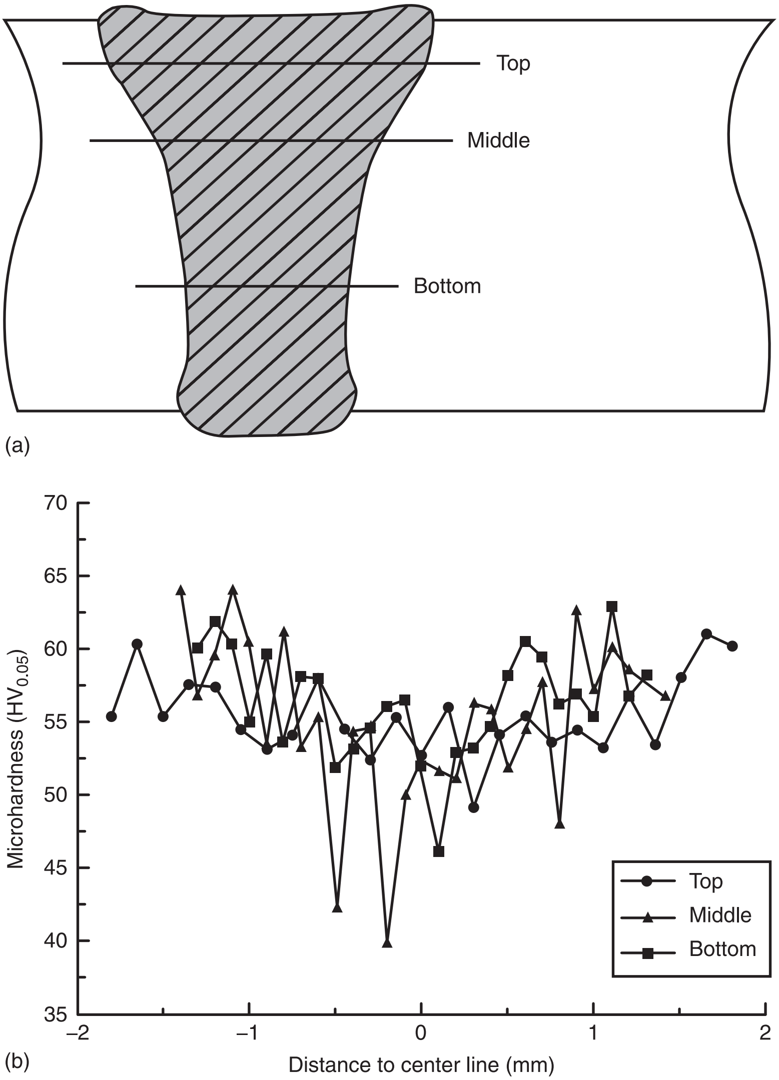

17.20 Distribution of microhardness of weld: (a) sketch of the zone of measuring microhardness; (b) distribution of microhardness in width; and *opposite* (c) distribution of microhardness in depth.

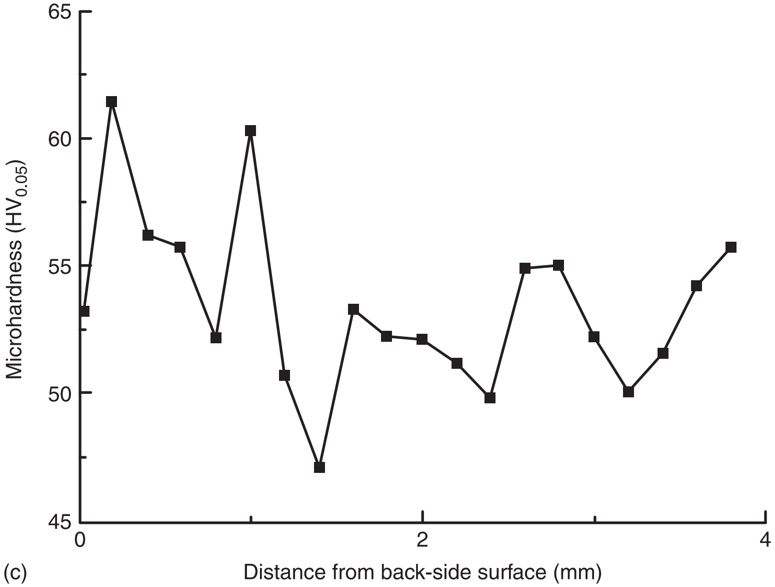

17.20 Continued.

principle that the grain size changes in the depth direction of the weld, which proves that the microhardness of the weld increases with the decreasing grain size.

Tensile strength

The tensile strength of a welded joint is an important aspect of service performance. Tensile strength (σ_b), yield strength (σ_s) and fracture elongation (δ_k) are measured by static tension test and results are lower than that of the base metal (Table 17.4).

All tensile test samples fracture in the weld. The strengthening effect of the weld is lost due to cold work and the strength of the weld is lower than that of the base metal. So, distortion takes place in the weld when supporting tensile load, and results in fracture in the weld.[55]

Table 17.4 Mechanical properties of base metal and welds of various welding parameters

Power (W)	Welding speed (mm/min)	Tensile strength (MPa)	Yield strength (MPa)	Elongation (%)
—	—	256	138	14.8
2300	3600	252	131	13.6
2300	2800	252	130	13.2
2300	2000	249	130	12.2
2300	1200	242	126	8.5

When the welding speed is between 2 m/min and 3.6 m/min, the shapes of fractures are very similar (Fig. 17.21a–c). There are dimples in some areas and a lot of quasi-cleavage steps around these dimples. According to this, we conclude that cracks initially sprout in a surface of impurities or porosities. With expansion in the cracks, inner necking of local metal increases continuously, which results in fracture; this leads to links in cracks, and finally, dimples form.[56,57] Crack expansion speed increases rapidly and once a crack size achieves a critical stage, then a low-density tear is visible in the metal. Hence, the smooth quasi-cleavage steps are formed without plastic deformation.[56,57]

When the welding speed is 1.2 m/min, the shape of the fracture is different from the shapes discussed above. The number of dimples decreases and a lot of irregular pits and white impurities are distributed on the boundary of the dimples (Fig. 17.21d). There are a lot of cleavage steps around the pits and white impurities.

By measuring the components of the white impurities by EDS (Fig. 17.22 and Table 17.5) it has been found that the oxygen content is higher than the weld. It is thought that the white impurities are oxides of Mg. High heat input results in

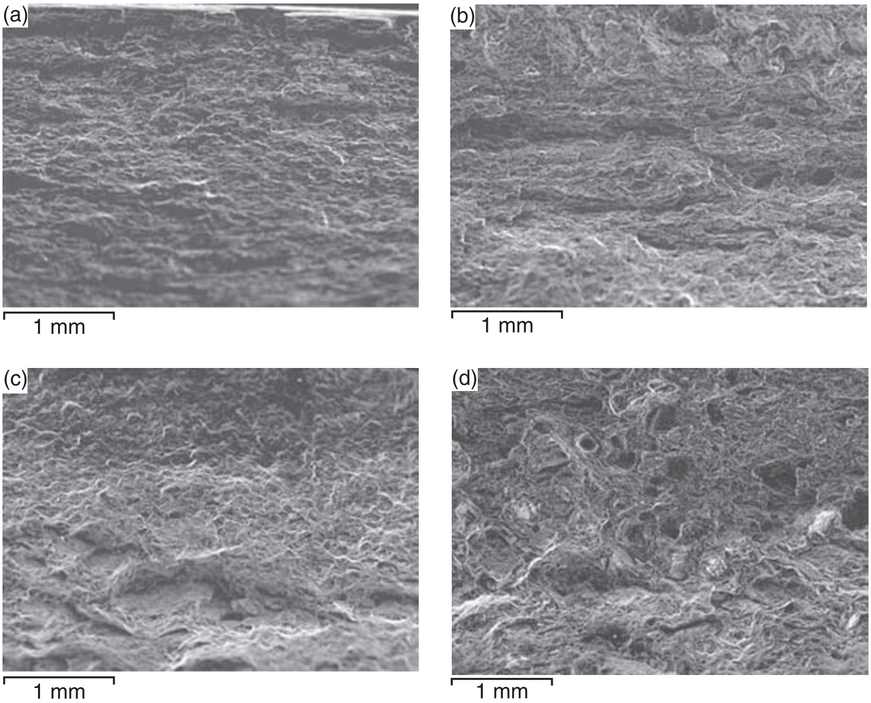

17.21 Fracture shapes of weld (SEM, secondary electrons): (a) 2300 W × 3600 mm/min; (b) 2300 W × 2800 mm/min; (c) 2300 W × 2000 mm/min; and (d) 2300 W × 1200 mm/min.

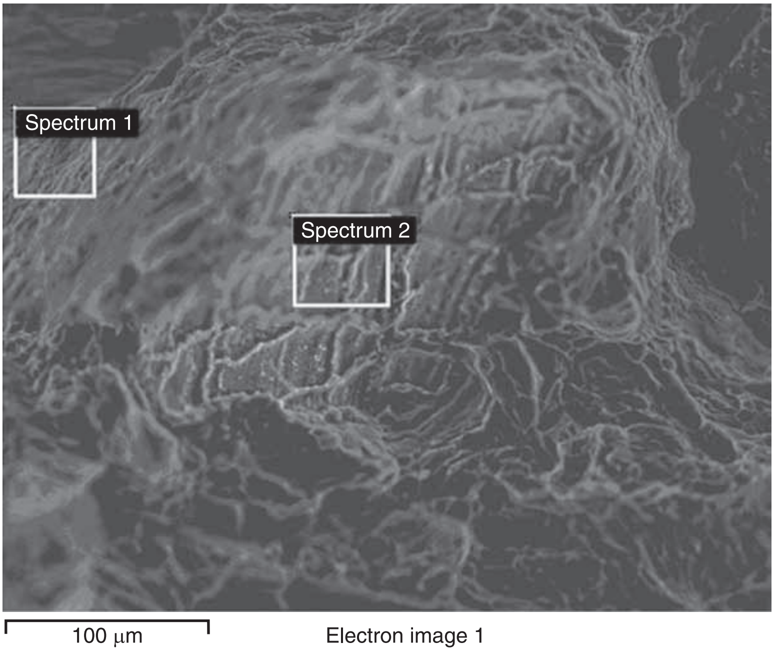

17.22 Area selection in the fracture of component measured (2300 W × 1200 mm/min).

Table 17.5 Component in selected area in the fracture (2300 W × 1200 mm/min)

	Spectrum 1		Spectrum 2	
Elements	wt.%	at.%	wt.%	at.%
Mg	95.67	95.35	84.44	80.42
Al	2.09	1.88	3.44	2.95
Zn	0.55	0.21	0.83	0.29
O	1.69	2.56	11.29	16.34

an increase in the width of the weld, and so shielding gas cannot protect the whole molten pool effectively. Hence, the metal is oxidized and white impurities are formed.

Based on the analysis of the microstructure and the shapes of the fractures we can conclude that welding parameters can result in crack origin changing. In high welding speed weld, the major crack originates from small impurities and pores. Therefore, the decreasing value of tensile properties of the weld is small. However, in low welding speed weld, the major origin of cracks is large oxide impurities. Since the oxide impurities bond weakly with metal, cracks easily sprout in the impurity surfaces. Therefore, the tensile properties of the weld decrease to a great extent.

17.5 Typical defects of laser welding of magnesium alloys

17.5.1 Welding problems of magnesium alloys

There are many kinds of alloy systems and types in magnesium alloys. The components of magnesium alloys have an influence on their process methods, and process methods and components of magnesium alloys both influence the kinds of welding defects. The main defects of wrought magnesium alloys in laser welding are weak surface formation and cracks; the main defects of sand cast magnesium alloys in laser welding are cracks and porosity; however, the main defect of die cast magnesium alloys in laser welding is a high porosity ratio.

17.5.2 Welding crack

Hot cracks have been one of the main welding defects of magnesium alloys. In most magnesium alloys, an increase in alloying elements will generally increase the solidification temperature range. The large freezing temperature range, large solidification shrinkage, high coefficient of thermal expansion and low melting point intermetallic constituents potentially make magnesium alloys susceptible to liquation cracking in the HAZ and solidification cracking in the fusion zone.[9,13,15]

Solidification cracking occurs regularly in alloys with large solidification interval, such as Mg-Zn-Zr, Mg-Al-Zn, etc. It is reported that some Mg-Zn-Zr alloys, such as M18 and M22, have solidification ranges much larger than 100 °C. Sand cast ZE41A alloy has an equilibrium freezing range of 120 °C; thus solidification cracking was observed in the joint (Fig. 17.23).[54] For Mg-Al-Zn alloys, solidification cracking starts to develop when the composition promotes a wide freezing range, which typically occurs at around ten percent Al. Generally speaking, the alloys containing up to six percent Al and up to one percent Zn possess good weldability, otherwise weld cracking becomes severe because of the occurrence of low melting point constituents ($Mg_{17}Al_{12}$).[9,16] Rare earth elements beneficially reduce the tendency of weld cracking and porosity in magnesium castings because they narrow the freezing range. For some alloys containing rare earth, such as QE22, however, cracking is still observed in the age-hardened condition.

Heat-treatable magnesium alloys, such as AZ80 and ZK60, are usually produced by extrusion processes at high cooling rates, which reduce segregation and thereby decrease the tendency for liquation. Die castings of Al-bearing Mg alloys, however, often exhibit low melting point intermetallic constituents, such as $Al_{12}Mg_{17}$ (melting point at 642 °C), at grain boundaries which promote liquation in the HAZ.[58] Baeslack III et al.[59] studied CO_2 laser welding of cast alloy WE54X indicating that the alloy may also be sensitive to HAZ liquation cracking. Near the fusion line, they observed a liquation of the intermetallic phase and additional melting into the surrounding matrix. On cooling, neodymium- and yttrium-rich liquid solidified to a lamellar eutectic structure at the grain boundaries, and fine intergranular cracks were observed in the HAZ along with some of these grain boundaries. Similarly, the HAZ liquation cracking was observed in ZE41A joints welded, as shown in Fig. 17.23.[54] The liquation cracking in the HAZ results

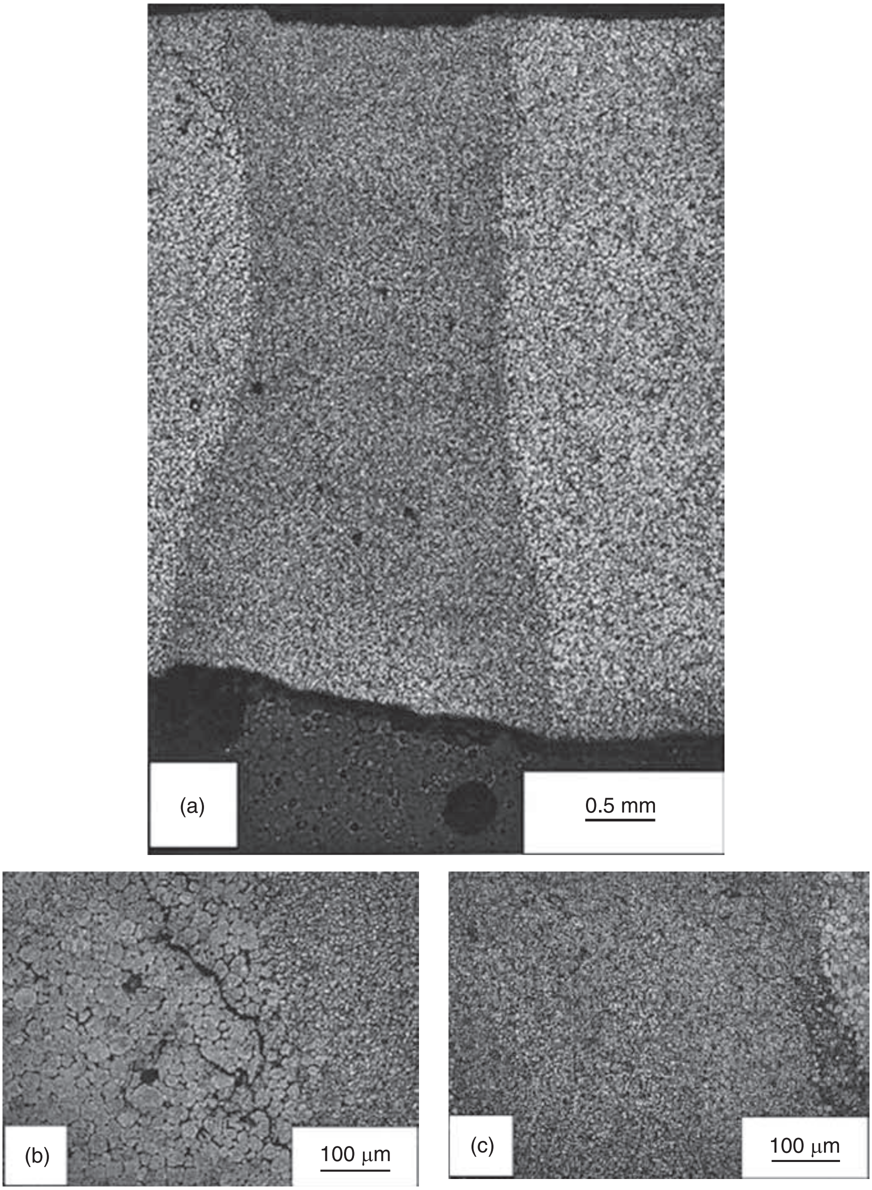

17.23 ZE41A-T5 alloy joint welded using a 4 kW CW Nd:YAG laser: (a) whole cross section; (b) cracks at the top left corner of HAZ; and (c) cracks at the top of weld.[54]

from the formation of liquid films at grain boundaries adjacent to the fusion boundaries during the weld thermal cycles, and the inability of the liquid films to accommodate thermally induced stresses experienced during cooling.[59] The cracks tend to disappear if they are refilled with the surrounding eutectic material of the low melting point.[60] The liquation cracking needs to be further investigated in laser welding of magnesium alloys because alloy composition, welding processing parameters, solidification rate and weld joint geometry can all influence the tendency to crack.

17.5.3 Collapse of the molten pool

The surface tension of liquid magnesium is small, and so the molten pool collapses in the laser welding process, which results in weak surface formation.

Research on laser welding of wrought magnesium alloy AZ31B proves that the flow and angle of shielding gas and welding parameters influence the surface formation in the laser welding process. The optimization of welding parameters can prevent the molten pool collapse and then obtain the weld with good surface formation.

The melting temperature, boiling temperature and ionization potential of magnesium alloys are low. Hence, the tendency of laser-induced plasma formation in laser welding process is strong. Shielding gas can protect the molten pool as well as blow down the plasma, which can suppress the effect of plasma on shielding laser to keep the welding process stable. However, if the parameters (flow, angle) of shielding gas are not suitable, the impact of shielding gas on the molten pool may result in intense oscillation of the keyhole and the molten pool, which may cause obvious deterioration of the surface in the formation process. Therefore the purpose of selecting the shielding gas is to enhance the effect of blowing down the plasma and suppress the impact of shielding gas to the molten pool.[61]

In various directions of shielding gas, including the axis direction and the various side directions, the side direction opposite the welding direction that forms a 30 ° angle with the horizontal plane is the most beneficial for the surface formation of the weld. The optimized flow of shielding gas is 2000 L/h in this direction, as shown in Fig. 17.24.

The side directions of shielding gas not only can blow down the plasma but can also suppress the disturbance of shielding gas on the forced balance of the molten pool and keyhole, which is more beneficial to the surface formation of the weld than the axis direction. When shielding gas forms a 45 ° angle with the horizontal plane, the axial component of shielding gas becomes too strong and enhances the impact on the molten pool, hampering the surface formation of the weld. Similarly, when the shielding gas forms a 15 ° angle with the horizontal plane, the horizontal component of the shielding gas becomes too weak and then weakens the effect of blowing down the plasma. The residual plasma above the keyhole can still shield the laser beam, thereby weakening the surface

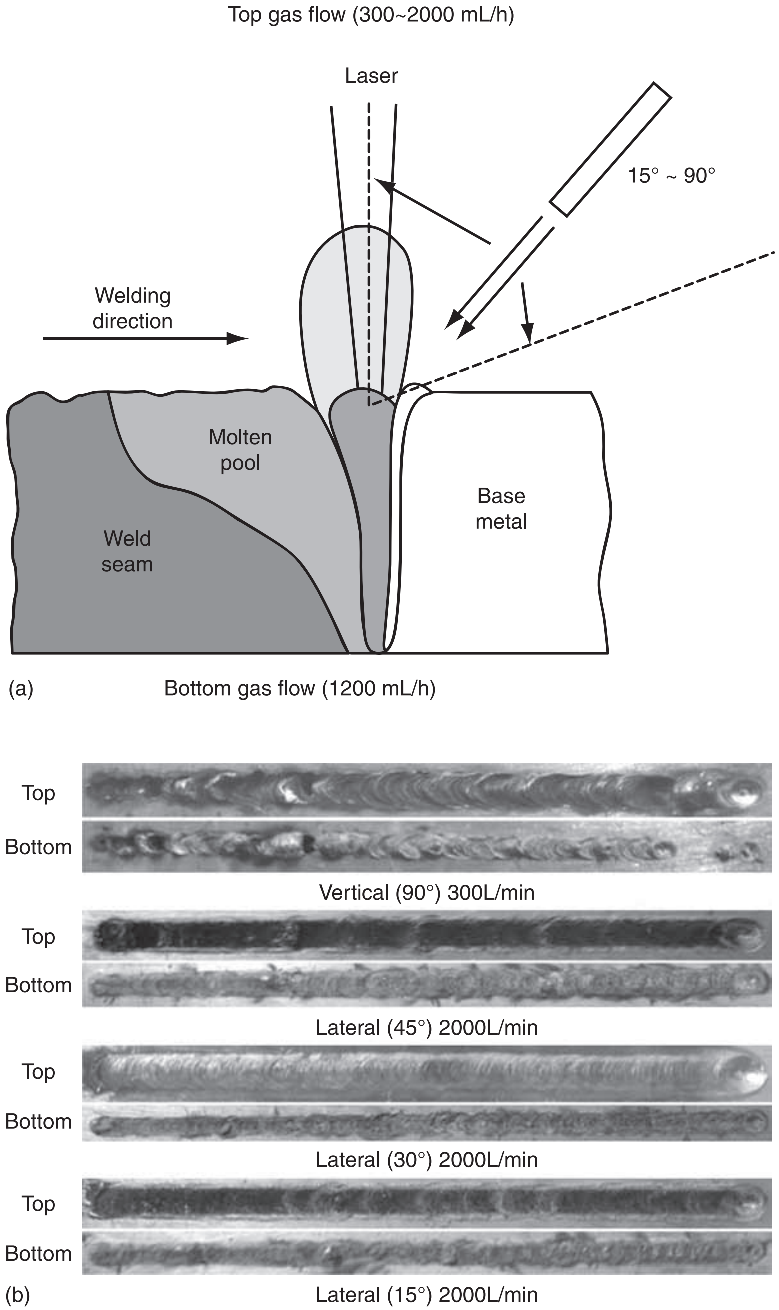

17.24 (a) Sketch of the angle of gas flow. (b) Relationship between weld surface formation and gas flow. Power: 2 kW; welding speed: 1.2 m/min.[61]

formation of the weld. When the shielding gas forms a 30° angle with the horizontal plane, the axial component and horizontal component of shielding gas are strengthened. The axial component of the shielding gas can slow down the spouting speed of the plasma, and the horizontal component can rapidly blow down the plasma to the trailing edge of the molten pool. So, the surface formation of the weld is successful.[61]

Increasing the power or decreasing the welding speed can both enlarge the heat input and change the penetration conditions of the weld. When the keyhole just penetrates the workpiece, the surface formation of the weld is successful, as shown in Fig. 17.25.

17.5.4 Porosity

Based on the characters of magnesium alloys and laser welding, the factors that cause the formation of porosity in the laser welding of magnesium alloys are as follows:[62–66]

1 Hydrogen pores: Most liquid magnesium alloys have a higher solubility for hydrogen than solid magnesium. The decrease in hydrogen solubility in the liquid, and relatively rapid solidification experienced during laser welding, still cause the formation of gas porosity within the weld.
2 Porosity caused by the collapse of unstable keyholes.
3 Porosity caused by the evaporation of elements such as magnesium and zinc.

The related research[9,24,25,67] showed that magnesium alloys, compared with aluminum and iron alloys, give rise to more stable keyholes due to a much higher equilibrium vapor pressure, lower boiling temperature and lower surface tension. So, the collapse of unstable keyholes is not the main factor in porosity formation. In addition, porosity caused by the evaporation of Mg and Zn only occurs in particular types of magnesium alloys manufactured by particular processes.[67] Hydrogen is the only gas that dissolves in molten magnesium, and hydrogen pores are considered the main cause of porosity formation.[13,24,54,62,67,68]

The formation of hydrogen pores in laser welding of magnesium alloys is closely related to the action of hydrogen in laser welding process. In laser welding of magnesium alloys, the hydrogen in the molten pool is mainly due to initial preexisting hydrogen in the base metal.[67] It is speculated that the initial preexisting hydrogen mainly results from the interaction of water vapor (H_2O) with magnesium alloys in the manufacturing process. The tendency of porosity formation in laser welding depends on the initial hydrogen contents of the base metal, which in the case of magnesium alloys are different under different manufacturing processes.[49,69] In the three main manufacturing processes, the initial hydrogen content of die cast magnesium alloys is much higher than that of sand cast magnesium alloys, and the initial hydrogen content of sand cast magnesium alloys is higher than that of wrought magnesium alloys.

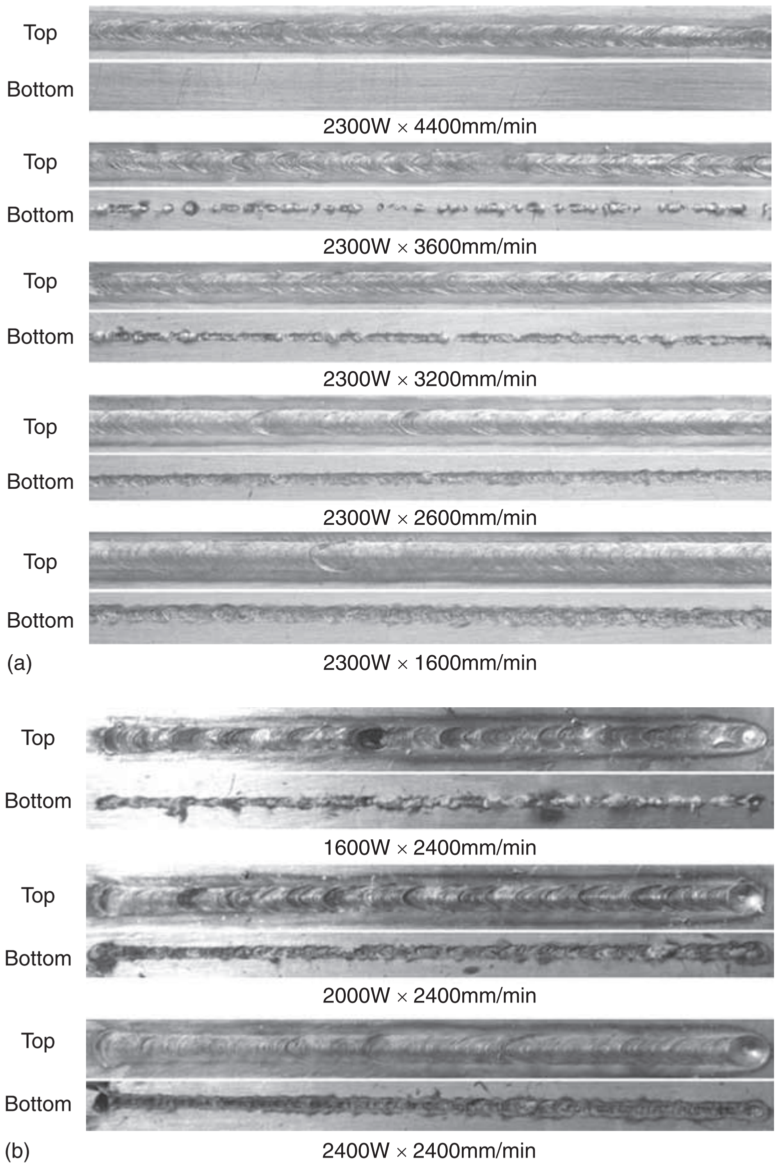

17.25 (a) Relationship between weld surface formation and welding speed (gas: 30°, 2000 L/min) (b) relationship between weld surface formation and power (gas: 30°, 2000L/min).[61]

Correspondingly, the tendency of porosity formation in die cast magnesium alloys during laser welding is the largest, in sand cast it is medium and in wrought magnesium alloys it is the smallest (Fig. 17.26). So, porosity of die cast magnesium alloys in laser welding is a severe problem.[62,63,69]

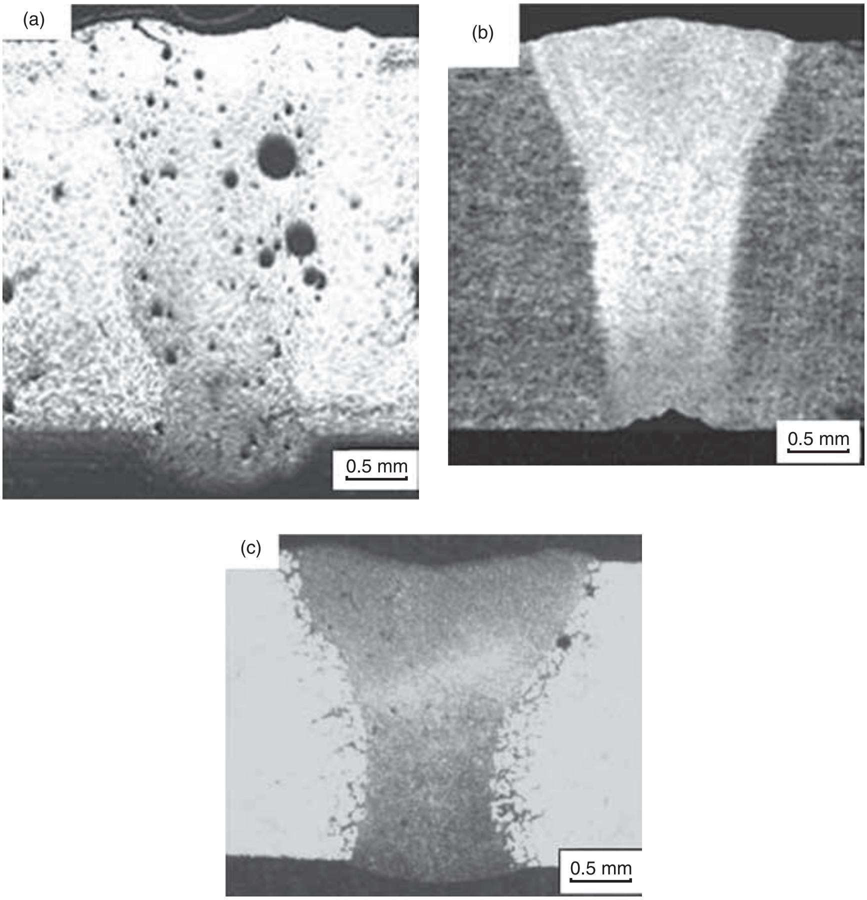

17.26 Pores in laser welding seam of various magnesium alloys under different manufacture processes: (a) AM50 die-cast magnesium alloy; (b) AZ31 wrought magnesium alloy; and (c) AZ91 sand-cast magnesium alloy.[69]

Because of the characteristics of die casting process, the hydrogen exists in die cast magnesium alloys in two forms: hydrogen gas (H_2) in high pressure pores and atomic hydrogen (H) oversaturated solid solution in the base metal. The hydrogen in the two forms has an important effect on porosity formation in the laser welding of die cast magnesium alloys. When die cast magnesium alloys are remelted during laser welding, H_2 pores may expand due to heating (thermal expansion), thereby leading to the release of high pressure in the preexisting pores.[52] The growth in porosity results from the expansion and coalescence of the pores, and causes the formation of large pores in the fusion zone as shown in Fig. 17.27.[67]

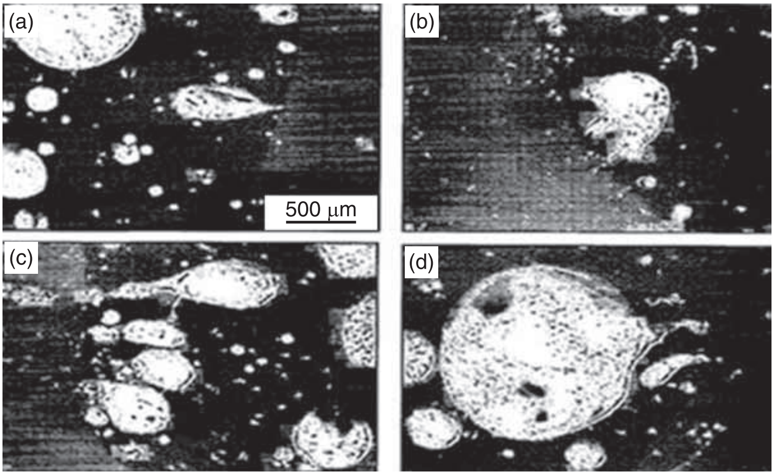

17.27 Formation of large pores in the fusion zone due to the expansion and coalescence of preexisting pores in the base die-cast AM60B alloy.[67]

The effect of H_2 on porosity formation in laser welding is analyzed taking account of the expansion of the pores caused by heating and the release of high pressure. The initial pressure in the preexisting H_2 pores can be calculated by Eq. 17.6.[69]

$$p = p_d + p_m + 2\sigma/r. \tag{17.6}$$

In Eq. 17.6, p is the initial interior pressure of the preexisting pores in base metal, p_d is the environmental pressure, p_m is the static pressure of liquid magnesium alloy, σ is the surface tensile and r is the radius of pores.

After the expansion of the pores, the volume of the pores can be calculated by Eq. 17.7.[69]

$$p_2 \cdot \frac{4}{3}\pi \cdot r^3 = (T/T_0) \cdot p_1 \cdot \frac{4}{3}\pi \cdot r^3. \tag{17.7}$$

In Eq. 17.7, p_1 is the interior pressure of the pores before welding, p_2 is the interior pressure of the pores after welding, r_0 is the radius of pores before welding, r is the radius of pores after welding, T_0 is the room temperature and T is the solid phase line temperature of the base metal.

According to Eq. 17.8, if the radii of the pores in the molten pool exceed the critical radius, the pores will escape from the molten pool.[69]

$$v = \frac{2gr^2(\rho_L - \rho_G)}{9\eta} > v_s \tag{17.8}$$

In Eq. 17.8, v is the escape speed, g is the acceleration of gravity, r is the radius of the pores, ρ_L is the density of the liquid base metal, ρ_G is the density of the gas in the pores, η is the viscosity of the liquid base metal, and v_s is the moving speed of the solidification interface.

Based on the related data, the last radii of pores in the base metal after welding are shown in Fig. 17.28. When the pressure in die cast process is 44 MPa, the pores with the initial diameters larger than 10.06 μm in the base metal can escape from the molten pool in the laser welding process. Based on Table 17.6, the porosity ratio of the pores with initial diameters smaller than 10.06 mm is 0.076% and in those larger than 10.06 μm it is 0.54%. This means that 87.66% hydrogen gas (H_2) in the base metal can escape from the molten pool in laser welding process.

Figure 17.29 shows the pressure and temperature changes in the vacuum heating of die cast magnesium alloy AM50 and wrought magnesium alloy

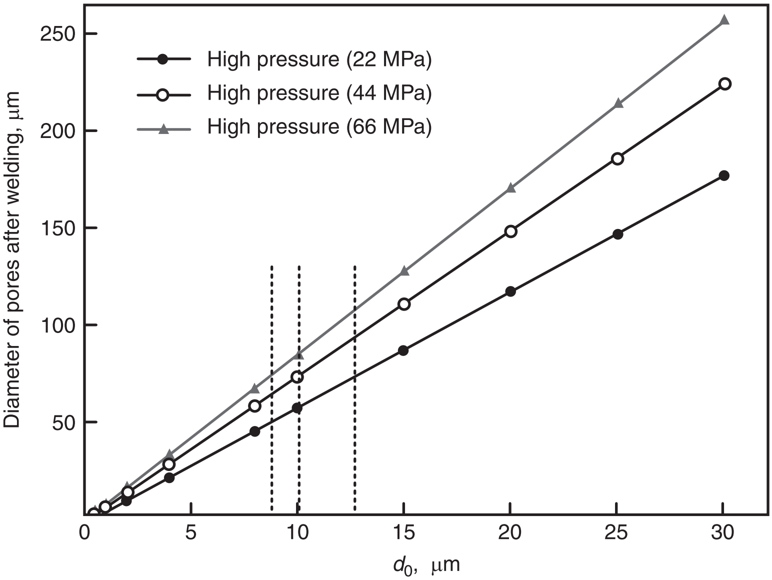

17.28 Final diameters of initial pores of different diameters in die-cast magnesium alloys after welding.[69]

Table 17.6 Characteristic parameters of pores in AM50 base metal[69]

Characteristic parameters of pores	Porosity (%)	Average diameter (μm)	Number density (mm^{-2})
Big pores ($d > 10$mm)	0.54	108.5	1.670
Small pores ($d \leq 10$mm)	0.076	0.6471	7.84×10^3

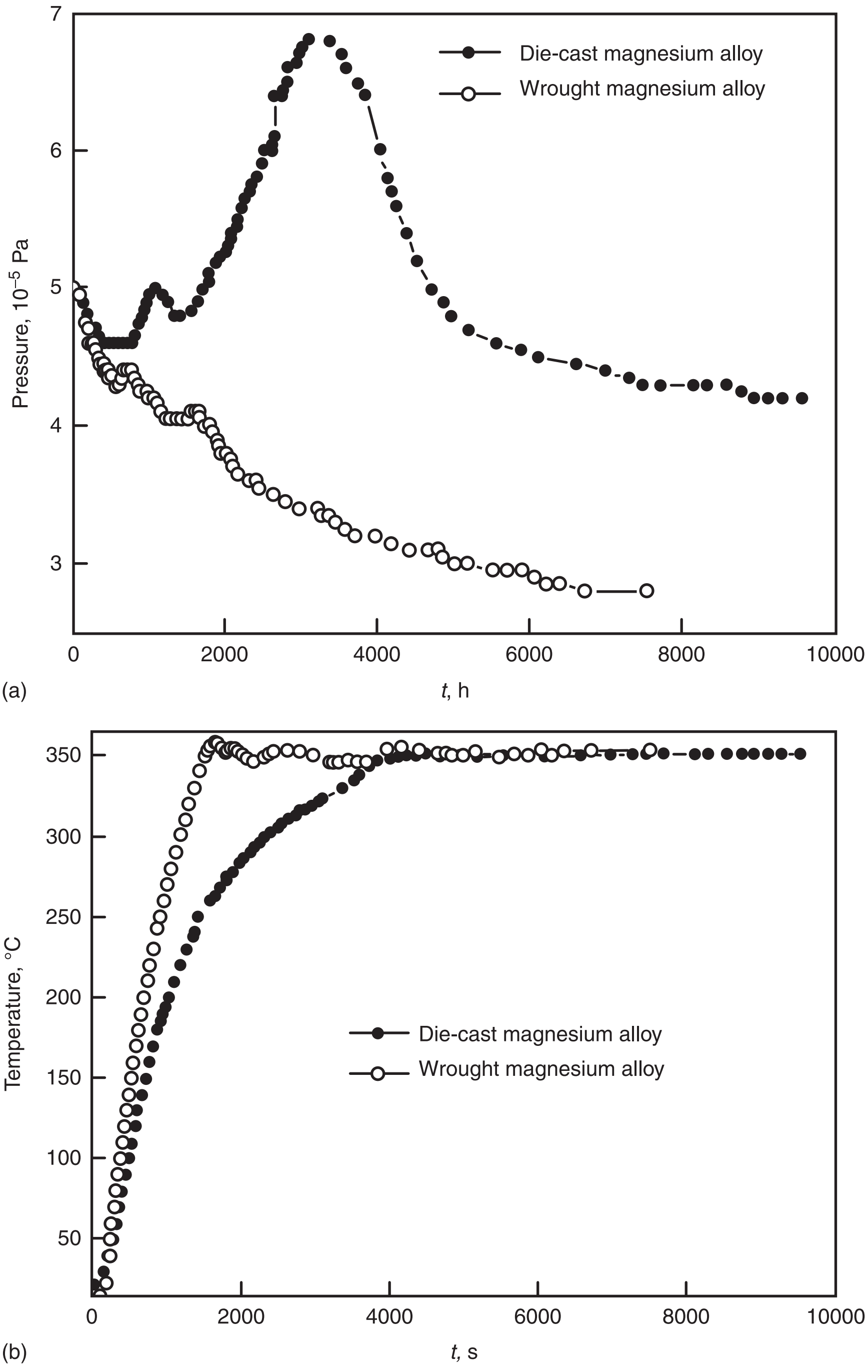

17.29 Changes of (a) pressure and (b) temperature during hot vacuum pumping.[69]

AZ31.[69] In the vacuum heating process, the pressure with AZ31 decreases continuously; however, the pressure with AM50 increases abruptly when the temperature is about 270 °C. At this temperature, the atomic hydrogen (H) can obviously diffuse into the vacuum. This means that die cast magnesium alloy AM50 has a high content of atomic hydrogen compared to wrought magnesium alloy AZ31.[69] The tendency of porosity formation in the base metal of die cast magnesium alloys with vacuum heating is weaker than that without vacuum heating (Fig. 17.30). Combining the calculations related to hydrogen gas (Eq. 17.5–17.7), we can consider that although hydrogen gas has some effect on porosity formation in laser welding, atomic hydrogen has the main effect here.[69]

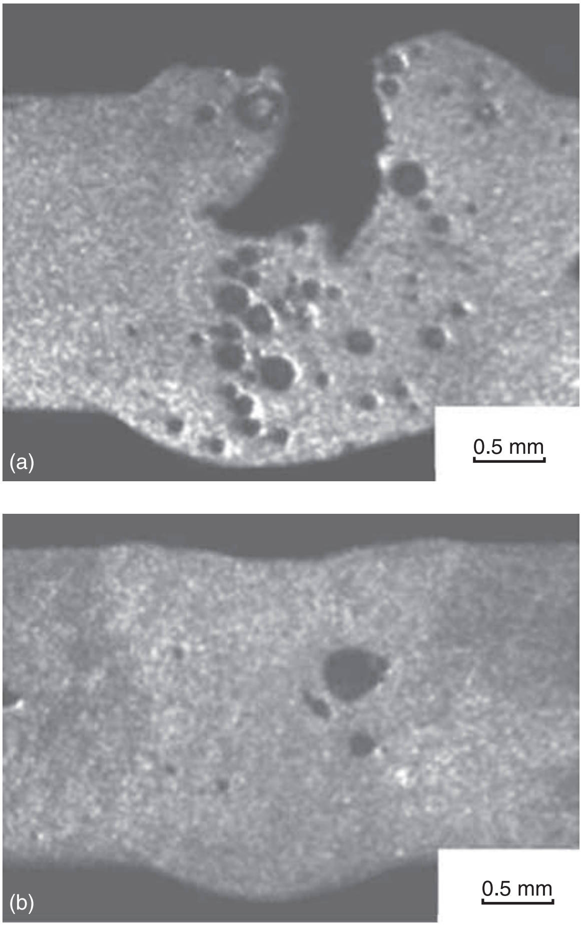

17.30 (a) Laser welding of AM50 without heating; and (b) laser welding of AM50 after heating.[69]

For wrought magnesium alloys, the effects of welding parameters (such as power, welding speed and so on) on the porosity ratio in laser welding are not obvious.[63] For sand cast magnesium alloys, the parameter of shielding gas has an obvious effect on porosity ratio in laser welding, but the effects of other welding parameters on the porosity ratio in laser welding are not obvious under the optimized parameter of shielding gas.[63] For die cast magnesium alloys, welding parameters have an important effect on the porosity ratio in laser welding; however, there are many contentions about the findings.[52,62,67] Jiguo Shan's research shows that increasing welding speed and decreasing power reduce the porosity ratio of the weld (Fig. 17.31 and Fig. 17.32). This means that the porosity ratio is lowest when a small amount of metal is melted, which is similar to the conclusions of article 67 (Fig. 17.33). However, Marya's research shows that the maximum of porosity ratio develops with the change of welding speed in laser welding of die cast magnesium alloys (Fig. 17.34).[53]

For wrought magnesium alloys and sand cast magnesium alloys, optimization of welding parameters can effectively prevent porosity formation in the laser weld[63] because of the low gas content in them. However, for die cast magnesium alloys, optimization of welding parameters cannot prevent porosity formation in the laser weld because of the high gas content in the base metal. Little has so far been done about porosity prevention in laser welding of die cast magnesium alloy. Jiguo Shan's research shows that removing hydrogen before welding can

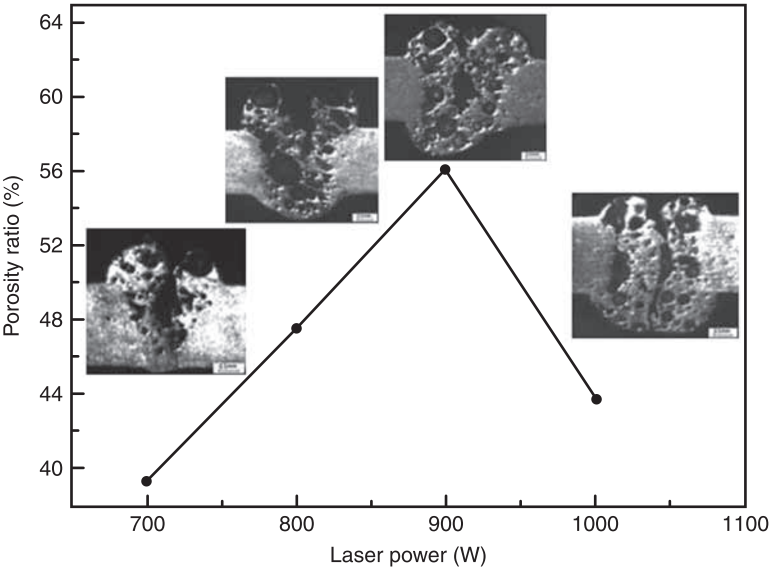

17.31 Porosity of laser welding of die-cast magnesium alloys under different power.[63]

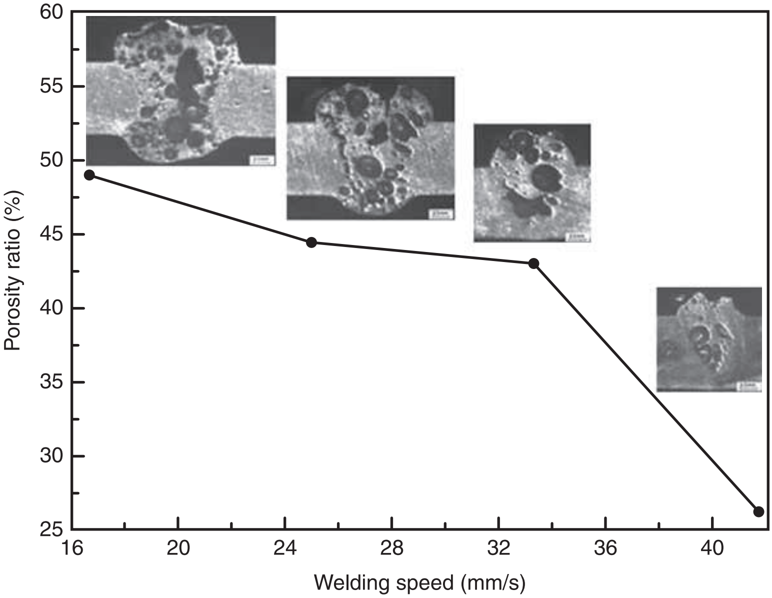

17.32 Porosity of laser welding of die-cast magnesium alloys under different speed.[63]

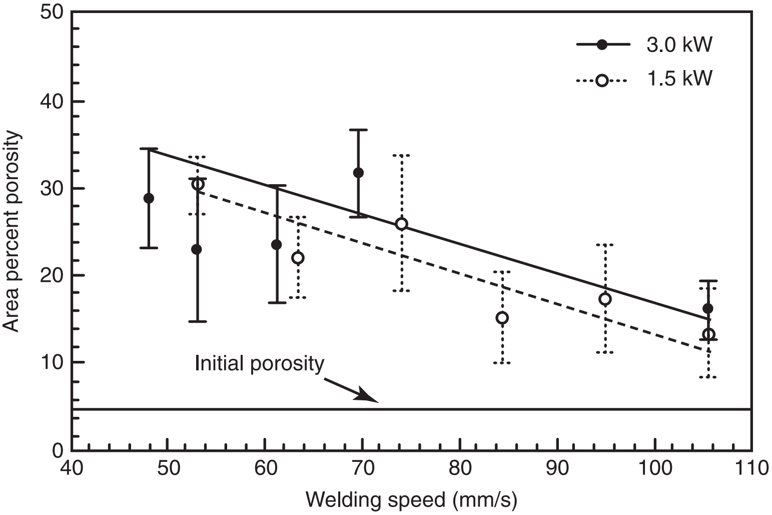

17.33 Relationship between porosity and welding speed in laser welds of die-cast AM60B.[52]

prevent porosity formation.[69] In addition, remelting after welding can also prevent porosity formation to a certain extent, and so can double side welding with one side being unaffected. The effects are shown in Fig. 17.35 and Fig. 17.36. Zhao also recommends remelting to prevent porosity formation (article 52).

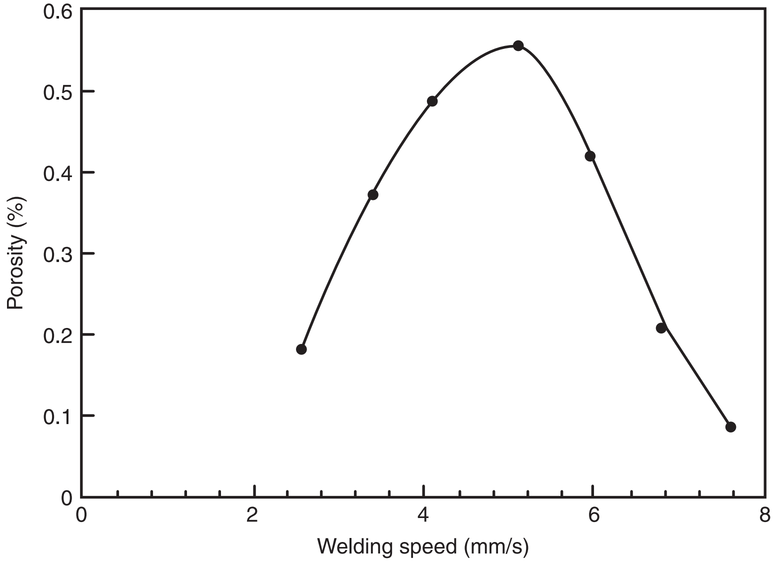

17.34 Porosity of laser welding of die-cast magnesium alloys under different speed.[53]

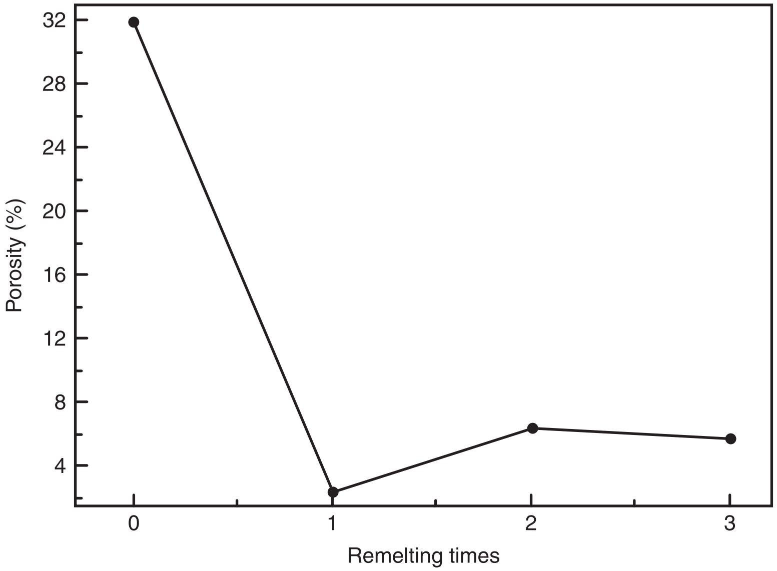

17.35 Porosity of laser welds of die-cast magnesium alloys change before and after remelting.[63]

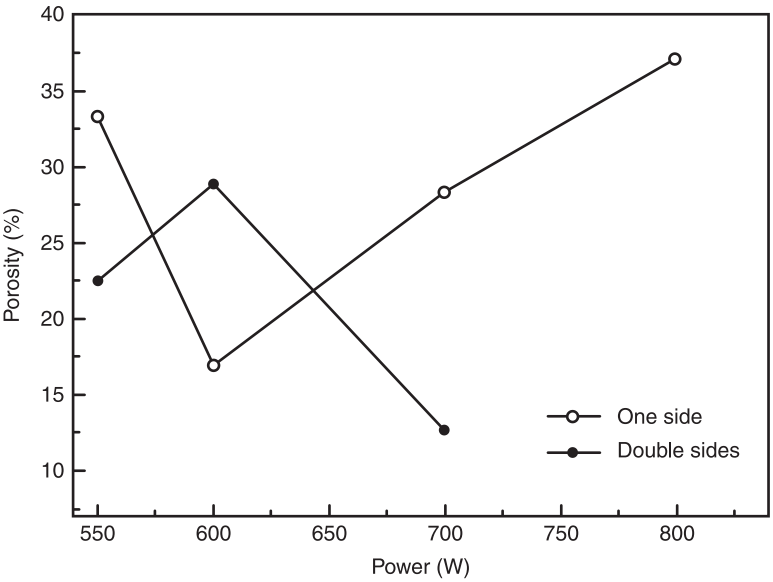

17.36 Comparing porosities of single-side welding and double-side welding of die-cast magnesium alloys under different welding conditions.[63]

17.6 Outlook and future trends

To weld magnesium joints and maintaining high productivity, high quality and low cost, a predictable, repeatable, consistent and reliable welding process needs to be developed. Wider welding operating windows are also welcomed for industrial applications. Thus, further efforts should concentrate on optimizing, controlling, regulating and defining laser welding parameter-operating windows for different magnesium alloys. Process specifications for laser welding should be developed to avoid the occurrence of welding defects for the reliable production of magnesium alloy joints. Research work on modeling and simulation will aid in the understanding of the welding processes involved. Little work in this aspect, however, has been conducted to date. No quality standards for laser-welded magnesium joints are available at the moment. Defect assessment procedures specific to the laser-welded joints are also needed. There is also a need to establish comprehensive relationships of material, welding processes for and defects in the mechanical properties of laser-welded joints including tensile, fatigue, fracture, formability and other static and dynamic properties, as well as corrosion. No work has ever been reported on the control of residual stress and distortion in laser-welded magnesium alloys.

Dissimilar joints between different magnesium alloys, dissimilar metals (such as Mg-Al, Mg-steel) and composites, with different geometries (thickness, shape), will probably be laser-welded in the future. Because of tight tolerances towards edge preparation, fit-up and sophisticated clamping jigs, hybrid processes, that is, laser beams combined with MIG, TIG and plasma arc processes or even combinations of similar or different lasers (such as multi-beam techniques) will possibly be used in the future. The easy manipulation and control of Nd:YAG lasers through optical fiber delivery provides welding opportunities for complex geometries where 3D welding may be carried out.

Castings are often complex in design and differ in section thickness. The constraints on laser welding could be quite severe. Thus, careful process control is necessary, especially for long freezing of range alloys, such as those with high zinc contents. Castings are also needed to repair some defects such as cracks, porosity, undersize, inclusions, broken and worn sections. However, no work has yet been carried out on repair welding using laser beams.

17.7 References

1. Zuo TC (2008). *Laser Materials Processing of High Strength Aluminum Alloys*. Beijing: National Defence Industrial Press.
2. Chen JM, Xu XY, Xiao RS (2007). *Modern Manufacturing Technology of Laser*. Beijing: National Defence Industrial Press.
3. Guan ZZ (2007). *Process Manual of Laser Processing*. Beijing: China Metrology Press.
4. Duley WW (1998). *Laser Welding*. New York: John Wiley.
5. Chen YB (2005). *Modern Laser Welding Technology*. Beijing: Science Press.
6. Liu LM, Xu GJ, Kutsuna MNH (2007). Laser and laser-MAG hybrid welding of high strength steel using fiber laser and CO_2 laser. *J Jpn Weld Soc* **25**(2): 254–60.
7. Zhang XD, Ren JL, Chen WZ (1997). Welding mode transition and process stability in high power laser welding. *Chin Weld* **6**(1): 61–6.
8. Yang YH, Zhong ML (1994). *High Power Laser Processing and Application*. Tianjin: Tianjin Science and Technology Press.
9. Chen ZH, Yan HG, Chen, JH (2004). *Magnesium Alloys*. Beijing: Chemical Industry Press.
10. Wang JJ (1992). *Laser Processing Technology*. Beijing: China Metrology Press.
11. Mazumder J, Ki H, Mohanty P S (2002). Modeling of laser keyhole welding: Part I. Mathematical modeling, numerical methodology, role of recoil pressure, multiple reflections, and free surface evolution. *Metall Mater Trans A* **33**(6): 1817–30.
12. Shan JG, Lei X (2008). Welding modes and weld formation characteristics of CO_2 laser welding of wrought magnesium alloy AZ31B. *Trans Chin Weld Inst* **29**(4): 9–13.
13. Cao X, Jahazi M, Immarigeon JP (2006). A review of laser welding techniques for magnesium alloys. *J Mater Process Technol* **171**(2): 188–204.
14. Ning XL (2002). The lightest metallic structure material: Mg-Li alloy. *Rare Met* **10**: 17–18.
15. Xu H, Liu JG, Xie SS (2007). *Manufacture and Processing Technology of Magnesium alloys*. Beijing: China Metallurgical Industry Press.

16. Liu Z, Zhang K, Zeng XQ (2002). *Theoretical Basis and Application of Mg-based Light Alloys*. Beijing: Mechanical Industry Press.
17. Zhang J, Zhang ZH (2004). *Magnesium Alloys and Application*. Beijing: Chemical Industry Press.
18. Pan HP, Ding ZY, Xie YS (2002). The study and application of processing technology of magnesium alloys. *Light Alloy Fabric Technol* **30**(7): 7.
19. Zhang TJ, Li XG (2002). Applications of magnesium alloys and progress of metallic magnesium industry in China. *Mater Rev* **16**(7): 11.
20. Yu K, Li WX, Wang RC (2003). Research, development and application of wrought magnesium alloys. *Chin J Nonferrous Met* **13**(2): 277.
21. Zhang GH, Zhang ZP, Pan JD (2003). Research and developments of magnesium and magnesium alloys. *World Sci-Technol R & D* **25**(1): 72.
22. Pan JL (2003). Structure of magnesium alloy and welding. *Electric Weld Mach* **35**(9): 1–7.
23. Wu J, Fang WY (1992). *Welding Handbook (2): Welding of Material*. Beijing: Mechanical Industry Press.
24. Feng JC, Wang YR, Zhang ZD (2005). Status and expectation of research on welding of magnesium alloy. *Chin J Nonferrous Met* **15**(2): 165–79.
25. Ding WB, Jiang HY, Jiang XQ (2005). Progress in welding technology of magnesium alloy. *Light Alloy Fabrication Technol* **33**(8): 1–6.
26. Stern A, Munitz A, Kohn G (2003). Application of welding technologies for joining of magnesium alloys: microstructure and mechanical properties. *Magnesium Technol* **33**(8): 163–8.
27. Xu JF, Zhai QY (2004). Microstructure and properties of TIG welding joint for AZ91B Mg alloy. *Spec Cast Nonferrous Alloy* **3**: 23–6.
28. Qu GX, Liu QZ, Guo DH (2002). Welding of thin plate of magnesium alloy AZ31B. *Weld Join* **2**: 44–5.
29. Zheng R, Lin R (2003). TIG welding of thin plate of magnesium alloy AZ31B. *Weld Join* **4**: 43–4.
30. Munitz A, Cotler C, Stern A (2001). Mechanical properties and microstructrue of gas tungsten arc welded magnesium AZ91D plates. *Mater Sci Eng* **A302**: 68–73.
31. Ashina T, Tokisue H (1995). Some characteristics of TIG welded joints of AZ31 magnesium alloy. *Jpn Inst Met* **45**(2): 70–5.
32. Wang HY, Liang XF (2005). Present research status and application of the laser welding technologies of magnesium alloys. *Weld Join* **11**: 10–14.
33. Dong CF, Liu LM, Zhao X (2005). Welding technology and microstructure of tungsten inert-gas welded magnesium alloy. *Trans Chin Weld Inst* **26**(2): 33–6.
34. Munitz A, Cotler C, Shaham H (2000). Electron beam welding of magnesium AZ91D plates. *Weld J* **79**(7): 202–8.
35. Bach FW, Szelagowski A, Versemann R (2003). Non-vacuum electron beam welding of light sheet metals and steel sheets. *Weld World* **47**(3–4): 4–10.
36. Bagger C, Olsen F (2005). Review of laser hybrid welding. *J Laser Appl* **1**(17): 2–14.
37. Wang W, Li LQ, Wang XY (2004). Laser arc hybrid welding technique. *Weld J* **3**: 6–9.

38. Taewon K, Jongcheol K, Yu H (2004). Welding of AZ31B magnesium alloy by YAG Laser/TIG arc hybrid welding process. *Mater Sci Forum* **449–52**(1): 417–20.
39. Liu LM, Song G, Wang JF (2004). Microstructure and mechanical properties of wrought magnesium alloy AZ31B welded by Laser-TIG hybrid. *Trans Nonferrous Met Soc Chin* [English Edition] **14**(3): 550–5.
40. Mishra RS, Ma ZY (2005). Friction stir welding and processing. *Mater Sci Eng R* 50: 71–8.
41. Esparza JA, Davis WC, Trillo EA (2002). Friction-stir welding of magnesium alloy AZ31B. *J Mater Sci Lett* **21**: 917–20.
42. Zhang H, Wu L, Lin SB (2004). Friction stir welding of AZ31 magnesium alloy. *Chin J Mech Eng* **40**(8): 123–6.
43. Seung HCP, Yutaka SS, Hiroyuki K (2003). Effect of micro-texture on fracture location in friction stir weld of Mg alloy AZ61 during tensile test. *Scr Mater* **49**: 161–6.
44. Zhang H, Wu HQ, Huang JH, Lin SB, Wu L (2007). Effect of welding speed on the material flow patterns in friction stir welding of AZ31 magnesium alloy. *Rare Met* **26**(2): 158–62.
45. Wang XH, Wang KS (2006). Microstructure and properties of friction stir butt-welded AZ31 magnesium alloy. *Mater Sci Eng A* **431**(1–2): 114–17.
46. Zhang DT, Suzuki M, Maruyama K (2005). Mircostructural evolution of a heat-resistant magnesium alloy due to friction stir welding. *Scr Mater* **52**(9): 899–903.
47. Stern A, Munitz A, Kohn G (2003). Application of welding technologies for joining of Mg alloys: microstructure and mechanical properties. Paper presented at Magnesium Technology 2003 Conference, Warrendale (PA): TMS.
48. Pan LK, Wang CC, Hsiao YC (2005). Optimization of Nd:YAG laser welding onto magnesium alloy via Taguchi analysis. *Opt Laser Technol* **37**(1): 33–42.
49. Weisheit A, Galun R, Mordike BL (2005). CO_2 laser beam welding of magnesium-based alloys. *Weld J* **77**(4): 148–54.
50. Dhahri M, Masse JE, Mathieu JF (2001). Laser welding of AZ91 and WE43 magnesium alloys for automotive and aerospace industries. *Adv Eng Mater* **3**(7): 504–7.
51. Wang JF, Liu LM, Song G (2004). Microstructure character of YAG laser welding AZ31B Mg alloy. *Trans Chin Weld Inst* **25**(3): 15–18.
52. Pastor M, Zhao H, DebRoy T (2000). Continuous wave-Nd: yttrium-aluminum-garnet laser welding of AM60B magnesium alloy. *J Laser Appl* **20**(3): 91–100.
53. Marya M, Edwards GR (2000). The laser welding of magnesium alloy AZ91. *Weld World* **44**(2): 31–7.
54. Cao X, Xiao M, Jahazi M (2005). Nd:YAG laser welding of magnesium alloy castings. Paper presented at Magnesium Technology 2005 Conference, Warrendale (PA): TMS.
55. Huo LX (2000). *Fracture Behavior and Evaluation of Welding Structure*. Beijing: Mechanical Industry Press.
56. Shu D (1982). *Mechanical Properties of Metal* (rev. ed.). Beijing: Mechanical Industry Press.

57. Shu D (1987). *Mechanical Properties of Metal*. Beijing: Mechanical Industry Press.
58. Baeslack WA, Savage SJ, Froes FH (1986). Laser weld heat affected zone liquation and cracking in a high strength Mg base alloy. *J Mater Sci* **5**(9): 935–8.
59. Marya M, Edwards GR (2002). Influence of laser beam variable on AZ91D weld fusion zone microstructure. *Sci Technol Weld Join* **7**(5): 286–93.
60. Lathabai S, Barton KJ, Harris D (2003). Welding and weldability of AZ31B by gas tungsten arc laser beam welding processes. Paper presented at Magnesium Technology 2003 Conference. Warrendale (PA): TMS.
61. Tan WD, Shan JG (2007). Influence of CO_2 laser welding process on weld surface formation of wrought magnesium alloy AZ31B. *Weld Join* **11**: 27–38.
62. Zhang J, Shan JG (2009). Research status and prospect of porosity problem in laser welding of magnesium alloys. *Weld Join* **7**: 37–41.
63. Shan JG, Zhang J (2009). Experimental study of porosity problem in laser welding of magnesium alloys. *Rare Met Mater Eng* **38**(3): 234–9.
64. Zhou MH, Yu MF (1984). *Welding Defects and Treatments*. Shanghai: Shanghai Scientific and Technical Literature Press.
65. Cao X, Wallace W, Poon C, Immarigeon JP (2003). Research and progress in laser welding of wrought aluminum alloys. I. Laser welding processes. *Mater Manuf Process* **18**(1): 1–22.
66. Cao X, Wallace W, Immarigeon JP, Poon C (2003). Research and progress in laser welding of wrought aluminum alloys. II. Metallurgical microstructures, defects and mechanical properties. *Mater Manuf Process* **18**(1): 23–49.
67. Zhao H, DebRoy T (2001). Pore formation during laser beam welding of die-cast magnesium alloy AM60B – mechanism and remedy. *Weld J* **80**(8): 204–10.
68. Quan YJ, Chen ZH, Yu ZH (2007). Defects analysis of AZ31 magnesium alloy joints by laser beam welding. *Hot Work Technol* **36**(3): 22–7.
69. Shan JG, Zhang J (2009). Experimental study on porosity in laser welding of die-cast magnesium alloys. *Acta Metall Sin* **45**(8): 1006–12.

18

Resistance spot welding of magnesium alloys

L. LIU, University of Waterloo, Canada, J. FENG,
Harbin Institute of Technology, China and Y. ZHOU,
University of Waterloo, Canada

Abstract: Resistance spot welding (RSW) of magnesium alloy is discussed in this chapter. Surface condition is important for RSW of magnesium due to the high chemical reactivity of magnesium and because oxides that form are hard, strong and electrically insulated. Expulsion, weld strength and electrode life are all related to surface conditions. Welding conditions (welding current, weld time, electrode force and weld spacing), nugget growth and dynamic resistance are discussed and compared with those of steel and aluminum alloys. Microstructure of the nugget and the influence of secondary particles are studied in detail. Technologies and mechanisms of dissimilar joining of magnesium alloy to steel and magnesium to aluminum alloys are also discussed.

Key words: resistance spot welding, magnesium alloy, surface condition, columnar-to-equiaxed transition (CET), dissimilar welding.

18.1 Introduction

In recent years, the increasing number of regulations relating to environmental protection has resulted in a demand for vehicles with lower fuel consumption and decreased emission of pollutants. Interest in magnesium alloys is rapidly increasing for use in automotive and aerospace equipment due to their low density and high strength. Resistance spot welding (RSW) is a primary joining method in the auto industry. If magnesium sheets can be successfully joined by RSW, the costs could be quite attractive due to less need for new equipment and the inherent low-cost characteristics of RSW. However, despite the ever-increasing demands to use RSW to join Mg alloys, only few feasibility studies have been published and detailed investigations are still needed. For example, the Resistance Welding Manual devotes 35 pages to introduce RSW of aluminum alloys but only eight pages to magnesium alloys. In this chapter, the fundamentals of RSW of Mg are introduced. The material preparation, welding process, mechanism of Mg nugget formation and welding metallurgy of RSW of Mg are discussed.

18.2 Fundamentals of resistance spot welding

18.2.1 General principles

As shown in Fig. 18.1, a resistance spot weld is made by pressing two or more overlapping pieces of metal together while an electric current is passed through a localized contact area to heat the metal forming the weld nugget to the welding. Generally, the application of heat is needed to weld two or more pieces of metal. For RSW, the heat is generated by the resistance of the weld assembly when a welding current passes between the electrodes through the welded plates. The heat generation in the weld zone should be very rapid so that the minimum amount of heat can dissipate for conduction to the cooler adjacent material. The rate of heat generation can be calculated by Joule's law:

$$W = I^2R \qquad [18.1]$$

where W is the electrical power, I is the welding current and R is the resistance. If the current is applied over a time interval of t, then the heat generated is

$$Q = I^2Rt \qquad [18.2]$$

where Q is watt seconds or joules. So, the heat generation can be controlled by changing the welding current, weld time and resistance. Part of the heat is used to melt the metal and part is lost to the surroundings, such as electrodes, surrounding solid workpieces and air.

Two kinds of resistance can be found in the RSW process (Fig. 18.1): contact resistances (R_3, R_4 and R_5) and bulk resistances (R_1 and R_2). The contact resistance includes resistance at electrode to workpiece interfaces (R_3 and R_5) and resistance

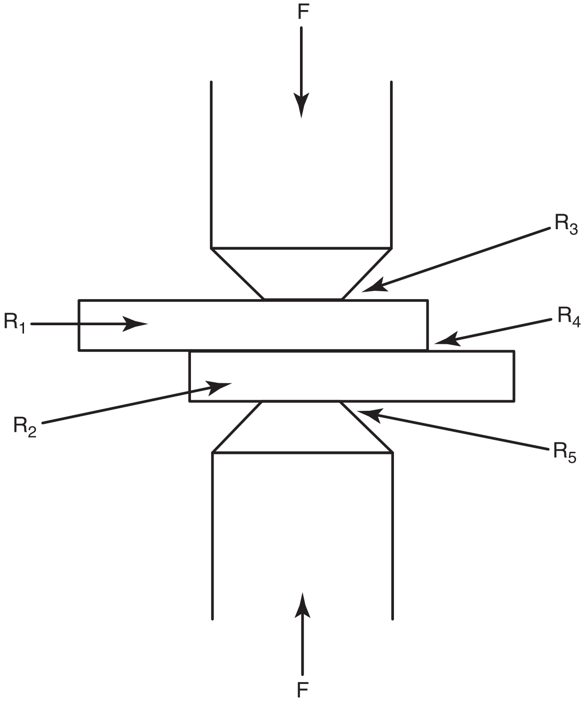

18.1 Resistances involved in a resistance spot weld.

at the faying interface between the two workpieces (R_4). The bulk resistances are directly proportional to the electrical resistivity and thickness of the welded materials, and inversely proportional to the cross-sectional area of the current path. Usually, the bulk resistances are smaller than the contact resistances, and it is desireable that the contact resistance at electrode to workpiece interfaces be smaller than that at the faying interface between the two workpieces. Therefore, the melting will start at the faying interface (RWMA, 1995).

18.2.2 Dynamic resistance

Usually, a constant welding current mode is programmed in RSW. On the basis of Eq. 18.2, the heat generation is determined by resistance R. During welding, the contact characteristics and areas, temperature and phases (solid or liquid) will change with weld time, causing changes in contact resistance and bulk resistance. So, the dynamic resistance is important and can be written as

$$V = IR + L\frac{dI}{dt} \qquad [18.3]$$

where R is the sum of the various component resistances and L is the inductance. The phase shift between voltage and current is a function of R and L. So, for an alternating current (AC) machine, the dynamic resistance data are measured once per half cycle when $\mathrm{d}I/\mathrm{d}t$ is zero at the peak. In the RSW of steel, the dynamic resistance decreases in the first few cycles due to surface oxide breakdown and the thermal softening/growing of constrictions, but then it increases because the elevated workpiece temperature leads to a major increase in bulk electrical resistivity (Dickinson et al., 1980). In the final stage, if the liquid nugget is allowed to grow too large, expulsion occurs resulting in a sudden drop of resistance. However, aluminum has a different characteristic shape in dynamic resistance during RSW. No peaks or increase of dynamic resistance is found during the RSW of aluminum alloys, which displays a continuously decreasing dynamic resistance. Because the bulk resistivity of Al alloys is very low and less dependent on temperature, almost all the heat-generating resistance is composed of faying surface and electrode workpiece contact resistances, which are reduced as the workpieces heat up and soften. The characteristic dynamic resistance of magnesium alloy is similar to that of aluminum alloy, which can be divided into three stages. In stage I, the dynamic resistance decreases rapidly and a nugget begins to form. In stage II, the increase of bulk resistance due to the elevated temperature results in a smaller rate of dynamic resistance decrease. In stage III, expulsion occurs and the dynamic resistance drops suddenly (Wang et al., 2007).

18.2.3 Weld nugget microstructure

Usually, the microstructure morphology is controlled by a combination of thermal gradient and cooling rate. During RSW, the water-cooled electrodes serve as a pair of efficient heat sinks and the base sheet material can also transfer heat radially outward from the nugget region. The liquid nugget is effectively in a chilled ingot mold and experiences a very high cooling rate (Zhang and Senkara, 2006). A columnar dendritic structure is the usual expected result under such thermal conditions. For example, the nugget microstructure in most metals (i.e., steel, Mo, Ni, Ti and Cu alloy) is a simple columnar dendritic structure; a few metals like Al alloys may show columnar grains around the periphery and equiaxed grains in the center (Wang et al., 2006). The main metallurgical defects in resistance spot welds are porosity and cracks (Sun et al., 2007). Pores are normally caused by either gas evolution in the nugget or liquid/solid shrinkage, the latter being sometimes related to liquid loss by expulsion. Cracks in a heat-affected zone (HAZ) (or liquation cracks) are frequently observed in some spot welded Al and Mg alloys and have an intergranular character. HAZ cracks have been suggested to have no significant effect on the static strength of spot welded AA5754 (Senkara and Zhang, 2000), but they may reduce the fatigue strength. The effect of porosity on the static weld strength is normally found to be significant, especially when the pores locate close to the notch tips (Zhang and Senkara, 2006).

18.3 Welding conditions: surface

As discussed in Section 18.2.2, the dynamic resistance of Mg alloys in RSW is different from that of steel. It decreases rapidly in the initial stage of RSW and no peaks can be found with the increase of weld time. So, the initial resistance (contact resistance) is very important for heat generation in RSW of Mg alloy. If the contact resistance is too low, heat generation at the faying surface will be insufficient to form a weld nugget. If the contact resistance is too high, expulsion could occur due to too much local heat generated at a few small contact spots. Moreover, since magnesium forms intermetallic alloys with copper, high contact resistance between the copper alloy electrodes and magnesium sheet could cause local melting of magnesium, leading to alloying, magnesium pickup and a lower electrode life.

Surface condition is one of the most important factors that can influence the contact resistance of the faying surface. In order to protect magnesium alloys from corrosion, various protective coatings, such as chrome pickle, anodizing, microarc oxidizing, etc., may be applied by sheet manufacturers. However, most added protective coatings show lower electrical conductivity or are even used as electrical insulators, in addition to the insulating effect of native surface oxide. Those coatings, as well as the excessive oxide films on unprotected sheets, must be removed before RSW (RWMA, 1995). For example, the contact resistance of faying surfaces varies significantly with surface conditions, as shown in Figure 18.2 (Liu, Zhou et al., 2009; Zhou et al., 2009). A-ARW, A-ARB, A-$H_2Cr_2O_7$ and A-HNO_3 are as-received-white (as-received sheet: looks white and bright),

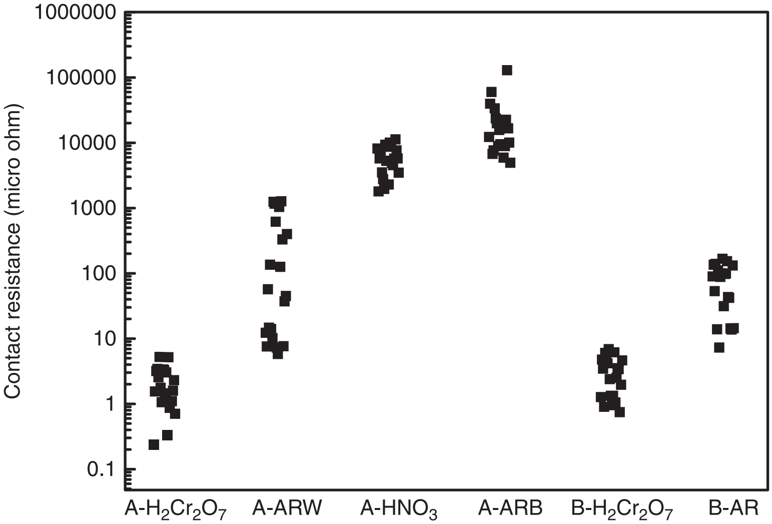

18.2 Contact resistance of different surface conditions (Liu et al., 2009c; Zhou et al., 2009).

as-received-black (as-received sheet: looks dark), chromic acid and nitric acid cleaned conditions of AZ31 sheets from supplier A. B-AR and B-$H_2Cr_2O_7$ are as-received and chromic acid cleaned conditions of AZ31 sheets from supplier B. The A-ARB condition produced the highest contact resistance, which is due to its thicker oxide film on the surface. Chromic acid treatment has been shown to remove the oxide layers efficiently, reduce the contact resistance and make the surface more uniform. However, diluted nitric acid cannot reduce the contact resistance. On the contrary, the contact resistance increased after nitric acid cleaning. These results suggest that the cleaning solutions for magnesium alloys should be selected carefully due to the high chemical reactivity of Mg alloys and the possibility of forming undesirable reaction products on the surface. The sheet processing can also change the surface condition. For example, the as-received contact resistance of sheet B was lower than that of sheet A. It may be because the conventional process of Mg alloy sheet production (sheet A, die casting and then warm rolling) had a higher finishing temperature than that of the new sheet process (sheet B, twin-roll strip casting). If no oxide is present on the surface of a metal sheet to be RSW, the contact resistance will be too low and not enough heat can be generated to make a weld. But for magnesium this situation is hard to meet, as after either chemical or mechanical cleaning, oxide will begin to reform on the surface immediately as long as the sheet is exposed to the air. So, the objective in pre-weld preparation is to ensure that the oxide layer will be moderate and consistent for making spot welds.

Expulsion is actually the ejection of molten metal during welding. It happens at either the faying surface or the electrode/workpiece interfaces. The latter may severely affect surface quality and electrode life. The former leads to loss of liquid metal from the nugget during welding that could cause voids and porosity in the nugget. Generally, the joint strength defined by joint breaking force in a standardized test such as tensile shear is roughly proportional to nugget size. However, as discussed in Section 18.2.3, defects in the nugget, such as pores, could obviously reduce the joint strength. Expulsion in steel RSW generally occurs in the last few cycles during welding according to its dynamic resistance curve in Section 18.2.2. Therefore, the expulsion of steel can be controlled by weld time. Expulsion from magnesium spot welds always occurs in the first few cycles during welding (Liu, Zhou et al., 2009), suggesting that surface condition plays an important role in the expulsion behavior and joint strength of magnesium alloys. As shown in Fig. 18.3, for the same nugget size, shear forces of spot welded chromic acid cleaned sheet were higher than those of A-ARW. The joint strength was not improved by nitric acid cleaning. Furthermore, nitric acid 'cleaning' increased the standard deviation of joint strength. Figure 18.4 shows fracture surfaces of welds in A-$H_2Cr_2O_7$, A-HNO_3 and A-ARW sheets. Elongated dimples were found on the fracture surface of shear tests (Fig. 18.4a). Large voids and shrinkages were always observed in the nuggets made in A-HNO_3 and A-ARW surface conditions (Fig. 18.4b and c). On close examination, the dendrite tips

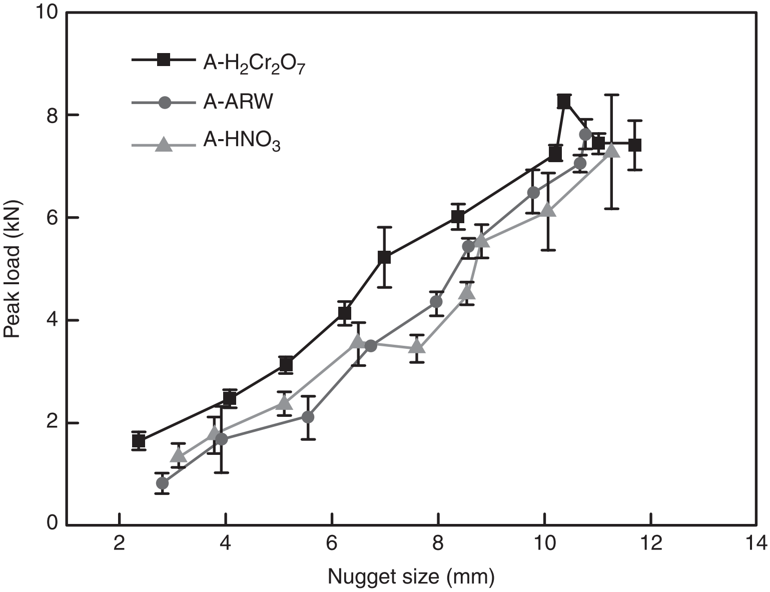

18.3 Weld strength versus nugget size of different surface conditions (Liu et al., 2009c).

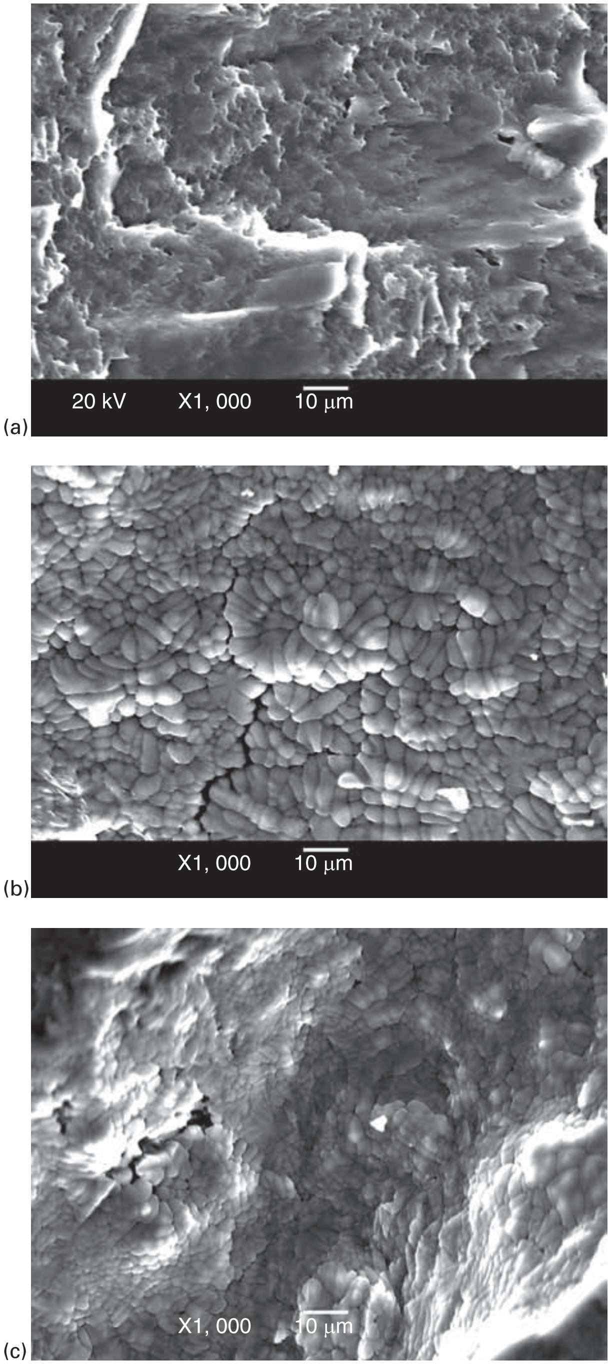

18.4 Fracture surfaces of different surface conditions: (a) A-$H_2Cr_2O_7$; (b) A-ARW; (c) A-HNO_3.

were smooth, undamaged and freely solidified, which was taken as evidence of formation during the later stages of the solidification process.

One of the major costs in the RSW of aluminum alloys and coated steel is short electrode life, which is due to metallurgical interactions between copper electrodes and aluminum or zinc. The brittle intermetallic phases formed on the surface of electrode tip faces could easily be pulled off by the workpiece at the end of the welding sequence, which results in cavitation on the electrode tip faces and consequently the reduction of electrode life (Lum et al., 2004). As magnesium reacts with copper and forms Cu-Mg intermetallic phases, electrode life should also be an issue in the RSW of magnesium alloys. Whenever a metal such as Al or Mg with hard, strong, insulating oxides is welded, the current constrictions during welding, induced by the fractures of surface oxides, may lead to spots of very high local current density, causing premature local melting at the workpiece/electrode interface (Liu, Zhou et al., 2009). The molten magnesium will result in Mg pickup on the electrode tip and the alloying of electrode (Cu) with magnesium. Therefore, the surface condition is also important for the electrode life. As suggested by the Resistance Welder Manufacturers' Association (RWMA), the electrodes should be cleaned after every 270 and 550 spots if dilute chromic acid is used to clean the sheets before welding, and every 15–40 spots if wire brush is used. Plate III (in color section between pages 210 and 211) shows the surface profiles of electrode tip faces after 40 welds made at 28 kA and eight cycles. It can be seen that much more surface damage was found on the electrode tip faces on welding sheets in the A-ARW (Plate IIIb) condition than with A-$H_2Cr_2O_7$ sheets (Plate IIIa).

18.4 Welding conditions: welding parameters

Welding current, weld time and electrode force are the most important parameters in the RSW of magnesium as they have a significant influence on the nugget diameter and joint strength. Typically, aluminum's high electrical and thermal conductivity requires about two or three times the amount of current and about one quarter of the weld time compared to spot welding of steel (RWMA, 1995). The thermal conductivity of magnesium alloy is smaller than that of aluminum alloy in the solid state, and the bulk electrical resistivity of magnesium alloys is close to that of aluminum alloys (Feng et al., 2006). As a result, the welding current required for magnesium alloys of a given thickness is slightly lower than that for aluminum alloys. For example, as suggested by RWMA, the welding current and weld time for a sheet 1.27 mm thick are 33 kA and eight cycles for aluminum alloy, and 29 kA and five cycles for magnesium (RWMA, 1995). Special features of the welding current schedule such as up and/or downslope control could also be applied to improve the weld quality. The upslope can reduce magnesium pickup on electrodes during welding and the downslope or postheat could reduce weld cracks (RWMA, 1995). A constant power mode could also be considered, as with a constant current weld controller, the rate of heat generation in the nugget region becomes very small once significant melting occurs and the interfacial oxide is dispersed.

The electrode force influences the RSW process mainly through its effects on the contact resistances and contact areas. Generally, the contact resistance decreases as the electrode force increases. Qiu et al. (2009) found that the nugget diameter and tensile shear load of magnesium alloy welds decreased with increasing electrode force. The electrode force should not be too low as the probabilities of excessive tip pickup, surface marking and greater inconsistency increase (RWMA, 1995). It should not be too high because extreme indentation, sheet separation, workpiece distortion and asymmetrical welds may occur. A dual force cycle has been suggested in the RSW of magnesium in which the welds are made at a low force followed by the application of a higher force called forging force (RWMA, 1995). The purpose of the forging force is to close internal defects such as voids and liquation cracks. The application time is extremely important as healing internal defects by forging force is only effective during the solidification process.

Spot spacing is another important parameter in making rows of Mg spot welds. This is because the second and succeeding welds in a row are affected by the current shunting effect from previous welds. The shunting effect is more obvious in alloys with high electrical conductivity such as magnesium and aluminum alloys. For example, the suggested minimum weld spacing when welding a 1.27 mm thick sheet is 6.4 mm for steel, 11.1 mm for magnesium and 12.7 mm for aluminum (RWMA, 1995).

Zhou et al. (2009) optimized RSW parameters for AZ31B Mg alloy and defined a process window by the minimum strength, expulsion and indentation, as shown in Fig. 18.5. The left and bottom boundaries are defined by the minimum strength required by AWS D17.2. For example, if the welding current is lower than 22 kA, the heat input would not be sufficient and the tensile shear load would be lower than the required value. The right and top boundary is defined by severe expulsion and indentation. The welding current should be limited to a certain critical value so as to avoid severe expulsion. Severe expulsion at the faying surface would reduce the strength and increase the indentation due to the loss of liquid metal. The expulsion boundary of the weld lobe in Fig. 18.5 corresponded roughly to an indentation of 15% (Zhou et al., 2009).

18.5 Nugget growth and microstructure

The growth of the nugget versus weld time for Al and Mg alloys has been suggested to be divided into three stages: incubation, growth and stabilization (Wang et al., 2007). An incipient nugget is formed in the incubation stage, which takes less than one cycle. In the growth stage, the nugget diameter increases, but the rate of increase drops with weld time. This is due to the increase in the contact area between the electrode and the workpiece with weld time, causing the decrease of current density and rate of heat generation. Eventually, the input thermal power

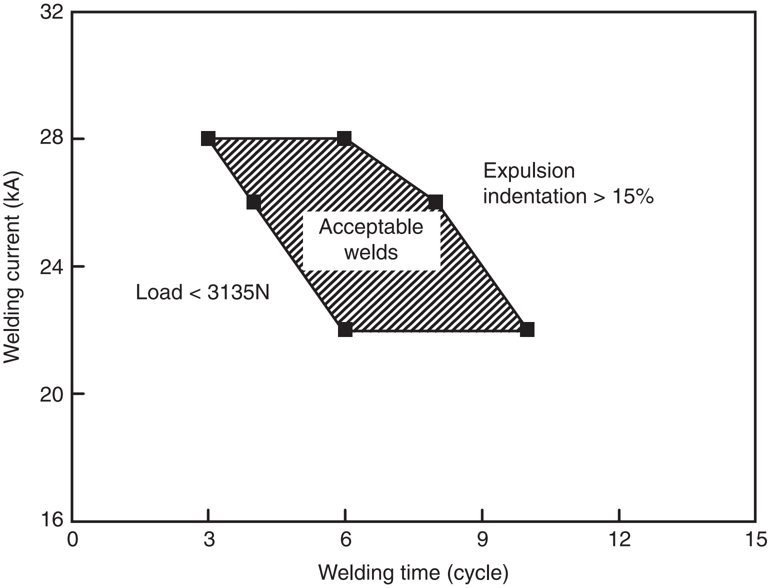

18.5 Process window (Zhou et al., 2009).

reaches a balance with the rate of heat loss and the nugget size stabilizes. Simulation results have compared the growth dynamics of Mg alloy with those of Al alloy and steel (Feng et al., 2006). The time span of the incubation stage of Mg alloy was similar to that of Al alloy, but different from steels that took five cycles to form the nugget. The simulation of temperature distribution indicated that the relatively high contact resistance at the faying surface was the main factor leading to a rapid increase in temperature at the faying surface. The temperature distribution along the radial direction of the faying surface was different for different materials. Steel was flatter than Mg and Al (Feng et al., 2006), suggesting that the heat generation of Mg and Al is more concentrated than that of steel, which has a positive effect on the formation of the nugget.

The typical microstructure of resistance spot welds in Mg alloys can be divided into four parts: base metal, HAZ, plastic ring and nugget (fusion zone) (Wang et al., 2006). The HAZ is characterized by recrystallization and grain growth. As in the case of some Al alloys, liquation cracks may be found in the HAZ of spot welded Mg alloy, adjacent to the fusion zone (nugget). The plastic ring is a special characteristic of RSW, which is located in the faying surface plane and within the range of the HAZ. Dynamic recrystallization occurs in this area due to the high temperature and plastic deformation by the electrode force. Generally, the nugget contains two kinds of microstructure: columnar dendritic and equiaxed dendritic structure (Sun et al., 2007). During solidification, columnar dendritic grains epitaxially grow from the partially molten base metal in the direction of the maximum local temperature gradient. The columnar-to-equiaxed transition (CET) occurs when the movement of the columnar front is blocked by enough equiaxed grains formed in the liquid ahead of the columnar front. Equiaxed grain structures are usually more desirable than columnar structures, for several reasons: the structures are more isotropic; equiaxed grains accommodate strains more uniformly; and segregation of alloying elements to the central plane or region is reduced (Villafuerte et al., 1995).

Secondary particles in base material that remain unmelted in the liquid nugget have been shown to promote the CET, increase the fraction of equiaxed dendritic structure and improve the joint strength. For example, Xiao et al. (2010) found that if Al_8Mn_5 particles are big enough, then the heterogeneous nucleation would occur ahead of the columnar front, block off the epitaxial columnar grains and promote the CET. Figure 18.6(a) and (b) show typical morphology of solidification structures of

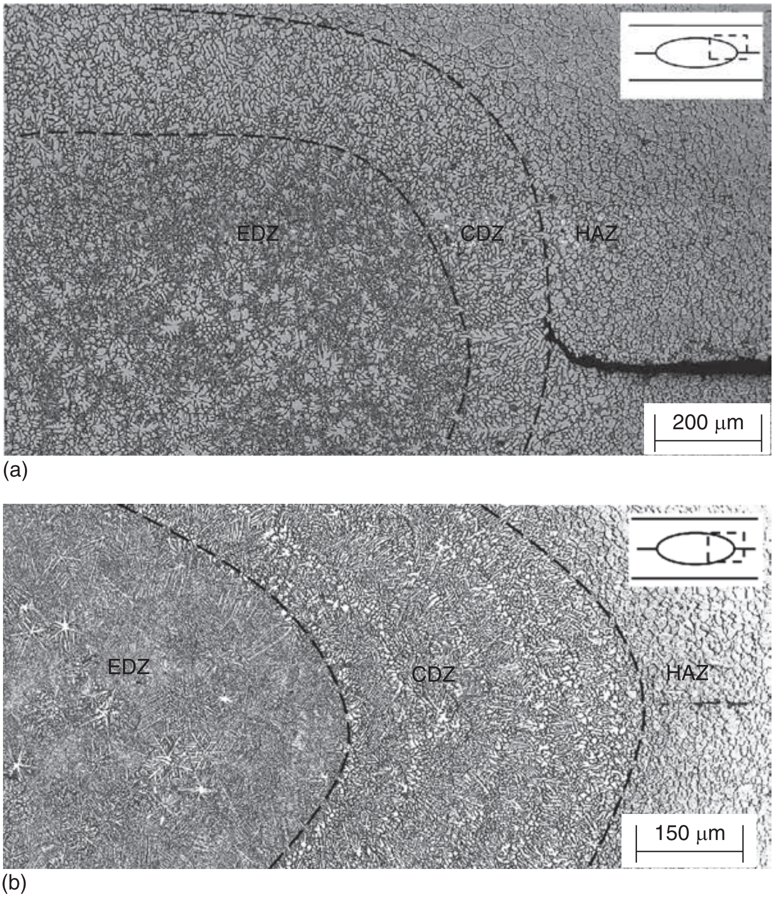

18.6 Microstructures along the notch of two AZ31 alloys: (a) AZ31-SA with micro-scale Al_8Mn_5; (b) AZ31-SB with nano-scale Al_8Mn_5 (Liu et al., 2009b).

two resistance spot welded AZ31B alloys containing different secondary particle populations, referred to as AZ31-SA and AZ31-SB, respectively (Liu, Xiao, Feng, Tian and Zhou Y et al., 2009). The AZ31-SA (Fig. 18.6a) was shown to contain both micro- and nano-scale Al_8Mn_5 particles whereas AZ31-SB (Fig. 18.6b) contained only nano-scale Al_8Mn_5 particles. Two zones in the nugget, with different microstructural features, that is, columnar dendritic zone (CDZ) and equiaxied dendritic zone (EDZ), were observed in the welds of AZ31-SA and AZ31-SB alloys. A dendritic structure with short primary arms was formed in AZ31-SA. However, typical columnar dendritic grains with long primary arms and large columnar dendritic regions were found in AZ31-SB. The width of the CDZ of AZ31-SB was larger than that of AZ31-SA. In order to confirm the effects of second-phase particles on the microstructure formed in AZ31 Mg alloy, coarse Mn particles, approximately 10 μm in length, were intentionally added into the fusion zone of the AZ31-SB welds. The changed microstructure showed that the addition of Mn particles would restrict the growth of columnar dendritic structure.

18.6 Welding of magnesium alloys to other alloys

Generally, the primary structural materials used in industry are steels and Al alloys. So, the development of technologies for dissimilar welding of Mg alloy to steel (Mg/steel) and Mg to Al alloys (Mg/Al) is very important. Magnesium and steel are difficult to join to one another due to the large difference in physical, chemical and mechanical properties between them. For example, the bulk resistance of magnesium is about one-third of that of steel and the thermal conductivity of magnesium is about twice the steel value (Feng et al., 2006). The melting point of steel is about 1500°C, which is even higher than the boiling point of magnesium (1090°C). The differences in bulk resistance and melting point between magnesium and aluminum are not particularly significant compared to those between magnesium and steel (Feng et al., 2006). The major problem of welding Mg to Al alloys is the formation of Mg-Al intermetallic compounds with a very high degree of hardness and brittleness. Those brittle intermetallic compounds formed between Mg and Al can generally act as crack sources that would reduce the mechanical properties significantly. Welding of Mg/Al and Mg/steel has been explored by various methods such as laser, friction stir and brazing (Chen and Nakata, 2009; Liu and Zhao, 2008; Zhao and Zhang; 2008). Only very few feasibility studies of dissimilar RSW have been published (Liu et al., 2009; Tomiharu, 2004).

If symmetric electrodes are used to weld Mg to steel, the peak temperature on the steel side would be much higher than that on the magnesium side due to the higher resistance and lower thermal conductivity of steel. The imbalance in heat generation would induce the melting of steel and boiling of magnesium and reduce the weld strength dramatically. Asymmetric electrodes should be used to balance the heat generation by reducing the current density and cooling rate of the steel side. For example, AZ31B Mg alloy and coated DP600 steel were

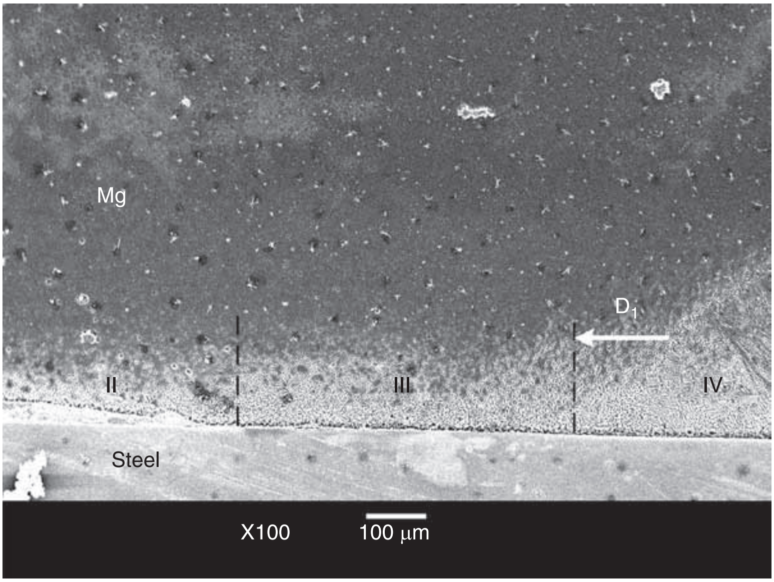

18.7 Typical cross-section of Mg/steel spot weld (Liu et al., 2009a).

successfully joined using a radiative electrode against the Mg side and a flat electrode against the steel side. The largest force in tensile shear testing of completed welds was around 5 kN that was above 95% of the strength of optimized AZ31B to AZ31B spot joints (Liu et al., 2010). These dissimilar joints were divided into three regions by solidification morphologies and chemical compositions as shown in Fig. 18.7 (Liu et al., 2010). In region II, soldering of magnesium to steel by zinc-based filler metal was observed. Equiaxed grains larger than those in the base metal were found in region III. It was determined that in region III, magnesium was partially melted and the joint was in fact formed by a combination of solid-state and fusion bonding. In region IV, magnesium alloy was melted and braze-welded to steel. No melt was found on the steel side, according to the microstructural evidence in the center of the steel side.

The strength of Mg/Al joints has been found to be extremely low (less than 1.0 kN) and brittle if directly welded by RSW due to Mg-Al intermetallic compounds that can readily be formed (Tomiharu, 2004). Weld bonding, which combines spot welding with adhesive bonding, was applied to RSW of Mg/Al (Tomiharu, 2004). The strength was improved considerably, but the intermetallic layers could not be avoided. Lots of work is still needed to be done in the field of RSW of Mg/Al.

18.7 Equipment for the welding of magnesium alloys

As discussed in Section 18.4, higher current density is needed for the RSW of magnesium alloys due to their high electrical and thermal conductivity. Therefore, the welding equipment for magnesium must have sufficient welding current available to make the weld in the shortest possible time, which is similar to the requirement for aluminum. So, equipment suitable for aluminum alloys should be used for spot welding magnesium alloys. The cost of a welding machine is proportional to its rating and secondary current capacity, suggesting that the cost of a machine for welding magnesium would be higher than that for welding steel of equivalent thickness. Generally, two kinds of RSW power supplies are used in the auto industry: single-phase AC and mid-frequency direct current (MFDC). The higher peak current of AC machine makes the process more susceptible to expulsion. The MFDC machine has advantages because the difference between peak and root mean square (RMS) current of the direct current (DC) machine is much smaller compared to an AC machine. Electrode life is less on AC welding machines than it is on DC, as the skin effect of AC leads to more current concentrated around the outside of the electrode tip. The advantage of AC is the generally lower capital cost than that of an MFDC machine due to much simpler power electronics. Positive control of welding force is also important and the force system should be air operated, as frictionless as possible and provided with a fast follow-up (RWMA, 1995).

The electrical rating of RSW machines in automobile body assembly lines is usually low, as the required welding current for RSW of steel body sheets is only between 6 and 12 kA (Qiu et al., 2009). A technique of RSW with cover plates has been developed to facilitate the welding of magnesium alloy, in which the magnesium alloy sheets are placed between cover plates (Qiu et al., 2009). The cover plates are metal sheets with a relatively lower electrical conductivity than magnesium alloy, such as cold rolled steel, so heat could be conducted from the cover plates into the magnesium sheets. Researchers have found that joints with high tensile shear strength can be obtained under relatively low welding current (Qiu et al., 2009).

As suggested by the RWMA, the best RSW electrode types for welding Mg alloys should have high thermal and electrical conductivity and a high degree of hardness or a resistance to deformation due to the high current typically needed for welding of magnesium. The electrodes should be cleaned or dressed regularly to remove Mg contamination that leads to the formation of Cu/Mg alloy buildup. Efficient electrode cooling is also necessary to maintain the electrode at a low temperature and reduce the Mg pickup and alloying.

18.8 Future trends

Sheet surface condition is important for RSW of magnesium due to the main effects of oxides and contaminants on contact resistance. Magnesium sheets should be cleaned before welding, as protective coatings and excess oxide films on the surface could induce expulsion and accelerate the damage to electrodes. Welding current, weld time, electrode force and weld spacing are the most important operating parameters. CET is always found in solidification structures of Mg nuggets and needs to be promoted because an equiaxed structure is more desirable. Technologies and mechanisms of dissimilar joining of magnesium alloy to steel and magnesium to aluminum alloys are also discussed.

This chapter has attempted to introduce various aspects of the RSW of magnesium alloy. However, as the RSW of magnesium alloy is immature compared to aluminum alloy and steel, the information in this chapter is far from comprehensive. In this regard, much more systematic research and development work is needed to study process, materials and control issues in the RSW of Mg alloys. Research on welding of wrought alloys has been more extensive since 2003, and lots of new magnesium alloys have been developed recently, such as AM, AZM and ZK series. Most of the limited publications on the RSW of magnesium alloy have been focused on AZ31 alloy. Weldability of other magnesium alloys and joining of different magnesium alloys need to be studied in the future. Nearly all the publications focused on the static mechanical properties. Fatigue properties of magnesium spot welds also need to be investigated further, as they are important for the practical use and safe application of welded structures. Poor corrosion properties are one of the factors that limit the usage of magnesium alloys. The corrosion properties of magnesium spot welds are nearly an unknown area. The RSW is the primary joining technique employed in automotive structures, in which corrosion behavior is very important for the life of vehicles. The RSW of magnesium alloy to other materials, such as steel and aluminum, has to be further developed because the predominant structural materials used in vehicles today are steel and aluminum.

18.9 References

Chen, Y.C. and Nakata, K., 2009. Effect of tool geometry on microstructure and mechanical properties of friction stir lap welded magnesium alloy and steel. *Materials and Design*, **30**: 3913–3919.

Dickinson, D.W., Franklin, J.E. and Stanya A., 1980. Characterization of spot welding behavior by dynamic electrical parameter monitoring. *Welding Journal*, **59**: 170S–176S.

Feng, J.C., Wang, Y.R. and Zhang, Z.D., 2006. Nugget growth characteristic for AZ31B magnesium alloy during resistance spot welding. *Science and Technology of Welding & Joining*, **11**: 154–162.

Liu, L., Xiao, L., Feng, J.C., Tian, Y.H., Zhou, S.Q. and Zhou Y., 2010. The mechanisms of resistance spot welding of magnesium to steel. *Metallurgical and Materials Transactions A*, in press.

Liu, L., Xiao, L., Feng, J.C., Tian, Y.H. and Zhou, Y., 2009. Resistance spot welded AZ31 magnesium alloy, Part II: Effects of welding current on microstructure and mechanical properties. *Metallurgical and Materials Transactions A*, in press.

Liu, L., Zhou, S.Q., Tian, Y.H., Feng, J.C., Jung, J.P. and Zhou, Y.N., 2009. Effects of surface conditions on resistance spot welding of Mg alloy AZ31. *Science and Technology of Welding & Joining*, **14**: 656–661.

Liu, L.M. and Zhao, X., 2008. Study on the weld joint of Mg alloy and steel by laser-GTA hybrid welding. *Materials Characterization*, **59**: 1279–1284.

Lum, I., Biro, E., Zhou, Y., Fukumoto, S. and Boomer, D.R., 2004. Electrode pitting in resistance spot welding of aluminum alloy 5182. *Metallurgical and Materials Transactions A*, **35**: 217–226.

Qiu, R.F., Satonaka, S. and Iwamoto, C., 2009. Mechanical properties and microstructures of magnesium alloy AZ31B joint fabricated by resistance spot welding with cover plates. *Science and Technology of Welding & Joining*, **14**: 691–697.

RWMA, 1995. *Resistance Welding Manual*, Philadelphia, PA: Resistance Welder Manufacturers' Association.

Senkara, J. and Zhang, H., 2000. Cracking in spot welding aluminum alloy AA5754. *Welding Journal*, **79**: s194–201.

Sun, D.Q., Lang, B., Sun, D.X. and Li, J.B., 2007. Microstructures and mechanical properties of resistance spot welded magnesium alloy joints. *Materials Science and Engineering*, **460**: 494–498.

Tomiharu, O., 2004. Resistance welding of aluminum alloy to dissimilar metals. *Journal of Light Metal Welding & Construction*, **42**: 2–15.

Villafuerte, J.C., Kerr, H.W. and David, S.A., 1995. Mechanisms of equiaxed grain formation in ferritic stainless steel gas tungsten arc welds. *Materials Science & Engineering A*, **194**: 187–191.

Wang, Y.R., Feng, J.C. and Zhang, Z.D., 2006. Microstructure characteristics of resistance spot welds of AZ31 Mg alloy. *Science and Technology of Welding & Joining*, **11**: 555–560.

Wang, Y.R., Mo, Z.H., Feng, J.C. and Zhang, Z.D., 2007. Effect of welding time on microstructure and tensile shear load in resistance spot welded joints of AZ31 Mg alloy. *Science and Technology of Welding & Joining*, **12**: 641–646.

Xiao, L., Liu, L., Zhou, Y. and Shahrzad, E., 2010. Resistance-spot-welded AZ31 magnesium alloys: Part I. Dependence of fusion zone microstructures on second-phase particles. *Metallurgical and Materials Transactions A*, **41**, 1511–1522.

Zhang, H. and Senkara, J., 2006. *Resistance Welding: Fundamentals and Applications*. Boca Raton, FL: CRC Press.

Zhao, L.M. and Zhang, Z.D., 2008. Effect of Zn alloy interlayer on interface microstructure and strength of diffusion-bonded Mg–Al joints. *Scripta Materialia*, **58**: 283–286.

Zhou, S.Q., Liu, L., Jung, J.P., Lee, M.Y. and Zhou, Y.N., 2009. Effects of welding parameters and surface pretreatments on resistance spot welding of AZ31B Mg alloy. *Metals and Materials International*, MMI09-221.

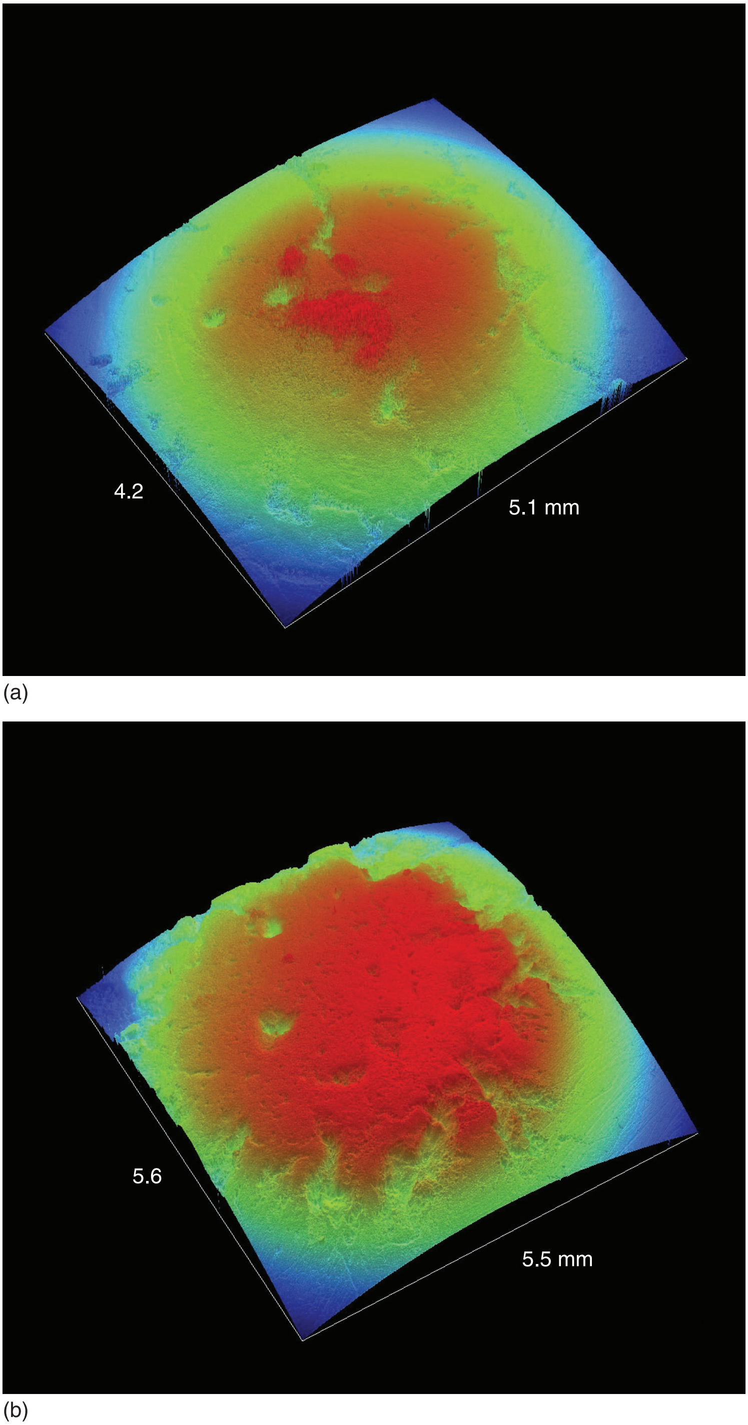

Plate III Profiles of electrode tip faces after 40 welds at 28 kA: (a) A-$H_2Cr_2O_7$; (b) A-ARW.

19

Electromagnetic pulse welding of magnesium to aluminium sheets

S. KORE, Indian Institute of Technology Guwahati, India
and J. IMBERT, Y. ZHOU and M. WORSWICK,
University of Waterloo, Canada

Abstract: Electromagnetic (EM) welding is based on application of Ampere's law. Due to the ease of controlling magnetic fields, EM technique is more suitable for joining axis symmetric components. With special coil design, it can also be used to join Mg to Al sheets. Lorentz force is induced by eddy current and magnetic field, both of which are generated in the workpiece by a transient current in a coil in the vicinity. The jetting action due to the high velocity of impact removes the oxide layer present on the metal surface and creates a defect-free weld. EM welds of Mg to Al sheets obtained at optimum process parameters are found to be stronger than the parent metal. As EM setups are of high-voltage, the safety measures related to high-voltage are considered very important.

Key words: electromagnetic, welding, strength, microstructure, intermetallics, safety.

19.1 Introduction

Aluminum alloys have good formability and weight savings. Hence, they are considered for the manufacture of vehicles. Magnesium alloys are lighter than other structural metals and their density is two-thirds that of aluminum. Mg alloys are also promising structural materials for vehicle manufacture. It is essential to develop reliable joints between Mg alloys and Al alloys to use them together to take advantage of their properties. There is no suitable technique available to weld these alloys using fusion welding technology because of the level of inter-metallic compounds formed in the weld, resulting in unacceptable mechanical properties.[1] Electromagnetic (EM) welding, being a solid-state welding technique, is potentially well suited to avoid this problem. EM welding technique is similar to explosive welding in terms of removal of the oxide layer by jetting action due to high velocity of impact. In EM welding process, the approach angle and velocity between the parts are sufficient to remove the oxide layer present on the surface of the sheets by jetting. Thus, two atomically clean surfaces are pressed together at very high pressures to obtain complete metallurgical continuity, thus forming an EM weld between the metals in question.

19.2 Fundamental theory of electromagnetic welding

The working principle of EM forming is based on the application of Ampere's law: 'Current-carrying conductors, when placed near each other, exert a force on each other,' as shown in Fig. 19.1.

If the currents flow in the same direction, there is a force of attraction, whereas if the currents flow in opposite directions, a repulsive force acts on the conductors. This repulsive force is used for the shaping and joining of metals by means of a high-strength transient magnetic field. The force between infinitely long parallel conductors is given by:[2]

$$F = \frac{\mu_0}{2\pi d} I_1 I_2 \qquad [19.1]$$

where F is force (N), I_1, I_2 is current (A) and μ_0 is permeability of free space (H/m).

To produce the current, energy stored in the capacitors, charged through a DC power supply, is discharged through the work coil. When the capacitors discharge, energy is transferred back and forth between the capacitor (where it is stored in electric fields) and the coil (where it is stored in magnetic fields). The current in the coil takes the form of a dampened sinusoidal function. The dampened sinusoidal current set up in the work coil produces a transient magnetic field. The metal sheets that are to be welded cut the transient magnetic field, and an electromotive force (EMF) is induced in them. The polarity of this EMF is such that the eddy currents induced in the sheets flow in the opposite direction to the ones in the coil. The induced currents depend upon the material conductivity. Finally, the work sheets are repelled away from the coil (towards each other) by Lorentz force (F), which is given by:

$$\mathrm{F} = \mathrm{J} \times \mathrm{B} \qquad [19.2]$$

where, J is current density and B is magnetic flux density.

The Lorentz force is an impulsive force that is applied for a time in the order of tens of microseconds.[3–8] The impact energy, and hence the occurrence of a weld, depends on parameters such as the inductance of circuit, frequency, capacitor

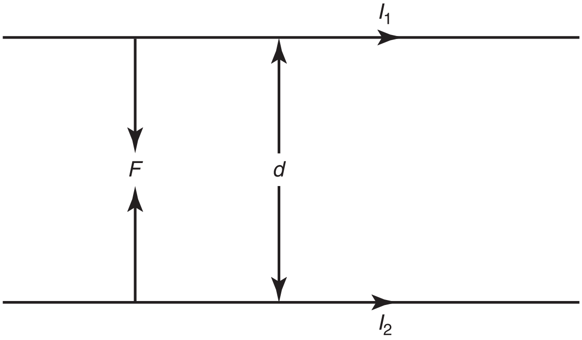

19.1 Principle of EM welding.

energy, voltage, current and standoff distance between the sheets. The standoff distance is the distance by which the sheets to be welded are separated from each other. The velocity acquired by the sheets prior to impact depends upon the energy imputed and the standoff distance. The kinetic energy achieved by the sheets due to the high velocity is converted into impact energy.

Skin depth is a measure of the distance an alternating current can penetrate beneath the surface of a conductor. It is defined as

$$\delta = \frac{\rho}{\pi \mu_0 \mu_r f} \qquad [19.3]$$

where ρ is the electrical resistivity of the workpiece; ρ_0 is permeability of free space ($4\pi \times 10^{-7}$); m_r is relative permeability and f is frequency.

In the case of sheet metal, the skin depth can be greater than the thickness, causing 'leaking' of the magnetic field through the other side, lowering the efficiency of the process. It is desirable for EM welding operations that the value of the frequency is selected in such a way that the skin depth of the induced currents in the workpiece is less than its thickness. Under this condition, an appreciable amount of magnetic field is confined within the thickness of the workpiece, and the diffusion of the field beyond it is reduced to a minimum value.

Since it is relatively easy to control the magnetic field for axi-symmetric components, such as tubes,[9,10] the EM technique has been studied in detail by many researchers for the formation and welding of tubes. EM impulse welding has similarities to explosive welding, such as the critical impact angle, the velocity for joining and a wavy interface after welding.[11–16] The EM welding has also been explored for joining similar and dissimilar metal tubes and structural applications.[17–25]

The EM welding technique has thus far mainly been studied and applied to tubular structures and has been much less researched for welding of flat sheets, due to the difficulties in designing EM coils and controlling the magnetic fields. Aizawa et al.,[3–5] Kore et al.[6–8,26–28] and Zhang et. al.[29] have reported the feasibility of EM welding of flat sheets. Kore et al.[7,8] have reported a detailed study of the effects of process parameters on the strength and width of EM welds of Al-to-Al and Al-to-SS sheets. Kore et al.[30] have reported the feasibility of EM welding of magnesium (AZ31) to aluminum (AA3003) flat sheets.

19.3 Equipment for electromagnetic welding

An EM-forming system comprises the following equipment connected electrically to form an RLC (resistance, R; inductance, L and capacitance, C) circuit.

19.3.1 Work coil

The work coil is that part of the RLC circuit through which a dampened sinusoidal current of high magnitude is passed, producing a transient magnetic field required for processing. Depending upon the EM metal-processing technique, different types of coil that can be used are described below.[31,32]

- *Solenoid coils*: This is a helical coil used for processing the axi-symmetric components. Depending upon their operation, these coils are further classified into two types:
  - *Expansion coil*: When a solenoid coil is kept inside a job piece (tube) and is used to expand the tube, then it is termed an expansion coil, as shown in Fig. 19.2(a).
  - *Compression coil*: When a solenoid coil is kept outside the job piece (tube) and is used to compress the tube, then it is termed a compression coil, as shown in Fig. 19.2(b).
- *Flat pancake type coil*: A spirally wound coil, as shown in Fig. 19.2(c), is used for the material processing of flat sheets. The magnetic field is uniformly developed above the coil. The end portion of the coil is its center, where the direction of current flow changes, which forms a dead zone.
- *Bar coil*: In case of bar coils, as shown in Fig. 19.2(d), due to its small cross-sectional area, the magnetic pressure is concentrated at the workpiece area which is directly facing the coil. This type of coil is mainly used for concentrating the repulsive force onto a localized area of the workpiece, in order to get the deformation or weld to the localized area.

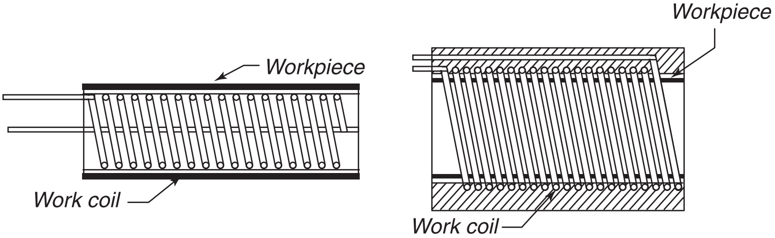

(a) Expansion coil

(b) Compression coil

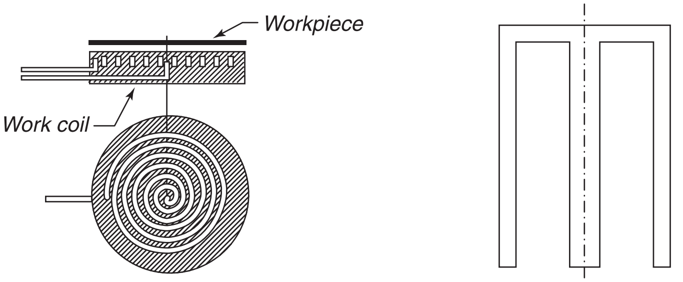

(c) Flat pancake type coil

(d) Bar coil

19.2 (a)–(d) Types of coil.

19.3.2 Capacitor

A capacitor is an energy storage device that is used for drawing a high current for forming and welding operations. Capacitors can be connected in parallel depending upon the energy requirement for the material-processing operation.

19.3.3 High-voltage power supply

High-voltage power supply is a capacitor-charging device. The capacitor bank can be charged from a variable voltage power supply. It consists of three basic elements: the step-up transformer, the rectifier and the current limiting device. It charges the capacitor by using a rectified current. A detailed discussion about the working of a variable power supply is given, in context, along with the experimental setup, in Section 19.3.

19.3.4 High-voltage switch (spark gap)

A high-voltage switch, like a spark gap switch, is used to close the RLC circuit and pass the high current through the work coil.

19.3.5 Field shapers

Field shapers are used to concentrate pressure to a specific location on the workpiece. They are also used to adapt large diameter compression coils to smaller diameter workpieces. Field shapers are single-turn coils. They are inserted between the work coil and the workpiece. They receive their energy from the work coil and transfer it to the workpiece by induction.[33] Thus, by using different sizes of field shapers, the same size work coil can be used for job pieces of different diameters. However, field shapers must be electrically insulated from the work coil and the workpiece. The use of field shapers increases the life of the coil by reducing the force acting on the coil.

The efficiency of the EM process can be calculated by using the plastic work done in deforming the tubes and the energy stored in the capacitor bank:[34]

$$\eta = \frac{W}{E_c} \times 100 \tag{19.4}$$

where η is the efficiency of the EM process; W is plastic work done during the forming process and E_c is energy stored in the capacitor bank.

The field shaper is inductively coupled to a forming coil and not directly connected to it. Hence, the efficiency of the EM-forming process using field shapers is less than that in which the forming coil is used without the field shaper. Designing a strong coil, which can sustain the mechanical stress arising from Lorentz force, is difficult. By introducing induction currents in the coil system, the Lorentz forces can be shifted towards the region of greater mechanical strength of the coil.[35] The other equipment of the EM welding includes a high-speed camera, an accelerometer, a load cell, a Rogowski coil[36] to measure the current and a memory oscilloscope to capture and analyze the signals obtained.

19.4 Welding technique and materials

A schematic representation of the EM setup used by Kore et al. for EM welding of flat sheets is shown in Fig. 19.3.

Kore et al. reported EM welding of Mg to Al sheets with single-turn copper coil. Dumbbell-shaped coil concentrates the current over the area to be welded. The coil was made from 3-mm-thick copper plate and was insulated with Kapton™ sheet. It was supported by a fixture to avoid bending from the induced forces during welding of the sheets.

Relatively poor electrical conductivity of the magnesium alloy led to a skin depth more than its thickness; hence, the field was not fully contained, thereby lowering the impact force. Magnesium sheets, being poor conductors of electricity as compared to Al, were not driven on their own. Since electrical conductivity of aluminum is higher, its skin depth at the experimental frequency condition was less than its thickness. Thus, frequency and skin depth conditions were appropriate for aluminum sheets. Kore et al.[30] used aluminum driver sheets to accelerate the

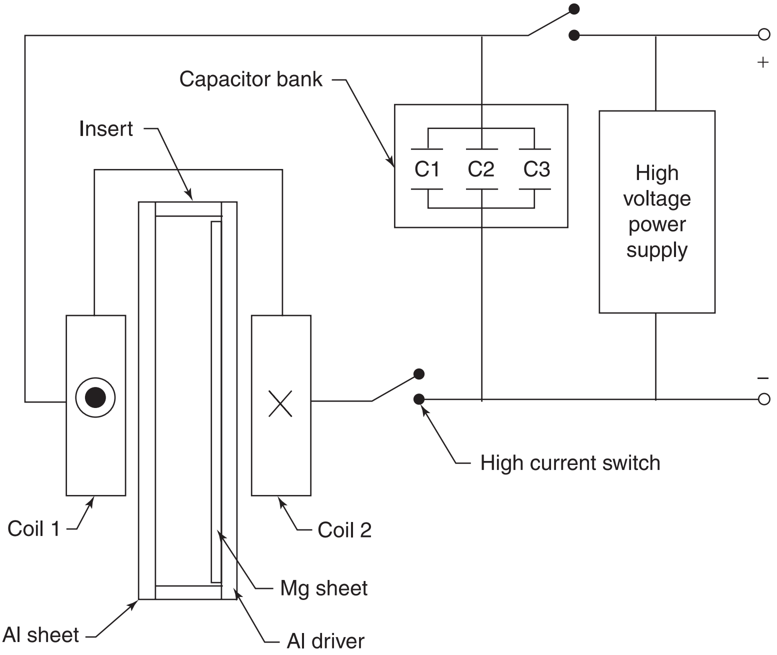

19.3 Schematic of electromagnetic impact welding set up.[30]

magnesium sheets. Each sheet of magnesium was backed up with an aluminum driver sheet. The magnesium sheet was insulated from the aluminum driver sheet to avoid sparking between them. The prepared samples were placed within the copper coil. Energies of 4.3–9.7 kJ were discharged from the capacitor bank. The current waveform obtained at 6.7 kJ discharge energy is shown in Fig. 19.4. A sample of Mg to Al sheet welded by EM welding technique is shown in Fig. 19.5.[30]

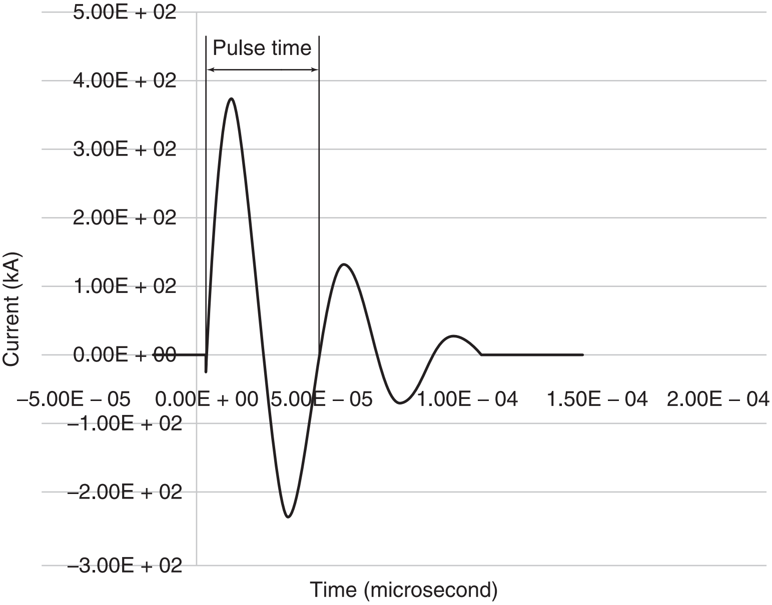

19.4 A typical current waveform showing peak current of 369 kA and pulse time of 42 ms (frequency 23.8 kHz) at 6.7 kJ discharge energy.[30]

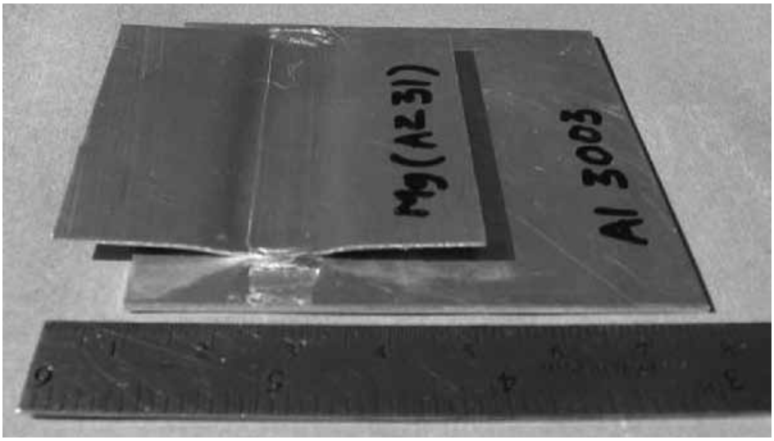

19.5 A typical EM weld of Mg to Al sheets.[30]

19.5 Mechanical and metallurgical testing of welds

Figure 19.6 shows the variation in shear strength of the welds with respect to the discharge energy used, for a constant standoff distance of 2.5 mm. With the experimental conditions described above, the minimum discharge energy required for EM welding of magnesium to aluminum sheets was 4.3 kJ. Samples welded with lower discharge energies showed interfacial failure, with less shear strengths. Higher values of discharge energies improved the shear strength and produced welded samples that exhibited two types of failure, as shown in Fig. 19.7.

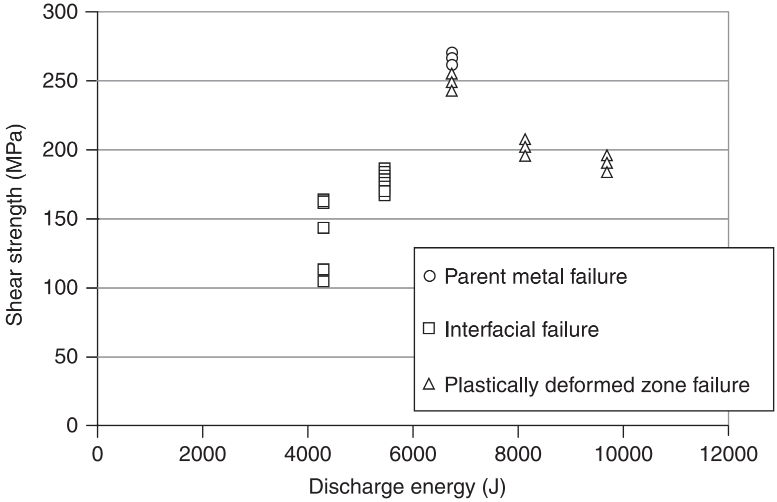

19.6 Shear strength of EM welds with variation in discharge energy.[30]

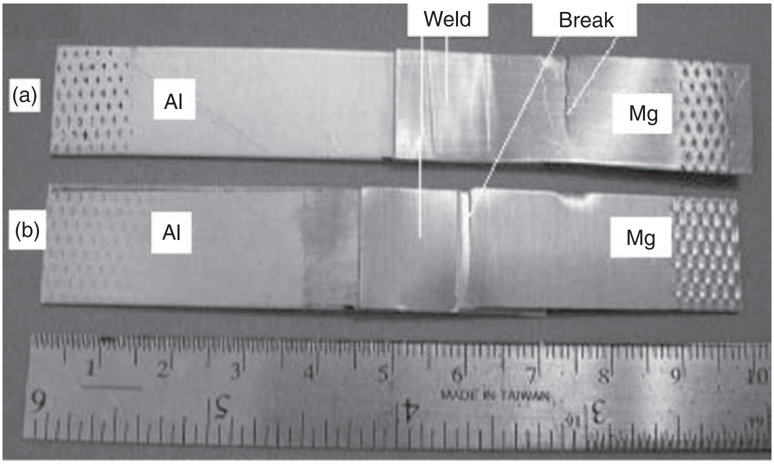

19.7 Shear-tested samples of Mg to Al welds with failure in (a) base metal and (b) plastically deformed zone.[30]

Samples welded at higher values of discharge energy failed either in the plastically deformed zone or in the base metal. At higher discharge energy values, the plastic deformation of the magnesium sheets was severe and failure occurred away from the weld in the severely plastically deformed zone. At the optimum value of standoff and discharge energy, the welds exhibited maximum value of strength.

The welded samples were cut across the weld, polished and observed under the microscope to analyze the weld interface. Compressed grains were observed at the weld interface. A scanning electron microscope (SEM) image of the weld interface is shown in Fig. 19.8. The image shows a wavy interface and complete metal continuity without any defect in the weld. No eutectic microstructure has been observed at the interface which indicates that any rise in temperature during the EM welding process is insufficient to cause melting. The wavy interface in these welds is due to the high velocity of impact between the two sheets. This phenomenon is similar to the one observed in the well-known explosive welding process.[37]

The representative results from X-ray diffraction, which are presented in Fig. 19.9, indicate that both the aluminum phase and the magnesium phase emitted the strongest signals.[30] These measurements could either suggest that the interfacial microstructure of these EM welds had no intermetallic phases, or that any intermetallic phase must have been exceptionally fine, thus undetectable by the X-ray diffraction technique used in this case. From the X-ray diffraction results, for the welds formed using the experimental conditions and material combinations studied, it is concluded that there is no melting and formation of intermetallic phases at the weld interface.

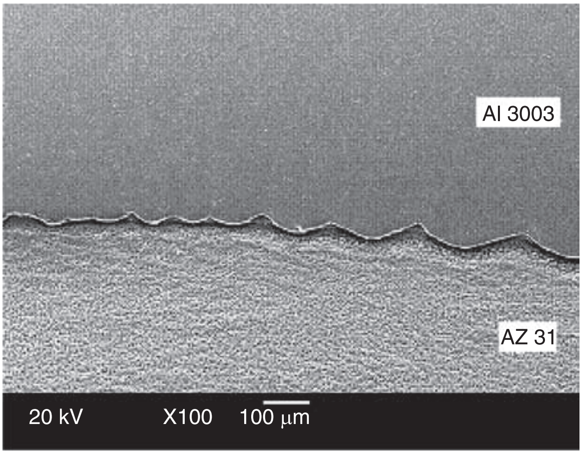

19.8 SEM image of Mg to Al weld cross-section showing wavy interface and complete metal continuity.[30]

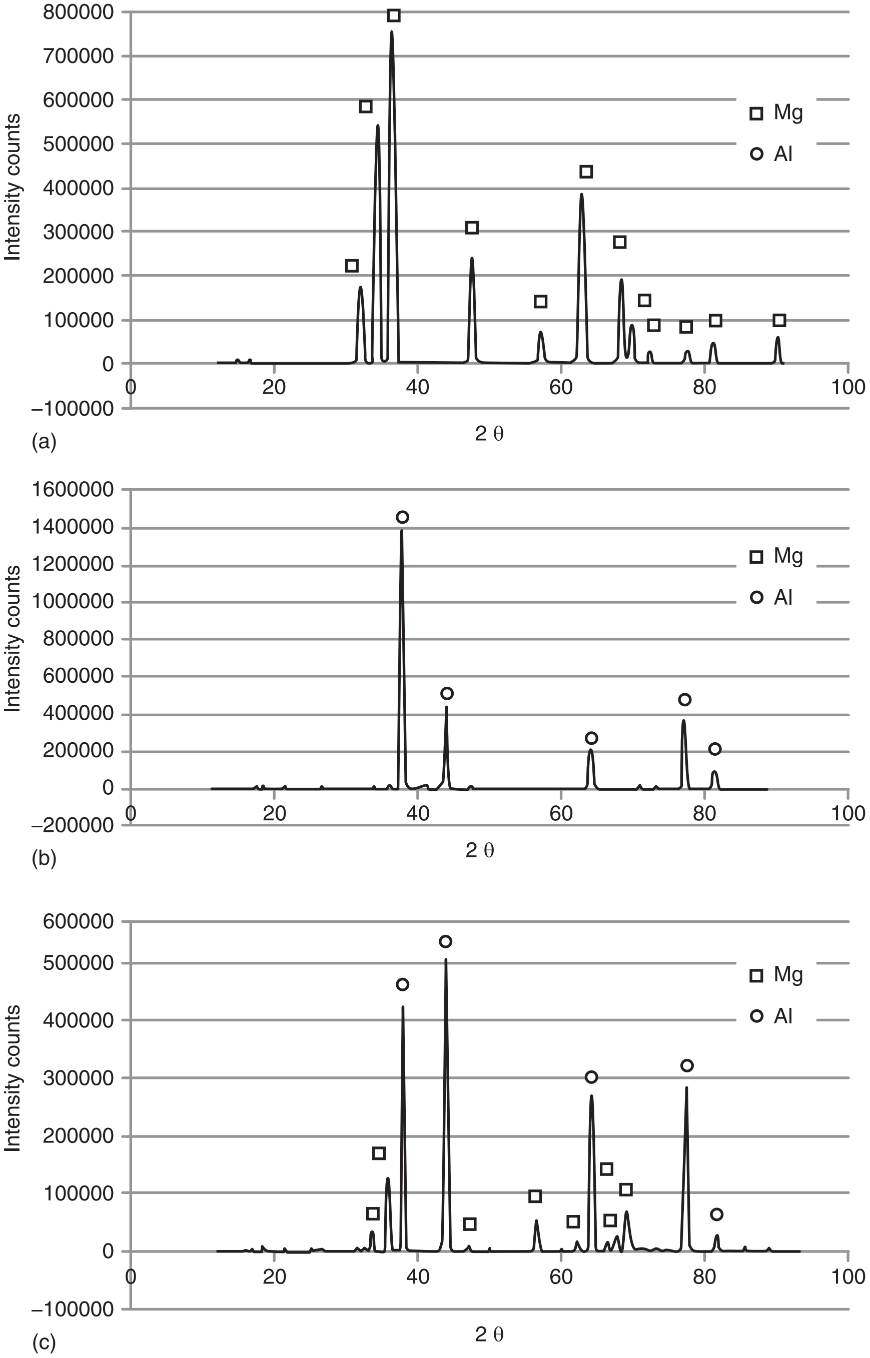

19.9 XRD spectra of Mg to Al weld at (a) opened weld interface Mg side; (b) opened weld interface Al side; and (c) Al-Mg weld cross-section.[30]

19.6 Safety guidelines while handling the electromagnetic welding setup

As electromagnetic setups are high-voltage setups, the safety measures related to them are considered very important. The danger is most lethal in the body providing a conducting path, particularly through the heart. Also any involuntary muscle contractions caused by a shock, while perhaps harmless in them, may cause collateral damage. There may be many sharp edges and points inside the setup, like metal inserts, nut bolts, metal sheets and left out spanners or other such instruments which may be lethal if not properly taken care of. In addition, the reflex may result in contact with other electrically live parts and further unfortunate consequences. The guidelines mentioned below help to protect people from potential deadly electrical shock hazards as well as the equipment from accidental damage.

- Do not work alone – in the event of an emergency another person's presence will be essential.
- Wear rubber sole shoes or sneakers. An insulated floor is best option than metal or bare concrete, but this is sometimes difficult to maintain. A rubber mat is an acceptable alternative. No carpet of any thickness will serve as insulator.
- Try to keep one hand in your pocket when working anywhere around a powered line-connected or high-voltage system.
- Wear ear muffs for the protection from the spark gap triggering sound.
- Wear eye protection – large plastic-lensed eyeglasses or safety goggles.
- Do not wear any jewelry or other articles that could accidentally contact circuitry and conduct current.
- Stand away from the setup behind the protection wall to protect yourself from exposure to the EM field and the stray components, if any, which may accelerate like bullets.
- Always keep the capacitor banks shorted when not in use.
- Make sure to dump all the charge on the capacitor.
- Manual dumping by using a dead stick confirms the complete discharge of the capacitors.
- Do not use capacitors to full rating to avoid possible explosion due to weakening of the capacitor wall after repeated use.
- Set up your work area away from possible grounds that you may accidentally contact.
- Have a fire extinguisher rated for electrical fires readily accessible in a location.
- Finally, never assume anything without checking it out. Avoid taking shortcuts and monotony.

19.7 References

1. Liu L, Wang H, Song G, Ye J (2007). Microstructure characteristics and mechanical properties of laser weld bonding of magnesium alloy to aluminum alloy. *J Mater Sci* **42**: 565–72.
2. Moon FC (1984). *Magneto Solid Mechanics*. New York: John Wiley.
3. Aizawa T, Okogawa K, Yoshizawa M, Henmi N (2001). Impulse magnetic pressure seam welding of aluminium sheets. *Impact Eng Appl* 827–32.
4. Aizawa T, Okogawa K (2004). Impact seam welding with magnetic pressure for Aluminium sheets. *Mater Sci Forum* **465**: 231–6.
5. Aizawa T (2004). Methods for electromagnetic pressure seam welding of Al/Fe sheets. *Weld Int* **18**(11): 868–72.
6. Kore SD, Date PP, Kulkarni SV (2006). AWS's sheet metal welding conference XII, Livonia/Detroit, MI, Paper 2.
7. Kore SD, Date PP, Kulkarni SV (2007). Effect of process parameters on electromagnetic impact welding of Al sheets. *Int J Impact Eng* **34**: 1327–41.
8. Kore SD, Date PP, Kulkarni SV (2008). Electromagnetic impact welding of aluminum to stainless steel sheets. *J Mater Process Technol* **1–3**: 486–93.
9. Mamalis AG, Manolakos DE, Kaldas AG, Koumoutsos AK (2004). Electromagnetic forming and powder processing: trends and developments. *Appl Mech Rev* **57**(4): 299–324.
10. El-Azab A, Garnich M, Kapoor A (2003). Modeling of the electromagnetic forming of sheet metals: state of art and future needs. *J Mater Process Technol* **142**: 744–54.
11. Zhang P (2003). Joining enabled by high velocity deformation. PhD. Thesis in OhioLink ETD, Ohio State University. Available from: http://www.ohiolink.edu/etd/view.cgi?acc_num=osu1061233577.
12. Masumoto I, Tamaki K, Kojima M (1985). Electromagnetic welding of aluminium tube to aluminium or dissimilar metal cores. *Trans Jpn Weld Soc* **16**(2): 110–6.
13. Kojima M, Tamaki K (1990). Electromagnetic Welding of tubes. The 5th international symposium of the Japan Welding Society, Tokyo, pp. 201–6.
14. Kojima M, Tamaki K (1988). Factors affecting the electromagnetic welding of aluminium tube. *Trans Jpn Weld Soc* **19**(1): 35–43.
15. Kojima M, Tamaki K, Furuta T (1989). Effect of collision angle on the result of electromagnetic welding of aluminium. *Trans Jpn Weld Soc* **20**(2): 36–42.
16. Kojima M, Tamaki K, Suzuki J, Sasaki K (1990). Flow stress, collision velocity and collision acceleration in EM welding. *Weld Int* **4**: 684–90.
17. Hwang WS, Kim NH, Sohn HS, Lee JS (1992). Electromagnetic joining of aluminium tubes on plyurethane cores. *J Mater Process Technol* **34**: 341–8.
18. Hwang WS, Lee JS, Kim NH, Sohn HS (1993). Joining of copper tube to polyurethane tube by electromagnetic pulse forming. *J Mater Process Technol* **37**: 83–93.
19. Powers HG (1967). Al by the capacitor discharge magnetic forming process. *Weld J* 507–10.
20. Marya M, Marya S (2004). Interfacial microstructures and temperatures in aluminum—copper electromagnetic pulse welds. *Sci Technol Weld Join* **9**(6): 541–7.
21. Stern A, Aizenshtein M (2002). Bonding zone formation in magnetic pulse welds. *Sci Technol Weld Join* **7**(5): 339–42.

22. Marya M, Marya S, Priem D (2005). On the characteristics of electromagnetic welds between aluminum and other metals and alloys. *Weld World* **49**: 74–84.
23. Shribman V, Stern A, Livshitz Y, Gafri O (2002). Magnetic pulse welding produces high strength aluminum welds. *Weld J* **81**(4): 33–7.
24. Kimchi M, Saho H, Cheng W, Krishnaswamy P (2004). Magnetic pulse welding of aluminum tubes to steel bars. *Weld World* **48**: 19–22.
25. Ben-Artzy A, Stern A, Frage N, Shribman V (2008). Interface phenomena in aluminum–magnesium magnetic pulse welding. *Sci Technol Weld Join* **13**(4): 402–9.
26. Kore SD, Date PP, Kulkarni SV, Kumar S, Rani D, Kulkarni MR, et al. Electromagnetic impact welding of Cu to Cu sheets. *Int J Mater Form*. Accepted September 2009, doi: 10.1007/s12289-009-0661-z.
27. Kore SD, Date PP, Kulkarni SV (2010). Numerical modeling of electromagnetic welding. *Int J Appl Electromagnet Mech* **32**(1): 1–19.
28. Kore SD, Date PP, Kulkarni SV, Kumar S, Rani D, Kulkarni MR, et al. (2009). Electromagnetic welding of Al-to-Al-Li sheets. *ASME J Manuf Sci Eng* 131, 131,034502-1-4.
29. Zhang Y, Babu SS, Zhang P, Kenik EA, Daehn GS (2008). Microstructure characterisation of magnetic pulse welded AA6061-T6 by electron backscattered diffraction. *Sci Technol Weld Join* **13**(5): 467–71.
30. Kore SD, Imbert J, Worswick MJ, Zhou Y (2009). Electromagnetic impact welding of Mg to Al sheets. *Sci Technol Weld Join* **14**(6): 549–53.
31. Davis R, Austin ER (1970). *Developments in High Speed Metal Forming*. New York: Industrial Press.
32. Panshikar HM (2000). Computer modeling of electromagnetic forming and impact welding. MS Thesis, Ohio State University [cited 2010 Feb 1]. Available from: http://www.er6.eng.ohio-state.edu/;DAEHN/hyperplasticity.html.
33. Wilson MN, Srivastava KD (1965). Design of efficient flux concentrators for pulsed high magnetic fields. *Rev Sci Instrum* **36**(8): 1096–1100.
34. Suzuki H (1987). The effect of a field shaper in EM tube bulging. *J Mater Process Technol* **15**: 229–40.
35. Kim YB, Platner ED (1959). Flux concentrator for high intensity pulsed magnetic fields. *Rev Sci Instrum* **10**: 524–33.
36. Ramboz JD (1996). Machinable Rogowski coil, design and calibration. *IEEE Trans Instrum Meas* **45**(2): 445–8.
37. Cowan GR (1971). Mechanism of Bond zone wave formation in explosion clad metals. *Metall Trans* **2**: 3145–55.

Index

- abrasion methods, 150
- ACEN *see* alternating current electrode negative
- ACEP *see* alternating current electrode positive
- acetone, 150
- activating flux tungsten inert gas welding, 253–72
  - base metal and melted materials oxygen contents, 271
  - effect of activating fluxes
    - surface appearance, 266
    - weld morphology, 266
    - future trends, 272
  - joints microstructure, 267–71
    - crystal grain size, 268
    - EDS analysis, 269
    - fusion zone XRD analysis, 270
    - secondary electron images, 269
  - mechanical properties, 271–2
    - room temperature tensile test results, 271
  - weld penetration
    - activating flux coating density, 264
    - argon shielding gas flowrate, 262
    - penetration depth vs arc length with different activating fluxes, 261
    - welding current effect, 259
    - welding speed, 263
    - with vs without activating flux, 265
  - welding mechanism, 254–8
    - arc image of Mg alloy with oxide fluxes on one side, 256
    - effects of fluxes on weld shape, 257, 258
    - flux application on one side of the joint, 257
    - mechanisms affecting the penetration characteristics, 257
    - Mg alloy with and without oxide fluxes arc image, 255
    - specimen used in TIG/ATIG welding trials, 254
    - welding configuration, 255
  - welding parameters, 258–67, 265
    - arc length, 260
    - flux thickness, 263–7
    - Mg alloy welds produced with and without activating flux, 259
    - shielding gas flowrate, 261–2
    - welding current, 259–60
    - welding speed, 262
- adhesive bonding
  - applications, 154, 157–8
    - adhesive layer containing SiO_2, 158
    - automotive magnesium parts, 157
    - magnesium alloy door inner panel, 157
    - specimens with SiO_2 particles, 157
  - future trends, 158
  - magnesium alloys, 149–58
    - adhesives characteristics, 155–6
    - adhesives used, 154
    - cure for the bonding, 154
  - surface treatments, 149–53
    - group pre-treatment/coating/adhesive combinations, 152
    - Lap-shear peak stress before and after corrosion testing, 152
    - Lap-shear samples before and after corrosion testing, 153
    - pre-treatment and powder coating process, 150
- aerodynamic forces, 256
- airborne grit blasting, 150
- AlF_3 flux, 260
- alkaline detergent solution, 150
- alternating current electrode negative, 199
- alternating current electrode positive, 200
- alternating current MIG welding, 185–94
- aluminium, 7
- aluminium alloys
  - welding and joining with magnesium alloys, 38–61
    - diffusion bonding, 44–9
    - future trends, 60–1
    - hybrid laser-tungsten inert gas welding, 39–44
    - laser weld bonding, 49–60
- aluminium coating, 91
- aluminium rivets, 131
- Ampere's law, 367
- antimony, 6
- arc spraying
  - post-treatment technology, 87–91
    - Al-rich epoxy resin based paint on aluminium coating, 88
    - arc-sprayed Al and MAO coating

      polarisation curves, 92
    coating morphologies, 90
    corrosion kinetics of epoxy resin and paint sealed coatings, 89
    epoxy resin sealed coating and Al-rich paint, 88
    epoxy resin sealing treatment, 87–9
    hydrothermal sealing technology, 89–90
    MAO coating surface images, 92
    micro-arc oxidation treatment, 90–1
    SSIT coatings corrosion kinetics, 91
  technology, 86–7
arc welding, 320
argon, 160, 316
argon gas, 261
ASTM D 1384, 293
ASTM D 2651, 150, 151
AZ31
  arc-sprayed aluminium coating on welded joint, 86
  cross-sectioned weld joint images, 83
  longitudinal section morphologies of lap joints, 87
  low-power laser-TIG hybrid welded alloy to mild steel polarisation curves, 85
AZ31B, 178, 180, 186, 211
  EPMA patterns after hybrid overlaps welding, Plate V
AZ91
  corrosion potential and corrosion current density, 81
  different zones microstructure, 82
  laser-arc hybrid welded joint cross-section macrostructure, 80
  laser-TIG hybrid welded alloy polarisation curves, 81
  magnification microstructure, 82

bar coil, 370
bimetallic corrosion, 292
blind riveting, 124–7
  additional terms of connection, 125
  blind rivet with closed rivet body, 126
  body folding blind rivet made of aluminium, 126
  nuts/thread bolts, 126–7
    blind rivet nuts with a closed body, 127
    setting process, 127
  process steps, 125
  unprocessed body folding blind rivet, 124
BMW 5 series, 129
bolt, 132
brazing, 97–117
  compositions and melting temperatures
    commercial brazing filler metals, 107
    low-temperature brazing filler metals, 107
  compositions, hardness, liquidus and brazing temperature
    In-Mg-Zn system filler metals, 108
    Mg-Sn-In-Al system filler metals, 111
  microstructures of brazed layer performed with applying time
    0.5 to 4.0 seconds, 116
    2.0 to 8.0 seconds, 115
    6.0 seconds, 114
  ultrasonic brazing with no flux, 112–17
    apparatus, 113
    applying time and tensile strength, 115
    AZ31B polished surface before and after heating, 117
    bonding process, 116–17
    fracture path in joint brazed, 114
    joining temperatures and tensile strength, 113
    processes schematic, 117
    ultrasonic vibration temperature and applying time effect on brazing, 112–15
  using flux and filler metal, 103–12
    brazeable magnesium alloys compositions and melting temperatures, 106
    $CaCl_2$-LiCl-KCl equilibrium phase diagrams, 105
    filler metal development, 105–12
    flux development, 103–5
    fluxes compositions, 105
    joint broken at base metal after cross-tensile test, 109
    joint broken at base metal and fillet appearance, 112
    magnesium brazing fluxes compositions and operational temperatures, 104
    Mg-In system equilibrium phase diagram, 108
    spread area for fluxes, 106
brazing temperature, 112, 114
buoyancy forces, 256

calcium, 103
carbon dioxide, 318
castings, 20, 21
$CdCl_2$ flux, 261
cerium, 40, 43–4, 48, 60
chemical methods, 149
chromating pre-treatments, 151
chrome conversion coatings, 151
classical hemming process, 146
clinching, 142–5
  alloy AZ31 characteristic joining elements, 145
  joining element characteristics, 144–5
  process steps using a split die, 143
CO_2 laser welding, 311
coarse grains, 11
coefficient of thermal expansion, 65
cold cracks, 13
cold forming screws, 137
columnar dendritic zone, 362
columnar-to-equiaxed transition, 361
compression coil, 370
contact reaction brazing, 38–9
conventional riveting, 130–1
  magnesium connection using aluminium solid rivet, 131
  process steps using solid rivet, 131
conversion coatings, 151
corrosion, 13–14
cutting clinch processes, 143

DC pulsed MIG welding, 186
deep penetration welding, 310–11
degreasing methods, 150
depth-to-width ratio (DWR), 72
diffusion bonding, 44–5

- magnesium to aluminium, 44–9
  - interfacial microstructure, 45
  - joint microstructure, 45–8
  - mechanical properties, 48–9
  - Mg-Al joint with zinc bond region analysis results, 47
  - Mg-Al joints with zinc alloy interlayer, 46
  - welding mechanism, 49
- direct joining techniques, 69–74
- direct screwing
  - with pre-punching and one-sided accessibility, 128–9
    - thread-forming self-tapping screw application, 130
    - thread-forming self-tapping screw processing, 129
  - without pre-punching and one-sided accessibility, 134–7
    - cold-forming screws, 137
    - flow drill screws, 135–7
    - process steps of cold forming screw, 137
- dissimilar metal welding, 38
- drop shot transfer, 191

- electrode negative, 186
- electrode positive, 186
- electromagnetic forces, 256
- electromagnetic induction, 144
- electromagnetic property, 65–6
- electromagnetic welding, 367–77
  - equipments, 369–72
    - capacitor, 371
    - coil types, 370
    - field shapers, 371–2
    - high-voltage power supply, 371
    - high-voltage switch, 371
    - work coil, 369–70
  - fundamental theory, 367–9
  - mechanical and metallurgical testing, 374–5
    - Mg to Al welds shear-tested samples, 374
    - opened weld interface and cross-section XRD spectra, 376
    - shear strength with variation in discharge energy, 374
    - wavy interface and complete metal continuity, 375
  - principle, 368
  - safety guidelines, 377
  - welding technique and materials, 372–3
    - current waveform, 373
    - Mg to Al sheet weld, 373
    - welding set-up, 372
- electromotive force, 368
- electron beam welding, 321
- electron probe microanalysis, 213, 214, 237, Plate I, Plate IV, Plate V
- EPMA *see* electron probe microanalysis
- epoxy adhesive, 211, 222
- epoxy resin sealing treatment, 87–9
- equiaxed dendritic zone, 362
- ER AZ101A filler metal, 23
- ER AZ61A filler metal, 23
- ER AZ92A filler metal, 23
- ER EZ33A filler metal, 23
- European End-of-Life Vehicle Directive, 151
- evaporation, 10–11, 13
- expansion coil, 370
- expulsion, 356

- filler metals, 23, 244
  - development for brazing magnesium alloys, 105–12
  - In-Mg-Zn system, 107–10
    - brazed joints strength, 108
    - compositions, hardness, liquidus and brazing temperature, 108
  - joint crossed section brazed with In-4Zn, 110
  - Mg-Sn-In-Al system, 110–12
    - compositions, hardness, liquidus and brazing temperature, 111
    - strength of brazed joints, 111
  - recommended for arc welding, 24
- filler wire, 169
  - welding, 16
- flanging, 140
  - process steps, 141
  - typical joints, 141
- flat pancake type coil, 370
- flow drill screws, 135–7
  - functional sections and process steps, 136
  - joining process
    - with pre-punching, 136
    - without pre-punching, 137
- focal position, 313
  - mode transition curve
    - determined by laser power and focal position, 317
    - determined by welding speed and focal position, 318
  - relationship with spot size and power density, 317
  - sketch, 315
- friction stir welding, 4, 7, 38, 274–301, 321
  - advantages, 275
  - applications, 300
  - future trends, 301
  - joint configurations, 276
  - parameters and procedures, 276–80
    - effect of welding speed on pore area in stir zone, 279
    - friction stir welds at different welding pressures, 280
    - temperature distributions, 277
    - tilt angle, 279
    - ultimate strength and welding parameters, 278
    - welding and rotation speed, 276–9
    - welding pressure, 280
  - salt spray tested-FSW AZ31 Mg sample
    - macrograph, 293
    - micrograph, 294
  - sample materials, 282
  - schematic drawing, 275
  - tools and equipment, 280–2
    - selection of tools designed at TWI, 281
  - weld defects, 295–300
    - defects at different welding speeds, 297
    - FSW AZ31 Mg typical defects, 296
    - micro-pore fill procedure, 298
    - micro-pore produced during welding, 298
    - void formation, 300

- welded alloy microstructures, 282–8
  - advancing and retreating side microstructures, 287
  - friction stir welded AZ31 alloy macrograph, 282
  - heat-affected zone, 285–6
  - mechanism of microstructure evolution, 288
  - microstructure evolution on weld nugget, 289
  - nugget zone, 283–5
  - onion rings in the weld nugget, 283
  - thermo-mechanically affected zone, 285
  - weld nugget microstructure, 284
  - zone microstructures along TMAZ line, weld nugget and crown, 286
- welded alloys properties, 289–95
  - corrosion properties, 291–4
  - crack cross-section, 291
  - fatigue properties, 291
  - Hall–Petch type relationship, 295
  - other mechanical properties, 294–5
  - tensile fracture location, 290
  - tensile properties, 289–91
  - typical fracture modes, 292

fusion stir welding, 61
fusion zone, 79, 81, 82, 181

galvanic corrosion, 152, 292
gas metal arc welding, 23, 197
gas-tungsten arc filler welding, 160–75
- hardness testing, 175
- mechanical properties, 172–5
- principle, 161
- tensile properties, 172–4
  - geometry size and location, 174
  - specimens fractography, 174
  - specimens properties, 174
- welded joint
  - grain size contrast, 173
  - GTAF and GTA appearance contrast, 171
  - hardness analysis, 175
  - macro-morphology, 171
  - microstructure, 171–2
  - transition zone, 172
- welding parameters, 169–71
  - effect on weld shape, 170–1
  - normative interval, 169
  - wire feed rate effect, 170

gas-tungsten arc welding, 23, 160–75, 197
- *see also* gas-tungsten arc filler welding; gas-tungsten arc welding without filling wire
- GTAF and GTA-welded joints appearance contrast, 171
- welded joint microstructure, 173

gas-tungsten arc welding without filling wire, 161–8
- hardness testing, 167–8
  - hardness distribution, 168
  - weld joints average hardness, 167
- mechanical properties, 165–8
- preparing for welding, 161–2
- tensile properties, 165–7
  - AZ31B size and position, 165
  - heat input and strength relationship, 166
  - specimens properties, 165
  - tensile fractures, 167
- welded joint
  - AZ31B microstructure observation and results, 163
  - heat input, HAZ and grain size relation, 164
  - macrograph, 162
  - macrophotograph under heat input conditions, 162
  - microstructure observation and analysis, 163–5
  - microstructures, 164

GMAW *see* gas metal arc welding
grain bit vector, 288
GTAW *see* gas-tungsten arc welding

Hall–Petch relationship, 295
HAZ *see* heat-affected zone
heat capacity, 65
heat stress, 11–12
heat-affected zone, 79, 81, 82
- friction stir welding, 285–6
- gas-tungsten arc welding, 160
- laser-arc hybrid welding, 231
- metal inert gas welding, 181
- resistance spot welding, 354, 360
- variable polarity plasma arc welding, 205

helium, 316
hemming, 145–7
- magnesium sheet roller hemming, 147
- process steps, 146

hot chromic acid, 151
hot cracks, 11, 179, 332
hot extrusion process, 27–32
- extrusion device, 30
- extrusion steps, 30
- fluxing agent composition, 27
- magnesium alloy ingot
  - after machining, 29
  - extrusion, 29–30
  - preparation, 27–9
- process flowchart, 31
- processing parameter, 31–2

hot pull process, 34–5
- hot pull equipment diagram, 34
- process parameters, 34–5

hybrid lap welding process, 43
hybrid laser-tungsten inert gas welding, 4, 66, 67, 69–70
- magnesium and aluminium, 39–44
  - Ce added joint major elements EPMA image and distribution maps, Plate I
  - configuration, 40
  - direct joint fractography, 44
  - fusion zone microstructure and composition, 42
  - joint interface, 43
  - joint with cerium fractography, 44
  - lap joint microstructures, 41
  - strength of samples with different cerium foil thickness, 40
  - weld pool bottom microstructures, 42

hydrogen, 11, 339–40

intermetallic compound layer (IMC), 68–9, 77
iron, 84

joining *see* specific joining technique
Joule's law, 352

Kapton sheet, 372
keyhole, 309

Langrangian–Eulerian formulation, 299
lanthanum, 6
lap joining method, 66
laser bond welding, 7
laser power, 312
  and heat input on welding mode, 312
  effect on welding seam depth and width, 313
  mode transition curve determined by laser power and focal position, 317
laser weld bonding, 49–50
  magnesium to aluminium, 49–60
    binary equilibrium phase diagram, 53
    different zones in joint, 58
    elements distribution in fusion zone, 54–6
    fracture location with favourable and imperfect infusion, 60
    joint microstructure, 50–60
    joint transverse section, 55
    joints tensile shear strength, 59
    laser welding and LWB joint images and quantitative analysis, 56
    magnesium fusion zone microstructure, 52
    mechanical properties, 56
    Mg-Al interface in fusion zone microstructure, 54
    Mg-$Mg_{17}Al_{12}$ microstructure, 52
    quantitative analysis, 57
    transverse section of joints, 51
    welding mechanism, 59–60
laser welding, 306–47
  absorption of metals
    as function of laser radiation wavelength, 308
    as function of temperature, 308
  AM50 without heating and after heating, 342
  focal position, 313–14
    depth and mode, 316
    relationship with spot size and power density, 317
    sketch of, 315
  influence of parameter combination on weld shape parameter, 316
  magnesium alloys, 318–19
    advantages in welding, 320–2
    physical properties of Mg, Al, Fe, 319
    weldability, 319–20
  microstructure and properties, 322–31
    base metal and welds mechanical properties, 329
    components in selected area in the fracture, 331
    different zones in depth direction of weld, 326
    different zones in width direction of weld, 325
    laser welds microstructure, 323–7
    microhardness distribution, 328–9
    weld centre microstructure, 323
    weld components, 324
    weld fracture shapes, 330
    weld XRD analysis, 324
    white impurities components, 331
    ZE41A-T5 sand casting Mg alloy microstructure, 327
  mode transition curve
    determined by laser power and focal position, 317
    determined by welding speed and focal position, 318
  outlook, 346–7
  porosity, 336–45
    change before and after remelting, 345
    die-cast Mg alloys initial pores final diameters, 340
    large pores formation, 339
    pores characteristic parameters in AM50 base metal, 340
    pores in laser welding seam, 338
    relationship with welding speed, 344
    single-side welding vs double-side welding, 346
    under different power, 343
    under different speed (Jiguo Shan's research), 343
    under different speed (Marya's research), 343
  pressure and temperature changes during hot vacuum pumping, 341
  process character, 307–11
    heat input and laser power on welding mode, 312
    influence of plasma, 311
    laser multiple reflection on keyhole surface, 310
    physical process, 307–11
    various processes in different power density laser radiations, 309
  typical defects, 332–45
    magnesium alloys welding problems, 332
    molten pool collapse, 334–6
    shielding gas optimised flow, 335
    weld surface formation, 337
    welded ZE41A-T5 alloy joint liquation cracking, 333
    welding crack, 332–4
  welding parameters, 311–18
    complex influence of several factors, 314–15
    laser beam character, 311–12
    laser power, 312
    shielding gas, 315–16, 318
    welding speed, 313
  welding seam depth and width
    laser power, 313
    welding speed, 314
  welds mechanical properties, 327–31
    microhardness, 327–9
    tensile strength, 329–31
laser-arc hybrid welding, 321
  application, 250
    autocycle products, 250
    bicycle products, 250
  AZ31B EPMA patterns after hybrid overlaps welding, Plate V

  future trends, 251
  hybrid welding process with filler metal, 244–50
    distance between laser and arc influence on weld formation, 247
    filler wire feeding modes, 245
    fracture scanned photograph, 249
    hybrid welding modes appearances, 245
    joint with back-feeding filler wire microstructure, 249
    tensile strength, 248–50
    weld joints vs back-feeding filler wire, 246
    weld microstructure, 248
    welding defects, 247–8
    welding defects under unsuitable parameters, 248
    welding mode, 245–6
    welding parameters, 246–7
  low-power laser/arc hybrid welding, 230–44
    AZ31 to AZ91 joint microstructure, 237
    AZ31 weld hardness profile, 239
    AZ31, AZ61 and AZ91 alloys microstructure, 236
    AZ31B weld joint macrographs, 241
    AZ61 to AZ31weld hardness profile, 240
    AZ61weld hardness profile, 240
    AZ91 to AZ31weld hardness profile, 241
    AZ91weld hardness profile, 240
    defocusing value effect, 233
    dissimilar welds cross-sections, 232
    distance between laser and arc effect on weld seam formation, 235
    fatigue test results, 239
    hybrid welding joint microstructure, 235
    joints appearance of A131 to AZ31 and AZ31 to AZ91, 231
    mechanical properties, 237–41
    microstructure, 235–7
    optimal hybrid welding parameters, 234
    pore element distribution, 242
    pore formation sketch map, 243
    pores in weld metal using laser coaxial shielding, 243
    pores in weld metal using laser lateral shielding, 244
    porosity, 241–4
    tensile test results, 238
    TIG welded joint microstructure, 236
    weld depths variation, 232
    weld metal, 237
    welded joints macro-sections and appearances, 231
    welded seam morphology, 231
    welding speed effect on weld seam, 234
  magnesium alloys, 229–51
    hybrid laser-tungsten inert gas welding, 230
  welding parameters influence, 232–4
    arc power, 232
    defocusing value, 233
    distance between laser and arc, 234
    welding speed, 233
laser-tungsten inert gas welding, 40, 231
  see also hybrid laser-tungsten inert gas welding
liquation cracking, 333–4
lithium, 103
local thermodynamic equilibrium, 225
lock-ring bolts, 132–3
  processing steps, 133
Lorentz forces, 256, 368, 371–2
LWB *see* laser weld bonding

magnesia, 10
magnesium, 3, 242
  physical and chemical properties of magnesium and steel, 65–6
  physical properties, 10
  welding and joining techniques, 3–7
    alloys to other metals dissimilar welding, 6–7
    efficient gas metal arc welding, 5–6
    welded joints characteristics under dynamic load, 4–5
magnesium alloy welds
  corrosion and protection, 79–93
  corrosion characteristics, 80–4
    corrosion current densities and corrosion potentials, 84
    laser-arc hybrid welded AZ91 magnesium sheet behaviour, 80–3
    magnesium alloy to dissimilar metals joints, 83–4
    soldered joint between magnesium and aluminium, 85
    weld joint corrosion macrostructures, 84
  corrosion resistance improvement, 86–91
    arc spray technology, 86–7
    post-treatment technology of arc spraying, 87–91
magnesium alloys, 3, 79
  activating flux tungsten inert gas welding, 253–72
    future trends, 272
    mechanical properties, 271–2
    welding joints microstructure, 267–71
    welding mechanism, 254–8
    welding parameters, 258–67
  adhesive bonding, 149–58
    adhesives used, 154
    applications, 154
    characteristics, 155–6
    cure for the bonding, 154
    future trends, 158
    surface treatments, 149–53
  brazing and soldering, 97–120
    brazing using flux and filler metal, 103–12
    soldering, 117–20
    ultrasonic brazing with no flux, 112–17
  classification, 322
  dissimilar welding to other metals, 6–7
  efficient gas metal arc welding, 5–6
  electromagnetic welding, 367–77
    equipments, 369–72
    fundamental theory, 367–9
    mechanical and metallurgical testing, 374–5
    safety guidelines, 377
    welding technique and materials, 372–3
  friction stir welding, 274–301
    applications, 300
    future trends, 301
    materials that have been or are being friction stir welded, 282

    - parameters and procedures, 276–80
    - tools and equipment, 280–2
    - typical microstructures, 282–8
    - weld defects, 295–300
    - welded alloys properties, 289–95
  - gas-tungsten arc welding, 160–75
    - principle, 161
    - with filler wire, 168–75
    - without filler wire, 161–8
  - laser welding, 306–47
    - alloys weldability, 318–22
    - microstructure and properties, 322–31
    - outlook, 346–7
    - process character and influence of welding parameters, 307–18
    - typical defects, 332–45
  - laser-arc hybrid welding, 229–51
    - application, 250
    - future trends, 251
    - hybrid welding process with filler metal, 244–50
    - low-power laser/arc hybrid welding, 230–44
  - mechanical joining techniques, 122–47
    - hemming, 145–7
    - with pre-punching and one-sided accessibility, 123–9
    - with pre-punching and two-sided accessibility, 130–3
    - without pre-punching and one-sided accessibility, 133–7
    - without pre-punching and two-sided accessibility, 138–45
  - metal inert gas welding, 178–94
    - alternating current MIG welding, 185–94
    - future trends, 194
    - pulsed MIG welding, 179–85
  - preheating and postweld treatments, 20–2
    - castings, 21
  - preparation for welding, 16–22
  - resistance spot welding, 351–65
    - electrode tip profiles after 40 welds, Plate III
    - equipment, 363–4
    - fundamentals, 351–4
    - future trends, 364–5
    - magnesium alloy welding to other alloys, 362–3
    - nugget growth and microstructure, 359–62
    - surface welding conditions, 354–8
    - welding parameters, 358–9
  - slip systems, 32
  - steel joining techniques, 63–77
    - direct joining, 69–74
    - existing problems, 64–6
    - future trends, 77
    - Mg, Ni and Fe element distribution maps, Plate II
    - nickel-added joining, 74–7
    - welding principle, 66–9
  - surface preparation before joining, 97–103
    - aluminium and magnesium alloys joinability, 98
    - brazing filler metal solidified on surfaces, 102
    - Mg2p photoelectron XPS spectra, 99
    - microphotographs around ultrasonically welded interfaces, 102
    - surface film on magnesium, 97–8
    - surface film on magnesium and aluminium, 98
    - surface film thickness and components, 100
    - surface treatment on ultrasonic welds strength, 101
    - surface treatment to improve joinability, 98–103
    - weld fracture surface, 101
  - surface treatment, 16–18
    - chemical pre-treatment methods, 17
    - pre-treatment methods for wire, 18
    - welding defects, 17
    - wires and weld, 18
  - variable polarity plasma arc weld bonding, 211–26
  - variable polarity plasma arc welding, 199–211
    - process, 198
  - welding and joining with aluminium alloys, 38–61
    - diffusion bonding, 44–9
    - future trends, 60–1
    - hybrid laser-tungsten inert gas welding, 39–44
    - laser weld bonding, 49–60
  - welding groove, 18–20
    - types for repairing welding, 20
    - types for welding, 19
  - welding materials, 23–36
    - component design, 32–3
    - hot extrusion process, 27–32
    - hot pull process, 34–5
    - microstructure and strength, 35–6
  - welding metallurgy, 9–14
    - other metals, 12–14
    - relative weldabilities with common grades, 12
    - weldability, 10–12
  - welding problems, 332
- magnesium chloride, 27
- magnesium oxide, 11
- manganese coating conversion, 151
- MAO *see* micro-arc oxidation
- Marangoni effect, 256, 265, 270
- mechanical joining techniques, 122–47
  - hemming, 145–7
    - magnesium sheet roller hemming, 147
    - roller hemming and bonding procedure, 146
  - pre-punching and one-sided accessibility, 123–9
    - blind rivet nuts/thread bolts, 126–7
    - blind riveting, 124–6
    - direct screwing, 128–9
    - functional element Rivkle Elastic, 127–8
  - pre-punching and two-sided accessibility, 130–3
    - conventional riveting, 130–1
    - lock-ring bolts, 132–3
    - screw nut joint, 132
  - punctual joining techniques classification, 123
  - without pre-punching and one-sided accessibility, 133–7

    - direct screwing, 134–7
    - tac setting, 133–4
  - without pre-punching and two-sided accessibility, 138–45
    - clinching, 142–5
    - flanging, 140
    - self-piercing riveting with semi-tubular rivet, 138–40
    - self-piercing riveting with solid rivet, 141–2
- melting point, 64–5
- metal inert gas welding, 178–94
  - alternating current MIG welding, 185–94
    - arc and weld appearance, 190
    - arc morphological change, 187
    - base metal and weld beads microstructure, 193
    - butt and lap joint appearances, 191
    - butt joints weld appearance, 192
    - designed current waveform, 186
    - metal transfer arc, 188
    - parameters plates with different thickness, 191
    - parameters range for metal transfers, 190
    - weld beads appearance, 189
    - weld beads macrostructures, 193
    - wire speed parameters, 192
  - future trends, 194
  - pulsed MIG welding, 179–85
    - base metal and weld beads microstructures, 183
    - drop detachment, 184
    - force on the drop from the detached wire, 185
    - pulse frequency effect on joint formation, 182
    - spatters and hot cracking, 180
    - weld appearances, 182
    - weld beads microstructures, 184
    - weld width and pulse rework current, 180
    - welding speed effect on joint formation, 181
- metal inner gas welding, 5
- $Mg(OH)_2$ coating, 151
- micro-arc oxidation treatment, 90–1
- MIG *see* metal inert gas welding
- momentum theory, 299

- nickel-added joining techniques, 74–7
- nitric acid cleaning, 356
- nitrogen, 316, 318
- non-chrome conversion coatings, 151
- non-cutting round clinch processes, 143
- nugget
  - friction stir welding, 283–5
  - resistance spot welding, 359–62

- oxidation, 10–11, 13
- oxide films, 292
- oxidisability, 66

- PAW *see* plasma arc welding
- Pilling–Bedworth ratio, 97
- plasma arc welding, 197
- polypropylene sheet, 154
- pores, 11
- porosity, 241–4, 336–45
- porosity ratio, 343
- pulse current, 185
- pulse tungsten inert gas welding, 11
- pulsed MIG welding, 179–85
- pulsed rework current, 180, 187

- recrystallised, 283
- resistance spot welding, 351–65
  - electrode tip profiles after 40 welds, Plate III
  - equipment, 363–4
  - fundamentals, 351–4
    - dynamic resistance, 353
    - general principles, 351–3
    - involved resistances, 352
    - weld nugget microstructure, 353–4
  - future trends, 364–5
  - magnesium alloy welding to other alloys, 362–3
    - Mg/steel spot weld cross-section, 363
  - nugget growth and microstructure, 359–62
    - AZ31-SA with micro-scale Al_8Mn_5, 361
    - AZ31-SB with micro- and nano-scale Al_8Mn_5, 361
  - surface welding conditions, 354–8
    - contact resistance of different surface conditions, 355
    - electrode tip faces surface profiles, Plate III
    - fracture surface, 357
    - weld strength vs nugget size, 356
  - welding parameters, 358–9
    - process window, 360
- Rivkle Elastic
  - functional element, 127–8
    - connection, 128
    - unprocessed and processed state, 128
- roll-hemming process, 146
- rolling deformation, 166

- screw nut joint, 132
- screws *see* specific screw
- self-locking, 132
- self-piercing riveting
  - semi-tubular rivet, 138–40
    - AZ31 monotype joint, 140
    - joining process with increasing setting speed, 140
    - joint set at room temperature, 139
    - terms and process steps, 138
  - solid rivet, 141–2
    - joining element characteristic, 143
    - process steps, 142
- shear strength tests, 46, 48
- skin depth, 369
- soldering, 117–20
  - AZ31/AZ31 joint interfaces, 119
  - new solders compositions and melting temperatures, 119
  - soldered joints tensile strength, 119
  - solders for magnesium, 118
- solenoid coils, 370
- solidification cracking, 332
- solubility, 66
- spot spacing, 359
- steel joining techniques, 63–77
  - direct joining, 69–74
    - defocus on joint strength, 70–2

    - defocusing amount on weld bead strength and width, 71
    - direct joint microstructures, 73
    - laser power on joint strength, 69–70
    - laser power on weld bead strength, 70
    - mechanical properties, 74
    - microstructure characteristics, 73–4
    - sample in tensile shear test, 74
    - tungsten inert gas current on joint strength, 72–3
    - welding current on weld bead strength, 72
    - welding speed on joint strength, 70
    - welding speed on top weld width and weld bead strength, 71
  - existing problems, 64–6
  - future trends, 77
  - Mg, Ni and Fe element distribution maps, Plate II
  - nickel-added joining, 74–7
    - interface between magnesium alloy and nickel interface, 76
    - joint with nickel interlayer microstructure, 75
    - microstructure characteristics, 74–6
    - microstructure SEM images, 75
    - nickel distribution, 76
    - shear test results, 77
    - welded joint properties, 76–7
    - welding procedure, 74
  - physical and chemical properties of magnesium and steel, 65–6
  - welding principle, 66–9
    - direct joining principle, 67–8
    - interfacial microstructure, 68
    - joint cross-section, 68
    - Mg-Ni-Fe joint, 69
    - principle of interlayer into lap joint, 68–9
    - test specimens, 67
    - welding method, 66–7
- superplastic deformation, 288
- surface tension, 267
- surface treatment
  - magnesium alloys to improve joinability, 98–103
    - surface film thickness and components, 100
    - surface treatment and ultrasonic weldability, 100–2
    - surface treatment and wettability in brazing, 102–3
    - x-ray photoelectron spectroscopy analysis on treated surface, 99

- tabletop hemming, 146
- tac setting, 133–4
  - connection and process steps, 134
  - joining element characteristic, 135
- target depth, 280
- thermal conductivity, 9, 65
- thermal spray technology, 93
- thermo-mechanically affected zone, 279, 285
- thread-forming self-tapping screws, 128–9
- TIG *see* tungsten inert gas
- tin coating conversion, 151
- TiO_2 flux, 260, 261
- transition layer, 68–9
- trichloroethylene, 150
- tungsten inert gas, 230
- tungsten inert gas current, 72–3
- tungsten-arc inert gas welding, 160

- vacuum diffusion bonding, 39
  - *see also* diffusion bonding
- variable polarity plasma arc weld bonding
  - arc behaviour observation, 224–6
    - ACEN stage ionisation atmosphere, 225
    - argon and CO_2 physical properties, 226
    - VP-PAW and VP-PAWB process, 224
  - keyhole mode process investigation, 211–13
    - weld bead surfaces, 212
  - magnesium alloys, 211–26
    - elements distribution measurement, 222–3
    - transverse section EPMA analyses, Plate IV
  - mechanical property measure, 223–4
    - tensile shearing test results, 223
  - pores behaviour investigation, 213–19
    - cross-section with different flow rates of plasma gas, 215
    - EPMA analysis, 214
    - joint cross-section, 213
    - joint porosity, 213–14
    - molten width change with different welding currents, 216
    - molten width change with different welding speeds, 217
    - plasma gas flow rate, 214–15
    - pores total area and heat input relationship, 218
    - remedy for eliminating pores, 217–19
    - welding current, 215–16
    - welding joint cross-section by optimal welding parameters, 219
    - welding parameters effect, 214
    - welding speed, 216–17
  - welding joint morphology and microstructure, 219–22
    - VP-PAW vs VP-PAWB transverse section, 221
    - weld pool shape, 221
    - welding seam morphology, 220
- variable polarity plasma arc welding, 197–227
  - alternating current electrode negative time to cycle ratio, 199–202
    - magnesium alloy butt welding, 200
    - tungsten melting loss comparison, 201
    - variable polarity current waveform, 199
    - welding joints failure loads, 201
  - catelectrode clean effect on welding joint mechanical property, 204–6
    - variations effect on joint dimension and strength, 205
  - magnesium alloy with lap joint, 206–11
    - alloy weld pool shape, 210
    - AZ31B weld microstructure, 210
    - hardness distribution in joint, 209
    - magnesium alloy welding appearance, 206
    - schematic diagram, 207
    - tensile test results, 207
    - test specimens, 208
    - welding characters, 206–7
    - welding joints mechanical properties, 207–8

    - welding joints microstructure, 209–11
  - magnesium alloys, 199–211
    - AZ31 alloy plasma arc welding appearance, 199
    - process, 198
  - welding parameters effect on welding process, 202–4
    - nozzle structure, 203
    - processing parameter on AZ31B alloy, 202
    - welding currents and speeds effect on welding width, 203–4
- VP-PAW *see* variable polarity plasma arc welding
- VP-PAWB *see* variable polarity plasma arc weld bonding

- waterborne grit blasting, 150
- weight loss method, 33
- welding
  - *see also* specific type of welding
  - magnesium alloys preparation, 16–22
    - preheating and postweld treatments, 20–2
    - surface treatment, 16–18
    - welding groove, 18–20
  - magnesium alloys to aluminium alloys, 38–61
    - diffusion bonding, 44–9
    - future trends, 60–1
    - hybrid laser-tungsten inert gas welding, 39–44
    - laser weld bonding, 49–60
    - main problem, 39
- welding defects, 10–12, 17
- welding groove, 18–20
- welding materials
  - component design, 32–3
    - boiling point of Mg-Zn with different composition, 33
  - hot extrusion process, 27–32
    - extruding process flowchart, 31
    - extrusion device, 30
    - extrusion steps, 30
    - fluxing agent composition, 27
    - magnesium alloy ingot after machining, 29
    - magnesium alloy ingot extrusion, 29–30
    - magnesium alloy ingot preparation, 27–9
    - processing parameter, 31–2
  - hot pull process, 34–5
    - hot pull equipment diagram, 34
    - process parameters, 34–5
  - magnesium alloys, 23–36
    - filler metals for arc welding, 24
    - melting flow process chart, 29
    - slip systems, 32
    - welding wire composition, 24
    - welding wire selection, 26
  - microstructure and strength, 35–6
    - magnesium alloy welding wire microstructure, 35
    - welding wire ultimate tensile strength and elongation, 35
- welding metallurgy
  - magnesium alloys, 9–14
    - magnesium, aluminium and iron physical properties, 10
    - relative weldabilities with common grades, 12
    - weldability, 10–12
    - weldability to other metals, 12–14
- welding wire
  - composition, 24
  - microstructure, 35
  - selection, 26
  - ultimate tensile strength and elongation, 36
- Whorl and MX-Triflute, 281

- zinc, 45, 49, 60